JP Journal of Heat and Mass Transfer

http://www.pphmj.com
http://dx.doi.org/10.17654/HM022020201
Volume 22, Number 2, 2021, Pages 201-216 **ISSN: 0973-5763**

DUSTY GAS FLOW OVER A SEMI-INFINITE VERTICAL CONE

G. Palani* and E. J. Lalith Kumar

Department of Mathematics
Dr. Ambedkar Government Arts College
Chennai 600 039, Tamil Nadu, India
e-mail: gpalani32@yahoo.co.in

Department of Mathematics
SRM Arts and Science College
Kattankulathur, Chengalpet District - 603 203
Tamil Nadu, India

Abstract

This work is focused on 2-D unstable convective dusty gas flow over a semi-infinite plumb (vertical) cone. The ruling PDE's are solved numerically using a finite difference algorithm. Our current numerical outcomes are compared with the available published paper and it is concluded that they are in an outstanding agreement with each other. Mathematical results are presented in favor of transient dusty gas momentum, dust particles velocity, temperature contour, local as well as average skin friction. Nusselt number on selected values of dust mass concentration and dust parameters are presented graphically and discussed briefly. This is done in order to make clear the influence of the various parameters involved in the problem.

Received: October 23, 2020; Accepted: December 10, 2020
Keywords and phrases: apex, dusty gas, finite difference, shearing stress, vertical cone.
*Corresponding author

sciendo

Int. J. of Applied Mechanics and Engineering, 2021, vol.26, No.1, pp.215-225
DOI: 10.2478/ijame-2021-0013

EFFECTS OF PRESSURE WORK OVER A SEMI-INFINITE VERTICAL OSCILLATING CYLINDER

A.SAROJINI and G.PALANI*
PG & Research Department of Mathematics, Dr. Ambedkar Govt. Arts College
Chennai 600 039, Tamil Nadu, INDIA
E-mail: gpalani32@yahoo.co.in

An arithmetical methodology is used to study natural convection with properties of pressure work over a semi-infinite vertical oscillating cylinder. The governing partial differential equations are set up and the resulting equations are changed into a non-dimensional form using the proper non-dimensional quantities. The set of non-dimensional partial differential equations is solved arithmetically using a well-organized method known as the Crank-Nicolson method. The velocity, as well as temperature profiles for different values of parameters are studied with the assistance of graphs.

Key words: cylinder, finite difference, pressure work, oscillating, skin friction.

1. Introduction

Heat transfer by free convection frequently occurs in our environment and is used in engineering devices. Two dimensional free convection flows past a semi-infinite vertical oscillating cylinder have received the attention of many researchers because of their extensive application in industry and engineering fields.

Dring and Gebhart [1] analysed the transient natural convection in association with the thin wires in liquids. In their study, the quasi static solution predictions are given only for transients in air. Velusamy and Garg [2] obtained the numerical solution for the transient natural convection adjacent to heat generating, vertical cylindrical fuel rods with constant surface heat flux. In particular, they paid special attention the rate of propagation of the leading edge. Lee *et al.* [3] considered the natural convection along a slender vertical cylinder with varying surface temperature. The solution of steady governing equations was achieved through a spline interpolation system. Collins and Dennis [4] considered a numerical calculation of the system of development in the powers of time for an impulsively started circular cylinder by a numerical integration technique. The acquired outcomes agree very well with earlier numerical as well as experimental work. Collins and Dennis [5] studied a symmetrical flow along over a uniformly accelerated circular cylinder.

Alam *et al*. [6] studied the convective flow over a permeable cone with variable surface temperature with pressure work term. The non-similarity solution is found for the governing equations of the flow. Rashad [7] discussed the effect of thermal radiation and pressure stress work on free convective flows of a Newtonian fluid-saturated porous medium. Elbashbeshy *et al*. [8] analyzed pressure work and heat generation along a cone with variable surface heat flux. The equations were analysed and numerical results were presented for the local skin friction and Nusselt number.

Alam *et al*. [9] considered the Joule heating, heat conduction and stress work on convective flow over a vertical plate. They found a similarity solution of the problem, the developed equations were made dimensionless using suitable transformations. Asma Begum *et al*. [10] focused on natural convective flow past an inclined plate with pressure effect. The boundary layer equations were solved approximately by means of the Nachtsheim-Swigert shooting technique along with Runge-Kutta method of sixth order. They consider two cases of motion of the flow, one with impulsive force and the other one was the uniformly accelerated motion.

* To whom correspondence should be addressed

Solid State Technology
Volume: 63 Issue: 5
Publication Year: 2020

Effects of Mass Transfer on Varying Viscosity and Thermal Diffusivity over a Vertical Plate with Applied Magnetic Field and Heat Flux

M. Radhakrishnan [1], G. Palani [2]
[1] Department of Mathematics, Sri Venkateswara College of Engineering, Sriperumbudur 602117, Tamil Nadu, India
[2] Department of Mathematics, Dr. Ambedkar Govt. Arts College, Chennai 600039, Tamil Nadu, India
[1]*mrk@svce.ac.in*, [2] *gpalani32@yahoo.co.in*

***Abstract*—** The existing exploration deals with the impact of heat as well as mass transfer over a vertical plate with changing viscosity besides thermal diffusivity under the impact of magnetic induction. We deliberate two dimensional laminar unsteady boundary layer equations. The appearance of dimensional structure of equations is converted into dimensionless format. These equations are solved numerically by well-organized finite difference scheme (implicit). Calculated outcomes are attained and offered through graphs.

Keywords- *Heat flux, Vertical plate, Variable viscosity, Finite differences, Nusselt number.*

I. INTRODUCTION

In the natural environment, not only by differences in temperature, concentration differences are also generated currents. Transfer of heat as well mass is the drought of pond water in the air owing over it. There are some situations where transfer of mass is very significant and transfer of heat is not important; But in the other scenario, together is equally important and, just like the temperature gradient in heat transfer, the absorption gradient serves as a motivating force in mass transfer. Transfer of heat along with mass on natural convective flow on a plumb plate is discussed by Gebhart and Pera [1]with varying diffusion in addition to the different external temperatures. Callahan and Marner [2] explored convection(free) motion above a plumb plate with constant wall temperature also mass transfer by applying explicit finite difference scheme. Soundalgekar and Ganesan [3] obtained a solution for a free convective motion with transfer of mass on a plumb plate by an implicit method. Elbashbeshy [4] considered the integrated buoyancy impacts of thermal and species diffusion with magnetic induction. Ganesan and Palani [5] studied free convection MHD motion on a semi-infinitely slant plate with heat and mass flux by an implicit scheme. Abbas and Palani [6] obtained the approximate result of the effects of magnetic hydrodynamic on a plumb plate with varying surface temperatures. The pertinent equations are changed to dimensionless form, which are solved by finite element method.

Previous studies have all linked to a fluid with stable properties. The key to the theory of lubrication fluids, the heat created by internal friction as well as temperature growth affects the thermal conductivity and viscosity is no longer considered to be stable. The physical liquid properties, for instance thermal conductivity as well as viscosity may be substantial with temperature proposed by Schlichting [7]. The problem of temperature-associated property is quite complex by the fact that many liquid properties make differently with temperature. Kays and Crawford [8] offered some associations between the physical liquid characteristics with temperature. Ockendon and Ockendon [9] provided the analysis of the Newtonian fluid

Some aspects on cubic fuzzy $\beta-$subalgebra of $\beta-$algebra

P Muralikrishna[1], R Vinodkumar[2] and G Palani[3]

[1]PG & Research Department of Mathematics,Muthurangam Govt. Arts College(Autonomous), Vellore - 612 001,Tamilnadu, India.
[2]Department of Mathematics, Prathyusha Engineering College, Aranvoyalkuppam, Thiruvallur-602 025, Tamilnadu, India.
[3]Department of Mathematics, Dr. Ambedkar Government Arts College, Chennai-600 039,Tamilnadu, India.

E-mail: pmkrishna@rocketmail.com

Abstract. The theory of fuzzy set was introduced by Zadeh and he has shown meaningful applications of this notion in many fields of Engineering and Mathematical studies. Later Atanosov extended the fuzzy set into Intuitionistic fuzzy set by introducing a non-member. Recently the idea of cubic sets and related properties are investigated by Jun et al. All these fuzzy concepts were applied in various algebraic structures. Neggers and Kim presented the thought of $\beta-$algebras in which two operations are coupled in such a way that as to reflect the natural coupling which exists between the usual group operation. This study is to propose a new approach on a $\beta-$algebra using Cubic fuzzy set.
Keywords: $\beta-$algebra, $\beta-$subalgebra, fuzzy set, Cubic fuzzy set, Cubic fuzzy $\beta-$subalgebra

1. Introduction

In the presentation of Zadeh's [12] fuzzy sets, there have been various speculations of this crucial idea. Zadeh [13] likewise the author presented the idea of interval valued fuzzy subsets where the estimations of the membership functions are intervals of numbers rather than the numbers. The notion of Intuitionistic fuzzy sets were explored by Atanassov [3] in 1986. The study of fuzzy subgroups with interval valued membership functions has been initiated by Biswas et al. [4] in 1994. The thought of $\beta-$algebra was started by Neggers et al. [8]. Renugha et al. [9] proposed the concept of Cubic BF-algebra in 2014. In 2013, Aub Ayub Ansari et al. [1] proposed the concept of fuzzy $\beta-$subalgebras of $\beta-$algebra. Hemavathi et al.[5,6] discussed the concept of interval valued fuzzy $\beta-$subalgebras and also they have extended the concept of interval valued intuitionistic fuzzy $\beta-$subalgebras with interesting results. Sujatha et al.[10] depicted the thought of intuitionistic fuzzy $\beta-$subalgebras of $\beta-$algebras. In 2012, Jun et al. [7] presented cubic sets, and then this notion is applied to many algebraic structures. Akram et al.[2] proposed the concept of Cubic KU-subalgebras and provided useful results.Young Bae Jun et al.[11] applied Cubic interval valued intuitionistic fuzzy sets into BCK/BCI algebras. With all these inspiration, this paper intends to study about the cubic fuzzy $\beta-$subalgebra.
The paper is classified into the following sections:

Section 1 shows the introduction, section 2 gives some basic definitions and properties of $\beta-$algebra, cubic fuzzy set and so on, Section 3 deals the concept and operations of cubic fuzzy

ADV MATH SCI JOURNAL
Advances in Mathematics: Scientific Journal **9** (2020), no.3, 1359–1365
ISSN: 1857-8365 (printed); 1857-8438 (electronic)
https://doi.org/10.37418/amsj.9.3.82 Spec. Issue on ICNTMMA

APPLICATIONS OF CUBIC LEVEL SET ON β-SUBALGEBRAS

P. MURALIKRISHNA[1], B. DAVVAZ, R. VINODKUMAR, AND G. PALANI

ABSTRACT. In this paper, the notion of cubic level set on fuzzy $\beta-$subalgebras has introduced and investigated few of its related outcomes.

1. INTRODUCTION

Neggers et al. [3] initiated the notion of $\beta-$algebra where two operations are coupled in such a way to reflect the natural coupling, which exists between the usual group operation and its associated B-algebra. The concept of fuzzy sets has been originated by Zadeh [7], which created a pathway for many researchers. Using a fuzzy set and interval valued fuzzy set, Jun et al. [4] introduced the concept of cubic sets in which the fascinating results have studied. In [6], Vijayabalaji et al. proposed the concept of cubic set theoretical approach to linear space. The thought of interval valued intuitionistic fuzzy $\beta-$subalgebras presented by Hemavathi et al. [1,2] and the level sets has extended in interval valued fuzzy $\beta-$subalgebra. Recently, Muralikrishna et al. [5] investigated the properties of cubic fuzzy β-subalgebras. This paper deals with the cubic level sets on $\beta-$subalgebra and its associated properties.

[1]*corresponding author*

2010 *Mathematics Subject Classification.* 06F35, 03G25, 08A72, 03E72.

Key words and phrases. $\beta-$algebra, Level set, Cubic set, Cubic level set.

ISSN No:-2456-2165

Exact Solutions for Couple Stress Fluid with Slip Boundary Conditions in Porous Plane-Poiseuille Flow

G. Palani[1] and Santhana Krishnan Narayanan[2]
[1] PG and Research Department of Mathematics, Dr. Ambedkar Government Arts College, Chennai-600039, India
[2] PG and Research Department of Computer Science, Dr. Ambedkar Government Arts College, Chennai-600039, India

Abstract:- In this paper, an exact solution of plane-poiseuille flow of a couple stress fluid with slip boundary conditions between porous parallel plates are obtained. The solution for the liming case as $a \to 0$ or $b \to \infty$ for Newtonian flow in the absenteeism of couple stresses are obtained and compared with viscous Newtonian fluid. It is found that the occurrence of couple stresses has a reducing impact on the velocity of fluid and the volume flow rate.

I. INTRODUCTION

Stokes [1] offered the principle of couple stress fluids and has attracted the attention of many researchers in fluid mechanics. The [2,3] adequately explains the flow behavior of fluids containing a substance such as lubricants with animal blood, liquid crystals and polymer additives. Navier [4] proposed a general boundary condition that presents the possibility of slip at the solid boundary. Neto *et al*. [5] gives an analysis of experimental studies concerning the slip of Newtonian fluids at solid interface. Svetlana *et al*. [6] invented that the Poiseuille flow is one of the creeping flow with numerous applications in polymer processing such as blow molding, extraction and die flow. Sundarammal *et al*.[7] studied about MHD squeeze film features among finite porous parallel rectangular plates with surface roughness. Santhana Krishnan Narayanan *et al*. [8] invented about Squeeze film behavior in porous transversely circular stepped plates with a couple stress fluid. Ellahi *et al*. [9] and Devakar *et al*. [10] invented the precise answers for three fundamental flows namely, Couette, Poiseuille and generalized Couette flow with nonlinear slip conditions. Ferras *et al*. [11] acquired analytical solutions in Couette and Poiseuille flows for both Newtonian and inelastic non-Newtonian with slip boundary conditions. This motivates us to produce exact solutions of plane poiseuille flow of couple stress fluid between parallel porous plates with slip boundary conditions.

II. CONSTRUCTION OF THE PROBLEM

Consider a unidirectional steady flow of the incompressible couple stress fluid in between two infinitely long horizontal parallel porous plates $y = \bar{} h$ and $y = h$ as shown in Figure 1. Both the upper and lower plates are porous faced with uniform thickness which are placed at rest.

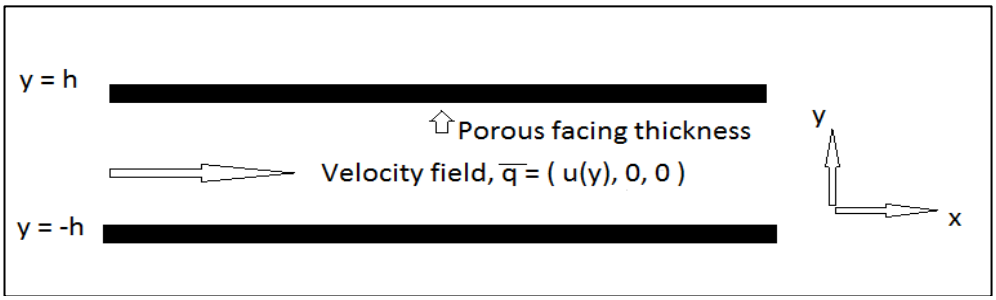

Fig 1:- Flow Configuration of the Plane-Poiseuille flow of couple stress fluid

The flow is due to the constant pressure gradient G in the positive x-direction with velocity field $\bar{q} = (u(y), 0, 0)$. In the porous medium, Darcy law

$$\bar{q}^{*} = (0,0,h) - \frac{\varphi(x,y,z)}{\eta}.\nabla\left(p_1 + p^{*}\right)$$

Where h film thickness, φ permeability, η couple stress viscosity coefficient, p_1 pressure in the porous matrix, p^{*} is the pressure in the film region and pressure $p = p_1 + p^{*}$.

The governing equation of an incompressible couple stress fluid in the absence of body forces is given by [10],

$$\eta\frac{d^4u}{dy^4} - \mu\frac{d^2u}{dy^2} + \frac{dp}{dx} = 0$$

where p is the fluid pressure at any point, μ viscosity material constant and η couple stress viscosity coefficient. The slip boundary condition is

$$u(h) = \beta\left[\frac{du}{dy} - \frac{\eta}{\mu}\frac{d^3u}{dy^3}\right] \quad \text{at } y = -h$$

ISSN No:-2456-2165

Thermal Radiation, Heat Generation and Soret Effects on Vertical Oscillating Cylinder

G. Palani* and A. Sarojini
Department of Mathematics, Dr. Ambedkar Govt, Arts College
Chennai 600 039, Tamil Nadu, India

Abstract:- An arithmetical methodology is castoff towards study the natural convection with properties of thermal radiation, heat generation and Soret effects on a vertical oscillating cylinder. The governing equations are set up and the resulting equations are changed into a non-dimensional form using the proper non-dimensional quantities. The set of non-dimensional partial differential equations are solved arithmetically using a well-organized method known as Crank-Nicolson method. The velocity, as well as temperature profiles and concentration profiles for different values of parameters taking place into the problem are studied with the assistance of graphs.

Keywords:- *Cylinder, Finite Difference, Heat Generation, Oscillating, Soret Effects.*

I. INTRODUCTION

Convective heat transference stands as one of the most important categories of heat transference and likewise convection is a major kind of mass transference in liquids. Joint hotness as well as mass transference procedure in normal convection captivating the consideration of number of investigators owing to their uses in several twigs of science and engineering. The marvel of natural convective ascends in the liquid what time heat vicissitudes which reason density difference leading to resistance force performing on the liquid elements. This know how to be seen in our routine life in the atmospheric flow which is caused by temperature changes. There are several transportation procedures occurring in environment owed to heat and species concentration changes.

Chen and Yuh [1] studied the steady heat and mass transfer process near cylinders with uniform wall heat and mass fluxes, and wall temperature numerically. Ganesan and Rani [2] premeditated unstable convective movement along a straight up cylinder with collective resistance force effects. Finite-difference process is hired to solve the principal equations approximately. An arithmetical analysis for hotness and concentration driven fleeting free convective nearby a straight up drum was carried out by Rani [3]. The level of temperature and concentration at the cylinder shallow are supposed to fluctuate with exponents n and m correspondingly in the stream wise coordinate. Approximate outcomes are achieved and exposed with numerous power law changes, thermal as well as mass Grashof numbers. Ganesan and Loganathan [4] inspected transitory natural convective movement of an incompressible liquid along a moving straight up cylinder. They presumed that the heat in addition to absorption of the cylinder exterior remained unvarying. Transitory impact of velocity, temperature as well as concentration sketches are revealed through the assistance of charts.

Heat generation is the energy transported as a result of a divergence in temperature. Heat absorption is the transfer of heat that happens between two bodies, it may occur through by three modes of heat transfer. It is an endothermic reaction so a cooler object absorbs the heat of hotter object. Heat generation/absorptions may be important in weak electrically conducting polymeric liquids due to no change taking place at constant temperature situation and also because of cation and anion salts dissolved in them.

Several procedures in novel engineering regions befall by high temperatures as well as familiarity of radiative heat transference also the convective warmth transference develops an essential for the design of the appropriate paraphernalia. Atomic power plants, fume turbines as well as the numerous driving force devices used for air crafts, arms, satellite broadcasting and interplanetary vehicles are instances of such engineering regions. Furthermore, radiative warmth transference taking place in the liquid intricate know how to be electrically conducting namely ionized owing to extraordinary operative temperature.

Mahfooz *et al*. [5] scrutinized the radiative effects on a transient convective current of optically dense and viscid electrically conducting liquid along a flat surface with heat generation. Sanatan Das *et al* [6] deliberated things of radiations and heat generation on MHD couette movements started exponentially with non-constant wall temperature. Analytical solutions were obtained for the flow problem. Chamkha *et al* [7] tested numerically effects of chemical reaction, Joule-Heating, and thermal emission on MHD unstable natural convective from a porous plate in a micropolar liquid.

The warmth production impact on normal convective movements as well as transmission inside a plumb level plate remains examined. The established controlling equations through the linked boundary environments are rehabilitated to non-dimension forms by means of a local non-similar conversion premeditated by Mamun *et al* [8]. Alam *et al* [9] deliberated numerically for joint free-forced convection and mass transference movement along a plumb permeable level plate, in existence of warmth generation as well as thermal diffusion. Zueco and Ahamed [10] inspected a precise as well as approximate answers of a

Applied Mathematics and Computation 372 (2020) 124963

Contents lists available at ScienceDirect

Applied Mathematics and Computation

journal homepage: www.elsevier.com/locate/amc

Oscillation criteria for advanced difference equations of second order

E. Chandrasekaran[a], George E. Chatzarakis[b,*], G. Palani[c], E. Thandapani[d]

[a] Department of Mathematics, Vel Tech Rangarajan Dr.Sagunthala, R and D Institute of Science and Technology, Chennai 600062, India
[b] Department of Electrical and Electronic Engineering Educators, School of Pedagogical and Technological Education, 14121, N.Heraklio, Athens, Greece
[c] Department of Mathematics, Dr.Ambedkar Government College, Chennai 600039, India
[d] Ramanujan Institute For Advanced Study in Mathematics University of Madras, Chennai 600005, India

ARTICLE INFO

Article history:
Received 28 August 2019
Revised 27 November 2019
Accepted 8 December 2019

MSC:
39A10

Keywords:
Oscillation
Second order difference equation
Advanced argument

ABSTRACT

This paper involves a new improved method for establishing the oscillation of second order advanced difference equation of the form

$$\Delta(a(\ell)\Delta\upsilon(\ell)) + p(\ell)\upsilon(\sigma(\ell)) = 0$$

using the difference equation

$$\Delta(a(\ell)\Delta\upsilon(\ell)) + q(\ell)\upsilon(\ell+1) = 0.$$

The results that we obtain are new and improve the existing criteria. We illustrate the results by various examples, at the end of the paper.

1. Introduction

In this paper, we study the second order advanced difference equation

$$\Delta(a(\ell)\Delta\upsilon(\ell)) + p(\ell)\upsilon(\sigma(\ell)) = 0, \ \ \ell \geq \ell_0, \tag{1.1}$$

where $\ell \in \mathbb{N}(\ell_0) = \{\ell_0, \ell_0+1, \ell_0+2, \ldots\}$, ℓ_0 is a nonnegative integer, and

(H_1) $\{a(\ell)\}$ and $\{p(\ell)\}$ are positive real sequences with $a(\ell) \geq 1$ for $\ell \geq \ell_0$;
(H_2) $\{\sigma(\ell)\}$ is a monotone increasing sequence of integers with $\sigma(\ell) \geq \ell+1$ for $\ell \geq \ell_0$;
(H_3) $\mathcal{H}(\ell) = \sum_{s=\ell_0}^{\ell-1} \frac{1}{a(s)} \to \infty$ as $\ell \to \infty$.

By a solution of (1.1), we mean a nontrivial sequence $\{\upsilon(\ell)\}$ that satisfies (1.1) for all $\ell \geq \ell_0$. A solution $\{\upsilon(\ell)\}$ of (1.1) is called *oscillatory* if it is neither eventually negative nor eventually positive, otherwise, it is called *nonoscillatory*. Eq. (1.1) is called oscillatory if all its solutions are oscillatory.

Recently, several criteria have appeared in the literature, on the oscillation of (1.1) for the delay case, that is, $\sigma(\ell) \leq \ell - 1$ and $\lim_{\ell\to\infty} \sigma(\ell) = \infty$. On the majority, these studies use the comparison method, which is considered the most plausible

* Corresponding author.
E-mail addresses: gea.xatz@aspete.gr, geaxatz@otenet.gr (G.E. Chatzarakis).

https://doi.org/10.1016/j.amc.2019.124963
0096-3003/

Journal of Superconductivity and Novel Magnetism (2021) 34:971–980
https://doi.org/10.1007/s10948-020-05777-8

ORIGINAL PAPER

Effect of Sr^{2+} Ion–Substituted Nickel Ferrite Nanoparticles Prepared by a Simple Microwave Combustion Method

M. Vanitha[1,2] · G. Ramachandran[2] · A. Manikandan[3] · Y. Slimani[4] · M. A. Almessiere[4] · A. Baykal[5] · Chandra Sekhar Dash[6]

Received: 27 October 2020 / Accepted: 5 December 2020 / Published online: 21 January 2021

Abstract

Microwave combustion technique (MCT) was used to synthesize of spinel $Ni_{1-x}Sr_xFe_2O_4$ ($x = 0.0$, 0.1, 0.3 and 0.5) nanoparticles (NPs) by employing the fuel L-arginine. The physical characteristics of the as-prepared NPs were obtained by following methods, viz., powder X-ray diffraction (XRD), high-resolution scanning electron microscope (HR-SEM), energy-dispersive X-ray (EDX), UV-visible diffuse reflectance spectra (UV-Vis DRS), Fourier-transform infrared spectra (FT-IR), and vibrating sample magnetometer (VSM) techniques. The diffraction studies revealed that the average crystallite size exists in the band of 14.25 to 27.52 nm. The HR-SEM pictures revealed the agglomerated and spherical morphology of spinel $Ni_{1-x}Sr_xFe_2O_4$ ($x = 0$ to 0.5) nanoparticles. Elemental analysis ensured the existence of Ni, Sr, O, and Fe ions. The energy band gap of the NPs was observed to exist in the range of 2.95 to 3.39 eV upon varying the concentration of Sr^{2+} dopant. The broad peaks at 437 cm^{-1} and 582 cm^{-1} correspond to octahedral (B-) metal stretching (Ni-O) and tetrahedral (A-) metal stretching (Fe-O) of nickel ferrite respectively. Magnetic results revealed that the prepared NPs are ferromagnetic in nature. The antibacterial activity (ABA) of gram-positive *Staphylococcus aureus* and *Bacillus subtilis* and gram-negative *Escherichia coli* and *Klebsiella pneumonia* has been investigated using pure and Sr^{2+}-substituted $NiFe_2O_4$ NPs. It was found that the improved activity is intensified with smooth Sr^{2+} doping as it causes a decrease in the grain size.

Keywords Spinel $NiFe_2O_4$ · Nanostructures · Ionic radius · Crystallite size · Band gap · Magnetic measurements

1 Introduction

Recently, magnetic spinel ferrites are greatly important in the field of materials science, due to their enhanced structural, morphology, optical, magnetic, and vibrational properties and also they have been widely used for applications such as magnetic fluid for the purpose of information storage, drug delivery, MRI, RRAM, and many more [1–3]. The general formula for cubic spinal structure-based ferrite is MFe_2O_4, (M = Metal). The M^{2+} and Fe^{3+} ions occupy two distinct sites namely tetrahedral (A^{2+}) and octahedral sites (B^{3+}) [4, 5]. Based on the theory of Wyckoff positions, the spinels exhibit three different crystal structures namely normal, inverse, and mixed. In the case of normal spinel structure, M^{2+} and Fe^{3+}

✉ G. Ramachandran
ramuvec@gmail.com

✉ A. Manikandan
manikandana.che@bharathuniv.ac.in; mkavath15@gmail.com

[1] Department of Chemistry, Sri Sairam Engineering College, West Tambaram, Chennai, Tamil Nadu, India

[2] Department of Chemistry, Dr. Ambedkar Government Arts College (affiliated to University of Madras), Vyasarpadi, Chennai, Tamil Nadu, India

[3] Department of Chemistry, Bharath Institute of Higher Education and Research (BIHER), Bharath University, Chennai, Tamil Nadu 600 073, India

[4] Department of Biophysics, Institute for Research & Medical Consultations (IRMC), Imam Abdulrahman Bin Faisal University, P.O. Box 1982, Dammam 31441, Saudi Arabia

[5] Department of Nano-Medicine Research, Institute for Research & Medical Consultations (IRMC), Imam Abdulrahman Bin Faisal University, P.O. Box 1982, Dammam 31441, Saudi Arabia

[6] Department of Electronics and Communication Engineering, Centurion University of Technology and Management, Bhubaneswar 752050, India

Chinese Journal of Physics 67 (2020) 27–36

Contents lists available at ScienceDirect

Chinese Journal of Physics

journal homepage: www.elsevier.com/locate/cjph

Growth, structural, spectral, thermal, electrical and optical characterization of a novel optical material: Triethanolamine picrate single crystals for optical applications

Raja Raghavan[a,*], Seshadri Srinivasan[b], Santhanam Venkatakrishnan[c], Kurinjinathan Panneerselvam[d], Suvasini Chandramouleeswaran[a]

[a] Department of Physics, Sri Chanderasekarendra Viswa mahavidhyalaya, Tamil Nadu 631561, India
[b] Department of Physics, Ambedkar Government College, Tamil Nadu 600039, India
[c] Department of Chemistry, Sri Chanderasekarendra Viswa mahavidhyalaya, Tamil Nadu 631561, India
[d] Department of Physics, Academy of Maritime Education and Training, Tamil Nadu 603112, India

ARTICLE INFO

Keywords:
TEAP crystal
dielectrics
hardness
FTIR
NLO

ABSTRACT

The Triethanolamine picrate (TEAP) single crystal was grown by slow evaporation technique. The grown crystal crystallizes in monoclinic system and $P2_1/C$ is the space group determined by Single crystal X-Ray diffraction method. The vibrational modes and functional groups were elucidated from Fourier Transform InfraRed (FTIR) spectra and Fourier Transform Raman (FT-Raman) spectra. The Ultraviolet - Visible (Uv-Vis) studies accomplished the excitation wavelength of the grown crystal is around 203 nm and 354 nm and it is suitable to exhibit second harmonic generation signal. From the absorption data, remarkable optical properties such as optical band gap energy, extinction coefficient were evaluated. The mechanical strength of the grown crystal was examined by Vickers micro hardness test. The temperature of decomposition was confirmed by Thermo Gravimetric / Differential Thermal Analysis (TG/DTA). Kurtz and Perry technique were confirmed the Non-Linear Optics (NLO) property of the crystal. The electrical properties were explained using Dielectric studies.

1. Introduction

In recent years, communication technology needs a device that utilizes photons instead of electrons for ultra-fast transmission of information and data. Organic materials plays an immense role in the field of photonic device fabrication like solar cells, optical modulators, frequency conversion devices and light emitting diodes due to its high optical nonlinearity, high optical threshold and wide transparency range [1-3]. Further, Non Linear Optical materials based on metal-organic frameworks finds place in applications like Ultrafast Photonics with enhanced stability, nano perovskite materials for LEDs and deep ultraviolet applications were already reported [4–11]. The optical non linearity is based on the materials which manipulates the phase amplitude polarization and frequency of optical beams [12–13]. The important requirement for optical non linearity is intermolecular hydrogen bonding and the crystal chirality which is achieved by connecting a donor and acceptor group [14]. Organic crystal attracts a great attention because they have large optical susceptibilities and high optical thresholds [15,16]. Among the organic materials the hyper polarizability possess the charge transfer between donor and acceptor [17]. Picric acid is an organic acid, it drawn more attention due to its

* Corresponding author.
E-mail address: sridev_raja@yahoo.com (R. Raghavan).

https://doi.org/10.1016/j.cjph.2019.11.017
Received 8 September 2019; Received in revised form 31 October 2019; Accepted 24 November 2019
Available online 30 November 2019

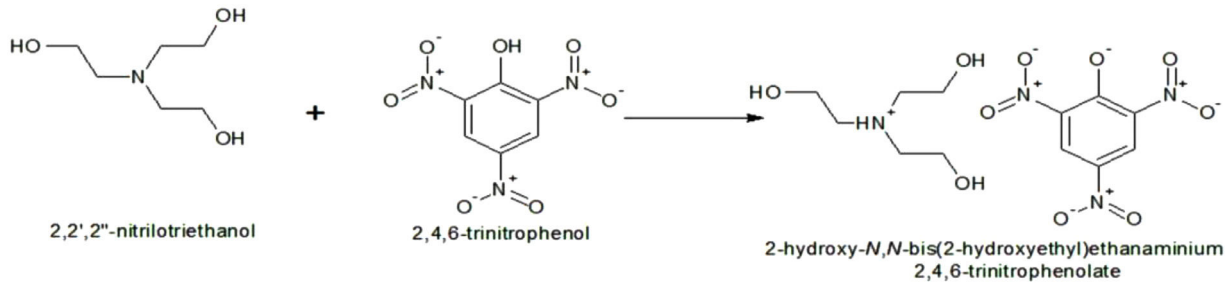

Fig. 1. Reaction Scheme.

tendency to form molecular complexes with many organic compounds [18]. Crystalline picrate serves as a better acidic ligand to give π–π interaction or hydrogen bonding interaction with amines [19], pyridine [20] and piperazines [21]. The Second Harmonic Generation materials requires non-centrosymmetric molecular packing arrangement unless a magnetic dipole or an electric quadrupole [22]. Picrate crystals were extensively investigated due to its high optical non linearity, wide bandgap and high laser damage threshold. In the present work, an attempt is made to synthesize and grow an organic charge transfer complex NLO material triethanolamine picrate (TEAP) using triethanol amine and picric acid. The grown crystals were subjected to structural, thermal, vibrational, linear and non-linear optical evaluation and electrical properties are evaluated.

2. Materials and methods

2.1. Materials

The title compound was grown by using AR grade Picric acid $(O_2N)_3C_6H_2OH$ and Triethanol amine $(C_6H_{15}NO_3)$ and Acetone (C_3H_6O).

2.2. Method

The saturated solution of Picric acid was prepared by using acetone as a solvent in room temperature. Triethanolamine was dissolved in acetone separately. Then the solutions were gently mixed in magnetic stirrer until the homogeneity achieved. The obtained yellow solution was filtered and allowed to evaporate in the room temperature. The well sized crystal was harvested by continuous recrystallization process. The reaction scheme and photograph of grown crystal are shown in Figs. 1 and 2.

3. Results and discussion

3.1. Single crystal X-Ray diffraction analysis

The structural analysis and refinement of TEAP crystals were done using Bruker Kappa APEX II single crystal CCD X-ray

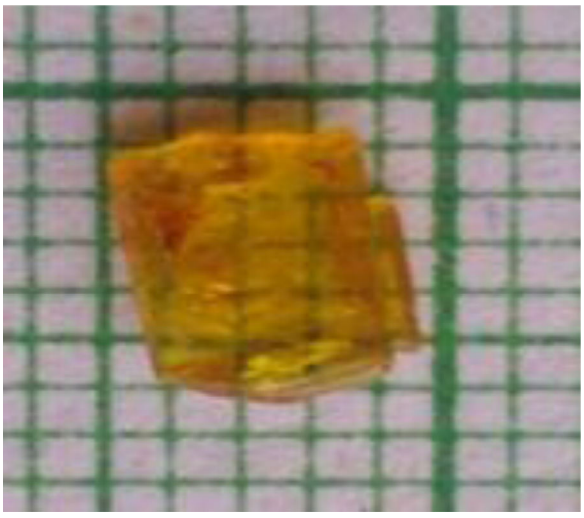

Fig. 2. Grown Crystal.

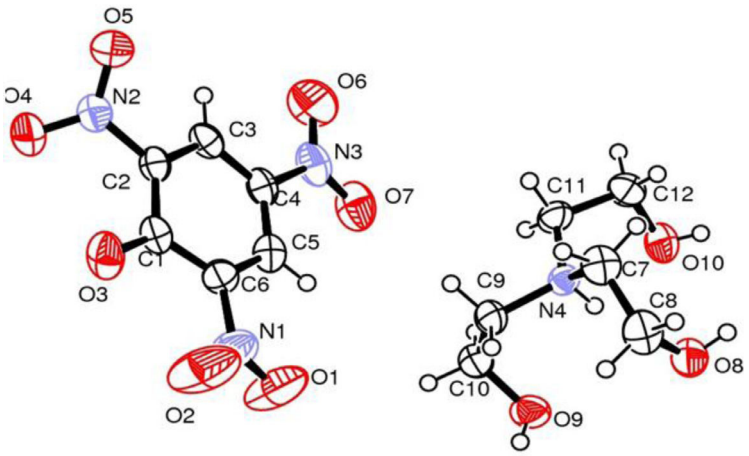

Fig. 3.1. ORTEP diagram of TEAP crystal.

diffractometer equipped with graphite-monochromated MoKα radiation (λ = 0.71073 Å) at the temperature of 293(2) K well sized crystal was employed for analysis. The crystal structure was solved by direct methods procedure and the non-hydrogen atoms were subjected to anisotropic refinement by full-matrix least squares on F^2 using SHELXL-97 program. From the analysis, the results reveals that the crystal belongs to space group of P2(1)/c monoclinic structure, the obtained lattice parameters based on set of reflections of TEAP are a = 13.4431 Å, b = 8.3921 Å, c = 14.8385 Å and the cell volume is 1668.09 (Å)^3 [23]. The titled compound having the elemental composition $C_{12}H_{18}N_4O_{10}$ and the systematic name is 2-hydroxy-N,N-bis(2-hydroxyethyl) ethanaminium 2, 4, 6 trinitro phenolate. The asymmetric unit of triethanolamine picrate consists of a unit of nitrilotriethanol and trinitrophenol molecules. Fig. 3.1 represents the ORTEP diagram of TEAP crystal.

The bond length of C - C atom in benzene ring is in the order of 1.37 Å – 1.43 Å. The N–O—H and O–H—O hydrogen bonds and π−π interactions connects the components of the structure into a three-dimensional network as a ring structure. The angle between C—C—C varies from 116°−120° and thus confirms that the molecules are slightly perturbed from the regular hexagonal symmetry. The molecular parameter O4-N2-O5 exhibits an angle of 122.3°. The other two angles O6-N3-O7 and O2-N1-O1 shows 123.6° and 121.6° respectively. The nitrilotriethanol and trinitrophenol interacts through the N—O—H bond of lengths 1.9789 Å and 2.5682 Å, respectively [24]. The crystal data and refinement details were showed in Table 1.

3.2. Thermal analysis

The thermal property is one of the influential criteria for an NLO crystal to attain as the practical device. In the nonlinear process,

Table 1
Crystal data and structure refinement details.

Empirical formula	C_{12} H_{18} N_4 O_{10}
Formula weight	378.30
Temperature	296(2) K
Wavelength	0.71073 A
Crystal system, space group	Monoclinic, P2(1)/c
Unit cell dimensions	a = 13.4431(3) A alpha = 90 deg.
	b = 8.3921(2) A beta = 94.8233(11) deg.
	c = 14.8385(3) A gamma = 90 deg.
Volume	1668.09(6) A^3
Z, Calculated density	4, 1.506 Mg/m^3
Absorption coefficient	0.133 mm^{-1}
F(000)	792
Crystal size	0.250 × 0.220 × 0.130 mm
Theta range for data collection	1.520 to 24.998 deg.
Limiting indices	$-15<=h<=15$, $-8<=k<=9$, $-17<=l<=14$
Reflections collected / unique	13,187 / 2929 [R(int) = 0.0208]
Completeness to theta	= 24.998 100.0%
Refinement method	Full-matrix least-squares on F^2
Data / restraints / parameters	2929 / 0 / 252
Goodness-of-fit on F^2	1.022
Final R indices [I>2sigma(I)]	R1 = 0.0383, wR2 = 0.0953
R indices (all data)	R1 = 0.0477, wR2 = 0.1027
Extinction coefficient	0.0269(17)
Largest diff. peak and hole	0.299 and −0.263 e.A^−3

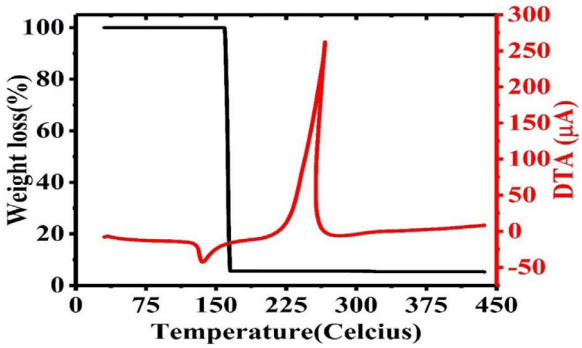

Fig. 3.2. TGA/DTA of TEAP crystal.

a considerable amount of heat is generated by the high power lasers. In order to improve the better performance for the devices, thermally stable NLO crystals are very much needed. The TGA/DTA studies were carried out in the nitrogen atmosphere at a heating rate of 20 °C min^{-1} from 30 °C to 1000 °C. From the Fig. 3.2, the TEAP crystal is stable from room temperature to 160 °C and the Thermogram shows the single step decomposition of the TEAP crystal due to the elimination of all major functional groups. The DTA curve of TEAP gives one sharp endothermic peak at 135.1 °C which corresponds to the melting point of the sample and one exothermic peak at 265.8 °C indicate the major decomposition and volatilization of the material. The sharpness of the endothermic peak shows the well crystalline nature and purity of the TEAP crystal [25].

3.3. FTIR and FT-Raman analysis

The infra-red spectra of TEAP crystal was recorded in the region of 4000–400 cm^{-1} analysed by using KBr pellet technique was shown in Fig. 3.3 a. The FT-Raman spectrum of the title compound was recorded in the region of 4000–50 cm^{-1} and was shown in Fig. 3.3 b. The spectral investigation reveals the functional group associated with the crystal structure. The sharp peak at 3356 cm^{-1} in the IR spectrum is due to the N—H asymmetric stretching and superimposed OH bending. The stretching at 1630 cm^{-1} in the IR spectrum and at 1614 cm^{-1} in the FT-Raman spectrum is observed for corresponding picrate salt [26]. The IR and Raman band associated with ~1552 cm^{-1} is due to the asymmetric stretching vibration of $–NO_2$. The scissoring vibrational mode of $–NO_2$ is observed at ~908 cm^{-1} in the IR spectrum and the same is observed in the FT-Raman spectrum at 914 cm^{-1}. The rocking vibration of $–NO_2$ appears at ~547 cm^{-1} and 545 cm^{-1} in the IR and Raman spectrum respectively. The three nitro groups confirm the formation of picric in ring structure. The NO_2 groups are involved in the intramolecular charge–transfer, intermolecular hydrogen bond and dipole – dipole interactions. The IR and Raman bands between 1400 and 1650 cm^{-1} in benzene derivatives are due to aromatic C—C stretching vibrations. The observed frequencies are well agreed with the previous reports [27–29]

3.4. UV–Vis studies

The UV–Vis spectra recorded in the range of 190–800 nm. The observation of spectra gives important structural information in the event of absorption of UV and visible light incorporating lifting of electrons into p and n orbital's from the ground state to higher

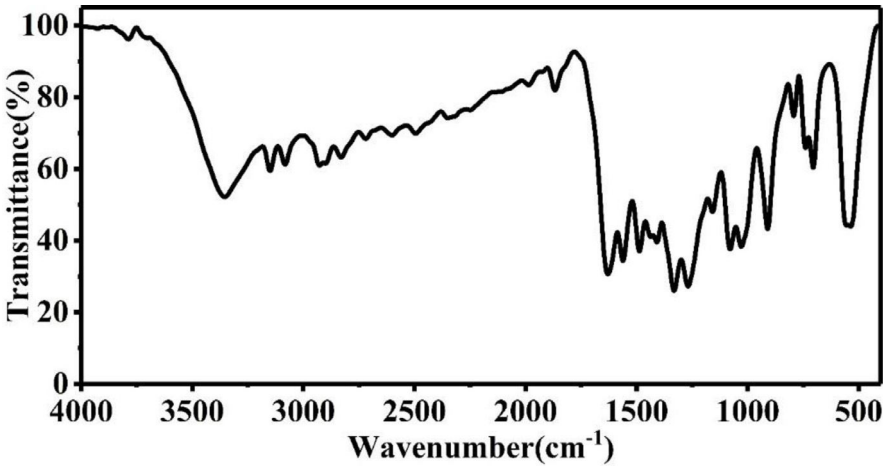

Fig. 3.3 a. FTIR spectrum of TEAP crystal.

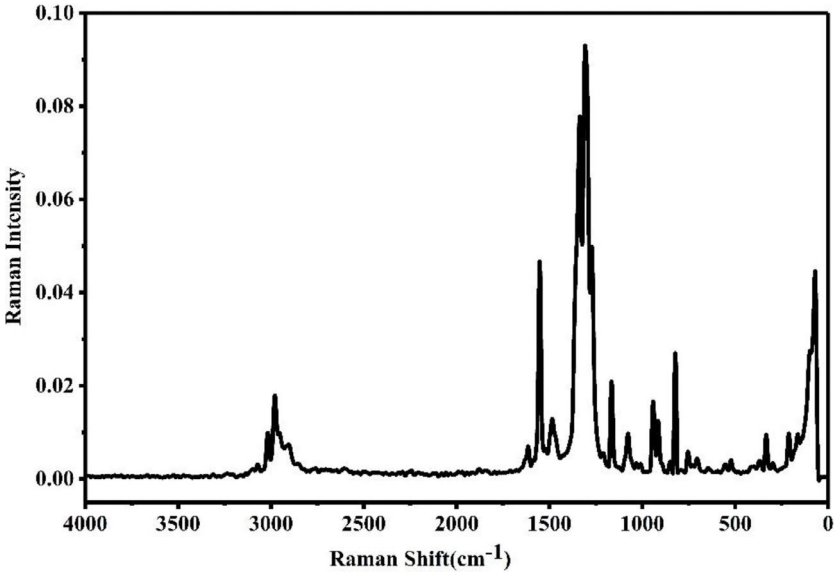

Fig. 3.3 b. FT-Raman spectrum of TEAP crystal.

energy states [30]. From Fig. 3.4.1, the absorption of the grown crystal TEAP is around 203 nm and 354 nm. This may be due to the π→π* and n→π∗ transitions taking place in the grown crystal. The nitro (–NO_2) groups present in the grown crystal are the chromophores which are responsible for the yellow color [31]. The absorption enhancement is due to auxochromophores such as O—H present in TEAP crystal. The observed spectra clearly depeicts the absence of absorption in the region of 450 nm – 800 nm that helps in the frequency doubling process in the second harmonic generation [32].

The optical energy band gap (Eg) is closely connected to the atomic and electronic band structures utilized in electro-optic field. The plot drawn between $(\alpha h\nu)^2$ vs $h\nu$ gives optical energy gap of the grown TEAP crystal. The dependence of optical absorption coefficient (α) with the photon energy helps to study the band structure and the type of transition of electrons [33]. The optical absorption coefficient was calculated from the absorbance (A) using the following relation

$$\alpha = \frac{2.303}{t}\log(A)$$

where t is the path length and A is the absorbance of TEAP crystal. The absorption coefficient is used to determine optical energy gap of the TEAP crystal by using Tauc relation

$$\alpha h\nu = A(h\nu - Eg)^x$$

where, A is the band edge constant that depends on the transition probability. x is the index that characterizes the optical absorption process, theoretically equal to 1/2, 3/2, 2, and 3 depends on the transitions such as direct allowed, direct forbidden, indirect allowed,

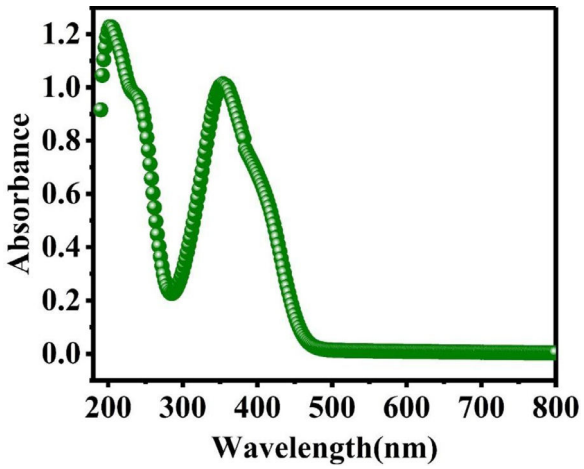

Fig. 3.4.1. UV–Vis of TEAP crystal.

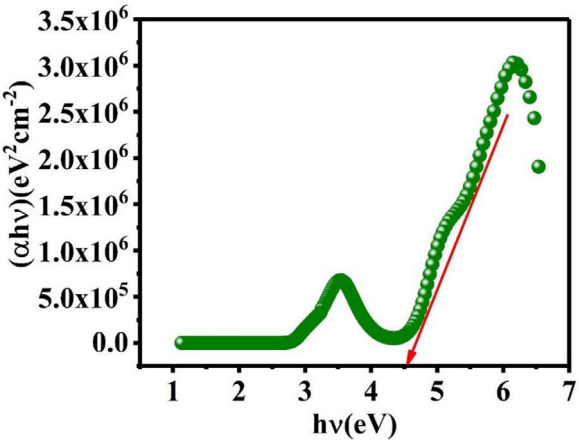

Fig. 3.4.2. Energy gap of TEAPcrystal.

and indirect forbidden transitions, respectively [34]. The plot is observed to be a straight line in the region of high absorption. The extrapolating of the linear portion to zero abscissa gives the band gap for TEAP crystal. The optical band gap 4.49 eV is found to be the predominant transition. This transition takes place due to proton donor (–OH) group and proton acceptor amine (–NH) group present in the TEAP crystal resulting in charge asymmetry. This charge asymmetry is required for second order nonlinearity of the TEAP crystal. Fig. 3.4.2 represent the energy bandgap of TEAP crystal.

3.5. Second harmonic generator (SHG)

The level of SHG response of a given material is dependent on its structural features. The structure should lack center of symmetry. On a molecular scale, the extent of charge transfer (CT) across the NLO chromophores determines the level of SHG output. It can be noted that the intermolecular N—H—O hydrogen bonding network formed between hydrogen atoms of a triethanolamine cation and oxygen atoms of adjacent picric anions. The compound crystallizes in a P2(1)/c space group [35]. The presence of strong intermolecular hydrogen bonds interactions can extend this level of charge transfer into the supramolecular realm, owing to their electrostatic and directed nature, thereby enhancing the SHG response. The second harmonic generation efficiency of the grown TEAP crystal was measured using Kurtz and Perry method [36]. For the SHG efficiency measurements, microcrystalline material of KDP was used for comparison. The sample was illuminated using Q-switched mode locked Nd:YAG laser with input pulse of 3.2 mJ. The emission of green radiation from the crystal confirmed the second harmonic signal generation in the crystal. The generated SHG signal at 532 nm was split from the fundamental frequency using an IR separator. A detector was used to detect second harmonic intensity connected to a power meter to read the energy input and output. The Kurtz powder SHG measurement shows that the efficiency of TEAP single crystal is 8.85 mJ with the reference of KDP 17.3 mJ using input efficiency of 0.68 J. The SHG efficiency of TEAP crystal 0.5 times more than that of KDP.

3.6. Dielectric study

The dielectric characteristics of the material are vital parameter to examine the electrical response of the crystal which is an essential requirement for optoelectronics devices. The dielectric constant of the material is fundamentally contributed by ionic, electronic, dipolar and space charge polarization which might be controlled by applying an external electric field and temperature. The knowledge about the nature of the atoms, ions and their bonding in a material is also given by dielectric studies. The dielectric study of TEAP crystal was carried out using HIOKI 3532–50 LCRHITESTER instrument for the frequency ranges from 50 Hz to 5 MHz at different temperatures of 313 K, 333 K, 353 K and 373 K. For these different temperatures, the dielectric constant or relative permittivity (ε_r) was determined by the relation

$$\varepsilon_r = \frac{Cd}{\varepsilon_0 \, A}$$

where d is the thickness of the sample, ε_r is the capacitance, A is the area of the crystal and ε_o is the absolute permittivity of free space which is equal to 8.854×10^{-12} Fm^{-1}. The graph drawn between the logarithm of the frequency (log f) and dielectric constant (ε_r) for different temperatures of 323 K, 333 K, 343 K, 353 K and 363 K is shown in Fig. 3.6.1. The curve shows that the value of dielectric constant is high in the lower frequency region for all the temperatures and then it decreases with increase in frequency. The high value dielectric constant at low frequency range is consequent to space charge polarization in addition to electronic, ionic and orientation polarizations [37]. The low value of dielectric constant at high frequency shows the way to enhance the nonlinear optical applications.

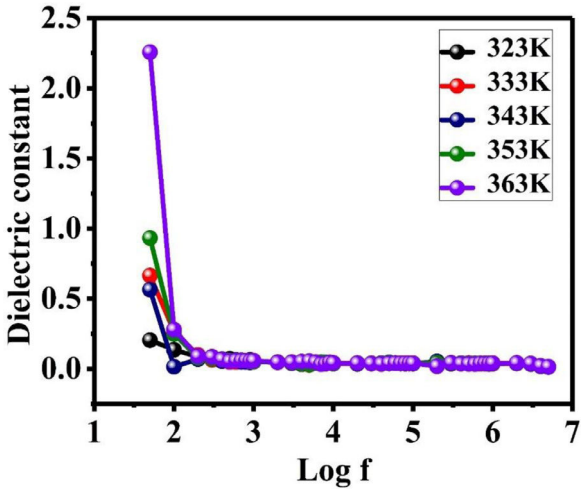

Fig. 3.6.1. Dielectric study of TEAP crystal.

3.6.2. Dielectric loss

The dielectric loss (tan δ) were calculated by the equation

$$\tan\delta = \varepsilon_r D$$

where D is the dissipation factor.

The high values of tan δ at low frequencies are due to the presence of all the form of polarizations. As the frequency increases, the space charge cannot sustain and comply with external field and hence the polarization decreases. According to miller rule, the low value of dielectric loss at high frequency revealed the high optical quality of the crystal with less electrically active defects, which is a desirable property for NLO applications. The dielectric loss of TEAP crystals as a function of various temperatures at different frequencies are shown in Fig. 3.6.2

It is observed from the figure that the dielectric constant decreases sharply with the increase in frequency in almost all temperatures but achieves saturation in the higher frequency region. This is because, beyond a certain frequency of the electric field the dipoles do not follow the alternating field. It is also observed that at low frequencies, when the temperature is high, the larger is the dielectric constant. This is mainly due to blocking of charge carriers at the electrodes. Because of the impedance to their motion at the electrodes, space charge and macroscopic distortion which causes larger values of dielectric constant at lower frequencies. At high frequencies, the low values of dielectric loss indicate that the crystal possess lesser number of electrically active defects

3.6.3. AC conductivity

The ac conductivity (σ_{ac}) of the TEAP crystals were concluded from the relation

$$\sigma_{ac} = \omega\varepsilon_o\varepsilon_r \tan\delta\,(\Omega^{-1}m^{-1})$$

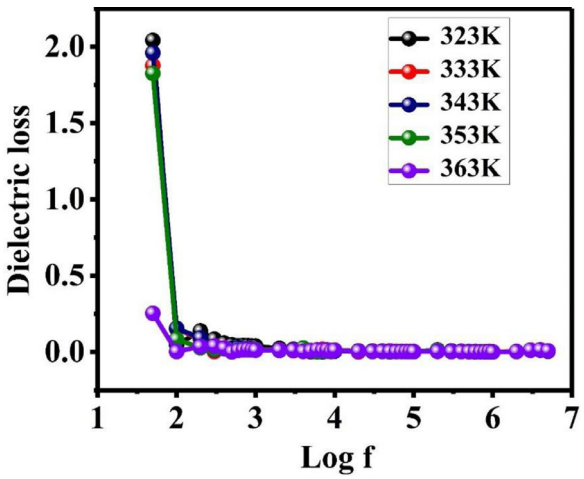

Fig. 3.6.2. Dielectric loss of TEAP crystal.

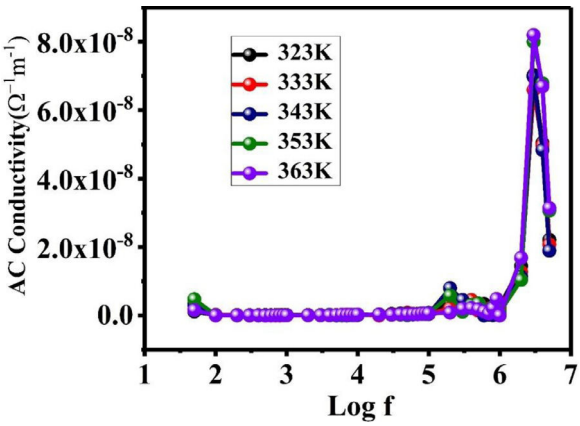

Fig. 3.6.3. AC Conductivity of TEAP crystal.

where ω the angular frequency

The Fig. 3.6.3 shows the variation of ac conductivity for different frequencies, at higher frequencies, the conductivity spectrum exhibits dispersion and indicates the onset of ac conductivity which increases with the increasing frequency could be attributed due to the forward and backward ion displacements occurring at the same time thus making the frequency dependence of ionic motion easier [38].

3.7. Microhardness study

Mechanical stability of the grown TEAP crystals was revealed by Vickers microhardness study. The Vickers hardness number (Hv) was calculated using the standard formula:

$$Hv = 1.8544\,P/d^2(kg/mm^2)$$

where P is the applied load in kg and d is the diagonal lengths obtained from the indenter impression. From the Fig. 3.7.1 the variation of Vicker's hardness number with the applied load P. It is observed that the hardness number increases with the increasing load which is termed as reverse indentation size effect (ISE) [39]. Thus, the material is well suitable for optical device fabrication.

3.7.2. Meyer work hardening coefficient

According to Meyer hardness analysis, the relation between load P and indentation length d is given by

$$P = kd^n$$

where P is the applied load, d is the observed mean diagonal length of indentation, k is the standard hardness constant and n is the Meyer micro hardening index or work hardening coefficient.

The above equation can be rewritten as follows:

$$\log P = \log k + n \log d$$

The Meyer micro hardening index n was determined from the slope of the curve drawn between log d and log P as shown in Fig. 3.7.2. According to Onitsch et al., for hard materials the n value lies between 1 and 1.6 and it is higher than 1.6 for soft materials.

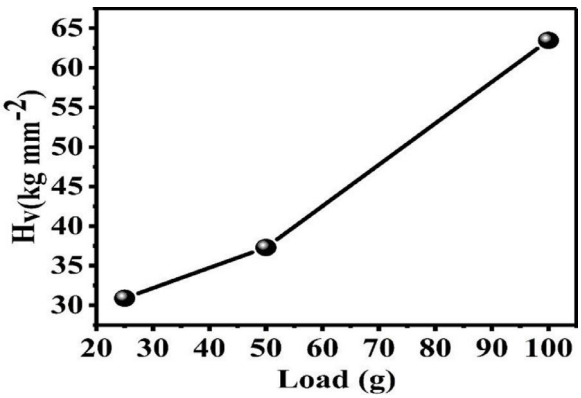

Fig. 3.7.1. Mechanical stability of TEAP crystal.

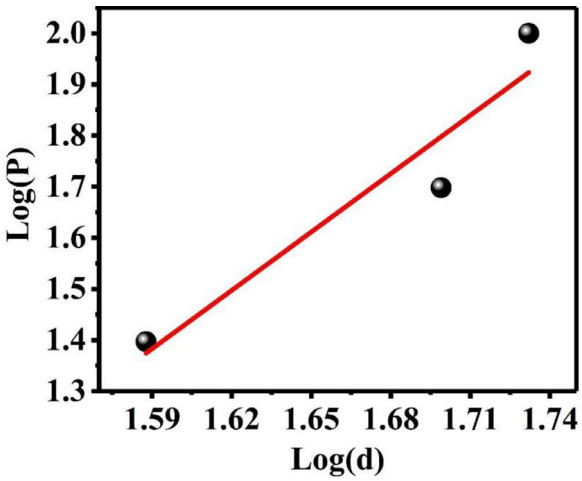

Fig. 3.7.2. Microhardening index of TEAP crystal.

The work hardening coefficient of the grown TEAP crystal is found to be 3.80 by applying least square fitting. The calculated n value depicts that the grown crystal belongs to soft material category.

3.7.3. Elastic stiffness constant

The elastic stiffness constant (C_{11}) is also calculated from Wooster's empirical formula

$$\mathbf{C}_{11} = (\mathbf{Hv})^{7/4}$$

The elastic stiffness constant gives confess the nature of bonding between neighbouring atoms. A graph is plotted between load P vs stiffness constant C11 is shown in figure. The Fig. 3.7.3 evidences that the stiffness constant increases with increase of load. The higher the stiffness constant C11 point out that the binding forces between the ions are quite strong.

4. Conclusion

Single crystal of TEAP was grown by slow evaporation method. XRD analysis confirmed monoclinic crystal structure with a space group of $P2_1/C$. The UV-Vis spectral analysis of TEAP crystal reveals absorption peaks around 203 nm and 354 nm. TG/DTA analysis shows that TEAP crystal have thermal stability upto 135.1 °C. The SHG efficiency of TEAP crystal is 0.5 times more than that of KDP. From Vickers microhardness study, the crystal is found to be a soft material.

Declaration of Competing Interest

The authors declare that they have no known competing financial interests or personal relationships that could have appeared to

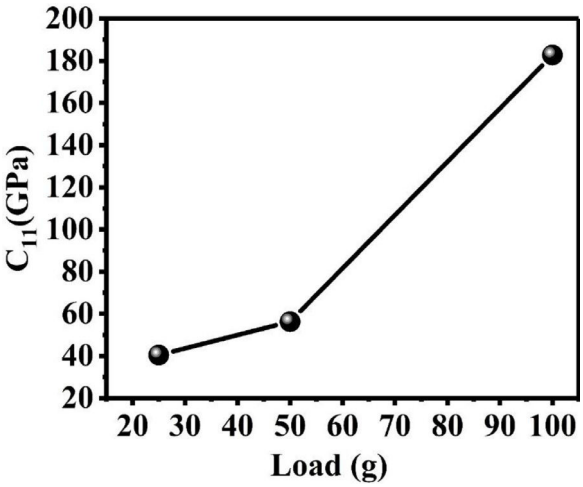

Fig. 3.7.3. Elastic stiffness constant of TEAP crystal.

influence the work reported in this paper.

References

[1] Z. Zhang, Y.H. Zhou, W.Q. Zheng, R.M. Chen, B.W. Wang, X.G. Zheng, C.L. Ni, X.P. Liu, J.R. Zhou, W.X. Zheng, Synthesis, crystal structure, thermal and optical properties of an organic material: benzyl isoquinolinium picrate single crystal, Synth. Met. 222 (2016) 267–273.

[2] J. Uma, V. Rajendran, Growth and properties of semi-organic nonlinear optical crystal: L-Glutamic acid hydrochloride, Prog. Nat. Sci. 26 (2016) 24–31.

[3] S.R. Forrest, The path to ubiquitous and low-cost organic electronic appliances on plastic, Nature 428 (2004) 911.

[4] X. Jiang, L. Zhang, S. Liu, Y. Zhang, Z. He, W. Li, F. Zhang, Y. Shi, W. Lü, Y. Li, Q. Wen, J. Li, J. Feng, S. Ruan, Y.J. Zeng, X. Zhu, Y. Lu, H. Zhang, Ultrathin metal–organic framework: an emerging broadband nonlinear optical material for ultrafast photonics, Adv. Opt. Mater. 6 (2018) 1800561.

[5] L. Lu, X. Tang, R. Cao, L. Wu, Z. Li, G. Jing, B. Dong, S. Lu, Y. Li, Y. Xiang, J. Li, D. Fan, H. Zhang, Broadband nonlinear optical response in few-layer antimonene and antimonene quantum dots: a promising optical kerr media with enhanced stability, Adv. Opt. Mater. 5 (2017) 1700301, , https://doi.org/10.1002/adom.201700301.

[6] J. Zheng, Z. Yang, S. Chen, Z. Liang, X. Chen, R. Cao, Z. Guo, K. Wang, Y. Zhang, J. Ji, M. Zhang, D. Fan, H. Zhang, Black phosphorus based all-optical-signal-processing: towards high performances and enhanced stability, Adv. Opt. Mater. 6 (4) (2017) 1701166.

[7] Y. Zhang, C.K. Lim, Z. Dai, G. Yu, J.W. Haus, H. Zhang, P.N. Prasad, Photonics and optoelectronics using nano-structured hybrid perovskite media and their optical cavities, Phy. Rep. 795 (2019) 1–51 ISSN 0370-1573.

[8] X. Jiang, S. Liu, W. Liang, C.S. Luo, Z. He, Y. Ge, H. Wang, R. Cao, F. Zhang, Q. Wen, J. Li, Q. Bao, D. Fan, Broadband nonlinear photonics in Few-Layer MXene Ti_3C_2 T_x (T = F, O, or OH), Laser Photon. Rev 12 (2018) 1700229.

[9] L. Lu, Z. Liang, L. Wu, Y.X. Chen, Y. Song, S. Dhanabalan, J. Ponraj, B. Dong, Y.J. Xiang, F. Xing, D. Fan, Few-layer bismuthene: sonochemical exfoliation, nonlinear optics and applications for ultrafast photonics with enhanced stability, Laser Photon. Rev 12 (2018) 1700221.

[10] M. Mutailipu, M. Zhang, B.B. Zhang, L.Y. Wang, Z.H. Yang, X. Zhou, S.L. Pan, $SrB_5O_7F_3$ functionalized with $[B_5O_9F_3]$ 6- chromophores: accelerating the rational design of deep-ultraviolet nonlinear optical materials, Angew. Chem. Int. Ed. 57 (2018) 6095–6099.

[11] H.P. Wu, H.W. Yu, Z.H. Yang, X.L. Hou, X. Su, S.L. Pan, X. Su, K.R. Poeppelmeier, J.M. Rondinelli, Designing a deep ultraviolet nonlinear optical material with large second harmonic generation response, J. Am. Chem. Soc. 135 (2015) 4215–4219.

[12] D. Arivuoli, Fundamentals of nonlinear optical materials, Pramana 57 (2001) 871–883.

[13] P. Paramasivam, C.R. Raja, Synthesis, growth and characterization of a new nonlinear optical crystal: glycinium hydrogen squarate (GHS), Spectrochim. Acta Part A. 93 (2012) 81–85.

[14] P. Pandi, G. Peramaiyan, G. Bhagavannarayana, R.M. Kumar, R. Jayavel, Growth, structural, optical and laser damage threshold studies of organic picolinium picrate monohydrate single crystals, Optik 124 (2013) 5792–5796.

[15] A. Rathika, R.G. Raman, Growth and characterization of an efficient nonlinear optical single crystal: urea p-nitrophenol, Optik 125 (2014) 2978–2982.

[16] X. Xu, Z. Sun, K. Fan, Y. Jiang, R. Huang, Y. Wen, Q. He, T. Ao, Conversion of 4-N, N-dimethylamino-4'-N'-methyl-stilbazolium tosylate (DAST) from a simple optical material to a versatile optoelectronic material, Sci. Rep. 5 (2015) 12269.

[17] B.F. Levine, Donor—acceptor charge transfer contributions to the second order hyperpolarizability, Chem. Phys. Lett. 37 (1976) 516–520.

[18] C. Indumathi, S.G. TC, K. Anitha, Structural, thermal, optical and nonlinear optical properties of ethylenediaminium picrate single crystals, J. Phys. Chem. Solids. 106 (2017) 37–43.

[19] A.A. Prasad, K. Muthu, M. Rajasekar, V. Meenatchi, S.P. Meenakshisundaram, Synthesis, crystal growth, characterization and theoretical studies of 4-amino-benzophenonium picrate, Spectrochim. Acta, Part A 135 (2015) 46–54.

[20] A.N. Talukdar, B. Chaudhuri, The crystal and molecular structure of pyridine picrate, Acta Crystallogr. Sect. B Struct. Sci. 32 (1976) 803–808, https://doi.org/10.1107/S056774087600397X.

[21] Z.L. Wang, L.H. Jia, Three-dimensional network in piperazine-1, 4-diium–picrate–piperazine (1/2/1), Acta Crystallogr. Sect. E: Struct. Rep. Online. 64 (2008) o665–o666.

[22] G.J. Ashwell, G. Jefferies, D.G. Hamilton, D.E. Lynch, M.P.S. Roberts, G.S. Bahra, C.R. Brown, Strong second-harmonic generation from centrosymmetric dyes, Nature 375 (1995) 385.

[23] H.A. Ghabbour, H.A. Abdel-Aziz, H. AlRabiah, O.S. Alruqi, Crystal structure of 4, 5-diphenylthiazol-2-amine, $C_{15}H_{12}N_2S$, Z. Kristallogr. - New Cryst. Struct. 231 (2016) 861–862.

[24] C.N. Kavitha, M. Kaur, J.P. Jasinski, H.S. Yathirajan, 4-Acetylpiperazinium picrate, Acta Crystallogr. Sect. E Struct. Rep. Online. 70 (2014) o717–o718.

[25] G.A. Babu, A. Chandramohan, P. Ramasamy, G. Bhagavannarayana, B. Varghese, Synthesis, structure, growth and physical properties of a novel organic NLO crystal: 1, 3-Dimethylurea dimethylammonium picrate, Mater. Res. Bull. 46 (2011) 464–468.

[26] A. Tarai, J.B. Baruah, Different self-assemblies and absorption–emission properties of the picrate salts of aromatic amine or heterocycle linked oximes, New J. Chem. 42 (2018) 4757–4765.

[27] A.A. Prasad, K. Muthu, V. Meenatchi, M. Rajasekar, S.P. Meenakshisundaram, S.C. Mojumdar, Growth and characterization of 2-amino-5-nitrobenzophenonium picrate crystals, J. Therm. Anal. Calorim. 119 (2015) 885–890.

[28] M. Vimalan, A. Ramanand, P. Sagayaraj, Synthesis, growth and characterization of l-alaninium oxalate-a novel organic NLO crystal, Cryst. Res. Technol. 42 (2007) 1091–1096.

[29] T. Dhanabal, G. Amirthaganesan, M. Dhandapani, S.K. Das, Synthesis, structure, thermal and NLO characterization of 4-hydroxy tetramethylpiperazinium picrate crystals, J. Chem. Sci. 124 (2012) 951–961.

[30] P. Jayaprakash, P. Sangeetha, C.R.T. Kumari, M.L. Caroline, Investigation on the growth, spectral, lifetime, mechanical analysis and third-order nonlinear optical studies of L-methionine admixtured D-mandelic acid single crystal: a promising material for nonlinear optical applications, Physica B (Amsterdam, Neth.). 518 (2017) 1–12.

[31] N. Sudharsana, S. Muthunatesan, G.J. Priya, V. Krishnakumar, R. Nagalakshmi, Experimental and theoretical studies of 2, 5-dichloroanilinium picrate, Spectrochim. Acta Part A. 121 (2014) 53–62.

[32] N. Sudharsana, B. Keerthana, R. Nagalakshmi, V. Krishnakumar, L.G. Prasad, Growth and characterization of hydroxyethylammonium picrate single crystals for third-order nonlinear optical applications, Mater. Chem. Phys. (2012) 736–746.

[33] S. Muhammad, M. Shkir, S. AlFaify, A. Irfan, A.G. Al-Sehemi, Combined experimental and computational insights into the key features of L-alanine L-alaninium picrate monohydrate: growth, structural, electronic and nonlinear optical properties, RSC Adv 5 (2015) 53988–54002.

[34] A. Jagadesan, G. Peramaiyan, T. Srinivasan, R.M. Kumar, S. Arjunan, Crystal structure, thermal and optical properties of Benzimidazole benzimidazolium picrate crystal, J. Cryst. Growth. 436 (2016) 40–45.

[35] V. Nalla, R. Medishetty, Y. Wang, Z. Bai, H. Sun, J. Wei, J.J. Vittal, Second harmonic generation from the 'centrosymmetric' crystals, IUCrJ 2 (2015) 317–321, https://doi.org/10.1107/S2052252515002183.

[36] S.K. Kurtz, T.T. Perry, A powder technique for the evaluation of nonlinear optical materials, J. Appl. Phys. 39 (1968) 3798–3813.

[37] M. Prakash, D. Geetha, M.L. Caroline, Crystal growth and characterization of L-phenylalaninium trichloroacetate—A new organic nonlinear optical material, Physica B (Amsterdam, Neth.). 406 (2011) 2621–2625.

[38] P. Sangeetha, P. Jayaprakash, M. Nageshwari, M.P. Mohamed, G. Vinitha, M.L. Caroline, Growth and characterization of L-phenylalanine nitric acid (LPN) and tris L-(phenylalanine)-phenylalanininum nitrate (TPLPN) as second and third order nonlinear optical materials, Chin. J. Phys. 56 (2018) 721–739.

[39] M. Nageshwari, C.R.T. Kumari, G. Vinitha, S. Muthu, M.L. Caroline, Growth and characterization of L-Serine: a promising acentric organic crystal, Physica B (Amsterdam, Neth.). 541 (2018) 32–42.

DR.LYDIA CAROLINE MANOHAR

PUBLICATIONS YEAR 2020-2021

Journal of Molecular Structure 1200 (2020) 127123

Contents lists available at ScienceDirect

Journal of Molecular Structure

journal homepage: http://www.elsevier.com/locate/molstruc

Spectroscopic and DFT studies, structural determination, chemical properties and molecular docking of 1-(3-bromo-2-thienyl)-3-[4-(dimethylamino)-phenyl]prop-2-en-1-one

P. Ramesh [a, b, e], M. Lydia Caroline [a, c], S. Muthu [a, *], B. Narayana [d], M. Raja [e], S. Aayisha [f, g]

[a] Department of Physics, Arignar Anna Govt. Arts College, Cheyyar, 604407, Tamilnadu, India
[b] Thiruvalluvar University, Serkkadu, Vellore, 632 115, Tamilnadu, India
[c] Department of Physics, Dr.Ambedkar Government Arts College, Chennai, 39, Tamilnadu, India
[d] Department of Chemistry, Mangalore University, Mangalagangotri, 574 199, Karnataka, India
[e] Department of Physics, Govt. Thirumagal Mills College, Gudiyatham, Vellore, 632602, Tamilnadu, India
[f] Department of Physics, Meenakshi College for Women, Chennai, 600024, Tamilnadu, India
[g] Research and Development Centre, Bharathiar University, Coimbatore, 641046, Tamilnadu, India

ARTICLE INFO

Article history:
Received 5 July 2019
Received in revised form
20 September 2019
Accepted 24 September 2019
Available online 30 September 2019

Keywords:
DFT
FT-IR
FT-Raman
Molecular docking
Condensed Fukui function

ABSTRACT

The bromo based theyophen chalcone derivative 1-(3-Bromo-2-thienyl)-3-[4-(dimethylamino)-phenyl] prop-2-en-1-one (BTDAP) has been investigated by spectroscopy and quantum chemistry methods using Gaussian09 software package. The stable conformation of molecular structure, vibrational frequencies and electronic absorption spectra were established using B3LYP/6-311++G(d,p) and M062x/6-311++G(d,p) calculations. The Infrared intensities, Raman scattering active regions have been calculated. UV–Visible absorption spectrum has showed the best agreement with their experimental results. The formation of the donor and the acceptor stabilization energies, molecular bonding which is composed from orbitals that have been localized on different atoms and molecular bond angular properties were investigated using NBO, NLMO and NHO calculations. Frontier molecular orbital analysis which explains the energy gap between the ground state HOMO and first excited state LUMO energies were determined. Besides, the chemical properties of condensed Fukui function, MEP and electron-hole charge transfer within the molecule due to excitation for three excited states were obtained by multiwfn software. Molecular docking studies were performed for the title compound with Monoamine oxidase A and B inhibitions.

1. Introduction

The title compound which is known as bromo substituted thienyl chalcone has multiple biological activities including anti-bacterial, antifungal, anti-inflammatory and anticancer agents [1]. The chemical formula of BTDAP is $C_{15}H_{14}BrNOS$ and its chemical formula weight is 353.23 kg/mol. Previously, several natural and synthetic chalcone derivatives were reported at where they inhibit Monoamine oxidase A, B, and MAO-A, MAO-B which are the two isoenzymes responsible for catalyzing the oxidative deamination of neurotransmitters and for dietary amines [2]. MAO-A is best the known powerful anti-depressants, clinical depressants and anxiolytics as well as effective therapeutic agents for bulimia, social phobia, and panic disorder. They are particularly effective in treatment of resistant depression and atypical depression [3]. MAO-B is also used in the treatment of Parkinson's disease, at where the symptoms associated with Alzheimer's disease and several other disorders [4]. Further insight into the biological evaluation of the possible interactions between the title compound and monoamine oxidases (MAO-A and MAO-B) inhibitor active site proteins have been developed through docking studies.

In this work, conformation stability actions of PES were investigated. The structural characterization of the compound was accomplished theoretically and experimentally by FT-IR and FT-Raman spectroscopic methods. The molecular electron transactions (UV–Vis) have been discussed using TD-DFT method. The chemical reactivity of the given molecule is calculated with the help of molecular reactivity descriptors such as condensed Fukui

* Corresponding author.
E-mail address: mutgee@gmail.com (S. Muthu).

https://doi.org/10.1016/j.molstruc.2019.127123
0022-2860/

Table 1
Geometrical parameters optimized in bond length (Å) and bond angle (°) for BTDAP with 6−311++G (d,P) basis set.

Parameters	Experimental[a]	B3LYP/6-311++G(d,p)	Parameters	Experimental[a]	B3LYP/6-311++G(d,p)
Bond length(Å)			Bond angle(°)		
Br_1-C_2	1.886	1.896	$C_3-C_7-O_{19}$	117.00	119.90
C_2-C_3	1.400	1.380	$S_4-C_5-C_6$	114.43	112.00
C_2-C_6	1.444	1.422	$S_4-C_5-H_{20}$	123.80	120.10
C_3-S_4	1.735	1.758	$C_6-C_5-H_{20}$	124.70	128.00
C_3-C_7	1.480	1.489	$C_5-C_6-H_{21}$	122.30	124.40
S_4-C_5	1.735	1.722	$C_8-C_7-O_{19}$	122.60	122.60
C_5-C_6	1.369	1.365	$C_7-C_8-C_9$	121.20	120.30
C_5-H_{20}	0.930	1.080	$C_7-C_8-H_{22}$	118.90	118.70
C_6-H_{21}	0.930	1.081	$C_9-C_8-H_{22}$	119.40	121.00
C_7-C_8	1.480	1.476	$C_8-C_9-C_{10}$	123.50	128.40
C_7-O_{19}	1.225	1.225	$C_8-C_9-H_{23}$	116.30	115.70
C_8-C_9	1.332	1.350	$C_{10}-C_9-H_{23}$	118.30	115.90
C_8-H_{22}	0.930	1.084	$C_9-C_{10}-C_{11}$	121.20	119.30
C_9-C_{10}	1.443	1.450	$C_9-C_{10}-C_{15}$	123.40	124.00
C_9-H_{23}	0.960	1.088	$C_{10}-C_{11}-C_{15}$	116.90	116.60
$C_{10}-C_{11}$	1.407	1.406	$C_{10}-C_{11}-C_{12}$	121.20	122.30
$C_{10}-C_{15}$	1.401	1.408	$C_{10}-C_{11}-H_{24}$	118.90	118.90
$C_{11}-C_{12}$	1.368	1.384	$C_{10}-C_{15}-C_{14}$	121.20	121.90
$C_{11}-H_{24}$	0.930	1.085	$C_{10}-C_{15}-H_{27}$	118.80	119.80
$C_{12}-C_{13}$	1.403	1.414	$C_{12}-C_{11}-H_{24}$	118.80	118.80
$C_{12}-H_{25}$	0.960	1.081	$C_{11}-C_{12}-C_{13}$	121.00	120.80
$C_{13}-C_{14}$	1.403	1.418	$C_{11}-C_{12}-H_{25}$	118.90	118.70
$C_{13}-N_{16}$	1.367	1.378	$C_{13}-C_{12}-H_{25}$	119.40	120.50
$C_{14}-C_{15}$	1.368	1.381	$C_{12}-C_{13}-C_{14}$	116.90	117.10
$C_{14}-H_{26}$	0.930	1.081	$C_{12}-C_{13}-N_{16}$	122.00	121.60
$C_{15}-H_{27}$	0.960	1.084	$C_{14}-C_{13}-N_{16}$	121.00	121.30
$N_{16}-C_{17}$	1.445	1.455	$C_{13}-C_{14}-C_{15}$	121.10	121.20
$N_{16}-C_{18}$	1.453	1.455	$C_{13}-C_{14}-H_{26}$	119.40	120.20
$C_{17}-H_{28}$	0.960	1.098	$C_{13}-N_{16}-C_{17}$	120.40	119.90
$C_{17}-H_{29}$	0.960	1.089	$C_{13}-N_{16}-C_{18}$	121.00	120.10
$C_{17}-H_{30}$	0.930	1.094	$C_{15}-C_{14}-H_{26}$	119.40	118.60
$C_{18}-H_{31}$	0.960	1.094	$C_{14}-C_{15}-H_{27}$	119.40	118.20
$C_{18}-H_{32}$	0.930	1.089	$C_{17}-N_{16}-C_{18}$	121.40	118.70
$C_{18}-H_{33}$	0.960	1.098	$N_{16}-C_{17}-H_{28}$	109.50	109.40
			$N_{16}-C_{17}-H_{29}$	109.50	109.10
Bond angle(°)			$N_{16}-C_{17}-H_{30}$	109.50	109.50
$Br_1-C_2-C_3$	126.34	126.00	$N_{16}-C_{18}-H_{31}$	109.50	111.30
$Br_1-C_2-C_6$	119.00	119.50	$N_{16}-C_{18}-H_{32}$	109.50	109.00
$C_3-C_2-C_6$	114.70	114.50	$N_{16}-C_{18}-H_{33}$	109.50	112.30
$C_2-C_3-S_4$	108.81	108.90	$H_{28}-C_{17}-H_{29}$	109.50	108.20
$C_2-C_3-C_7$	127.50	129.50	$H_{28}-C_{17}-H_{30}$	109.50	108.20
$C_2-C_6-C_5$	112.00	112.30	$H_{29}-C_{17}-H_{30}$	109.50	107.70
$C_2-C_6-H_{21}$	124.00	123.30	$H_{31}-C_{18}-H_{32}$	109.50	107.60
$S_4-C_3-C_7$	123.80	121.60	$H_{31}-C_{18}-H_{33}$	109.50	108.20
$C_3-S_4-C_5$	92.33	92.40	$H_{32}-C_{18}-H_{33}$	109.50	108.20
$C_3-C_7-C_8$	116.30	117.60			

[a] Ref. [5].

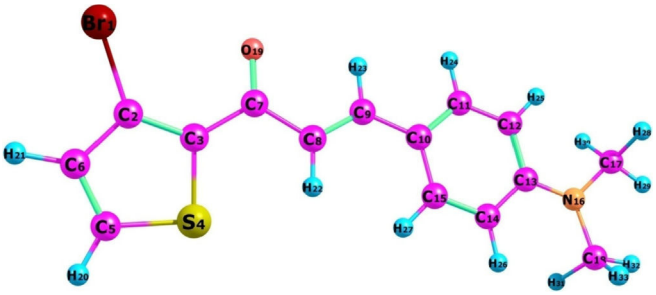

Fig. 1. Optimized structure of 1-(3-Bromo-2-thienyl)-3-[4-(dimethylamino)-phenyl] prop-2-en-1-one.

functions, HOMO- LUMO analyses, NHO, NLMO, NBO and MEP analyses. The ligand-receptor interaction of the compound was explored by the molecular docking and the human MAO-A and MAO-B inhibitors (PDB Code: 2BXR and 2BYB) have been identified as the potential target proteins.

2. Experimental methods

FT-IR spectra were recorded on PerkinElmer spectrum (resolution 1.0 cm^{-1} and scale range 450−4000 cm^{-1}) is dispersed in KBr pellets depending on the region of interest. FT-Raman spectrum has been recorded on BRUKER RFS 27 spectrometer in scale range 50−4000 cm^{-1} and resolution 2 cm^{-1}. The electronic transition (UV−Vis) spectra were recorded on JASCO spectrometer with the model name UV-670 in cell length 10 mm. Ray J. Butcher et al. reported the syntheses procedure of the present molecule [5].

3. Computational details

The title compound is optimized and their vibrational frequencies, Frontier molecular orbitals and bonding-antibonding stabilization energies are computed using the B3LYP/6-311++G(d,p) level of GAUSSIAN 09Wprogram package [6]. The theoretical UV−Visible spectrum was obtained by performing the TD-DFT method [7]. The electron-hole overlapping, HOMO-LUMO interaction, molecular electrostatic potential and Fukui functions

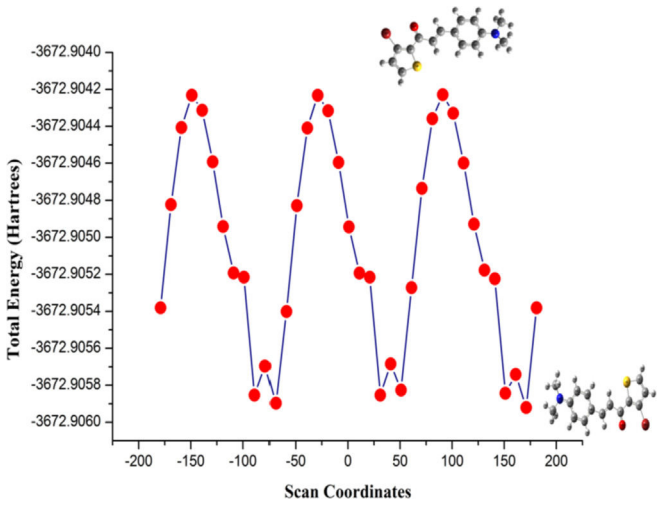

Fig. 2. Potential energy surface scan of 1-(3-Bromo-2-thienyl)-3-[4-(dimethylamino)-phenyl] prop-2-en-1-one.

were investigated by Multiwfn 3.4.1 [8]. AutoDock 4.2.1 program was used to find out the binding energy, inhibition constant and other biological parameters of the ligand-protein interactions [9].

4. Results and discussion

4.1. Potential energy surface (PES)

The potential energy surface curve was carried out by taking C_{13}—N_{16}—C_{18}—H_{31} as torsion angle for the present molecule. It has been determined in 36 steps of 10°. The angles are taken at every −180° up to 180°rotations. It's designated as the strongest confirmation about the rotational angle. The molecule structure of the transition state of saddle point and the minimum energy conformers for torsion angles have been given in Fig. 2. For this saddle point the torsion angles have been found out as −149°, −29°, and 90.99°, and the global maximum energy has been obtained at −3672.9042 Hartree. For this local minimum energy curve for the torsion angles has been found as −69°, 31°, global minimum energy curve for the torsion angles has been found as 171° the local and global minimum energy obtained at −3672.9058, −3672.9042 and −3672.9059 Hartree which have been shown in Fig. 2.

4.2. Geometrical structure analyses

The stable conformation of optimized structural parameters of BTDAP molecule is listed in Table 1 and optimized molecular structure with atom numbering scheme is shown Fig. 1. The molecule has six C═C and seven C—C bonds, thirteen C—H bonds, one C—Br bond, two C—S bonds, three C—N bonds, and one C═O bond. Theoretical bond length computed at C_2—Br_1, C_3—S_4, C_5—S_4 (1.896 Å, 1.758 Å, 1.722 Å) is almost equal to observed bond length (1.886 Å, 1.735 Å, 1.735 Å) which agrees on the X-ray diffraction [5].

The C—Br, C—S bonds are non-polar covalent bonds because they have almost equal sharing electrons due to the electronegativity difference which is less than 0.5 (ΔEN < 0.5), and due to the higher bond length. The sulphur atom is more polarized than a carbon atom. Although carbon and sulphur have similar electronegativities (EN = 2.55, 2.58), the bond is not polar based on electronegativity considerations. The effect of this increased polarizability for sulphur is that sulphur reacts as if the bond is polar in nature and the polarizability of the sulphur allows the bond to react as if it is polar when it has a nucleophilic approach.

The non-polar C_8═C_9 bond length is compared with other non-polar C═C bond length at where the value is low because, the adjacent C_7═O_{19} group undergo keto-enol tautomerism which refers to chemical equilibrium. The bond angles depend upon electronegativity difference (ΔEN) at where the electronegativity difference increases with the bond angle increment. For the present molecule, bromo substituted thienyl ring bond angles have been computed and observed at (C_3—C_2—Br_1, C_6—C_3—Br_1, C_3—S_4—C_5, S_4—C_5—H_{20}, C_6—C_5—S_4) as (126/126.34°, 119.5/119°,92.4/92.33°, 120.1/123.3°, 108.9/108.88°). The other functional group bond angles of (C_{13}—N_{16}—C_{18}, N_{16}—C_{17}—H_{28} and C12—C_{13}—N_{16}) are (120/120.1°, 109.4/109.5° and 121.6/122°). The carbon-carbon and carbon-hydrogen bond lengths for the phenyl ring of the title compound are almost same and their values from 1.38 Å −1.41 Å and 1.08 Å showing a closer agreement with the experimental data.

The theoretical optimized parameters and vibrational wavenumber values have small variations from the experimental values due to the isolated state of molecule in the gaseous phase in theoretical calculations; meanwhile the experimental results of the molecule are in the solid state.

4.3. Vibrational analysis

The FT-IR, FT-Raman spectra and fundamental vibration frequencies are computed at DFT method. The title molecule is having 33 atoms (N) which corresponds to (3N-6) = 93 modes of fundamental vibrations lively in both IR and Raman spectra. The vibrational frequencies are obtained for the title compound with the unscaled force field which is detected to be slightly greater than the experimental values. The unscaled vibrational wavenumber is scaled by a factor of 0.961. The potential energy distributions are calculated by the VEDA programme [10]. The theoretical and experimental wavenumbers, IR-Intensity, Raman activity and the percentage of PED are depicted in Table 2. The comparative FT-IR and FT-Raman spectra are shown in Figs. 3 and 4.

4.3.1. 3-Bromo-2-thienyl ring vibration

The 3-Bromo-2-thienyl ring has two C—H stretching vibrations in FT-IR (3130 cm^{-1}) and FT-Raman (3081 cm^{-1}) spectrums and their corresponding theoretical vibrations are at 3117, 3095 cm^{-1}which have a pure mode of PED 99, and 100%. The non-polar covalent S—C stretching and C—S—C bending vibrations were obtained theoretically at 845, 796, 757, and 621 cm^{-1} which has relevant mixed vibration of PED values in stretching 13, 16, 29, 20% and in bending 10, 17, 33%. The corresponding experimental stretching and bending vibrations of FT-IR are seen at 863, 819, 758 and 660 cm^{-1} and FT-Raman experimental stretching vibration has been seen at 874 cm^{-1} spectra.

The stretching vibration Br—C of the FT-IR and FT-Raman are scaled values obtained in the region 290 cm^{-1} and observed FT-Raman was seen at 246 cm^{-1} with relevant PED value of 54%. Along with Br—C—C bending vibration which is present at 326 cm^{-1} in FT-Raman spectrum with the consequent theoretical vibrations of 330, 260 cm^{-1}, the PED occupying value is noted as 16%. The C—C stretching vibrations, C—C—C bending vibrations which have PEDs are scheduled in Table 2.

4.3.2. C═O vibration

The polar covalent stretching vibration of carboxylic acid (C═O) is expected in the region 1740–1660 cm^{-1} [11]. The band is reasonably easy to be recognized due to its high intensity, strong polarizations and dipole moment [12]. This multiple bonded group is highly polarized and therefore gives rise to an intense infrared absorption band. In the present molecule, spectra were identified at

Table: 2
Comparison of the experimental and calculated vibrational spectra and proposed assignments of BTDAP at B3LYP method with 6−311++G(d,P) basis set.

Mode	Experimental wave number (cm^{-1})		Theoretical wave number(cm^{-1})		I_{IR}[c]	I_{RAMAN}[d]	Assignments (PED)[a]
	FT-IR	FT-Raman	Unscaled	Scaled[b]			
1	3130(w)		3243	3117	0	3	rCH(99)
2		3081(vw)	3221	3095	0	1	rCH(100)
3			3213	3088	1	1	rCH(93)
4	3071(m)		3210	3085	1	1	rCH(91)
5			3178	3054	1	0	rCH(95)
6			3170	3046	0	0	rCH(95)
7		3025(vw)	3166	3043	0	1	rCH(95)
8			3143	3020	0	0	rCH(97)
9	3012(w)		3134	3012	3	2	rCH(93)
10		3002(vw)	3121	2999	0	0	rCH(92)
11			3050	2931	3	1	rCH(90)
12	2905(m)	2919(vw)	3048	2929	2	1	rCH(91)
13		2096(vw)	2991	2874	9	3	rCH(85)
14	2863(s)		2984	2868	6	2	rCH(82)
15	1613(vs)	1622(vw)	1704	1638	10	0	rOC(59)+rCC(19)
16		1606(vw)	1659	1594	3	0	rCC(43)
17	1563(s)		1613	1550	100	100	rOC(21)+rCC(24)
18	1522(vs)	1538(s)	1579	1517	5	5	rCC(35)+θCCC(12)
19			1557	1496	33	0	rNC(16)+θHCC(31)
20		1475(vw)	1531	1471	0	3	rCC(10)+θHCH(32)
21			1530	1470	12	1	rCC(52)
22	1448(w)	1439(m)	1515	1456	1	0	θHCH(54)
23	1433(w)	1408(m)	1494	1436	1	0	θHCH(90)
24			1487	1429	2	0	θHCH(75)
25			1485	1427	1	0	θHCH(74)
26	1406(w)		1468	1411	6	1	rCC(39)+θHCC(17)
27	1397(vw)		1446	1390	2	0	θHCH(71)
28	1371(vw)	1373(m)	1442	1386	16	10	rCC(73)
29			1386	1332	28	3	rNC(37)
30			1376	1322	8	1	rCC(22)+θHCS(22)+θHCC(19)
31		1314(m)	1365	1312	1	0	rCC(14)
32			1361	1308	7	1	θHCC(68)
33			1341	1289	4	5	rCC(18)+θHCC(35)
34		1293(m)	1325	1273	2	0	rCC(32)+θHCC(20)
35	1224(m)	1232(vw)	1265	1216	2	0	rNC(34)+rCC(16)+θHCC(11)
36		1182(m)	1248	1199	1	0	rCC(12)+θHCC(35)
37	1166(vw)		1212	1165	8	7	θHCC(42)
38	1174(vw)		1198	1151	7	0	rCC(14)+θHCC(10)
39			1189	1143	25	1	rCC(17)+θHCC(13)
40			1155	1110	1	0	rCC(11)+θHCC(50)
41			1147	1102	6	0	rCC(12)+θCCC(21)+θHCS(16)
42			1138	1094	5	1	φHCNC(63)+θHCH(10)
43	1087(m)	1089(vw)	1133	1089	0	0	φHCNC(64)+θHCH(10)
44			1102	1059	7	1	rCC(12)+θHCS(36)+θHCC(30)
45	1057(s)		1077	1035	2	0	rNC(28)+φHCNC(52)
46			1036	996	14	3	rCC(46)+θCCC(10)
47			1019	979	2	0	φHCCC(77)
48	986(w)	988(vw)	1017	977	1	0	θCCC(76)
49			963	925	0	0	φHCCC(64)+φHCCN(19)+φCCCC(13)
50	942(s)		961	924	2	0	rNC(46)
51			951	914	0	0	φCCCC(73)+φCCCC(15)
52			895	860	0	0	φHCSC(82)+φSCCC(12)
53			894	859	1	0	rCC(20)+θOCC(10)+θCCC(14)
54	863(m)	874(vw)	879	845	3	0	rSC(13)+θSCC(10)+θCCC(42)
55			865	831	1	0	φHCCC(70)
56			828	796	5	0	φHCCN(30)+φHCCC(46)
57	819(w)		819	787	1	1	rSC(16)+θSCC(17)
58			808	776	0	0	φHCCN(30)+φHCCC(65)
59	758(w)		788	757	3	0	rSC(29)
60			761	731	1	0	ψOCCC(30)+ψNCCC(10)
61			731	702	1	0	φHCSC(39)+φHCCS(11)+ψNCCC(11)
62	697(w)	702(vw)	717	689	2	0	rNC(21)+θCCC(17)
63			704	677	1	0	ψOCCC(31)+φHCSC(26)
64			655	629	1	0	θCCC(36)
65	660(w)		646	621	3	0	rSC(20)+θSCC(33)
66			605	581	0	0	φCCCC(45)+ψBrCCC(24)+φHCCS(13)
67	545(w)	538(vw)	551	530	3	0	θCCC(25)+θCNC(19)
68	517(w)		524	504	1	0	ψCCCC(10)+ψNCCC(37)
69		479(wv)	511	491	1	0	θNCC(10)+θCCC(10)+θCNC(20)
70			473	455	0	0	θCNC(28)+θNCC(13)+θCCC(10)
71			459	441	0	0	φSCCC(62)
72		420(vw)	429	412	0	0	φCCCC(49)+φHCCC(23)

Table: 2 (*continued*)

Mode	Experimental wave number (cm^{-1})		Theoretical wave number(cm^{-1})		I_{IR}[c]	I_{RAMAN}[d]	Assignments (PED)[a]
	FT-IR	FT-Raman	Unscaled	Scaled[b]			
73			417	401	0	0	θOCC(12)+θCNC(14)
74			401	385	0	0	rCC(19)+θCNC(19)
75			378	363	0	0	φCCCC(32)+ψCCCC(34)
76		326 (w)	343	330	1	0	θCCC(30)+θBrCC(16)+θOCC(10)
77		246 (vw)	302	290	0	0	rBrC(54)+θCCC(17)
78			271	260	0	0	θCNC(18)+θBrCC(16)+θNCC(17)
79			247	237	0	0	ψCCCN(32)+φCCCC(25)
80			228	219	0	0	φCCCC(21)+ψBrCCC(22)
81			221	212	0	0	θCCC(11)+φCCCC(13)+ψBrCCC(15)
82		171(vw)	185	178	0	0	φCNCC(12)+φHCNC(25)
83			155	149	0	0	θCCC(14)+φCCCC(38)
84			152	146	0	0	θCCC(14)+φCCCC(46)+ψBrCCC(12)
85		116(vw)	136	131	0	0	φCCCC(52)+φCCNC(10)+φHCNC(10)
86			102	98	0	0	θCCC(18)+θBrCC(17)+φCCCC(12)
87			98	94	0	0	φCCCC(41)+θCCC(13)
88		72(vw)	75	72	1	0	φHCNC(44)
89			72	69	0	0	φCNCC(63)
90			47	45	0	0	φCCCC(11)+ψCCCN(27)+ψCCCC(11)
91			39	37	0	0	θCCC(85)
92			21	20	0	0	φCCCC(70)
93			9	9	0	0	φCCCC(77)

[a] r-stretching, θ-bending, , φ-torsion, ψ-out, vs-very strong, s-strong, m-medium, w-weak.
[b] Scaling factor: 0.961 for B3LYP/6-311 + G(d,p).
[c] Relative absorption intensities normalized with highest peak absorption equal to 100.
[d] Relative Raman intensities normalized to 100.

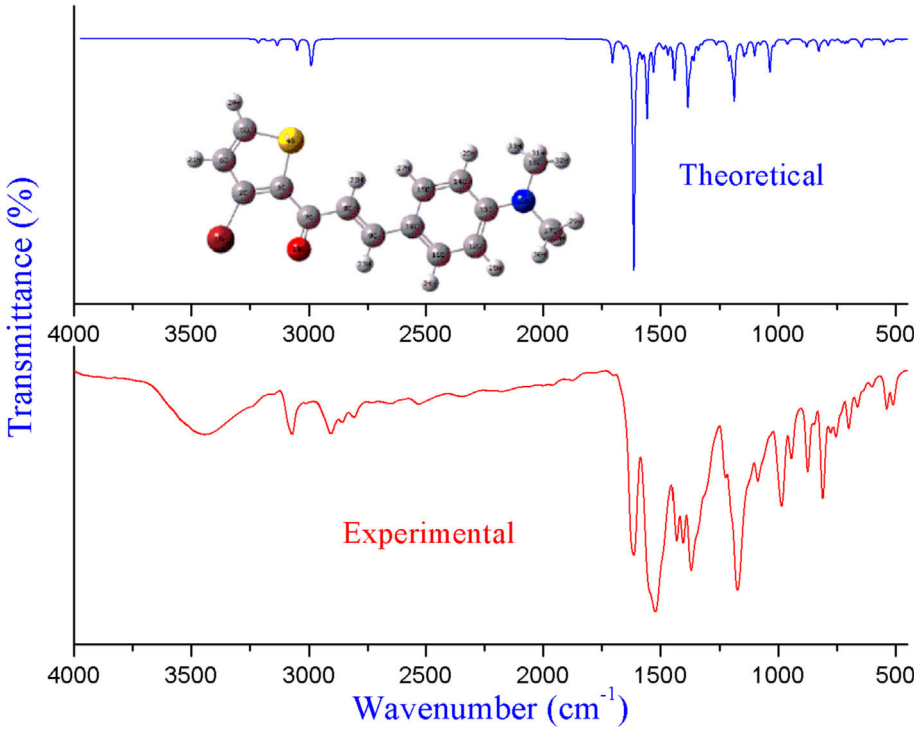

Fig. 3. FT-IR spectra of 1-(3-Bromo-2-thienyl)-3-[4-(dimethylamino)-phenyl] prop-2-en-1-one using B3LYP/6-311++G(d.p) and experimental data{{}}

1613 cm^{-1} in FT-IR and 1622 cm^{-1} in FT-Raman which is assigned for C═O vibrations at 1638 cm^{-1} with PED contributions of 59%.

4.3.3. Phenyl ring vibrations

The aromatic C–H stretching wavenumbers generally exhibit multiple peaks in the spectral range of 3100–3000 cm^{-1} [13]. In the present investigation, the title compound observed C–H stretching wavenumber at 3071 cm^{-1} in FT-infrared and 3025 cm^{-1}in FT-Raman with the theoretical wavenumber between 3088, 3085, 3054, 3044 cm^{-1} which is a pure mode of PED values between 91 and 95%.The aromatic and hetero-aromatic compounds in C–C stretching wavenumbers are expected to arise at 1650-1400 cm^{-1} [14]. In the present molecule, the C–C stretching bands at 1563, 1522, 1406, 1371,986 cm^{-1} in FT-IR and 1606, 1538, 1373, 1293,

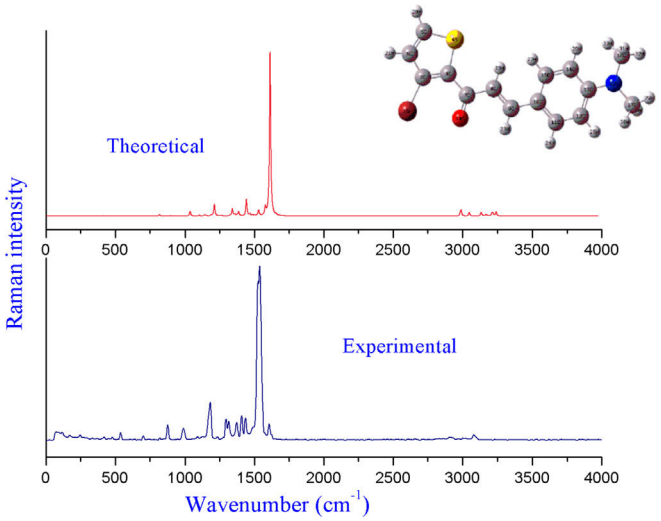

Fig. 4. FT-RAMAN spectra of 1-(3-Bromo-2-thienyl)-3-[4-(dimethylamino)-phenyl] prop-2-en-1-one using B3LYP/6-311++G(d.p) and experimental data.

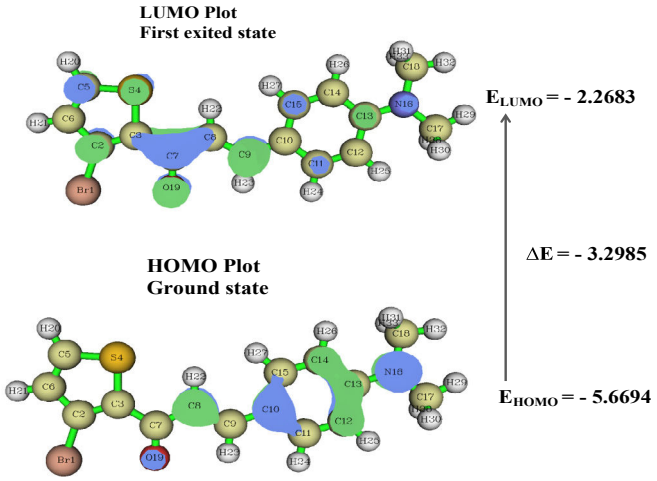

Fig. 5. Atomic orbital HOMO - LUMO composition of the frontier molecular orbital of the 1-(3-Bromo-2-thienyl)-3-[4-(dimethylamino)-phenyl] prop-2-en-1-one.

Table 3
The calculated quantum chemical parameters of title compound.

Chemical parameters	B3LYP/6-311++G(d, p)
HOMO(eV)	−5.566
LUMO(eV)	−2.268
Ionization potential(IP)	5.5669
Electron affinity(EA)	2.2684
Energy gap(eV)	3.2986
Electronegativity (χ)	3.9176
Chemical potential (μ)	−3.9176
Chemical hardness (η)	1.6493
Chemical softness (S)	0.3032
Electrophilicity index(ω)	4.6529
Electronic charge	2.3753
Electron donating capability (w^-)	6.8178
Electron accepting capability (w^+)	2.9002

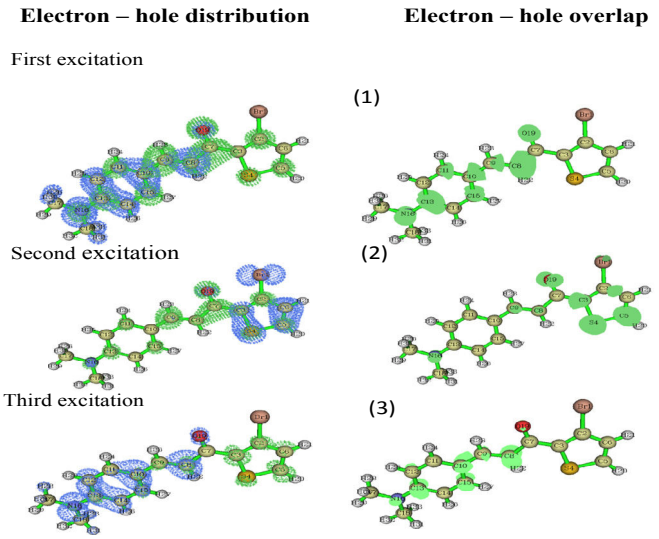

Fig. 6. Electron – hole distribution, Electron – hole overlap for the three excited states of the title compound.

988 cm^{-1} in FT-Raman have been measured with their scaled values 1594, 1550, 1517, 1417, 1385, 1276, 977 cm^{-1}. The C–C–C scaled bending vibrations are also found from 1517(1522/1538 exp. FT-IR/FT-Raman), 977(986/1988 exp. FT-IR/FT-Raman) $cm^{-1}$with relevant mixed stretching and bending potential energy distribution values and are listed in Table .2.

4.3.4. C–N Vibration

In present investigation, the molecule has C–N stretching bands at 1224, 1057, 942, 697 cm^{-1} in FT-IR and 1232, 702 cm^{-1} in FT-Raman with their scaled values at1496, 1332, 1216, 1035, 924 and 689 cm^{-1} with PED contributions of 16, 37, 34, 28, 46, 21%.

4.3.5. Methyl group vibration

In the current study, the methyl (CH_3) group C–H stretching vibrationis established at 3012 cm^{-1} in FT-IR and at 3002 cm^{-1} in FT –Raman with their corresponding assigned values at 3012, 2999 cm^{-1} at where the related potential energy occupying values are above 93, 92%. The asymmetric and symmetric C–H stretching modes of CH_3 occurs at 2982–2962 cm^{-1} and 2882–2862 cm^{-1} [15]. The asymmetric stretching wavenumber is observed at 2905 and 2919 cm^{-1} in FT-IR & FT-Raman spectra and this computed scale value is 2931, 2927 cm^{-1} (PED 90, 91%). The CH_3 symmetric stretching wavenumber has been observed at 2863 and 2906 cm^{-1} in the FT-IR & FT-Raman spectra and calculated theoretically at 2874, 2863 $cm^{-1}$with good PED values.

The symmetric and anti-symmetric bending vibrations of the methyl deformations normally emerges in the range 1355–1395 and 1430 - 1470 cm^{-1} [16]. The asymmetrical bending observed at 1433 and 1408 cm^{-1} in FT-IR & FT-Raman spectra are assigned as the CH_3 asymmetrical deformation and their calculated scale value is reported at 1436, 1427 cm^{-1} (PED 90, 74%). The CH_3 symmetric bending vibration has been observed at 1397 cm^{-1} in the FT-IR spectrum and their computed values are reported at 1429, 1390 cm^{-1} with PED at 75, 71%. The bending vibrations of CH_2 deformations are expected in the region 1480–1400 cm^{-1}(scissoring) [17]. The scissoring vibration of CH_2 is assigned at 1471, 1456 cm^{-1} theoretically and observed in FT-IR spectrum at 1448 $cm^{-1}$and observed in FT-Raman spectrum at 1475, 1439 cm^{-1}.

Table: 4
Three excited states, excitation energy, hole-electron distribution, transition density, Δr index, and charge-transfer length (CT) for.

Parameters	First Transition	Second Transition	Third Transition
Excitation energy (eV)	3.1454	3.4545	4.3055
λ max value (nm)	394.44	359.15	288.16
Oscillator strength	0.9563	0	0.0537
Integral of transition density	−0.0004	0.0003	0.0007
Integral of overlap of hole-electron distribution	0.3130	0.2599	0.1690
CT length- Distance between centriod of hole electron (Å)	3.3911	2.9294	5.8566
Δr −index (Å)	4.2272	3.0792	4.4827

BTDAP.

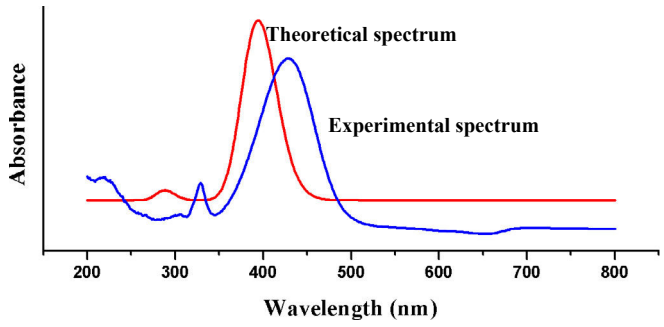

Fig. 7. Experimental and theoretical UV−Vis spectra of the BTDAP.

5. Frontier molecular orbital energy analysis

Frontier molecular orbital theory is an application of the MO theory that describes the interactions of HOMO and LUMO interactions. The energy of HOMO indicates nucleophilicity, and LUMO indicates electrophilicity [18]. The HOMO-LUMO energy gap reflects chemical reactivity and provides an essential approach into its bioactivity from the charge transfer interactions within the molecule. Title molecule computed band gap energy difference between ground state HOMO energy (−5.5669eV) and first excitation state of LUMO energy (−2.2683eV) was found as ΔE = 3.2985 eV at where the energy gap was reflected due to the bioactive molecules [19]. HOMO − LUMO energy difference plot of the frontier molecular orbital for the present compound is represented in Fig. 5 using Multiwfn programand the global reactivity descriptors calculated from the HOMO and LUMO energies with respect to the chemical parameters are listed in Table 3. The present molecule has a low softness value (0.3). The calculated maximum value of Ionization potential (IP = 5.56 eV), electronegativity (χ = 3.9 eV), Electron donating capability (w^{-} = 6.81 eV) electrophilicity index (ω = 5.28) describes the biological activity.

The study of the correlation between Molecular orbital energy gaps give rise to the electron-hole charge transfer due to the excitation, transition density, λ max value, oscillator strength (f), charge-transfer length (D), excitation energy (E), Δr index and so on for different electron transition modes of the title compound at where Multiwfn program is used.

Isosurface of electron-hole (green-blue) distributions and the electron-hole overlap for the three excited states are shown in Fig. 6. The electron−hole charge transition parameter values of the title compound have been scheduled in Table 4. The overlap integral of electron-hole distribution (S) measures the spatial separation of electrons and holes. The charge transfer is expected to be more when the integral of overlap of electron-hole distribution is less. Charge transfer length (CT) gives the distance between the centroid of hole and electron at where greater the value of electron-hole distance longer the charge transfer within the molecule. The movement of charge density from one place to another place is expected to occur when the spatial separation of hole and electron is largely leading to charge transfer excitation. The Δr index is a quantitative indicator of electron excitation mode and also a measure of CT length [20] at where the larger Δr value indicates more charge transfer within the molecule at the corresponding excited state with the first and third mode for the present molecule. From the above summarised list of the table, the Charge-transfer excitation (CT) of the first and third excitation state has large value and Δr is also higher for the same mode indicating the fact that the first and third excitation mode corresponds to a strong charge transfer excitation. The overlap integral of electron-hole distribution was found to be small in the third excited state when comparing its first and second excited states.

The experimental electronic absorption spectrum (UV−Vis) of the title compound in the region 200−800 nm was attained in organic solvent acetone and the theoretical BTDAP molecule is calculated using TD-DFT method. The BTDAP compound has been observed and simulated by UV−Vis spectra and displayed in Fig. 7. The three excitation energies, λ-max values, oscillator strengths (f), HOMO and LUMO major contributions are listed in Table 5. One can note that there are two peaks observed at 429 and 326 nm in experimental spectra (see Fig. 7). These peaks are calculated theoretically at 394.18 and 287.97 nm which shows a better agreement with the experimental one. The first transition energy gap of title molecule calculated experimentally by UV−Visible spectrum is 2.89 eV and theoretically by TD-DFT (DMSO) method is 3.15eV with HOMO-LUMO energy gap of 3.29 eV. From multiwfn, the first order excitation energy has been found as 3.15eV which shows that all energy gap values are in good agreement.

Table 5
The UV−Vis wavelength (λ), band gap energy (ΔE) and oscillator strength (f) for BTDAP calculated by #td M062x/6-31++g(d,p) scrf=(solvent = Acetone) method.

Experimental			TD-DFT/m062x-6311++G(d,p) Solvent = Acetone			
Methanol solvent						
λ (nm)	E (eV)	Abs.	λ (nm)	E (eV)	*f* (a.u)	Major contribs
429	2.8977	0.3850	394.18	3.1551	0.9563	HOMO- > LUMO (91%)
_	–	–	358.91	3.4627	0	H-6- > LUMO (12%), H-3- > LUMO (77%)
326	3.8016	0.0912	287.97	4.3164	0.0537	HOMO- > L+1 (33%), HOMO- > L+6 (51%)

Table 6
Fukui Condensed Functions are evaluated by Frontier Molecular Orbital Method for BTDAP.

Atoms	Atomic No.	HOMO Electrophilic attack	LUMO Nucleophilic attack	Radical attack	Dual-Descriptor	Hardness	Local eletrophilic	Local nucleophilic
(N)	(Z)	(f_r^-)	(f_k^+)	(f_k^0)	(Δf_r)	(au)	W-(eV)	W+(eV)
Br_1	35	0.0029	0.0223	0.0126	0.0194	−0.001	0.0054	0.0414
C_2	6	0.0025	0.1184	0.0605	0.116	−0.0076	0.0046	0.2192
C_3	6	0.0024	0.0538	0.0281	0.0513	−0.0032	0.0045	0.0995
S_4	16	0.0009	0.0845	0.0427	0.0836	−0.0055	0.0017	0.1565
C_5	6	0.0023	0.1091	0.0557	0.1068	−0.007	0.0043	0.202
C_6	6	0.0009	0.0018	0.0014	0.0008	0.0001	0.0017	0.0033
C_7	6	0.0024	0.1163	0.0593	0.1138	−0.0074	0.0045	0.2152
C_8	6	0.1187	0.0386	0.0787	−0.0802	0.0194	0.2198	0.0714
C_9	6	0.0056	0.1561	0.0809	0.1505	−0.0095	0.0104	0.2889
C_{10}	6	0.1387	0.0016	0.0702	−0.1371	0.0256	0.2568	0.0030
C_{11}	6	0.0154	0.0276	0.0215	0.0122	0.0010	0.0285	0.0512
C_{12}	6	0.0916	0.0001	0.0458	−0.0916	0.0170	0.1696	0.0001
C_{13}	6	0.0448	0.0377	0.0413	−0.0071	0.0058	0.0830	0.0698
C_{14}	6	0.0731	0.0012	0.0371	−0.0718	0.0135	0.1352	0.0023
C_{15}	6	0.0163	0.0358	0.0261	0.0195	0.0006	0.0302	0.0663
N_{16}	7	0.3473	0.0244	0.1858	−0.3229	0.0627	0.6427	0.0451
C_{17}	6	0.0028	0.0004	0.0016	−0.0025	0.0005	0.0053	0.0007
C_{18}	6	0.0028	0.0005	0.0016	−0.0023	0.0005	0.0051	0.0009
O_{19}	8	0.0384	0.1611	0.0998	0.1227	−0.0038	0.0711	0.2982

6. Condensed Fukui function

The Fukui function describes the electron density after adding or removing some amount of electrons. Atomic charges are used to get the condensed Fukui function. There are several ways to split the atomic charges. R. G. Parr and W. Yang [21] reported condensed Fukui function and frontier function. The local reactivity descriptor like Fukui function indicates the preferred regions at where a molecular chemical species will alter its density when numbers of electrons are customized or it indicates propensity of electronic density to deform at a given position over accepting or donating electrons [22] to the HOMO or LUMO, respectively, i.e. the frontier orbitals whose importance was emphasized by Fukui. These concepts can be analyzed quantitatively using the DFT method.

Condensed Fukui function and local softness are one of the broadly used local density functional descriptors to find chemical reactivity and selectivity of the specific atomic site in a molecule [23,24]. The Fukui functions at the atom k results to be:

$$f_k^{\alpha} = \sum_{v=k}\left[|C_{v\alpha}|^2 + \sum_{x\notin\mu} C_{x\alpha}^{*} C_{v\alpha} S_{xv}\right] \quad (1)$$

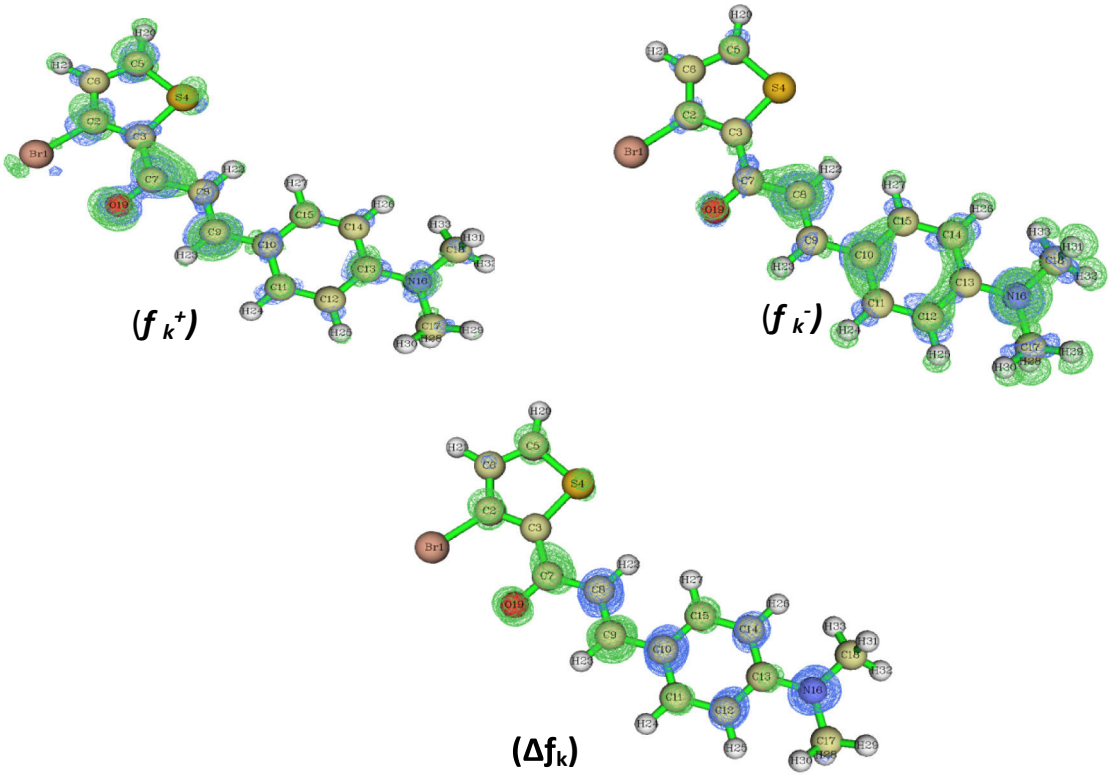

Fig. 8. Condensed Fukui function (f^+, f^-, Δf) of BTDAP.

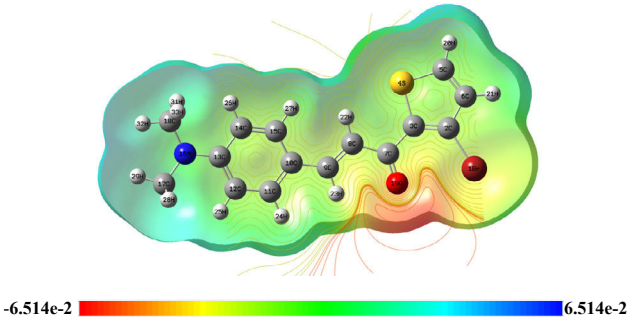

Fig. 9. Molecular Electrostatic Potential (MEP) of 1-(3-Bromo-2-thienyl)-3-[4-(dimethylamino)-phenyl] prop-2-en-1-one.

where $C_{v\alpha}$ are the molecular frontier orbital coefficients and S_{xv} are the atomic orbital overlap matrix elements

$$f_k^- = \sum_{v\in k}\left[|C_{vH}|^2 + \sum_{\chi\notin v} C_{\chi H}^* C_{vH} S_{\chi v}\right] \quad \left(\text{for HOMO electrophonic attack}\right) \tag{2}$$

$$f_k^+ = \sum_{v\in k}\left[|C_{vL}|^2 + \sum_{\chi\notin v} C_{\chi L}^* C_{vL} S_{\chi v}\right] \quad \left(\text{for LUMO Nucleophilic attack}\right) \tag{3}$$

$$f_k^0 = \frac{1}{2}\left(f_k^+ + f_k^-\right) \quad \left(\text{for radical attack}\right) \tag{4}$$

The sub-indexes "H" and "L" are referenced to the HOMO and LUMO orbitals. When the molecule gains electrons (electron removal to the LUMO of the neutral molecule) it has reactivity site of the electrophilic attack f_k^-, when the molecule losses electrons (electron addition from the HOMO of the neutral molecule) it has reactivity site of the nucleophilic attack f_k^+ and when the molecule has neutral electrons then they are in radical attack f_k^0.

Local electrophilicity (nucleophilic attack), Local nucleophilicity (electrophilic attack), and local Hardness and the second order Fukui function are called Dual-Descriptor $\Delta f(r)$. Using a finite difference approximation [25,26] it has been defined as:

Table 7
Hirshfeld atomic charges for BTDAP.

Element name,	Atomic charge
Br_1	−0.01
C_2	−0.01
C_3	−0.04
S_4	0.10
C_5	−0.06
C_6	−0.06
C_7	0.12
C_8	−0.08
C_9	0.00
C_{10}	−0.02
C_{11}	−0.03
C_{12}	−0.07
C_{13}	0.05
C_{14}	−0.06
C_{15}	−0.03
N_{16}	−0.04
C_{17}	−0.03
C_{18}	−0.03
O_{19}	−0.26

$$w_k^+ = w f_k^+ \quad \text{For local Electrophilicity} \tag{5}$$

$$w_k^- = w f_k^- \quad \text{For local Nucleophilicity} \tag{6}$$

$$\eta_k = \in_L f_k^+ - \in_H f_k^- \quad \text{For local Hardness} \tag{7}$$

$$\Delta f(r) = |f_r^+ - f_r^-| \quad \text{For duel} - \text{descriptor} \tag{8}$$

By using FMO theory, local descriptors are calculated for the selected atomic site of BTDAP which has been listed in Table 6 and maximum tenancy of electrophilic, nucleophilic and dual-descriptor were shown in Fig. 8. The individual atoms are compared to maximum electrophilic attack (f_k^- = 0.3473 eV), Radical attack (f_k^+ = 0.1858 eV), Dual-Descriptor ($\Delta f(r) = -0.3229$ eV), Hardness (0.62 au) and Local electrophilic (w_k^- = 0.64 eV), nitrogen atom and oxygen atom maximum nucleophilic attack (f_k^+ = 0.16 eV), Local nucleophilic (w_k^+ = 0.29 eV) of

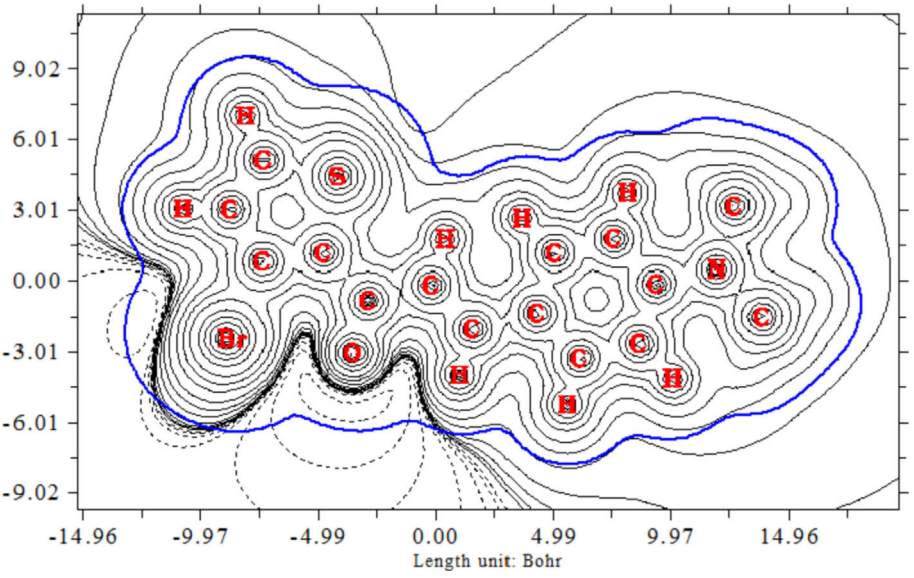

Fig. 10. Molecular Electrostatic Potential (MEP) contour map of BTDAP obtained by multiwfn method.

Table 8
Second order perturbation theory analysis of Fock matrix in NBO basis for title molecule.

Donor(i)	Type	ED/e	Acceptor(i)	Type	ED/e	[a]E(2) (Kcal mol^{-1})	[b]E(J)-E(i) (a.u.)	[c]F(I,j) (a.u.)
C_2—C_3	π	1.80191	C_7—O_{19}	π*	0.26326	18.30	0.32	0.070
C_8—C_9	π	1.83251	C_7—O_{19}	π*	0.26326	22.90	0.29	0.075
C_{14}—H_{26}	σ	1.97471	C_{13}—N_{16}	σ*	0.03369	198.24	0.30	0.219
N_{16}—C_{17}	σ	1.9903	C_{11}—H_{24}	σ*	0.01459	170.15	0.50	0.260
N_{16}—C_{18}	σ	1.99029	C_{14}—C_{15}	σ*	0.01521	130.04	0.91	0.307
C_{17}—H_{28}	σ	1.99058	C_{11}—H_{24}	σ*	0.26326	72.96	0.30	0.132
C_{18}—H_{33}	σ	1.98836	Br_1—C_2	σ*	0.04	101.77	0.41	0.183
C_{18}—H_{33}	σ	1.98836	N_{16}—C_{18}	σ*	0.01522	45.65	0.65	0.153
Br_1	LP(1)	1.9938	C_5—H_{20}	σ*	0.01388	35.20	0.48	0.116
Br_1	LP(1)	1.9938	C_{11}—H_{24}	σ*	0.26326	13.29	0.75	0.089
Br_1	LP(1)	1.9938	C_{13}—N_{16}	σ*	0.03369	12.94	0.76	0.089
Br_1	LP(2)	1.9708	C_{13}—N_{16}	σ*	0.03369	4.23	0.06	0.014
Br_1	LP(3)	1.91247	C_2—C_3	σ*	0.40297	13.86	0.28	0.061
S_4	LP(2)	1.62182	Br_1—C_2	σ*	0.04	21.13	0.31	0.079
S_4	LP(2)	1.62182	C_2—C_3	π*	0.40297	13.16	0.32	0.058
S_4	LP(2)	1.62182	C_8—H_{22}	σ*	0.02079	7.97	0.67	0.072
S_4	LP(2)	1.62182	C_{14}—C_{15}	σ*	0.01521	52.07	0.47	0.155
S_4	LP(2)	1.62182	N_{16}—C_{18}	σ*	0.01522	10.49	0.55	0.075
S_4	LP(2)	1.62182	C_{18}—H_{31}	σ*	0.0179	5.31	3.67	0.138
N_{16}	LP(1)	1.72109	Br_1—C_2	σ*	0.04	4.18	0.24	0.030
N_{16}	LP(1)	1.72109	C_{11}—H_{24}	σ*	0.01459	130.16	0.02	0.046
N_{16}	LP(1)	1.72109	C_{12}—C_{13}	π*	0.43102	33.16	0.27	0.087
O_{19}	LP(2)	1.97997	C_3—C_7	σ*	0.06541	19.73	0.71	0.107
O_{19}	LP(2)	1.88023	C_7—C_8	σ*	0.0555	17.47	0.72	0.101
O_{19}	LP(2)	1.88023	C_8—H_{22}	σ*	0.02079	0.72	0.60	0.019

[a] $E^{(2)}$ means energy of hyper conjugative interaction (stabilization energy).
[b] Energy difference between donor and acceptor i and j NBO orbitals.
[c] F(i,j) is the Fock matrix element between i and j NBO orbitals.

Table 9
NLMO analysis for BTDAP.

NLMO	Occupancy	Polarization coefficient	Parant NBO Bond (A-B)	Percent of the NLMO each atom	Hybrid composition ratio of the NAOs	S(%)	P(%)
3	1.80191	0.6818*	π(C_2—C_3)	46.48%	$C_2SP^{(1.00)}$	0.00%	99.95%
		0.7316*		53.52%	$C_3SP^{(1.00)}$	0.00%	99.97%
16	1.83251	0.7495*	π(C_8—C_9)	56.17%	$C_8SP^{(1.00)}$	0.00%	99.96%
		0.6621*		43.83%	$C_9SP^{(1.00)}$	0.00%	99.93%
32	1.97471	0.7758*	σ(C_{14}—H_{26})	60.18%	$C_{14}SP^{(2.50)}$	28.54%	71.42%
		0.6310*		39.82%	$H_{26}SP^{(0.00)}$	99.95%	0.05%
34	1.9903	0.7928*	σ(N_{16}—C_{17})	62.85%	$N_{16}SP^{(2.15)}$	31.78%	68.19%
		0.6095*		37.15%	$C_{17}SP^{(3.3)}$	23.23%	76.64%
36	1.99058	0.7732*	σ(C_{17}—H_{28})	59.78%	$C_{17}SP^{(2.94)}$	25.36%	74.58%
		0.6342*		40.22%	$H_{28}SP^{(0.00)}$	99.97%	0.03%
41	1.98836	0.7743*	σ(C_{18}—H_{33})	59.95%	$C_{18}SP^{(2.84)}$	26.01%	73.93%
		0.6329*		40.05%	$H_{33}SP^{(0.00)}$	99.96%	0.04%
78	1.9938	—	LP(1)Br_1	—	$Br_1SP^{(0.16)}$	86.33%	13.66%
80	1.91247	—	LP(3)Br_1	—	$Br_1SP^{(1.00)}$	0.00%	99.97%
82	1.62182	—	LP(2)S_4	—	$S_4SP^{(1.00)}$	0.00%	99.91%
83	1.72109	—	LP(1)N_{16}	—	$N_{16}SP^{(1.00)}$	0.00%	100.00%
84	1.97997	—	LP(1)O_{19}	—	$O_{19}SP^{(0.72)}$	58.29%	41.69%
505	0.04	0.7201*	σ*(Br_1—C_2)	51.86%	$Br_1SP^{(6.39)}$	13.49%	86.11%
		−0.6939*		48.14%	$C_2SP^{(3.08)}$	24.48%	75.41%
507	0.40297	0.7316*	π*(C_2—C_3)	53.52%	$C_2SP^{(1.00)}$	0.00%	99.95%
		−0.6818*		46.48%	$C_3SP^{(1.00)}$	0.00%	99.97%
510	0.06541	0.6882*	σ*(C_3—C_7)	47.36%	$C_3SP^{(1.72)}$	36.72%	63.24%
		−0.7255*		52.64%	$C_7SP^{(1.94)}$	34.05%	65.90%
518	0.26326	0.8265*	π*(C_7—O_{19})	68.31%	$C_7SP^{(1.00)}$	0.00%	99.62%
		−0.5630*		31.69%	$O_{19}SP^{(1.00)}$	0.00%	99.89%
520	0.13742	0.6621*	π*(C_8—C_9)	43.83%	$C_8SP^{(1.00)}$	0.00%	99.96%
		−0.7495*		56.17%	$C_9SP^{(1.00)}$	0.00%	99.93%
528	0.01459	0.6264*	σ*(C_{11}—H_{24})	39.24%	$C_{11}SP^{(2.55)}$	28.15%	71.79%
		−0.7795*		60.76%	$H_{24}SP^{(0.00)}$	99.94%	0.06%
533	0.03369	0.7848*	σ*(C_{13}—N_{16})	61.59%	$N_{16}SP^{(1.74)}$	27.19%	72.71%
		−0.6197*		38.41%	$C_{11}SP^{(2.55)}$	36.42%	63.54%

the title compound.

7. Molecular electrical potential surface

The molecular electrostatic potential maps help to visualize charge distribution, and other charge related properties of

Table 10
NHO analysis for BTDAP.

NBO		Line of Centers		Hybrid 1			Hybrid 2		
		Theta	Phi	Theta	Phi	Dev	Theta	Phi	Dev
1	$\sigma(Br_1-C_2)$	90	64.8	90	63.1	1.8	–	–	–
2	$\sigma(C_2-C_3)$	90	8.2	89.9	2.6	5.7	–	–	–
3	$\pi(C_2-C_3)$	90	8.2	0.2	143.1	90.1	180	0	90
4	$\sigma(C_2-C_6)$	90.2	121.5	90.2	126.6	5.1	89.9	299.6	1.9
5	$\sigma(C_3-S_4)$	90	79.2	90	75.3	3.9	90	266.6	7.4
6	$\sigma(C_3-C_7)$	90	313.7	90	317.2	3.5	90	135.1	1.4
7	$\sigma(S_4-C_5)$	90	167.6	89.9	158.8	8.7	89.9	350.1	2.5
8	$\sigma(C_5-C_6)$	90.3	236.6	90.3	238.5	1.9	–	–	–
9	$\pi(C_5-C_6)$	90.3	236.6	0.2	229.5	90.1	179.8	359.2	90.2
10	$\sigma(C_5-H_{20})$	90	112.1	90	109.7	2.4	–	–	–
12	$\sigma(C_7-C_8)$	90	13.7	–	–	–	90	192.2	1.5
14	$\pi(C_7-O_{19})$	90	253.7	0	0	90	0	0	90
16	$\pi(C_8-C_9)$	90	313.7	0	0	90	0	0	90
19	$\sigma(C_9-H_{23})$	90	253.7	90	255.2	1.6	–	–	–
21	$\pi(C_{10}-C_{11})$	90	313.8	0.2	87	90.2	180	0	90
23	$\sigma(C_{11}-C_{12})$	90	13.9	89.9	15.8	1.9	–	–	–
26	$\pi(C_{12}-C_{13})$	90	73.8	179.8	103.7	89.8	179.9	264.2	89.9
28	$\sigma(C_{13}-C_{14})$	90	133.6	90.1	132.4	1.2	–	–	–
30	$\sigma(C_{14}-C_{15})$	90.2	193.5	90.5	194.9	1.4	–	–	–
31	$\pi(C_{14}-C_{15})$	90.2	193.5	0.2	185.9	90	179.9	278.8	90.3
32	$\sigma(C_{14}-H_{26})$	90	73.5	90.1	72.5	1	–	–	–
36	$\sigma(C_{17}-H_{28})$	160.5	313.7	162.4	313.7	1.9	–	–	–
37	$\sigma(C_{17}-H_{29})$	61.9	21.5	61.6	23.1	1.5	–	–	–
38	$\sigma(C_{17}-H_{30})$	61.9	245.9	61.5	244.7	1.1	–	–	–
39	$\sigma(C_{18}-H_{31})$	19.5	73.7	17.6	73.9	1.8	–	–	–
40	$\sigma(C_{18}-H_{32})$	118.1	5.9	118.3	4.3	1.5	–	–	–
41	$\sigma(C_{18}-H_{33})$	118.1	141.5	118.5	142.7	1.1	–	–	–
79	$LP(2)Br_1$	90.1	154.7	–	–	–	–		
80	$LP(3)Br_1$	179.9	338.5	–	–	–	–		
81	$LP(1)S_4$	89.9	32.2	–	–	–	–		
82	$LP(2)S_4$	179.9	114.6	–	–	–	–		
83	$LP(1)N_{16}$	179.9	89.5	–	–	–	–		
84	$LP(1)O_{19}$	90	251.6	–	–	–	–		
85	$LP(2)O_{19}$	90	342.9	–	–	–	–		
507	$\pi^*(C_2-C_3)$	90	8.2	0.2	143.1	90.1	180	0	90
513	$\pi^*(C_5-C_6)$	90.3	236.6	0.2	229.5	90.1	179.8	359.2	90.2
518	$\pi^*(C_7-O_{19})$	90	253.7	0	0	90	0	0	90
520	$\pi^*(C_8-C_9)$	90	313.7	0	0	90	0	0	90
525	$\pi^*(C_{10}-C_{11})$	90	313.8	0.2	87	90.2	180	0	90
530	$\pi^*(C_{12}-C_{13})$	90	73.8	179.8	103.7	89.8	179.9	264.2	89.9
535	$\pi^*(C_{14}-C_{15})$	90.2	193.5	0.2	185.9	90	179.9	278.8	90.3
535	$\pi^*(C_{14}-C_{15})$	90.2	193.5	0.2	185.9	90	179.9	278.8	90.3

molecules [27]. Title compound has a color scale that indicates the negative and positive value is reported in Fig. 9. From this surface, one can interpret where the most electron density resides (in the more red areas), and where the least electron density resides (deep blue areas). The electrostatic potential increases in the order red < orange < yellow < green < blue. The colour code of the maps was found to be in the range −6.514e-2 a. u (deepest red color has negative extreme) to 6.514e-2 a. u. (deepest blue color has positive extreme). The highest negative potential with the red region is visible over the regions close to O_{19} atom of the carbonyl group as potential sites for the electrophilic attack. The yellowish blob reflects less negative potential which is visible above the Br atom. A positive charge is localized near the hydrogen atoms of the methyl group as possible sites for nucleophilic attack.

From Fig. 10, multiwfn program was used to examine MEP contour map, it is clear that C_7, O_{19} atoms are negatively charged because the local vdW surface which is closed to C_7 and O_{19} atom has largely intersected solid contour line (corresponds to positive MEP). This point can be further verified when we calculate Hirshfeld atomic charges for this molecule which is listed in Table 7.

8. NBO-NLMO-NHO analyses

The NBOs are one of the sequences of natural localized orbital sets that include natural atomic orbitals (NAO), natural hybrid orbitals (NHO), natural bonding orbitals (NBO) and natural localized molecular orbitals (NLMO). These natural localized sets are intermediate one between basis atomic orbitals (AO) and molecular

Table: 11
Molecular docking energy data for mentioned ligand and Hydrogen bonding with MAO-A (PDB ID: 2BXR) and MAO-B (PDB ID: 2BYB) inhibitors protein.

Protein (PDB ID)	Bonded residues	No. of hydrogen bond	Bond distance (Å)	Estimated Inhibition Constant (μm)	Binding energy (kcal/mol)	Intermolecular energy (kcal/mol)	Reference RMSD (Å)
2BXR	TYR444	1	1.7	8.23	−6.94	−8.13	40.51
2BYB	SER59	2	1.9	2.23	−7.77	−8.96	129.19
	TYR60		2.2				

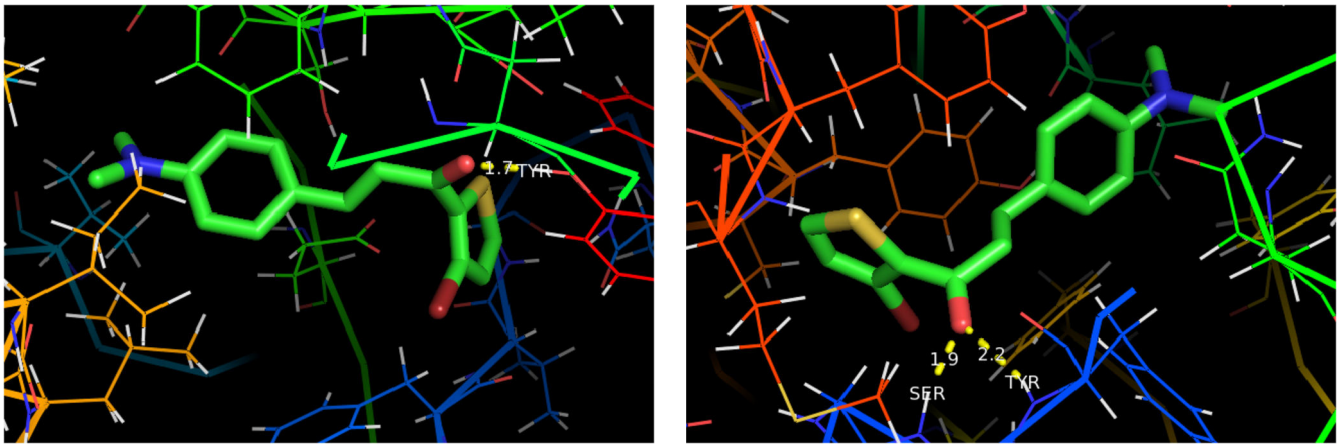

Fig. 11. (a): Docking and Hydrogen bond interactions of BTDAP with 2BXR protein. (b) Docking and Hydrogen bond interactions of BTDAP with 2BYB protein.

orbitals (MO):

Atomic orbital → NAO → NHO → NBO → NLMO → Molecular orbital

The useful application of NBO was analyzed by molecular bonding-antibonding stabilization energy. NLMO shows how bonding is formed in a molecule which is composed of orbitals localized on different atoms. NHO summarizes the molecular bond angular properties. The derivation of NLMOs from NBOs gives direct insight into the nature of the localized molecular orbital's delocalization tails [28].

The natural bond orbital (NBO) analysis provides an efficient method for studying intra-molecule and inter-molecular bonding orbital with maximum electron density, interaction among bonds and also provides supportive information for examining charge transfer or conjugative interaction in molecular systems [29]. The second-order Fock-matrix was carried out to evaluate different types of bonding and anti-bonding interactions and their E(2) stabilization energies in the NBO approach [30].

The NBO analyses for BTDAP have been carried out by B3LYP method in order to elucidate the delocalization of electron density within the molecule. The BTDAP intramolecular interaction is formed by the orbital overlap between bonding and antibonding orbitals which result in intermolecular charge transfer basis electron density and stabilization of the system. The intramolecular hyperconjugative interaction of the bonding $\sigma(C_{14}{-}H_{26})$ distributes to anti-bonding $\sigma^*(C_{13}{-}N_{16})$ leading to stabilization energy of 198.24 kcal/mol and increasing electron density as shown in Table 8.

The Natural localized molecular orbital (NLMO) analysis of BTDAP is an important electron overlap which is listed in Table 9 and which shows that NLMO is slightly delocalized NBO [31].

$$BD(1) = \sigma_{CH} = 0.775(sp^{2.50})_C + 0.631(sp^{0.00})_H \quad (9)$$

$$BD^*(1) = \sigma_{NC} = 0.784(sp^{1.74})_N - 0.619(sp^{2.55})_C \quad (10)$$

The NBO orbital output $\sigma(C_{14}{-}H_{26})$ orbital with 1.97471electrons occupancy has 60.18% C_{14} character in a $sp^{2.50}$ hybrid, polarization coefficient 0.7758 (71.42% *p*-character, 28.54% S- character) and has 39.82% H_{26} character in a $sp^{0.00}$ hybrid, polarization coefficient 0.6310 (99.95% *p*-character, 0.05% S- character). The related anti-bond output $\sigma^*(C_{13}{-}N_{16})$ is the 2-center bond (with 0.03369 electrons occupancy) has 61.59%, N_{16} character is formed from an $sp^{1.74}$ hybrid, polarization coefficient 0.7848 (72.71% *p*-character, 27.19% S- character) and has 38.41% C_{13} character in a $sp^{2.55}$ hybrid, polarization coefficient −0.6197 (63.54% *p*-character, 36.42% S-character).

The angular properties of the natural hybrid orbital's (NHO) are direction' of a hybrid specified in terms of the polar (θ) and azimuthal (φ) angles of the vector describing its *p*-component. The hybrid direction is compared with the direction of the line of centers between the two nuclei to determine the 'bending' of the bond, and expressed as the deviation angle (Dev) between these two directions. The NHO information is often useful in anticipating the direction of geometry changes resulting from geometry optimization. For title compound shown above, the NHO of the $\sigma(S_4{-}C_5)$ bond is bent away from the line of centers polar angle 90, azimuthal angle 167.6 by hybrid (1) polar angle(θ) 89.9, azimuthal angle(ϕ) 158.8, and deviation angle(Dev) 8.7° and hybrid(2) polar angle(θ) 89.9, azimuthal angle(ϕ) 350.1, and deviation angle(Dev) 2.5°. The direction of geometry changes due to the geometrical optimization can be expected using the vital data attained from Table 10.

9. Molecular docking

Molecular docking is a powerful computational tool in predicting the binding affinity of a ligand with proteins which is useful in modern structure based drug designing. Molecular docking study can be carried out by AutoDock which is automated docking software [32]. Molecular docking is used to predict the ideal bonded residues, hydrogen bond, estimated inhibition constant, binding energy, RMSD of the drug molecule and their protein targets, to predict how small the molecule binds to a receptor of the known 3D structure. Monoamine oxidases (MAO) inhibitor activity of title bromo substituted thienyl chalcone molecule has been explained here. There are two types of monoamine oxidases (MAO-A and MAO-B) which are enzyme family and the MAO-A inhibitors act as an antidepressant and anti-anxiety agents, whereas MAO-B inhibitors are used alone or in combination to treat Alzheimer's disease and Parkinson's disease. The Food and Drug Administration (FDA) has approved these MAO inhibitors to treat depression [33]. The docking protocol is verified by monoamine oxidases (MAO) inhibitor into the active site of the human MAO-A(PDB Code: 2BXR) and MAO-B (PDB Code: 2BYB) proteins, which was obtained from the Protein Data Bank. From the docking study, it was found that the ligand BTDAP shows the best affinity towards both of the proteins. The molecular docking binding energies (kcal/mol),

intermolecular energy ((kcal/mol) and inhibition constants (μm) were also obtained and listed in Table 11. The interactions of the title compound were taken for the ligand with proteins (2bxr/2byb) has been shown in Fig. 11 (a) and (b) at where the minimum binding energies of 2bxr/2byb are −6.94/−7.77 kcal/m, the intermolecular energies are −8.13/−8.96 kcal/mol and RMSD values are 40.51/129.19 Å which can be seen during the interaction. The 2bxr protein bonded residue such as TYR-444 was observed with shortest hydrogen interaction bond length 1.7 Å and various bonded residues of 2byb protein such as SER-59, TYR-60 were observed with shortest hydrogen interaction bond length 1.9/2.2 Å.

10. Conclusion

In this present study, the versatile quondam computational chemical calculations were performed for 1-(3-Bromo-2-thienyl)-3-[4-(dimethylamino)-phenyl]prop-2-en-1-one molecule. The geometrical optimized bond lengths and bond angles were calculated theoretically and compared with experimental data. The FT-IR and FT-Raman spectra of the title molecule have been observed, calculated and mentioned with PED values. NHO, NLMO and NBO analysis was employed to comprehend the angular properties, electrons occupancy, the stability of the title molecule which occurs from the hyperconjugative interaction and the charge delocalization. The maximum absorption wavelength in the UV−Visible spectrum has been observed at 429 and 326 nm. The TD-DFT calculations also show a good agreement with the observed values insolvent case. Furtheremore, the significant difference in HOMO and LUMO energy gap supports the charge transfer model of interaction within the molecule. The condensed fukui function and MEP map were shown to reveal the negative and positive regions of the molecule. The title compound might be a significant one in medicinal chemistry due to its higher electrophilicity index value. The molecular docking protocol established by monoamine oxidases (MAO) inhibitor into the active site of the human MAO-A(PDB Code: 2BXR) and MAO-B (PDB Code: 2BYB) proteins shows its minimum binding energy as −6.94/-7.77 kcal/mol respectively. There is **a** binding mode analysis about their molecular recognition process to provide information which is helpful in designing other selective and reversible MAO-inhibitors in future.

References

[1] Y. Zhenga, X. Wanga, S. Gaoa, M. Maa, G. Rena, H. Liua, X. Chena, Synthesis and antifungal activity of chalcone derivatives, Nat. Prod. Res.: Formerly Nat. Prod. Lett., DOI: 10.1080/14786419.2015.1007973, 12 Feb 2015.

[2] B. Mathew, A. Haridas, G. Ucar, I. Baysal, M. Joy, G.E. Mathew, B. Lakshmanan, V. Jayaprakash, Synthesis, biochemistry, and computational studies of brominated thienyl chalcones: a new class of reversible MAO-B inhibitors, ChemMedChem 11 (2016) 1161−1171.

[3] J.C. Shih, K. Chen, M.J. Ridd, Monoamine oxidase: from genes to behavior, Annu. Rev. Neurosci. 22 (1999) 197−217.

[4] C.J. Fowler, A. Wiberg, L. Oreland, J. Marcusson, B. Winblad, The effect of age on the activity and molecular properties of human brain monoamine oxidase, J. Neural Transm. 49 (1980) 1−20.

[5] Ray J. Butcher, H.S. Yathirajan, B.V. Ashalath, B. Narayana, B.K. Sarojini, 1-(3-Bromo-2-thienyl)-3-[4-(dimethylamino)-phenyl]prop-2-en-1-one, Acta Crystallogr. E63 (2007) o1005−o1007.

[6] M.J. Frisch, G.W. Trucks, H.B. Schlegel, G.E. Scuseria, M.A. Robb, J.R. Cheeseman, Gaussian 09, C3 Revision B.01, Gaussian, Inc, Walling- ford CT, 2010.

[7] A.H. Kianfar, H. Farrokhpour, P. Dehghani, H.R. Khavasi, Experimental and theoretical spectroscopic study and structural determination of nickel(II) tridentate Schiff base complexes, Spectrochim. Acta Part A: Mol. and Biomol. Spect. 150 (2015) 220−229.

[8] B. Fathima Rizwana, S. Muthu, J.C. Prasana, C.S. Abraham, M. Raja, Spectroscopic (FT-IR, FT-Raman) investigation, Topology (ESP, ELF, LOL) analyses, Charge transfer excitation and Molecular docking (Dengue, HCV) studies on Ribavirin, Chem. Data coll. 17−18 (2018) 236−250.

[9] M. Raja, R. Raj Muhamed, S. Muthu, M. Suresh, Synthesis, spectroscopic (FT-IR, FT-Raman, NMR, UV−Visible), NLO, NBO, HOMO-LUMO, Fukui function and molecular docking study of (E)-1-(5-bromo-2- hydroxybenzylidene)semicarbazide, J. Mol. Struct. 1141 (2017) 284−298.

[10] S. Muthu, E.I. Paulraj, Molecular structure, vibrational spectra, first order hyper polarizability, NBO and HOMO−LUMO analysis of 4-amino-3(4-chlorophenyl) butanoic acid, Solid. State Sci. 14 (2012) 476−487.

[11] N. Swarnalatha, S. Gunasekaran, S. Muthu, M. Nagarajan, Molecular structure analysis and spectroscopic characterization of 9-methoxy-2H-furo[3,2-g] chromen-2-one with experimental (FT-IR and FT-Raman) techniques and quantum chemical calculations, Spectrochim. Acta Part A: Mol. Bio. Mol Spectrosc. 137 (2015) 721−729.

[12] J. Dong, Y. Ozaki, K. Nakashima, Infrared, Raman, and near-infrared spectroscopic evidence for the coexistence of various hydrogen-bond forms in poly(acrylic acid), Macromolecules 30 (1997) 1111−1117.

[13] G. Socrates, Infrared and Raman Characteristic Group Frequencies: Tables and Charts, 2001 west London, UK.

[14] V. Balachandran, A. Lakshmi, A. Janaki, Conformational stability, vibrational spectral studies, HOMO−LUMO and NBO analyses of 2-hydroxy-4-methyl-3-nitropyridine and 2-hydroxy-4-methyl-5-nitropyridine based on density functional theory, J. Mol. Struct. 1013 (2012) 75−85.

[15] N.B. Colthup, L.H. Daly, S.E. Wiberley, Introduction to Infrared and Raman Spectroscopy, Academic Press, New York, NY, USA, 1990.

[16] G. Varsanyi, Vibrational Spectra of Benzene Derivatives, Academic Press, New York, NY, USA, 1969.

[17] B.C. Smith, Infrared Spectral Interpretation: A Systematic Approach, CRC Press, New York, NY, USA, 1999.

[18] N. Balamurugan, C. Charanya, S. SampathKrishnan, S. Muthu, Molecular structure, vibrational spectra, first order hyper polarizability, NBO and HOMO−LUMO analysis of 2-amino-5-bromo-benzoic acid methyl ester, Spectrochim. Acta Part A: Mol. Bio. Mol Spectrosc. 137 (2015) 1374−1386.

[19] B. Fathima Rizwana, J.C. Prasanaa, S. Muthu, C.S. Abrahama, Molecular docking studies, charge transfer excitation and wave function analyses (ESP, ELF, LOL) on valacyclovir : a potential antiviral drug, Comput. Biol. Chem. 78 (2019) 9−17.

[20] C.A. Guido, P. Cortona, B. Mennucci, C. Adamo, On the metric of charge transfer molecular excitations: a simple chemical descriptor, J. Chem. Theory Comput. 9 (7) (2013) 3118−3126.

[21] R.G. Parr, W. Yang, DFT approach to the frontier-electron theory of chemical reactivity, J. Am. Chem. Soc. 106 (1984) 4049−4050.

[22] R.G. Parr, L.V. Szentpaly, S. Liu, Electrophilicity index, J. Am. Chem. Soc. 121 (9) (1999) 1922−1924.

[23] T.C. Allison, Y.J. Tong, Application of the condensed Fukui function to predict reactivity in core−shell transition metal nanoparticles, Electrochim. Acta. 101 (2013) 334−340.

[24] P. Fuentealba, P. Pérez, On the condensed Fukui function, J. Chem. Phys. 113 (2000) 7−15.

[25] J. Sanchez-Marquez, D. Zorrilla, Introducing "UCA-FUKUI" software, reactivity-index calculations, J. Mol. Model. 20 (2014) 2492.

[26] C. Morell, A. Grand, A. Toro-Labbe, New dual descriptor for chemical reactivity, J. Phys. Chem. 109 (2005) 205−212.

[27] B. Kosar, C. Albayrak, Spectroscopic investigations and quantum chemical computational study of (E)-4-methoxy-2-[(p-tolylimino)methyl]phenol, Spectrochim. Acta Part A: Mol. Bio. Mol Spectrosc. 71 (2011) 160−167.

[28] A.E. Reed, L.A. Curtiss, F. Weinhold, Intermolecular interactions from a natural bond orbital, donor-acceptor viewpoint, Chem. Rev. 88 (1988) 899−926.

[29] P. Rajesh, S. Gunasekaran, T. Gnanasambandan, S. Seshadri, Experimental, quantum chemical and NBO/NLMO investigations of pantoprazole, Spectrochim. Acta Part A: Mol. Bio. Mol Spectrosc. 136 (2015) 247−255.

[30] V. Balachandran, A. Lakshmi, A. Janaki, Conformational stability, vibrational spectral studies, HOMO−LUMO and NBO analyses of 2-hydroxy-4-methyl-3-nitropyridine and 2-hydroxy-4-methyl-5-nitropyridine based on density functional theory, J. Mol. Struct. 1013 (2012) 75−85.

[31] S. Ghammamy, A. Lashgari, Structural properties, natural bond orbital, theory functional calculations (DFT) and energies for the 3-Methyl-4-(2-phenyl-1,2,4-triazolo-[1,5-a]pyrimidin-7-yl)furazan compound, J. Sci. Res. 17 (8) (2013) 1080−1086.

[32] G.M. Morris, R. Huey, W. Lindstrom, M.F. Sanner, R.K. Belew, D.S. Goodsell, A.J. Olson, AutoDock4 and auto DockTools4, J. Comput. Chem. 30 (2009) 2785−2791.

[33] A. Khan, R.M. Leventhal, S.R. Khan, W.A. Brown, Severity of depression and response to antidepressants and placebo: an analysis of the food and drug administration database, J. Clin.Psychopharmacol. 22 (2002) 40−45.

Journal of Molecular Structure 1213 (2020) 128187

Contents lists available at ScienceDirect

Journal of Molecular Structure

journal homepage: http://www.elsevier.com/locate/molstruc

Crystal growth, spectroscopic, optical, thermal and hirshfeld surface analysis of glycinium hydrogen fumarate glycine solvate monohydrate (GHFGSM): A third harmonic nonlinear optical organic crystal

P. Sangeetha [a], P. Jayaprakash [b], P. Ramesh [c, d], S. Sudha [d], G. Vinitha [e], M. Nageshwari [f], M. Lydia Caroline [d, g, *]

[a] Department of Physics, Government Arts and Science College, Thennangur, Vandavasi-604408, Tamil Nadu, India
[b] Department of Physics, St.Joseph's Institute of Technology, OMR, Chennai, 600119, TamilNadu, India
[c] Department of Physics, Govt. Thirumagal Mills College, Gudiyatham, 632602, Tamil Nadu, India
[d] PG & Research Department of Physics, Arignar Anna Govt. Arts College, Cheyyar, 604407, Tamil Nadu, India
[e] Department of Physics, School of Advanced Sciences, VIT, Chennai, 600127, Tamil Nadu, India
[f] Department of Physics, Peri Institute of Technology, Mannivakkam, Chennai, 600048, Tamil Nadu, India
[g] Department of Physics, Dr. Ambedkar Govt. Arts College, Vyasarpadi, Chennai, 600039, TamilNadu, India

ARTICLE INFO

Article history:
Received 6 November 2019
Received in revised form
11 March 2020
Accepted 1 April 2020
Available online 4 April 2020

Keywords:
Nonlinear optics
GHFGSM
Optical absorbance
Hirshfeld surface
Lifetime
Z-Scan technique

ABSTRACT

An efficient nonlinear optical single crystal, GHFGSM was grown by solvent evaporation method. Single crystal XRD evince that GHFGSM crystallized in monoclinic system with centric space group $P2_1/n$. The composition of different functional groups in GHFGSM was identified with FTIR spectral investigation. The UV−visible and fluorescence spectrum proved the optical and electronic properties respectively for the grown crystal. The various optical parameters such as extinction coefficient, reflectance, and linear refractive index, electrical and optical conductivity were also determined. Inter molecular interaction in the compound was studied using Hirshfeld Surface generated by crystal explorer 3.1 program. The thermal firmness of the grown crystal was decided by thermogravimetric analysis and accurate melting point was confirmed from differential scanning calorimetry. The dielectric property of the grown crystal was examined for different temperatures. The third harmonic generation in GHFGSM has been investigated using Z-scan technique employing Nd:YAG laser and thus this technique clearly suggest its suitability in emerging technologies such as optoelectronics and third order nonlinear optical applications.

1. Introduction

Much evolution has been made in the new materials with high optical nonlinearities because their practical applications in harmonic generation, amplitude and phase modulation, laser technology, switching and other signal processing devices [1,2]. Nonlinear optical (NLO) materials have attracted many researchers due to their huge range of applications in the area of photonics, lasers, electro-optic switches and frequency conversion devices [3]. The interaction between the electric field of the wave and the nonlinear optical medium giving out the output possessing three times that of the original frequency executes third harmonic generation (THG) effect. In certain cases when the THG is not acquired directly, then in such case firstly a fraction of the fundamental is converted into second harmonic and thereafter that unconverted fundamental and second harmonic generated signal are coupled to tripler to produce third harmonic signal. The third order nonlinear optical (NLO) materials have been actively employed as promising materials in photonics, communications devices, information processing, optoelectronic switching devices which forms the basis for future optical systems [4,5] and also in photodynamic therapy [6]. The NLO properties can be utilized as sensitive probes in biomedical and environmental fields [7,8]. Especially two-photon absorption is utilized in the field of medicine and photonics [9]. From the computer and telecommunication advances, inherent high nonlinearity, synthetic flexibility and scope to alter their properties

* Corresponding author. Department of Physics, Dr. Ambedkar Govt. Arts College, Vyasaradi, Chennai-600039, Tamil Nadu, India.
E-mail address: lydiacaroline2006@yahoo.co.in (M.L. Caroline).

https://doi.org/10.1016/j.molstruc.2020.128187
0022-2860/

by functional substitutions mould the organic materials as highly versatile [10,11]. At present, organic crystals with strong third-order nonlinear optical absorptions are significant requirements owing to their potential applications such as 3D optical memory, optical switching, optical modulating, optical communication and high-speed information processing. Glycine is well known amino acid that crystallizes from its aqueous solution in different polymorphic forms (α, β, γ) [12] of which alpha and beta glycine crystallizes in centric symmetric space groups $P2_1/n$ and gamma glycine crystallizes in noncentrosymmetric space group $P3_1$ [13]. Glycine is essential for the biosynthesis of nucleic acid as well as other amino acids explained by Nataraj et al., who solved the structure of GHFGSM [14]. Also Riscob et al. reported glycine based centric organic crystal presenting explication on the physicochemical properties [15]. Fumaric acid among the organic compounds is widely found in nature and is a main median in the biosynthesis of organic acids [14]. Earlier fumaric acid based crystal structures have been by Alagar et al. [16,17]. Quite some time researchers have shown interest to work on fumaric acid based materials and described as good NLO materials [18,19] suitable for photonic and optoelectronic applications. In the present work, the synthesis was carried out with glycine and fumaric acid and subsequently followed by crystal growth of GHFGSM by slow solvent evaporation method with optical, dielectric, fluorescence and lifetime studies. Also work includes to the evaluation of nonlinearities by Z-scan technique from open and closed apertures is reported for the first time.

2. Materials and methods

2.1. Synthesis and crystal growth of GHFGSM

Starting materials Glycine (SRL, 99%) and Fumaric acid (LOBA, 99%) were taken to synthesize GHFGSM in stoichiometric molar (1:1) ratio using aqueous solution. The scheme of reaction shown in the following reaction in the right hand side depicts the chemical formula moiety of Glycinium hydrogen fumarate glycine solvate monohydrate (GHFGSM) [14].

$$2C_2H_5NO_2 + C_4H_4O_4 \rightarrow C_2H_6NO_2^+.C_4H_3O_4^-.\ C_2H_5NO_2.H_2O$$

After the solution was stirred well utilizing magnetic stirrer for about 8 h at 45 ∘C, homogenous saturated solution was filtered off to remove insoluble impurities and transferred to 250 ml beaker for crystallization process. By means of homogenous nucleation, in a period of two weeks, optically colorless crystals appeared in the beaker. The photograph of harvested GHFGSM crystals is shown in Fig. 1.

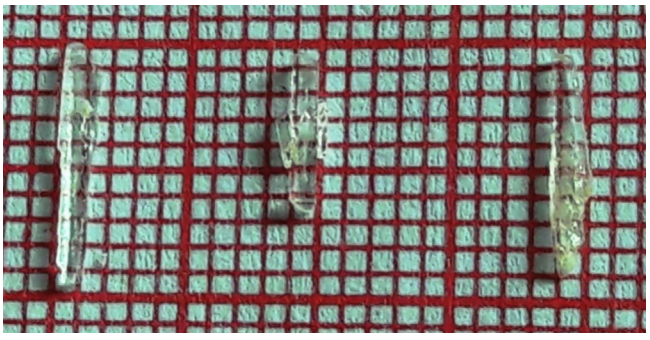

Fig. 1. The photograph of as-grown GHFGSM single crystals.

2.2. Characterization techniques

The harvested crystal of GHFGSM was exposed to MoKα (λ = 0.71073 Å) radiation to measure the Lattice parameters by employing a BRUKER KAPPA APEX II CCD diffractometer. The FTIR spectrum was recorded using PERKIN ELMER Fourier transform infrared spectrometer in the range 4000–450 cm^{-1} by KBr pellet technique at room temperature. The UV–visible spectrum of GHFGSM was obtained at room temperature by employing a PERKIN ELMER LAMADA 35 spectrophotometer with a wide wavelength range 200–700 nm. The TG/DSC of GHFGSM has been recorded by NETZSCH STA 449F3 thermal analyser. The dielectric loss and dielectric constant as a function of frequency in the temperature range (313 K, 333 K, 353 K and 373 K) was explained using a HIOKO 3532-50 LCR HiTESTER meter. The fluorescence and lifetime measurement were performed with the help of FLUOROCUBE (JOBIN-VYON M/S) spectrofluorometer. Open aperture and closed aperture of Z-scan study was carried out using a Field master GS-coherent digital power meter.

3. Results and discussion

3.1. Single crystal X-ray diffraction study

The single crystal XRD investigation revealed that GHFGSM corresponds to the monoclinic system having space group $P2_1/n$ and the lattice parameter values *a,b,c* and the volume of the unit cell are enumerated in Table 1 represents no modulation in crystal structure and are in accordance with literature [14] solved by the authors Nataraj et al., and the crystallographic data have been deposited with the Cambridge Crystallographic Data Centre, citing the title of this paper by the authors Nataraj et al. [14] with the CCDC No. 722874.

3.2. Infrared (IR) spectral analysis

The recorded FTIR spectrum of GHFGSM is presented in Fig. 2. The protonation of amino group in GHFGSM (Glycinium hydrogen fumarate glycine solvate monohydrate) can be confirmed by the occurrence of peaks at 3081 cm^{-1} (asymmetric stretching of NH_3^+) [20] and 2529 cm^{-1} (existence of $-NH_3^+$) [18]. The C–H aromatic stretching mode is due to band seen at 2898 cm^{-1}. The CH_2 stretching vibrations occurs due to band positioned at 2687 cm^{-1} and 886 cm^{-1} respectively [13]. The band that appears at 1686 cm^{-1} is due to the presence of COOH in GHFGSM crystal. The protonation of carboxyl group COO^- deformation is confirmed due to the bands situated around 1422 cm^{-1} and 1499 cm^{-1}. The C–N stretching vibrations is seen occurring at wavenumber positioned at 1010 cm^{-1}. The band that is seen at 926 cm^{-1} indicates OH out of plane deformation [18].

Table 1
Single crystal XRD crystallographic data of GHFGSM.

Cell parameters	Present work	Reported work [14]
	Monoclinic	Monoclinic
Space group	$P2_1/n$	$P2_1/n$
a (Å)	13.05	13.05
b (Å)	6.80	6.85
c (Å)	15.29	15.32
β (°)	112.38	112.65
Volume ($Å^3$)	1257	1260.6

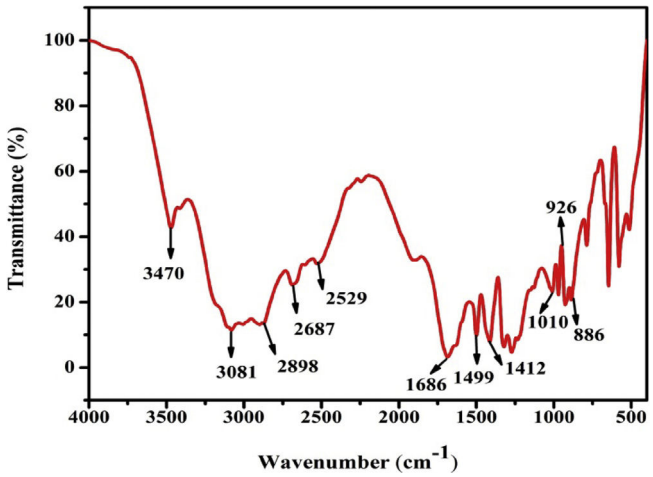

Fig. 2. FTIR profile of GHFGSM.

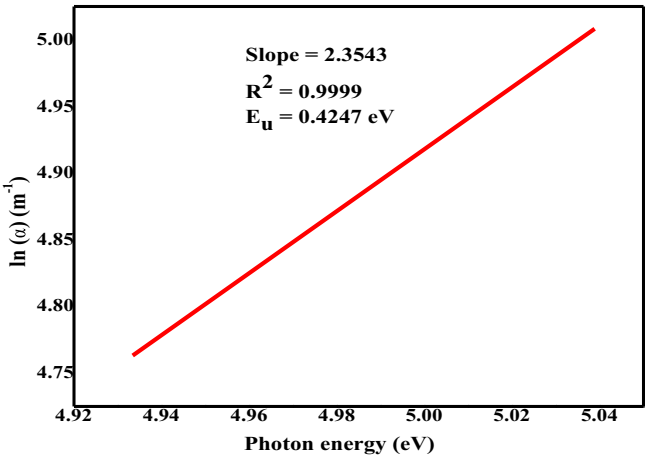

Fig. 4. Plot ln (α) vs. hυ for the GHFGSM.

3.3. Optical studies

The linear optical properties of GHFGSM crystal was analyzed for understanding the transmission nature in the UV–visible region. The recorded GHFGSM spectrum was recorded in the range 200–700 nm shown in Fig. 3(a). From the figure, it is clear that the title compound GHFGSM possess good transmittance in the visible and infrared region with lower cut-off wavelength of 252 nm contribute to the crystal usefulness in the field optical applications.

The optical absorption coefficient (α) was computed using the following formula:

$$\alpha = \frac{2.3026 \log(1/T)}{t} \quad (A.1)$$

Where 'T' is the transmittance (%), t the thickness of the crystal. The optical band gap energy (E_g) was calculated from the transmission (T) data and the optical absorption coefficient (α) near the absorption edge is related as presented below [17],

$$h\upsilon\alpha = A(h\upsilon - E_g)^{1/2} \quad (A.2)$$

In the above equation 'E_g' is electronic band gap energy, 'h' the Planck's constant, 'υ' is frequency of the incident photons, 'A' is a constant. The band gap energy of Glycinium hydrogen fumarate glycine solvate monohydrate (GHFGSM) single crystal was evaluated from linear part of the Tauc's plot by plotting $(\alpha h\upsilon)^2$ vs. photon energy (hυ) as shown in Fig. 3(b) and E_g value is evaluated to be 5.19 eV. The wide band gap of the GHFGSM crystals confirms the large transmittance in the visible region and defect less concentration in the grown crystal [18]. Hence GHFGSM crystal possessing wide optical band gap can be a suitable candidate for UV tunable laser and NLO device applications.

3.3.1. Urbach energy

In the exponential-edge region, the absorption coefficient below the fundamental absorption edge for the crystalline materials exhibit an exponential dependence on the photon energy (hυ) are related by so called Urbach relationship [4],

$$\alpha(h\upsilon) = \alpha_0 \exp\left(\frac{h\upsilon}{E_u}\right) \quad (B.1)$$

where α_0 is a constant and E_u the Urbach energy, which gives information about depth-of tail levels extending in to the forbidden electronic band gap below the absorption edge, h is Planck's constant and υ is the frequency of radiation. Whenever the degree of

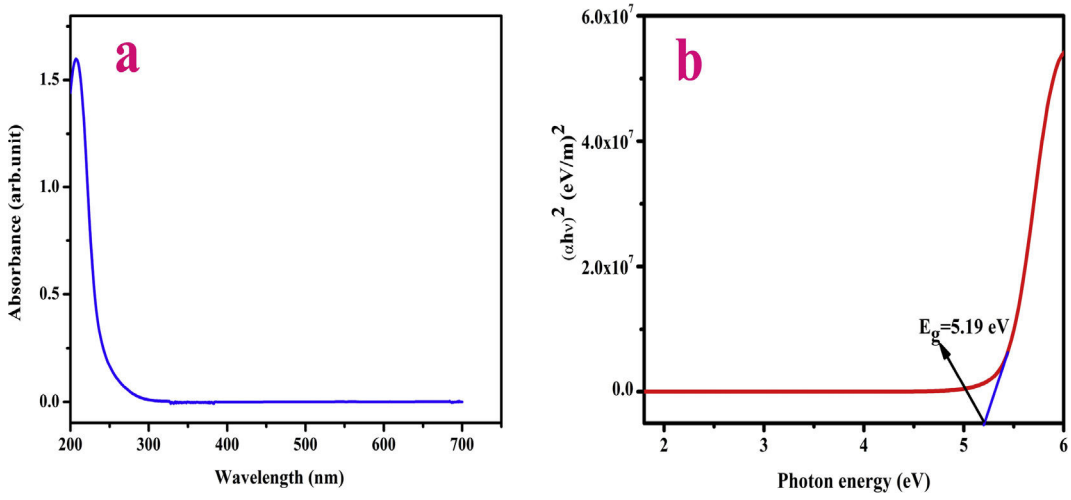

Fig. 3. (a) UV–vis profile and (b) Tauc's plot of GHFGSM.

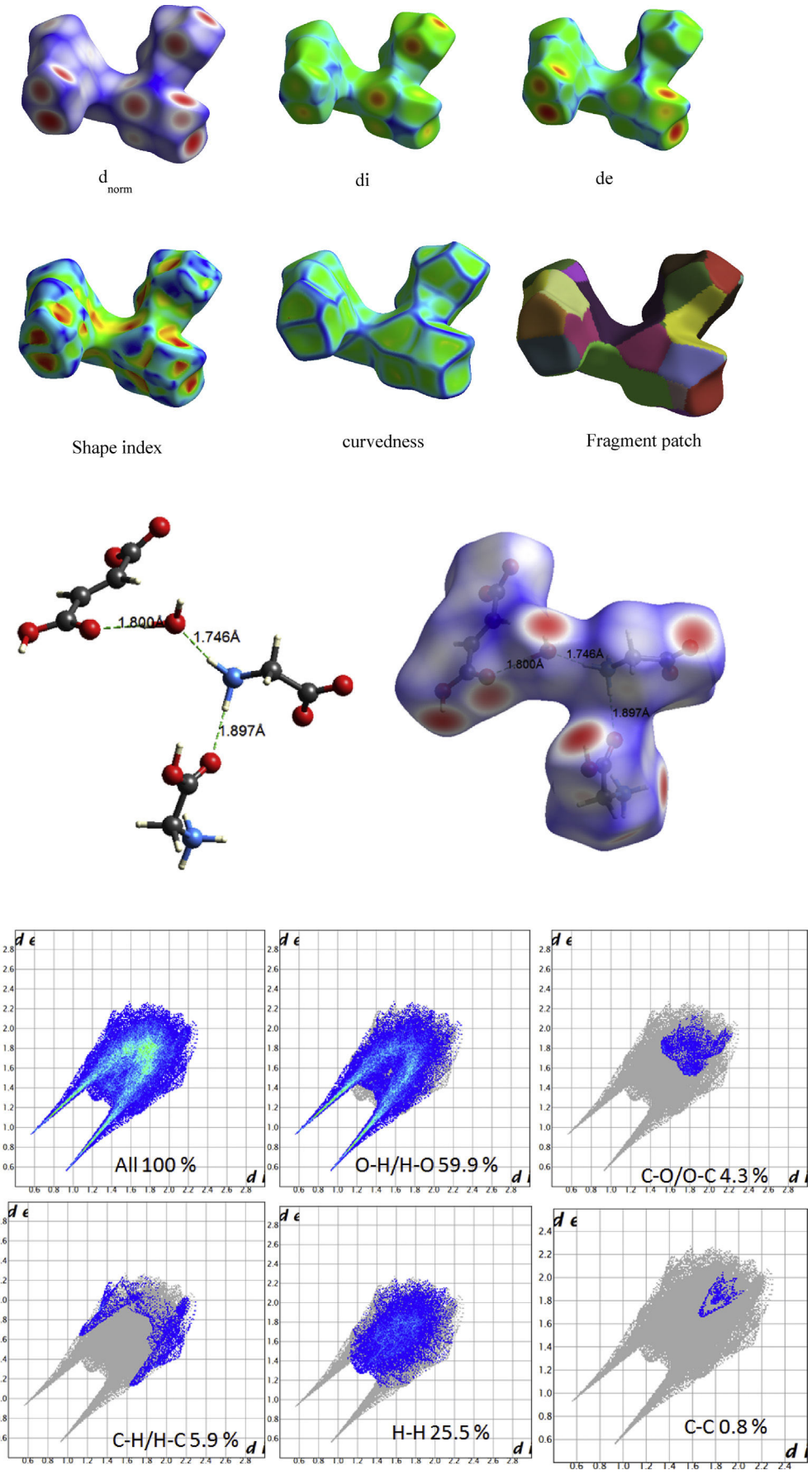

Fig. 5. a: Hirshfeld surfaces for d-norm, di, de, Shape index, Curvedness and Fragment patch for title compound .**5b**: N–H···O, O–H···O, C–O···H intermolecular interactions mapped on d_{norm} surface. **5c**: 2D Fingerprint plots of the title compound resolved into O···H/H···O (59.9%), O···C/C···O (4.3%), C···H/H···C (5.9%), H···H (25.5%), C···C (0.8%) contacts showing the percentages participations to the Hirshfeld surface area.

crystallinity increases, the slope of this region will increase. The observed slope 2.3543 of the linear portion of the plot was found from logarithm of the absorption coefficient (ln(α)) with function of high photon energy (hυ) which interprets that the crystal is highly crystalline in nature. Urbach energy E_u was calculated by taking the reciprocal of the slope of linear portion of the plot drawn between ln(α) and hυ depicted in Fig. 4. The calculated Urbach energy value is 0.4247 eV for GHFGSM crystal. The low value of Urbach energy (0.4247 eV) is an indicative of decrease in structural defect in as-grown GHFGSM crystal, supports its good NLO performance [4].

3.4. Hirshfeld surface analysis

The hirshfeld surface and 2d-fingerprind of the compound were generated by the crystal explorer 3.1 program [20]. The molecular Hirshfeld surface *d*norm, di, de, shape index, curvedness and fragment path for the title compound is depicted in Fig. 5(a) and mapped over intermolecular interaction *d*norm which ranges −0.8674 to 1.2731 Å. The intermolecular distance O—H is shown in Fig. 5(b). The full 2D fingerprint plots are critically investigated to get the contribution of O—H/H—O (59.9%), C—O/O—C (4.3%), C—H/H—C (5.9%), H—H (25.5%) and C—C (0.8%) intermolecular interactions which have comprised to total Hirshfeld surface (Fig. 5(c)). The title molecule intermolecular interactions are evidently given in fingerprint plots (Fig. 5(c)) and the de and di spikes in the FP illustrate that the values (de + di = 0.9 + 0.9) is 1.8 Å for O—H/H—O interaction and other molecular interaction shown in Fig. 2. This FP interaction de and di graphical slope values are in good agreement for intermolecular interactions shown in the same figure (Fig. 2). This interaction is the shortest and the strongest, were in good agreement with the structural study when the structure was dominated by N—H···O, C—O···H and O—H···O interactions in the crystal.

3.5. Thermal analysis

TG-DSC (Thermogravimetric-Differential scanning calorimetry) study provides the information about distinct stages of decomposition, phase analysis, stability and melting point of the crystal system. In the temperature range 20—700 °C at a heating rate of 20 °C min^{-1} in nitrogen atmosphere and the simultaneously recorded TG and DSC curves are depicted in Fig. 6. From the TG spectrum the presence of monohydrate in the title compound is predicted from a small dip spotted at around 97 °C, represented by the appearance of small endothermic peak in the DSC curve. The evaporation of water occurs between 97°C-161 °C. The decomposition of the sample launch with the weight loss at the temperature 161 °C also represented by the broad exothermic peak in the DSC curve. The next stage of decomposition gets started at around 185 °C goes up to 236 °C coincides with a broad exothermic peak in the DSC profile. After 250 °C the residual mass is negative manifest small amount of residue of the sample after the completion of evaporation process. Henceforth further decomposition of the sample is indicated by the multiple broad exothermic peaks of very less intensity in the DSC curve. Finally it infers from the result of TG-DSC, that maximum temperature for nonlinear optical implementation for this sample is limited to 160 °C without weight loss.

3.6. Dielectric studies

The dielectric characteristics of the material is a salient feature to know about the electro-optical molecular response, transport phenomena, lattice dynamics, nature of atoms, ions, polarization mechanism and quality of the crystalline material [21]. The dielectric permittivity and dielectric loss of GHFGSM crystal was

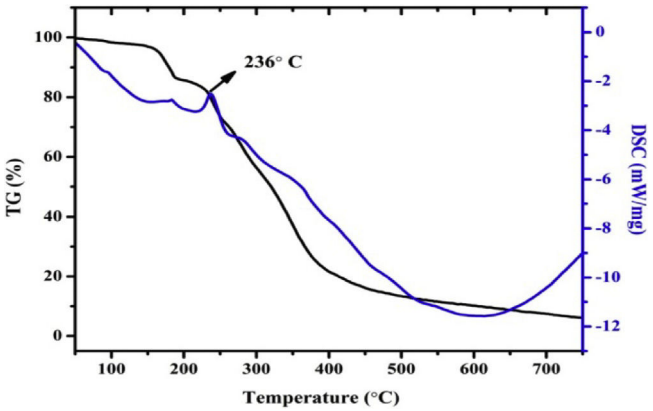

Fig. 6. TG/DSC profile of GHFGSM.

carried out as a function of frequency varying from 50 Hz to 5 MHz at various temperatures (313 K, 333 K, 353 K and 373 K0. The dielectric constant and dielectric loss were elucidated using the relation:

$$\varepsilon' = \frac{Cd}{A\varepsilon_0} \quad \text{(C.1)}$$

$$\varepsilon'' = \varepsilon' \tan \delta \quad \text{(C.2)}$$

where C is the capacitance in μF, d is the thickness of the sample in mm, $\varepsilon_0 = 8.854 \times 10^{-12}$ Fm^{-1} is the vacuum dielectric constant, A-Area of the sample in mm^2 and tan δ is the dissipation factor. The variation of dielectric constant and dielectric loss as function of logarithm of frequency for the grown crystal at various temperatures are shown in Fig. 7(a) and (b) respectively. From the graphs, it clearly depicts that the dielectric constant and dielectric loss decreases as the frequency increases. The very high value of dielectric constant at low frequencies assigns presence of all the four polarizations namely electronic, space charge, orientation and ionic polarizations. Also very low dielectric constant and dielectric loss at high frequencies reveals enhanced optical quality with lesser defects. Hence, GHFGSM crystal could be utilized for optoelectronic applications and NLO applications [22].

3.6.1. A.C conductivity

The a. c conductivity σ_{ac} (Ω^{-1} m^{-1}) is evaluated using the relation:

$$\sigma_{ac} = 2\pi f \varepsilon_0 \varepsilon' \tan \delta \quad \text{(D.1)}$$

where f is the applied frequency of ac field (Hz). The mechanism of conduction is expressed as a plot of log σ_{ac} vs. log ω at various temperatures has been plotted and represented in Fig. 7(c). From this graph it is clear that the low frequency conductivity data show small variation, corresponding to the frequency-independent part, σ_{dc} which is due to the random diffusion of the ionic charge carriers via activated hopping. At high frequencies, the conductivity spectrum shows dispersion, indicating the onset of ac conductivity. At higher frequencies, the ionic conductivity increases with the increasing frequency which may be due to the forward and reverse ion displacements occurring simultaneously thus facilitating the frequency dependence of ionic motion.

3.6.2. Activation energy

The activation energy (E_a) is an electrical process evaluated from

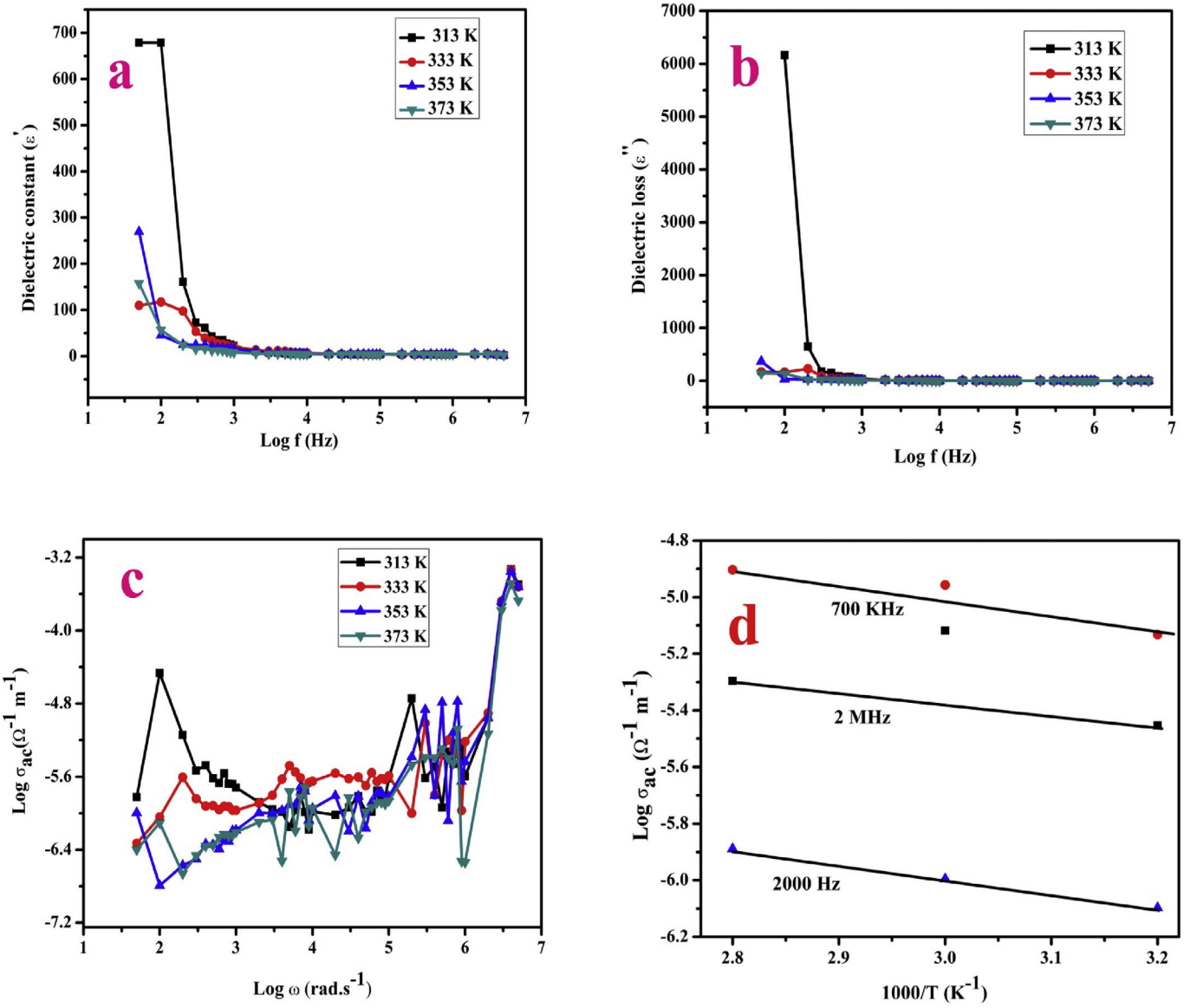

Fig. 7. Plot of (a) Log f vs. dielectric constant (b) Log f vs. dielectric loss (c) Log σ_{ac} vs. log ω and (d) Log σ_{ac} vs. 1000/T.

the plot drawn between log σ_{ac} and inverse of temperature using the relation:

$$\sigma = \sigma_0 \exp\left(-\frac{E_a}{k_B T}\right) \quad \text{(E.1)}$$

where σ_{ac} is the conductivity at temperature T, E_a - activation energy for the electrical process and $k_B = 1.38 \times 10^{23}$ J/K is the Boltzmann constant. Fig. 6(d) shows the variation of log σ_{ac} versus 1000/T. From this graph is almost linear in behavior and the slope of this graph is used to calculate activation energy using the formula,

$$E_a = \text{-Slope x 1000 x } k_B \quad \text{(E.2)}$$

The values of the activation energy come out to be 0.00892 eV, 0.0255 eV and 0.0327 eV at frequencies of 1 KHz, 2 KHz and 8 KHz respectively. The lower activation energy value establishes that the GHFGSM crystal contain very less number of defects. Defect less crystals become more useful materials for device fabrications.

3.7. Fluorescence and life time measurement

The fluorescence spectrum of GHFGSM crystal was measured denotes the emission spectrum concerned with that particular excited state of the system and decaying components [23]. The fluorescence emission spectrum of GHFGSM shown in Fig. 8(a), was recorded with respect to the corresponding excitation wavelength of 252 nm. The emission peaks with maximum intensity is seen occurring at 503 nm (2.465 eV), which lies in the visible region in accordance with the electromagnetic spectrum. The remaining peak observed at 393 nm (3.158 eV) was assigned to the defects present inside the crystal. The existence of 2-day (prompt and delayed) component of fluorescence materials lead to the neutron-gamma discrimination. The most prominent feature of the organic scintillator as a detector application is to predict various lifetime (prompt-τ_1, delay1-τ_2 and delay2-τ_3) at the emission wavelength

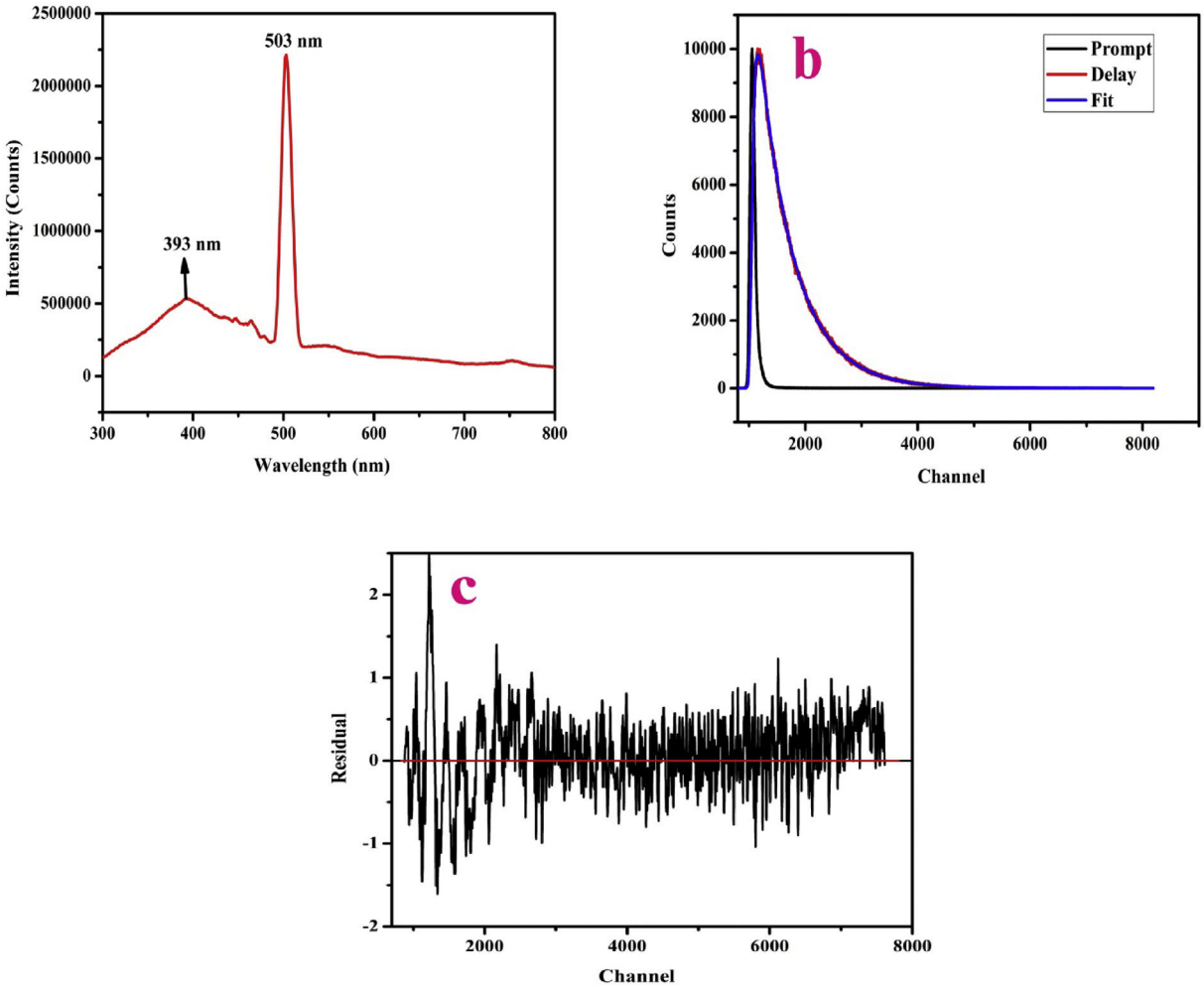

Fig. 8. (a) Emission spectrum (b) Fluorescence lifetime spectrum (c) Residual fit of GHFGSM.

Table 2
Fluorescence lifetime analysis data of GHFGSM crystal.

Single crystal	Analysis	Lifetime (ns)			Amplitude			
		τ_1	τ_2	τ_3	A_1	A_2	A_3	$\chi 2$
GHFGSM	Three exponential	2	4	5	11.76	85.28	2.96	1.15

corresponding to 503 nm. The lifetime measurement was carried out using pulsed-Diode excitation sources. The lifetime profile was evaluated by time-correlated single photon counting method (TCSPC) [24]. Fig. 8(b) reveals the three exponential decay time spectrum of the GHFGSM single crystal. The analysis of decay time measurement was fitted with a three exponential decay function of the form,

$$F(t) = A_1 e^{-t/\tau_1} + A_2 e^{-t/\tau_2} + A_3 e^{-t/\tau_3} \quad \text{(F.1)}$$

Where A_1, A_2 and A_3 are amplitudes corresponding to prompt and delayed emissions, τ_1, τ_2 and τ_3 refer to lifetimes respectively. The residual fit shown in Fig. 7(c) indicates the extent of best fitting done to the actual decay curve. The quality of the curve fit was calculated by the inspection of the residuals, and the value of the reduced χ^2 ratio. The present study exhibited the shortest decay component of lifetime and amplitude is presented in Table 2.

3.8. Z -Scan studies

The Z-Scan technique is a simple, highly popular and accurate method for ascertain the magnitude and sign of nonlinear refractive index (n_2) of solids, liquid solutions and thin films [25]. The change in phase imparted on a diode pumped Nd:YAG laser of wavelength 532 nm was used as source produces both the sign and magnitude of the phase change. The propagation of the incident laser beam on the sample is scanned along the z-axis direction and so it is named as Z scan.

A tightly focused Gaussian laser beam was made to incident on a convex lens with a focal length of 30 mm. The transmittance of the Gaussian laser beam was measured by changing a position of the sample with respect to the focal plane of a field lens, which is set at $z = 0$. Thus the Z-scan technique also elucidates the transmission change created by nonlinear absorption which is connected to change in the absorption coefficient. The sample was translated in $+z$ to $-z$ axial direction. Initially, the measurement starts far away from the focus along negative z direction showing the transmittance to be relatively constant. Further if the sample is moved towards the focus along positive z direction depicts the transmittance graph showing valley first and then peak predicts the positive non linearity ($n2>0$) of the sample. For a sample with ($n2<0$) the transmittance graph is exactly opposite showing peak first and then valley represents the negative nonlinearity of the

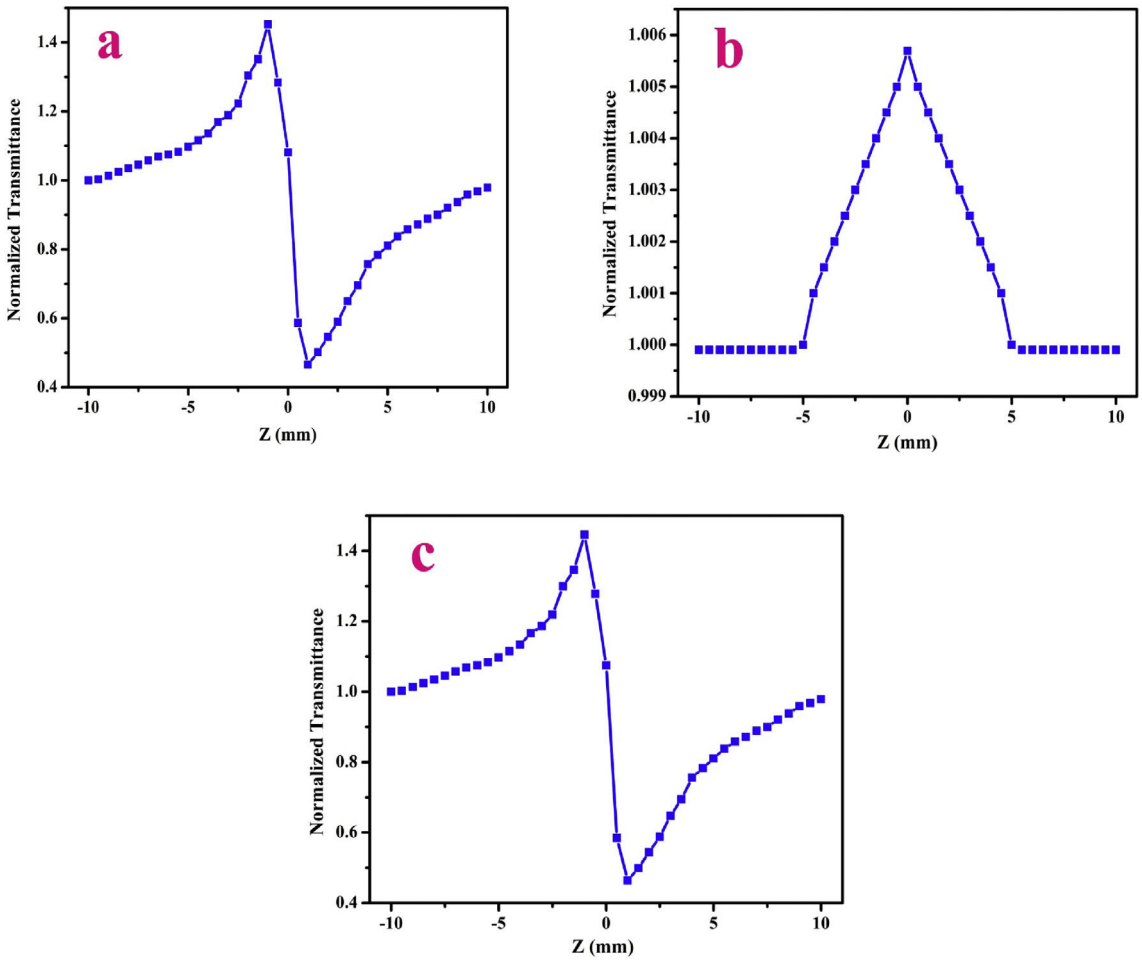

Fig. 9. (a) Closed aperture and (b) Open aperture (c) Ratio of the closed-to-open Z-scan traces of GHFGSM.

Table 3
Obtained nonlinear optical parameters from Z-scan measurements for GHFGSM.

Parameters	Measured values for GHFGSM crystal
Laser beam wavelength (λ)	532 nm
Linear absorption coefficient (α)	116.87
Nonlinear refractive index (n_2)	4.80×10^{-8} cm^2/W
Nonlinear absorption coefficient (β)	0.00×10^{-4} cm/W
Real part of the third-order susceptibility [Re (χ^3)]	1.31×10^{-6} esu
Imaginary part of the third-order susceptibility [Im (χ^3)]	0.02×10^{-6} esu
Third-order nonlinear optical susceptibility (χ^3)	1.13×10^{-6} esu

Table 4
Comparison of $\chi^{(3)}$ values of GHFGSM with other NLO materials.

Crystal	Third-order susceptibility $\chi^{(3)}$	Reference
GHFGSM	1.13×10^{-6} esu	**Present work**
DLMA	4.18×10^{-6} esu	[11]
BZP	6.20×10^{-8} esu	[28]
VMST	9.69×10^{-12} esu	[29]

sample. The variation in far field transmittance beam intensity of GHFGSM sample was measured through the closed aperture.

The recorded normalised transmittances of closed aperture, open aperture and ratio of the closed to open normalised Z-scan traces are illustrated in Fig. 9(a–c). In closed aperture pattern (Fig. 9(a)), the pre-focal maximum (peak) is been followed by a post-focal minimum (valley) which proves an indication of the signature of negative nonlinearity,i.e., the occurrence of self-defocusing [26]. The enhanced open aperture (Fig. 8(b)) Z-scan transmittance near the focus is a suggestive of the saturable absorbance (SA) at high intensity [27]. The measurable quantity (ΔT_{P-V}) is the characteristic difference between the transmittance change of peak and valley transmission given by the relation,

$$\Delta T_{P-V} = 0.406(1-S)^{0.25}|\Delta\Phi_0| \quad \text{(G.1)}$$

$$S = 1 - \exp\left(\frac{-2r_a^2}{\omega_a^2}\right) \quad \text{(G.2)}$$

where S,r_a, ω_a represents linear transmittance, radius of the aperture, beam radius at the aperture. The third-order nonlinear

refractive index (n_2) of the GHFGSM crystal were calculated by using the following relation,

$$n_2 = \frac{\Delta\Phi_0}{KI_0L_{eff}} \quad (G.3)$$

where I_0 is the intensity of the laser beam at focus (Z = 0) ($I_0 = 26.31\ MWm^{-2}$), $K = 2\pi/\lambda$(λ is the laser wavelength), L_{eff} is an effective thickness of the crystal which can be calculated using the relation $L_{eff} = [1 - \exp(-\alpha L)]/\alpha$. Where α and L is the linear absorption coefficient and the thickness of the crystal respectively. From the open aperture trace, the nonlinear absorption coefficient (β) can be estimated using the following relation,

$$\beta = \frac{2\sqrt{2}\Delta T}{I_0L_{eff}} \quad (G.4)$$

where ΔT is the one valley value at the open aperture Z-scan trace. The experimental determination of n_2 and β were used to calculate the real and imaginary parts of the third-order nonlinear optical susceptibility for the study of third order nonlinear response:

$$\mathrm{Re}\chi^{(3)}(esu) = \frac{10^{-4}\left(\varepsilon_0 C^2 {n_o}^2 n_2\right)}{\pi}\left(\frac{cm^2}{W}\right) \quad (G.5)$$

$$\mathrm{Im}\chi^{(3)}(esu) = \frac{10^{-2}\left(\varepsilon_0 C^2 n_0 \lambda\beta\right)}{4\pi^2}\left(\frac{cm^2}{W}\right) \quad (G.6)$$

where ε_0 is the permittivity of free space ($8.8518 \times 10^{-12} Fm^{-1}$), n_0 is the linear refractive index of the sample and C is the velocity of the light in a vacuum. The magnitude of third-order nonlinear optical susceptibility $\chi^{(3)}$ was calculated according to the following relation,

$$\left|\chi^{(3)}\right| = \sqrt{\left(\mathrm{Re}\chi^{(3)}\right)\left(\chi^{(3)}\right)^2 + \mathrm{Im}\left(\chi^{(3)}\right)^2} \quad (G.7)$$

The third order nonlinear optical susceptibility is obtained to be comparably larger than the other reported samples in Table 4.

4. Conclusion

A proton transfer organic complex GHFGSM was synthesized and its single crystals were grown by the slow solvent evaporation method at an elevated temperature. The lattice parameters and monoclinic crystal system of GHFGSM with space group $P2_1/n$ was revealed by single crystal XRD. The presence of distinct functional groups was identified by FTIR spectral analysis. The UV–vis spectra of the GHFGSM revealed that they are highly transparent in nature in the visible region, with the cut-off wavelength at 252 nm and optical direct band-gap as 5.19 eV using Tauc's plot including parameters such as absorption coefficient (α), reflectance (R), extinction coefficient (K) refractive index (n_0), electric susceptibility (χ_c) and optical conductivity (σ_{op}) was calculated and optical properties were explored. The melting point and crystallization of GHFGSM was confirmed by TG-DSC analysis. The dielectric character of the crystal is understood from the dielectric study from which favouring parameters like a. c conductivity (σ_{ac}) and activation energy (E_a) were calculated, established presence lesser defects in the GHFGSM crystal. Fluorescence lifetime proved the emission characteristics of the crystal. Closed aperture Z-scan studies affirm its negative nonlinearity (self-defocusing) in the GHFGSM crystal and open aperture Z-scan evinces the saturation absorption. Hence, the nonlinear optical study obviously suggests GHFGSM as a promising third order NLO material which can find applications in domain of optoelectronics and photonics.

Acknowledgements

The authors acknowledge to SAIF, IIT Madras for providing single crystal XRD, FTIR, Thermal studies and Fluorescence & life time measurement.

References

[1] A. Kandasamy, R. Mohan, M. Lydia Caroline, S. Vasudevan, Nucleation kinetics, growth, solubility and dielectric studies of L-Proline cadmium chloride monohydrate semiorganic nonlinear optical single crystal, Cryst. Res. Technol. (2007), https://doi.org/10.1002/crat.200710980.
[2] M. Peer Mohamed, P. Jayaprakash, M. Nageshwari, C. Rathika Thaya Kumari, P. Sangeetha, S. Sudha, G. Mani, M. Lydia Caroline, Crystal growth, structural, spectral, thermal, linear and nonlinear optical characterization of a new organic nonlinear chiral compound: L-tryptophan-fumaric acid-water (1/1/1) suitable for laser frequency conversion, J. Mol. Struct. 1141 (2017) 551–562.
[3] G. Maruthu, S. Krishnan, T. Thilak, P. Samuel, G. Vinitha, G. Pasupathi, Optical, thermal and mechanical studies of nonlinear optical materials diglycine barium chloride monohydrate (DGBCM) single crystal, J. Non. Phys. Mater. 22 (2013) 1350043.
[4] P. Sangeetha, P. Jayaprakash, M. Nageshwari, M. Peer Mohamed, G. Vinitha, M. Lydia Caroline, Growth and characterization of L-phenylalanine nitric acid (LPN) and Tris L-(phenylalanine)-phenylalanininum nitrate (TPLPN) as second and third order nonlinear optical materials, Chin. J. Phys. (2018), https://doi.org/10.1016/j.cjph.2017.12.026.
[5] M. Nageshwari, C. Rathika Thaya Kumari, G. Vinitha, M. Peer Mohamed, S. Sudha, M. Lydia Caroline, Crystal growth, structural, spectral, thermal, dielectric, linear and nonlinear optical characteristics of a new organic acentric material: L-methionine-succinic acid (2/1), J. Mol. Struct. 1155 (2018) 101–109.
[6] Hamed Ghanadan, Mehdi Hoseini, Ameneh Sazgarnia, Soheil Sharifi, Effect of ion pairs on nonlinear optical properties of crystal violet: surfactants, nanodroplets, and in vitro culture conditions, J. Electron. Mater. 48 (2019) 7417–7426, https://doi.org/10.1007/s11664-019-07516-9.
[7] Sergiu Draguta, Marina S. Fonari, Artem E. Masunov, Joel zazueta, Shannon Sullivan, Mikhail Yu Antipin, TatianaV. Timofeeva, New acentric materials constructed from aminopyridines and 4-nitrophenol, CrystEngComm 5 (2013) 4700.
[8] Mehdi Hoseini, Ameneh Sazgarnia, Soheil Sharifi, Effect of environment on protoporphyrin IX: absorbance, fluorescence and nonlinear optical properties, J. Fluoresc. 29 (2019) 531–540, https://doi.org/10.1007/s10895-019-02366-4.
[9] Afshin Azarpour, Soheil Sharifi, Forough Rakhshanizadeh, Nonlinear optical properties of crocin: from bulk solvent to nano-confined droplet, J. Mol. Liq. 252 (2018) 279–288.
[10] R. Jothi Mani, P. Selvarajan, H. Alex Devadoss, D. Shanthi, Second order, third order NLO and other properties of L-alanine crystals admixtured with perchloride acid (LAPA), Optik 126 (2014) 213.
[11] P. Jayaprakash, P. Sangeetha, M. Peer Mohamed, G. Vinitha, S. Muthu, M. Prakash, M. Lydia Caroline, Growth and characterization of DL-Mandelic acid (C6H5CH(OH)CO2H) single crystal for third-order nonlinear optical applications, J. Mol. Struct. 1148 (2017) 314–321.
[12] K. Ambujam, K. Rajarajam, S. Selvakumar, I. Vetha Potheher, P. Joseph Ginson, P. Sagayaraj, Growth and Characterization of a noval NLO crystal bis-glycine hydrogen chloride (BGHC), J. Cryst. Growth 286 (2006) 440–444.
[13] P. Kalaiselvi, S. Alfred Cecil Raj, N. Vijayan, D. Haranth, Growth, structural, spectral, optical and mechanical studies of gamma glycine bis glycin oxalate (GBGOX) new NLO single crystal by SEST method, Optik 125 (2014) 1825–1828.
[14] S. Natarajan, A. Kalyanasunder, J. Suresh, S.A. Martin Britto Dhas, P.L. Nilantha Lakshman, Glycinium hydrogen fumarate glycine solvate monohydrate, Acta Crystallogr. E 65 (2009) o462.
[15] B. Riscob, Mohd Shakira, J. Kalyana Sundar, S. Natarajan, M.A. Wahab, G. Bhagavannarayana, Synthesis, growth, crystal structure and characterization of a new organic material: Glycine glutaric acid, Spectrochim. Acta, Part A 78 (2011) 543–548.
[16] M. Alagar, R.V. Krishnakumar, K. Rajagopal, M. Subha Nandhini, S. Natarajan, L-Phenylalanine fumaric acid, Acta Crystallogr. E 59 (2003) o952–o954.
[17] M. Alagar, R.V. Krishnakumar, M. Subha Nandhini, S. Natarajan, DL-Valine-fumaric acid (2/1), Acta Crystallogr. E 59 (2003) o857–o859.
[18] M. Prakash, D. Geetha, M. Lydia Caroline, Growth and characterization of Nonlinear Optics (NLO) active L-phenylalanine fumaric acid (LPFA) single crystal, *Materials and Manufacturing processes*, Taylor & Francis 27 (2012) 519–522.
[19] C. Ramachandra Raja, A. Antony Joseph, Crystal growth and characterization of new nonlinear optical single crystals of L-alaninium fumarate, Mater. Lett. 63 (2009) 2507–2509.
[20] A. Sowmya, G.N. Anil Kumar, Sujeet Kumar, Subhas S. Karki, Crystal structure,

quantum chemical and Hirshfeld surface analysis substituted imidazo- thiadiazole-5-carbaldehyde, Chem. Data Collect. 17–18 (2018) 431–441, doi.org/10.1016/j.cdc.2018.11.002.
[21] A. Jayarama, H.J. Ravindra, S.M. Dharmaprakash, Crystal growth, characterization, structural characteristics and second harmonic generation in N-benzoyl glycine crystals, Mater. Chem. Phys. 113 (2009) 91–95.
[22] K. Senthil, S. Kalainathan, A. Ruban Kumar, P.G. Aravindan, Investigation of synthesis, crystal structure and third-order NLO properties of a new stilbazolium derivative crystal: a promising material for nonlinear optical devices, RSC Adv. 4 (2014) 56112.
[23] Joseph R. Lakowicz, Principles of Fluorescene Spectroscopy,Kluiver Academic Plenum Publishers, third ed., Springer, New York, 2006.
[24] M.B. Mallick, S.V.G. Ravindranath, N.C. Das, Development of Windows Based Software to Analyze Fluorescence Decay with Time-Correlated Single Photon Counting (TCSPC) Setup, BARC–2002/E/016), India, 2002, pp. 1–20.
[25] P.B. Chapple, J. Staromlynska, J.A. Hermann, T.C. Mckay, Single beam Z-Scan :Measurement techniques and analysis, J. Nonlinear Opt. Phys. Mater. 6 (1997) 251–293.
[26] T.C. SabariGirisun, S. Dhanuskodi, G. Vinitha, $\chi^{(3)}$ measurement and optical limiting properties of metal complexes of thiourea using Z-scan, Mater. Chem. Phys. 129 (2011) 9–14.
[27] N. Sudharsana, B. Keerthana, R. Nagalakshmi, V. Krishnakumar, L. Guru Prasad, Growth and characterization of hydroxyethylammonium picrate single crystals for third-order nonlinear optical applications, Mat. Chem. Phys. 518 (2017) 736–746.
[28] M. Sukumar, R. Ramesh Babu, K. Ramamurthi, Etching, dielectric and third order nonlinear optical studies on Czochralski grown Bi2ZnB2O7 single crystal, Mater. Res. Innovat. (2017), https://doi.org/10.1080/14328917.2016.1193362, 21 79-85.
[29] M.K. Kumar, S. Sudhahar, P. Pandi, G. Bhagavannaranya, R.M. Kumar, Studies of the structural and third-order nonlinear optical properties of solution grown 4-hydroxy-3-methoxy-4-N-methylstibazoliumtosylate monohydrate crystals, Opt. Mater. 36 (2014) 988.

J Mater Sci: Mater Electron

Synthesis, growth, optical and third order nonlinear optical properties of L-Phenylalanine D-Mandelic acid single crystal for photonic device applications

P. Jayaprakash[1,*], M. Lydia Caroline[2], S. Sudha[3], R. Ravisankar[4], G. Vinitha[5], P. Ramesh[6], and E. Raju[3]

[1] Department of Physics, St. Joseph's Institute of Technology, OMR, Chennai, Tamil Nadu 600119, India
[2] Department of Physics, Dr. Ambedkar Govt. Arts College, Vyasarpadi, Chennai, TamilNadu 600039, India
[3] Post Graduate and Research Department of Physics, Arignar Anna Govt. Arts College, Cheyyar, TamilNadu 604 407, India
[4] Post Graduate and Research Department of Physics, Government Arts College, Tiruvannamalai, TamilNadu 606603, India
[5] Division of Physics, School of Advanced Science, VIT University, Chennai, TamilNadu 600 127, India
[6] Department of Physics, Govt. Thirumagal Mills College, Gudiyattam, TamilNadu 632602, India

Received: 20 July 2020
Accepted: 29 September 2020

ABSTRACT

Organic nonlinear optical L-phenylalanine D-mandelic acid (LPDMA) single crystals have been harvested adopting slow solvent evaporation solution growth technique (SSEST) with growth period of 15 days. The XRD studies of the crystal confirm the non-centrosymmetric nature of the crystal. The presence of functional groups for the formation of the compound was confirmed by Fourier Transform Infrared (FTIR) analysis. The UV–Visible spectral studies ascertained linear optical quality and estimation of optical parameters. The nonlinear optical property was studied from Kurtz-Perry powder technique and *Z*-scan technique. The quantum chemical calculations such as HOMO–LUMO and Molecular Electrostatic Potential (MEP) were calculated and presented. In order to find out various mechanical parameters such as Vicker's hardness number (H_v), Mayer's index (n), yield strength (σ_y) and stiffness constant (C_{11}), Vicker's microhardness tester was utilized.

1 Introduction

Design and synthesis of newer organic materials with well built third-order nonlinear optical (NLO) absorptions are in great demand because of their potential applications extending from optical communication to optical computing and essential role in biological and medical sciences [1]. The NLO behavior of organic molecules possesses high nonlinearities and ultra-fast response. The third-order NLO crystals possessing weak nonlinear absorption (NLR) can be utilized in applications such as opto-electronic and photonic switching devices [2]. The formation of a molecule such as donor–acceptor–

Address correspondence to E-mail: jayajp85@gmail.com

https://doi.org/10.1007/s10854-020-04565-3
Published online: 15 October 2020

donor (D–A–D), donor–π–donor (D–π–D), donor–π–acceptor (D–π–A) and acceptor–donor–acceptor (A–D–A) makes organic molecules superior [1].

Of all the NLO materials available and developed so far, amino acids are found to display better non-optical properties. Amino acids exhibit molecular chirality, hydrogen bonds and the absence of strongly conjugated bonds, wide transparency ranges in the visible and UV spectral regions, and zwitterionic nature of the molecule which favors crystal hardness [3]. Amino acids showed potential candidature for non-linear optical applications for their specific features of interest such as zwitterionic nature of the molecule and ability to crystallize into non-centrosymmetric space groups makes importance of the compound selection. L-phenylalanine is commonly used to build neurotransmitters and is one of the most essential amino acids. It finds application in the field of food and beverage manufacturing and is often sold out as supplements. It is also known for its analgesics and antidepressant effects [4].

Materials such as L-phenylalanine benzoic acid [5], L-phenylalanine D-methionine (LPDM) [6] and L-phenylalanine nitrate (LPN) and L-(phenylalanine) L-phenylalaninium nitrate (TPLPN) [7] have been synthesized which possess third order nonlinear optical sequence. As a part of our research to identify for an advanced NLO material, growth of L-phenylalanine D-mandelic acid (LPDMA) at room temperature by slow solvent evaporation solution growth technique was done to report on various characterization analysis such as SXRD, spectral, linear optical studies, microhardness, antimicrobial activity, HOMO–LUMO and MEP. Also second harmonic generation (SHG) and third harmonic generation (THG) studies were conducted for LPDMA organic chromophore using Kurtz-Perry and *Z*-scan technique, in order to understand its suitability in the field of nonlinear optical applications.

2 Experimental

L-Phenylalanine (Spectrochem 99%) and D-mandelic acid (SRL 99%) were taken in stoichiometric molar (1:1) ratio for synthesis. L-Phenylalanine was added step by step into the solution of deionized water dissolved with D-madelic acid. Crystal was grown using slow evaporation technique under the ambient temperature by transferring the filtered L-Phenylalanine D-mandelic acid solution to crystal growth vessels. The synthesis scheme of LPDMA is depicted in Fig. 1.

The colorless transparent single crystal were obtained in a period of 15 days. The harvested optically transparent LPDMA crystal is shown in Fig. 2.

3 Results and discussion

3.1 Single crystal X-ray diffraction analysis

This study was performed to know the crystallinity and lattice parameters of the crystal. From the specimen reflections a specific number of planes were collected. The reflection indicates the presence of monoclinic system and space group C2. The lattice parameters are a = 19.88 Å, b = 5.58 Å, c = 17.07 Å, $\alpha = 90°$, $\beta = 123°$, $\gamma = 90°$ and the volume of the material is found to be 1572 Å. The obtained crystallographic data was compared with that of kimio Okamura et al. and are in accordance with literature [8].

3.2 FTIR spectral analysis

FTIR spectrum is essential to analyze the structure of a material from its vibration related interactions in its different functional groups. Figure 3 shows the FTIR spectrum of LPDMA. A peak observed of 3089 cm^{-1} is related to NH_3^+ showing an asymmetric stretching [9]. The stretching of CH_2 is seen at 2871 cm^{-1}. The CH stretching vibrations give rise to a peak at 2096 cm^{-1} and the C=O stretching appears at 1607 cm^{-1} [10]. The peak at 1495 cm^{-1} is assigned to COO^- symmetric stretching. The peak around 1359 cm^{-1} indicates the presence of C–N stretching vibration. The wave number occurring at 1328 cm^{-1} may be attributed due to OH in plane bending. The sharp peak at 1034 cm^{-1} is assigned to C–NH_2 stretching vibration. The benzene ring deformation is due to bands at 869 cm^{-1}. The vibration of CH_2 is seen at 745 cm^{-1}. The absorption bands at 588 cm^{-1} and 484 cm^{-1} related to C–C stretching are seen in the FTIR spectrum.

3.3 UV–Visible studies

LAMBDA-35 spectrophotometer of wavelength 200–700 nm as shown in Fig. 4a was used to obtain

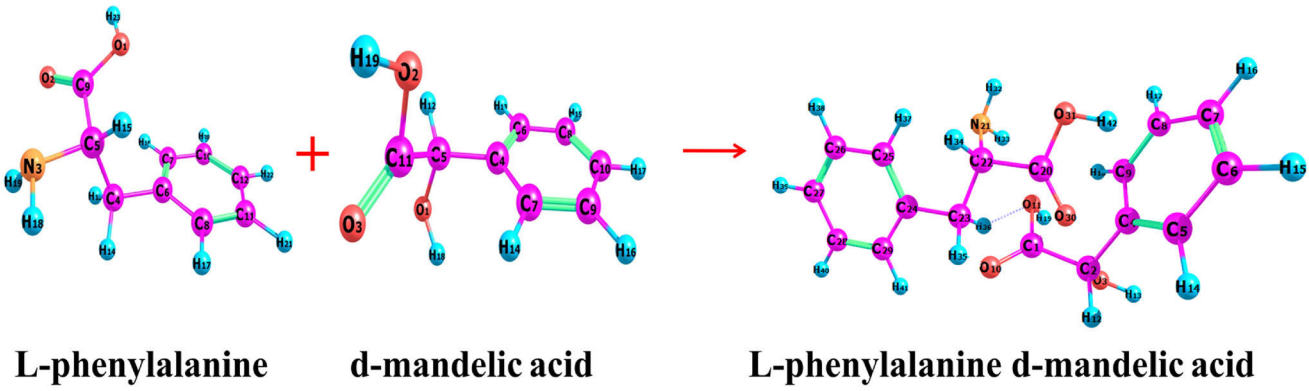

Fig. 1 Synthesis scheme of LPDMA compound

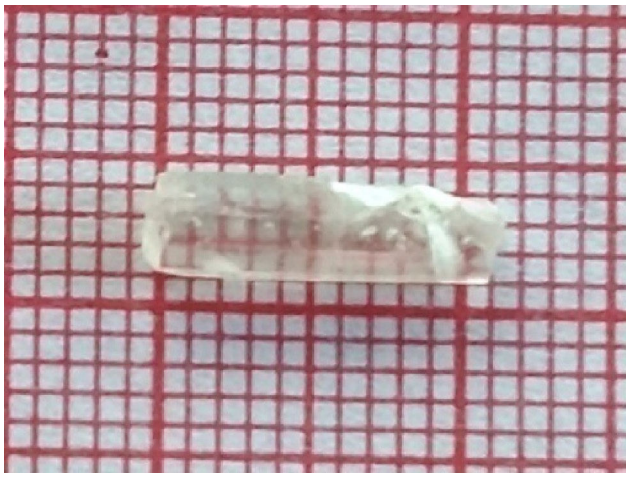

Fig. 2 Photograph of the grown LPDMA crystal

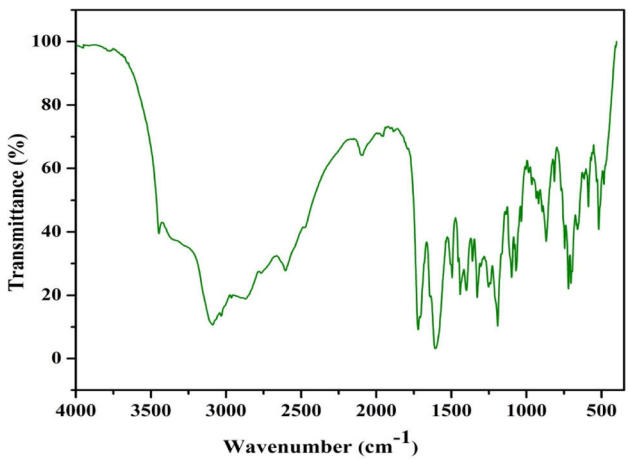

Fig. 3 FTIR spectrum of LPDMA

the absorption spectrum for LPDMA. It shows an extended transparent spectrum towards the UV region due the presence of lower absorbance. The lower cut-off wavelength observed at 256 nm stipulate the suitability for frequency conversion applications in NLO [11]. The Tauc's plot of $(\alpha h\upsilon)^2$ vs. $h\upsilon$ was manipulated to evaluate the band gap of the LPDMA crystal by extrapolation of the linear part of the graph as illustrated in the Fig. 4b. The value of E_g is found to be 4.62 eV. The wide band gap confirms the suitable material for the opto-electronic applications.

3.3.1 *Optical constant characteristics*

The various optical parameters like refractive index which are important in frequency doubling experiments when utilizing NLO crystals were evaluated using the formulae given below. Extinction coefficient (K) and reflectance (R) depend on the energy of the photon (Fig. 5a and b) [12].

$$K = \frac{\alpha\lambda}{4\pi} \tag{1}$$

$$R = \frac{\exp(-\alpha t) \pm \sqrt{\exp(-\alpha t)T - \exp(-3\alpha t)T + \exp(-2\alpha t)T^2}}{\exp(-\alpha t) + \exp(-2\alpha t)T} \tag{2}$$

$$n_0 = \frac{-(R+1) \pm 2\sqrt{R}}{(R-1)} \tag{3}$$

As observed from the Fig. 5c, the variation of the refractive index (n_0) with photon energy ($h\upsilon$) reveals the refractive index (n_0) to be 1.2097 for the LPDMA crystal at λ_{exe} = 294 nm, support LPDMA as a suitable material for antireflection coating in solar thermal devices and NLO applications [13].

Also the optical conductivity (σ_{op}) of the grown crystal when illuminated with light is found to depend on refractive index (n_0) and the speed of light (c) as per the the following relation:

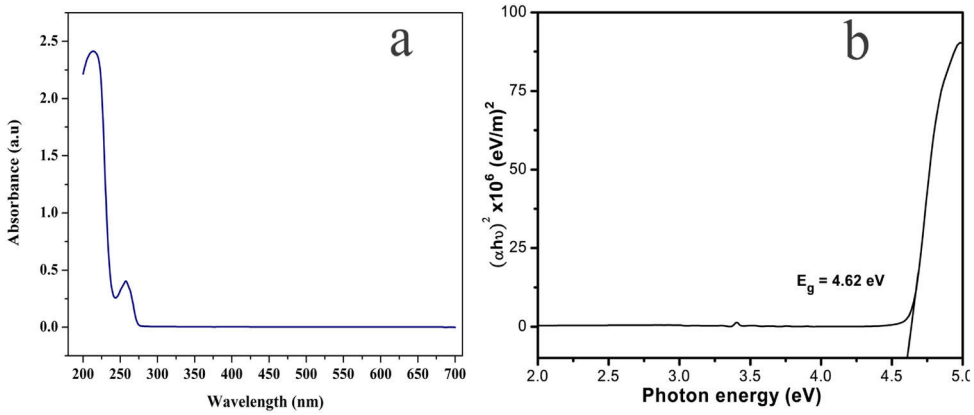

Fig. 4 **a** UV–Vis spectrum and **b** Band gap energy of LPDMA

$$\sigma_{op} = \frac{n_0 \alpha c}{4\pi} \tag{4}$$

and also the electrical conductivity is associated to the optical conductivity of the LPDMA crystal as follows,

$$\sigma_{ele} = \frac{2\lambda\sigma_{op}}{\alpha} \tag{5}$$

Figure 5e illustrates the response of the optical conductivity (σ_{op}) with photon energy (hυ). Figure 5e and d indicate low extinction value (10^{-5}) and electrical conductivity (8×10^{10} $(\Omega\ m)^{-1}$) exhibits the semiconducting nature of the material.

The electric susceptibility (χ_c) is closely correlated to the optical constants given by,

$$\varepsilon_r = \varepsilon_0 + 4\pi\chi_c = n_0^2 - K^2 \tag{6}$$

$$\chi_c = \frac{n_0^2 - K^2 - \varepsilon_0}{4\pi} \tag{7}$$

At λ = 293 nm, the calculated value of electric susceptibility χ_c is found to be 0.1719.

3.4 Nonlinear optical characterizations

3.4.1 SHG measurement

LPDMA's SHG was tested using the [14] Kurtz-Perry Powder technique. To illuminate the LPDMA sample, the fundamental beam of 1064 nm Q-switched Nd:YAG laser with pulse width 10 ns and repetition rate 10 Hz was employed. The method of frequency doubling paved the way for green light emission (532 nm), which was observed via a photomultiplier tube and eventually shown on a storage oscilloscope. This process shows LPDMA crystal's conversion efficiency as 0.41 times greater than that of typical single-crystal KH_2PO_4 (KDP).

3.4.2 THG measurement (Z-scan technique)

Z-scan technique was employed to analyse the Third order NLO behavior of the crystal. The laser source used was Nd:YAG, focused using a convex lens of focal length 3.5 cm. Intensity dependent nonlinear index of refraction (n_2), nonlinear absorption coefficient (β) and third-order nonlinear optical susceptibility ($\chi^{(3)}$) by closed and open aperture signatures etc. can be easily and accurately be obtained using this method [15]. The schematic diagram of Z-scan technique is as illustrated in Fig. 6a. Quantification of the aperture when closed, open and the ratio of closed is to open are shown in Fig. 6b–d.

In order to measure the non-linear refractive index n_2 closed aperture Z-scan was performed. Non-linear refraction is defined as the phenomenon wherein the refractive index is said to vary when there is a high intensity source. An aperture is placed in front of detector 2 in closed aperture Z-scan. When a Gaussian laser beam is made to pass through the material medium, it acts like an intensity dependent lens. Along the beam path, the effective focal length of medium changes due to the change in input intensity. This results in the intensity distribution at the far field aperture. The sign of non-linear refractive index n_2 and the location of the sample decide the amount of energy that can get transmitted. In cases where the sample is placed at a far of distance from the focus the intensity of the beam is weak to cause non-linearity. The power that is measured by the detector remains a constant.

The sample behaves like a variable lens when it is moved towards the focus. The non-linear absorption and its refraction get enhanced. There is an increase in the transmittance when a small amount of light

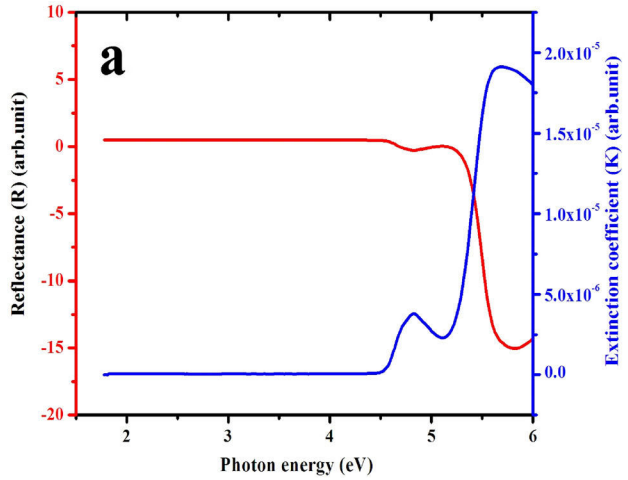
a
Reflectance (R) (arb.unit)
Extinction coefficient (K) (arb.unit)
Photon energy (eV)

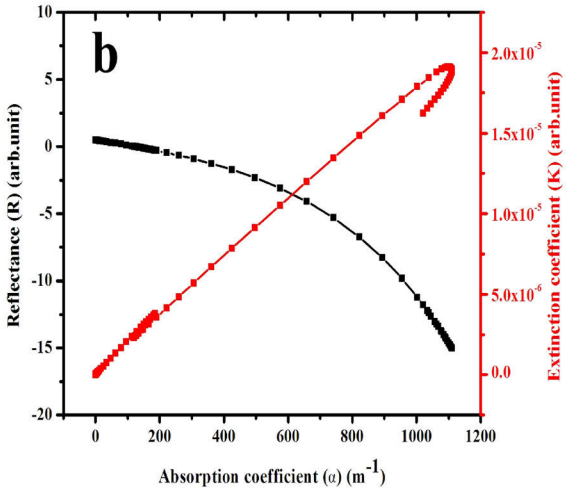
b
Reflectance (R) (arb.unit)
Extinction coefficient (K) (arb.unit)
Absorption coefficient (α) (m-1)

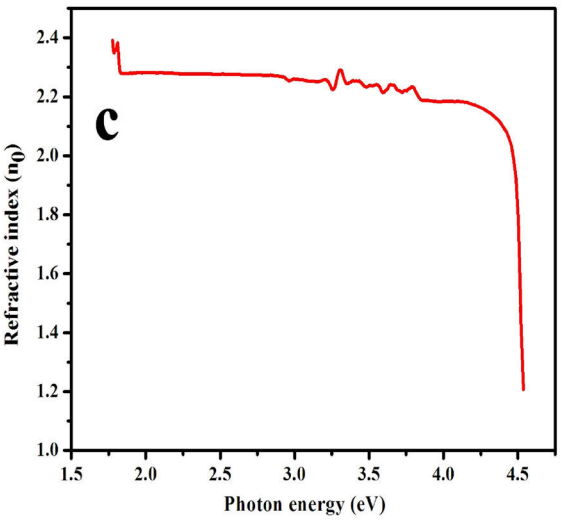
c
Refractive index (n0)
Photon energy (eV)

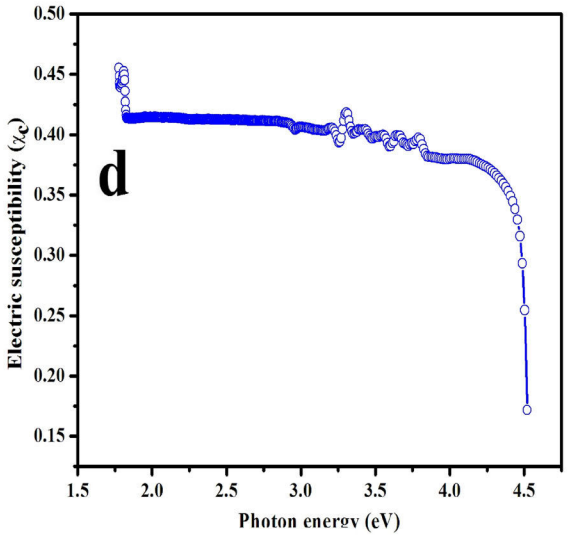
d
Electric susceptibility (χe)
Photon energy (eV)

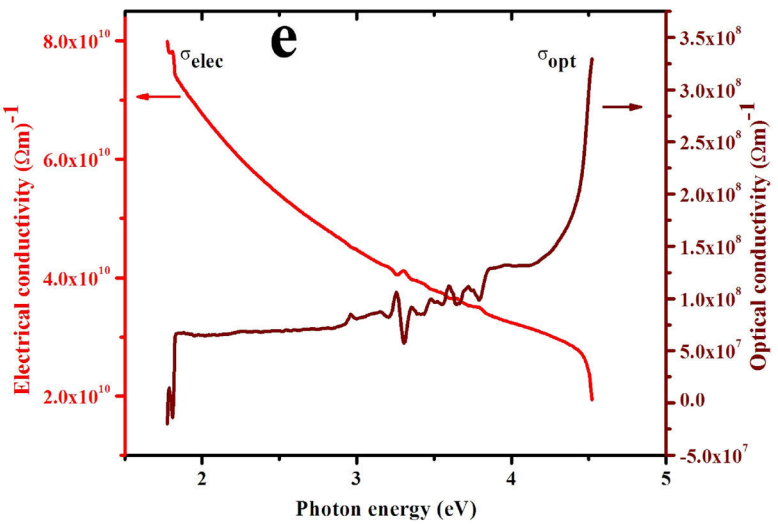
e
σelec
σopt
Electrical conductivity (Ωm)-1
Optical conductivity (Ωm)-1
Photon energy (eV)

◀**Fig. 5** **a** Plot of reflectance (R) and extinction coefficient (K) vs. photon energy **b** Variation of reflectance (R) and extinction coefficient (K) with absorption coefficient (α) **c** Plot of refractive index (n_0) vs. photon energy (d) electric susceptibility (χ_c) vs. photon energy (e) Variation of electrical conductivity and optical conductivity vs. photon energy

falls on the detector as the sample diverges the beam that falls on it. The sample does not have any effect on the beam. As the sample moves away from the focus, the strength of the refraction decreases due to lower intensity. This results in decrease in measured transmittance. Finally, when the sample reaches far field, the intensity is weak to initiate nonlinearity, so the measured power on the detector remains constant. The pre-focal transmittance maximum (peak) followed by post focal transmittance minimum (valley) behavior as shown in Fig. 6b is the characteristic of a material with a negative nonlinear refractive index [6].

There is good change in the optical properties of the medium when a Gaussian laser beam is incident on the nonlinear medium. Nonlinear absorption coefficient β of the nonlinear medium can be calculated using the open aperture Z-scan method. $S = 1$ is insensitive in open aperture z-scan experiments. That is, there is no aperture in front of detector 2. The z-scan traces obtained with no aperture is expected to be symmetric with respect to the focus ($z = 0$) where the transmittance is minimum. In this experiment, the sample is made to traverse from one end of the far field to the other end through the focus ($z = 0$).

At the far field, the intensity is low and hence linear absorption occurs. In other words, the intensity is not sufficient to induce any nonlinear absorption in the far field region. A graph of normalized transmission versus sample position has been plotted. As the sample is brought close to the focus there is peak formed in the measured transmittance. The saturable absorption is shown in Fig. 6c and it corresponds to the measured transmittance peaks. Non-linear refraction and absorption are shown when the aperture is closed whereas pure non-linear absorption is seen when the aperture is open. Figure 6d shows the closed to open ratio of aperture that is used to eliminate any absorption.

The difference in the permeability among peak and valley (ΔT_{P-V}) is given by

$$\Delta T_{P-V} = 0.406\,(1-S)^{0.25}|\Delta\Phi_0| \tag{8}$$

where $|\Delta\Phi_0|$ represents the on-axis phase shift, S is the linear transmittance aperture and it is found using the relation

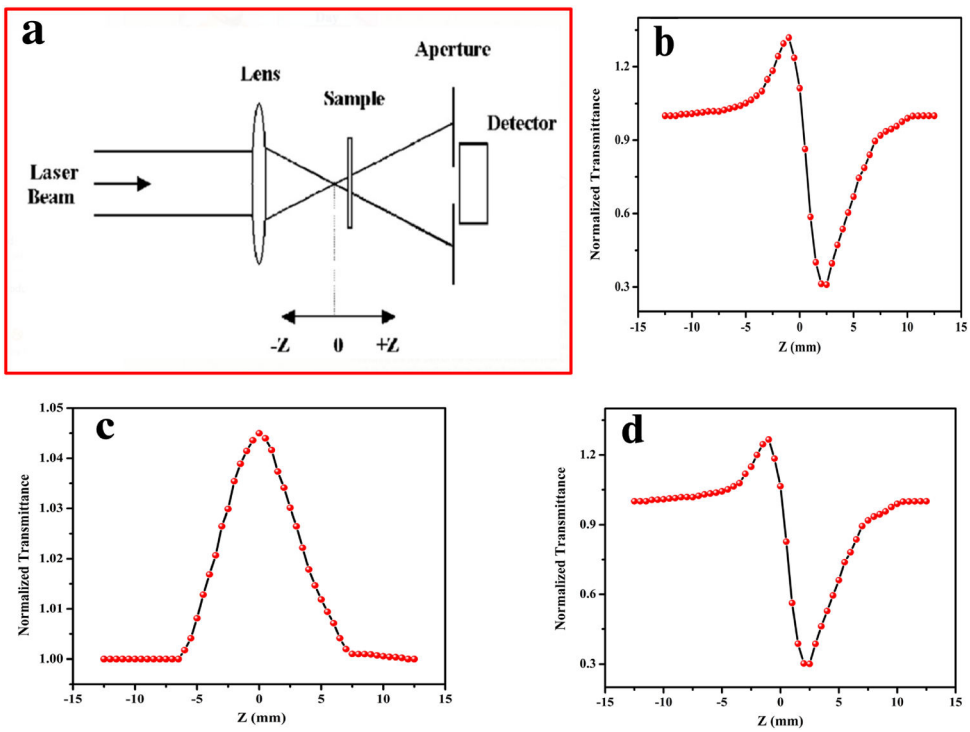

Fig. 6 **a** Schematic diagram of Z-scan technique **b** Closed aperture trace **c** Open aperture trace and **d** Ratio of the closed-to-open Z-scan trace of LPDMA

Table 1 Obtained nonlinear optical parameters from Z-scan measurements for LPDMA

Parameters	Measured values for LPDMA crystal
Laser beam wavelength (λ)	532 nm
Linear absorption coefficient (α)	1.264
Nonlinear refractive index (n_2)	7.835×10^{-8} cm^2W^{-1}
Nonlinear absorption coefficient (β)	0.052×10^{-4} cmW^{-1}
Real part of the third-order susceptibility [Re (χ^3)]	10.280×10^{-6}esu
Imaginary part of the third-order susceptibility [Im (χ^3)]	0.320×10^{-6}esu
Third-order nonlinear optical susceptibility (χ^3)	10.285×10^{-6}esu

$$S = 1 - \exp\left(\frac{-2r_a^2}{\omega_a^2}\right) \tag{9}$$

where r_a denoting the radius of the aperture and ω_a is the beam radius at the aperture.

Third-order nonlinear refractive index of the crystal is associated with on-axis phase shift

$$n_2 = \frac{\Delta\Phi_0}{KI_0L_{\text{eff}}} \tag{10}$$

where I_0 is the intensity of the laser beam at focus ($Z = 0$) ($I_0 = 26.31$ MWm^{-2}) and L_{eff} is the effective thickness of the crystal which is evaluated from the formula $L_{\text{eff}} = [1 - \exp(-\alpha L)]/\alpha$. Where α and L represent linear absorption coefficient and the thickness of the crystal respectively.

Nonlinear absorption coefficient (β) can be evaluated by applying the following formula,

$$\beta = \frac{2\sqrt{2}\Delta T}{I_0L_{\text{eff}}} \tag{11}$$

Third-order nonlinear optical (TONLO) susceptibility is denoted by the following relations. TONLO susceptibility of real and imaginary part of the susceptibility is calculated by the formulae

$$\text{Re}\chi^{(3)}(esu) = \frac{10^{-4}(\varepsilon_0C^2n_o^2n_2)}{\pi}\left(\frac{cm^2}{W}\right) \tag{12}$$

$$\text{Im}\chi^{(3)}(esu) = \frac{10^{-2}(\varepsilon_0C^2n_0\lambda\beta)}{4\pi^2}\left(\frac{cm^2}{W}\right) \tag{13}$$

$$|\chi^{(3)}| = \sqrt{(\text{Re}(\chi^{(3)}))^2 + (\text{Im}(\chi^{(3)}))^2} \tag{14}$$

Table 1 portrays the calculated TONLO parameters of LPDMA crystal. Thus, the LPDMA could be a suitable candidate for the NLO device fabrications.

3.5 Frontier molecular orbitals (FMOs)

Frontier molecular orbitals included the doubly occupied molecular orbital and unoccupied molecular orbitals [16]. FMOs are said to play a vital role in the study of optical and electric properties. The HOMO and LUMO energies rely on certain effects like substituents and electronegativity. The chemically hard molecules are less polarizable than the soft ones due to need of large energy for excitation. The susceptibility of the molecule due to electrophilic attack is mainly due to HOMO energy occurring on account of electron donation. The gap in the middle of HOMO and LUMO indicate the stability in the molecule. Molecular energy gap take part in deciding the optical and chemical properties. The easiest approach would be taking into consideration Koopman's theorem, where the negative HOMO energy estimates the ionization potential (IP) and the negative LUMO energy point out the electron affinity (EA). From the Mulliken's definition of electronegativity we can see that the sum of both IP and EA, (IP + EA/2) serve as a good approximation to the electronegativity [17].

Using Gauss view 0.5 program the illustrations of the doubly occupied (HOMO) and unoccupied (LUMO) orbitals for the molecule are calculated by the DFT. The topology of HOMO and LUMO energy level plots are shown in Fig. 7. Red colour is used to denote the position of the electron donating (positive) position whereas green colour is used to denote the electron accepting (negative) one. The energy gap of occupied and unoccupied orbitals indicates the total charge transfer that occurs due to interaction within the molecule. The energy gap of present molecule is − 5.9836 eV and − 5.1081 eV for HOMO and LUMO respectively both at an energy level of ΔE = 0.8755 eV. The energy values of the orbitals that corresponding to various energy gaps, related quantum chemical descriptors like Ionization potential (IP), Electron affinity (EA), Electro negativity (χ), Chemical hardness (η), Chemical softness (S), Electrophilicity index (ω), Chemical potential (μ),

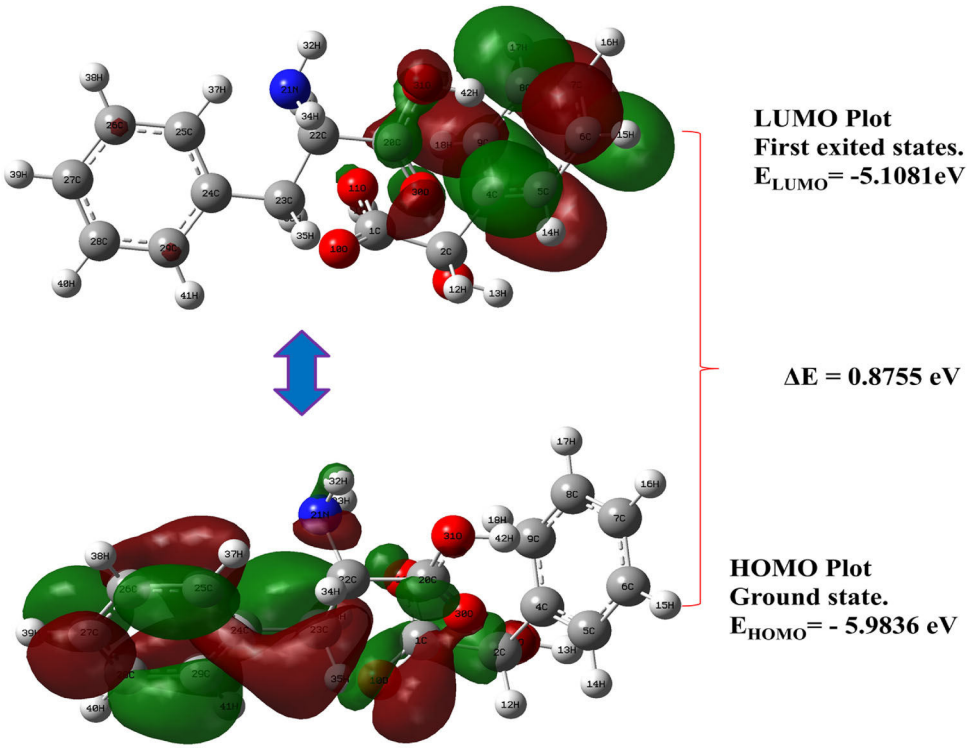

Fig. 7 Atomic orbital HOMO—LUMO composition of the frontier molecular orbital of the LPDMA

Table 2 The calculated quantum chemical parameters of LPDMA compound

Chemical parameters	DFT/B3LYP/ 6–311+ +G(d, p)
HOMO (eV)	− 5.9836
LUMO (eV)	− 5.1081
Ionization potential b IP)	5.9836
Electron affinity (EA)	5.1081
Energy gap (eV)	0.8755
Electronegativity (χ)	5.5458
Chemical potential (μ)	− 5.5458
Chemical hardness (η)	0.4378
Chemical softness (S)	1.1422
Electrophilicity index (ω)	35.1297
Electronic charge	12.6690
Electron donating capability (w−)	37.95780049
Electron accepting capability (w+)	32.41195049

Electronic charge, Electron donating capability (W+) and Electron accepting capability (W−) are shown in Table 2.

3.6 Molecular electrostatic potential (MEP)

Figure 8 shows the computed 3D plot of the molecular electrostatic potential (MEP) map defined as the potential energy of a proton at a particular position

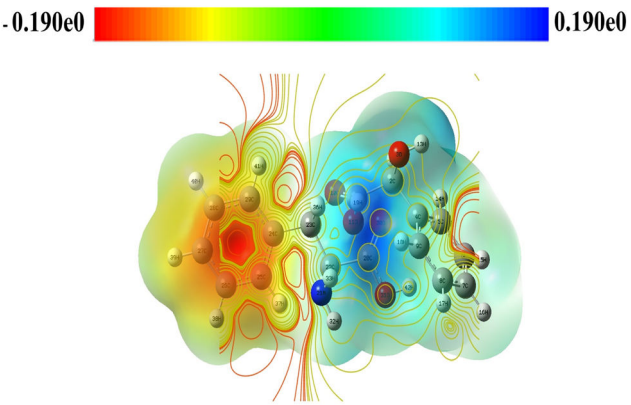

Fig. 8 Molecular electrostatic potential (MEP) of LPDMA

near a molecule for the title compound. The earnest red potential value in this molecule starts from − 0.90e0 a.u and the earnest blue potential possess the value up to + 0.190e0 a.u. which refer to the electron density at different points on the molecule. The electrostatic potential is depicted by different colors. Potential increases in the order red < orange < yellow < green < blue [18]. Regions of negative V(r) are usually associated with the lone pair of electronegative atoms. The red color on the map displays the negative electrostatic potential regions and electrophilic reactions. The blue color indicates positive

or nucleophilic reactivity. As it has been observed from the map in the regions surrounding the L-phenylalanine molecule, the carbon atoms are attributed to a strongly negative character, while the C=O is positive and d-mandelic acid remains in C=O are positive.

3.7 Mechanical (micro) hardness study

The study of micro hardness of the crystal is connected to the physical resistance of the material, with a combined effect of utilization of material leading to mechanical stability and deformation characteristics. Further it is also providing information about the material's physical limit [19]. The hardness properties are basically related to the crystal structure of the material and hardness studies are carried out to understand the plasticity of the crystal [20, 21]. The high hardness values can assure a better polish and quality of the laser surfaces for solid-state laser and optical applications [22].

At an ambient temperature with an applied load P (gm) in the range 25–100 g and indentation time 10 s, the Vicker's hardness number (H_v) associated with below relation was calculated for each load,

$$H_v = 1.855\left(P/d^2\right) \tag{15}$$

A graph is drawn between hardness number (H_v) and applied load P (Fig. 9a). It is seen from the figure that H_v increases with increase in applied load termed as reverse indentation size effect [RISE]. Log P versus Log d is observed to be a straight line and its gradient is determined using least square fitting method. The slope was utilized to find the Mayer's index (n). The value of Mayer's index (n) value denotes the work hardening coefficient for LPDMA crystal which is found to be 3.85 belongs to soft material category.

The yield strength (σ_y) for hardness can be found using the relation (for $n > 2$)

$$\sigma_y = \frac{H_v}{3}(0.1)^{n'-2} \tag{16}$$

where $n' = n + 2$.

A graph is plotted between load P against yield strength (σ_y) and is illustrated in Fig. 9c. According to Wooster's empirical formula, the stiffness constant (C_{11}) for different loads were calculated using the relation,

$$C_{11} = H_v^{7/4} \tag{17}$$

A graph is drawn between load P versus stiffness constant as represented in Fig. 9d. The calculated yield strength (σ_y), stiffness constant (C_{11}) and Vicker's hardness values for different loads are portrayed in Table 3.

3.7.1 Hays–Kendall (HK) approach

The analytical explanation of Hays and Kendall (HK) approach about the nonlinear behavior of hardness material may be conveyed by the following expression [19],

$$P = W + A_1 d^n \tag{18}$$

where W is the minimum applied load to initiate plastic (permanent) deformation (in grams), A_1 is the load independent hardness constant and the value n is 4.17. The values of W and A_1 were evaluated by plotting the applied load P vs. d^2 depicted in Fig. 9e. The resultant value of W is found to be negative, indicates that the crystal own a strong Reverse Indentation Size Effect (RISE) [19]. The hardness H_{HK} value of the LPDMA crystal is shown in Table 4 and is calculated using the formula below.

$$H_{HK} = 1854.4A_1 \tag{19}$$

3.8 Conclusion

Single crystals of L-phenylalanine D-mandelic acid (LPDMA) were grown by slow solvent evaporation solution growth technique and the structure was analyzed by employing XRD techniques. Various functional group assignments were confirmed in the title compound using FTIR analysis. UV–Visible spectral studies of the LPDMA crystal were done to evaluate its optical characteristics. The crystal exhibits high transparency in the visible region when the cut-off wavelength is 256 nm. The value of direct band gap energy is estimated to be 4.62 eV. Optical parameters such as absorption coefficient (α), reflectance (R), extinction coefficient (K), refractive index (n_0), electric susceptibility (χ_c) and optical conductivity (σ_{op}) were evaluated to examine its optical properties. Micro hardness study showed that the LPDMA belongs to softer material category. Kurtz Perry technique establishes that the SHG efficiency of LPDMA is 0.41 times that of KDP. The estimated values of Molecular

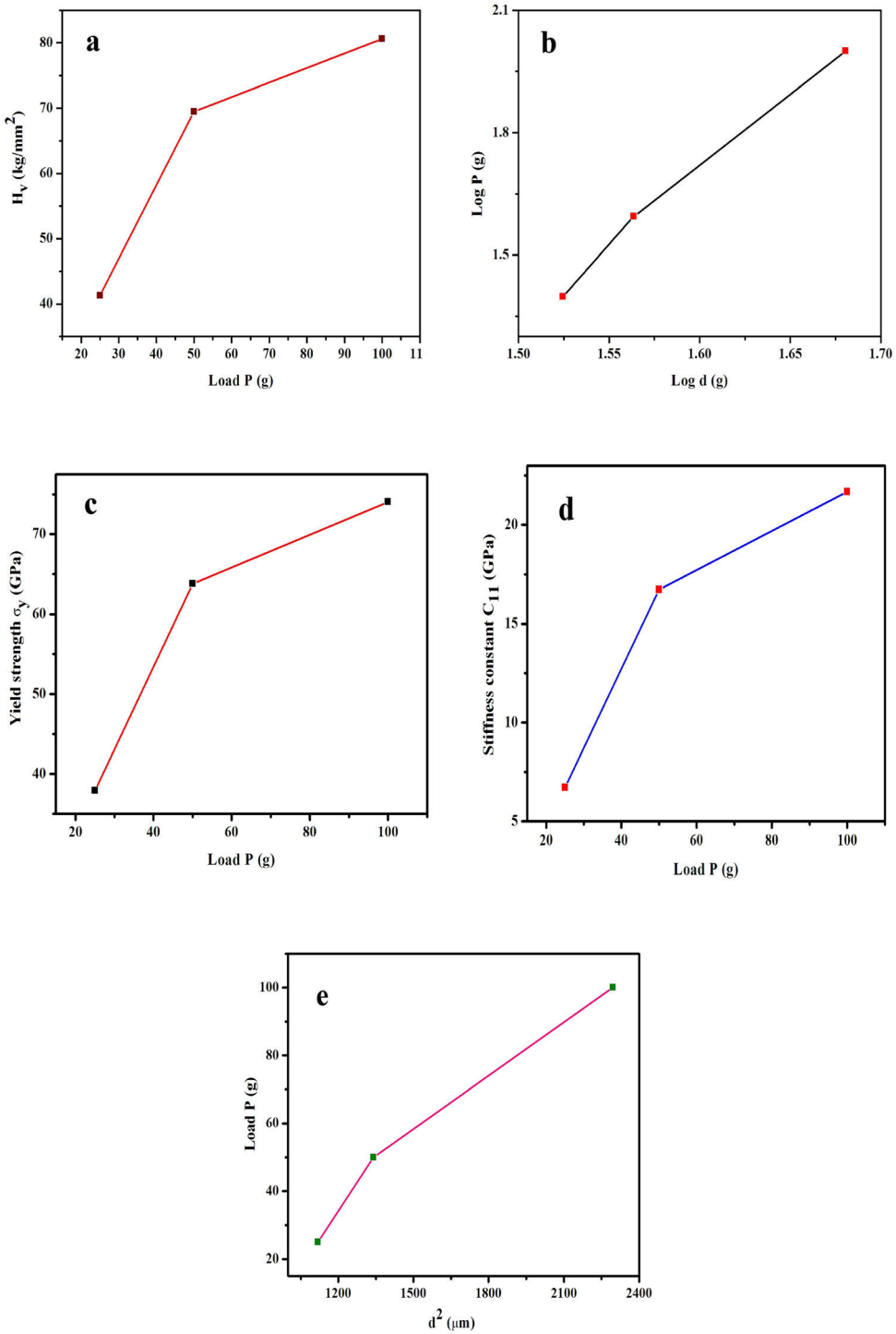

Fig. 9 **a** Hardness value, **b** Mayers plot, **c** yield strength, **d** stiffness constant, **e** plot log P vs. d^2

Table 3 Calculated mechanical parameters of LPDMA

Load P (g)	H_v (kg mm^{-2})	n	σ_y (GPa)	C_{11} (GPa)
25	41.3	3.85	37.91	6.72
50	69.5	3.85	63.80	16.72
100	80.65	3.85	74.04	21.68

Electrostatic Potential (MEP) and HOMO–LUMO energies attest to the high-ranking of the material. The Third-Order Nonlinear Optical (TONLO) properties of LPDMA was analyzed by adopting Z-scan technique. By these concerns, the LPDMA crystal proves to be a versatile candidate for the

Table 4 Calculated HK constant W, A_1 and H_{HK} for LPDMA

HK constant	Results
Resistance pressure (W)	− 37.28 (g)
Load independent constant (A_1)	0.0603 (g/μm^2)
Corrected load independent hardness (H_{HK})	111.8203 (g/μm^2)

future opto-electronic, photonic and NLO applications.

References

1. C.S. Chidan Kumar, T.C.S. Shetty, T.S. Chia, S. Chandraju, S.M. Dharmaprakash, H.K. Fun, C.K. Quah, Third order nonlinear optical properties and crystal structures of (*E*)-1 (3,4-dimethoxyphenyl)-3-(4-(trifluoromethyl)phenyl)prop-2-en-1-one. Mater. Res. Innov. (2017). https://doi.org/10.1080/14328917.2016.1199134
2. A. Muthuraja, S. Kalainathan, Study on growth, structural, optical, thermal and mechanical properties of organic single crystal ethyl p-amino benzoate (EPAB) grown using vertical Bridgman technique. J. Cryst. Growth **459**, 31–37 (2017)
3. M. Prakash, D. Geetha, M. Lydia Caroline, P.S. Ramesh, Crystal growth, structural, optical, dielectric and thermal studies of an amino acid based organic NLO material: l-Phenylalanine l-phenylalaninium malonate. Spectrochim. Acta Part A **83**, 461–466 (2011)
4. R. Surekha, R. Gunaseelan, P. Sagayaraj, K. Ambujam, L-Phenylalanine L-phenylalaninium bromide-a new nonlinear optical material. CrystEngComm **16**, 7979–7989 (2014)
5. M.L. Caroline, S. Vasudevan, Growth and characterization of L-phenylalanine nitric acid, a new organic nonlinear optical material. Mater. Lett. **63**, 41–44 (2009)
6. P. Sangeetha, P. Jayaprakash, M. Nageshwari, C.R.T. Kumari, S. Sudha, M. Prakash, G. Vinitha, M.L. Caroline, Growth and characterization of an efficient new NLO single crystal L-phenylalanine D-methionine for frequency conversion and optoelectronic applications. Phys. B **525**, 164–174 (2017)
7. P. Sangeetha, P. Jayaprakash, M. Nageshwari, M.P. Mohamed, G. Vinitha, M.L. Caroline, Growth and characterization of L-phenylalanine nitric acid (LPN)and tris L-(phenylalanine)-phenylalanininum nitrate (TPLPN) as second and third order nonlinear optical materials. Chin. J. Phys. **56**, 721–739 (2018)
8. K. Okamura, K. Aoe, H. Hiramatsu, N. Nishimura, T. Sato, K. Hashimoto, Crystal structures of diastereomeric 1:1 complexes of (R)- and (S)- phenylalanine (S)- mandelic acid. Anal. Sci. **13**, 315 (1997)
9. M. Prakash, D. Geetha, M.L. Caroline, Crystal growth, structural, optical, spectral and thermal studies of tris(l-phenylalanine)l-phenylalaninium nitrate: a new organic nonlinear optical material. Spectrochim. Acta Part A **81**, 48–52 (2011)
10. G. Socrates, *Infrared and Raman characteristic group frequencies*, 3rd edn. (Wiley, London, 2001)
11. M.R. Jagadeesh, H.M. Suresh Kumar, R.A. Kumari, Growth and characterization of mercuric chloride doped urea single crystals. Mater. Res. Innov. (2017). https://doi.org/10.1080/14328917.2016.1265245
12. M.P. Mohamed, S. Sudha, P. Jayaprakash, G. Vinitha, M. Nageshwari, P. Sangeetha, C.R.T. Kumari, M.L. Caroline, Growth and characterization of L-histidinium fumarate fumaric acid monohydrate single crystal: a promising second and third ordernonlinear optical material. Chin. J. Phys. (2019). https://doi.org/10.1016/j.cjph.2019.05.032
13. P. Jayaprakash, M.P. Mohamed, M.L. Caroline, Growth, spectral and optical characterization of a novel nonlinear optical organic material: D-Alanine DL-Mandelic acid single crystal. J. Mol. Struct. **1134**, 67–77 (2017)
14. S. Sudha, P. Jayaprakash, C.R.T. Kumari, M. Nageshwari, M.L. Caroline, Growth and characterization of Catena-((μ4-dihydrogen oxalate)-bis(μ3-hydrogenoxalato)-(μ2-dihydrogenoxalate)-tetra-aqua-rubidium){Rb(HC2O4)(H2C2O4)(H2O)2}1∞ single crystal for nonlinear optical. Chin. J. Phys. (2020). https://doi.org/10.1016/j.cjph.2019.08.017
15. M. Sheik-Bahae, A.A. Said, E.W. Van Stryland, High-sensitiity, single-beam $n_2$measurement. Opt. Lett. **14**, 955–957 (1989)
16. S. Muthu, J.U. Maheswari, Quantum mechanical study and spectroscopic(FT-IR, FT-Raman, 13C, 1H, UV) study, first order hyperpolarizability, NBO analysis, HOMO and LUMO analysis of 4-[(4-aminobenzene) sulfonyl] aniline by ab initio HF and density functional method. Spectrochim. Acta Part A **92**, 154–163 (2012)
17. N. Issaoui, H. Ghalla, F. Bardak, M. Karabacak, N.A. Dlala, H.T. Flakus, B. Oujia, Combined experimental and theoretical studies on the molecular structures, spectroscopy and inhibitor activity of 3-(2-thienyl) acrylic acid through AIM, NBO, FT-IR, FT-RAMAN, UV and HOMO-LUMO analyses and molecular docking. J. Mol. Struct. **1130**, 659–668 (2017)
18. N. Issaoui, H. Ghalla, S. Muthu, H.T. Flakus, B. Oujia, Molecular structure, vibrational spectra, AIM, HOMO-LUMO, NBO, UV, first order hyperpolarizability, analysis of 3-thiophenecarboxylic acid monomer and dimer by Hartree-Fock and density functional theory. Spectrochim. Acta Part A **136**, 1227–1242 (2015)

19. P. Rekha, P. Jayaprakash, G. Rajasekar, R. Mohan Kumar, G. Vinitha, R. Kanagadurai, Synthesis, growth, structural and optical properties of a novel organic third order nonlinear optical crystal: piperazinediium trichloroacetate. J. Mol. Struct. **1177**, 579–593 (2019)
20. R.E. Vizhi, D.R. Babu, K. Sathiyanarayanan, Study of microhardness and its related physical constants of ferroelectric glycine phosphite (gpi) single crystals. Ferroelectr. Lett. **37**, 23–29 (2010)
21. K. Li, P. Yang, L. Niu, D. Xue, Group electronegativity for prediction of materials hardness. J. Phys. Chem. A **116**, 6911–6916 (2012)
22. M.C. Pujol, X. Mateos, A. Aznar, X. Solans, S. Surinach, J. Massons, F. Dıaza, M. Aguilo, Structural redetermination, thermal expansion and refractive indices of $KLu(WO_4)_2$. J. Appl. Crystallogr. **39**, 230–236 (2006)

Journal of Materials Science: Materials in Electronics
https://doi.org/10.1007/s10854-020-04015-0

Linear and nonlinear optical investigation of L-arginium adipate single crystal for photonic applications

P. Sangeetha[1] · M. Nageshwari[2] · C. Rathika Thaya Kumari[3] · S. Sudha[4] · P. Jayaprakash[5] · M. Lydia Caroline[6] · G. Mathubala[7] · G. Vinitha[8] · A. Manikandan[7]

Received: 20 May 2020 / Accepted: 13 July 2020

Abstract
The L-arginium adipate (LAA) single crystal, is an organic component material efficiently grown by a simple technique called slow evaporation solution technique at ambient temperature. The monoclinic crystal system with the space group of $P2_1$ is exhibited for LAA from the X-ray diffraction analysis. FTIR spectroscopy that designates different molecular vibrations existing in LAA crystal was studied. The absorbance spectrum from the UV profile proclaims very less cut-off wavelength down to 206 nm and its wide optical band gap is also calculated. The perfection of the crystal is shown from Urbach's energy determination. The extent of polarization phenomena was examined for selected temperatures at dissimilar frequencies from the dielectric studies. The double harmonic output and triple-order nonlinear response for LAA are inspected from Kurtz-Perry and Z-scan technique, respectively.

1 Introduction

The focus on the development of new nonlinear optical crystals and its designing technology creates a good exposure in the domain of photonics and optoelectronics. Young scientific researchers explore this technique for assembling suitable materials among various applications for diverse device fabrication. The NLO third-order material with feeble nonlinear absorption and durable refraction has extensive courtesy because of their potential use in signal processing. The existence of strong nonlinear absorption enables the optical limiting property of an organic crystals [1–3]. The potentialities of different organic and inorganic materials with good nonlinear optical properties involve its application over vast image and information processing, terahertz wave generation, optoelectronic modulators etc. through engineering procedures [2, 3].

Mostly, primary amines act as strong bases among carboxylic acid groups because it can easily make bond among different organic acids. Organic materials offer more attention due to their capable application in adipic acid over higher (third) order harmonic generation based on their elevated NLO efficiency with strong optical (laser) damage threshold and show good stability over temperature dependence [4–7]. The nonlinear optical materials grown from low-temperature solution growth techniques stand as a new focus of science and development of technologies of photonics which effectively show more application in the field information domain, optical data transfer, laser, and optical power limiting [8].

Moreover, the crystal structure may be obtained due to fundamental forces through inter-molecular interactions and form the supra assembly of molecules. The hydrogen bondings are more dominant over engineering categories

✉ M. Lydia Caroline
lydiacaroline2006@yahoo.co.in

1 Department of Physics, Thiruvalluvar University College of Arts & Science, Thennangur Village, Vandavasi, Tamil Nadu, India

2 Department of Physics, Peri Institute of Technology, Chennai, Tamil Nadu, India

3 Department of Physics, Bharath Institute of Higher Education and Research, Chennai, Tamil Nadu, India

4 Department of Physics, Arignar Anna Govt. Arts College, Cheyyar, Tamil Nadu, India

5 Department of Physics, St. Joseph's Institute of Technology, OMR, Chennai, TamilNadu, India

6 Department of Physics, Dr. Ambedkar Govt. Arts College, Vyasarpadi, Tamil Nadu, India

7 Department of Chemistry, Bharath Institute of Higher Education and Research, Chennai, Tamil Nadu, India

8 Department of Physics, School of Advanced Sciences, VIT, Chennai, Tamil Nadu, India

Published online: 20 July 2020

and the strong H bond with N and O bond creates one-, two-, and three-dimensional networks in a crystal [9–11]. An adipic acid complex and the crystallographic structure were reported by Roy et al. [12] followed by Saravanan et al. [13] who therein proved it to be a suitable second harmonic generation material for nonlinear optical device fabrications [14]. Recently, characterization on centric L-arginine adipate crystal in 1:1 stoichiometry was reported by Ramya et al. [15].

Hence, here, we report the growth, investigation, and characterization of LAA crystal and its suitability for nonlinear optical applications which exhibit higher harmonic generation of input frequency of the laser source.

2 Experimental processes

2.1 Material synthesis—LAA

The parent compounds L-arginine and adipic acid are taken in molar ratio of 2:1 and diffused in an aqueous solution. This mixture was stirred using a magnetic stirrer for about 5 h duration with double-distilled water as a solvent. After 5 h duration, the solution attains a homogeneous mixture and is filtered with Whatmann filter paper to remove impurities present in the solution. This was covered and kept stable for slow evaporation to occur . After 2 weeks of time, optically exceptional crystals of LAA are harvested and are recrystallized to attain more purity and transparency. The recrystallized crystals are harvested and the image is shown in Fig. 1a. The complete reaction procedure [12] was revealed in Fig. 1b.

3 Results and discussion

3.1 Single crystal X-ray diffraction study

This investigation is executed by BRUKER KAPPA APEX II CCD diffractometer to find the crystal system and cell parameters for LAA crystal. The conventional cell parameters obtained are 12.60 Å, 5.99 Å, and 16.8 Å, respectively, with a space group $P2_1$. The defined unit cell parameters are in good occurrence with the reported literature value [12]. The crystallographic data for LAA is presented in Table 1.

3.2 FTIR profile of LAA

The powdered sample of LAA is subjected to FTIR spectral investigation using PERKIN ELMER Fourier transform infrared spectrometer in the range 4000–500 cm^{-1} and is displayed in Fig. 2. The wave number and their tentative assignments are tabulated in Table 2.

The pointed bend positioned in 2127 cm^{-1} arises mainly due to the zwitterion formation showing asymmetric bending of NH_3^+ [14]. The carboxyl COO^- vibration is defined from 1164 and 1084 cm^{-1} followed by 1084 cm^{-1} assigned in the plane deformation of C–H [16]. Hence the protonation from adipic acid to the amino acid L-arginine portrayed the zwitterionic nature in the organic complex (LAA) is thus revealed by the above vibrational modes.

Thus, the presence of functional groups for LAA crystal are identified from the corresponding absorption bands and they agreed well with other organic materials.

3.3 Optical studies

The crystals with good transmittance and absorption are the essential constraint for their application in photonics and optoelectronics. The LAA compound undergoes UV–Vis spectrum using PERKIN ELMER LAMADA 35 spectrophotometer with a wavelength range of 200–700 nm to notify its optical transmission and absorption. Figure 3a clearly depicts that LAA have a least cut-off wavelength down to 206 nm. The least absorbance with very high transmittance indicates its efficiency in exhibiting nonlinear properties [17].

The information about electronic and atomic band structure of materials can be concluded from the optical band gap.

The optical band gap energy (E_g) of the material is estimated from the following [18]:

$$\alpha = \frac{2.3026}{t} \times \log\left(\frac{1}{T}\right) \tag{1}$$

$$h\upsilon\alpha = A(h\upsilon - E_g)^{1/2} \tag{2}$$

The band gap energy of LAA is determined from Tauc's plot by plotting $(\alpha h\upsilon)^2$ verses photon energy ($h\upsilon$) as shown in Fig. 3b and is resolved to be 5.75 eV. The wide-ranging band gap of the LAA confirms large transmittance in the visible region and less flaws in the grown crystal [19] make it an appropriate material over NLO device implementation.

3.3.1 Urbach energy

The empirical Urbach relation was expressed as follows:

$$\alpha(h\upsilon) = \alpha_0 \exp\left(\frac{h\upsilon}{E_u}\right) \tag{3}$$

This relation follows when the absorption coefficient α displays an exponential rely on the incident photon energy near the fundamental absorption edge [19]. The E_u shows the Urbach energy which signifies the width of the localized

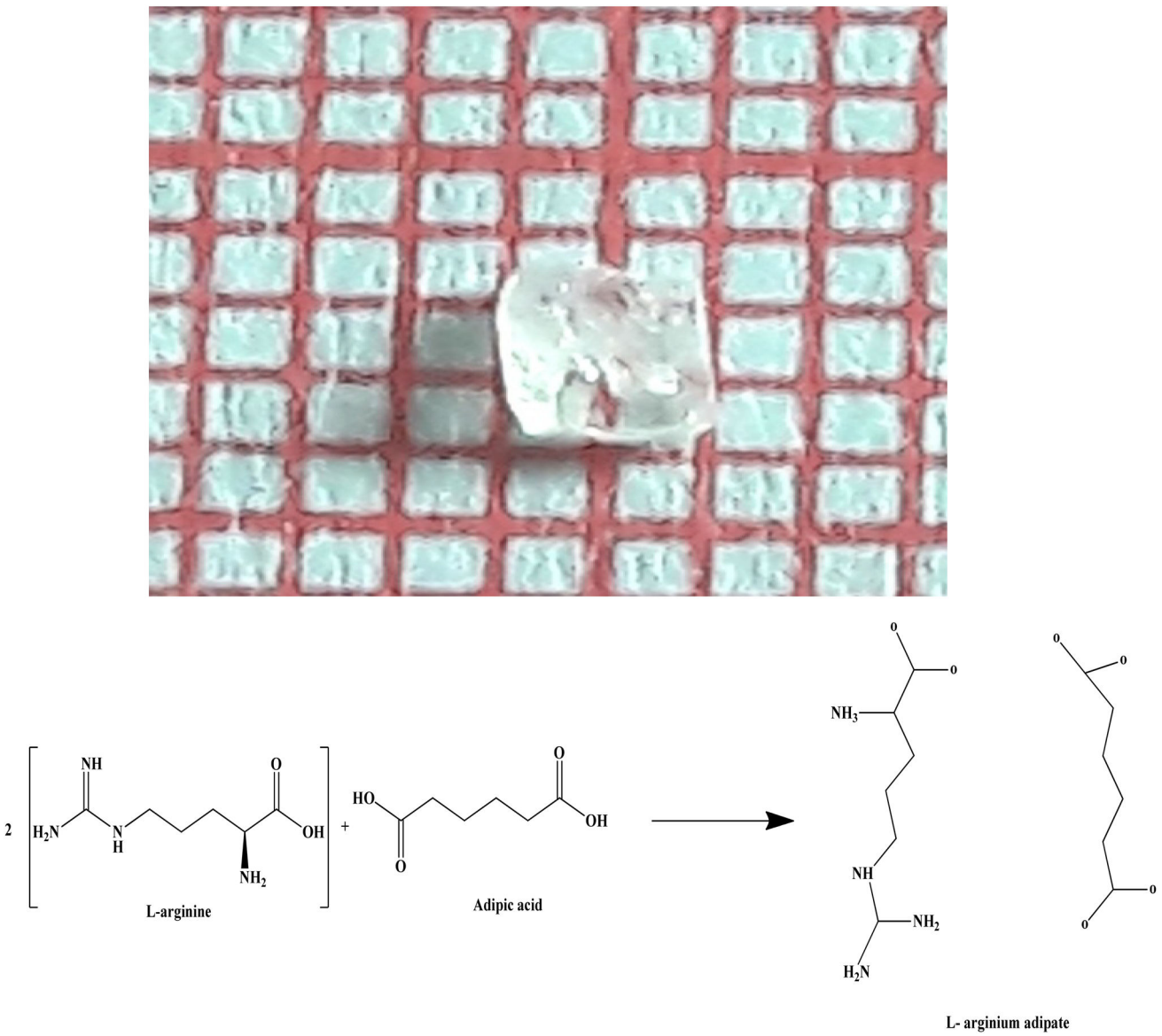

Fig. 1 Photograph of as-grown LAA single crystals (**a**) and Reaction scheme for LAA compound (**b**)

Table 1 Single crystal XRD crystallographic data of LAA

Cell parameters	Present work
Crystal system	Monoclinic
Space group	$P2_1$
a (Å)	12.60
b (Å)	5.99
c (Å)	16.87
β (°)	105.82
Volume (Å^3)	1226

states accompanying with the atomic arrangement present in the band gap of the material. It is calculated by taking the inverse of the slope from the linear portion of the graph drawn between ln (α) and $h\upsilon$. The high value of E_u shows more structural disorder and low value shows less structural disorder. For LAA, the E_u was calculated to be 0.1638 eV from the Fig. 4. Thus, the low value indicates the presence of lesser disorder stands as a support towards NLO performance of the material.

3.4 Dielectric studies

The study of dielectric permittivity (ε') and dielectric loss (ε'') of the grown crystal was carried out as a function of frequency varying from 50 Hz to 5 MHz at selected temperatures 313 K, 333 K, 353 K, and 373 K using a HIOKO

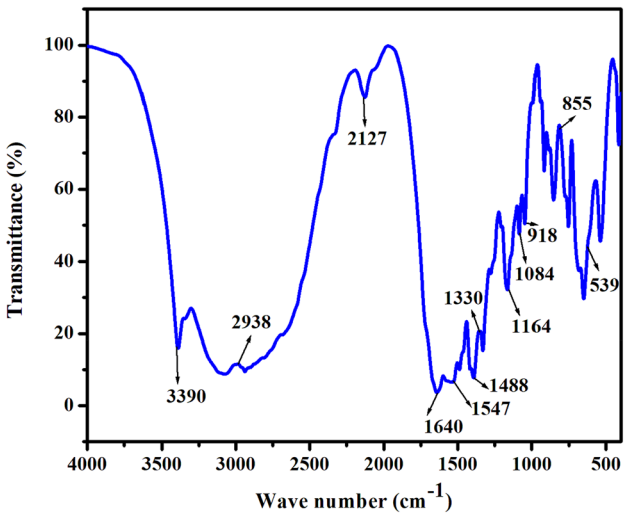

Fig.2 FTIR profile of LAA

Table 2 Vibrational allotments of LAA

FTIR—wave number (cm^{-1})	Assignments
3390	OH stretching
2938	CH_3 asymmetric stretching
2127	NH_3^+ asymmetric bending
1640	NH_2 plane bending
1488	CH_3 asymmetric bending
1392, 1330	CH_3 symmetric plain bending
1164, 1084	COO^- vibration
1084	C–H in plane deformation
918, 855	C–C stretching
537	C–O bending

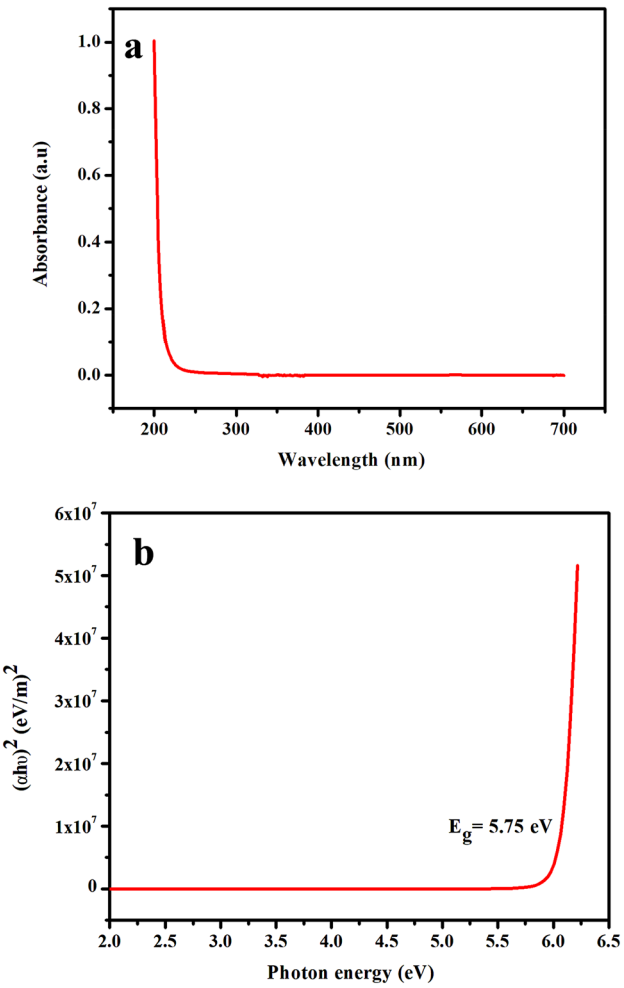

Fig. 3 UV–Vis absorbance spectra (**a**) and Tauc's plot of LAA (**b**)

3532-50 LCR HiTESTER meter and evaluated using the following relation [19]:

$$\varepsilon' = \frac{Cd}{A\varepsilon_0} \tag{4}$$

$$\epsilon'' = \epsilon' \tan \delta \tag{5}$$

From the graphs (Fig. 5a, b), we observe that dielectric constant and dielectric loss steep as the frequency raises, at mentioned range of temperatures. From the measured value, the high value of dielectric constant at low frequencies varies due to the presence of all electronic, space charge, orientation, and ionic polarizations, respectively. The much reduced dielectric constant and dielectric loss at raised frequencies declare superior optical quality of the crystal with lower defects. Thus, the LAA could be replaced as a functional material in optoelectronic applications and NLO applications [20].

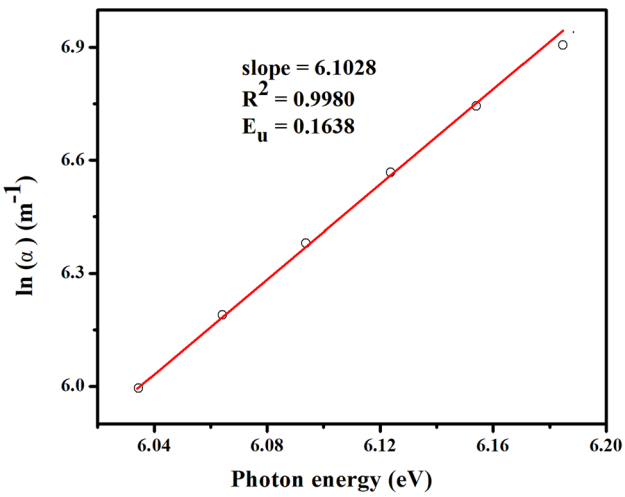

Fig. 4 Plot ln (α) vs. $h\upsilon$ for LAA

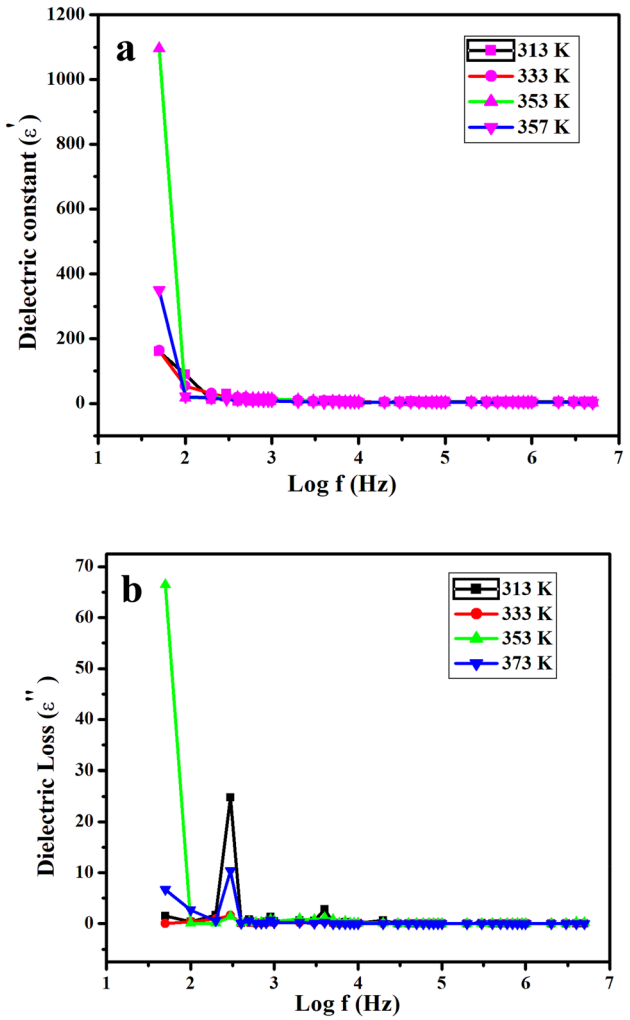

Fig. 5 Log f verses dielectric constant (**a**) and log *f* versus dielectric loss (**b**)

3.4.1 AC conductivity

The ac conductivity σ_{ac} (Ω^{-1} m^{-1}) is determined using the formula,

$$\sigma_{ac} = 2\pi f \epsilon_0 \epsilon' \tan\delta \tag{6}$$

The capability of conduction is represented in Fig. 6, as a plot of log σ_{ac} verses log ω at various temperatures. From this graph, it is understood that the low-frequency conductivity data depicting small variation corresponds to the frequency-independent part, σ_{dc} that emerges due to the random diffusion of the ionic charge carriers via activated hopping [20]. At high frequencies, forward and reverse ion displacement takes place which is responsible for increased ionic conductivity.

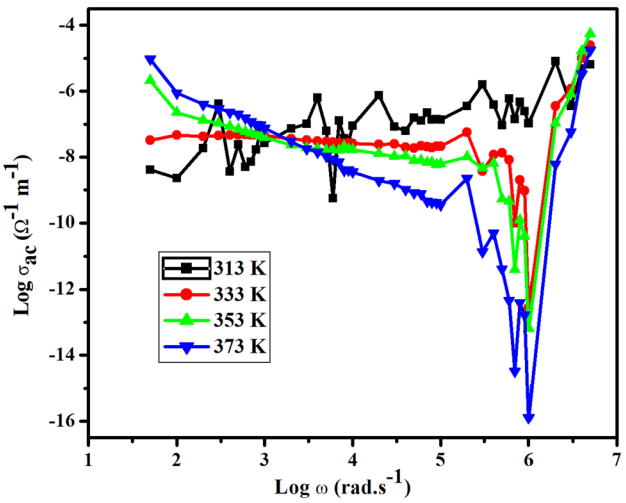

Fig. 6 Plot of log ω versus log σ_{ac}

3.4.2 Activation energy

The activation energy (E_a) of the electrical process is evaluated from the graph drawn between log σ_{ac} and inverse of temperature using the following relation:

$$\sigma = \sigma_0 \exp\left(-\frac{E_a}{k_B T}\right) \tag{7}$$

where σ_{ac} is the conductivity at temperature T, E_a—activation energy for the electrical process, and $K_B = 1.38 \times 10^{23}$ J/K is the Boltzmann constant. Figure 7 presents the variation of log σ_{ac} versus 1000/T. The graph shows almost linear behavior and the slope of this graph is used to calculate activation energy using the formula [18],

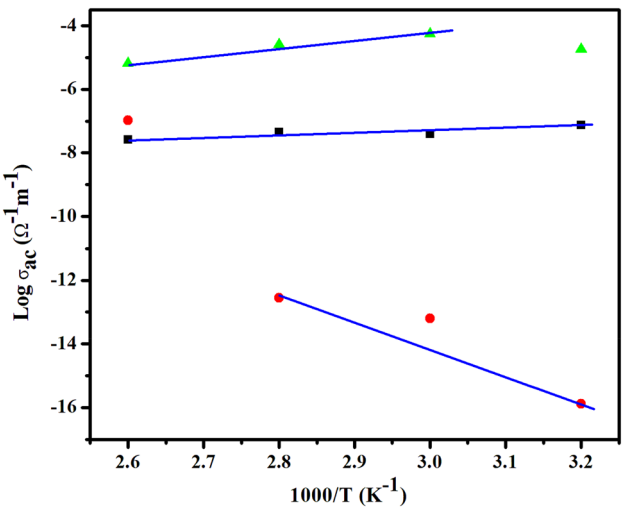

Fig.7 Plot of log σ_{ac} vs. 1000/T

$$-E_a = -\text{slope} \times 1000 \times K_B. \quad (8)$$

The values of the activation energy come out to be 0.1314, 0.1734, and 0.4982 eV at frequencies of 50 Hz, 6 kHz, and 1 MHz, respectively. The lower activation energy value proves that the LAA sample contains very less number of defects, supporting its usefulness in device fabrications.

3.5 SHG study

Second harmonic generation (SHG), a frequency-doubling process, is studied by employing Kurtz and Perry technique [21] which utilizes spectra physics quanta Nd:YAG laser with first harmonics output (1064 nm, 10 ns, 10 Hz) passing 0.705 J pulse power as the radiation source. The efficacy of LAA crystal was compared with the microcrystalline fine particles of KH_2PO_4 (KDP). The frequency-doubling process is confirmed from the output emission of green radiation ($\lambda = 532$ nm) from the samples [19]. The KDP crystal gave an SHG signal of 7.11 mJ for the same input energy, thus proving the efficiency of LAA as 0.80 times that of KDP. Hence this LAA material is considered for photonic applications [19].

3.6 Z-scan measurement

This method was first introduced by Sheik-Bahae et al. and this method is otherwise called as Sheik-Bahae method [22]. In this technique, the sample is placed in a Cuvette in a translation stage. The translation stage can move the sample along Z direction i.e., along the mid portion of the Gaussian beam and the transmittance is quantified using photo detector [23]. Nonlinear absorption is determined using open aperture experiment. In open aperture, photo detector was kept completely with no use of aperture. Nonlinear refraction is measured with the help of closed aperture and the an aperture is placed before the photodetector. Generally, the closed aperture experiment is done with 50% aperture [23].

The third-order optical nonlinearities for the LAA crystal was estimated. The Kerr nonlinearity (n_2), nonlinear absorption coefficient (β), and third-order nonlinear optical susceptibility ($\chi^{(3)}$) are achieved by Z-scan technique using open and closed apertures.

From the obtained data of Z-scan, the measurable quantity (ΔT_{P-V}) between the transmittance change of peak and valley $T_P - T_V$ is observed. The on-axis phase shift at the focus $|\Delta\Phi_0|$ is given by [22],

$$\Delta T_{P-V} = 0.406(1 - S)^{0.25}|\Delta\Phi_0| \quad (9)$$

$$S = 1 - \exp\left(\frac{-2r_a^2}{\omega_a^2}\right) \quad (10)$$

where S is the linear transmittance aperture, r_a denotes the radius of the aperture, and ω_a is the beam radius at the aperture. The on-axis phase shift $|\Delta\Phi_0|$ associated with the third-order nonlinear refractive index of the crystal is given by,

$$n_2 = \frac{\Delta\Phi_0}{KI_0L_{eff}} \quad (11)$$

The real and imaginary part of the LAA material was determined using,

$$\text{Re}\,\chi^{(3)}(\text{esu}) = \frac{10^{-4}(\varepsilon_0 C^2 n_o^2 n_2)}{\pi}\left(\frac{\text{cm}^2}{\text{W}}\right) \quad (12)$$

$$\text{Im}\,\chi^{(3)}(\text{esu}) = \frac{10^{-2}(\varepsilon_0 C^2 n_0 \lambda\beta)}{4\pi^2}\left(\frac{\text{cm}^2}{\text{W}}\right) \quad (13)$$

The absolute value of LAA material explains the magnitude of the extent of polarization process in response to applied electric field was assessed according to the following relation,

$$\left|\chi^{(3)}\right| = \sqrt{(\text{Re}(\chi^{(3)}))^2 + (\text{Im}(\chi^{(3)}))^2} \quad (14)$$

In the closed aperture graph in Fig. 8a, for LAA, we observe that there is a peak and it is followed by valley [23, 24]. This type of graph is observed due to Saturable absorption effect. Saturable absorption effect occurs when the absorption area of excited state is small when compared to the ground state so that the transmittance increases when the system is highly excited. From the open aperture curve for LAA in Fig. 8b, the value of β was calculated and its positive value refers to two-photon absorption effect (TPA) that is mainly focussed in the field of optical power limiting applications. The ratio of the closed to open normalized Z-scan traces of LAA are illustrated in Fig. 8c.

Thus, LAA crystals have feeble nonlinear absorption, but strong nonlinear refraction results to gain more interest because of their usage in optical and signal processing devices [24]. The calculated third-order nonlinear optical parameters is enumerated in Table 3.

4 Conclusions

In summary, single crystals of L-arginium adipate harvested through slow evaporation process crystallized to acentric space group $P2_1$ with monoclinic system. The various functional groups were identified by the FTIR spectrum. From the UV–visible spectrum, the optical direct band gap (6.03 eV) and Urbach energy (0.1638 eV) were evaluated. The dielectric studies revealed parameters like ac conductivity (σ_{ac}) and activation energy (E_a) calculated exhibits lower

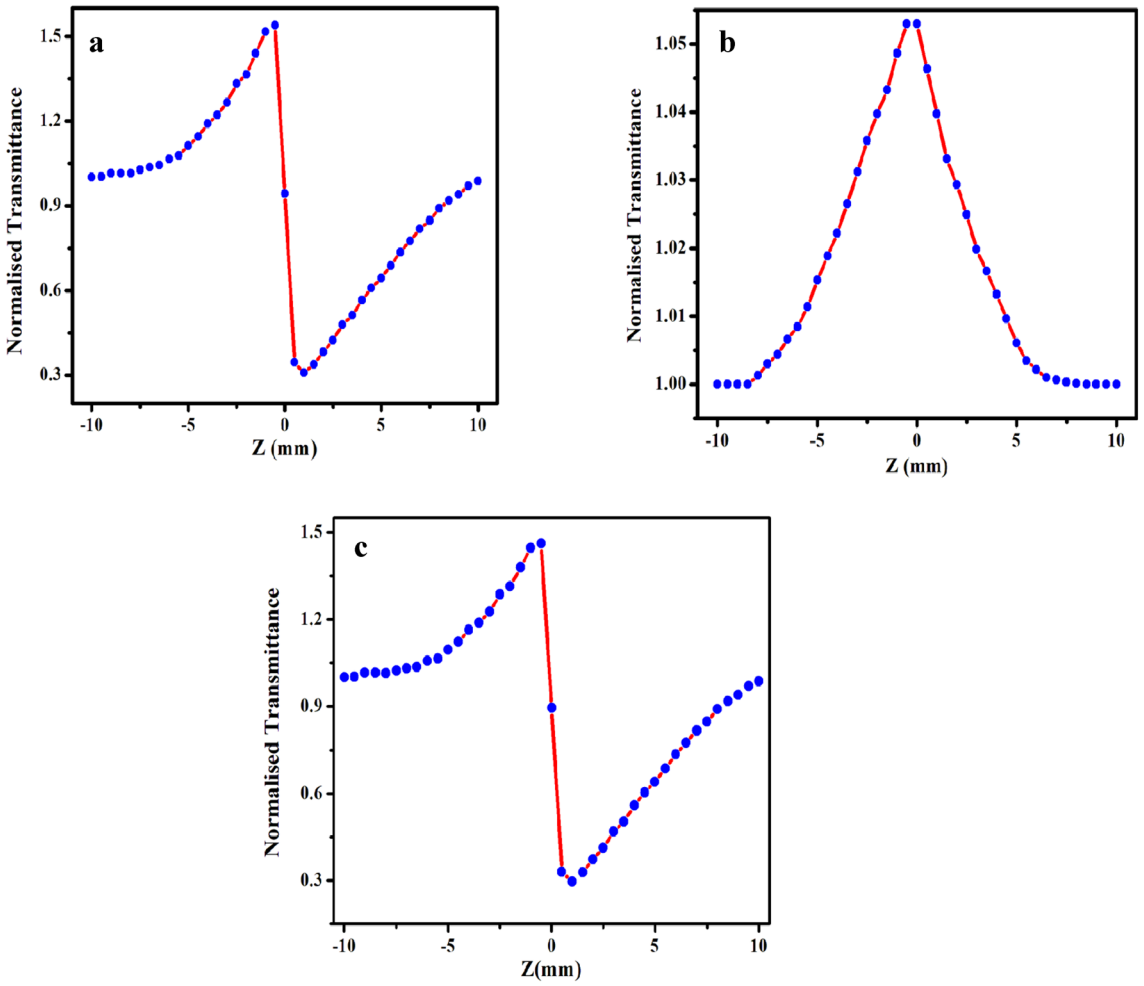

Fig. 8 Closed aperture (**a**), open aperture (**b**), and ratio of the closed to open Z-scan traces of LAA (**c**)

Table 3 Measured details and values from Z-scan for LAA

Third-order properties	Measured values
Laser beam wavelength (λ)	532 nm
Linear absorption coefficient (α)	401.45
Nonlinear refractive index (n_2)	6.52×10^{-8} cm^2 W^{-1}
Nonlinear absorption coefficient (β)	0.04×10^{-4} cm W^{-1}
Real part of the third-order susceptibility [Re (χ^3)]	1.97×10^{-6}esu
Imaginary part of the third-order susceptibility [Im (χ^3)]	0.26×10^{-6}esu
Third-order nonlinear optical susceptibility (χ^3)	1.31×10^{-6}esu

value, proving presence of lesser defect in the crystal. The Kurtz-Perry technique revealed that LAA exhibits SHG efficiency of 0.80 times that of KH_2PO_4 (KDP). The nonlinear refractive index (n_0), absorption coefficient (β), and third-order nonlinear susceptibility (χ^3) estimated for LAA using the technique of Z-scan revealed negative nonlinearity from closed aperture and two-photon absorption from open aperture proves it as an appropriate candidate in future optical limiting, switching, photonic, and NLO device fabrication.

Acknowledgements The scientific support is rendered by SAIF, IIT Madras for providing Single Crystal XRD and FTIR measurement. Also, the facility rendered by Department of Physics and Chemistry of BS Abdul Rahman University (BSAU), Chennai is greatly acknowledged for providing SHG measurement. The authors express their sincere thanks to VIT University, Chennai for providing Z-scan facility.

References

1. A. Priyadharshini, S. Kalainathan, J Mater Sci: Mater Electron. **29**, 2698 (2018)
2. A. Aravindan, P. Srinivasan, N. Vijayan, R. Gopalakrishnan, P. Ramasamy, Cryst. Res. Technol. **42**, 1097 (2007)
3. M. Prakash, D. Geetha, M. Lydia Caroline, Mater. Manuf. Process. **27**, 519 (2012)
4. J.J. Rodrigues Jr., L. Misoguti, F.D. Nunes, C.R. Mendonca, S.C. Zilio, Opt. Mater. **22**, 235 (2003)
5. M. Lydia Caroline, S. Vasudevan, Mater. Lett. **63**, 41 (2009)
6. K. Senthil, S. Kalainathan, A. Ruban Kumar, P.G. Aravindan, RSC Adv. **4**, 56112 (2014)
7. R. Mohankumar, N. Gopalakrishnan, R. Jayavel, P. Ramasamy, Cryst. Res. Technol. **34**, 1265 (1999)
8. P. Jayaprakash, P. Sangeetha, C. Rathika Thaya Kumari, I. Baskaran, M. Lydia Caroline, J. Mater. Sci.: Mater. Electron. **28**, 18787 (2017)
9. W.J. Liu, C. Ferrari, M. Zha, L. Zanotti, S.S. Jiang, Cryst. Res. Technol. **35**, 1215 (2000)
10. S. Mukerji, T. Kar, Cryst. Res. Technol. **34**, 1323 (1999)
11. G. Auvert, J. Bournay, Chem. Phys. **32**, 397 (1978)
12. S. Roy, D.D. Singh, M. Vijayan, Acta. Cryst. B **61**, 89 (2005)
13. M. Saravanan, A. Senthil, S. Abraham Rajasekar, Optik **127**, 1372 (2015)
14. A. Priyadharshini, S. Kalainathan, J. Mater. Sci.: Mater. Electron. **28**, 7401 (2017)
15. K. Ramya, N.T. Saraswathi, C. Ramachandra Raja, Optik **127**, 2495 (2016)
16. P. Jayaprakash, M. Peer Mohamed, M. Lydia Caroline, J. Mol. Struct. **1134**, 67 (2017)
17. Y. Slimani, A. Selmi, E. Hannachi, M.A. Almessiere, A. Baykal, I. Ercan, J. Mater. Sci.: Mater. Electron. **30**, 9520 (2019)
18. C. Rathika Thaya Kumari, P. Jayaprakash, M. Nageshwari, M. Peer Mohamed, P. Sangeetha, M. Lydia Caroline, Mol. Crystals Liq. Crystals **658**, 186 (2017)
19. M. Nageshwari, C. Rathika Thaya Kumari, G. Vinitha, M. Peer Mohamed, S. Sudha, M. Lydia Caroline, J. Mol. Struct. **1155**, 101 (2018)
20. S. Shettigar, G. Umesh, K. Chandrasekaran, B. Kalluraya, Synth. Met. **57**, 142 (2007)
21. S.K. Kurtz, T.T. Perry, J. Appl. Phys. **39**, 3798 (1968)
22. U.T. Sakshi, Spectrochim. Acta Part A: Mol. Biomol. Spectrosc. **223**, 117319 (2019)
23. X. Mathew, H. Juarez Santiesteban, H. Pacio Castillo, O. Portillo Moreno, Super Lattices Microstruct. **98**, 242 (2016)
24. S. Sudha, P. Ramesh, C. Rathika Thaya Kumari, P. Jayaprakash, M. Kumar, M. Kumar, M. Lydia Caroline, J. Mol. Struct. **1209**, 127946 (2020)

Journal of Materials Science: Materials in Electronics
https://doi.org/10.1007/s10854-020-04066-3

Crystal growth, optical, spectroscopic studies, PL behaviour and Hirshfield surface analysis of a third-order nonlinear optical Cesium Hydrogen Oxalate Dihydrate (CHOD) single crystal

S. Sudha[1] · C. Rathika Thaya Kumari[2] · M. Nageshwari[3] · P. Ramesh[4] · G. Vinitha[5] · M. Lydia Caroline[6] · G. Mathubala[7] · A. Manikandan[7]

Received: 2 March 2020 / Accepted: 16 May 2020

Abstract
Single crystal of oxalato-bridged, Cesium-extended frame work, Cesium Hydrogen Oxalate Dihydrate (CHOD), has been synthesized by slow evaporation solution growth technique. Diffraction studies were used to identify the geometry of the atoms present in the primitive cell of the crystal. The title compound has crystallized in triclinic category-bearing space group P-1. Spectroscopic investigation of the compound was done by FTIR and FT-Raman techniques. From UV–Vis studies, optical absorption edge was ascertained as 241 nm. It has excellent optical transmission window throughout the visible region. Energy dispersive X-ray analysis (EDAX) affirms the presence of Cesium in the compound. Fluorescence decay of the molecules present in the excited state for the crystal was studied. Hirshfield surface maps intermolecular contacts present in the crystal and the contributions made by the contacts were assessed by 2D Finger print plots. Z-Scan studies ascertain the magnitude of nonlinear refractive index and nonlinear refraction.

1 Introduction

Metal Organic frameworks (MOF) are porous, crystalline and robust hybrid materials of organic and inorganic constituents with inconceivable tunability of geometry, size and chemical nature. Tunability of MOFs can be made without change in their underlying topology [1,2]. It consists of ordered, crystalline and extended array of charge compensating metal ions coordinated to organic linkers. MOFs are known for astounding void fraction i.e. only 10% area of the material is occupied and it has expansive interior region without occupation of molecules and large void space. Their high porosity leads MOFs to be used in energy storage devices. They are used in batteries and superconductors.

✉ M. Lydia Caroline
lydiacaroline2006@yahoo.co.in

S. Sudha
sudhavaidhy@gmail.com

C. Rathika Thaya Kumari
rathikak06@gmail.com

M. Nageshwari
nageshwari.sb@gmail.com

P. Ramesh
gayaram0212@gmail.com

G. Vinitha
vinitha.g@vit.ac.in

G. Mathubala
madhu2705@gmail.com

A. Manikandan
mkavath15@gmail.com;
manikandana.che@bharathuniv.ac.in

[1] PG& Research Department of Physics, Arignar Anna Govt. Arts College, Cheyyar 604 407, Tamil Nadu, India

[2] Department of Physics, Bharath Institute of Higher Education and Research, Agaram Road, Chennai 600073, Tamil Nadu, India

[3] Department of Physics, Peri Institute of Technology, Chennai, Tamil Nadu, India

[4] Department of Physics, Govt. Thirumagal Mills College, Gudiyattam, 632602 Vellore, Tamil Nadu, India

[5] Department of Physics, School of Advanced Sciences, VIT, Chennai 600127, Tamil Nadu, India

[6] Department of Physics, Dr. Ambedkar Govt. Arts College, Vyasarpadi, Chennai 600039, Tamil Nadu, India

[7] Department of Chemistry, Bharath Institute of Higher Education and Research, Agaram Road, Chennai 600073, Tamil Nadu, India

Published online: 31 July 2020

Hottest topic in MOF research in recent years is CO_2 capture similar to that of the process done by plants to make environment clean [3]. They are widely used in catalysis, molecular separation, micro-electronics and sensors. They have possible applications in optoelectronics and nonlinear optics (NLO). NLO has wide application in optical switch-integrated photonics, high-speed information processing, optoelectronic modulators [4] and terahertz wave generation and detection. Numerous publications have been made on oxalate ion and its bonding with metallic ion. The Oxalate ions have actively constructed huge collection of molecular structures and frame works by merging alkali ions into lattice [5].

In this compound, neutral dihydrate of the acid and the hydrated trimeric anion are bonded by moderately stable hydrogen bonds. This association is attached into three-dimensional frame works. Cesium ions are situated in the cavity of the frame work [6,7]. In this paper, we have investigated experimental procedures like X-ray diffraction, FTIR and FT-Raman, SEM, EDAX, Mechanical studies, Fluorescence Life time techniques and Third harmonic generation techniques for this CHOD crystal. To best of our knowledge, apart from X-ray diffraction, all the above studies were investigated for the first time by us.

2 Experimental

2.1 Material synthesis and crystal growth

Parent compounds, Cesium iodide and Oxalic acid in the molar ratio 1:1, were diffused in millipore water. Then, it was thoroughly mixed by a stirrer for about 8 h and was filtered to a beaker using Whatmann filter paper to remove insoluble impurities. It was allowed to undergo slow evaporation. The beaker was covered with perforated cover to avoid dust and impurities penetrating into the solution. After a span of 20 days, optically, exceptional crystals of CHOD were harvested and the image is shown in the Fig. 1.

3 Results and discussion

3.1 Single crystal XRD diffraction

Single crystal XRD Investigation was executed by employing BRUKER Enraf Nonius CAD 4 single crystal X-ray diffractometer to find the unit cell dimensions of the crystal. The crystal's space group is Triclinic (P-1). Lattice parameters of the crystal $(C_8H_{14}CS_2O_{20})_n$ are found out to be 6.28 Å, 7.44 Å and 10.78 Å, respectively. Crystallographic axes were found out to be 94.61°, 99.43° and 95.34° and the cell volume was found out to be 492 $Å^3$. The perceived unit cell parameters are in good concurrence with reported literature values [8].

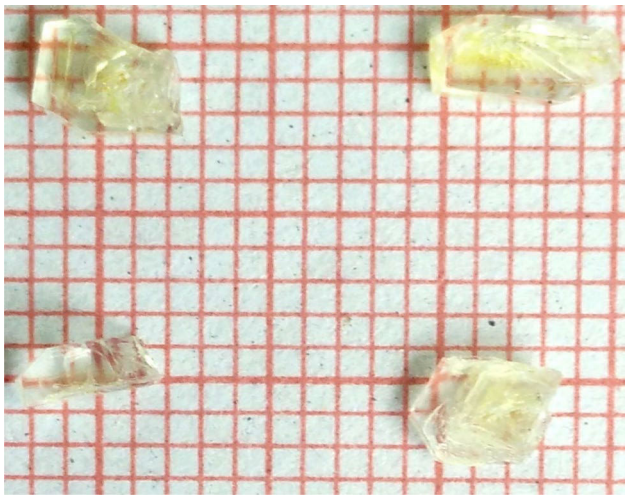

Fig. 1 Image of a CHOD Crystal

3.2 FTIR and FT-Raman vibrational analysis

The powdered sample was subjected to FTIR and FT-Raman techniques using PERKIN ELMER Spectrophotometer and BRUKER: RFS 27 spectrometer, respectively, in 4000–500 cm^{-1} wave number range and the spectrum obtained is shown in the Fig. 2a, b. The wavenumbers and their tentative assignments are given in Table 1.

Absorption band from 2500 to 3600 cm^{-1} corresponds to symmetric and asymmetric stretching vibrations of water molecules [9,10]. The presence of these vibrations confirms the presence of water molecule in the compound. The peak at 1691 cm^{-1} in FTIR and its counterpart 1713.33 cm^{-1} corresponds to C=O stretching of COOH [11,12]. The wave numbers 1401 cm^{-1} in FTIR and 1360.63 cm^{-1} represent stretching vibrations of C–O and vibrations of C–C ,respectively. Repentance noticed at 1253 cm^{-1} is attributed to C–O vibrations. The frequency at 1119 cm^{-1} is the deformation vibration of C–OH. C–O stretching is found at 1019 cm^{-1} [11]. C–C stretching vibrations were observed at 867.53 cm^{-1}. The absorption band at 785 cm^{-1}in FTIR is attributed to in plane bending motion of δ(O–C=O). Metal–oxygen bond vibrations appear at 488.09 cm^{-1} [13,14]. Rocking vibrations produce a sharp intense peak at 367.74 cm^{-1}.

3.3 UV–Vis studies

Single crystals are of great demand in optic field. Therefore, optical transmission range and cut-off wavelength are vital for measuring the potential of nonlinear optical crystals. Efficient NLO crystals have cut-off between 200 and

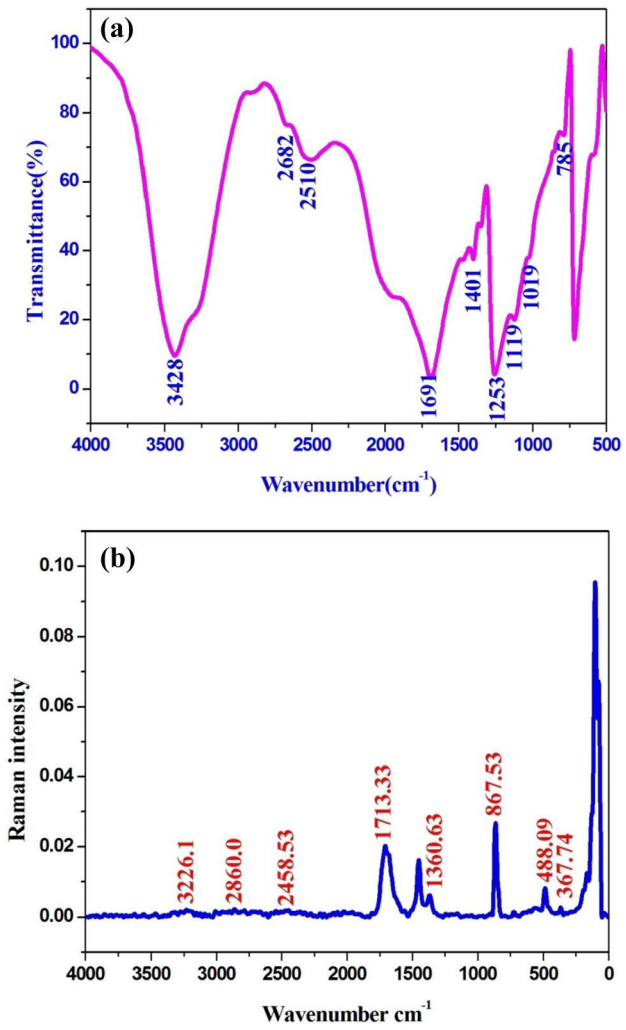

Fig. 2 **a**, **b** FTIR (**a**) and FT-Raman (**b**) Vibrational allotments of the CHOD crystal

400 nm [15]. The UV–Vis spectrum was recorded in the range 200–1200 nm availing LAMBDA-35 UV–visible spectrophotometer and the absorbance spectra is exhibited in the Fig. 3a. The spectra show a cut-off wavelength of 241 nm, which shows its ability in nonlinear optical applications [16]. In near-ultra violet region, there is an absorbance which is attributed to transition of nonbonded electron of the carbonyl group to π orbital [17].

The absorption coefficient (α) close to the absorption edge can be calculated as follows:

$$\alpha = \frac{2.3026 \log(1/T)}{d} \tag{1}$$

where d is the thickness of the crystal and T denotes transmittance.

From the absorption coefficient and other factors, optical band gap can be got from Tauc's relation[18,19]

$$\alpha = A\frac{(h\nu - E_g)^2}{h\nu} \tag{2}$$

where A denotes constant, h denotes planck's constant *and* ν represents frequency of the radiation. A graph is drawn between $(\alpha h\nu)^2$ and Photon energy (eV) [20] and extrapolating the linear part with abcissa, direct band gap energy can be found. From the Fig. 3b, the optical band gap was found to be 5.43 eV.

3.4 Fluorescence life time

Molecule's fluorescence is not only designated by its emission intensity and emission spectrum, but also by its life time [21]. Fluorescence lifetime is the time taken by the molecules of fluorophore to reduce to 1/e times of its original population [22]. In TCSPC, an pulse whose life time is less is allowed to excite the sample and a graph is drawn between the decayed pulse from the sample and time and shown in the Fig. 4a. In TCSPC, every single photon is observed and its arrival time is measured with respect to

Table 1 IR and Raman molecular vibrational assignments of CHOD

Wave numbers		Assignments
FTIR	FT-RAMAN	
3428, 2682, 2510	3226.1, 2860, 2458.53	Symmetric and asymmetric stretching vibrations of water molecule
1691	1713.33	C=O stretching of COOH
1401	1360.63	Stretching vibrations of C–O + vibrations of C–C
1253		ν(C–O)
1119		Deformation vibration of C–OH
1019		C–O Stretches
	867.53	C–C stretching
785		Inplane bending motion of O–C=O
	488.09	Metal–oxygen bond
	367.74	Rocking vibration

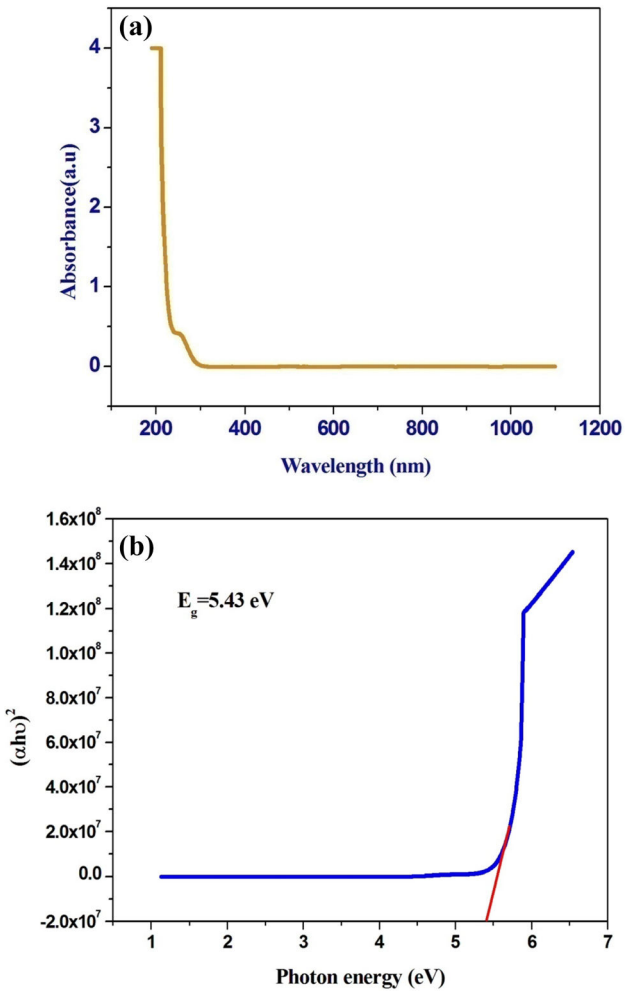

Fig. 3 **a** UV–Visible spectrum of CHOD and **b** Graph between $(\alpha h\nu)^2$ and Photon energy

the laser reference signal. Decay time is resolved using the following formula,

$$F(t) = A_1 e_1^{-t/\tau} + A_2 e_2^{-t/\tau} + A_3 e_3^{-t/\tau} \quad (3)$$

Prompt emission's amplitude and delay emission's amplitude are given by A_1, A_2 and A_3 and lifetimes are given by τ_1, τ_2 and τ_3, respectively. The prompt fluorescence lifetime (τ_1) and delayed fluorescence life time (τ_2) occur due to the direct de-excitation of singlet energy-level transition and collisional interaction pairs of molecules in lowest excited triplet states [23]. The observed decay time contains distortion caused by instrumental response. To minimize this instrumental distortion, deconvolution technique is used i.e. least square fitting (χ^2). For a good fit, χ^2 should be less than 1.2 and the obtained χ^2 is estimated in the table. Also for a good fit, weighted residuals should be randomly distributed and it is shown in Fig. 4b. The lifetime and amplitudes of the decays are shown in the Table 2. Smaller lifetime of the molecules concludes good crystalline nature of the title compound.

3.5 SEM studies

Topography of crystals was identified using SEM by operating FE1 quanta FEG 200 High-resolution scanning electron microscope with acceleration voltage of 30 kV. Crystals are flat and exhibit well-defined faces with smooth surfaces [24,25]. Multi-layered deposition of crystals was exhibited (Fig. 5a). Large grain size of the atoms were seen and these grains might be used as a Positive charge electrode in lithium batteries which have the distinct feature of both charging and discharging [26] (Fig. 5b). Sufficient space between the grains indicates the porous nature of the material. Aggregation of some grains may be due to the evolution of heating during the formation of crystal and weak Vander Waals forces may be responsible for this collection of grains [27,28]. Figure 5a and b indicate SEM mapping of the crystals with the magnification of 50 µm and 20 µm.

3.6 Energy dispersive X-ray analysis (EDAX)

EDAX deals about the recognition of different atoms present in the sample. Figure 6 shows the energy dispersive spectrum of the sample and the presence of various elements were identified by their characteristic peaks. Energy of the X-rays released from the atoms correspond to the difference in energy levels [24].

3.7 Hirshfeld surface analysis

Hirshfeld surface analysis is a graphical tool for visualizing and understanding intermolecular associations in the compound. 2D Finger print plots also quantitatively analyse the inter- and intra-molecular contacts [29]. The molecular Hirshfeld surface d_{norm}, d_i, d_e, shape index, curvedness and fragment path for the title compound were illustrated in Fig. 7 with the d_{norm} scale ranging from − 1.0965to 1.1342 Å, d_i ranging from 0.5805 to 2.8835 Å and d_e ranging from 0.5817to 2.5498 Å. The intermolecular distances O–H and Cs–O were displayed in Fig. 8. Entire 2D fingerprint plots are probed to obtain the allotment of O–H/H–O (53.4%), Cs–O\O–Cs (13.7%), Cs–H\H–Cs (1.8%), C–H/H–C (2.5%) and C–O/O–C (7.5%); inter-molecular and intra-molecular associations have built total Hirshfeld surface (Fig. 9). The title compound intermolecular interactions are specified in fingerprint (FP) plots and the d_e and d_i spikes in the FP give the values ($d_e + d_i = 0.9 + 0.9$) of 1.8 Å for O–H/H–O interaction and ($d_e + d_i = 1.7 + 1.7$) 3.4 Å for O–Cs/Cs–O molecular interaction shown in Fig. 9. This FP interaction

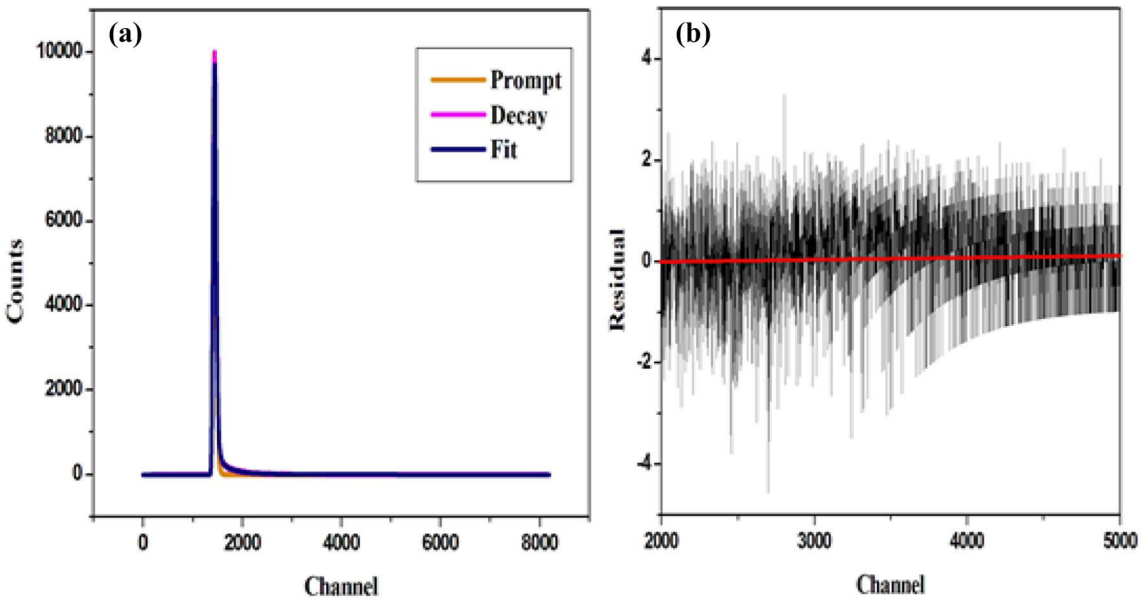

Fig. 4 **a**, **b** Time domain life time computation and residual fit

Table 2 Fluorescence decay life time measurement

Scrutiny of material	Life time(ns)			Amplitude			χ^2
	τ_1	τ_2	τ_3	A_1	A_2	A_3	
CHOD three exponential	1.55	5.11	6.12	6.2	84.8	8.9	1.133

Fig. 5 **a**, **b** SEM mapping of the crystal

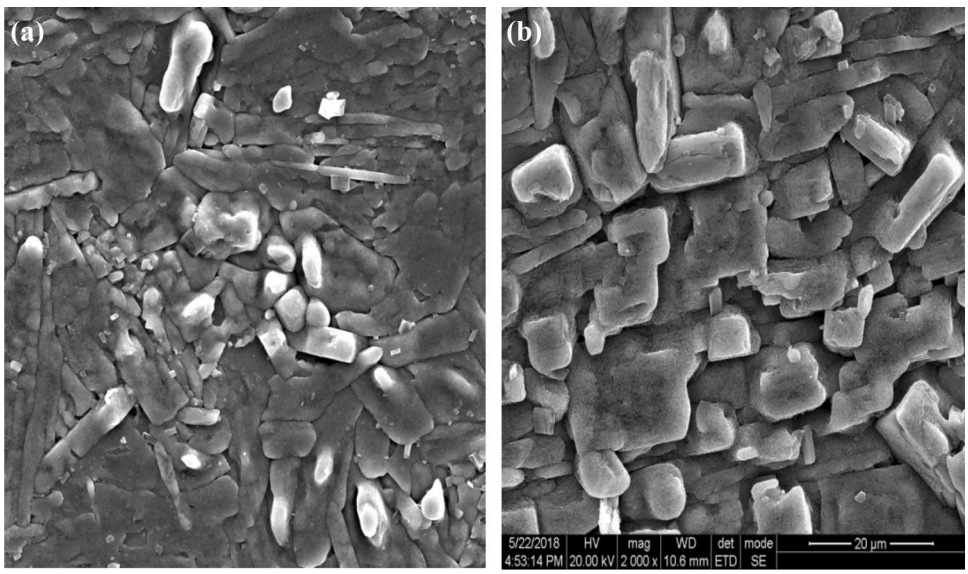

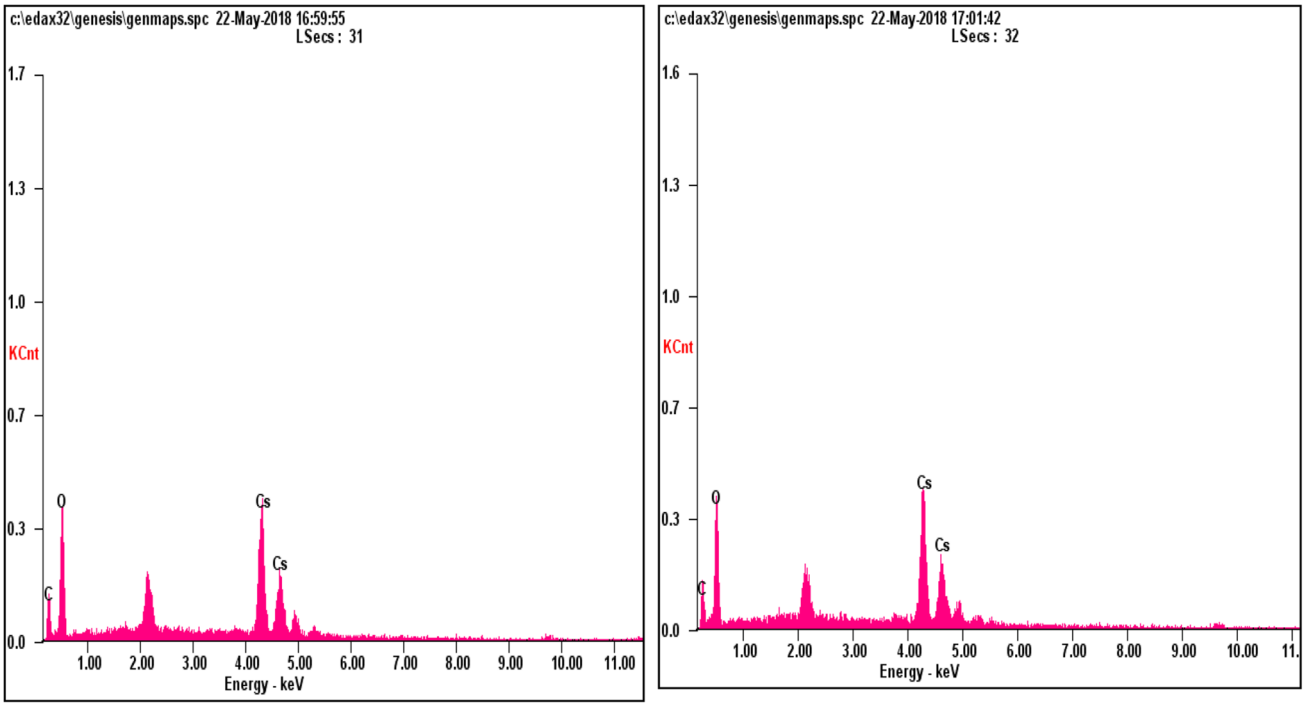

Fig. 6 EDAX spectrum of CHOD crystal

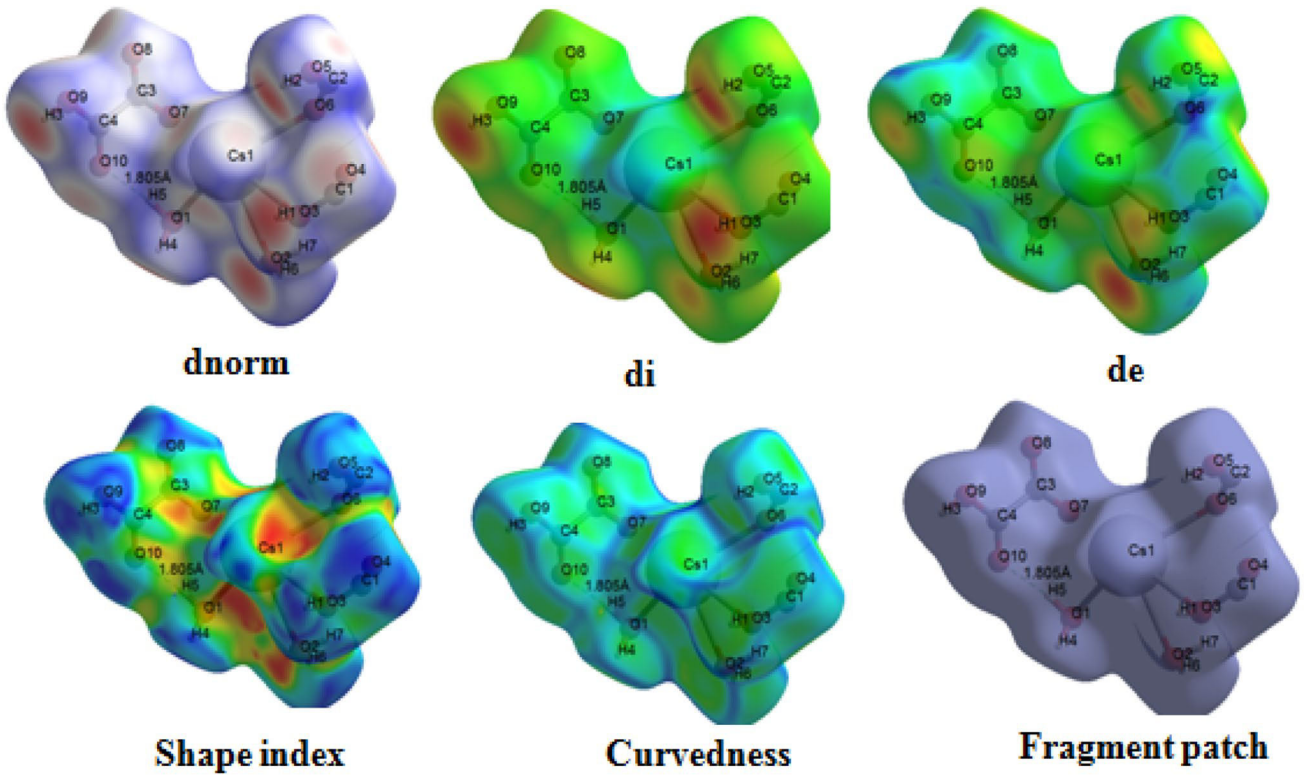

Fig. 7 3D Hirshfeld surfaces for d-norm, di, de, Shape index, Curvedness and Fragment patch for title compound

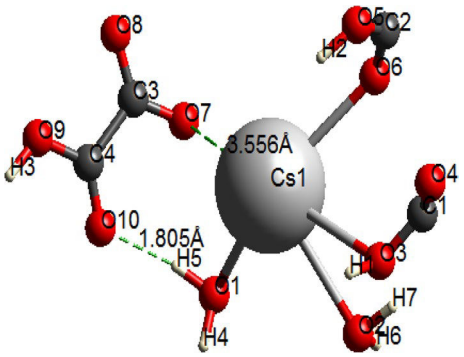

Fig. 8 Visualizing Intermolecular contacts plotted on d_{norm} surface

d_e and d_i graphical slope values are in fine accordance (Cs–O = 3.5 Å, O–H = 1.8 Å) with intermolecular interactions that were shown. This bond length is the smallest one, but associations between these atoms are more powerful. The structure was par amounted by C–O…Cs, C–O…H and O–H…O interactions in the crystal.

3.8 Z-scan method

Z-Scan is a bench mark, accurate rapid technique for measuring third-order nonlinear properties [30,31]. Crystals having third-order nonlinearities have expansive utilization in optical power confining, 3D storing optical information, two photon up conversion lasing, lithography and photodynamic applications. Z-scan is sensitive to all kind of effects which produces third-order nonlinearities such as ultrafast nonlinear absorption process, stimulated Raman scattering and AC stark effect.

In this Z-scan technique; He–Ne laser of 5mw intensity was used. This laser beam was modified into gaussian beam by Gaussian filter and it is allowed to fall on the convex lens. The focus of the convex lens reckon on the diameter of the Gaussian beam. The sampled is translated along Positive Z direction-Negative Z direction. Z denotes the focal position of the beam. Nonlinear refraction and nonlinear absorption can be found out using closed aperture and open aperture, respectively.

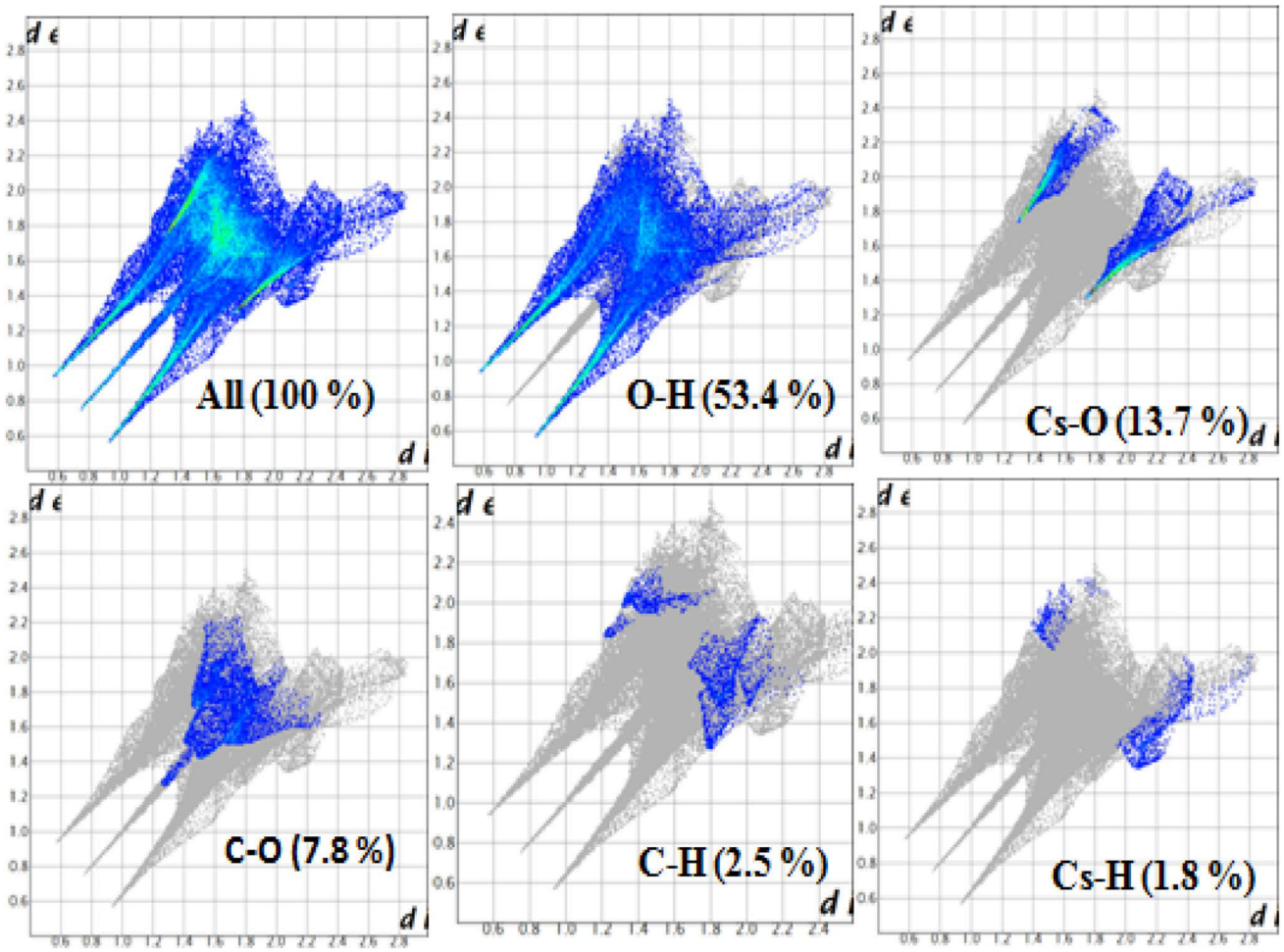

Fig. 9 2D Fingerprint plots represented for whole compound and deconstructed finger prints representing various interactions

Arrangement in which a detector is set behind the aperture is named as closed aperture. Figure 10a represents closed aperture picture for this compound. Nonlinear refraction can be found out using this method [32]. In this method, when a highly intensed laser light falls on the crystal, different portions of the material experience different temperatures. Temperature in the central portion will be high; it goes on decreasing and it will be minimum in the periphery. Due to the temperature differences in different parts of the crystal, difference in the value of refractive index is observed. These effects will be more pronounced, when the laser light's focal point is close to the sample, as it experiences more intensity. Therefore, the crystal acts as thermal lens, and depending on the internal structure, crystal self-focuses or defocuses the beam. In this method, from this graph, peak succeeds the valley representing self-defocusing effect. The sign of nonlinear refractive index is negative.

The arrangement in which aperture is taken off to converge all the transmitted light into detector is known as open aperture. Figure 10b represents the open aperture for this crystal.

The difference in permeability among peak and valley (ΔT) is interpreted in this technique as,

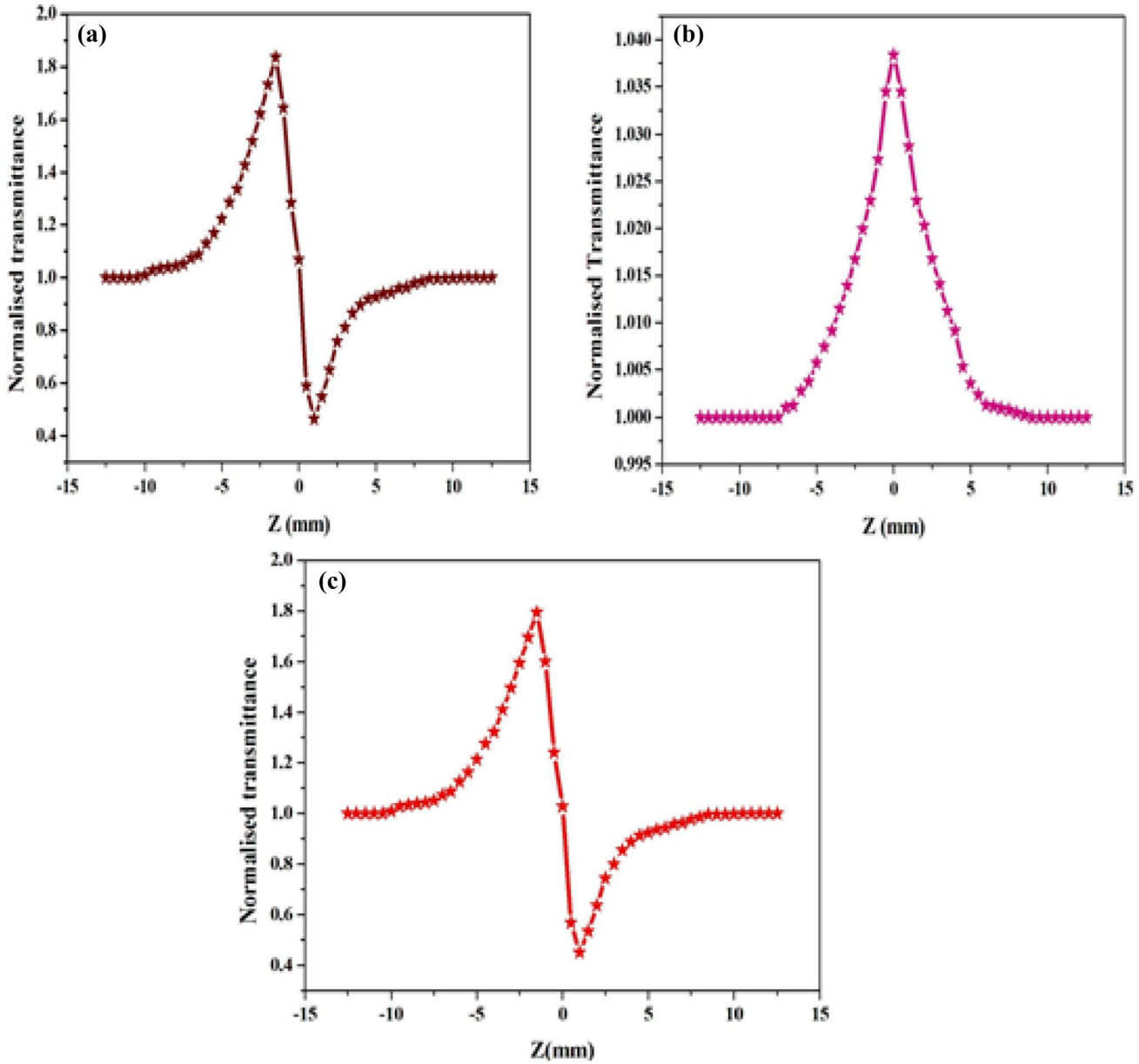

Fig. 10 Closed (**a**), Open (**b**) and Ratio (**c**) of closed to open aperture

$$\Delta T = 0.406(1 - S)^{0.25}|\phi| \tag{4}$$

where $|\phi|$ represents the on-axis phase shift, S is the aperture's linear transmittance and it is found using the formula,

$$S = 1 - \exp(-2r_a^2/\omega_a^2) \tag{5}$$

where ra is the radius of the aperture and ω_a is the beam radius at the aperture.

Third-order nonlinear refractive index is associated with on-axis phase shift

$$|\phi| = k\, n_2 L_{\text{eff}} I_0 \tag{6}$$

where I_0 is the intensity of the laser beam at focus ($Z=0$) ($I_0 = 26.31\ \text{MWm}^{-2}$) and L_{eff} is an effective thickness of the crystal which is evaluated from the formula$L_{\text{eff}} = [1 - \exp(-\alpha L)]/\alpha$where α and L correspond to linear absorption coefficient and the thickness of the crystal, respectively.

Nonlinear absorption coefficient (β) can be evaluated by applying the following formula

$$\beta = \frac{2\sqrt{2},\ \Delta T}{I_0,\ L_{\text{eff}}} \tag{7}$$

Third-Order Nonlinear Optical susceptibility ($n2$) has been assigned by the successive formulas

Real part of the abovementioned susceptibility is calculated by the formula

$$\text{Re}\ \chi^{(3)}(\text{esu}) = 10^{-4}\frac{\varepsilon_0 C^2 n_0^2}{\pi} n_2 \left(\frac{\text{cm}^2}{W}\right) \tag{8}$$

Third-order NLO susceptibility's imaginary part is given as

$$\text{Im}\ \chi^{(3)}(\text{esu}) = 10^{-2}\frac{\varepsilon_0 C^2 n_0^2 \lambda}{4\pi^2}\beta\left(\frac{\text{cm}^2}{W}\right) \tag{9}$$

$$\left|\chi^{(3)}\right| = \sqrt{\left(\text{Re}\left(\chi^{(3)}\right)\right)^2 + \left(\text{Im}\left(\chi^{(3)}\right)\right)^2} \tag{10}$$

Figure 10c represents ratio of closed to open aperture graph.

Table 3 displays the values of the nonlinear optical parameters of CHOD. The nonlinear parameters are refractive index n_2, absorption coefficient β, real section of susceptibility $\chi_R^{(3)}$, imaginary section of susceptibility $\chi_I^{(3)}$ and complete section of susceptibility as $\chi^{(3)}$

Table 3 Z-Scan parameters of the CHOD crystal

Third order nonlinear characteristics	Computed values
(n_2)	9.568×10^{-8} cm^2/W
(β)	0.039×10^{-4} cm/W
($\chi_R^{(3)}$)	5.678×10^{-6}esu
($\chi_I^{(3)}$)	0.239×10^{-6}esu
$\lvert\chi^{(3)}\rvert$	5.6838×10^{-6}esu

4 Conclusions

A potential, Oxalato-bridged nonlinear optical CHOD crystals were synthesized by slow evaporation technique. XRD technique interprets the geometry of the crystal. Spectroscopic analyses of the compound were performed by Fourier transform IR and Raman techniques. From UV–Vis spectrum, the absorption edge was found to be 241 nm. SEM divulges the porous nature of the crystal and big sized grains were seen. The lifetime of fluorophore was ascertained. Topology of the grown crystals was indexed by SEM and presence of cesium is confirmed by EDAX technique. Hirshfield analysis show that the main contribution to intermolecular contacts comes from O–H/H–O (53.4%) and Cs–O\O–Cs (13.7%) contacts. In Z-scan technique, the compound exhibits self-defocusing effect in closed aperture and saturable absorption behaviour in open aperture. Saturable absorption behaviour can be used for producing ultra-short laser pulse generation in fibre laser.

Acknowledgements Authors extend their thanks to SAIF IITM Chennai, St. Joseph's College, Trichy and VIT Chennai for accomplishing characterization techniques.

References

1. A. Priyadharshini, S. Kalainathan, J. Mater. Sci. **29**, 2698 (2018)
2. M. Nageshwari, C.R. Kumari, S. Sudha, G. Vinitha, M.L. Caroline, G. Mathubala, A. Manikandan, Phys. B **582**, 411980 (2020)
3. A. Priyadharshini, S. Kalainathan, J. Mater. Sci. **28**, 7401 (2017)
4. J. Jeyaram, K. Varadharajan, B. Singaram, R. Rajendhran, J. Cryst. Growth **486**, 96 (2018)
5. A. Priyadharshini, S. Kalainathan, J. Mater. Sci. **28**, 5089 (2017)
6. V.K. Trunov, V.A. Efremov, N.B. Tskhelashvili, J. Struct. Chem. **31**, 702 (1991)
7. Y. Slimani, M.A. Almessiere, S. Güner, N.A. Tashkandi, A. Baykal, M.F. Sarac, M. Nawaz, I. Ercan, J. Mater. Sci. **30**, 9143 (2019)
8. C.M. Mary, G. Vimal, K.P. Mani, G. Jose, P.R. Biju, C. Joseph, N.V. Unnikrishnan, M.A. Ittyachen, J. Mater. Res. Technol. **5**, 268 (2016)
9. C.R. Kumari, S. Sudha, G. Vinitha, M. Nageshwari, M.L. Caroline, G. Mathubala, A. Manikandan, Phys. B **577**, 411804 (2020)
10. H. Kherfi, M. Hamadène, A. Guehria-Laïdoudi, S. Dahaoui, C. Lecomte, Materials **3**, 1281 (2010)
11. B.C. Smith, Spectroscopy **33**, 20 (2018)
12. S. Sudha, P. Jayaprakash, C.R. Kumari, M. Nageshwari, G. Vinitha, R.G. Raman, M.L. Caroline, Chin. J. Phys. (2019). https://doi.org/10.1016/j.cjph.2019.08.017
13. Y. Slimani, A. Selmi, E. Hannachi, M.A. Almessiere, A. Baykal, I. Ercan, J. Mater. Sci. **30**, 9520 (2019)
14. S. Sudha, M.P. Mohamed, G. Vinitha, C.R. Kumari, P. Sangeetha, M.L. Caroline, Chin. J. Phys. **57**, 211 (2019)

15. P. Krishnan, K. Gayathri, P.R. Rajakumar, V. Jayaramakrishnan, S. Gunasekaran, G. Anbalagan, Spectrochim Acta A. **131**, 114 (2014)
16. R.P. Jebina, T. Suthan, N.P. Rajesh, G. Vinitha, Opt. Laser Technol. **115**, 500 (2019)
17. P. Krishnan, K. Gayathri, N. Sivakumar, S. Gunasekaran, G. Anbalagan, J. Cryst. Growth **396**, 85 (2014)
18. J. Tauc, *Amorphous and Liquid semiconductors* (Plenum Press, London and New York, 1974)
19. Y. Slimani, M.A. Almessiere, M. Nawaz, A. Baykal, S. Akhtar, I. Ercan, I. Belenli, Ceram. Int. **45**, 6021 (2019)
20. M.A. Almessiere, Y. Slimani, A.D. Korkmaz, S. Guner, M. Sertkol, E.S. Shirsath, A. Baykal, Ultrason. Sonochem. **54**, 1 (2019)
21. Ewald Terpetschnig and M.David Jameson, Fluorescence Lifetime 2 (1) ISS Inc. (2.) Department of Cell and Molecular Biology; John A. Burns School of Medicine 1960 East-West Rd.; University of Hawaii, HI 96822–2319.
22. S. Kandhan, B.T. Arasan, P. Krishnan, S. Aravindhan, S. Srinivasan, S. Gunasekaran, J. Mol. Struct. **1180**, 512 (2019)
23. A.C. Munson, L.J. Gottfried, C.F. De Lucia, L.K. McNesby, W.A. Miziolek, *Counterterrorist Detection Techniques of Explosives* (Elsevier, Amsterdam, 2007), pp. 279–321
24. S.J. Nandre, S.J. Shitole, R.R. Ahire, Study of growth, EDAX. J. Nano Elect. Phys. **4**, 04013–4021 (2012)
25. A.P.M. Manzoor, M. Mujeeburahiman, S.R. Duwal, P.D. Rekha, Biocatal. Agric. Biotechnol. **17**, 566 (2019)
26. M.A. Rahman, M.A.R. Sarker, J. Alloys Compd. **797**, 630 (2019)
27. M.A. Almessiere, Y. Slimani, H.S. El-Sayed, A. Baykal, J. Sol-Gel Sci. Technol. **88**, 628 (2018)
28. M.A. Almessiere, Y. Slimani, S. Güner, A. Baykal, I. Ercan, J. Rare Earth **37**, 871 (2019)
29. A. Sowmya, G.N.A. Kumar, S. Kumar, S.S. Karki, Chem. Data Collect. **17–18**, 431 (2018)
30. S.P. Ramteke, M.I. Baig, M. Shkir, S. Kalainathan, M.D. Shirsat, G.G. Muley, M. Anis, Opt. Laser Technol. **104**, 83 (2018)
31. M.G. Kuzyk, C.W. Dirk, *Characterization Techniques and Tabulations for Organic Nonlinear Materials* (Marcel Dekkar Inc., New York, 1998), pp. 655–692
32. S.A. Jabbar, I.S. Abbas, H.M. Al-zubaidy, Studying the linear and nonlinear optical properties by using Z-Scan technique for CdS thin films prepared by CBD technique. Appl. Phys. Res. **10**, 7 (2018)

Research Article

Spectral profile index changes as biomarker of toxicity in *Catla catla* (Hamilton, 1822) edible fish studied using FTIR and principle component analysis

M. Mohan Kumar[1] · S. Binu Kumari[1] · E. Kavitha[2] · B. Velmurugan[3] · S. Karthikeyan[4]

Received: 23 March 2020 / Accepted: 3 June 2020

Abstract

The study was carried out to evaluate the toxicity in gill tissue of edible fish *Catla catla* using FTIR spectra. Fourier self-deconvolution obtained by curve fitting was applied in the lipid (3000–2800 cm^{-1}), carbohydrates (1000–1100 cm^{-1}) and in the amide region (1700–1600 cm^{-1}). These spectral changes were used as biochemical parameters to assess the degree of toxicity. A disorder in lipid changes was measured by frequency shift and intensity changes in the CH_2 asymmetric stretching band. This change in the fatty acid composition in fish could be used as biomarkers of toxic effect. Decreases in lactic acid (6–16%) clarify the lipid peroxidation which is the primary mechanism of toxicity. The deconvolution in the amide region shows peaks at 1621 cm^{-1}, 1637 cm^{-1} due to β sheet; 1652 cm^{-1} and 1667 cm^{-1} due to α helix and 1683 cm^{-1} due to antiparallel β sheet. The results show a decrease by (3–7%) in α helix and increase by (13–40%) in β sheet structure. This shows β sheet formation of protein secondary structure due to toxicity. PCA plots indicate protein and lipids have strong positive loadings. The study shows the spectral variation is considered as an ideal biomarker with a high degree of accuracy of test organism to examine the toxicity of pollutants.

✉ S. Karthikeyan, physicskarthik@gmail.com | [1]PG and Research Department of Zoology, Kongunadu Arts and Science College, Coimbatore, Tamil Nadu 641029, India. [2]Department of Physics, Dr. MGR Educational and Research Institute, Chennai, Tamil Nadu 600095, India. [3]PG and Research Department of Department of Zoology, Sir Theagaraya College, Chennai, Tamil Nadu 600021, India. [4]Department of Physics, Dr. Ambedkar Government Arts College, Chennai, Tamil Nadu 600039, India.

SN Applied Sciences (2020) 2:1233 | https://doi.org/10.1007/s42452-020-3001-z

Published online: 16 June 2020

Graphic abstract

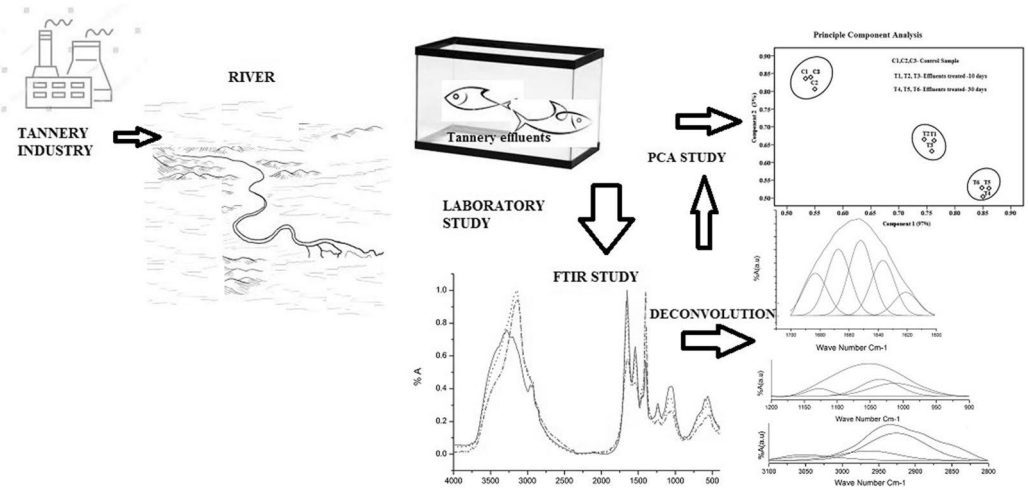

Keywords Deconvolution · Toxicity · FTIR · Lipids · Proteins · PCA

1 Introduction

Air, water and land are the basic components of life. They are defiled because of increasing population, fast urbanization and industrialization. Extensive industrialization measurably influences the quality of water in lakes, ponds, and rivers especially in India [1]. Natural waters are adulterated by untreated wastes of industry and often contain different metallic compounds. At present, the bioaccumulation of heavy metals in the environment is a remarkable threat to human. Water contamination caused by modern wastage is frequent as they fall into natural water sources and agricultural environment. Leather industry is one of the traditional industries in the world. The demand of leather products led to the emergence of huge commercial tanneries. They meet the huge demands of leather footwear, drums and musical instruments. In India production of leather and the leather industry contributes a major share to the nation's export earnings. The use of a large number of chemicals by tanning industries discharges toxic wastes into the rivers and land. The wastes deliver wide varieties of high strength toxic chemicals. A serious concern to the regulatory bodies and the general public is the safe and long-term management of chromium-containing waste effluents from the tanneries.

Leather industries cause a serious environmental threat due to the discharge of heavy metals, organic and inorganic matter, suspended solids etc. [2, 3]. It is the major source of water pollution with high chemical oxygen demand (COD) and chromium content. The accumulation of effluents becomes hazardous to the marine organisms and the surrounding human population. Fish is considered an ideal test species in the ecotoxicological studies, to examine the toxicity of pollutants. The wide use of fish is most likely due to their availability and adaptability to laboratory conditions to varying degrees of sensitivity to the toxic substances [4]. Fishes are the most widely distributed aquatic organisms that are susceptible to environmental pollution in the waters. They are also used to evaluate the health of aquatic systems and serve as biomarkers of environmental pollution. They are used in the quality assessment of the marine system due to pollution [5]. The freshwater fish, *Catla catla* are the most common fish consumed due to its high commercial importance worldwide. Therefore, it can be a good model to study the responses to various environmental contaminations. It is the best indicator of aquatic pollution and it is a good choice when compared to other aquatic animals. It is considered for perfect ecotoxicology test, to analyse all probabilities of changing levels of sensitivity to the toxic substance. Biochemical factors such as protein and glucose are highly sensitive and they are used in the detection of stress condition [6]. The alterations of these parameters are mainly used to identify target organs of toxicity. Proteins and lipids are biomarkers commonly used for detecting or diagnosing the pollution level of the environment. These parameters are suitable tools for surveying ecological impacts and stress of aquatic organisms. FTIR is a simple and rapid method to study the cellular changes in biological samples at the molecular level. It is easier to detect

the conformational changes in bimolecular components as well as intermolecular or intermolecular interaction in tissue samples [7, 8]. The change in the spectral alteration can be used in both qualitative and quantitative study of the molecular changes occurring in them [9, 10]. Studies due to the effect of an environmental pollution on the biological sample using FTIR paved the way for better understanding the biomonitoring process for qualitative and quantitate analysis [11, 12]. Hence, the present investigation was made to examine the biochemical changes in gill tissues of *Catla catla* under tannery effluents using the FTIR technique in conjunction with principle component analysis.

2 Description of the study area

The study area and the effluent discharge points in the river are shown in Fig. 1. The Kaveri river considered for this study travels into various districts of Tamil Nadu. The latitude of Kaveri river is 11.0585435 N and longitude is 79.5787168 E. The total length of this river is 765 km with an average rainfall of 812 mm. The major uses of the river water are agricultural consumption, household consumption and for drinking purpose. But nowadays the quality of the river water is deteriorating because of the discharge effluents from tannery industries and pollution due to sewage wastes, washing, bathing and miscellaneous activities. Kaveri River runs over several km and it reaches the domestic area Ramanathapuram Pudur where it receives effluents discharged from local tannery industries. The effluent samples are measured for the major physical and chemical parameters and heavy metal analysis. The effluents flowing into the river are collected from the discharge point (S1, S2, S3 and S4) to assess the toxicity due to tannery effluents in the nearby the residential area.

3 Materials and methods

3.1 Measurement of tannery effluent concentration by atomic absorption spectrometer

The collected effluents from sampling points are analysed for heavy metals concentration using Atomic absorption Spectrometer (model AL168 Elico, India) available at ALPHA Lab, Coimbatore, Tamil Nadu. The major concentrations of heavy metals are chromium 6.10 mg/l, Cd 2.93 mg/l, Pb 4.78 mg/l, Cu 0.07 mg/l and Mg 0.89 mg/l. Among the metals, Cu and Mg are below the limit as recommended by the Central pollution control board of India whereas the rest of the metals are found to be above the permissible limit. Further, the chlorides have 2388.36 mg/l and TDS 4080 mg/l. This shows that tannery effluents have higher chromium contents followed by Pb and Cd collected from the sampling points.

3.2 Toxicity study of tannery effluent—determination of LC_{50}

A static bioassay method was used in our laboratory. The experimental fish, *Catla catla* (average length: 7.5 ± 0.5 cm and weight: 6.5 ± 0.5 g) were obtained from Tamil Nadu Fisheries Development Corporation Limited, Aliyar Fish

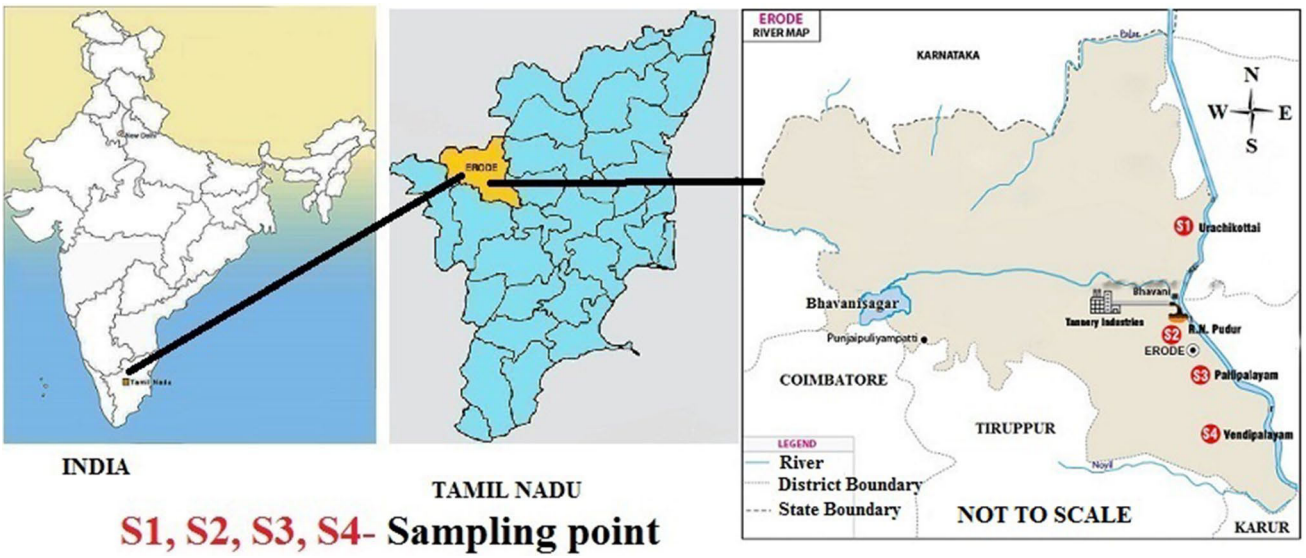

Fig. 1 Map of sampling station showing a collection of tannery effluents at different sampling point of Kaveri River flowing at Tamilnadu, India

Farm, Tamil Nadu, India. The fish were adapted to laboratory conditions for 15 days in a large tank (1000 l capacity) and fed with groundnut oil cake. Water was renewed daily to avoid accumulation of excretory materials. During acclimatization, the fish were maintained at a natural photoperiod at ambient temperature. The chlorine-free water was used in the present experiment. The physico–chemical parameters of the water were measured following the method of APHA [13]. They are temperature (29.0 ± 12 °C), pH (7.4 ± 0.03), dissolved oxygen (6.8 ± 0.5 mg/l), total alkalinity (164 ± 7.8 mg/l), total hardness (152 ± 4 mg/l) and salinity (0.04 ± 0.02 mg/l).

Preliminary tests were conducted to find out the median lethal concentration of fish due to tannery effluent for 96 h. For finding LC_{50}, circular plastic container of 20 l capacity was used. Ten fishes were introduced in each container having different concentrations of tannery effluent (1.0, 1.1, 1.2, 1.3, 1.4, 1.5, 1.6, 1.7, 1.8, 1.9 and 2.0 mg l^{-1}) for 96 h treatment. The fishes served without the addition of toxicants act as a control. Acute toxicity is determined using a standard static-renewal technique described by the US environmental protection agency for the measurement of toxicity of effluents [14]. The 96 h LC_{50} was calculated by the probit method [15] and found to be 1.9 mg/l. For chronic toxicity study 1/10th of LC_{50} concentration of tannery effluent (0.19 mg/l) was taken and exposed for 10 and 30 days treatments in our study. The samples were grouped into control—group 1, the effluents treated for 10 days and 30 days were grouped as group 2 and 3 respectively. The experiment was carried out with three replicates along with control groups. Upon completion of the stipulated exposure period, the gill tissues selected fish from the control and tannery effluent were taken for further analysis.

3.3 Sample preparation

The gill tissues were lyophilised for 12 h to remove its water content completely. The samples were then ground with the help of an agate mortar and pestle to bring it in powdered form. Finely powdered tissues were mixed with pre-dried potassium bromide in a ratio of 1:100 respectively. It was subjected to a high pressure (3000 Psi) for 5 min in an evacuated die to produce a transparent sample pellet of 1 mm thickness and 13 mm diameter for use in FTIR spectrophotometer.

3.4 FTIR analysis

FT-IR spectra were recorded on NEXUS 470 spectrophotometer installed at the Karunya University, Coimbatore, India. A total of 256 scans were taken at a resolution of 4 cm^{-1} and averaged. A blank KBr disk was used as background. Pellets were scanned at room temperature (25 ± 1 °C) in the 4000–400 cm^{-1} spectral range. Background spectra were subtracted from the sample automatically. Each sample was scanned under the same conditions with three different pellets. The software OPUS version 6.5 was used to carry out the baseline correction and vector normalization. The spectral deconvolution was obtained using the Origin 8.0 software.

A baseline was subtracted before the curve fitting. To start the curve fitting iteration, peak position, peak height and half bandwidth were chosen. The initial values were taken from second derivatives smoothed by the Savitzky and Golay method with a 9-point window. Gaussian function was used to resolve peak pattern with least goodness-of-fit explained in our earlier study [16].

3.5 Statistical analysis

The results were expressed as ± standard error of mean (SEM). Gill tissues of *Catla catla* tannery effluent treated group vs control group were analysed using the one-way ANOVA test using SPSS 16.0. *P* values of less than 0.05 were considered as statistically significant.

3.6 Principle component analysis (PCA)

The principle component analysis (PCA) was carried out using SPSS16.0 programming. It is used for data reduction from a larger sample. The PCA was used to our mean-centered, second derivative, and vector normalized spectral data. The results were displayed as score plots. The input value of the samples (both control and treated) is formed as data matrices. The inputs change into scores and loadings which are the characteristics of principal components. It is used for quantitative approaches in discriminating the samples. The scores of the component were plotted to gather data responsible for the variation.

4 Results and discussion

Figure 2 indicates the average spectra of gill tissues of *Catla catla* of control and chronic exposures of tannery effluents for two different periods. The major and minor bands of the infrared spectra of the control groups, tannery effluents treated gill tissues were recorded in Table 1. As observed from Fig. 2 the bands centred at ~ 3291 cm^{-1} and 3089 cm^{-1} corresponds to amide A and amide B of proteins due to N–H/O–H modes of proteins. The bands rise at ~ 3013 cm^{-1} which indicates the presence of HC=CH group olefinic molecules. This band is used as a varying measure of degrees of unsaturation of phospholipids [17]. Lipids give rise to a number of absorption in FTIR spectra.

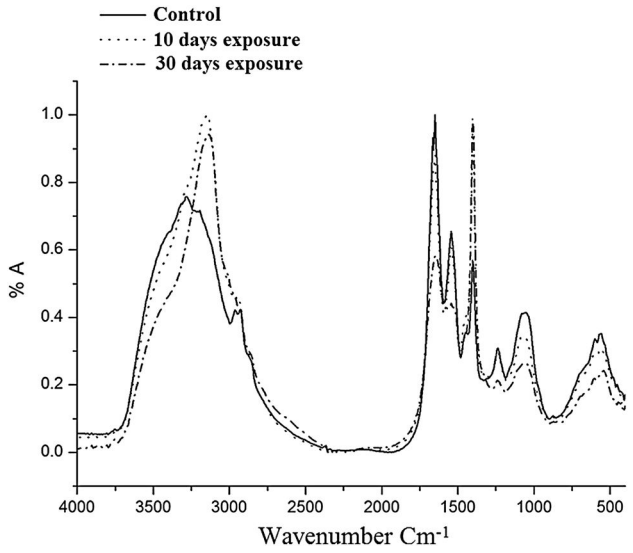

Fig. 2 Average FTIR spectra of *Catla catla* showing control and tannery effluents exposed to different days of exposure in the region of 4000–400 cm^{-1}

The medium band which rises at ~ 2957 cm^{-1} is assigned CH_3 asymmetric stretching. The peak at 2927 cm^{-1} and 2855 cm^{-1} can be assigned to asymmetric and symmetric stretching mode of CH_2 modes [18]. This band is mainly screened for the lipids present in the biological system. Strong band ~ 1645 cm^{-1} is assigned to amide I and arises due to C=O of protein. Amide II bands appear ~ 1536 cm^{-1} due to N–H/C–N mode of vibration [19, 20]. As observed from the Fig. 2 the intensity of amide bands decreases significantly due to the tannery effluents treated for both acute and chronic exposures. Medium intensity bands ~ 1392 cm^{-1} arise mainly from COO—symmetric stretching modes of fatty acids. The band is seen at ~ 1231 cm^{-1}, and 1083 cm^{-1} were primarily assigned to the asymmetric and symmetric stretching modes of nucleic acids instead of phospholipids [21]. This band may overlap in the carbohydrates region, as revealed by the deconvolution [22]. There are several bands which appear in the 3000–2800 and 1800–1000 cm^{-1} region. These bands need extraordinary administration to information investigation since they comprise of several unresolved bands. We used Fourier self deconvolution techniques in the lipid regions (3000–2800 cm^{-1}), carbohydrates region (1000–1100 cm^{-1}) and amide region (1700–1600 cm^{-1}).

4.1 FTIR self deconvolution deduced by curve fitting analysis in the fatty acids region

An interesting observation was made by examining the curve fitting in the region 3050–2800 cm^{-1} shown in Fig. 3. The investigation in the region 3050–2800 cm^{-1} indicates band ~ 3013 cm^{-1} is because of the HC=CH stretching modes. As observed from Fig. 3 the band area 3013 cm^{-1} diminishes demonstrating the population of unsaturated lipids. It was observed that the band of olefinic group reduced by 12% and 73% for tannery effluents when compared to control (Table 2). This reduction in the band area and the shift in the frequency value of this band were because of alterations in lipid metabolism induced by tannery treatment. These changes were monitored by the CH_3 asymmetric stretching mode observed in ~ 2960 cm^{-1}. Considering the control a decrease in the band area of the CH_3 asymmetric stretching vibration by 25% and 56% were observed as the outcome of tannery effluent treatment. This indicates the release of the phospholipids in the gill tissues of *Catla catla*. The shift in frequency and intensity changes in CH_2 asymmetric stretching band ~ 2927 cm^{-1} gives information regarding the degree of conformational disorder. In the current work, the shift in peak position to lower values indicates that the lipid disorder increases and

Table 1 Tentative frequency assignment and their functional groups for the Control and tannery effluents treated gill tissues of *Catla catla*

Control	10 Days exposure	30 Days exposure	Frequency assignment
3291 (m)	3298 (m)	3293 (w)	Amide A: mainly N–H stretching of proteins
3089 (w)	3081 (w)	3079 (w)	Amide B: N–H stretching of proteins
2957 (s)	2953 (m)	2955 (m)	CH_3 asymmetric stretching, mainly lipids
2927 (s)	2928 (m)	2927 (w)	CH_2 asymmetric stretch: mainly lipids
2855 (vw)	2852 (vw)	2858 (vw)	CH_2 symmetric stretch: mainly lipids
1645 (s)	1644 (m)	1642 (m)	Amide I: C=O stretching of proteins
1536 (s)	1527 (vw)	1529 (m)	Amide II: N–H bending and C–N stretching of proteins
1441 (m)	1444 (m)	1446 (vw)	CH_2 bending: mainly lipids
1398 (m)	1395 (vw)	1397 (vw)	COO^- symmetric stretch: fatty acids and amino acids
1231 (m)	1229 (vw)	1226 (vw)	PO^{2-} asymmetric stretch
1169 (m)	1164 (m)	1167 (vw)	C–O asymmetric stretching of glycogen

s strong, *m* medium, *w* weak, *vw* very weak

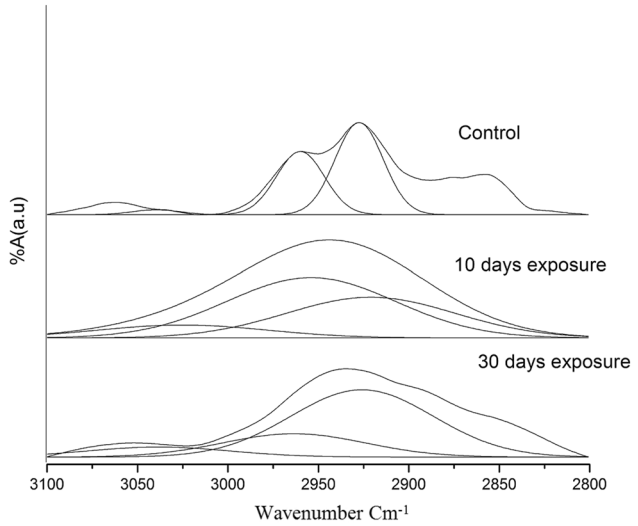

Fig. 3 FTIR spectra deduced by curve fitting analysis in the region 3100–2800 cm^{-1} of *Catla catla* showing control and tannery effluents exposed to different days of exposure

acyl chain flexibility decreases [23, 24] (disorder state of lipids). It was observed that the shift in frequency intensity of the band in the lipid region shows adverse in lipid fluidity due to exposure of tannery effluents. In addition, the band area of the CH_2 stretching band was found to be significantly increased at 30 days exposure compared to 10 days exposure. These results suggest an increase in the lipid contents has occurred for 30 days exposure when compared to 10 days. This could be due to the usage of lipid to satisfy the additional energy requirement under stress [25]. Similarly an increase in CH_2 stretching was observed in liver tissues of *rainbow trout* due to estradiol, which was studied using FTIR spectroscopy [26]. Loss of lipids noticed in this study results in lipid synthesis and mobilizing of the stored unsaturated lipid molecules as suggested by Jha [27]. This change in the fatty acid content of fish phospholipid is used as a biomarker indication thus helping in the diagnosis of aquatic pollution [28].

4.2 FTIR self deconvolution deduced by Curve fitting analysis in the carbohydrates region

The results of deconvolution in the region 1200–900 cm^{-1} shows the existence of glycogen ~ 1013 cm^{-1}, glucose ~ 1038 cm^{-1} and lactic acid ~ 1126 cm^{-1} respectively. From Fig. 4a remarkable decrease in glycogen level was perceived due to tannery effluent toxicity. The band area decreases by 5–15% due to effluent treatment (Table 3). This decrease in glycogen has additionally been recommended by Shaffi [29], to clarify consumption in glycogen. Comparable consumption in glycogen content in the current study might be credited to the usage of glycogenolysis due to effluents stress [30]. From Fig. 4 a 5% reduction in glucose was observed due to tannery effluent exposed for a period of 10 days. But there is a slight increment (18%) in the glucose concentration noted at 30 days exposure. This mobilization of glucose is due to its availability for utilization by the tissues in the normal metabolic process which is inevitable when exposed to the toxic medium.

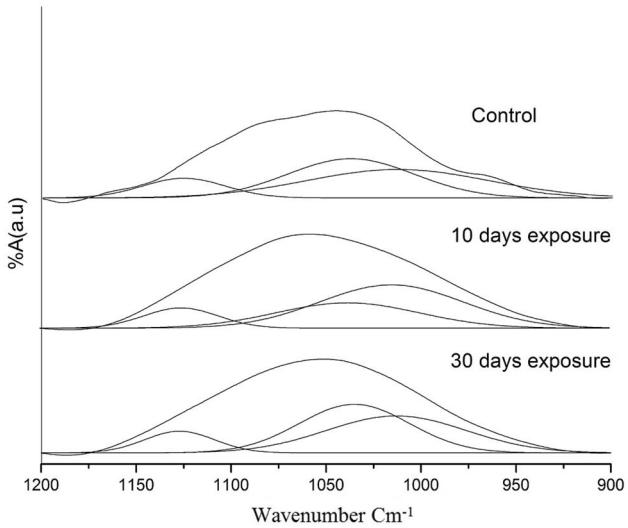

Fig. 4 FTIR spectra deduced by curve fitting analysis in the region 1200–900 cm^{-1} of *Catla catla* showing control and tannery effluents exposed to different days of exposure

Table 2 Results of curve fitting analysis for the Control and tannery effluents treated gill tissues of *Catla catla* in the fatty acids region (3050–2800 cm^{-1}) and their band assignments

Control		10 Days exposure		30 Days exposure		Assignments
Wave number (cm^{-1})	% Area	Wave number (cm^{-1})	% Area	Wave number (cm^{-1})	% Area	
2927	37.49 ± 0.79	2921	51.48 ± 0.94	2925	72.88 ± 1.25	CH_2 asymmetric stretching lipids
2960	52.59 ± 0.64	2954	39.48 ± 1.74	2963	23.18 ± 0.96	CH_3 asymmetric stretching Lipids
3013	11.24 ± 0.56	3015	9.93 ± 0.46	3018	3.03 ± 0.24	Olefinic HC=CH lipids

The values are the mean ± SE for each group ($n = 3$). The degree of significance was $P < 0.05$

Table 3 Results of curve fitting analysis for the control and tannery effluents treated gill tissues of *Catla catla* in the carbohydrates moiety region (1000–1150 cm^{-1}) and their band assignments

Control		10 Days exposure		30 Days exposure		Assignments
Wavenumber (cm^{-1})	% Area	Wave number (cm^{-1})	% Area	Wave number (cm^{-1})	% Area	
1013	50.77 ± 0.85	1014	48.12 ± 1.04	1013	42.95 ± 1.47	Glycogen
1038	37.73 ± 0.46	1037	35.96 ± 0.69	1035	44.36 ± 0.58	Glucose
1126	14.58 ± 0.64	1125	12.26 ± 0.38	1127	13.75 ± 0.26	Lactic acid

The values are the mean ± SE for each group ($n = 3$). The degree of significance was $p < 0.05$

The by-product lactic acid formed is put to use for cell functions. This clarifies the possible synthesis of carbohydrates to overcome the glucose level under stress conditions. The decrease in glycogen results in higher demand for carbohydrate to meet energy demands during stress conditions. The reduction in glycogen level is considered as the result of greater stress the organs experience during the detoxification process. An unusual lactic acid is found to diminish radically (6–16%) for both treatments which could clarify the lipid peroxidation which is the primary mechanism of toxicity. It is seen at chronic exposure concentration lactic acid raises, proposing oxidative stress resulting in altered levels of lipid metabolism due to toxicants. A similar effect was studied by Jerome et al. [31], due to the effect of industrial effluent on gill tissues of *Callinectes amnicola* resulting in a decrease lipid peroxidation. This brings about the disruption of enzymes associated with carbohydrate metabolism. The consumption of glycogen level by fish may because of the utilization of energy due to toxic stress. Similar result in a reduction in carbohydrate metabolism was reported by Tilak et al. [32] in *Channa punctatus* due to exposure of thermal power plant effluent. The decrease in the glycogen concentration is increased by the utilization of energy resource to overcome the toxic stress which normally enhances glycogen utilization [33]. In addition, the decline in glycogen may be due to use in the formation of glycoproteins and glycolipids of various cells and other membranes. Similar results in carbohydrates reduction were observed by Muley et al. [34], due to the toxic effect of industrial effluents in *Labeo rohita*. Sobha Rani et al. [35], observed a huge exhaustion in carbohydrate metabolism in different tissues of freshwater fish *O. mossambicus* under toxic conditions. Perceptions of the present review demonstrated that effluents to sublethal concentrations causes a decrease in the biochemical composition (glycogen, protein and lipid). Umminger [36] hypothesized that glycogen is utilized as the immediate energy source by the fish under stress conditions. Our FTIR study supports the decline in the glycogen level in fish tissues exposed to sub-lethal concentrations when compared to control. This may be due to the reduction of Cr(VI) to Cr(III) which is a major component in tannery effluents. Further, this Cr(III) ions can bring about the production of reactive oxygen species (ROS) leading to oxidative stress in the exposed animals [37, 38]. Chen et al. [39], studied the effect of chromium on tissues, organs of *Oryzias latipes* with respect to biochemical changes leading to an increase in lipid peroxidation and histopathological alteration. We can get from the eventual outcomes of the present study that the dynamic gathering of tannery effluents in gill target tissues influenced the decline in the glycogen level. The present work shows that tannery effluents brought about changes in the carbohydrate metabolism in *Catla catla*, resulting in a further decrease in glycogen values. Subsequently an increase in glucose content resulting in a decrease in lactic acid which are more pronounced due to anaerobic metabolism to make a by-product during ATP synthesis.

4.3 FTIR self deconvolution deduced by curve fitting analysis in the amide I region

Understanding of the protein components of the cell seems to be distinctly vital in studying fundamental changes in the secondary structure of protein among tannery intoxication. The synthesis of protein and degradation are sensitive due to varying physical and chemical modulators. Deconvolution made in the amide I region of 1720–1600 cm^{-1} are used to study the secondary structural changes in proteins. The Fig. 5 shows the presence of five peaks 1683, 1667, 1652, 1637 and 1621 cm^{-1} obtained after the results of the curve fitting analysis for control and treated samples. The peak due of 1621 cm^{-1}, 1637 cm^{-1} assigns to β sheet; 1652 and 1667 cm^{-1} assigns to α helix and 1683 cm^{-1} due to antiparallel β sheet [16, 40]. It is observed from Table 4 that the percentage area of α helix declines by 3–7% and an increase in β sheet structure by 13–40% was noticed. This may be because of the changes or synthesis of proteins which were consistent with the mechanisms of β sheet formation. The β-sheet structure in the effluents treated gill tissues was formed because of the intermolecular hydrogen-bond interaction that modifies the secondary structure of proteins in the gill tissues [41, 42]. The further antiparallel β sheet was formed and an increase in band area 9–12% was observed with respect to control. This change in the secondary structure

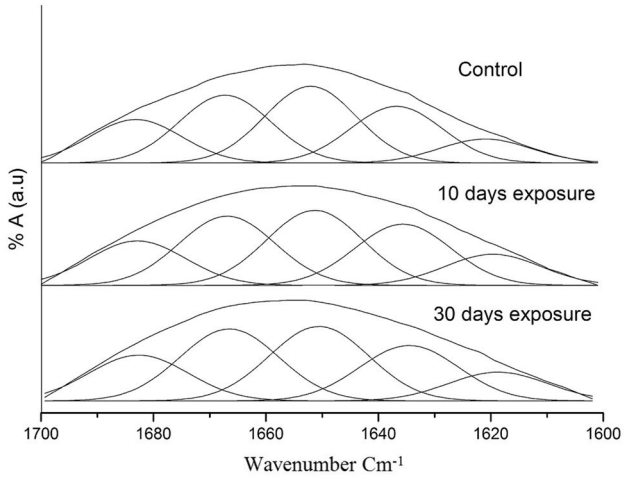

Fig. 5 Secondary structure of protein deduced by curve fitting analysis in the region 1720–1600 cm^{-1} of *Catla catla* showing control and tannery effluents exposed to different days of exposure

is in agreement with our earlier studies using FTIR on fish tissues [17]. Similar results of a decrease in the protein profile exposed to effluent toxicity of *Channa punctatus* (Bloch) were reported by Maruthi and Subba Rao [43]. Proteins possess a remarkable position in the metabolism of cells and enzymes, which intervene at different metabolic pathways. These results suggest that the structural changes in the protein of the gill tissues were significantly affected by tannery effluents. In the present study, protein compositions were altogether decreased in the tannery treated group when contrasted with the control group proposing solid markers of stress impact of the tannery treatment. Khan et al. [44], studied the toxic impact of Cd and Pb resulting in changes in lipids, proteins on *Crucian carp* (*Carassius auratus gibelio*) using FTIR analysis. The outcomes revealed that toxicity due to tannery influences the intermediary metabolism of *Catla catla* utilizing FTIR can fill in as incredible biomarkers of tannery effluent contamination.

4.4 Principle components analysis of the gill tissue of *Catla catla* exposed to tannery effluents

PCA enables quantitative changes among the spectra in terms of principle components, based on the criteria of uncorrelated difference. The PCA obtained from infrared spectra are better reflected from higher eigenvalues and % of the variance as shown in Fig. 6a. The plots indicate that the control and tannery treated samples are successfully well discriminated with each other. Control and tannery treated samples have a strong separation in the positive components of the score plots. The highest absolute eigenvalue corresponds to components 1 and 2. The first principal components describe over 97% of all spectral features. The component 2 accounts for 3% difference of the spectral values. The third component is neglected due to lower eigenvalues. The results of the PCA are best displayed graphically, as loading plots versus the wavenumber showing significant variation in the biochemical composition (Fig. 6b). By reviewing the loading plots, it is clear that protein and fatty acids have a positive loading showing highest variation obtained from our sample. A distinct variation was evident from the infrared spectra of the samples studied. The glycogen, glucose and lactic acid of the carbohydrate moieties are having the least variation of loading values due to effluent treatment.

5 Conclusion

Spectral bands obtained by deconvolution technique were used for a quantitative measure of toxicity on gill tissues of *Catla catla*. The decrease in the frequency and intensity changes of asymmetric CH_2 stretching showed a reduction in lipid contents due to tannery effluents. This reduction is more pronounced with exposure periods. Changes in carbohydrate metabolism bring about an increase in glucose level in both the types of treatment of gill tissues of *Catla catla*. The decrease in lipid and protein contents is

Table 4 Results of curve fitting analysis expressed as a function of percentage areas of protein secondary structures for the control and tannery effluents treated gill tissues of *Catla catla* in the Amide I region and their band assignments

Control		10 Days exposure		30 Days exposure		Assignments
Wave number (cm^{-1})	% Area	Wave number (cm^{-1})	% Area	Wave number (cm^{-1})	% Area	
1621	8.89 ± 0.46	1619	11.05 ± 0.73	1618	14.38 ± 0.64	β Sheet
1637	20.34 ± 0.61	1636	22.09 ± 0.65	1634	26.77 ± 0.68	β Sheet
1652	28.58 ± 0.71	1651	26.72 ± 0.32	1656	26.95 ± 0.14	α Helix
1667	26.03 ± 0.56	1666	25.26 ± 0.27	1665	24.64 ± 0.39	α Helix
1683	14.81 ± 0.48	1682	16.18 ± 0.52	1683	16.58 ± 0.63	β Sheet antiparallel structure

The values are the mean ± SE for each group ($n = 3$). The degree of significance was $P < 0.05$

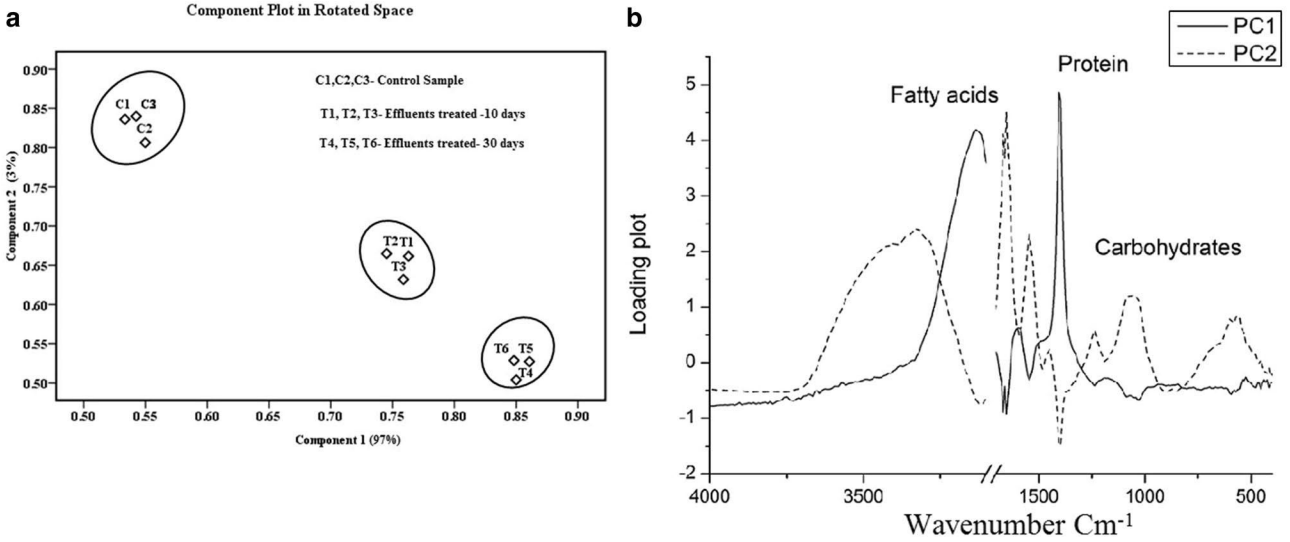

Fig. 6 **a** PCA plots showing distinct variation in the biochemical composition of gill tissues of *Catla catla* showing Control and tannery effluents exposed to different days of exposure. **b** Variation of the factor loading obtained from the PCA method with the corresponding wavenumber

because of the repair mechanism of the gill tissues with the creation of lipoproteins, key constituents of cell membranes. Further, the depletion of tissue proteins is due to lower protein synthesis because of metallic stress with the secretions of mucoproteins, which are eliminated in the form of mucus. PCA study shows the distinct variation among the samples studied when compared with control. It shows that the major component responsible for variation is proteins due to β sheet formation, followed fatty acids and carbohydrates. The results conclude that the use of infrared spectroscopy with self deconvolution and PCA techniques serve to assess the toxicity of the effluent in aquatic organisms. Further, the selected spectral bands are used as a potential tool in assessing the toxicity in the marine system with better reliability and accuracy.

Acknowledgements The authors thank Karunya University, Coimbatore, Tamil Nadu, India in helping with recording FTIR for the sample.

Compliance with ethical standards

Conflict of interest The authors have declared no conflict of interest.

Ethical approval Ethical approval is not required for carrying out experiments with fishes in India.

References

1. Beaumont MW, Butler PJ, Taylor EW (2000) Exposure of Brown trout, *Salmo trutta* to a sublethal concentration of copper in soft acidic water: effects upon muscle metabolism and membrane potential. Aquat Toxicol 51:259–272
2. Chaudry MA, Ahmad S, Malik MT (1997) Supported liquid membrane technique applicability for removal of chromium from tannery wastes. Waste Manag 17(4):211–218
3. Apte AD, Verma S, Tare V, Bose P (2005) Oxidation of Cr(Ш) in tannery sludge to Cr(VI): field observations and theoretical assessment. J Hazard Mater B 121:215–222
4. Javed M, Usmani N (2015) Stress response of biomolecules (carbohydrate, protein and lipid profiles) in fish, *Channapunctatus* inhibiting river polluted by thermal power plant effluent. Saudi J Biol Sci 22:237–242
5. Zhang Y, Sun H-J, Zhang J-Y, Ndayambaje E, Chen J, Hong H (2019) Chronic exposure to dichloroacetamide induces biochemical and histopathological changes in the gills of zebrafish. Environ Toxicol 34:781–787
6. Magazu S, Calabro E, Caccamo MT (2018) Experimental study of thermal restraint in bio-protectant disaccharides by FTIR spectroscopy. Open Biotechnol J 12:123–133
7. Osman AGM, Kouth M, Sayed AED (2010) Use of haematological parameters to assess the efficiency of quince leaf extract in alleviation of the effect of UV radiation on African catfish, *Clarias gariepinus*. J Photochem Photobiol 99:1–8
8. Gupta AD, Karthikeyan S (2016) Individual and combined toxic effect of nickel and chromium on biochemical constituents in *E. coli* using FTIR spectroscopy and principle component analysis. Ecotoxicol Environ Saf 130:289–294
9. Caccamo MT, Cannuli A (2019) PEG acoustic levitation treatment for historic wood preservation investigated by means of FTIR spectroscopy. Curr Chem Biol 13(1):60–72
10. Caccamo MT, Gugliandolo C, Zammuto V, Magazu S (2020) Thermal properties of an exopolysaccharide produced by a marine thermotolerant *Bacillus licheniformis* by ATR-FTIR spectroscopy. Int J Biol Macromol 145:77–83
11. Depciuch J, Kasprzyk I, Sadik O, Parlinka-Wojtan M (2017) FTIR analysis of molecular composition changes in hazel pollen from unpolluted and urbanized areas. Aerobiologia 33:1–12

12. Depciuch J, Kasprzyk I, Roga E, Parlinska-Wojtan M (2016) Analysis of morphological and molecular composition changes in allergenic *Artemisia vulgaris* L. pollen under traffic pollution using SEM and FTIR spectroscopy. Environ Sci Pollut Res 23:23203–23214
13. APHA (2015) Standard methods for the examination of water and waste water, 21st edn. American Public Health Association, Washington, DC, p 1085
14. Methods for measuring the acute toxicity of effluents and receiving waters to freshwater and marine organisms, 5th edn. October 2002 41–44 U.S. Environmental Protection Agency Washington, DC
15. Finney DJ (1971) Probit analysis. Cambridge University Press, Cambridge, p 333
16. Karthikeyan S, Easwaran R (2013) Analysis of a curve fitting model in the amide region applied to the muscle tissues of an edible fish: *Labeo rohita* fingerlings. J Biol Phys Chem 13:125–130
17. Velmurugan B, Senthilkumaar P, Karthikeyan S (2018) Toxicity impact of fenvalerate on the gill tissue of *Oreochromismossambicus* with respect to biochemical changes utilizing FTIR and principal component analysis. J Biol Phys 45:1563–1567
18. Moise MM (2019) FTIR study of the binary effect of titanium dioxide nanoparticles ($nTiO_2$) and copper (Cu_{2+}) on the biochemical constituents of liver tissues of catfish (*Clarias gariepinus*). Toxicol Rep 6:1061–1070
19. Depciuch J, Stanek-Widera A, Lange D, Biskup-Frużyńska M, Stanek-Tarkowska J, Czarny W, Cebulski J (2018) Spectroscopic analysis of normal and neoplastic (WI-FTC) thyroid tissue. Spectrochim Acta A 204:18–24
20. Depciucha J, Stanek-Widerab A, Warchulskac M, Langeb D, Sarwac K, Koziorowskad A, Kulae M, Cebulskic J (2019) Identification of chemical changes in healthy breast tissue caused by chemotherapy using Raman and FTIR spectroscopy: a preliminary study. Infrared Phys Technol 102:102989
21. Dogan A, Siyakus G, Severcan F (2007) FTIR spectroscopic characterization of irradiated hazelnut (*Corylus avellana* L). Food Chem 100:1106–1114
22. Cakmak G, Togan I, Uguz C, Severcan F (2003) FTIR spectroscopic analysis of rainbow trout liver exposed to nonylphenol. Appl Spectrosc 57:835–841
23. Wong PTT, Papavassiliou ED, Rigas B (1991) Phosphodiester stretching bands in the infrared spectra of human tissues and cultured cells. Appl Spectrosc 45:1563–1567
24. Cakmak G, Togan I, Severcan F (2006) 17β-Estradiol induced compositional structural and functional changes in rainbow trout liver, revealed by FTIR spectroscopy: a comparative study with nonylphenol. Aquat Toxicol 77:53–63
25. Rao KSP, Rao KRS, Sahib IKA, Rao KVR (1985) Combined action of carbaryl and phenthoate on tissue lipid derivative of muscle of *Channa punctatus* (Bloch). Ecotoxicol Environ Saf 9(1):107–111
26. Dicko A, Morissette M, Ameur SB, Pezolet M, Paolo T (1999) Effect of estradio and tamoxifen on brain membranes: investigation by infrared and fluorescence spectroscopy. Brain Res Bull 49:401–405
27. Jha BS, Pandey S (1989) Alteration in the total carbohydrate level of intestine, liver and gonad induced by lead nitrate in the fish Channa punctatus. In: Sahai YN, Deshmukh PN, Mathai TA, Pillai KS (eds) Environmental risk assessment. The Academy of Environ Biology, Lucknow, pp 207–211
28. Magazu S, Calabro E, Campo S (2010) FTIR spectroscopy studies on the bioprotective effectiveness of trehalose on human hemoglobin aqueous solutions under 50 Hz electromagnetic field exposure. J Phys Chem B 114:12144–12149
29. Shaffi SA (1978) Cadmium intoxication on tissue glycogen content in three freshwater teleost. Curr Sci 47:868–870
30. Cengiz EI, Bayar AS, Kizmaz V (2016) The protective effect of vitamin E against changes in fatty acid composition of phospholipid subclasses in gill tissue of *Oreochromis niloticus* exposed to deltamethrin. Chemosphere 147:138–143
31. Jeromea FC, Hassanb A, Omoniyi-Esanc GO, Odujokoc OO, Furlan PY, Scott SA, Peaslee MH (2007) FTIR STR study of pH effect on egg albumin secondary structure. Spectosc Lett 40:475–482
32. Tilak KS, Wilson Raju P, Butchiram MS (2009) Effects of alachlor on biochemical parameters of the freshwater fish, *Channa punctatus* (Bloch). J Environ Biol 30(3):421–426
33. Dezwaan A, Zandee DI (1973) Body distribution and seasonal changes in glycogen content of the commonsea mussel, *Mytilus edulis*. Comp Biochem Physiol 43:53–55
34. Muley DV, Karanjkar DM, Maske SV (2007) Impact of industrial effluents on the biochemical composition of fresh water fish *Labeo rohita*. J Environ Biol 28(2):245–249
35. Shobha Rani A, Sudharsan R, Reddy TN, Reddy PVM, Raju TN (2000) Effect of sodium arsenite on glucose and glycogen levels in freshwater teleost fish, *Tilapia mossambica*. Pollut Res 19(1):129–131
36. Umminger BL (1970) Physiological studies on supercooled kill fish *Fundulus heteroclitus*. III: carbohydrate metabolism and survival at sub zero temperature. J Exp Zool 173:159–174
37. Valko M, Morris H, Cronin M (2005) Metals, toxicity and oxidative stress. Curr Med Chem 12:1161–1208.29
38. Van der Putte I, Lubbers J, Kolar Z (1981) Effect of pH on uptake, tissue distribution and retention of hexavalent chromium in rainbow trout (*Salmo gairdneri*). Aquat Toxicol 1:3–18
39. Chen H, Mu L, Cao J, Mu J, Klerks PL, Luo Y, Guo Z, Xie, L (2016) Accumulation and effects of Cr (VI) in Japanese medaka (*Oryzias latipes*) during chronic dissolved and dietary exposures. Aquat Toxicol 176:208–216
40. Galassi VV, Salinas SR, Montich GG (2018) Conformational changes, from β strand to α helix, of the fatty acidbinding protein ReP1 NCXSQ in anionic lipid membranes: dependence with the vesicle curvature. Eur Biophys J 47(2):165–177
41. Thomas E (1984) Creighton, Pathways and mechanisms of protein folding. Adv Biophys 18(1–20):34
42. Palaniappan PLRM, Vijayasundaram V (2009) The effect of arsenic exposure and the efficacy of DMSA on the proteins and lipids of the gill tissues of *Labeo rohita*. Food Chem Toxicol 47(8):1752–1759
43. Maruthi YA, Subba Rao MV (2000) Effect of distillery effluent on biochemical parameters of fish *Channa punctatus* (Bloch). J Environ Pollut 7(2):111–113
44. Khan SA, Liu X, Li H, Li J, Zhou P, Rehman Z, Khan U (2017) Cd^{2+} and Pb^{2+} induced structural, functional and compositional changes in the liver and muscle tissue of crucian carp (*Carassiusauratusgibelio*): an FT-IR study. Turk J Fish Aquat Sci 17:135–143

Indian Journal of Biochemistry & Biophysics
Vol. 57, June 2020, pp. 277-282

Mineralization changes substituted type B carbonate of PO_4^{3-} ion in the bone minerals of an archaeological sample studied using fourier self deconvolution technique

G Velraj[1], S Karthikeyan[2]* & A Chitra[3]

[1]Department of Physics, Anna University, Chennai-600 025, Tamil Nadu, India

[2]Department of Physics, Dr. Ambedkar Government Arts College, Chennai-600 039, Tamil Nadu, India

[3]Department of Physics, S.I.V.E.T College, Chennai-600 073, Tamil Nadu, India

Received 26 January 2019; *revised 21 December 2019*

The aim of this study was to describe the compositional changes in the archaeological specimen using FTIR. Fourier deconvolution was applied in the carbonate (500-650 cm^{-1}), phosphate (900-1200 cm^{-1}), and in the amide region (1700-1600 cm^{-1}). The deconvolution of the spectra in the phosphate region 1200-900 cm^{-1} reveals six components 960 cm^{-1}, 1010 cm^{-1}, 1020 cm^{-1}, 1030 cm^{-1}, 1110 cm^{-1} and 1120 cm^{-1}. The bone mineral such as CO_3^{2-}, PO_4^{3-} particle, collagen, and organic materials were studied in detail from the infrared spectra. The computed parameters such as collagen development, mineralization index, C/P proportion, crystalline index, and maturing of bone help us in characterizing the bone samples. The Low estimation of C/P proportion resulted in changes in Type B carbonate (PO_4^{3-}) substitution. The absence of phosphate band ~1100 cm^{-1} and formation of β sheet structure were observed in the samples studied. Increased level of mineralization resulted in the increased in the crystalline nature of the bone samples. The study indicates the utilization of FTIR using self deconvolution technique which helps in understanding the compositional changes in the archaeological sample.

Keywords: Collagen matrix, FTIR, Bone, Mineralization index, β sheet structure

The characteristic bone tissues are calcium phosphates, water, and collagen alongside the other natural materials in small amounts. Collagen is the most abundant protein of the organic matrix in mineralizing tissues[1]. The bone crystals were found to contain significant and differing measures of carbonate and HPO_4^{2-} ions. The level of mineralization is steady with bone maturing/development and it is helpful for the portrayal of the archaeological specimens. The mineral part of the bone was poorly crystalline hydroxyapatite in which CO_3^{2-} particle can substitute for either the phosphate or the hydroxyl group prompting to nonstoichiometric apatite mineral[2]. This substitution creates vacancies and distortion that may influence the crystal lattice and influence the mechanical quality of the bone. This progression is studied by Fourier self deconvolution in the selected region of 500-650 cm^{-1}, 850-890 cm^{-1}, 900-1200 cm^{-1}. Delphine Farlay *et al*. showed that mineral maturity and crystallinity index are utilized to analyze the bone quality for a better understanding of the mechanism of bone fragility[3]. IR spectroscopy has wide application in biomedical fields and has been utilized to assess the mineral substance, mineral crystallinity, phosphate, carbonate, and collagen substance in bones[4-6]. Various techniques, such as X-ray diffraction, FTIR, NMR, ESR are utilized to study bone tissue and other biological material to decide mineral structures[7,8]. FTIR is a nondestructive tool and it gives the conformation regarding the changes in absorption frequency and intensity of the various functional groups in the specimen[9]. Hence it is appropriate to assess the variation in the chemical composition and mineralogy in the bone specimen. The most characteristic chemical groups such as PO_4^{3-}, CO_3^{2-}, HPO_4^{2} present in the bone specimen was studied using FTIR spectrum[9,10]. It gives an efficient way of checking various characteristic groups and vibrations. Further, it gives data about the location of peak, intensity, width, and wavenumber range. FTIR allows to describe the nature of both mineral and collagen in bone tissue.

The structure and the chemical composition of archaeological bone material may be modified by

*Correspondence:
Phone: +91 7395992195 (Mob)
E-mail: physicskarthik@gmail.com

interaction with the burial environment. Archaeological bone constitutes an important in the understanding of ancient societies as they can give evidence of human or faunal occupation. As biomaterials, they register for their chemical and isotopic composition information on climate and environmental conditions[11]. Hence, the study aims to assess the crystallinity of HA minerals, collagen, and the changes in phosphate and carbonate content based on the Fourier self deconvolution method. Deconvolution of FTIR spectra offers a detailed qualitative and quantitative analysis of carbonate and orthophosphates ($HPO_4^{2-}$and PO^{3-}). Keeping in view of the above discussion, the present study aims to look at the portrayal of the archaeological bone revealed from Kerala state of Kotapuram area, India utilizing Fourier transform infrared spectroscopy.

Site Details of Kottapuram Fort

Kottapuram Fort is an old stronghold territory close to Kodungalur Taluk, Thrissur area, Kerala state, India. Kottapuram is a piece of the Thrissur region and at the southernmost peripheral of the Kodungallur region. This region of Kerala is rich in the history and social convention of all the regulatory divisions of the state. Different sorts of ceramic, red ornamented pots, stoneware, globules, human and animal bones were found. This was exhumed by the archaeological study of India, Trivandrum, in the year April 2007. In 2007, the state branch of paleontology, Government of Kerala investigated this site deliberately and laid out a few trial trenches.

Materials and Methods

The two animal bones (Fig. 1A) KHB- Horse bone, KGB-Goat bone were gathered from the archaeological review in the location of Kotapuram region, Kerala, India. The bone specimen was cut with a microtome. A representative portion from the bone was ground into powder with steel mortar. For KBR pelleting sample 1-3 mg of ground, bone was blended with 100 mg of KBR using a hydraulic press tomake KBr pellets. FTIR spectra were acquired utilizing a Nicolet FTIR spectrometer controlled by OMNIC programming. The spectra were recorded in the region of 4000-400 cm^{-1} with a spectral resolution of 4 cm^{-1}. Each spectrum was the result of an average of 16 scans. The curve fitting calculation utilizes Gaussian bands to deliver the computed spectrum, which is compared with the experimental spectrum. The procedure is iterated until an acceptable fit is acquired by a least square regression analysis. Initial peak positions were acquired from the second derivative spectra of the raw data information. In every situation, the goodness of fit (GOF) parameters was resolved to locate the best fit from the different algorithm. The measured % area of the computed band was utilized for the quantitative change in the compositions of the sample studied[12].

Results and Discussion

Figure 1B demonstrates the normal FTIR spectra of the archaeological bone specimen collected at Kotapuram, Kerala state, India. Table 1 shows the tentative frequency assignment of the archaeological bone samples. A broad and weak band ~3444 cm^{-1} relates to the OH group. The Amide I band emerges because of C=O stretching from collagen. It relates to ~1633 cm^{-1} of the bone specimen. A strong band

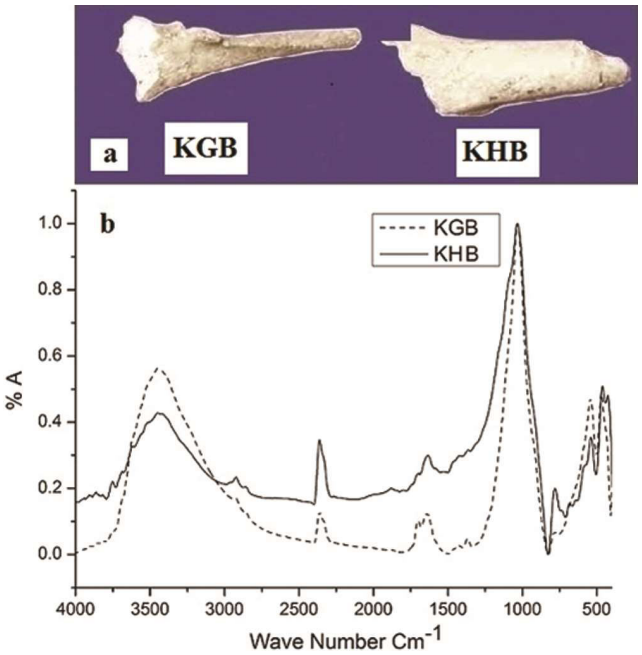

Fig. 1 — (A) A Photograph showing archaeological sample extracted from Kottapuram region, Kerala, India; and (B) Average FTIR spectra of bone sample

Table 1 — Tentative frequency assignment of the archaeological sample recently excavated from kottapuram place, India

KHB	KGB	Frequency Assignment
3435 (vw)	3444 (w)	OH group
1634 (w)	1634 (vw)	Amide I group
1030 (vs)	1029 (vs)	Phosphate group
542 (w)	544 (w)	PO_4^{3-}
476 (m)	479 (m)	

VS-Very Strong, m-Medium, W-Weak, VW-Very Weak

Table 2 — Computed values obtained from the FTIR spectra of the archaeological sample

Parameter	KHB	KGB
C/P	0.03	0.03
Collagen maturity	0.27	2.59
Crystalline Index	2.41	3.89
Degree of mineralization	18.61	23.28
Mineralization index	27.41	29.31

~1028 cm^{-1} associates to phosphate content. A weak band ~ 542 cm^{-1} and medium band ~ 476 cm^{-1} corresponds to the bending vibration of (PO_4^{3-}) phosphate anion. For a quantitative study the ratio of the band region 900-1200/1600-1700 results in the degree of mineralization or maturing of bone[13]. The observed values show KGB has higher maturity and KHB has a lower maturity of the sample studied (Table 2).

The ratio of C/P demonstrates the level of carbonate substitution of the collagen framework in the bone specimens. The least value was observed for both the sample studied. The measured value of the C/P ratio by Melainc *et al*. falls within our results and it was in good agreement with the present findings distinguishing prehistoric bone samples[14]. This change in C/P proportion is credited by the reduction in substitution of Type B carbonate (PO_4^{3-} substitutions) and increment to Type A carbonate (OH substitutions) as shown in (Fig. 2A& 2B). The phosphate band was obtained from the results of curve fitting in the region 1200-900 cm^{-1} (Fig. 2C). Consequently, phosphate substitution in mineral lattice demonstrates the increase in age of bone sample or development. The clearest change observed is an expansion in bone mineral crystallinity with maturing, demonstrating that mineral crystallinity increases with aging bones. This change is also correlated with an increase in the degree of mineralization of bone tissue.

It is observed in our case that the degree of mineralization increases in the KGB when compared to KHB. Crystallinity is contrarily identified with carbonate-to-phosphate proportion *i.e*., lower carbonate-to-phosphate proportion should be connected with large crystals[15]. Carbonate-to-phosphate proportion was additionally connected with delicacy crack[13]. In bone, carbonate ions can substitute for both phosphate and hydroxide ions when the hydroxyapatite crystal lattice is formed[16]. The collagen maturity of the sample was calculated using the band area ratio of 1660/1690 which was obtained as results of the curve fitting

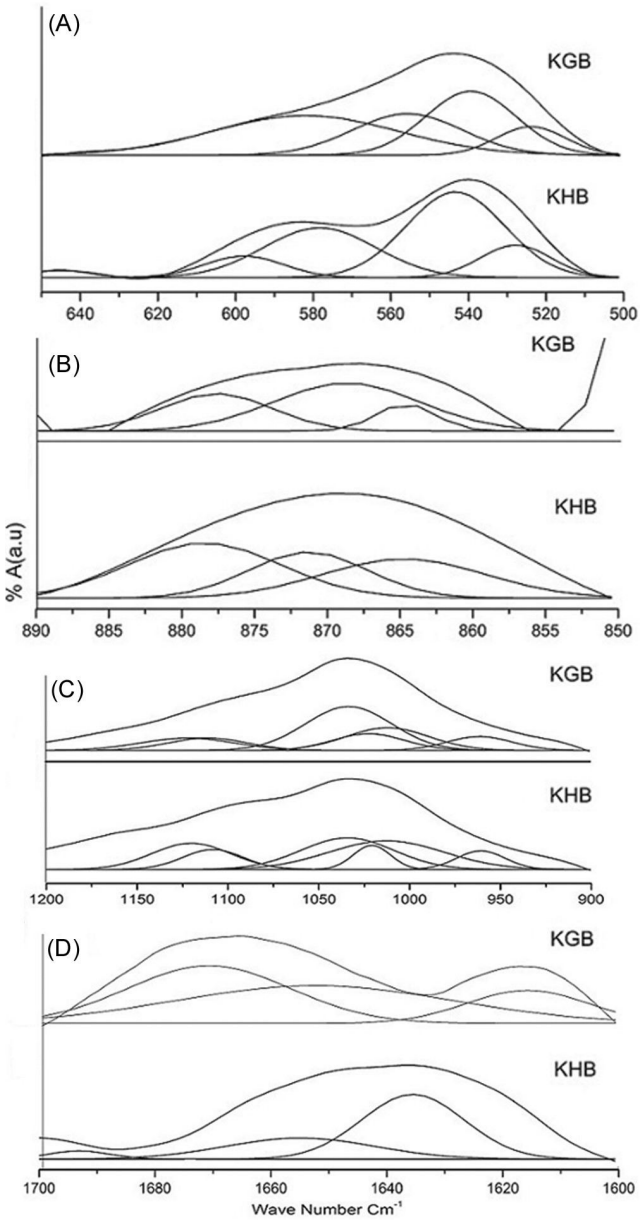

Fig. 2 — (A) Deduced curve fitting spectra of the bone sample in the region 640-500 cm^{-1} of HPO_4 band; (B) Deduced curve fitting spectra of the bone sample in the region 890-850 cm^{-1} of carbonate band; (C) Deduced curve fitting spectra of the bone sample in the region 1200-900 cm^{-1} of phosphate band; and (D) Deduced curve fitting spectra of the bone sample in the region 1700-1600 cm^{-1} Amide region

analysis[17]. These studies demonstrate that its value washigh for KGB when compared to KHB samples (Table 2). FTIR information reflects the persistence of both existing mineral and further collagen maturity. Failure of reabsorbs of the collagen matrix of the bone would bring about increased mineral content clarifying the distinction between the mineral of the

Table 3 — The results of curve fitting analysis of the archaeological sample in 500-650 cm^{-1} region

Sample Compositions	KHB	KGB	KHB	KGB
	Frequency (Cm^{-1})	% Area	Frequency (Cm^{-1})	% Area
Labile HPO4	530	12.53	524	10.02
Acid Phosphate	540	45.65	539	29.43
PO_4^{3-}	578	30.31	556	23.22
Labile PO_4^{3-}	597	9.21	582	37.33

bone specimen[18]. This increased collagen cross-link ratios (collagen maturity) could basically reflect the persistence of older bone.

Increasing mineralization density builds the quality of bone. Mineralization is a vital determinant of the micro hardness. Bone micro hardness is connected to Young's modulus of bone and is emphatically related to mineralization. The degree of mineralization of bone (DMB) not just impacts the mechanical resistance of bone additionally somewhat decides the bone mineral density. The crystallinity index was computed[19] using the ratio between the peak areas ~1030 to 1010 cm^{-1}. The high value of the C.I index was observed for the KGB when compared to the KHB bone sample. This band ~1110 cm^{-1} has great reproducibility in assessing the composition of the bone sample in an archaeological study[20]. The weakening of the crystallinity index (CI) may happen because the development of the β sheet arrangement as proved from curve fitting analysis which was discussed in the section Amide region.

Fourier self deconvoluted spectral analysis in the carbonate region

Figure 2A demonstrates the consequences of the curve fitting investigation performed in the region of 650-500cm^{-1}. It indicates wide band focused ~524 cm^{-1} and 540 cm^{-1} is assigned to acid phosphate contents whereas HPO_4^{2-} particle is promptly substituted *via* carbonate group. The decrease in the band area was seen at 530 cm^{-1} and 540 cm^{-1} for the KGB and when compared with the KHB sample (Table 3). Similar results were obtained from human and rabbit bone by Lisa *et al.* using infrared microspectroscopy[1]. As a result, in KHB sample the increase in HPO_4^{2-} ions creates an anionic vacancy which is compensated by the removal of Ca^{2+} from the lattice as it is proven from the C/P proportion. The principal PO_4^{3-} υ_4 mode shows up at 561 cm^{-1} comparing to the crystalline apatite environment[21] with the band of 580 cm^{-1}.

Table 4 — The results of curve fitting analysis of the archaeological sample in 850-890 cm^{-1} region

Sample Compositions	KHB		KGB	
	Frequency (Cm^{-1})	% Area	Frequency (Cm^{-1})	% Area
Liabile Co_3^{2-}	865	32.63	866	26.87
B Type Co_3^{2-}	872	42.12	873	57.09
A Type Co_3^{2-}	879	20.25	879	16.04

Utilizing curve fitting examination, we assessed the relative site of carbonate substitutions for the bone sample as shown in (Fig.2B). The three sub-bands of the CO_3^{2-} are 879, 872, and 865 cm^{-1} are known as Type A (OH substitution) Type B (PO_3^{4-}) and unstable CO_3^{2-} non- apatite carbonate band separately. The type B ~872 cm^{-1} is suitable for the quantitative calculation of carbonate in the bone minerals. These changes in the molecular structure are recognized by FTIR. It is because the different ionic radii of the substitutions cause changes in the environment of the molecular group, which results in alterations to the characteristic vibration modes that are reflected in their infrared absorption spectra[21]. It is seen from the (Table 4) the band area of 872 cm^{-1} in KGB has a higher concentration of carbonate and smallest value as observed for KHB. The (Fig.2B) demonstrates Type A carbonate reductions and portion of Type B carbonate increments in the KGB sample. This shows the development of bone towards by substitution of OH group by PO_3^{4-} a group of hydroxyapatite of bone specimen. Additionally a weak band ~865 cm^{-1} unstable CO_3^{2-} was observed in our study of the specimens.

Fourier self deconvoluted spectral analysis in the phosphate region

The deconvolution of the spectra in the region 1200-900 cm^{-1} reveals six components that were needed to get a satisfactory best fit for poorly crystalline apatite bone samples. (Fig. 2C). The position, intensity, and band area of each component were analysed. The results demonstrate critical distinction in the % area of the sub-bands of 960, 1010, 1020, 1030, 1110, and 1120 cm^{-1} (Table 5). The band ~960 cm^{-1} corresponds to a symmetric stretching mode of phosphate (PO_4^{3-}) consolidation. The intensive absorption band in the range of 1040-1090 cm^{-1} corresponds to the asymmetric stretching mode of PO_4^{3-}. The band ~1020 cm^{-1} is connected with non- stoichiometric apatite (containing HPO_4^{2-}/or CO_3^{2-}) and at ~1030 cm^{-1}

Table 5 — The results of curve fitting analysis of the archaeological sample in 900-1200 cm^{-1} region

Sample Compositions	KHB		KGB	
	Frequency (Cm^{-1})	% Area	Frequency (Cm^{-1})	% Area
PO_4^{3-} υ_1 symmetric stretch	961	8.02	961	9.13
PO_4^{3-} υ_3 asymmetric stretch	1013	29.09	1012	19.06
PO_4^{3-} υ_3 asymmetric stretch	1020	7.89	1022	12.11
PO_4^{3-} υ_3 asymmetric stretch	1034	26.00	1033	38.29
PO_4^{3-} $\upsilon_3$symmetric stretch	1108	10.73	1110	9.80
PO_4^{3-} $\upsilon_3$symmetric stretch	1120	18.27	1122	11.59

to stoichiometric apatite[22]. Additionally the band ~1030 cm^{-1} is connected with crystallinity.

The peak area ratio of 1030/1020 was measured to quantify the crystalline nature of the sample. The peak area ratio of 1030/1020 decreases with the KHB sample showing a decrease in crystalline nature. This information concurs with the finding in the KHB sample. Further the increase in the band area of the band ~1120 cm^{-1} of the KHB and KGB sample prompting to development of maturation of bone, which, is supported by the increase in the mineralization index as seen from (Table 2). The increase in the band area of ~ 1020 cm^{-1} emerges from HPO_4^{2-} substitute for the apatite lattice of a bone sample. This band decreases with KHB and increases in the KGB sample. As a result, the bone sample of KGB at higher age attains changes in mineral constitutions because of substitution of CO_3^{2-} by HPO_4^{2-} ions. This might be supported by an increment in Type B CO_3^{2-} in KGB when compared with KHB (Table 4).

Fourier self deconvoluted spectral analysis in the Amide region

The curve fitting was performed in the amide I band demonstrates the presence of a secondary structure of the collagen matrix. The adjustments in the collagen cross- linked peptides in the amide I region were resolved to examine the secondary structure of proteins. Amide I band (Peptide bond C=O extends ~ 1650 cm^{-1} is particularly sensitive to the secondary structure of proteins[23]. The (Fig. 2D) indicates FTIR spectra of the collagen framework of the archaeological specimen of the determined hidden groups in the amide I region as deduced from a curve fitting examination. The band centred ~ 1624 cm^{-1} allocates to β sheet, 1660 to α helix, and 1693 to β turns of the secondary structure of proteins. For lower mature bone (KHB) increase in β sheet and decrease in α helix and β turns was observed when compared with the KGB. For α helix structure, it increases as the bone matures. This is contradictory to our study that an increase in βsheet and α helical results from diminishing in collagen development which was observed for the KHB sample (Table 6). This confirms the collagen development is because of β sheet arrangement of the protein structure. This might be because of the impact of the burial environment of the bone sample where structural alteration happens and this procedure is called a digenesis[23]. Comparable results were gotten for an archaeological specimen of animal bone where a reduction in the band area of α helix and an expansion at random coils has been observed.

Table 6 — The results of curve fitting analysis of the archaeological sample in Amide I region

Sample Compositions	KHB		KGB	
	Frequency (Cm^{-1})	% Area	Frequency (Cm^{-1})	% Area
β sheet	1625	64.56	1624	39.32
α helices	1654	30.49	1656	43.84
β turns	1693	4.95	1695	16.84

Conclusion

The change in the various functional groups of an archaeological bone sample was studied from FTIR spectra utilizing the Fourier self deconvolution technique. The computed parameters like crystalline index, collagen maturity and maturing of bone were obtained from the spectra. They were high for the sample KGB and low for the KHB sample. The phosphate band 1022 cm^{-1} accounted for a high crystalline index of the samples studied. It was in good agreement with the results of the deconvolution technique applied in the region 900-1200 cm^{-1}. The curve fitting in the Amide I region demonstrates the β sheet development of the secondary structure of the protein. Investigation in the 850-890 cm^{-1} demonstrates the substitution of phosphate ions by Type B carbonate indicating maturation of bone in

the studied samples. This Type B carbonate observed at 872 cm^{-1} was suitable for the quantitative measurement in the bone minerals of the samples studied. It was clear from the IR spectra that both carbonate and phosphate ions have a significant impact on the pool of bone minerals. The results conclude that the various compositional changes in the archaeological bone studied might be altered by interaction with the burial environment. In this way, the utilization of FTIR spectra with self deconvolution strategies serves to describe the chemical compositions and in understanding the biochemical changes in the archaeological specimen.

Conflict of interest

All authors declare no conflict of interest.

Acknowledgment

The authors are grateful to the Archaeological Survey of India (ASI), Trivandrum, Kerala for providing the archaeological bone specimens. Similarly, the authors are grateful to the DST-FIST lab of the Department of Physics, Periyar University for taking the FTIR spectra.

References

1 Lisa M, Miller, Vidyasagar V, Mark R, Richard M, Eleftherios P, Paschalis, Foster B & Adele L, *In situ* analysis of mineral content and crystallinity in bone using infrared microspectroscopy of the υ4 PO_4^{3-} vibration Boskey. *Biochimica et Biophysica Acta*, 1527 (2001) 11.

2 Bonel G, Cotribution a l'etude de la carbonation des apatites. PartI. *Ann Chim*, 7 (1972a) 127.

3 Farlay D, Panczer G, Rey C, Delmas P & Boivin G, Mineral maturity and crystallinity index are distinct characteristics of bone mineral. *J Bone Miner Metab*, 28 (2010) 433.

4 Yamamoto T, Uchida K, Naruse K, Suto M, Urabe K, Uchiyama K, Suto K, Moriya M, Itoman M & Takaso M, Quality assessment for processed and serialized bone using raman spectroscopy. *Cell Tissue Bank*, 13 (2012) 409.

5 Salesse K, Dufour E, Lebon M, Wurster C, Castex D, Bruzek J & Zazzo A, Variablity of bone preservation in a confined environment: the case of the catacomb of Sts peter and Marcellinus (Rome, Italy). *Palaeogeogr Palaeoclimatol Palaeoecol*, 416 (2014) 43.

6 Vincke D, Miller R, Stassart E, Otte M, Dardenne P, Collins M, Wilkinson K, Stewart J, Baeten V & Fernandez Pierna JA, Analysis of collagen preservation in bones recovered in archaeological contexts using NIR hyper spectral imaging. *Talanta*, 125 (2014)181.

7 Boseky AL, Pleshko N, Doty SB & Mendelsohn R, Applications of Fourier Transform Infrared (FT-IR) Microscopy to the Study of Mineralization in Bone and Cartilage.*Cells Mater*, 2 (1992) 209.

8 Fernandes MC & Sellappan K, Elemental compositions and X ray diffraction studies of *Strobilanthes* species, *Indian J Biochem Biophys*, 56 (2019) 144.

9 Subashini S & Kumar KS, Physicochemical characteristics of calcium oxalate crystals in *Spinacia oleracea* L. *Indian J Biochem Biophys*, 54 (2017) 156.

10 Rai DV, Darbari R& Aggarwal LM, Age related changes in the elemental constituents and molecular behaviour of bone. *Indian J Biochem Biophys*, 42 (2005) 127.

11 Basu A, Sarkar A, Maulik U & Basak P,Three dimensional structure prediction and ligand-protein interaction study of expansion proteinATEXPA23 from *Arabidopsis thaliana* L. *Indian J Biochem Biophys*, 56 (2019) 20.

12 Karthikeyan S & Easwaran R, Analysis of a curve fitting model in the amide region applied to the muscle tissues of an edible fish: *Labeo rohita* fingerlings. *J Biol Phys Chem*, 13 (2013) 125.

13 Chadefaux C, Ho ASL, Gurlet LB & Reiche I, Cure fitting micro ATR FTIR studies of the amide I and amide II bands of Tyoe U collagen in archaeological bone materials. *e Pres Sci*, 6 (2009) 129.

14 Beasley MM, Bartelink EJ, Taylor L, Miller RM, Comparison of transmission FTIR, ATR and DRIFT spectra: implications for assessment of bone bio apatite diagnosis. *J Archaeol Sci*, 46 (2014) 16.

15 Soejoko DS, Sari YW, Dewi SU, Nurizati, Dahlan K & Atmadja DS, Composition of human bone mineral by FTIR and its relationship to the age. *J Med Phys Biophys*, 1 (2014) 1.

16 Gourion-Arsiquaud S, Lukashova L, Power J, Loveridge N, Reeve J & Boskey AL, Fourier transform infrared imaging of femoral neck bone: reduced heterogeneity of mineral-to-matrix and carbonate to phosphate and more variable crystallinity in treatment-naive fracture cases compared with fracture- free controls. *J Bone Miner Res*, 28 (2013) 150.

17 Fleet ME, The carbonate ion in hydroxyapatite: recent X-ray and infrared results. *Front Biosci (Elite Ed)*, 5 (2013) 643.

18 Paschalis EP, Verdelis K, Doty SB, Boskey AL, Mendelsohn R & Yamauchi M, Spectroscopic characterization of collagen cross links in bone. *J Bone Miner Res*, 16 (2001) 893.

19 Enzo S, Bazzoni M, Mazzarello V, Piga G, Bandieray P & Melis P, A study by thermal treatment and X-ray powder diffraction on burnt fragmented bones from tombs II, IV and IX belonging to the hypogeic necropolis of Sa Figu near lttiri, Sassari (Sardinia, Italy). *J Archaeol Sci*, 34 (2007) 1731.

20 Legros R, Balmain N & Bonel G, Age related changes in mineral of rat and bovine Cortical bone. *Calcif Tissue Int*, 41 (1987)137.

21 Rey CM, Shimuzu B, Collins B & Glimcher MJ, Resolution enhanced Fourier transform infrared spectroscopy study of the environment of phosphate ions in the early deposits of a solid phase of calcium phosphate in bone and enamel and their evolution with age I. Investigation in the υ3 PO4 domain. *Calcif Tissue Int*, 46 (1990) 384.

22 Rey C, Shimuzu M, Collins B & Glimcher MJ, Resolution enhanced fourier transform infrared spectroscopy study of the environment of phosphate ion in the early deposits of a solid phase of calcium phosphate in bone and enamel and their evolution with age: 2. Investigations in the υ3 PO4 domain.*Calcif Tissue Int*, 49 (1991) 383.

23 Legeros RZ, Apatites in biological systems. *Prog Cryst Growth Charact*, 4 (1981) 1.

Food Research International 138 (2020) 109783

Contents lists available at ScienceDirect

Food Research International

journal homepage: www.elsevier.com/locate/foodres

Effects of drying techniques on the physicochemical, functional, thermal, structural and rheological properties of mung bean (*Vigna radiata*) protein isolate powder

Fatema Hossain Brishti [a], Shyan Yea Chay [a], Kharidah Muhammad [a], Mohammad Rashedi Ismail-Fitry [b], Mohammad Zarei [c], Sivakumaran Karthikeyan [d], Nazamid Saari [a,*]

[a] Department of Food Science, Faculty of Food Science and Technology, Universiti Putra Malaysia, 43400 UPM Serdang, Selangor, Malaysia
[b] Department of Food Technology, Faculty of Food Science and Technology, Universiti Putra Malaysia, 43400 UPM Serdang, Selangor, Malaysia
[c] Department of Food Science and Technology, School of Industrial Technology, Faculty of Applied Sciences, Universiti Teknologi MARA, 40450 Shah Alam, Selangor, Malaysia
[d] Department of Physics, Dr. Ambedkar Government Arts College, Chennai, Tamil Nadu 600 039, India

ARTICLE INFO

Keywords:
Functional properties
Mung bean
Pilot scale extraction
Protein characterization
Sustainable food

ABSTRACT

Mung bean is an inexpensive yet sustainable protein source. Current work compared the effects of freeze (FD), spray (SD) and oven drying (OD), on mung bean protein isolate (MBPI) produced on pilot scale. All samples showed no dissociation of protein subunits and were thermally stable (T_d = 157.90–158.07 °C). According to morphological studies, FD formed a porous protein while SD and OD formed wrinkled and compact crystals, respectively. FD and SD formed elastic gels with better gelling capacity than OD (aggregated gel). FD showed exceptional protein solubility, water and oil absorption capacity (4.23 g/g and 8.38 g/g, respectively). SD demonstrated the smallest particle size, excellent emulsion activity index (29.21 m^2/g) and stability (351.90 min) and the highest β-sheet amount (37.61%). FTIR spectra for all samples showed characteristic peaks which corresponded well to the secondary structure of legume proteins. Rheological analysis revealed that gelation temperature for all MBPI lied around 90 °C. Current work described the different final properties achieved for MBPI produced under different drying techniques that allowed tailoring for different food systems, whereby FD is ideal for meat extender, SD is suitable for meat emulsion while OD is suitable in general protein-based application.

1. Introduction

Mung bean (*Vigna radiate* L.), a leguminous crop which is predominantly grown in Asia and other parts of the world, demonstrates high potential as a sustainable protein source due to their lower carbon footprint compared to other protein sources such as cattle and poultry. In South Asia, the demand for mung bean reached 5.4 million tons between year 2015–2016 (Schreinemachers et al., 2019). Its popularity is credited to high protein (25–28%) and low fat content (1–2%) (Khaket, Dhanda, & Jodha, 2015). Additionally, mung bean protein contains a high amount of essential amino acids to meet the human body requirement (Du et al., 2018). Mung bean extracts have been reported to possess various biological activities such as ACE inhibitory, anti-diabetic, anti-tumor, and antioxidant activities (Xie et al., 2019). Above all, low-cost and easy digestibility makes mung bean an invaluable source for those who could not afford animal proteins (Hou et al., 2019). Hence, it is gaining recognition as a significant source of sustainable dietary protein in recent years.

Proteins from different plant sources display variations in functional properties including solubility, gelation, water/oil absorption capacity, emulsion and foam stability, due to their heterogeneous structure and composition. Successful utilization of plant protein in food processing largely depends on their functional properties, which is then highly dependent on the protein extraction process and drying techniques. For a protein obtained from the same source, different extraction and drying procedures would yield proteins with different functional properties.

* Corresponding author.
E-mail address: nazamid@upm.edu.my (N. Saari).

https://doi.org/10.1016/j.foodres.2020.109783
Received 5 June 2020; Received in revised form 30 September 2020; Accepted 4 October 2020
Available online 15 October 2020

Drying technique is crucial in the preparation of protein isolate powders. While drying could improve storage stability, it causes protein to form irreversible, insoluble aggregates due to partial protein denaturation, shifting its functional properties (Vojdani, 2006). The commonly used protein drying techniques are freeze, spray, and oven drying. Freeze drying is commonly used to characterize protein functionality while spray drying is used for commercial large scale protein production. Oven drying is comparatively less expensive and drying temperature could be set below protein denaturation temperature (Feyzi et al., 2017) but the residence time is much longer.

Previously, it has been reported that drying has a noticeable effect on the structural and functional properties of chia, fenugreek, soybean and rice dreg protein powders (Timilsena et al., 2016; Feyzi et al., 2017; Rasli & Sarbon, 2015; Zhao et al., 2013). However, no comparative study is made on the properties of mung bean protein isolates (MBPI) as affected by different drying techniques. Current work compares, for the first time, the effects of three drying techniques (freeze, spray and oven drying) on the physicochemical, functional, structural and rheological properties of MBPI, a plant-based protein source that is highly potential in the production of sustainable food.

2. Materials and methodology

2.1. Raw material and chemicals

Mung bean flour was purchased from Spicon products Sdn Bhd (Melaka, Malaysia). Hydrochloric acid, sodium hydroxide, sulfuric acid (97%), α-amino butyric acid (AABA) and amino acid standards AAS18 were purchased from Sigma- Aldrich (St. Louis, USA). Phenyl-isothiocyanate (PITC), Triethylamine (TEA) and methanol were purchased from Merck (Darmstadt, Germany).

2.2. Preparation of protein isolate

The protein isolate was prepared by following the method of Thompson (1977) with slight modification. Briefly, 10 kg of mung bean flour was dispersed in 100 L of distilled water. The dispersion was adjusted to pH 9.0 with 3 N NaOH, stirred at 2000 rpm in a stirred tank bioreactor equipped with six-bladed Rushton turbine (B. Braun Biotech International GmbH, Melsungen, Germany) for 1 h at 30 °C and then centrifuged at 8586*g* using a continuous centrifuge machine (Model AS16VBNF, Alfa Laval, Lund, Sweden). The supernatant was adjusted to pH 4.5 with 3 N HCl to precipitate the protein. The protein curd was then recovered via centrifugation at 8586*g* and subjected to three different drying techniques.

2.3. Drying of protein isolate

For freeze-drying, the protein curd was first frozen at −18 °C for 48 h. The frozen sample was then freeze-dried using freeze dryer (VirTis Benchmark Freeze Dryer, SP Scientific, Pennsylvania, USA) at temperature −30 °C, pressure 120 Pa for 48 h. To produce spray-dried powder, the protein curd was diluted with distilled water at a ratio of 1: 4 (w/v), mixed thoroughly and spray-dried on a pilot scale spray dryer (Model Niro 2000 type A; GEA Niro A/S, Soeborg, Denmark) at 185 °C inlet, 90 °C outlet temperatures and 6 ml/min flow rate on a rotary atomizer. To produce oven-dried powder, the protein curd was dried at 50 °C for 24 h in a convective oven (Memmert GmbH + Co. KG, Schwabach, Germany). The resulting mung bean protein isolate (MBPI) powders were grounded using an electric grinder and stored at −20 °C for further analysis.

2.4. Proximate analysis

Proximate analysis of MBPI powder was carried out according to the AOAC (2005) official methods and carbohydrate was calculated by difference (Vogelsang-O'Dwyer et al., 2020). Specifically, protein content was analysed following Kjeldahl's method (AOAC, 2005).

2.5. Physical properties

2.5.1. Color parameters and browning index

In order to measure the colour parameters, a digital colorimeter (Model CR-410, Konica Minolta, Tokyo, Japan) was used. The instrument calibration was performed using a white standard with L* = 88.05, a* = 1.44, b* = −4.27 prior to color determination.

The browning index was calculated using Eq. (1) from Gonzales, Burin, and del Pilar Buera, (1999) and Ding and Ling (2014):

$$\text{Browning index} = \frac{x - 0.31}{0.172} \times 100 \quad (1)$$

where x = (a* + 1.75L*)/(5.645L* + a* − 0.3012b*)

2.5.2. Particle size analysis

The particle size distribution of MBPI was evaluated using a laser diffraction particle size analyzer (Model Mastersizer 2000, Malvern Instruments Ltd., Worcestershire, UK). The dispersant (water) and particle refractive index were 1.33 and 1.44, respectively. Four size distribution features were determined at D_{10}, D_{50}, D_{90} and $D_{[4,3]}$.

2.6. Morphological analysis

Scanning electron microscope (Model JSM-5200, JEOL Ltd., Tokyo, Japan), at an accelerating voltage of 15 kV, was used to view the surface feature of the MBPI powder. Sample was directly deposited on aluminum stubs using double-sided adhesive carbon conductive tapes and coated with gold layer using a gold sputter prior to viewing. Micrographs were taken at 500x and 1.00kx magnification.

2.7. SDS-PAGe

SDS-PAGE was performed following the method of Laemmli (1970). A 50 g/l stacking gel and 125 g/l separating gel were used in current work. Protein solution (10 g/l) was prepared by dispersing MBPI into phosphate buffer (10 mM, pH 7.0). The content was stirred for 12 h to be homogenized and then, 20 μL of the protein solution was mixed with 20 μL of sample buffer [0.125 M Tris-HCl buffer, pH 8.0 containing 10 g/l SDS, 0.5 g/l bromophenol blue, 30% glycerol (v/v)]. The mixture was then heated for 5 min at 90 °C and centrifuged at 8000*g* for 10 min. An aliquot of 10 μL supernatant was loaded into the gel well and electrophoresis was performed at 100 V for first 10 min and then 140 V for the next 30 min until the tracking dye reached the bottom of the gel. Finally, the gel was stained with Coomassie Blue R250 and destained with ethanol and acetic acid.

2.8. Amino acid profile

The amino acid profile of MBPI was determined using Pico-tag method with slight modification (Shang-gui et al., 2004). First, 50 mg of sample was treated with 6 N HCl for 24 h at 110 °C to achieve complete hydrolysis. To perform profiling, HPLC equipped with C18 reversed phase column (Hypersil GOLD, Thermo Scientific, 250 mm × 4.6 mm ID, 5 μm particle size) was used. The mobile phases consisted of buffer A (0.1 M ammonium acetate, pH 6.5) and buffer B (0.1 M ammonium acetate + acetonitrile + methanol, 44:46:10 v/v/v, pH = 6.5). The sample was injected into HPLC system and eluted using a gradient of buffer A (100–0%) and buffer B (0–100%) at a flow rate of 1 ml/min for a total run time of 50 min. Absorbance was recorded at 254 nm. Quantification of amino acid was performed by comparing the peak area of individual amino acid in sample to the peak area of individual amino acid in standard using Eq. (2). Results were reported as mg amino

acid/g sample.

$$\text{Amino acid content (mg/g)} = \left[\frac{\text{RRF} \times \text{Peak area of individual amino acid in sample} \times \text{concentration of individual amino acid in the standard}}{\text{Peak area of AABA in sample} \times \text{weight of sample}}\right] \times \text{molecular weight of individual amino acid} \quad (2)$$

where RRF (Relative Response Factor) = $\frac{\text{Peak area of internal standard (AABA)}}{\text{Peak area of individual amino acid in standard}}$

2.9. Functional properties

2.9.1. Protein solubility

Protein solubility was determined at different pHs of 2–12. Briefly, 0.5 g of MBPI powder was dispersed into 50 ml distilled water. The dispersion was maintained at constant pH by adding 1 N NaOH or HCl. The protein slurry was centrifuged at 5000*g* for 15 min, filtered through Whatman No. 1 filter paper and analyzed for soluble protein content via Lowry's method (Lowry et al., 1951) using bovine serum albumin as standard.

2.9.2. Water and oil absorption capacity

Water absorption capacity was determined by the method of Bencini (1986) with slight modification. Three grams of MBPI powder were dispersed in 50 ml distilled water. The dispersion was thoroughly stirred for 1 h and then centrifuged at 5000*g* for 30 min in pre-weighed centrifuge tubes. After centrifugation, the supernatant was discarded and the centrifuge tubes containing the protein isolate were re-weighed. The oil absorption capacity was determined by the method of Beuchat (1977) with slight modification. One gram of sample was mixed with 10 ml of corn oil. The content was stirred for 1 h and then centrifuged at 5000*g* for 15 min in pre-weighed centrifuge tubes. The supernatant was drained by inverting the tubes for 25 min. The tubes were then re-weighed. The water and oil absorption capacities were calculated using Eq. (3) and expressed as gram of water/oil bound per gram of protein isolate.

$$\text{Water/Oil absorption capacity (g/g)} = \frac{W_2 - W_1}{W_0} \times 100 \quad (3)$$

where W_2 = Weight of tube plus the sediment (g), W_1 = Weight of tube plus dry sample (g), and W_0 = Weight of the dry sample (g)

2.9.3. Emulsion activity index (EAI) and emulsion stability index (ESI)

The EAI and ESI were determined by the method of Pearce and Kinsella (1978) with slight modification. Emulsion was prepared by homogenizing 50 ml of 10 g/l protein solution with 2 ml of corn oil (water/oil ratio = 25:1) using a homogenizer (Model ULTRA-TURRAX® T25, IKA-Werke GmbH & Co.KG, Staufen, Germany) at 20,000 rpm for 1 min. Then, 50 μL of emulsion sample was immediately taken from the bottom of the tube and diluted in 50 ml of 1 g/l sodium dodecyl sulfate solution at 0 min and then again at 15 min. The absorbance of diluted emulsions was measured at 500 nm using a UV–visible spectrophotometer (Model GENESYS™ 10S, Thermo Scientific, Massachusetts, USA).

EAI and ESI were calculated according to Eqs. (4) and (5):

$$\text{EAI} = (4.606 \times A_0 \times N)/(\Phi \times C \times 10000) \quad (4)$$

$$\text{ESI} = [A_0/(A_0 - A_{15})] \times t \quad (5)$$

where A_0 is the absorbance of the diluted emulsion at 0 min, N is the dilution factor (×1000), C is the weight of protein per volume of aqueous phase (g/ml), Φ is the oil fraction of the emulsion, (A_0-A_{15}) is the change in absorbance between 0 and 15 min and t is the time interval, 15 min.

2.9.4. Least gelation capacity (LGC)

Protein isolates at different concentrations of 8, 10, 12, 14, 16, 18 and 20%, (w/v) were heated at 100 °C for 1 h. The samples were immediately cooled under running tap water and kept at 4 °C for another 2 h. The strength of the coagulum formed was measured by turning the tube upside down. The lowest concentration of protein, which formed a stable gel, was considered as LGC (Sathe et al., 1981).

2.10. Thermal properties

A differential scanning calorimetry (Model DSC-823E, Mettler-Toledo International Inc., Ohio, USA) was used to determine the thermal properties of MBPI. Samples (8–10 mg) were weighted in aluminium pans (for thermal analysis) and sealed hermetically. The pans were heated from 25 to 300 °C at a heating rate of 10 °C/min. The calibration was performed with indium. The denaturation peak temperature (T_d), onset temperature (T_o), endset temperature (T_e) and enthalpy (ΔH) was calculated using Mettler-Toledo STARe software system, version 9.x (Mettler-Toledo International Inc., Ohio, USA).

2.11. Structural properties

2.11.1. Surface hydrophobicity (H_0)

H_0 was determined according to the method of Nakai (2003) using a fluorescent probe, ANS (8-anilinonaphthalene-1-sulfonic acid). MBPI samples were suspended in phosphate buffer (10 mM, pH 7.0) to prepare protein solutions at 0.035, 0.075, 0.15, 0.3 and 0.6 g/l. Four milliliter of each of these solutions were mixed with 20 ml of freshly prepared ANS solution (8 mM ANS in 10 mM phosphate buffer, pH 7.0), shaken vigorously and kept in the dark for 10 min. The relative fluorescent intensity (RFI) was measured using a microplate spectrofluorophotometer (Model SpectraMax Gemini XPS, Molecular Devices LLC., California, USA) at $\lambda_{excitation}$ = 390 nm and $\lambda_{emission}$ = 470 nm. H_0 was calculated from the slope by plotting RFIs versus protein concentrations (%) as linear regression.

2.11.2. Sulfhydryl groups (SH) and disulfide bonds (SS)

The sulfhydryl groups and disulfide bonds were estimated according to the method of Shimada and Cheftel (1988) with slight modification. In brief, 30 mg of MBPI powder was dispersed in 10 ml of Tris-Glycine buffer (0.086 M Tris, 0.09 M Glycine and 0.04 M EDTA, pH 8.0) containing 8 M urea (total SH) or without 8 M urea (free SH). An aliquot of 4 ml was mixed with 0.1 ml Ellman's reagent [5,5′-dithiobis-(2-nitrobenzoic acid) in Tris-Glycine buffer, 4 mg/ml, pH 8.0]. The mixture was incubated in dark at room temperature for 1 h, followed by centrifugation at 5000*g* for 10 min. The supernatant was collected and the absorbance was measured at 412 nm against a reagent blank. Same procedure was followed for determination of free SH content. Free SH and total SH contents were calculated according to Eq. (6):

$$\mu\text{mol SH/g} = \frac{73.53 \times A412 \times D}{C} \quad (6)$$

where A_{412} = absorbance at 412 nm; C = concentration of sample (mg/ml), D = dilution factor (1.01)

To determine SS content, 1 ml of protein dispersion was added to 0.05 ml of β-mercaptoethanol and 4 ml of Tris-Glycine buffer. The content was incubated for 1 h at room temperature. Then, 10 ml of trichloroacetic acid (12%) was added and the mixture was centrifuged at 5000*g* for 10 min. The precipitate was resuspended in 10 ml of Tris-Glycine buffer and then 0.04 ml of Ellman's reagent was added. The mixture was incubated in dark at room temperature for 30 min, followed by centrifugation at 5000*g* for 10 min. The absorbance of the supernatant was measured at 412 nm against a reagent blank. SS bond was calculated according to Eq. (7):

$$\mu\text{mol SS/g} == \left(\frac{73.53 \times A412 \times D}{C} - \text{SHfree}\right) \Big/ 2 \quad (7)$$

where A_{412} = absorbance at 412 nm; C = concentration of sample (mg/ml), D = dilution factor (6.08)

2.11.3. Secondary structure characterization

The secondary structures of MBPI powder samples were characterized using FTIR spectrometer (Model Spectrum-100, PerkinElmer, Inc., Connecticut, USA). The spectra were recorded in the region of 4000–400 cm^{-1} with a spectral resolution of 10 cm^{-1} and 32 scans. The FTIR spectra were analyzed using OriginLab software (OriginLab Corporation, Massachusetts, USA). Fourier self-deconvolution was conducted on the second derivative function of amide I region (1600–1700 cm^{-1}) by Gaussian curve-fitting to get detailed information on the secondary structures.

2.12. Dynamic rheological properties (Temperature sweep study)

The rheological evaluation was carried out using a controlled stress rheometer (Model Rheostress RS600, Thermo Scientific, Massachusetts, USA) with a 35 mm diameter parallel plate geometry (Joshi et al., 2011). MBPI was dispersed in phosphate buffer (10 mM, pH 7.0) to form a protein dispersion of 250 g/l. Then 1 ml of the dispersion was loaded onto the lower plate of rheometer, set at 25 °C, and the upper plate was lowered to get contact with the sample. The gap between the two plates was maintained at 1 mm. A thin layer of silicon oil was used to minimize evaporation. Temperature sweep was conducted by heating from 25 to 90 °C with a heating rate of 2 °C/min. The samples were held for 10 min at 90 °C then cooled from 90 to 25 °C at a cooling rate of 0.8 °C to form gel strips. The cooled gels were held for 30 min at 25 °C. Storage modulus (G′), loss modulus (G″) and loss tangent (δ) were determined at a constant frequency of 1 Hz and shear stress of 1 Pa as a function of temperature. These constants were obtained from the linear viscoelastic range during a preliminary work involving stress sweep study.

2.13. Statistical analysis

All results were analyzed using one-way ANOVA followed by independent *t*-test using SPSS software (version 17, SPSS Inc., Illinois, USA). The data was expressed as means ± standard deviations from triplicate readings. The sample means were significantly different at $p \leq 0.05$.

3. Results and discussion

3.1. Physicochemical properties

3.1.1. Proximate composition

The proximate composition of mung bean protein isolate (MBPI) prepared by freeze, spray and oven drying are presented in Table 1. The protein contents of all MBPI were comparable to other legume protein isolates which ranged above 70% (Kudre, Benjakul & Kishimura, 2013). Freeze dried MBPI (FD) showed the highest protein content of 86.15%, compared to spray dried MBPI (SD) and oven dried MBPI (OD) of 75.85% and 77.27%, respectively. The difference in protein contents among FD, SD and OD was mainly due to different drying methods, of which FD was not exposed to heat treatment but SD and OD did. When protein curd received heat under moist condition in SD and OD, thermal denaturation was facilitated, as water molecules caused protein to swell, increasing the dynamic flexibility (Damodaran, 2008) and eventually forming complexes that no longer resembled nitrogen-based compounds for detection in Kjeldahl analysis. Agoreyo et al. (2011) reported that heating would cause Maillard reaction which resulted in complex changes due to the reaction between carbohydrate and amino acids, thus reducing the protein content. Heating could also result in the formation of tannin-protein complex which consequently reduced the protein content (Akpan & Umoh, 2004). These observations explained the lowered protein content in SD and OD as compared to FD. In terms of fat and ash content, OD recorded values lower than FD and SD, owing to the different drying techniques using different temperatures and drying duration. (Bawa, Songsermpong, Kaewtapee, & Chanput, 2020).

Table 1
Proximate composition, color parameters, particle size distribution, functional, and thermal properties of FD, SD and OD mung bean protein isolates.

Properties	FD	SD	OD
Proximate analysis (%)			
Protein	86.15 ± 0.74^{a}	75.85 ± 0.19^{b}	77.27 ± 2.22^{b}
Fat	1.11 ± 0.06^{a}	1.23 ± 0.07^{a}	0.67 ± 0.08^{b}
Moisture	4.49 ± 0.08^{a}	3.59 ± 0.45^{ab}	4.77 ± 0.18^{a}
Fiber	0.55 ± 0.07^{a}	0.17 ± 0.04^{ab}	0.25 ± 0.14^{a}
Ash	0.49 ± 0.00^{a}	0.48 ± 0.00^{a}	0.06 ± 0.03^{b}
Carbohydrate	7.21 ± 0.43^{b}	18.68 ± 0.50^{a}	16.98 ± 1.31^{a}
Color parameters			
L*	56.70 ± 0.80^{b}	63.22 ± 1.23^{a}	52.26 ± 1.02^{c}
a*	9.24 ± 0.03^{a}	5.74 ± 0.16^{c}	8.8 ± 0.17^{b}
b*	24.42 ± 0.38^{a}	17.75 ± 0.87^{b}	18.94 ± 0.63^{b}
Browning index	15.73 ± 0.00^{a}	9.25 ± 0.19^{b}	15.84 ± 0.09^{a}
Particle size distributions (μm)			
D_{10}	78.72 ± 1.44^{a}	6.75 ± 0.18^{c}	48.92 ± 0.69^{b}
D_{50}	251.71 ± 9.13^{a}	14.87 ± 0.04^{c}	233.17 ± 1.22^{b}
D_{90}	559.89 ± 10.93^{a}	31.28 ± 1.15^{c}	532.88 ± 3.10^{b}
$D_{[4,3]}$	287.01 ± 4.62^{a}	17.77 ± 0.09^{c}	268.62 ± 1.24^{b}
Functional properties			
Water absorption capacity (g/g)	4.23 ± 0.49^{a}	3.03 ± 0.11^{b}	4.78 ± 0.15^{a}
Oil absorption capacity (g/g)	8.38 ± 0.22^{a}	4.00 ± 0.86^{c}	5.58 ± 0.57^{b}
Emulsion activity index (m^2/g)	23.56 ± 0.47^{b}	29.21 ± 0.06^{a}	21.88 ± 0.20^{c}
Emulsion stability (min)	72.61 ± 0.45^{b}	351.90 ± 21.24^{a}	64.74 ± 6.54^{b}
Least gelation concentration (%w/v)	12%	12%	18%
Thermal properties			
T_d (°C)	158.00 ± 0.33^{a}	158.07 ± 0.25^{a}	157.90 ± 0.10^{a}
T_o (°C)	155.50 ± 0.29^{a}	155.59 ± 0.26^{a}	155.48 ± 0.06^{a}
T_e (°C)	158.49 ± 0.31^{a}	158.59 ± 0.28^{a}	158.32 ± 0.13^{a}
ΔH(J g^{-1})	19.90 ± 2.11^{b}	24.38 ± 4.30^{a}	17.23 ± 3.55^{b}

FD = Freeze dried; SD = Spray dried; OD = Oven dried; Mean ± s.d. in a row followed by different letters are significantly ($p \leq 0.05$) different; n = 3.

Likewise, Ghribi et al. (2015) found that conventional drying at 40 °C (60 h) and 50 °C (48 h) reduced fat and ash content of chickpea protein concentrate compared to freeze drying most likely due to the long drying duration.

3.1.2. Color and particle size distribution

Table 1 shows the color parameters for MBPI samples. All samples demonstrated little red/green hue but are richer in yellow/blue hue, as indicated by small a* and large b*values. SD showed the highest L* value but lowest a* and b* values compared to FD and OD, indicating its higher degree of lightness, as seen from its creamy white appearance. This finding is in line with the lower browning index in SD compared to FD and OD (Table 1), as well as that reported by Joshi et al. (2011) who observed the highest L* but lowest a* and b* values for spray dried lentil protein isolate. On the other hand, OD recorded the lowest L* value (52.26), indicating that OD is the darkest product. This could be attributed to the formation of brown pigments, such as melanoidins, by Maillard reaction under heated condition during oven drying. This finding is in accordance with the lowest amount of lysine content in OD (Table 2), as lysine takes part actively in Maillard reaction and lower lysine content confirms the occurrence of Maillard reaction (Feyzi et al., 2017). The intense Maillard reaction in OD is further supported by its high browning index (Table 1).

Table 1 shows the particle size distributions for MBPI samples. In brief, FD had the highest D_{10}, D_{50}, D_{10} and $D_{[4,3]}$ followed by OD then SD. It has been reported that the formation of ice crystal during freeze drying could cause the particles to aggregate and recombine into larger particles (Yao et al., 2016), thus FD exhibited the highest particle size among three samples. In contrast, SD had the smallest particle size and this is in line with its highest L* value. Small particle size allows larger surface area to reflect more light compared to FD and OD. Similar findings were reported by Ghribi et al. (2015) for freeze and convective dried chickpea protein concentrates, as well as Hu et al. (2010) for freeze, spray and vacuum dried soy protein isolates.

Table 2
Amino acid profile of FD, SD and OD mung bean protein isolates.

Amino acid (mg/g of sample)	FD	SD	OD
Aspartic acid	249.99 ± 4.12^{a}	258.85 ± 0.32^{b}	251.89 ± 1.40^{ab}
Glutamic Acid	379.68 ± 2.72^{a}	392.27 ± 0.38^{b}	380.85 ± 2.40^{a}
Serine	118.70 ± 6.40^{a}	118.41 ± 6.40^{a}	114.95 ± 0.19^{a}
Glycine	72.19 ± 6.60^{a}	70.52 ± 0.86^{a}	67.48 ± 0.04^{a}
Histidine	54.50 ± 1.09^{a}	56.36 ± 2.08^{a}	54.30 ± 4.74^{a}
Arginine	153.52 ± 2.80^{a}	159.84 ± 0.09^{a}	155.28 ± 2.10^{a}
Threonine	131.36 ± 7.94^{a}	145.59 ± 6.08^{a}	136.13 ± 1.33^{a}
Alanine	79.23 ± 13.71^{a}	74.14 ± 0.169^{a}	70.94 ± 7.25^{a}
Proline	168.86 ± 0.37^{a}	165.14 ± 0.14^{b}	143.81 ± 0.20^{c}
Tyrosine	141.84 ± 1.41^{b}	151.96 ± 0.98^{a}	149.19 ± 2.28^{a}
Valine	76.45 ± 0.93^{a}	78.04 ± 0.43^{a}	77.31 ± 2.96^{a}
Methionine	206.18 ± 8.29^{a}	208.24 ± 0.15^{a}	208.77 ± 5.99^{a}
Cystine	290.80 ± 0.00^{b}	366.93 ± 0.00^{a}	161.03 ± 0.00^{c}
Isoleucine	114.10 ± 1.49^{b}	121.17 ± 1.91^{a}	110.94 ± 0.34^{b}
Leucine	139.59 ± 14.79^{b}	178.14 ± 1.23^{a}	144.61 ± 0.00^{b}
Phenylalanine	547.77 ± 31.35^{a}	524.65 ± 0.00^{a}	162.93 ± 0.00^{b}
Lysine	48.63 ± 8.54^{b}	81.60 ± 0.00^{a}	33.21 ± 7.77^{b}
Acidic	629.66 ± 6.85^{b}	651.12 ± 0.70^{a}	212.79 ± 0.93^{c}
Basic	256.65 ± 12.44^{b}	297.79 ± 1.97^{a}	242.79 ± 0.93^{a}
Polar-without-charge	391.90 ± 0.06^{a}	414.46 ± 8.98^{a}	400.26 ± 3.73^{a}
Hydrophilic	1278.21 ± 5.64^{b}	1363.38 ± 7.70^{a}	1275.79 ± 0.99^{b}
Hydrophobic	1723.44 ± 43.45^{a}	1751.71 ± 0.08^{a}	1278.64 ± 13.46^{b}

FD = Freeze dried; SD = Spray dried; OD = Oven dried; Mean ± s.d. in a row followed by different letters are significantly ($p \leq 0.05$) different; n = 2.

3.1.3. Morphological characteristics

Fig. 1 shows SEM micrographs of FD, SD and OD. All samples revealed distinct surface structures whereby FD showed non-collapsed, porous structure, SD exhibited wrinkled surface while OD showed compact crystalline structure. The porous structure of FD is due to the formation of ice crystal during freezing step which sublimes during freeze-drying (Zhao et al., 2013). For SD, the collapsed and wrinkled structure could be due to uneven shrinkage of particles containing protein and water (Gong et al., 2015). Additionally, in a spray drying environment, there is a complex interchange in the moisture diffusivity of protein and a high concentration gradient between the droplet-particle and drying media. The protein-water droplets would try to minimize water vapour diffusion path in order to expedite a higher moisture evaporation flux, resulting in wrinkled surface. On the other hand, the crystalline structure in OD could be due to long hour of drying at heated temperature (24 h, 50 °C), causing water molecules to transfer from the inside of the sample and evaporate from the surface rapidly (Rudra et al., 2016).

3.1.4. Protein profiling

SDS-PAGE was performed to evaluate the changes in the protein composition of MBPI. The protein molecular weight distribution profiles of FD, SD and OD are presented in Fig. 2. Despite different drying techniques, all MBPI depicted identical band pattern, indicating that drying processes do not cause dissociation of mung bean protein subunits at the quaternary structural level. This is in agreement with Zhao et al. (2013) who reported that spray and freeze-drying had no effect on the subunit constituents of rice protein isolate. In all three samples, five major bands were observed at 15, 25, 26, 50 and 65 kDa, of which 15 kDa represents 7S globulin subunit; 25 kDa represents 11S globulin while 26, 50 and 65 kDa correspond to 8S globulin subunit. This finding is very much comparable to the work from Mendoza, Adachi, Bernardo and Utsumi (2001) whereby 7S globulin is comprised of 16 kDa and 28 kDa; 11S is comprised of 24 kDa and 40 kDa while 8S is comprised of 26, 32, 48 and 60 kDa, as detected for mung bean protein.

3.2. Amino acid composition

Amino acid composition (hydrophobic, acidic, basic and charged residues) of a protein sample governs its functionality to a great extent. For instance, the relative ratio of acidic and basic amino acids helps to determine the net surface charge of a protein molecule. In this study, FD and SD demonstrated significantly higher content of acidic amino acid than OD (FD = 629.66 mg/g and SD = 651.12 mg/g *vs.* OD = 212.79 mg/g) (Table 2). The vast reduction in OD could be due to the slightly-heated temperature and prolonged oven drying (50 °C, 24 h) compared with FD (-30 °C, 48 h) and SD (185 °C inlet and 90 °C outlet temperature, drying residence time 30 s, total drying time 5 h). Similar result has been reported by Feyzi et al. (2017). It has been reported earlier that heating duration has a strong effect on the percentage of amino acid content and longer heating duration causes depletion of amino acid content (Taira et al., 1965). The hydrophobic amino acids are highly important for protein conformation stability whereby protein with higher amount of hydrophobic amino acids is more thermostable. In present study, irrespective of drying techniques, all MBPI show the highest amount of hydrophobic, followed by hydrophilic residues compared to acidic,

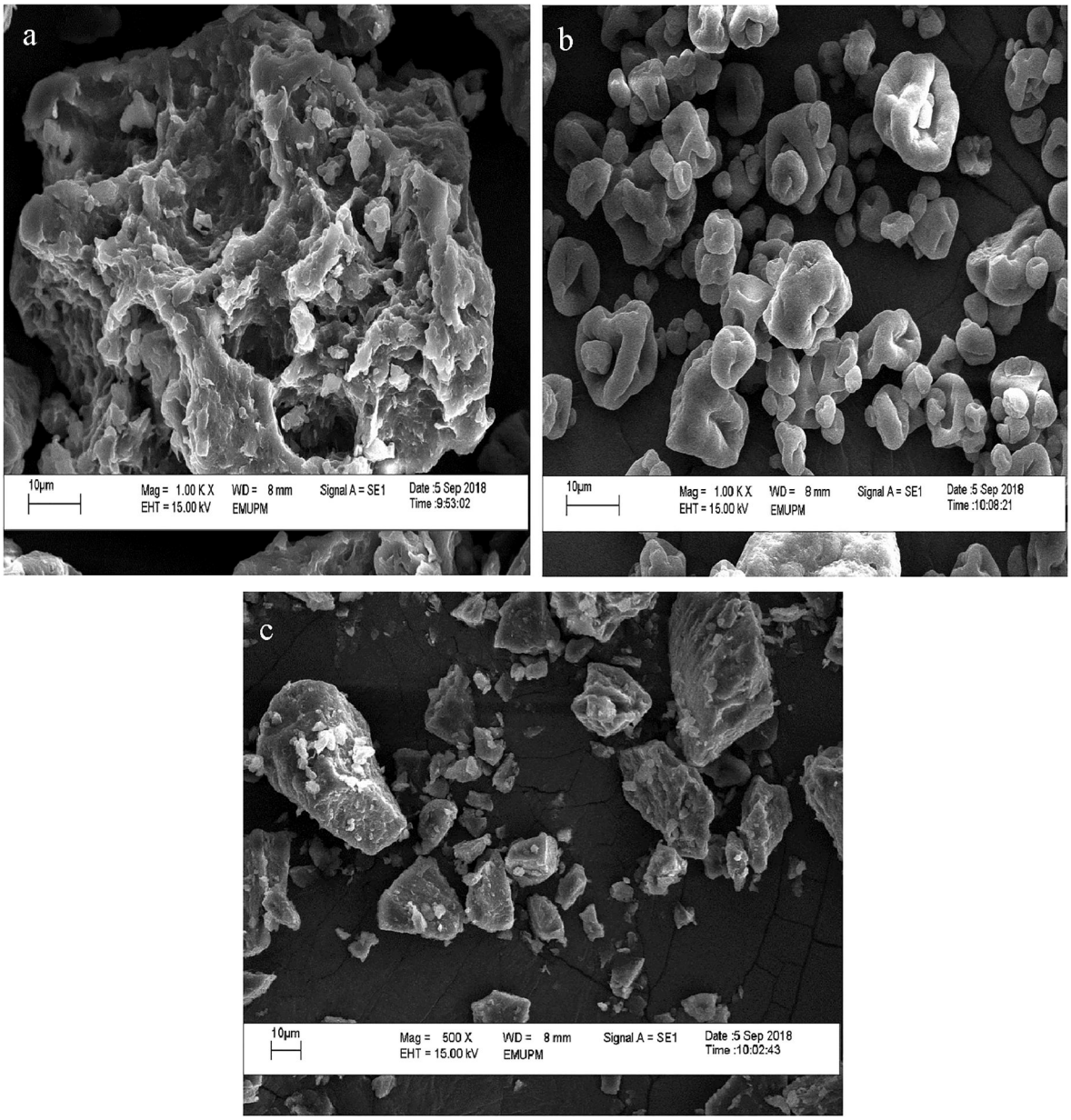

Fig. 1. Scanning electron micrographs of (a) freeze dried, (b) spray dried and (c) oven dried mung bean protein isolate.

basic and polar-without-charge residues, which explain the thermostability of MBPI, as detailed in Section 3.4.

Aspartic and glutamic acid are dominant in plant-based protein. All FD, SD and OD samples showed a high amount of aspartic and glutamic acid content. Similar result was found by Feyzi et al. (2017) who produced fenugreek protein isolates by freeze, spray and vacuum drying. Among all the amino acids, lysine is most heat sensitive and all the drying techniques significantly affect its content. OD revealed the lowest lysine content (33.21 mg/g protein) and this loss is due to Maillard reaction which is facilitated by heated temperature during oven drying (Bhandari, Bansal, Zhang, & Schuck, 2013). Furthermore, the lowest L* value justifies the formation of Maillard product in OD (Table 1). To conclude, the amino acid compositions are comparable between FD, SD and OD, except for lysine. The higher amount of acidic amino acid makes MBPI negatively charged and hydrophilic in nature.

3.3. Functional properties

3.3.1. Protein solubility

Protein solubility is a good indicator for the performance of protein isolates in new food product development. Fig. 3 shows the protein solubility of FD, SD and OD at pH 2–12. All samples demonstrated similar U-shaped curves. The highest solubility was observed in extreme acidic (pH 2) and alkaline (pH 12) media while the minimum solubility was found in pH 4.5 as the isoelectric point of MBPI lies in pH 4.5 region. The solubility of FD was comparatively higher than SD and OD in extreme acidic (pH 2) and alkaline (pH 8–12) media. This result is in line with the SEM result (Fig. 1) which shows that FD powder has porous particle morphology while SD and OD are compact. The porous structure in FD could facilitate protein solubility by easing protein hydration (Lili et al., 2015). At pH 8–12, the high protein solubility of FD could be due to the presence of water-soluble aggregates (Hu et al., 2010; Wagner, Sorgentini, & Añón, 2000) while the low protein solubility of SD and OD could be due to the formation of moisture resistant film during drying. The film is formed due to the unfolding of proteins at the particle-air

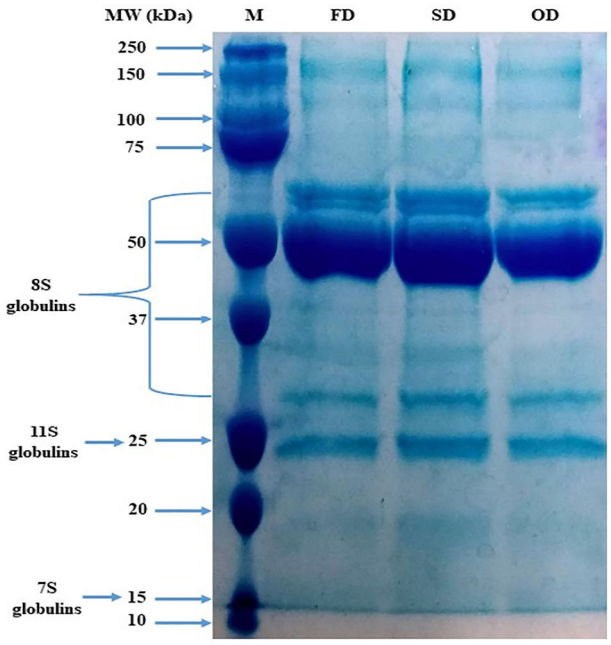

Fig. 2. SDS-PAGE protein bands of freeze, spray and oven dried MBPI. Lane 1: Marker (M); Lane 2: Freeze dried (FD); Lane 3: Spray dried (SD) and Lane 4: Oven dried (OD).

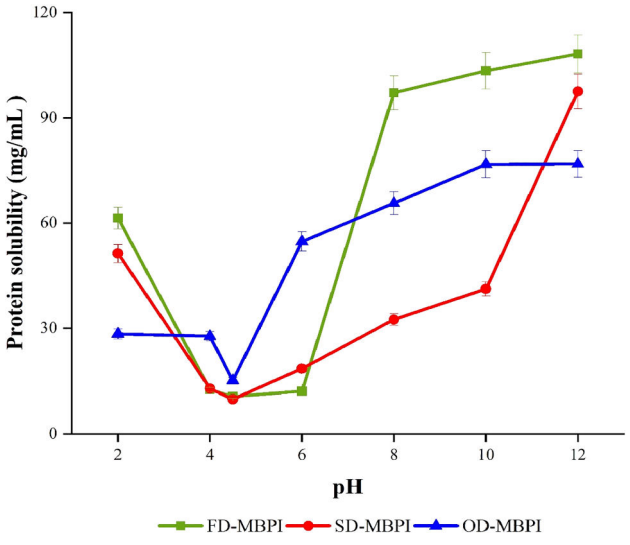

Fig. 3. Protein solubility profile of freeze (FD), spray (SD) and oven-dried (OD) MBPI at pH 2–12.

interface (Ghribi et al., 2015). Adhikari et al. (2007) confirmed the formation of smooth, thin and high-moisture resistant film during spray drying of whey protein isolate. A similar result was found by Joshi et al. (2011) reported that spray drying reduced the lentil protein isolate solubility due to the formation of moisture resistant film.

3.3.2. Water and oil absorption capacity

The water absorption capacity (WAC) of a protein is one of the most significant parameters to measure its techno-functionality. Generally, the sum of bound water, hydrodynamic water, and physically entrapped water contribute to the WAC of a protein. As shown in Table 1, the WAC of SD was significantly lower (3.03 g/g) than FD and OD. This lowered WAC could be attributed to the presence of moisture-resistant film that is formed during spray-drying. Ghribi et al. (2015) reported similar values for freeze and convective dried chickpea protein concentrates. In contrast, Du et al. (2018) reported the WAC for mung bean protein isolate to be 2.62 g/ml, which is significantly lower than the present findings. This difference could be attributed to different protein structures and changes in protein conformation as a result of different drying methods (Mune Mune, Sogi, & Minka, 2017). The findings of the current study imply that FD and OD could be added to food product formulation that requires high water entrapment.

Oil absorption capacity (OAC) measures the ability of protein molecules to bind with fat and enhance flavor retention in a food product. It is influenced by protein source, size and concentration, number of non-polar amino acids, processing method, and protein-lipid interactions. According to Table 1, the OAC of FD was significantly higher (8.38 g/g) than that of SD (4.00 g/g) and OD (5.58 g/g). This higher OAC could be attributed to the increased amount of protein-fat interaction and superior-fat binding ability of non-polar amino acid side chains. This finding is in line with the SEM results (Fig. 1) which shows that FD is light and porous to facilitate fat absorption while SD is sticky and OD is dense, which consequently hinder fat entrapment into protein matrix. Different studies reported different OAC for mung bean protein, ranging between 9.5 and 10.5 g/g (Du et al., 2018) and 3.07 ml/g (Liu et al., 2015). Current findings fall within this range. The exceptional fat-binding ability of FD makes it a useful meat substitute or extender to enhance flavour retention and improve mouthfeel in meat analogues.

3.3.3. Emulsion activity index (EAI) and emulsion stability index (ESI)

Protein act as emulsifiers by adsorbing at the oil-water interface and forming densely packed layers. The emulsifying property is determined by the emulsion activity index (EAI) and emulsion stability (ESI). EAI determines the amount of oil that can be emulsified per unit of protein and ESI determines the resistance of the emulsion over a prescribed period of time. EAI and ESI are substantially influenced by the distribution of hydrophobic and hydrophilic residues on the protein surface, conformational stability, and ease of folding-unfolding of the protein molecule at the oil-water interface (Damodaran, 2008). As demonstrated in Table 1, EAI for FD (23.56 m^2/g) and OD (21.88 m^2/g) were significantly lower than that for SD (29.21 m^2/g). On the other hand, ESI values for FD and OD were 72.61 min and 64.74 min, respectively, and again were significantly lower than that for SD (351.90 min). This higher EAI and ESI values of SD could be due to heating during spray drying (outlet temperature 90 °C) which causes the globular proteins to partially unfold, leading to the exposure of hydrophobic amino acid residues towards external environment which increases the adsorption at the oil-water interface. Similar results were reported by Feyzi et al. (2017) who found that EAI and ESI values for spray dried fenugreek protein isolate were higher than freeze and oven dried samples. High EAI and ESI values of SD makes it an ideal ingredient for the production of food involving meat emulsion system, such as meat loaf, bologna and sausages.

3.3.4. Gelation

Gelation capacity guides food manufacturers to achieve the right texture and elasticity in final products, particularly puddings and meat products. Gelling ability is typically measured as least gelation concentration (LGC). The LGC for FD and SD was 12% while OD required 18% protein to form a gel (Table 1). This result infers the superior gelling capacity of FD and SD compared to OD. Moreover, this finding is consistent with the protein solubility profile, as FD has the highest solubility hence requires a lower concentration of protein to form gel. This finding is in accordance with Joshi et al. (2011) who reported that freeze and spray dried lentil protein isolate required lower LGC (11%) than vacuum dried sample (14%). Different legume protein isolates showed a different range of LGC from 8% to 16% (Boye et al., 2010). The LGCs of FD, SD and OD in current study fall within this range.

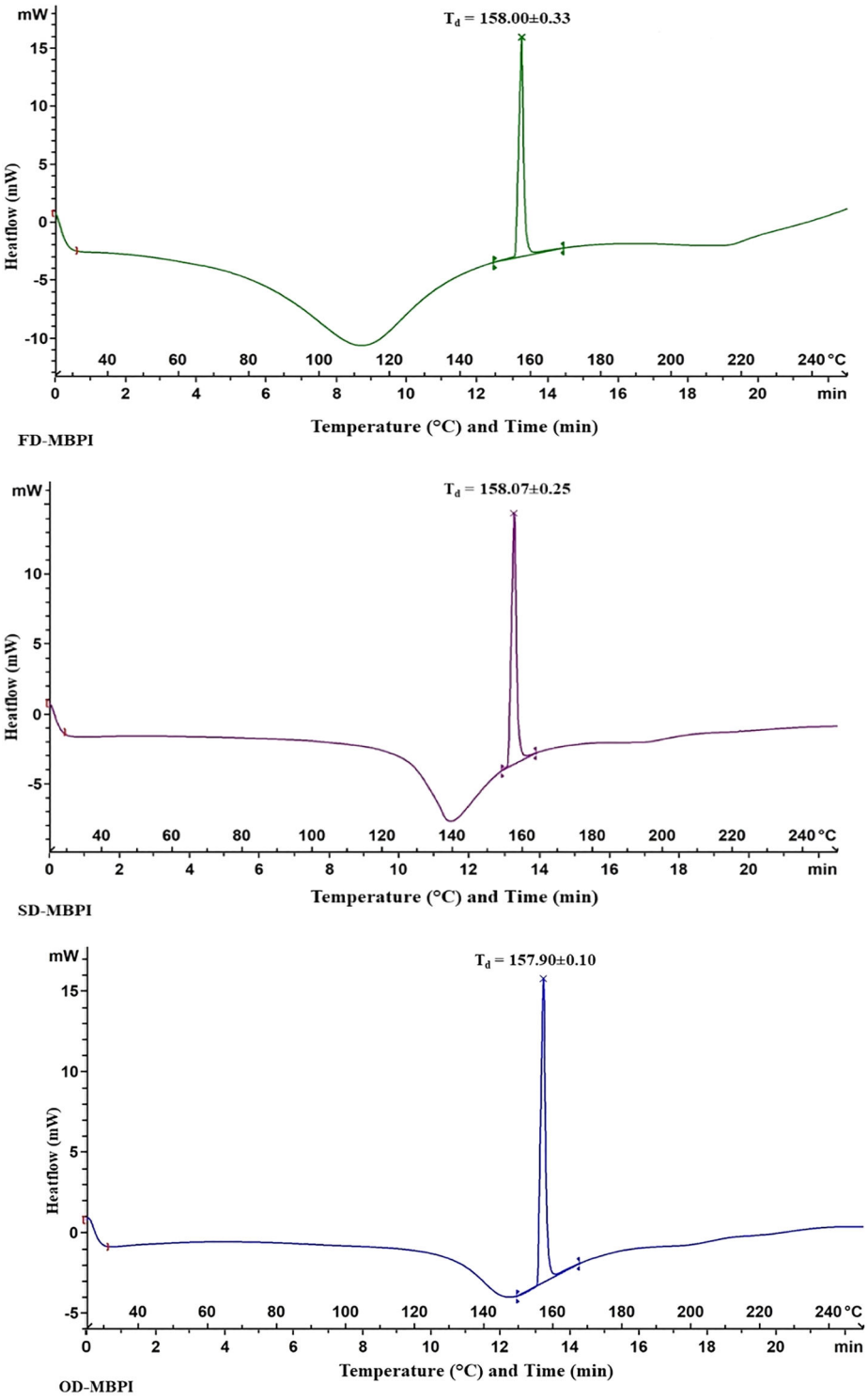

Fig. 4. DSC heating curves of freeze (FD), spray (SD) and oven-dried (OD) mung bean protein isolate.

3.4. Thermal properties

Differential Scanning Calorimetry (DSC) is frequently used to determine the degree of denaturation, structural and conformational changes in protein molecules. Denaturation temperature (T_d) indicates protein thermal stability, of which higher T_d reveals higher stability. ΔH indicates the amount of energy needed to denature the protein, which is the net energy value required to break hydrogen bonds (endothermic) and hydrophobic interactions (exothermic) (Ma & Harwalkar, 1991). Fig. 4 shows the DSC heating curves and Table 2 presents the denaturation peak temperature (T_d), onset temperature (T_o), endset temperature (T_e) and enthalpy (ΔH). From Table 1, all samples showed high T_d (157.90–158.07 °C), indicating good thermal stability of MBPI samples, making it a potential ingredient for food products where high processing temperature is required. Tang and Ma (2009) reported T_d for thermally treated kidney bean protein (treated at 95 °C for 30 min) to be 97.6 °C. In another study conducted by Kudre et al. (2013), the T_d were 86.23 °C, 82.13 °C and 79.56 °C for mung bean, black bean and bambara

groundnut protein isolate, respectively. The variations in T_d values between current and previous studies could be due to the application of different protein extraction methods and heating rates during DSC analysis (Feyzi et al., 2017). Another noteworthy observation was made on the gelling ability of MBPI at 100 °C, a temperature much lower than the denaturation temperature (T_d = 157.90–158.07 °C), despite the fact that both processes require denaturation of protein molecules. This is because MBPI exists in dried powder form that is thermally stable due to static structure (i.e. the polypeptide segments have restricted mobility). When protein is heated at 100 °C with water, gel formation becomes feasible because water molecule greatly reduces the T_d by increasing protein chain mobility and flexibility, whereby protein acquires a dynamic molten structure which allows easy denaturation upon heating to promote gel formation (Damodaran, 2008).

For ΔH, SD was significantly higher than FD and OD, indicating a lower degree of protein denaturation in SD compared to FD and OD. This is because spray drying is a fast process and the drying residence time of MBPI inside the drying chamber is short (30 s), leading to less protein denaturation. On the other hand, prolonged oven drying (24 h, 50 °C) denatures protein molecules to a greater extend, thus lower ΔH was observed. For FD, protein denaturation may be caused by intermolecular reactions through S-S bonds as a result of concentration by freezing (Sanfelice & Temussi, 2016).

3.5. Structural properties

3.5.1. Surface hydrophobicity

Surface hydrophobicity (H_0) identifies the changes in hydrophobic groups located on the surface of protein molecules, which occur as a result of molecular alteration during denaturation (Wang et al., 2014). Denaturation could lead to an increase in hydrophobicity by unfolding the proteins' secondary and tertiary structures to expose respective hydrophobic sites. H_0 significantly reduces ($p \leq 0.05$) in the order: FD > OD > SD (Table 3). SD depicted the lowest H_0 as a result of protein aggregation induced by heating during spray drying, causing a reduction in exposed hydrophobic sites which subsequently decreases its overall surface hydrophobicity (Hu et al., 2010). This finding is in accordance with that reported by Timilsena et al. (2016) who observed spray dried chia protein isolate possessed lower H_0 than freeze and vacuum dried samples.

To further support the lowest H_0 observed in SD, the thermal properties are referred. Hu et al. (2010) reported that protein unfoldment and denaturation are accompanied by enthalpy changes, and denatured proteins have lower enthalpies (ΔH) than native proteins. From Table 1, the enthalpy for SD was the highest (ΔH = 24.38 g^{-1}), indicative of the lowest degree of denaturation and thus lowest H_0. On the other hand, FD and OD showed higher surface hydrophobicity than SD, and this is in line with the higher oil absorption capacity of these two samples, as protein with high surface hydrophobicity can readily align and bind its hydrophobic residues towards the oil phase.

3.5.2. Sulfhydryl groups (SH) and disulfide bonds (SS)

SH and SS are functional groups which impose significant effects on the protein conformation and functional properties. SH and SS contents of FD, SD and OD are presented in Table 3. The total SH groups were significantly different ($p \leq 0.05$) among all MBPIs. OD and SD revealed higher total SH (19.06 μmol/g and 18.07 μmol/g, respectively) than FD (15.56 μmol/g). This could be due to the occurrence of higher protein denaturation which leads to the unfolding of protein structure and revealing more SH groups under heated environment in OD and SD. For exposed SH content, FD and OD recorded values that were slightly higher than SD. This infers that freeze, spray and oven drying expose half of the SH group from total SH. An increase number of exposed SH groups is important in heat-induced gel formation to strengthen the intermolecular network. It has been reported that gel strength increased with increasing number of exposed SH groups (Zayas, 2012).

There is no significant difference ($p > 0.05$) in the SS content for all samples. However, an interesting observation was made whereby the SS content was much higher than the SH content in all samples. Disulfide bonds (SS) in proteins are formed between the thiol groups by the process of oxidative folding. Since mung bean is rich in polyphenols, the sulfhydryl groups could readily oxidize with polyphenols (Tajoddin et al., 2014). Furthermore, heating during spray and oven drying could also initiate oxidation of SH groups into SS bonds. During freeze drying, the freezing and drying stress causes protein to denature to an extent that unfold protein structures and expose free sulfhydryl groups, which are further oxidized to SS bonds (Hu et al., 2010).

3.5.3. FTIR spectra analysis

Fig. 5a shows the FTIR spectra of FD, SD and OD in the range of 400–4000 cm^{-1} region while Fig. 5b depicts the curve-fitting spectra of FD, SD and OD specifically in 1600–1700 cm^{-1} region. From Fig. 5a, the wide bands observed at 3273 cm^{-1} (FD), 3276 cm^{-1} (SD) and 3272 cm^{-1} (OD) correspond to O—H stretching vibrations arising mainly from water or protein while the shoulder bands at 3069 cm^{-1} (FD), 3070 cm^{-1} (SD) and 3070 cm^{-1} (OD) are assigned to N—H stretching (amide B). In all three samples, the spectra demonstrated characteristic peaks in 1510–1580 cm^{-1} (amide II, N—H bending and C═N stretching) and 1600–1700 cm^{-1} (amide I, C═O stretching), which corresponded to main peaks for protein (Withana-Gamage et al., 2011). Amide I portrays the strongest vibration mode and is important to reveal and analyze protein secondary structure.

The main secondary structural components of legume and pulse protein isolates are α-helix (1650–1659 cm^{-1}), β-sheet (1615–1640 cm^{-1}), random coils (1641–1649 cm^{-1}) and β-turn (1660–1688 cm^{-1}) (Withana-Gamage et al., 2011; Du et al., 2018). The secondary structures for MBPI reported in current study fit well with the literature, whereby MBPI composes mainly of α-helix, β-sheet and random coil that absorb at maximum wavelength of 1655–1656 cm^{-1}, 1625–1638 cm^{-1} and 1641–1643 cm^{-1}, respectively (Fig. 5b and Table 3). The composition of secondary structures showed significant difference ($p \leq 0.05$)

Table 3
Structural properties and secondary structure composition of FD, SD and OD mung bean protein isolates.

Structural properties	FD		SD		OD	
Surface hydrophobicity	4691.65 ± 2.33^a		2154.65 ± 55.21^c		3466.85 ± 19.30^b	
Sulfhydryl groups and disulfide bonds						
Total SH groups (μmol/g)	15.56 ± 0.67^b		18.07 ± 0.16^a		19.06 ± 0.17^a	
Exposed SH groups (μmol/g)	9.61 ± 0.45^a		8.69 ± 0.07^b		9.20 ± 0.03^a	
S-S bonds (μmol/g)	54.66 ± 0.59^a		55.25 ± 0.13^a		54.25 ± 0.49^a	
Secondary structure composition	Peak (cm^{-1})	Area (%)	Peak (cm^{-1})	Area (%)	Peak (cm^{-1})	Area (%)
β-sheet	1627	4.27 ± 0.35^c	1625	21.65 ± 0.97^a	1626	6.41 ± 0.09^b
β-sheet	1638	19.82 ± 0.91^a	1638	15.96 ± 0.64^c	1638	18.72 ± 0.39^b
Random coil	1643	44.01 ± 1.2^a	1641	22.23 ± 0.29^c	1643	31.47 ± 0.24^b
α-helix	1656	27.54 ± 0.02^b	1655	36.41 ± 0.27^a	1656	36.47 ± 0.64^a
β-turn	1684	4.36 ± 0.02^b	1684	3.74 ± 0.23^c	1684	6.93 ± 0.29^a

FD = Freeze dried; SD = Spray dried; OD = Oven dried; Mean ± s.d. in a row followed by different letters are significantly ($p \leq 0.05$) different; n = 3.

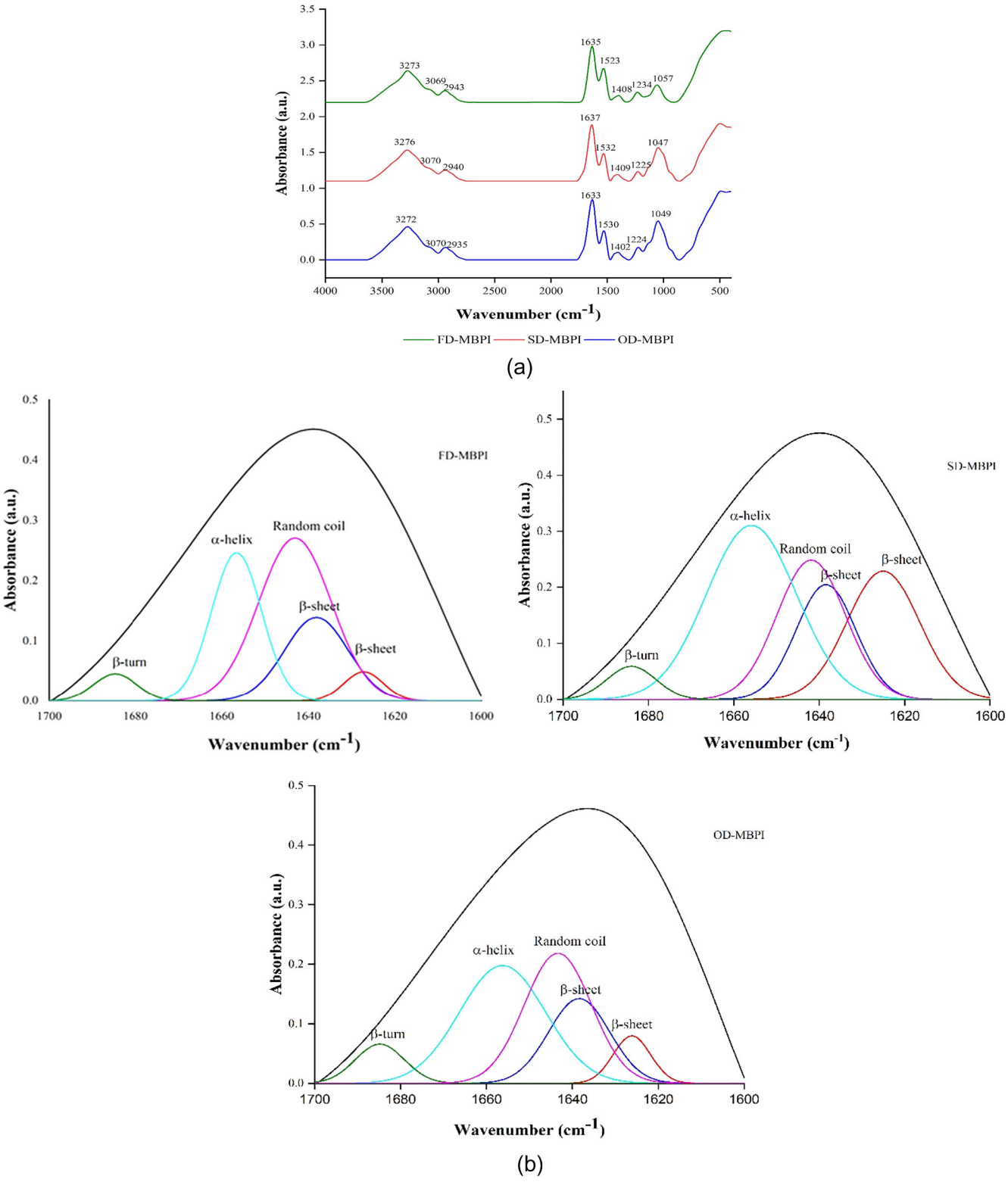

Fig. 5. (a) Characteristic region of absorption for freeze, spray and oven dried MBPI using FTIR (b) Fourier self-deconvoluted (FSD) curve-fitted spectra for freeze, spray and oven-dried MBPI.

when compared among FD, SD and OD, as observed in the % peak area in Table 3, indicating that drying techniques exert significant effect on the structural changes in protein molecules, causing alteration in their final functional properties. This shows that, different drying techniques can be suitably applied to cater for different desirable functional properties based on food manufacturers' requirements.

From Table 3, SD shows the highest amount of β-sheets (37.61%) compared to FD (24.09%) and OD (25.13%), indicating its highly ordered structure compared to other MBPIs (Mune Mune et al., 2017). This finding is in line with the DSC result where SD depicts the highest denaturation ΔH, i.e. it requires the most energy to be denatured, as a result of highly ordered, compact structure. Also, the increased amount

of β-sheet in SD favors the exposure of hydrophobic amino acids (Mune Mune et al., 2017) and thus reduces its solubility, as shown in Fig. 3. It was observed that some of the α-helix structure in FD has transformed into random coil, shown from the increased random coil percentage (44.01%). This could be due to partial unfolding of secondary structures during freeze drying (Kudre et al., 2013) supported by the high surface hydrophobicity recorded in Table 3. Also, the increased amount of unordered structure (random coil) and a low amount of β-sheet contribute towards high protein solubility in FD (Mune Mune et al., 2017). This would improve the gastrointestinal digestibility of FD, as more random structure makes it easily accessible by gastrointestinal enzyme upon ingestion. On the other hand, OD showed a comparatively higher amount of β-turn structure which could be due to the transformation from β-sheet during prolonged heating at 50 °C. It has been reported that β-turn structure plays an important role in the formation of protein aggregates (Wang et al., 2014).

3.6. Dynamic rheological characteristic

The small amplitude oscillatory shear measurement is valuable to determine the nature of protein matrix wherein temperature sweep provides information about the heat-induced gel structure of globular protein aggregates. In this study, temperature sweep was performed to observe the gel formation behavior of MBPI by measuring storage modulus (G′, elastic modulus), loss modulus (G″, viscous modulus) and loss tangent (δ, ratio of viscous to elastic modulus) as a function of temperature at fixed frequency and stress.

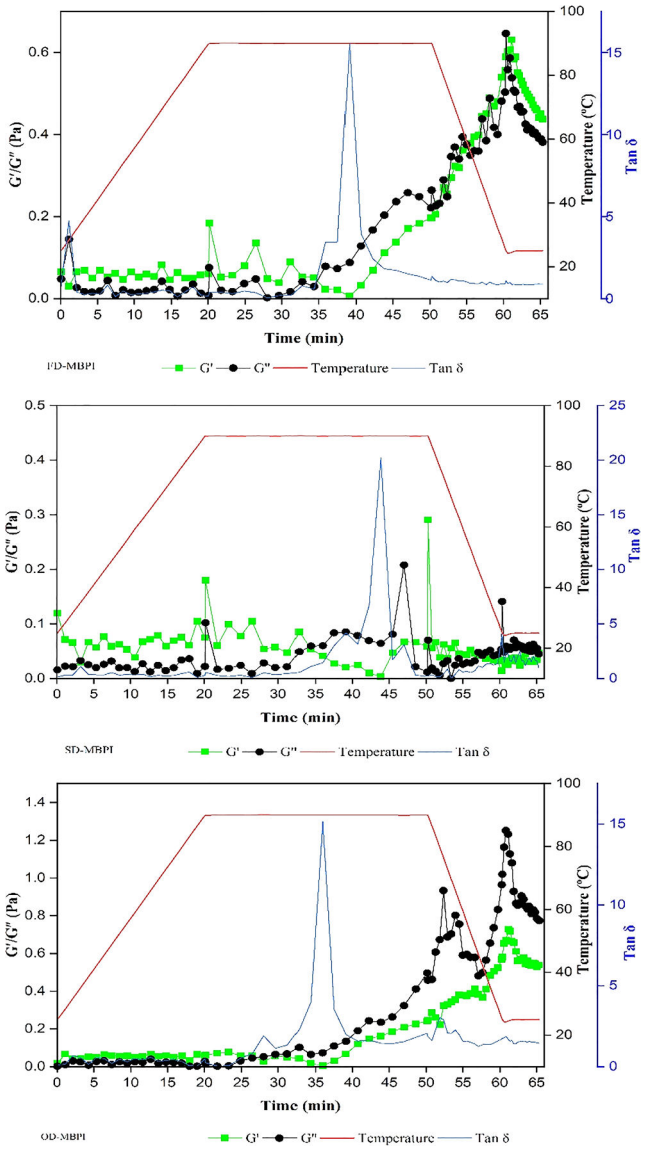

Fig. 6. Effect of temperature on the storage modulus (G′), loss modulus (G″) and loss tangent (δ) of protein dispersions (250 g/l) of freeze (FD), spray (SD) and oven-dried (OD) MBPI.

The gelation behavior of freeze, spray and oven dried MBPI are depicted in Fig. 6. For instance, the G′ of FD gel did not show any marked differences when the temperature was increased from 25 °C until 90 °C, but during holding at 90 °C, it dropped significantly and again increased dramatically during cooling phase. There is a clear cross-over between G′ and G″ at 32 min during the holding phase (90 °C). This cross-over point is defined as gelation temperature (Joshi et al., 2011). Similar results were obtained for SD and OD, whereby the cross-over took place at 35 min (89 °C) and 28 min (90 °C), respectively. These results show that the gelation temperature for MBPI, irrespective of drying techniques, was around 90 °C. For FD and OD, holding at 90 °C for 10 min reduced their G′ to some extent while subsequent cooling at 25 °C increased their G′ and G″ values. This increment in moduli is termed as $G_{reinforcement}$ and is attributed to the cold-induced strengthening of gel structure caused by the development of additional interactions (van der Waals and hydrogen bondings) between the disordered coils of protein molecules (Shevkani et al., 2015). In contrast, there is no such increment in the G′ and G″ values of SD, indicating that its gel structure is less rigid than FD and OD and gel structure is formed by the hydrophobic interactions only (Dapčević-Hadnađev, Hadnađev, Lazaridou, Moschakis, & Biliaderis, 2018).

The loss tangent (tan δ) is useful to evaluate the final gel network characteristics. It is interesting to note that for all the samples there is a peak in tan δ along with a drop in G′ value at holding phase at 90 °C. This is due to the increased protein molecular mobility and dissociation of the globulin subunits since the temperature reached well above the glass transition temperature. The tan δ then decreases dramatically at cooling phase, indicative of the formation of cross-linked polymer gel as well as their elastic nature (Bhandari & Roos, 2016; Dapčević-Hadnađev, 2018). A lower tan δ value indicates a more elastic network while higher value refers to an aggregated gel structure (Withana-Gamage et al., 2011). The tan δ values at different temperatures were 0.5–0.83, 0.3–0.9 and 1.12–1.14 for FD, SD and OD, respectively. This demonstrated that FD and SD developed gels with high elasticity while OD developed aggregated gel. The result suggests differences in gel structure formation by different sample which could be due to the differences in protein secondary structure. For instance, β-sheet plays an important role in gel formation and reinforcement. It is reported that intermolecular hydrogen bonds between β-sheets aid in stabilizing gel network (Joshi et al., 2011; Shevkani et al., 2015), i.e. higher amount of β-sheet would form gel with higher elasticity and results in smaller tan δ values.

4. Conclusion

Current work reports the thorough, complete profiling of mung bean protein isolate (MBPI) produced on a pilot-scale basis. MBPIs were obtained by three drying techniques, i.e. freeze, spray and oven drying, of which all techniques exerted profound effects on the final properties of MBPI. Irrespective of FD, SD and OD, all products showed no dissociation of protein subunit bands based on SDS-PAGE, were thermally stable (T_d = 157.90–158.07 °C) and recorded similar gelation temperatures around 90 °C. High thermal stability fosters the use of MBPI in food manufacturing that requires high heat. Other physicochemical, functional, thermal, structural and rheological properties were significantly influenced by drying techniques, as a result of different extent of protein denaturation. Morphological study showed that FD had a porous structure while SD and OD had wrinkled and compact crystalline structures, respectively. Based on LGC results, FD and SD demonstrated better gelling capacity than OD, which complemented the dynamic rheological

result whereby FD and SD formed elastic gels while OD formed aggregated gel. FD demonstrated exceptional protein solubility, water and oil absorption capacity, increased amount of unordered structure (random coil) and a low amount of β-sheet (thus good gastrointestinal digestibility). SD demonstrated the smallest particle size, excellent emulsion activity index and emulsion stability and the highest amount of β-sheet. Based on these, FD is ideal for the production of meat extender, SD is suitable for meat emulsion (meat loaf, bologna, sausages) while OD is appropriate as general protein-based food. Different quality attributes of mung bean protein are achieved by different drying techniques. This assists the selection of optimum drying technique to cater for different desirable functional properties, as needed for different food applications.

CRediT authorship contribution statement

Fatema Hossain Brishti: Conceptualization, Data curation, Formal analysis, Investigation, Methodology, Software, Writing - original draft. **Shyan Yea Chay:** Validation, Writing - review & editing. **Kharidah Muhammad:** Resources, Supervision, Validation. **Mohammad Rashedi Ismail-Fitry:** Resources, Supervision. **Mohammad Zarei:** Writing - review & editing. **Sivakumaran Karthikeyan:** Software. **Nazamid Saari:** Conceptualization, Funding acquisition, Project administration, Resources, Supervision, Validation, Writing - review & editing.

Declaration of Competing Interest

The authors declare that they have no known competing financial interests or personal relationships that could have appeared to influence the work reported in this paper.

Acknowledgement

The financial support from Universiti Putra Malaysia, Malaysia, under Putra grant scheme GP/2018/9643900 (Vote no: 9643900) and scholarship from Organization for Women in Science for the Developing World (OWSD) PhD fellowship and the Swedish International Development Cooperation Agency (SIDA) are gratefully acknowledged. The authors are grateful to Dr. Michael H Tunick and Dr. Mark Patrick for their valuable suggestions in rheology experiment.

References

Adhikari, B., Howes, T., Shresshta, A. K., & Bhandari, B. R. (2007). Development of stickiness of whey protein isolate and lactose droplets during convective drying. *Chemical Engineering and Processing: Process Intensification, 46*(5), 420–428.

Agoreyo, B., Akpiroroh, O., Orukpe, O., Osaweren, O., & Owabor, C. (2011). The effects of various drying methods on the nutritional composition of *Musa paradisiaca*, *Dioscorea rotundata* and *Colocasia esculenta*. *Asian Journal of Biochemistry, 6*(6), 458–464.

Akpan, E. J., & Umoh, I. B. (2004). Effect of heat and tetracycline treatments on the food quality and acridity factors in cocoyam [*Xanthosoma sagittifolium* (L.) Schott]. *Pakistan Journal of Nutrition, 3*, 240–243.

AOAC (2005). Official methods of analysis of AOAC International. In W. H. G. W. Latimer (ED.), Food composition; additives; natural contaminants (18th ed., Vol. II). California, USA.

Bawa, M., Songsermpong, S., Kaewtapee, C., & Chanput, W. (2020). Effects of microwave and hot air oven drying on the nutritional, microbiological load, and color parameters of the house crickets (*Acheta domesticus*). *Journal of Food Processing and Preservation, 44*(5), e14407.

Bencini, M. C. (1986). Functional properties of drum dried chickpea (*Cicer arietinum* L.) flour. *Journal of Food Science, 51*, 1518–1526.

Beuchat, L. R. (1977). Functional and electrophoretic characteristics of succinylated peanut flour protein. *Journal of Agricultural and Food chemistry, 25*(2), 258–261.

Bhandari, B., Bansal, N., Zhang, M., & Schuck, P. (2013). *Handbook of food powders: Processes and properties*. Amsterdam, Netherlands: Elsevier.

Bhandari, B. R., & Roos, Y. H. (Eds.). (2016). *Non-equilibrium states and glass transitions in foods: Processing effects and product-specific implications*. Woodhead Publishing.

Boye, J. I., Aksay, S., Roufik, S., Ribéreau, S., Mondor, M., Farnworth, E., & Rajamohamed, S. H. (2010). Comparison of the functional properties of pea, chickpea and lentil protein concentrates processed using ultrafiltration and isoelectric precipitation techniques. *Food Research International, 43*(2), 537–546.

Damodaran, S. (2008). Amino acids, peptides and proteins. *Fennema's Food Chemistry, 4*, 217–329.

Dapčević-Hadnađev, T., Hadnađev, M., Lazaridou, A., Moschakis, T., & Biliaderis, C. G. (2018). Hempseed meal protein isolates prepared by different isolation techniques. Part II. Gelation properties at different ionic strengths. *Food Hydrocolloids, 81*, 481–489.

Ding, P., & Ling, Y. S. (2014). Browning assessment methods and polyphenol oxidase in UV-C irradiated Berangan banana fruit. *International Food Research Journal, 21*(4), 1667.

Du, M., Xie, J., Gong, B., Xu, X., Tang, W., Li, X., Li, C., & Xie, M. (2018). Extraction, physicochemical characteristics and functional properties of Mung bean protein. *Food Hydrocolloids, 76*, 131–140.

Feyzi, S., Varidi, M., Zare, F., & Varidi, M. J. (2017). Effect of drying methods on the structure, thermo and functional properties of fenugreek (*Trigonella foenum graecum*) protein isolate. *Journal of the Science of Food and Agriculture, 98*(5), 1880–1888.

Ghribi, A. M., Gafsi, I. M., Blecker, C., Danthine, S., Attia, H., & Besbes, S. (2015). Effect of drying methods on physicochemical and functional properties of chickpea protein concentrates. *Journal of Food Engineering, 165*, 179–188.

Gong, K. J., Shi, A. M., Liu, H. Z., Liu, L., Hu, H., Adhikari, B., & Wang, Q. (2015). Emulsifying properties and structure changes of spray and freeze-dried peanut protein isolate. *Journal of Food Engineering, 170*, 33–40.

Gonzales, A. P., Burin, L., & del Pilar Buera, M. (1999). Color changes during storage of honeys in relation to their composition and initial color. *Food Research International, 32*(3), 185–191.

Hou, D., Yousaf, L., Xue, Y., Hu, J., Wu, J., Hu, X., … Shen, Q. (2019). Mung bean (*Vigna radiata* L.): Bioactive polyphenols, polysaccharides, peptides, and health benefits. *Nutrients, 11*(6), 1238.

Hu, X., Cheng, Y., Fan, J., Lu, Z., Yamaki, K., & Li, L. (2010). Effects of drying methods on physicochemical and functional properties of soy protein isolates. *Journal of Food Processing and Preservation, 34*, 520–540.

Joshi, M., Adhikari, B., Aldred, P., Panozzo, J. F., & Kasapis, S. (2011). Physicochemical and functional properties of lentil protein isolates prepared by different drying methods. *Food Chemistry, 129*(4), 1513–1522.

Khaket, T. P., Dhanda, S., Jodha, D., & Singh, J. (2015). Purification and biochemical characterization of dipeptidyl peptidase-II (DPP7) homologue from germinated *Vigna radiata* seeds. *Bioorganic Chemistry, 63*, 132–141.

Kudre, T. G., Benjakul, S., & Kishimura, H. (2013). Comparative study on chemical compositions and properties of protein isolates from mung bean, black bean and bambara groundnut. *Journal of the Science of Food and Agriculture, 93*(10), 2429–2436.

Laemmli, U. K. (1970). Cleavage of structural proteins during the assembly of the head of bacteriophage T4. *Nature, 227*(5259), 680–685.

Lili, L., Huan, W., Guangyue, R., Xu, D., Dan, L., & Guangjun, Y. (2015). Effects of freeze-drying and spray drying processes on functional properties of phosphorylation of egg white protein. *International Journal of Agricultural and Biological Engineering, 8*(4), 116–123.

Lowry, O. H., Rosebrough, N. J., Farr, A. L., & Randall, R. J. (1951). Protein measurement with the Folin phenol reagent. *Journal of Biological Chemistry, 193*, 265–275.

Ma, C. Y., & Harwalkar, V. R. (1991). Thermal analysis of food proteins. In *Advances in food and nutrition research* (Vol. 35, pp. 317–366). Academic Press.

Mendoza, E. M. T., Adachi, M., Bernardo, A. E. N., & Utsumi, S. (2001). Mungbean *[Vigna radiata* (L.) Wilczek] globulins: Purification and characterization. *Journal of Agricultural and Food Chemistry, 49*(3), 1552–1558.

Mune Mune, M. A., Sogi, D. S., & Minka, S. R. (2017). Response surface methodology for investigating structure–function relationship of grain legume proteins. *Journal of Food Processing and Preservation, 42*(2), e13524.

Nakai, S. (2003). Measurement of protein hydrophobicity. *Current Protocols in Food Analytical Chemistry, 9*, B5.2.1–B5.2.13.

Pearce, K. N., & Kinsella, J. E. (1978). Emulsifying properties of proteins: Evaluation of a turbidimetric technique. *Journal of Agricultural & Food Chemistry, 26*, 716–723.

Rasli, H. I., & Sarbon, N. M. (2015). Effects of different drying methods on the rheological, functional and structural properties of chicken skin gelatin compared to bovine gelatin. *International Food Research Journal, 22*(2), 584–592.

Rudra, S. G., Sethi, S., Jha, S. K., & Kumar, R. (2016). Physicochemical and functional properties of cowpea protein isolate as affected by the dehydration technique. *Legume Research, 39*(3), 370–378.

Sanfelice, D., & Temussi, P. A. (2016). Cold denaturation as a tool to measure protein stability. *Biophysical Chemistry, 208*, 4–8.

Sathe, S. K., Deshpande, S. S., & Salunkhe, D. K. (1981). Functional properties of lupin seeds (*Lupinus mutabilis*) proteins and protein concentrates. *Journal of Food Science, 47*, 491–497.

Schreinemachers, P., Sequeros, T., Rani, S., Rashid, M. A., Gowdru, N. V., Rahman, M. S., … Nair, R. M. (2019). Counting the beans: Quantifying the adoption of improved mungbean varieties in South Asia and Myanmar. *Food Security, 11*(3), 623–634.

Shang-gui, D., Zhi-ying, P., Fang, C., Ping, Y., & Tie, W. (2004). Amino acid composition and anti-anaemia action of hydrolyzed offal protein from *Harengula Zunasi* Bleeker. *Food Chemistry, 87*(1), 97–102.

Shevkani, K., Singh, N., Kaur, A., & Rana, J. C. (2015). Structural and functional characterization of kidney bean and field pea protein isolates: A comparative study. *Food Hydrocolloids, 43*, 679–689.

Shimada, K., & Cheftel, J. C. (1988). Determination of sulfhydryl groups and disulfide bonds in heat-induced gels of soy protein isolate. *Journal of Agricultural and Food Chemistry, 36*(1), 147–153.

Taira, H., Taira, H., Sugimura, K., & Sakurai, Y. (1965). Studies on amino acid contents of processed soybean. *Agricultural and Biological Chemistry, 29*(12), 1074–1083.

Tajoddin, M., Manohar, S., & Lalitha, J. (2014). Effect of soaking and germination on polyphenol content and polyphenol oxidase activity of mung bean (*Phaseolus aureus* L.) cultivars differing in seed color. *International Journal of Food Properties, 17*(4), 782–790.

Tang, C. H., & Ma, C. Y. (2009). Heat-induced modifications in the functional and structural properties of vicilin-rich protein isolate from kidney (*Phaseolus vulgaris* L.) bean. *Food Chemistry, 115*(3), 859–866.

Thompson, L. U. (1977). Preparation and evaluation of mung bean protein isolates. *Journal of Food Science, 42*, 202–206.

Timilsena, Y. P., Adhikari, R., Barrow, C. J., & Adhikari, B. (2016). Physicochemical and functional properties of protein isolate produced from Australian chia seeds. *Food Chemistry, 212*, 648–656.

Vogelsang-O'Dwyer, M., Petersen, I. L., Joehnke, M. S., Sørensen, J. C., Bez, J., Detzel, A., … Zannini, E. (2020). Comparison of faba bean protein ingredients produced using dry fractionation and isoelectric precipitation: Techno-functional, nutritional and environmental performance. *Foods, 9*(3), 322.

Vojdani, F. (2006). Solubility. In G. M. Hall (Ed.), Methods of testing protein functionality. St. Edmundsbury Great Britain, pp. 11–60.

Wagner, J. R., Sorgentini, D. A., & Añón, M. C. (2000). Relation between solubility and surface hydrophobicity as an indicator of modifications during preparation processes of commercial and laboratory-prepared soy protein isolates. *Journal of Agricultural and Food Chemistry, 48*(8), 3159–3165.

Wang, Z., Li, Y., Jiang, L., Qi, B., & Zhou, L. (2014). Relationship between secondary structure and surface hydrophobicity of soybean protein isolate subjected to heat treatment. *Journal of Chemistry, 2014*, 1–10.

Withana-Gamage, T. S., Wanasundara, J. P., Pietrasik, Z., & Shand, P. J. (2011). Physicochemical, thermal and functional characterisation of protein isolates from Kabuli and Desi chickpea (*Cicer arietinum* L.): A comparative study with soy (*Glycine max*) and pea (*Pisum sativum* L.). *Journal of the Science of Food and Agriculture, 91*(6), 1022–1031.

Xie, J., Du, M., Shen, M., Wu, T., & Lin, L. (2019). Physicochemical properties, antioxidant activities and angiotensin-I converting enzyme inhibitory of protein hydrolysates from Mung bean (*Vigna radiate*). *Food Chemistry, 270*, 243–250.

Yao, Y., Zhao, G., Yan, Y., Chen, C., Sun, C., Zou, X., … Wang, X. (2016). Effects of freeze drying and spray drying on the microstructure and composition of milk fat globules. *RSC Advances*, 2520–2529.

Zayas, J. F. (2012). *Functionality of proteins in food*. Springer Science & Business Media.

Zhao, Q., Xiong, H., Selomulya, C., Chen, X. D., Huang, S., Ruan, X., … Sun, W. (2013). Effects of spray drying and freeze drying on the properties of protein isolate from rice dreg protein. *Food and Bioprocess Technology, 6*(7), 1759–1769.

Spectrochimica Acta Part A: Molecular and Biomolecular Spectroscopy 249 (2021) 119220

Contents lists available at ScienceDirect

Spectrochimica Acta Part A: Molecular and Biomolecular Spectroscopy

journal homepage: www.elsevier.com/locate/saa

Nitrogen influenced biomolecular changes on *Physalis* L. species studied using 2DCOS spectral analysis coupled with chemometric and Receiver operation characteristics analysis

Romeu da Silva Leite [a,*], Karthikeyan Sivakumaran [b,*], Salvador Hernandéz-Navarro [c], Marilza Neves do Nascimento [a], Norlan Miguel Ruiz Potosme [d], Paula Carrión-Prieto [c], Elma dos Santos Souza [a]

[a] *Biological Sciences Department, State University of Feira de Santana, 44036-900 Feira de Santana, Bahia, Brazil*
[b] *Department of Physics, Dr. Ambedkar Government Arts College, 600039 Chennai, Tamil Nadu, India*
[c] *Agriculture and Forestry Engineering Department, Universidad de Valladolid, 34004 Palencia, Castilla y Leon, Spain*
[d] *Superior Polytechnic School, European University Miguel de Cervantes, 47012 Valladolid, Castilla y Leon, Spain*

HIGHLIGHTS

- 2DCOS FTIR spectral analysis was used in monitoring the biochemical changes due to *Physalis* L. species under nitrogen fertilization.
- ROC analysis shows the area under the curve ranges from 0.84 to 0.92 indicating good reliability of the study.
- PCA signifies protein predominant in discriminating against the variation among the samples studied.
- HCA analysis shows high dissimilarity obtained in the dendrogram scale.

GRAPHICAL ABSTRACT

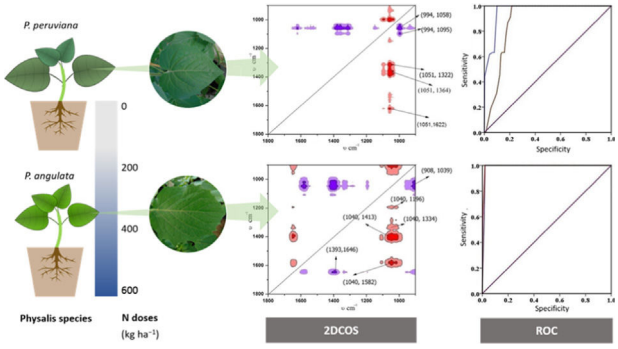

ARTICLE INFO

Article history:
Received 20 July 2020
Received in revised form 6 November 2020
Accepted 10 November 2020
Available online 16 November 2020

Keywords:
Fourier Transform Infrared Spectroscopy
2D correlation spectral analysis
Mineral nutrition
Physalis angulata
Physalis peruviana

ABSTRACT

The determination of the molecular composition of plant leaves is essential to assist in nutritional management, whether for cultivated or non-cultivated species. In this sense, the study aimed to apply FTIR technique in combination with chemometrics and ROC analysis for the evaluation of changes in compositional of plant leaves of *Physalis angulata* and *Physalis peruviana* due to nitrogen fertilization treatments. Both species were grown under different doses of nitrogen (0, 200, 400, and 600 Kg ha^{-1}) and leaf samples were evaluated using ATR-FTIR. Our results demonstrate that the spectra of both species were influenced by the nitrogen doses. The computed band area from the lipid/amide, lipid/carbohydrates, degree of esterification and calcium oxalate shows nitrogen fertilization due to 400 Kg ha^{-1} of N treatment is more effective for a better quality of yield. 2D correlation spectral analysis (2DCOS) reveals cellulose and pectin begins changes followed by amide of proteins due to nitrogen treatment in *P. peruviana* samples. The *P. angulata* plants shows hemicellulose changes predominating followed by proteins and polysaccharides. The obtained principle component analysis plot and loading values show the *Physalis* species samples distinctly separated from control with protein and carbohydrates are predominant in influencing separation among them. Receiver operation characteristic analysis shows a higher value of area under the curve reflecting better reliability of the experiments carried out. Hierarchical cluster analysis shows closed separation for a similar group on dissimilarity scale. Thus the use of 2DCOS coupled

* Corresponding authors.
E-mail addresses: leiteromeu@hotmail.com (R. da Silva Leite), physicskarthik@gmail.com (K. Sivakumaran).

https://doi.org/10.1016/j.saa.2020.119220

with chemometrics helps to identify changes in the composition of leaves of physalis species due to nitrogen doses, constituting a fast and precise measuring for the suitable management of this fertilization.

1. Introduction

The leaf is a vital organ of a plant due to its various functions such as gas exchange and storehouse of reserve substances [1]. The unique feature of the leaf consists of lipids compounds, cellulose and pectin; and its cell wall has a complex structure that consists of cellulose-hemicellulose embedded in a pectin matrix [2]. In addition to determining the cell size and shape, the plant cell wall can be a key component of the plant's response to abiotic stresses [3], such as the lack or excess of nutrients.

Apart from the organic compounds, the plant leaf has a common biomineral occurring as crystals of various shapes in tissues. This presence of calcium oxalate crystal plays a prominent role in calcium regulation, metal detoxification, and plant protection [4]. The other functions include cell wall rigidity and light gathering and reflection [5]. The key plant characteristics are related to leaf a chemical composition which contributes to feeding resource quality, and its production linked to the ecosystem [6,7]. The alteration of soil nutrient availability via fertilization concerning leaf composition has been important measures at the ecosystem level for agriculture production [8].

In cultivated plants, the nitrogen (N) is one of the most limiting factors considered for productivity and growth [9]. And, after being absorbed from the soil, nitrogen is distributed in various parts of plants. The major amount is accumulated in leaf as the main storage organs [10]. The nutritional status of these plants under the influence of nitrogen treatments can be assessed form leaves for effective crop yield [11]. Hence it is necessary to assess the biochemical changes occurring in leaves due to nitrogen supplement for effective crop yield using Fourier transform infrared spectroscopy (FTIR) techniques. It gives an idea for the requirement for optimum fertilization usage in plant production. Hence effective usage of required nitrogen for productive will reduce the cost and also reduces soil polluted with nitrogen supplements [12].

Infrared spectroscopy (IR) is a versatile tool in determining molecular compositions of the plant leaves. Understanding the response changes in the chemical composition of leaf helps in finding suitable fertilization required for sustainable growth. The advantage of FTIR enable is to examine the initial response to stimuli with high sensitivity from a small amount of samples [13]. Attenuated Total Reflectance (ATR) with FTIR has been extensively used for the chemical composition of biological samples with minimum sample requirement [14]. IR spectra give information about functional groups thus providing the biochemical nature of the samples. It helps to identify the cellular organic constituents such as lipids, proteins, and polysaccharides present in leaf samples [15]. Also, the use of multivariate statistical analysis is necessary to extract valuable information. In this study, Principle component analysis (PCA) and Hierarchical cluster analysis (HCA) were employed to explore the identification and classification of *Physalis* L. species treated to various nitrogen fertilization. Further Receiver operation characteristic (ROC) analysis was also carried out to demonstrate the accuracy of the outcome of the experiment. It is used in biomedical/biological functions to judge the quality of the diagnostic test. ATR combined with chemometrics was successfully applied to discrimination of plant chemical compositions [16].

Studies with FTIR analyzes in species of the *Physalis* genus are scarce, especially in terms of mineral nutrition and its influence on the biochemical composition. This is an American genus of importance for agriculture [17] and its main representatives are the species *Physalis angulata* and *Physalis peruviana*. These species are characterized by medicinal uses and fresh consumption, with *P. peruviana* being the main cultivated species, while *P. angulata* is an underexploited genetic resource, with potential prospection. Thus, the study aimed to apply the FTIR technique for evaluation of changes in compositional of plant leaves of *P. angulata* and *P. peruviana* due to nitrogen fertilization treatments in combination with chemometrics and ROC analysis.

2. Material and methods

2.1. Plant material and growth conditions

Three fertilization treatments in physalis species were conducted at the Higher Technical School of Agricultural Engineering, University of Valladolid, Palencia Campus, Spain. Two physalis species were grown in a greenhouse, *Physalis angulata,* and *Physalis peruviana*, and applied the following treatments: 200, 400, and 600 kg ha^{-1} of nitrogen (N), with control no fertilization, is required (0 kg ha^{-1} of N). Seedling production, substrate characteristics, and other cultural treatments were described in a previous study [18]. The cultivation with both species was terminated at 60 days after transplantation and the collected leaves were dried in an oven at 60 °C until reaching a constant weight and then crushed in an ultracentrifugal mill (1 mm).

2.2. FTIR measurements

The leaf samples of the different treatments were analyzed by infrared attenuated total reflectance spectroscopy with Fourier transform (ATR FTIR) using the ThermoNicolet iS50 spectrophotometer (Thermo Fischer Scientific, Waltham, MA, USA). The spectra were recorded in the medium infrared (4000–500 cm^{-1}) with a spectral resolution of 4 cm^{-1} and 32 scans per sample [18]. Before spectral analysis, the obtained FTIR data were baseline corrected and vector normalized using Origin 8.0. The Fourier self deconvolution techniques were used to resolve the hidden peak. A baseline was subtracted before the curve fitting. The initial values peak position, peak height, and half bandwidth were chosen and taken from second derivatives. The Savitzky and Golay method with a 9-point window was used for smoothing. The Gaussian function was used to resolve peak pattern with least goodness-of-fit was obtained as described by Karthikeyan and Eswaran [19].

2.3. Two dimensional correlation method

Two-dimensional correlation spectra are constructed using 2D shige v1.3 software [20–22]. 2D correlation spectroscopy provides the correlation information between absorption peaks of different functional groups. It gives one to one correspondence between external perturbation and characteristics information with good sensitivity. We obtained 2D COS a spectrum for *Physalis* L. species of three sample sets each. Before executing 2D correlation the FTIR data were smoothed, baseline corrected, and normalized to 3300 cm^{-1}. The application of nitrogen fertilization was regarded as an external perturbation. The information obtained from the

spectra are given characteristics information of the sample with good sensitivity.

2.4. Principle component analysis

The Principle component analysis (PCA) was done using SPSS 16.0 software. It is used for reducing a smaller number of factors from large data sets. FTIR data are mean-centered, with second derivative and vector normalized before subjected to PCA analysis. PCA was done in the region 4000–500 cm^{-1} for all samples each of two replicates which are obtained after five replication of spectral data measured. The input absorption values are supplied as n × n matrix. The output of PCA gives scores and loading which are characteristics of PCA. The score plot gives the variation among the samples studied.

2.5. Hierarchical cluster analysis

Hierarchical cluster analysis was utilized to know the difference among the samples of *Physalis* L. species. Pearson's product-moment correlation coefficient with the squared Euclidean distance method using the ward algorithm was applied using SPSS 16 Software. The dissimilarity scale on the Dendrogram shows group which is related by smaller distances represents closed separations. It gives information about the order of the clustering of the samples studied.

2.6. Receiver operation characteristics analysis

Receiver operation Characteristics (ROC) is a statistical decision theory widely used in medical, electronic, biology, radiology, etc. ROC curves allow us by direct comparisons of the effectiveness of different tests by the common unit called the area under the curve (AUC). It helps to compare the overall experimental outcome of the test. To form the ROC curve a plot, FTIR data obtained for treated samples was given as input variables and control taken as a reference point with a threshold of limit as 95% using SPSS 16.0 software. The results of ROC helps to determine the sensitivity and specificity associated with the chosen threshold of limits.

2.7. Statistical analysis

The student *t*-test was performed using SPSS19 for windows. The spectra for control and nitrogen treatment were calculated for 5 repeats individually. These replicates were averaged and these averaged spectra were used for statistical analysis. Differences between control and treated were analyzed by paired *t*-test. A p-value of less than 0.05 is regarded as significant.

3. Results and discussion

3.1. Phenotypical observations

Nitrogen fertilization was promoted to distinct phenotypic responses between the species and the treatments evaluated (Fig. 1). Control plants of *P. peruviana* showed chlorosis in the older leaves, however, this characteristic was less pronounced for the same treatment in *P. angulata*, probably due to the greater rusticity of this species. Leaves with dark green colorations were observed in plants grown with 400 Kg ha^{-1} of N. It is important to mention that plants of *P. peruviana* grown with 600 Kg ha^{-1} of N had smaller height and greater number of branches, although these variables were not measured in this work. This effect was not observed in *P. angulata*, which did not present visual characteristics of phytotoxicity due to the excess of N. The stress due to lack or excess of nitrogen can cause oxidative damage in cellular components [23], in the metabolism of proteins, amino acid and lipids [24], resulting in reduced growth rates and yield in plants [25]. Thus, it is essential to use methodologies that can assist in the adequate management of nitrogen fertilization.

3.2. Infrared spectral analysis and the band area measurement in the selected region in Physalis species exposed to nitrogen fertilization treatment

The supply of nitrogen fertilization changed the FTIR spectra of the evaluated physalis species. Fig. 2 shows typical FTIR spectra of *P. angulata* and *P. peruviana* leaves in the region 4000–500 cm^{-1}. Table 1 shows the band area measured for characteristic frequency assignment of physalis leaves. The spectra of plant leaves show the presence of lipids, proteins and carbohydrates [26,1]. Fig. 3 shows FTIR average spectra of physalis leaves in 1800–800 cm^{-1} normalized at amide I region. The most predominant changes of the bands are seen at spectral ranges 3000–2800 cm^{-1} and 1800–900 cm^{-1}. Fig. 3 shows that spectra consist of several bands arising from the vibrations of different groups such as proteins, lipids, carbohydrates, and nucleic acid. This signifying that the leaves are rich in biochemical compositions [27]. Thus, showing the biochemical potential of the species under study, mainly for *P. angulata*, which is an unexploited genetic resource.

The lipids bands due to CH stretching vibration arises in the region 3000–2800 cm^{-1} and protein bands due to amide I and amide II are located in 1630 cm^{-1} and 1543 cm^{-1} [28]. The carbohydrates and nucleic acid contributes in the 1500–1000 cm^{-1} region [29]. The peak seen at a ~2927 cm^{-1} was associated with C-H stretching vibrations. It was observed form the amide bands significant increase in band arises at 200 Kg ha^{-1} of N treatment and reaches higher values at 400 Kg ha^{-1} of N followed by a decrease in amide bands at 600 Kg ha^{-1} of N. This band forms an important role in assessing the leaf protein contents due influence of nitrogen status as amide is an important chemical form of nitrogen storage in plants [10]. The computed lipid/amide band ratio shows a consistent value shown in Fig. 4.

The nutritional status of *P. angulata* leaves is increased at 400 Kg ha^{-1} of N treatments as seen from the lipid/amide ratio. The amide bands are subjected to Fourier self deconvolution to find changes in the secondary structural variation of protein. The specific band area ratio of selected band lipid/amide I, lipid/total amide, lipid/-carbohydrates ratio was computed from the spectra. The changes in the band area measured are compared with control. It shows a variation in the main cellular compositions. The lower value of band area of lipid/total amide due to 600 Kg ha^{-1} of N treatment indicates possible phenolic constituents responsible for the activation of several molecular mechanisms [30]. Efstathia Skotti et al. [28] studied a similar approach in utilizing FTIR with PCA of the aromatic plant of Lamiaceae family.

The study is considered as the first which can identify the strong correlation between FTIR bands area ratio with different nitrogen treatments. The study shows growth enhancement of proteins in *P. angulata* and *P. peruviana* leaves due to nitrogen fertilization which, in addition to physiological functions, can be a promising indication of the role of this fertilization in promoting tolerance of physalis species to abiotic stresses. The result shows that conformational changes of lipid and protein in physalis leaves help to study the biological mechanism of nitrogen influences on plant growth and development. Detection of changes on the cellular component using FTIR technique in plants under unfavorable abiotic conditions, such as heat and mineral stresses, was observed in other studies [31,32].

The study shows a significant increase in lipid/carbohydrates for at 400 Kg ha^{-1} of N treatment, denoting an effective strategy

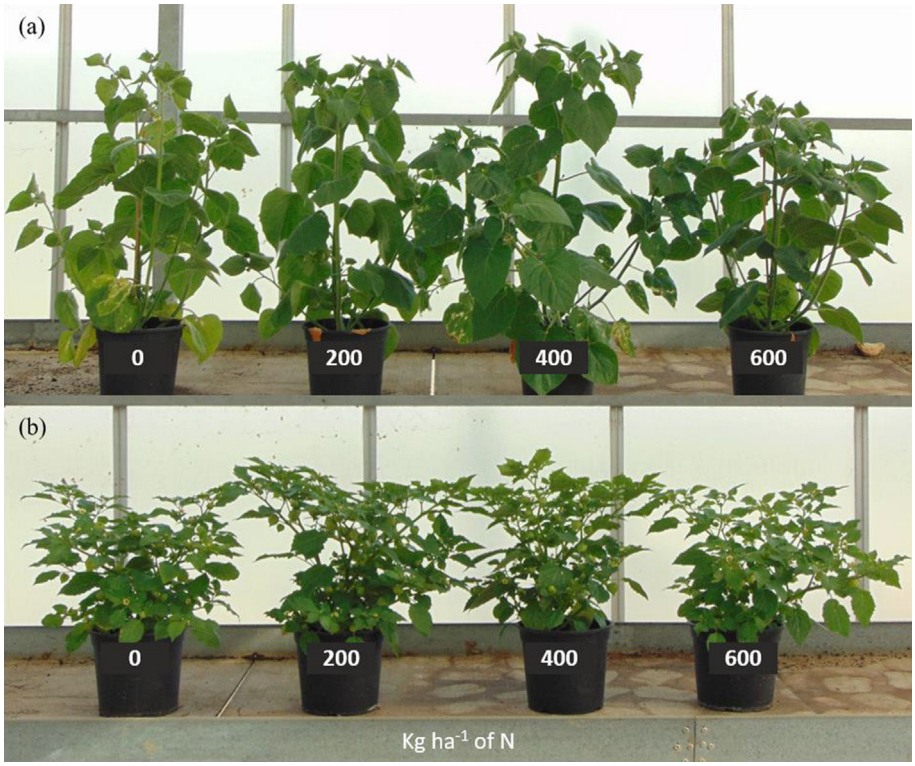

Fig. 1. Phenotypical observations of physalis species under nitrogen fertilization: (a) *Physalis peruviana* and (b) *Physalis angulata*.

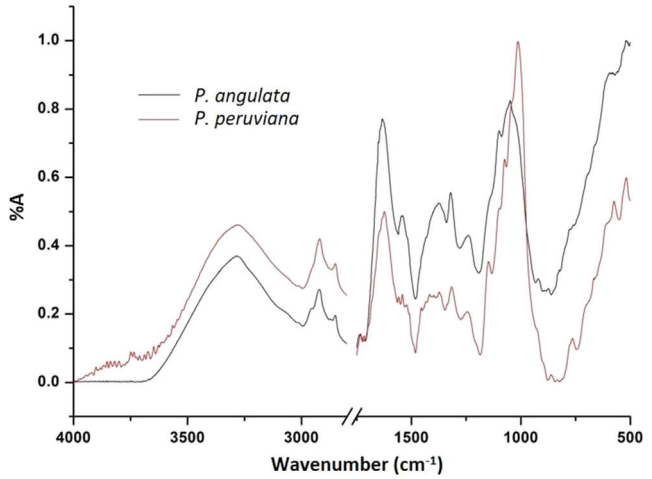

Fig. 2. Representative of FTIR spectra in *Physalis* L. species in the region 4000–500 cm^{-1}.

for nitrogen supply assessment in the selected species using FTIR (Fig. 4). The lipid/amide ratio shows a significant reduction due to nitrogen treatments when compared to control. This shows the influence of nitrogen in *P. angulata* leaves resulting in a change in biochemical compositions. Similar results were reported by Ke Wu et al. [10] for rice production under nitrogen fertilizer treatment. The observed band area ratio (0.52–0.43) is considered for sufficient nitrogen supplement for growth production. Any decrease in the ratio shows an excess of nitrogen supplements for the plants which is not utilized for growth factors and that can cause phytotoxicity or environmental contamination.

Our field experiment shows their ratio applies to all *Physalis* L. species. For the ratio of 0.43–0.52 likely reflects a suitable nitrogen status for plants. Less than 0.4 is considered insufficient whereas a ratio above 0.52 implies excess nitrogen which accumulated in the soil environment. Thus, FTIR and PCA can facilitate the effective assessment of the nitrogen status in plant production and gives relevant information on fertilization usage. However, nitrate accumulation depends on the plant species, growth stage, and fertilization used [33,34]. The amide bands influence the nitrogen storage in plants which occurs at 1630 cm^{-1} and 1543 cm^{-1}[35]. They are the main chemical form for nitrogen storage in plants. It is an essential nutrient for plant growth and development. Therefore, it was presumed that these two absorption bands (amide I or amide II) could be assessed for nitrogen status thus providing a potential tool for the diagnosis of the plant [10,35,36]. Equilibrium has reached between amide I and amide II at specific nitrogen supplement (400 Kg ha^{-1} of N). Any alteration in the amide bands provides a diagnosis for plant nitrogen requirement status [10]. The results of the study show significant variation for *P. angulate* for Lipid/amide regions compared to control. The frequency ~1374 cm^{-1} assigned to the carboxylate group. Pectin groups are assigned to 1320 cm^{-1} and, 1240 cm^{-1}.

In both plant species, the lipids and proteins are mainly affected as shown from the band area measured from spectra. Carbohydrates and pectin have no significant changes. Our study gives a way to characterize leaf compositions for nitrogen supplement for large production using FTIR spectra. In our study, protein band area amide I/amideII help in discriminating samples due to various treatments. Changes in fatty acids regions may be related to the richness of sesquiterpenes, flavonoids and other phenolic compounds characteristics [37], which are important compounds reported for the species of physalis in this study [38,39]. We found that infrared spectral regions of polysaccharides (cellulose) and proteins were +vely correlated with nitrogen treatment.

It was supported by band area measurement. The composition of a leaf is controlled by nitrogen fertilization where the proportion of nitrogen is present in the form of protein [40]. Studies by

Table 1
Frequency assignment and the band area of the *P. angulata* and *P. peruviana* plant leaves samples subjected to various nitrogen treatments.

Wavenumber (cm^{-1})	*P. angulate* Treatments (Kg ha^{-1} of N)				*P. peruviana* Treatments (Kg ha^{-1} of N)				Frequency assignment
	Control	200	400	600	Control	200	400	600	
2927	2.01 ± 0.01	2.86 ± 0.07	1.84 ± 0.02	1.82 ± 0.04	3.58 ± 0.05	3.31 ± 0.11	2.27 ± 0.13	3.58 ± 0.05	C-H stretching vibration
1749	1.69 ± 0.10	2.34 ± 0.05	1.82 ± 0.11	1.74 ± 0.26	0.48 ± 0.02	0.59 ± 0.03	0.41 ± 0.04	0.48 ± 0.02	Pectin C=O stretching vibration of alkyl ester
1630	35.16 ± 0.87	37.99 ± 0.56	46.83 ± 0.69	38.17 ± 1.56	19.2 ± 0.38	22.54 ± 1.29	32.59 ± 1.27	19.2 ± 0.38	Amide I
1543	1.36 ± 0.07	1.44 ± 0.17	1.23 ± 0.08	0.90 ± 0.07	0.28 ± 0.04	0.36 ± 0.04	0.42 ± 0.04	0.28 ± 0.04	Amide II
1507	0.16 ± 0.04	0.50 ± 0.06	0.24 ± 0.02	0.14 ± 0.02	0.21 ± 0.02	0.17 ± 0.02	0.19 ± 0.01	0.21 ± 0.02	lignin
1374	0.58 ± 0.01	7.20 ± 0.73	6.62 ± 1.80	7.17 ± 0.46	0.49 ± 0.02	0.19 ± 0.02	1.2 ± 0.06	0.49 ± 0.02	Carboxylate group
1320	2.86 ± 0.06	3.05 ± 0.03	2.76 ± 0.14	2.83 ± 0.46	2.51 ± 0.04	3.6 ± 0.17	1.55 ± 0.12	2.51 ± 0.04	Pectin
1240	0.50 ± 0.45	4.05 ± 0.98	3.19 ± 0.33	2.55 ± 0.12	3.18 ± 0.17	3.57 ± 0.16	2.21 ± 0.32	3.18 ± 0.17	Pectin
1070	0.48 ± 0.04	4.01 ± 0.05	2.76 ± 0.61	2.84 ± 0.40	0.39 ± 0.02	0.29 ± 0.04	0.21 ± 0.03	0.39 ± 0.02	hemicellulose

*p < 0.05 significant with control.

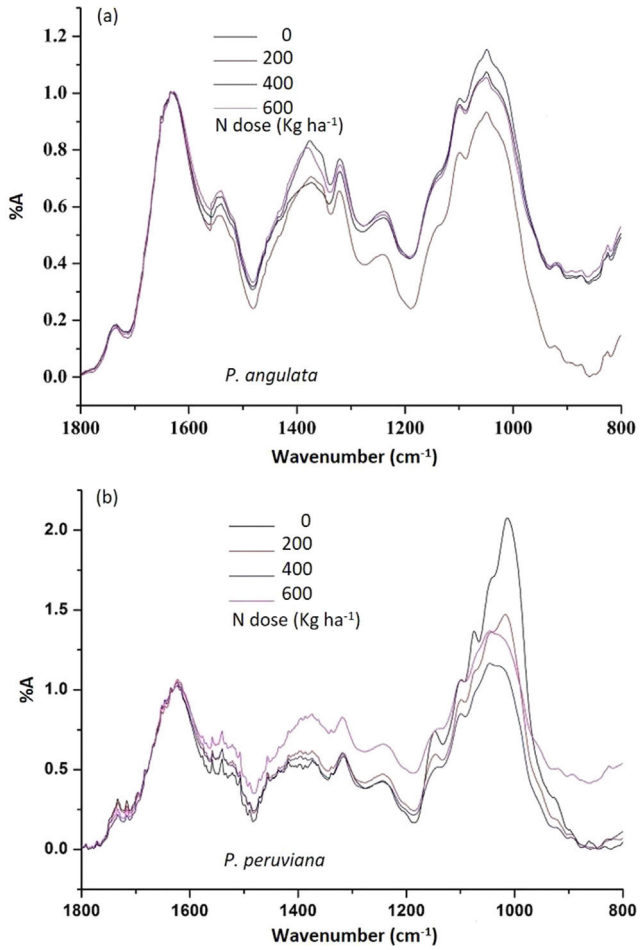

Fig. 3. FTIR spectra of *Physalis* species with in the region 1800–800 cm^{-1} normalized at amide I region: *Physalis angulata* (a) and *Physalis peruviana* (b).

Baldwin et al. [41], shows changes in cellulose content in plants occurs due to nitrogen fertilization. Rumana Rana et al. [8] found similar results for *Dactylis glomerata* plant where protein contents were affected by nitrogen fertilization. Increases in protein levels with nitrogen supply have been reported for other crops, such as potatoes [42] and lettuce [43].

Lipids/Carbohydrates band area ratio shows no significant increase due to nitrogen fertilizer in the case of *P. angulata*. This shows that *P. angulata* leaves reserves the carbohydrates energy for the growth where it contradicts with *P. peruviana* plant. The increase in carbohydrates was observed in the *P. angulata* whereas *P. peruviana* did not have any significant changes (Fig. 4). This difference in the spectral variation in carbohydrates (1200–900) region may be attributed to quantitative variation between the species [44]. The remarkable changes in protein, lipids, and cell wall pectin synthesis were pronounced in at 400 Kg ha^{-1} of N treatment. FTIR can be used to identify the structure of biochemical compositions and the spectra associated with molecular compositions [45]. The degree of methyl esterification and calcium oxalate was computed from the selected band area as suggested by Vincenzo Lionetti et al. [2]. The computed value of the degree of esterification form the selected band area shows at 400 Kg ha^{-1} of N treatment is more effective in bringing the high quality of production of plants with given nitrogen supplements (Fig. 4). The formation of calcium oxalate results in improving the nutritional quality of plants thereby improving in plant defense mechanism [46]. The presence of calcium oxalate primarily participates in the influence of photosynthesis. Hence higher the calcium oxalate production results in improved quality of plant nutritional status. The calcium oxalate measured value shows higher for at 400 Kg ha^{-1} of N treatment when compared to control and other treatment (Fig. 4). This supports of findings that nitrogen supplement due to at 400 Kg ha^{-1} of N treatment is more effective in improving the plant yield.

Overall the spectrum of control and nitrogen treated samples differ in the form absorption intensity and peak positions. This indicates noticeable changes in the structure and content of biological compositions. The obtained IR spectra were further processed by deconvolution using a curve fitting analysis. It is used for resolving the hidden peaks for the quantitative examination of structural changes.

3.3. Fourier self deconvolution (FSD) deduced by curve fitting analysis in the fatty acids region of Physalis L. species exposed to nitrogen fertilization treatment

Fourier self deconvolution in the lipid region 3000–2800 cm^{-1} represents CH_3 and CH_2 groups of lipids for *P. angulata* and *P. peruviana* shown in Fig. SF1. The respective band area measured is listed in Table S1. Fourier self deconvolution results in bands at 2959 cm^{-1} and 2880 cm^{-1} corresponding to asymmetric and symmetric of CH_3 stretching of lipids. The asymmetric and symmetric CH_2 stretching band arises at 2924 cm^{-1}, 2851 cm^{-1}. In the case of *P. angulata* leaves band area of symmetric CH_2 bands decreases after 400 Kg ha^{-1} of N treatment while symmetric CH_3 band increases. Less significant or no significant changes in band area observed for the bands 2959 cm^{-1}, 2924 cm^{-1}.

This result indicates a structural variation of lipids due to nitrogen fertilization. This variation in lipids is likely contributed to its physiological roles. The peak found at 2927 cm^{-1} is assigned to CH stretching of fatty acids. Zhelin Wei et al. [29] studied variation in

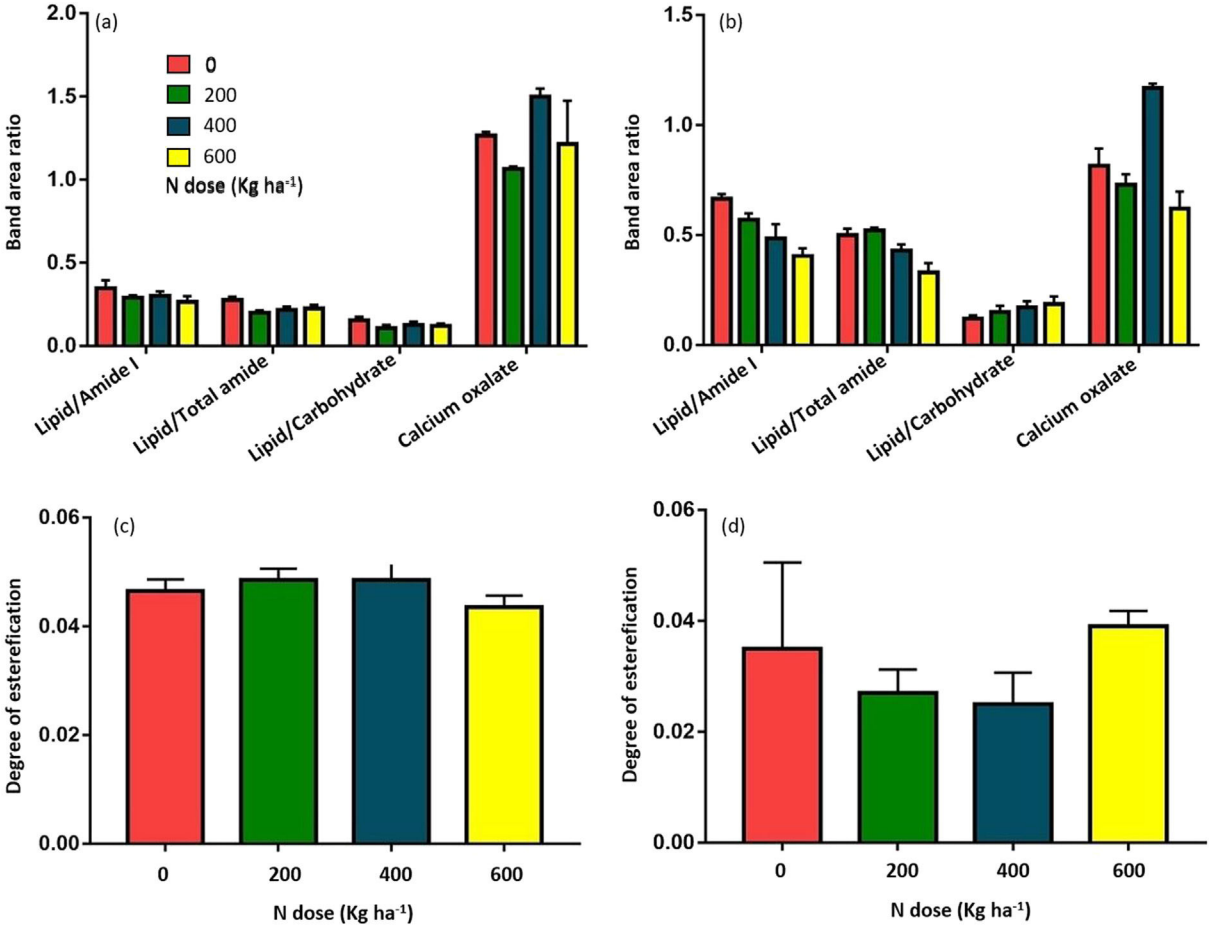

Fig. 4. Selected band area ratio of Lipid (3000–2800)/Amide I (1705–1575), Lipid (3000–2800)/Total Amide (1705–1480)+(1350–1240), Lipid (3000–2800)/Carbohydrates (1200–900) and Calcium oxalate (1318/2922) of (a) *P. angulata* and (b) *P. peruviana*, and degree of esterification of (c) *P. angulata* (d) and *P. peruviana* leaves.

lipids bands in wheat leaves due to magnetic field treatment. Since amides are major chemical structures for nitrogen storage in plants, the primary and secondary amides are the dominant forms of nitrogen, which synthesize amino acids and other macromolecules for plant metabolism and growth and development [10,35,36]. Baseri and Baker [47] describe the crucial role of protein of medicinal plants using FTIR. Wu et al. [10] studied the role of amide protein in diagnostic nitrogen metabolism concerning yield in the rice leaves using FTIR. Movasaghi et al. [48] studied the cell's protein content to analyze physiological phases of a cell's role in maintaining homeostasis in plants. Wu et al. [10] studied the role of amide protein in the rice leaves using FTIR. Considering the above discussion our results using FSD show under nitrogen supplements the proteins are very sensitive than lipids.

In the case of *P. peruviana* the band area of CH_2 group 2851 cm^{-1}, 2924 cm^{-1} decreases for all nitrogen treatment. Further decrease in CH_2/CH_3 ratio is observed indicating the lipid peroxidation which is considered as a biomarker of a plant under nitrogen fertilization. influences. Sharma and Uttam [49] studied the change in the band are of CH_3 and CH_2 group due to TiO_2 nanoparticles resulting in lipid peroxidation studied using FTIR spectra. This indicates lipid peroxidation due to nitrogen treatment. But for *P. angulata* has no significant changes occurs in 400 Kg ha^{-1} of N and 600 Kg ha^{-1} of N reflecting nitrogen fertilization is used for consistent improvement in protein in leaf for its growth performance. This was confirmed from band area measurement in the amide I bands.

3.4. Fourier self deconvolution deduced by curve fitting analysis in the amide I region of Physalis L. species exposed to nitrogen fertilization treatment

Fourier self deconvolution in the amide region of protein 1700–1600 cm^{-1} is shown in Fig. SF2 for physalis species. The band area of secondary structural changes is reported in Table S2. In the case of *P. angulata*, 7 peaks are observed whereas for *P. peruviana* 8 peaks were deduced from Fourier self deconvolution techniques. The peak at 1630 cm^{-1} is assigned to ß sheet structure and 1692 cm^{-1} is assigned to ß turn sturcture. Our results agree with other studies reported by Wolkers et al. [50] and Lahlai et al. [51] and Usoltsev et al. [52].

The α helix relates to the band at 1651 and 1661 cm^{-1}. Contribution to ß turn and pectin arises at 1669 and 1613 cm^{-1}. The measure total band area of ß sheet decreases whereas the increase in α helix was noted due to nitrogen treatments. It shows that ß sheet decreases by 40% reduction for 200 Kg ha^{-1} of N and 400 Kg ha^{-1} of N and where 34% for 600 Kg ha^{-1} of N when compared to control. The increase in α helix noted for 400 Kg ha^{-1} of N & 600 Kg ha^{-1} of N except for 200 Kg ha^{-1} of N for both the plant species studied.

As seen from Table S2, *P. peruviana* plant leaves show the peak at 1625 cm^{-1}, 1637 cm^{-1} 1669 cm^{-1}& 1674 cm^{-1} arise from ß sheet structure. The peak at 1646 $cm^{-1}$and 1653 cm^{-1} is due to α helix structure [43]. The ß turn structure arises at 1682 cm^{-1}. This change in the ß sheet structure is considered to be denatura-

tion of the protein. Similarly, in the case of *P. peruviana* leave samples shows an initial 200 Kg ha^{-1} of N treatment triggers total ß sheet variation by 7% followed by a decrease of 9–13% for 400 and 600 Kg ha^{-1} of N treatment when compared to control. 400 Kg ha^{-1} of N treatment shows consistency in secondary structural changes. Interestingly for this treatment, no significant or minimum variation of ß sheet and α helix was observed. This shows lipids supports for an ideal generation of protein for the development of plant which enriches in *Physalis* L. species studied. This was supported from the Lipid/Total amide band area ratio reported in our earlier sections.

The presence of α helix structure protects the bulk proteins due to influence nitrogen fertilization which results in effective growth for 400 Kg ha^{-1} of N treatments. Wolkers et al. [53] studied the similar effects of an increase in α helix and a decrease in ß sheet structure in the pollen grain using FTIR due to heat resistance. Lahlali et al. [51] reported higher amounts of α helix than ß sheet in the pollen grains due to heat stress studied using FTIR technique.

3.5. 2D COS dimensional correlation spectral analysis of Physalis L. species exposed to nitrogen supplements

The 2D COS FTIR is a good technique in the process of monitoring biochemical changes due to nitrogen fertilization. The synchronous and asynchronous correlation maps developed by Noda [20,22] allow changes due to interaction in the complex structure. In synchronous spectra of *P. angulata* and *P. peruviana* sample, the auto peaks describe the total changes under the influence of nitrogen fertilization.

The most prominent changes in the intensity of the bands are seen at spectral ranges 3000–2800 cm^{-1}, 1800–900 cm^{-1}. So 2D correlation analysis performed in this given region [1,54]. The positive cross peak appears to indicate a simultaneous increase or decrease of intensities of two variables. The –ve cross peak shows that decrease of intensity of one variable with others. The asynchronous maps of the plant leaves show changes sequence corresponding to the variable under the influence of external perturbation.

The synchronous maps of both species are shown in Fig. 5 and the peak assigned are listed in Tables 2 and 3, respectively. Synchronous maps of both *P. angulata* and *P. peruviana* leaves (Fig. 5) shows one strong auto peaks appears at 1040 cm^{-1} due to C-O & C-C stretching of hemicellulose and 1056 cm^{-1} of C-OH bending respectively which indicates the presence of cellulose with crystalline domains. In the case of *P. peruviana* there appear the less intense +ve cross-peaks. This shows cellulose band of leaf *P. peruviana* leaf changing similarly with Amide +(1056, 1628), polysaccharides (1056, 1380), and CH_2 bending cellulose pectin at (1056, 1318) and pectin (1056, 1095).

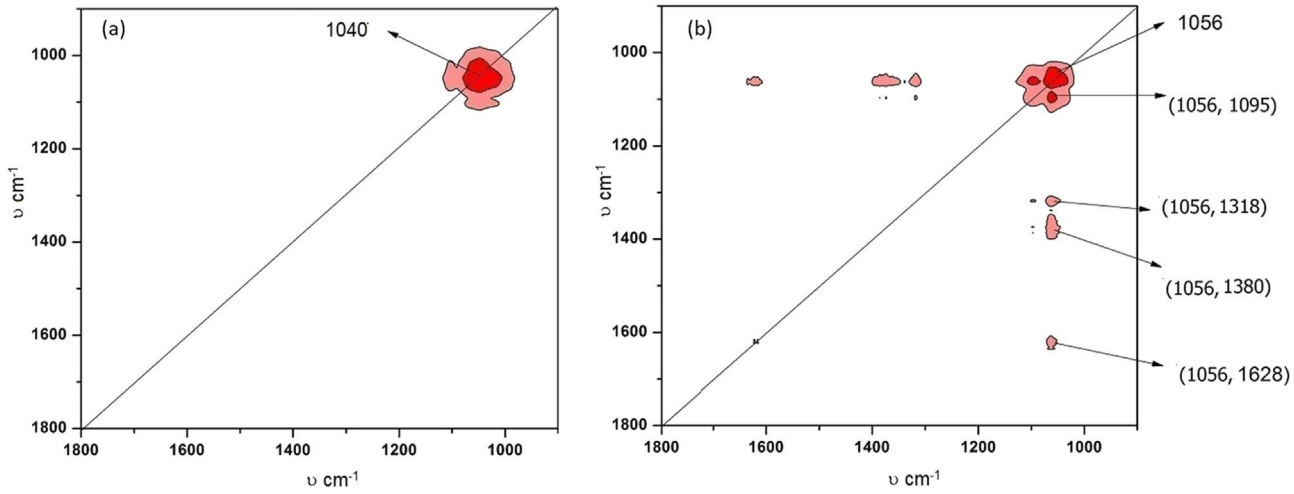

Fig. 5. Synchronous 2DCOS spectra obtained in the region 1800–1000 cm^{-1} of (a) *P. angulata* leaves; (b) *P. peruviana* leaves.

Table 2
Synchronous and asynchronous 2D correlation cross peaks and their assignments for *P. angulata* samples.

Synchronous Auto Peaks		Assignment	Asynchronous	Cross Peaks	Assignment
1040			υC-O, C-C hemicellulose	+(1040, 1582)	Amide II Proteins
			υC-O, C-C hemicellulose	+(1040, 1413)	Carboxylate; Asp Glu, COO Sym stretching
			υC-O, C-C hemicellulose	+(1040, 1334)	δ CH2, Cellulose
			υC-O, C-C hemicellulose	+(1040, 1196)	C-OH deformation & C-O stretching phenolic group
			Non Crystalline polysaccharide	−(908, 1039)	C-O stretching Cellulose
			COO^- Symm Stretching carboxylate	−(1393, 1646)	Amide I proteins
C-H Stretching, Cellulose	+(1709, 3298)	Hydroxyl contribution υ OH, υNH	Cellulose	+(1053, 3300)	Hydroxyl contribution υ OH, υNH
Polysaccharides υ C-O	+(1065, 3298)	Hydroxyl contribution υ OH, υNH			

The asynchronous maps of *P. angulata* and *P. peruviana* are shown in Fig. 6. The asynchronous map of *P. angulata* leaf shows several intense + and –ve cross-peaks. It is noted from the cross-peaks hemicellulose begins changes followed by Amide II proteins +(1040, 1582), carboxylate (1040, 1413), δCH_2 cellulose (1040, 1334) and phenolic group (1040, 1196) cm^{-1} due to nitrogen treatment. Changes in non-crystalline polysaccharides at 908 cm^{-1} occur after cellulose at 1039 cm^{-1} due to nitrogen treatment -(908, 1039). The observation from infrared region results primarily from the chlorophyll molecules masking suppressing the other bands which can be revealed by 2D FTIR spectra in the region 1800–800 cm^{-1}. The band at 1393 cm^{-1} assigned to COO^-symmetric stretching of carboxylates changes after that of amide I of proteins. The asynchronous maps of *P. peruviana* show both + and –ve cross-peaks. The positive cross-peaks that corresponds to cellulose begins changes followed by Amide I of proteins +(1051, 1622), xyloglucan (1051, 1364), and CH_2 bending of cellulose (1051, 1322). The negative cross-peaks show cellulose occurs after pectin – (994, 1095) and C-O & C-C stretching of cellulose – (994, 1058) respectively.

3.6. 2D hetero correlation analyses of Physalis L. species exposed to nitrogen supplements

The 2D hetero correlation in the ranges 3500–2700 cm^{-1} and 1900–900 cm^{-1} for *P. angulata* and *P. peruviana* are shown in Fig. 7. Synchronous 2D hetero correlation for both physalis species shows +ve crosses peaks. In the case of *P. angulata* leaves due to nitrogen fertilizer treatment bands at 1709 cm^{-1}, 1065 cm^{-1} of cellulose and polysaccharides are correlated with OH, NH stretching

Table 3
Synchronous and asynchronous 2D correlation cross peaks and their assignments for *P. peruviana* samples.

Synchronous Auto Peaks	Assignment		Asynchronous Assignment	Cross Peaks	Assignment
1056	Cellulose		Cellulose C-O-H bending	+(1051, 1622)	Amide II Proteins
Assignment	Cross Peaks	Assignment	Cellulose C-O-H bending	+(1051, 1364)	δ CH2, Cellulose
Cellulose	+(1056, 1628)	Amide I proteins	Cellulose C-O-H bending	+(1051, 1322)	C-OH deformation & C-O stretching phenolic group
	+(1056, 1380)	CH_2 bending Polysaccharides	υ C-O, υ C-C Cellulose	–(994, 1095)	C-O & C-C stretching pectin
	+(1056, 1318)	CH_2 bending Cellulose	υ C-O, υ C-C Cellulose	(994, 1058)	Cellulose C-O & C-C stretching C-O-H bending
	+(1056, 1095)	υC-O, C-C pectin			
υC-O, υC-C hemicellulose	+(1040, 3299)	Hydroxyl contribution υ OH, υNH	Keto C=O Chlorophyll	–(1703, 3296)	Hydroxyl contribution υ OH, υNH
υC-O, υC-C hemicellulose	+(1040, 2922)	CH_2 assym stretch lipids	Cell wall polysaccharides C-H bending	–(1431, 3296)	Hydroxyl contribution υ OH, υNH
			CH2 bending polysaccharides	–(1362, 3296)	Hydroxyl contribution υ OH, υNH
			C-O stretching pectin	–(1113, 3296)	Hydroxyl contribution υ OH, υNH
			Xyoglucan C-O; C-C stretching	–(1070, 3296)	Hydroxyl contribution υ OH, υNH
			Chlorophyll	–(1703, 2917)	CH2 assym stretching of lipids
			Cell wall polysaccharides	–(1431, 2917)	CH2 assym stretching of lipids
			CH2 bending polysaccharides	–(1362, 2917)	CH2 assym stretching of lipids
			Pectin	–(1113, 2917)	CH2 assym stretching of lipids
			δ C-O hemicellulose	–(1070, 2917)	CH2 assym stretching of lipids
			δ C-O hemicellulose	–(1070, 2857)	CH2 sym Stretching lipids, proteins carbohydrates

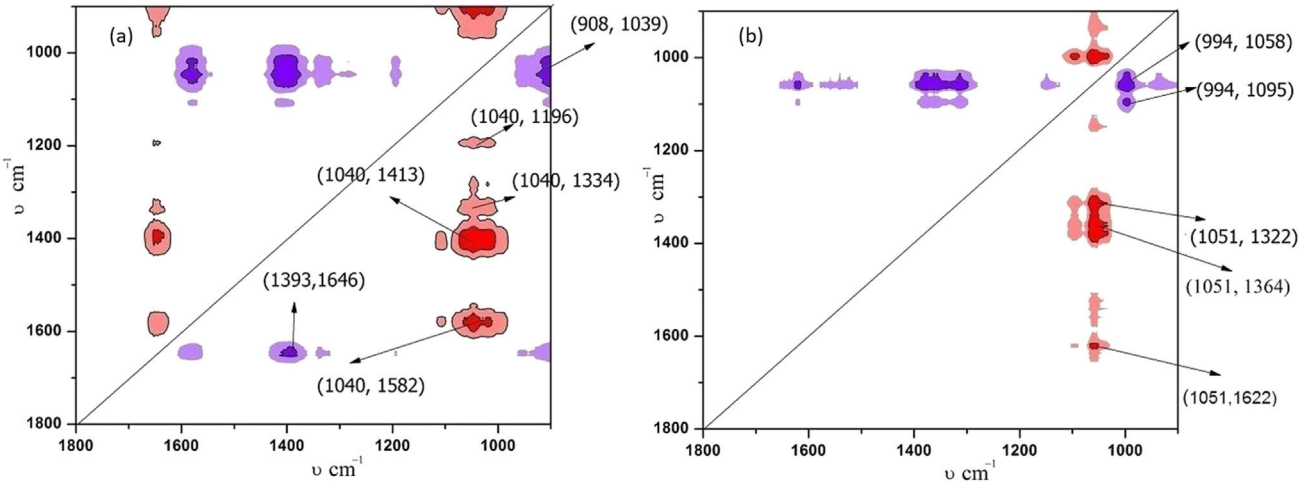

Fig. 6. Asynchronous 2DCOS spectra obtained in the region 1800–1000 cm^{-1} of (a) *P. angulata* leaves (b) *P. peruviana* leaves.

of vibrations near 3298 cm^{-1} (Fig. 7 a). The hetero correlations maps of *P. peruviana* samples indicate hemicellulose at 1040 cm^{-1} is correlated with OH/NH of 3229 cm^{-1} and CH_2 asymmetric stretching of lipids at 2922 cm^{-1} (Fig. 7 b).

Asynchronous 2D hetero correlation maps are studied in the region of 3500–2700 cm^{-1} and 1900–900 cm^{-1} for *P. angulata* and *P. peruviana* plant samples. *P. angulata* leaves show one +ve cross-peaks illustrates that cellulose bands at 1053 cm^{-1} occur

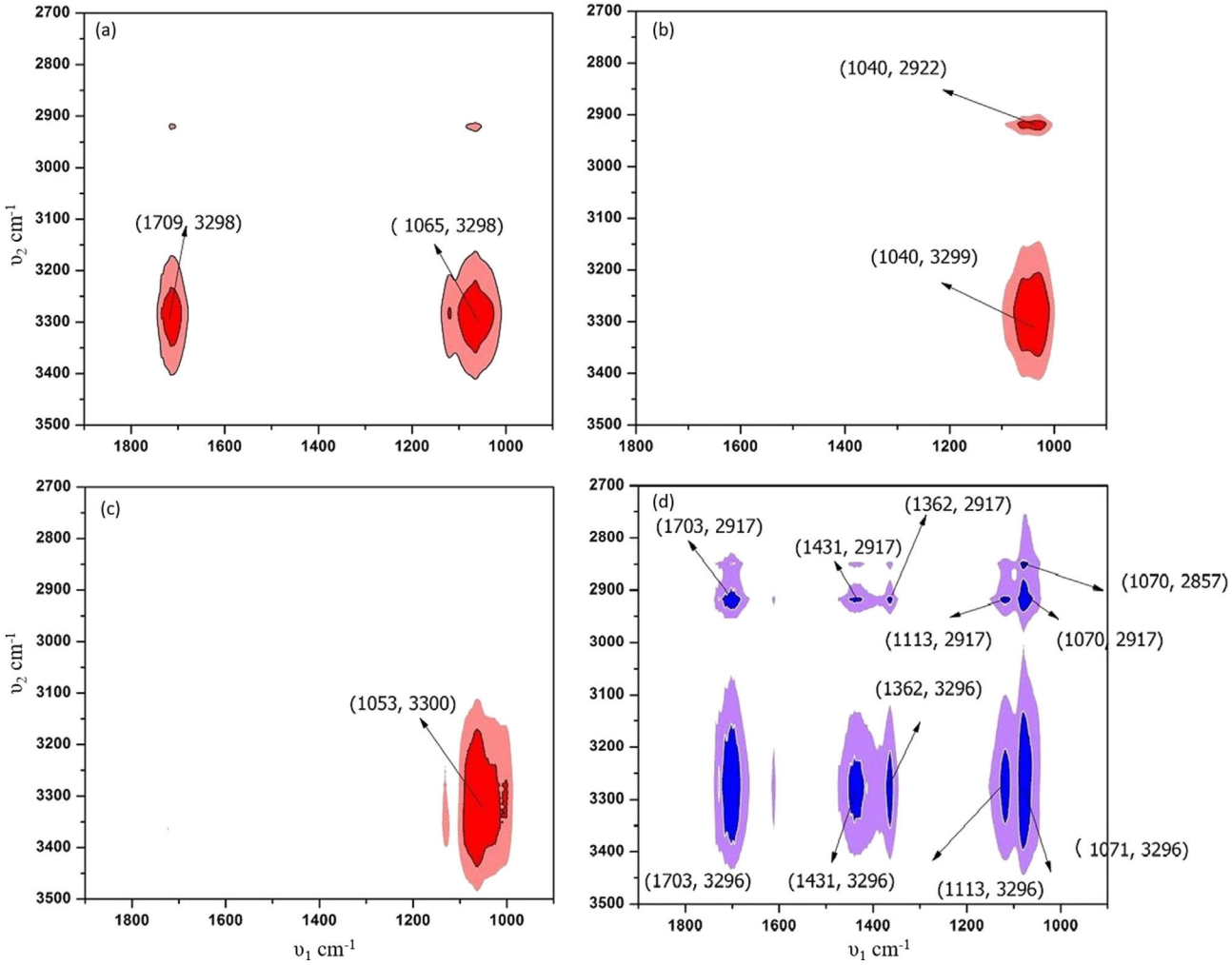

Fig. 7. 2D hetero correlation spectra of *Physalis* species: (a) Synchronous *P. angulata* leaves; (b) Synchronous *P. peruviana* leaves; (c) asynchronous *P. angulata* and (d) asynchronous *P. peruviana*.

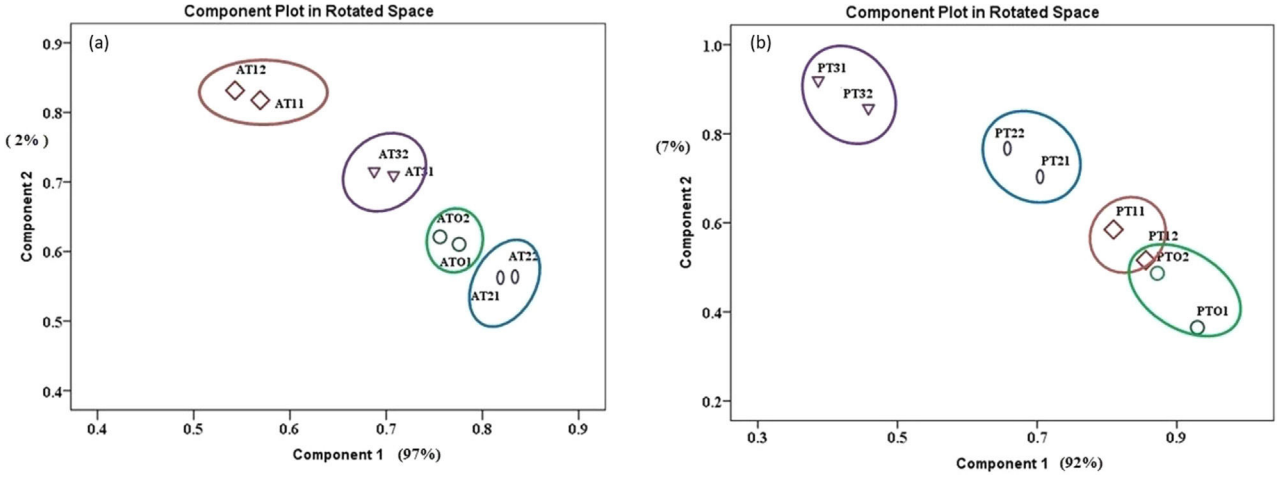

Fig. 8. PCA scatter plots of *Physalis* L. species: (a) *Physalis angulata* leaves and (b) *Physalis peruviana* leaves.

ahead of OH/NH stretching observed near 3300 cm^{-1} (Fig. 7 c). Asynchronous 2D hetero correlation of *P. peruviana* leaves shows –cross-peaks (Fig. 7d). The bands at 3296 cm^{-1} due OH/NH stretching changes before corresponding to chlorophyll 1703 cm^{-1}, polysaccharides 1431 cm^{-1} CH_2 bending polysaccharides 1362 cm^{-1}, pectin 1113 cm^{-1} and xyloglucan C-O; C-C stretching at 1071 cm^{-1}. The CH_2 asymmetric lipids bands observed at 2917 cm^{-1} changes before chlorophyll 1703 cm^{-1}, 1431 cm^{-1} cell wall polysaccharides, 1362 cm^{-1} CH_2 bending polysaccharides, pectin at 1113 cm^{-1} and hemicellulose at 1070 cm^{-1}.

Also peak of CH_2 symmetric of stretching of lipids 2857 cm^{-1} changes before hemicellulose at 1070 cm^{-1}. 2D hetro correlation of *P. angulate* leaves shows +ve major changes occur at cellulose 1709 cm^{-1} followed by hydroxyl contribution (1070, 3298). In the case of *P. peruviana* leaves -ve cross shows changes occur first at 2917 cm^{-1} due to CH_2 asymmetric stretching of lipids followed by chlorophyll, polysaccharides, pectin, and amide I of proteins. This indicates lipids changes predominates due to nitrogen fertilization which was not revealed form 1D FTIR spectra. Research shows that lipid compounds vary with plant genotypes and

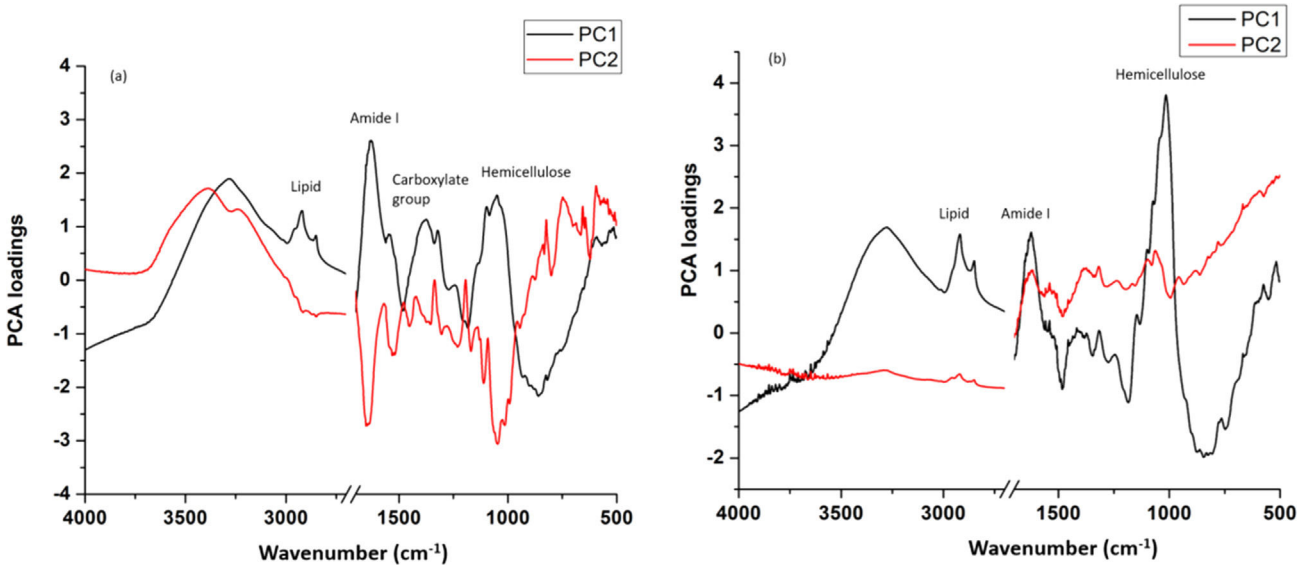

Fig. 9. Variation of the factor loading obtained from the PCA with the corresponding wave number of the *Physalis* L. species: (a) *Physalis angulata* leaves and (b) *Physalis peruviana* leaves.

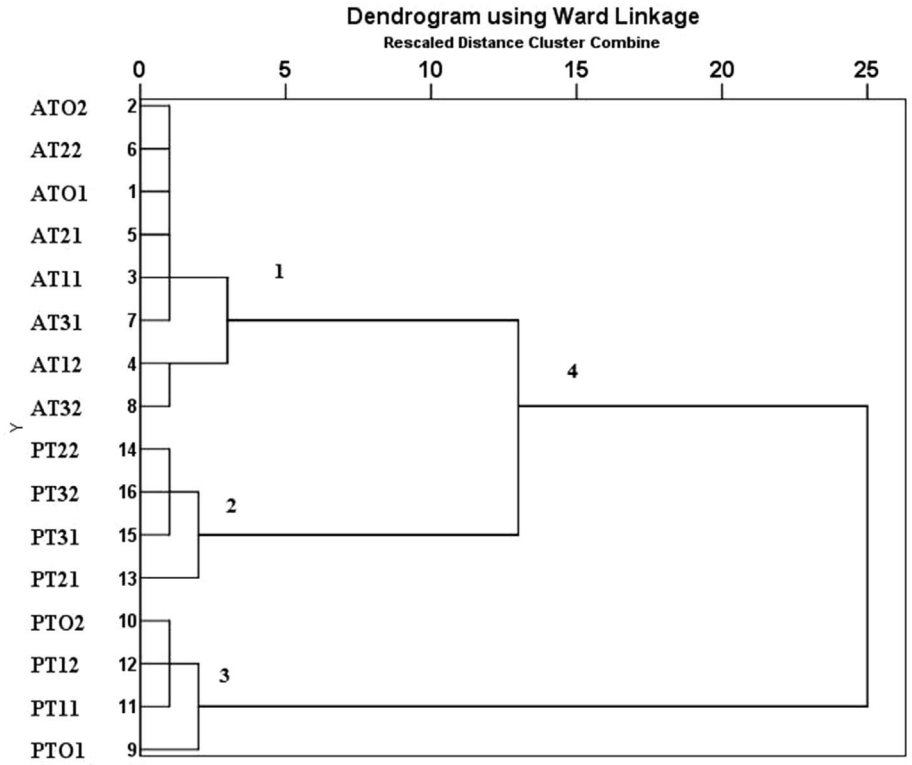

Fig. 10. Dendogram of physalis species populations treated with various nitrogen treatment showing group linkage obtained using ward algorithm.

according to nitrogen fertilization [55,56], besides, the mobilization of reserve lipids and other underlying processes are dependent on the relationship C/N [57].

3.7. Principle component analysis (PCA) of Physalis L. species exposed to nitrogen supplements

PCA is used to reduce smaller important variables from a large number of variables. PCA analysis of *P. angulata* and *P. peruviana* leaves shows clear discrimination of samples due to nitrogen treatments which are shown in score plots (Fig. 8). The plots are used to diagnosis the spectral variation due to biochemical changes. The output of the PCA results has three principle components. The first component PC1 obtained having higher variation and the second component PC2 has lower variation. The third component is neglected because of the least variation. In the case for *P. angulata* corresponds to PC1 of 97% variation and PC2 of 2% variation. *P. peruviana species* have PC1 (92%) and PC2 (7%). The score plots of PCA shows the highest eigenvalue for 400 kg of N treatment and lowest value for 200 kg of N treatment in *P. angulata*. *P. peruviana* samples show the control sample's highest eigenvalue followed by nitrogen treatment of increasing order. This difference in variation of existing in the species is due to variation in biochemical compositional changes occurring in response to nitrogen fertilization. Fig. 9 shows PCA loading Vs wavenumber for the *Physalis* L. species. From the PCA loading graph of *P. angulata* (Fig. 9a) the highest loading value corresponds to amide proteins followed by hemicellulose and lipids. Whereas in the graph of *P. peruviana it is* hemicellulose followed by proteins and lipids (Fig. 9b). This shows hemicellulose and proteins have a major contribution to data variation followed by lipids. This was well supported by the variation occurring the FTIR spectra of region 1700–1000 cm^{-1} (carbohydrates) as revealed from 2DCOS spectra.

3.8. Hierarchical cluster analysis of Physalis L. species exposed to nitrogen supplements

Fig. 10 shows the results of the hierarchical cluster analysis of *Physalis* L. species exposed to different nitrogen supplements. Cluster 1 results from a grouping of 2 sub-clusters in *Physalis angulata* which are closely separated. Cluster 2 results in the grouping of all *Physalis peruviana* with 3 sub-cluster with higher dissimilarity range from 4 to 9 as shown in Fig. 11. Cluster 3 corresponds to the distinct separation of two *Physalis* L. species studied having higher dissimilarity values. The results of the study show two species *P. angulata* and *P. peruviana* are well clustered within the same species and well separated among different spe-

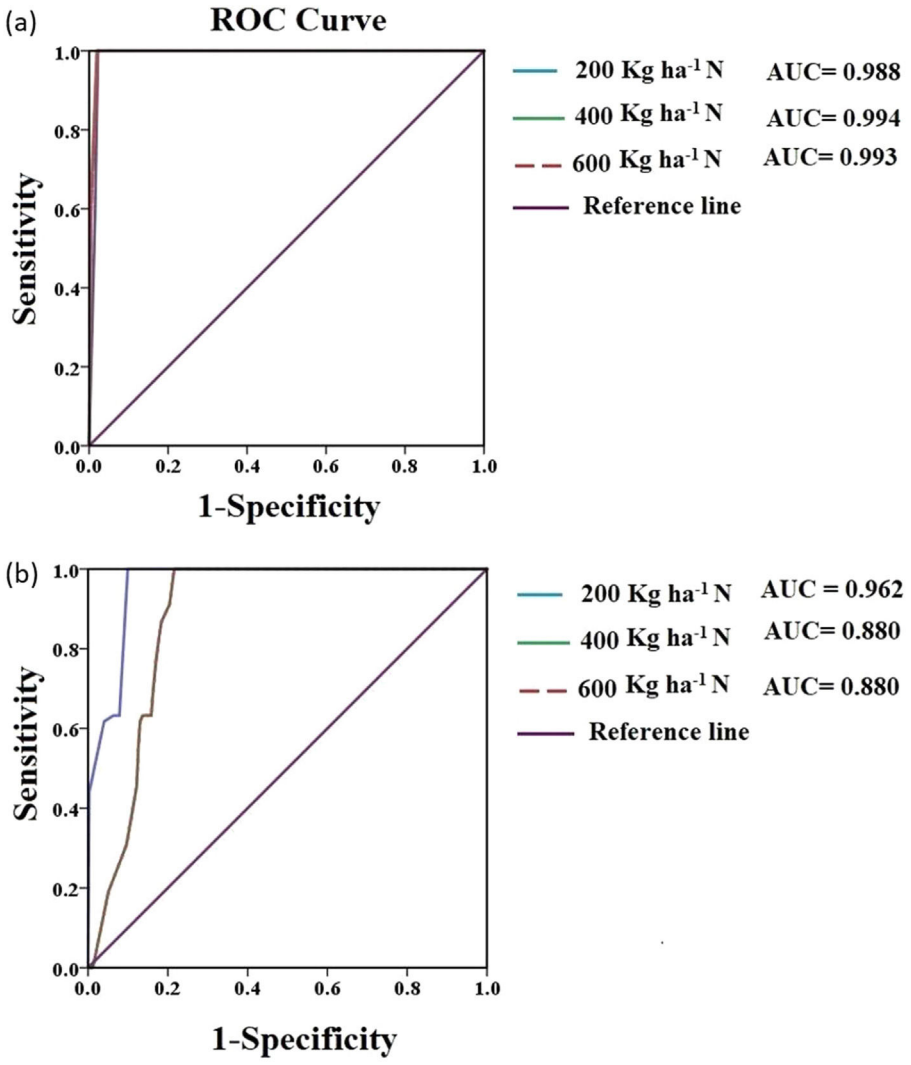

Fig. 11. Receiver operation characteristics curve of *Physalis* species treated with various nitrogen treatment: (a) *Physalis angulata* and (b) *Physalis peruviana*.

cies with high dissimilarity values which are reflected in the dendrogram.

3.9. Receiver operation characteristics (ROC) analysis of Physalis L. species exposed to nitrogen supplements.

ROC analysis helps to compare the overall efficiency of different experimental outcomes. The test is evaluated as a potential threshold separating different nitrogen treatments form control taken as a reference value (Fig. 11). For a given test a clear cut point exists above which the upper left-hand portion of the graph. This region of a curve that provides high sensitivity and specificity [58]. The lower left-hand side of the curve shows the ineffectiveness of the test. The measured area under the curve (AUC) in the upper left-hand side gives the information of higher reliability of the test having large value. The measured AUC test for our experiments ranges from 0.84 to 0.92 which is fairly high. This confirms the overall reliability of the study carried out in hence arriving better conclusion with low cost from the available experimental data.

4. Conclusions

The use of the FTIR technique, associated with deconvolution analysis, two-dimensional correlation spectroscopy, can identify changes in the composition of leaves of physalis species due to nitrogen doses. This constitutes a fast and precise method for the acceptable management of this fertilization. The computed band area ratio of lipid/amide, lipid/carbohydrates, degree of esterification, and calcium oxalate shows nitrogen fertilization due to 400 Kg ha^{-1} of N treatment is more effective for a better quality of yield. 2D correlation spectra show cellulose and pectin begins changes followed by amide of proteins due to nitrogen treatment in *P. peruviana* samples. The *P. angulata* plants show hemicellulose changes predominating followed by proteins and polysaccharides. These studies suggest that 2D correlation spectral analysis provides a biochemical change in *Physalis* L. species due to nitrogen treatment, which cannot be revealed from 1D FTIR spectra. The obtained loading plots from PCA show protein is predominant in influencing variation in both the samples followed by lipids and carbohydrates, especially for *P. peruviana* samples. These findings demonstrate the use of 2D COS analysis with chemometric and ROC is effective in studying the alteration in the composition of major cellular components in herbal plants.

CRediT authorship contribution statement

Romeu da Silva Leite: Conceptualization, Methodology, Investigation, Writing - review & editing. **Sivakumaran Karthikeyan:** Investigation, Formal analysis, Writing - original draft, Writing - review & editing. **Salvador Hernandéz-Navarro:** Project administration, Conceptualization, Resources. **Marilza Neves do Nascimento:** Project administration, Conceptualization, Writing - original draft. **Norlan Miguel Ruiz Potosme:** Conceptualization, Methodology, Supervision. **Paula Carrión-Prieto:** Methodology, Investigation, Supervision. **Elma dos Santos Souza:** Methodology, Supervision.

Declaration of Competing Interest

The authors declare that they have no known competing financial interests or personal relationships that could have appeared to influence the work reported in this paper.

Acknowledgment

This study was financed in part by Coordenação de Aperfeiçoamento de Pessoal de Nível Superior – Brasil (CAPES) – Finance Code 001. A special acknowledgment to the Special Advisory of Institutional Relations (AERI/UEFS).

Appendix A. Supplementary data

Supplementary data to this article can be found online at https://doi.org/10.1016/j.saa.2020.119220.

References

[1] P. Moskal, A. Wesełucha-Birczyńska, M. Łabanowska, M. Filek, Adaxial and abaxial pattern of *Urtica dioica* leaves analyzed by 2DCOS ATR-FTIR as a function of their growth time and impact of environmental pollution, Vib. Spectrosc. 104 (2019) 102948, https://doi.org/10.1016/j.vibspec.2019.102948.
[2] V. Lionetti, F. Cervone, D. Bellincampi, Methyl esterification of pectin plays a role during plant–pathogen interactions and affects plant resistance to diseases, J. Plant Physiol. 169 (2012) 1623–1630, https://doi.org/10.1016/j.jplph.2012.05.006.
[3] H. Le Gall, F. Philippe, J.-M. Domon, F. Gillet, J. Pelloux, C. Rayon, Cell wall metabolism in response to abiotic stress, Plants 4 (2015) 112–166, https://doi.org/10.3390/plants4010112.
[4] V.R. Franceschi, P.A. Nakata, Calcium oxalate in plants: formation and function, Annu. Rev. Plant Biol. 56 (2005) 41–71, https://doi.org/10.1146/annurev.arplant.56.032604.144106.
[5] V.R. Franceschi, H.T. Horner, Calcium oxalate crystals in plants, Bot. Rev. 46 (1980) 361–427, https://doi.org/10.1007/BF02860532.
[6] S. Wood, D. Karp, F. Declerck, C. Kremen, S. Naeem, C. Palm, Functional traits in agriculture agrobiodiversity and ecosystem services, Trends Ecol. Evol. 30 (2015) 531–539, https://doi.org/10.1016/j.tree.2015.06.013.
[7] K. Herz, S. Dietz, S. Haider, U. Jandt, D. Scheel, H. Bruelheide, Drivers of intraspecific trait variation of grass and forb species in German meadows and pastures, J. Veg. Sci. 28 (2017) 705–716, https://doi.org/10.1111/jvs.12534.
[8] R. Rana, K. Herz, H. Btuelheide, S. Dietz, S. Haider, U. Jandt, R. Pena, Leaf attenuated total reflection Fourier Transform Infrared (ATR-FTIR) biochemical profile of grassland plant species related to land use intensity, Ecol. Ind. 84 (2018) 803–810, https://doi.org/10.1016/j.ecolind.2017.09.047.
[9] J.B. Morgan, E.L. Connolly, Plant-soil interactions: nutrient uptake, Nat. Educ. Knowledge 4 (2013) 2.
[10] K. Wu, C. Du, F. Ma, Y. Shen, D. Liang, J. Zhou, Rapid diagnosis of nitrogen status in rice based on Fourier transform infrared photoacoustic spectroscopy (FTIR-PAS), Plant Methods 15 (2019) 94, https://doi.org/10.1186/s13007-019-0482-0.
[11] J.K. Ladha, G.J.D. Kirk, J. Bennett, S. Peng, C.K. Reddy, P.M. Reddy, U. Singh, Opportunities for increased nitrogen-use efficiency from improved lowland rice germplasm, Field Crops Res. 56 (1998) 41–71, https://doi.org/10.1016/S0378-4290(97)00123-8.
[12] Y. Wang, D.J. Wang, P.H. Shi, K. Omasa, Estimating rice chlorophyll content and leaf nitrogen concentration with a digital still color camera under natural light, Plant Methods 10 (2014) 36, https://doi.org/10.1186/1746-4811-10-36.
[13] L. Corte, P. Rellini, L. Roscini, F. Fatichenti, G. Cardinali, Development of a novel, FTIR (Fourier transform infrared spectroscopy) based, yeast bioassay for toxicity testing and stress response study, Anal. Chim. Acta 659 (2010) 258–265, https://doi.org/10.1016/j.aca.2009.11.035.
[14] C. Berthomieu, R. Hienerwadel, Fourier transforms infrared FTIR spectroscopy, Photosynth. Res. 101 (2009) 157–170, https://doi.org/10.1007/s11120-009-9439-x.
[15] B. Ribeiro da Luz, Attenuated total reflectance spectroscopy of plant leaves: a tool for ecological and botanical studies, New Phytol. 172 (2006) 305–318, https://doi.org/10.1111/j.1469-8137.2006.01823.x.
[16] C. Meinen, R. Rauber, Root discrimination of closely related crop and weed species using FT MIR-ATR spectroscopy, Front. Plant Sci. 6 (2015) 765, https://doi.org/10.3389/fpls.2015.00765.
[17] O. Vargas-Ponce, J.S. Martínez, M.P.Z. Tavares, L.E.V. Mares, Traditional management of a small-scale crop of *Physalis angulata* in Western Mexico, Genet. Resour. Crop Evol. 63 (2016) 1383–1395, https://doi.org/10.1007/s10722-015-0326-3.
[18] R.S. Leite, S. Hernandéz-Navarro, M.N. Nascimento, N.M.R. Potosme, P. Carrión-Prieto, E.S. Souza, Nitrogen fertilization affects Fourier Transform Infrared spectra (FTIR) in *Physalis* L. species, Comput. Electron. Agric. 150 (2018) 411–417, https://doi.org/10.1016/j.compag.2018.05.021.
[19] S. Karthikeyan, R. Easwaran, Analysis of a curve fitting model in the amide region applied to the muscle tissues of an edible fish: *Labeo rohita* fingerlings, J. Bio. Phy. Chem. 13 (2013) 125–130, https://doi.org/10.4024/13KA13A.jbpc.13.04.
[20] I. Noda, Generalized two-dimensional correlation method applicable to infrared, raman, and other types of spectroscopy, Appl. Spectrosc. 47 (1993) 1329–1336, https://doi.org/10.1366/0003702934067694.

[21] I. Noda, A.E. Dowrey, C. Marcoli, G.M. Story, Y. Ozaki, Generalized two-dimensional correlation spectroscopy, Appl. Spectrosc. 54 (2000) 236A, https://doi.org/10.1366/0003702001950454.
[22] I. Noda, Y. Ozaki, Two-dimensional correlation spectroscopy and applications in vibrational and optical spectroscopy, John Wiley and Sons, Chichester, 2004.
[23] Y. Wang, P. Zhang, M. Li, Z. Guo, S. Ullah, Y. Rui, I. Lynch, Alleviation of nitrogen stress in rice (*Oryza sativa*) by ceria nanoparticles, Environ. Sci. Nano 7 (2020) 2930–2940, https://doi.org/10.1039/D0EN00757A.
[24] F.-Y. Zhu, M.-X. Chen, W.-L. Chan, F. Yang, Y. Tian, T. Song, L.-J. Xied, Y. Zhoud, S. Xiaod, J. Zhang, C. Lo, SWATH-MS quantitative proteomic investigation of nitrogen starvation in Arabidopsis reveals new aspects of plant nitrogen stress responses, Proteomics 187 (2018) 161–170, https://doi.org/10.1016/j.jprot.2018.07.014.
[25] R.S. Leite, T.T. Tanan, M.N. Nascimento, L.M. Oliveira, P.A.S. Abreu, Hydroponic cultivation of *Physalis angulata* L.: growth and production under nitrogen doses, Pes. Agropec. Trop. 47 (2017) 145–151, https://doi.org/10.1590/1983-40632016v4744652.
[26] S.T. Gorgulu, M. Dogan, F. Severcan, The Characterization and differentiation of higher plants by Fourier Transform Infrared Spectroscopy, Appl. Spectrosc. 61 (2007) 300–308, https://doi.org/10.1366/000370207780220903.
[27] P. D'Souza, M.P. Divya Devi, C.G. Naik Shridhar, Use of Fourier Transform Infrared (FTIR) spectroscopy to study cadmium-induced changes in *Padina tetrastromatica* (Hauck), Anal. Chem. Insights (2008, 2008,) 135–143.
[28] E. Skotti, S. Kountouri, P. Bouchagier, D.I. Tsitsigiannis, M. Polissiou, P.A. Tarantilis, FTIR spectroscopic evaluation of changes in the cellular biochemical composition of the phytopathogenic fungus *Alternaria alternata* induced by extracts of some Greek medicinal and aromatic plants, Spectrochim. Acta A 127 (2014) 463–472, https://doi.org/10.1016/j.saa.2014.02.113.
[29] Z. Wei, D. Jiao, J. Xu, Using Fourier Transform Infrared Spectroscopy to study effects of magnetic field treatment on wheat (*Triticum aestivum* L.) seedlings, J. Spectrosc. 2015 (2015) 570190, https://doi.org/10.1155/2015/570190.
[30] G. Janicsák, I. Mathé, V. Miklóssy-Vári, G. Blunden, Comparative studies of the rosmarinic and caffeic acid contents of Lamiaceae species, Biochem. Syst. Ecol. 27 (1999) 733–738, https://doi.org/10.1016/S0305-1978(99)00007-1.
[31] J.C. Fernandes, P. García-Angulo, L.F. Goulao, J.L. Acebes, S. Amâncio, Mineral stress affects the cell wall composition of grapevine (*Vitis vinifera* L.), Plant Sci. 205–206 (2013) 111–120, https://doi.org/10.1016/j.plantsci.2013.01.013.
[32] N. Liu, C. Karunakaran, R. Lahlali, T. Warkentin, R.A. Buecker, Genotypic and heat stress effects on leaf cuticles of field pea using ATR-FTIR spectroscopy, Planta 249 (2019) 601–613, https://doi.org/10.1007/s00425-018-3025-4.
[33] I. Cechin, É.M. Valquilha, Nitrogen effect on gas exchange characteristics, dry matter production and nitrate accumulation of *Amaranthus cruentus* L, Braz. J. Bot. 42 (2019) 373–381, https://doi.org/10.1007/s40415-019-00542-1.
[34] O.R. Zandvakili, A.V. Barker, M. Hashemi, F. Etemadi, W.R. Autio, S. Weis, Growth and nutrient and nitrate accumulation of lettuce under different regimes of nitrogen fertilization, J. Plant Nutr. 42 (2019) 1575–1593, https://doi.org/10.1080/01904167.2019.1617313.
[35] C.L. Cao, S.X. Li, Effects of N form on some physiological characteristics and yield of wheat during the vegetative and reproductive growth stage, Acta Agron. Sin. 29 (2003) 258–262.
[36] H.M. Lam, K.T. Coschigano, I.C. Oliveira, R. Melo-Oliveira, G.M. Coruzzi, The thermolecular-genetics of nitrogen assimilation into amino acids in higher plants, Annu. Rev. Plant Phys. 47 (1996) 569–593, https://doi.org/10.1146/annurev.arplant.47.1.569.
[37] B. Benedek, N. Gjoncaj, J. Saukel, B. Kopp, Distribution of phenolic compounds in middleeuropean taxa of the *Achillea millefolium* L. aggregate, Chem. Biodivers. 4 (2007) 849–857, https://doi.org/10.1002/cbdv.200790072.
[38] S.-J. Wu, S.-P. Chang, D.-L. Lin, S.-S. Wang, F.-F. Hou, L.-T. Ng, Supercritical carbon dioxide extract of *Physalis peruviana* induced cell cycle arrest and apoptosis in human lung cancer H661 cells, Food Chem. Toxicol. 47 (2009) 1132–1138, https://doi.org/10.1016/j.fct.2009.01.044.
[39] N. Carniel, R.M. Dallago, C. Dariva, J.P. Bender, A.L. Nunes, O. Zanella, D. Bilbio, W. Luiz Priamo, Microwave-assisted extraction of phenolic acids and flavonoids from *Physalis angulata*, J. Food Process Eng. 40 (2016) e12433, https://doi.org/10.1111/jfpe.12433.
[40] J.L. Peyraud, L. Astigarraga, Review of the effect of nitrogen fertilization on the chemical composition intake digestion and nutritive value of fresh herbage: consequences on animal nutrition and N balance, Anim. Feed Sci. Technol. 72 (1998) 235–259, https://doi.org/10.1016/S0377-8401(97)00191-0.
[41] I. Baldwin, S. Glazowsk, J. Mravec, J. Fangel, H. Zhang, C. Felby, W.G. Willats, J.K. Schjoerring, External nitrogen input affects pre- and post-harvest cell wall composition but not the enzymatic saccharification of wheat straw, Biomass Bioener. 98 (2017) 70–79, https://doi.org/10.1016/j.biombioe.2017.01.009.
[42] P.C.R. Fontes, H. Braun, C. Busato, P.R. Cecon, Economic optimum nitrogen fertilization rates and nitrogen fertilization rate effects on tuber characteristics of potato cultivars, Potato Res. 53 (2010) 167–179, https://doi.org/10.1007/s11540-010-9160-3.
[43] Y. Fan, J. Xu, X. Gao, X. Fu, X. Yang, Effect of alginate on the release of amide nitrogen for soilless cultivation applications, Sci. Hortic. 256 (2019) 108545, https://doi.org/10.1016/j.scienta.2019.108545.
[44] R.A. Merts, T.P. Brutnell, Bundle sheath suberization in grass leaves: multiple barriers to characterization, J. Exp. Bot. 65 (2014) 3371–3380, https://doi.org/10.1093/jxb/eru108.
[45] W.K. Surewicz, A.F. Mantsch, D. Chapman, Determination of protein secondary structure by Fourier Transform Infrared Spectroscopy: a critical assessment, Biochemistry 32 (1993) 389–393, https://doi.org/10.1021/bi00053a001.
[46] P.A. Nakata, Advances in our understanding of calcium oxalate crystal formation and function in plants, Plant Sci. 164 (2003) 901–909, https://doi.org/10.1016/S0168-9452(03)00120-1.
[47] M.K. Baseri, S. Baker, Identification of cellular components of medicinal plants using FTIR, Romanian J. Biophys. 21 (2011) 277–284.
[48] Z.R.S. Movasaghi, S. Rehman, I. Rehman, Fourier transform infrared (FTIR) spectroscopy of biological tissues, Appl. Spectrosc. Rev. 243 (2008) 134–179, https://doi.org/10.1080/05704920701829043.
[49] S. Sharma, K.N. Uttam, Non-invasive monitoring of biochemical response of wheat seedlings toward titanium dioxide nanoparticles treatment using attenuated total reflectance Fourier transform infrared and laser induced fluorescence spectroscopy, Anal. Lett. 52 (2019) 1629–1652, https://doi.org/10.1080/00032719.2018.1563940.
[50] W.F. Wolkers, F.A. Hoekstra, Aging of dry desiccation-tolerant pollen does not affect protein secondary structure, Plant Physiol. 109 (1995) 907–915, https://doi.org/10.1104/pp.109.3.907.
[51] R. Lahlali, Y. Jiang, S. Kumar, C. Karunakaran, X. Liu, F. Borondics, E. Hallin, R. Bueckert, ATR–FTIR spectroscopy reveals involvement of lipids and proteins of intact pea pollen grains to heat stress tolerance, Front. Plant Sci. 5 (2014) 747, https://doi.org/10.3389/fpls.2014.00747.
[52] D. Usoltsev, V. Sitnikova, A. Kajava, M. Uspenskaya, Systematic FTIR spectroscopy study of the secondary structure changes in human serum albumin under various denaturation conditions, Biomolecules 9 (2019) 359, https://doi.org/10.3390/biom9080359.
[53] W.F. Wolkers, F.A. Hoekstra, Heat stability of proteins in desiccation tolerant cattail (*Typh latifolia* L.) pollen: a Fourier transform infrared spectroscopic study, Comp. Biochem. Physiol. A 117 (1997) 349–355, https://doi.org/10.1016/S0300-9629(96)00274-5.
[54] P. Moskal, A. Wesełucha-Birczyńska, M. Łabanowska, M. Kurdzie, M. Filek, 2D FTIR correlation spectroscopy and EPR analysis of *Urtica dioica* leaves from areas of different environmental pollution, Spectrochim. Acta A 189 (2018) 405–414, https://doi.org/10.1016/j.saa.2017.08.044.
[55] S.P. Devaiah, M.R. Roth, E. Baughman, M. Li, P. Tamura, R. Jeannotte, R. Welti, X. Wang, Quantitative profiling of polar glycerolipid species from organs of wild-type Arabidopsis and a PHOSPHOLIPASE Dα1 knockout mutant, Phytochemistry 67 (2006) 1907–1924, https://doi.org/10.1016/j.phytochem.2006.06.005.
[56] M.-Y. Liu, A. Burgos, L. Ma, Q. Zhang, D. Tang, J. Ruan, Lipidomics analysis unravels the effect of nitrogen fertilization on lipid metabolism in tea plant (*Camellia sinensis* L.), BMC Plant Biol. 17 (2017) 165, https://doi.org/10.1186/s12870-017-1111-6.
[57] T. Martin, O. Oswald, I.A. Graham, Arabidopsis seedling growth, storage lipid mobilization, and photosynthetic gene expression are regulated by carbon: nitrogen availability, Plant Physiol. 128 (2002) 472–481, https://doi.org/10.1104/pp.010475.
[58] J.P. Shine, C.J. Trapp, B.A. Coull, Use of receiver operating characteristic curves to evaluate sediment quality guidelines for metals, Environ. Toxicol. Chem. 22 (2003) 1642–1648, https://doi.org/10.1002/etc.5620220728.

Toxicity mechanism of Cu^{2+} ion individually and in combination with Zn^{2+} ion in characterizing the molecular changes of Staphylococcus aureus *studied using FTIR coupled with chemometric analysis*

Annika Durve Gupta, Esakimuthu Kavitha, Shikha Singh & Sivakumaran Karthikeyan

Journal of Biological Physics

ISSN 0092-0606

J Biol Phys
DOI 10.1007/s10867-020-09560-7

Springer

Journal of Biological Physics
https://doi.org/10.1007/s10867-020-09560-7

ORIGINAL PAPER

Toxicity mechanism of Cu^{2+} ion individually and in combination with Zn^{2+} ion in characterizing the molecular changes of *Staphylococcus aureus* studied using FTIR coupled with chemometric analysis

Annika Durve Gupta[1] · Esakimuthu Kavitha[2] · Shikha Singh[1] · Sivakumaran Karthikeyan[3]

Received: 29 July 2020 / Accepted: 8 November 2020/Published online: 25 November 2020

Abstract

Copper and zinc have a high binding affinity with a *Staphylococcus aureus* bacterial community. This causes a change in the biomolecular composition of *S. aureus*. Our study aims at understanding the resistance mechanism of Cu and Zn either or in various combinations using FTIR and chemometric techniques. Zn toxicity resulted in a significant change in lipid content (3100-2800 cm^{-1}) compared to Cu. A significant decrease in protein content is observed for Cu treatment in the amide region. The bio-concentration factor shows a higher value for Cu compared to Zn. The increase in band area of carbohydrates moieties 1059 cm^{-1} shows the secretion of EPS due to Cu toxicity. A significant change in nucleic acid compositions was noted in the region1200-900 cm^{-1} due to Zn treatment. Secondary structural change in protein shows β sheet formation. The result of the finding shows Cu has greater toxicity than Zn. Further toxicity effects were greatly enhanced for metal mixtures ratio (Cu:2Zn). This shows Zn exhibits synergism effect with Cu. The obtained ROC (receiver operating characteristic) curve area gives good reliability of the experiments. The study attempts to understand the mechanism of toxicity removal of Cu and Zn metal mixtures by bacterial population using FTIR coupled with chemometric techniques.

Keywords Cu-Zn interaction · BCF · Synergism · FTIR · PCA · ROC

Highlights Individual and combined toxicity of Cu and Zn are studied in *S. aureus*.
The synergism effect is exhibited by Zn in the presence of Cu.
Secondary structural protein changes show β sheet formation.
PCA plots clearly distinguish control and treated samples.
Receiver operating characteristic curves show a higher Youden index measured for Cu treatment.

✉ Sivakumaran Karthikeyan
physicskarthik@gmail.com

Extended author information available on the last page of the article

1 Introduction

Water pollution due to the presence of toxic metals remains a serious threat to the environment. Microorganisms are widely affected by the release of toxic metals existing in the environment. They play an effective role in resisting the toxicity and detoxify the metals from the environment by removing them. Bacterial populations have evolved specific resistance mechanisms to exist in a polluted environment. General bacterial resistance mechanisms are efflux pumping of harmful material out from the cell, bioaccumulation, and converting more toxic ion species into a less toxic one. Thus they act as bioremediation of toxic wastes. Efflux pumping is important in the resistance mechanism. Hence understanding the same necessitates developing a process suitable for cleaning the environment from pollutants [1]. Metal toxicity resistance varies widely in a bacterial population. These differences in mechanisms shown by the bacteria are due to varying cell wall features that exist among them. This can be understood from metal accumulation at the cellular level. The metals are stopped from entering into the cell by forming metal binding agents. These agents protect microbes and their control on metal uptake. Thus, it plays a major role in waste treatment processes. This metal transport mechanism is significant in the bacterial population. In the environment, copper serves at lower levels as a nutrient, but is toxic at a higher level. Copper and zinc are the highest affinity binders among the divalent metals present widely in nature. Various investigations of Cu and Zn in the bacterial community show the significance of the storage and development of enzyme activities. The bacterial systems separate and expel these metals to maintain balance for various cellular actions. The basic nature of copper is to cause multiple damages at the cellular level in bacterial systems. Zn (II) is an important micronutrient for bacteria. It has a considerable effect on toxicity at higher concentrations [2]. Mostly the microorganisms can resist heavy metals ions like Zn^{2+}, Cu^{2+}, Cd^{2+}, Ag^{2+}, etc. by limiting the penetration levels to prevent toxicity. Bacteria are very sensitive to surrounding environmental conditions even with small changes. They can sustain sharp changes in the surrounding environment. This proves their ecological supremacy under external stress conditions. They secrete a protective coating called extra polymeric substances (EPS). It comprises polysaccharides, proteins nucleic acids, and lipids. It plays a vital role in forming the biofilm and an external covering from toxic substances [3].

Staphylococcus aureus (*S. aureus)* is a gram-positive bacterium consisting of cytoplasm and rigid cell walls with a complex molecular network, made of peptidoglycan, which forms a strong mesh-like structure that covers the cell. It acts as a barrier and prevents drugs and toxicants from entering into it. The Gram-positive bacteria have an additional polymer, covalently bound to the peptidoglycan, the teichoic acid built of phosphate backbone with a side chain of variable composition [4, 5]. Hence understanding the activities of bacterial cells, at the interfaces due to toxicants plays a critical role in studying the structural and biochemical changes at their surfaces. The metal ion has a strong binding with various functional groups on the cell surfaces even at low concentrations. This leads to enzyme activity changes at the intracellular level [6]. Molecular composition changes occurring in the bacterial populations are studied using infrared energy. The interaction of energy provides fundamental information regarding the molecules that arise at a cellular level. With the help of this interaction, FTIR provides precise and rapid detection of biochemical changes arising in the microorganisms. The spectral analysis of whole organisms in fingerprint gives the biochemical characteristics present in the bacteria. It gives information regarding cellular compositions such as proteins, carbohydrates, nucleic acids, and phospholipids [7].

We have studied these changes in the molecular profile of *S. aures* populations due to Cu-Zn metal mixtures. IR spectra of *S. aureus* show several bands describing the molecular compositions of the cells. They are sensitive to structural changes like intermolecular H bonding and membrane constitution. Hence our study utilizes the IR spectra to visualise the molecular changes due to this metal resistance. Our earlier studies [8, 9] on Ni-Cr metal interaction on *E. coli* and in *S. aureus* populations proved effective ways of molecular changes using infrared spectral analysis. There has not been any analysis done in the case of Cu-Zn interaction for *S. aureus* using FTIR. Considering the above discussion our study aims to know how *S. aureus* reacts to extracellular metal ions Cu and Zn. We have also studied the individual and combined toxicity of Cu and Zn stress on *S. aureus* to find any significant role played in their resistance to intoxication. The outcome of the study explains how the metal stress impacts phenotypic/genotypic changes occurring in them using FTIR combined with chemometric analysis.

2 Materials and methods

2.1 Chemicals used

Chemicals used Copper sulphate ($CuSO_4$) and Zinc sulphate ($ZnSO_4$) were bought from Sigma Aldrich of analytical grade. All the standard solutions were made ready in deionized water.

Test micro-organisms: Pure culture of *Staphylococcus aureus* was brought from B. K. Birla College, Kalyan. These cultures were maintained with Sterile Nutrient broth. They were regularly sub cultured for proper maintenance.

2.2 Minimum inhibitory concentration (MIC)

The MIC is defined as the lowest concentration in which metal inhibits the visible growth in the test. *Staphylococcus aureus* was checked for heavy metal tolerance. The sterile Nutrient broth was used as a test medium. Varying concentration of $ZnCl_2$ and $CuCl_2$ were used (50–500 ppb for Zn and Cu). The tubes were incubated at 37 °C for 24 h. Growth in the form of turbidity was observed. The MIC values were interpreted when the culture reached an OD600 of 0.55–0.59 [CL157 (ELICO)]. All the tests were carried out in triplicates. The MIC results show that *S. aureus* could tolerate Zn at 350 ppb and Cu at 200 ppb. For metal interaction studies equal concentration of Cu and Zn salt solution were used in the range of 10–300 ppb. The MIC value for metal mixtures was found to be 250 ppb for *S. aureus*. Three flasks were maintained. One flask, containing Nutrient broth without any heavy metal and other flasks containing nutrient broth along with the 1/4th MIC value of the respective heavy metals Cu and Zn. For metal interaction study ¼ th MIC (62.5 ppb) at three different proportions of concentration of Cu and Zn (1:1, 1:2, 2:1) was taken and the sample was harvested at the end of the period.

2.3 Experimental study

The experiments were performed in aerobic conditions. Microorganisms were grown in proposed metal concentrations having 100 ml of Sterile Nutrient broth (Himedia) in 150 ml

Erlenmeyer flask at 30 °C at shaker conditions (90 rpm) for 18 h. The exponential phase culture was centrifuged at 5000Xg for 10 min and washed twice. The final sample was measured at OD600. Bacterial cells were collected from the liquid cultures by centrifugation (Remi, R-8C) at 10,000 rpm for 15 min. After removing the supernatants, the bacterial pellets were cleaned twice with phosphate buffer (pH 7.4; Na_2HPO_4-$7H_2O$ 20.214 g; $NaH_2PO_4H_2O$ 3.394 g; 1 L). They were used for further analysis in the FTIR spectrometer.

2.4 FITR analysis

The cells were separated by centrifugation at 10,000-g for 8 min. The pellet was resuspended in sterile normal saline (0.8% NaCl). All the samples were recorded in IIT SAIF, Bombay for FTIR analysis in the range 4000–400 cm^{-1} (Bruker, Germany; 3000 Hyperion Microscope with Vertex 80 FTIR System). The sample of 2 ml of *S. aureus* solution is used in the ATR cell for spectral measurement. A total of 20 scans were taken for each spectrum at 4 cm^{-1} resolution. All spectra were recorded for three identical samples. The collected spectra were vector normalized second derivatives with 15 points smoothing using the Savitzky–Golay algorithm using Origin 8.0 software. For curve fitting analysis Gaussian function was used to resolve peak pattern with least chi square value as described in our recent work [10].

2.5 Bioaccumulation of Cu, Zn, and its mixtures

Bioaccumulation of metals of Cu, Zn, and various combination ratios of the bacterial biomass was analysed using ICP-AES analysis (M/s. Spectro, Germany). Both the cells and the supernatant were analysed for residual heavy metal. The experiments were performed in triplicate. The bioconcentration factor (BCF) and metal removal efficiency (RF) were calculated as described by Phetsombat et al. [11] and Zhou et al. [12].

2.6 Principal component analysis (PCA)

Principal Component Analysis (PCA) was performed with SPSS 16.0. It is used commonly for multivariate data reduction. All spectral data are pre-processed before subjecting to PCA operations. The output of the PCA results in a small number of principal components. It explains the maximum variation of the data present in the samples. Each PC is composed of scores and loadings. It is utilized for quantitative approaches of discriminating samples. The scores of the component were plotted to gather data that accounts for variability in the FTIR information. The scores were plotted to obtain the data that describes the variation form the FTIR spectra.

2.7 Measurement of differentiation index

The reproducibility of the samples was found from Pearson's product-moment correlation coefficient (between replicates 1–2, 2–3, 3–1) which is expressed as the differentiation index (D) [4, 13]. It was calculated using the following equation:

$$r_{y1y2}\frac{\sum_{i=1}^{n} y_{1i}\ y_{2i} - n\overline{y_1}\overline{y_2}}{\sqrt{\sum_{i=1}^{n} y_{1i}^2 - n\overline{y_1^2}}\sqrt{\sum_{i}^{n} y_{2i}^2 - n\overline{y_2^2}}} \quad (1)$$

where y_1 and y_2 values mean observances of two kinds of comparative absorption spectra at a given wavelength; n represents the number of data points. From the correlation coefficient r_{y1y2}, the differentiation index Dy_1y_2 may be defined as

$$D_{y1y2} = \left(1 - r_{y1y2}\right) \times 1000 \tag{2}$$

The D value was measured for the selected region. This includes W_1 (3050-2800cm^{-1}), W_2 (1700–1600 cm^{-1}), W_3 (1200–900 cm^{-1}) and whole spectrum W_4 (4000–450 cm^{-1}).

2.8 Statistical analysis

The results were expressed as ± standard error of the mean (SEM). *S.aureus* heavy metal resistant groups of zinc and copper and their metal mixtures vs. control group were analysed using the one-way ANOVA test using SPSS 16.0. A probability level (p value) of less than 0.05, 0.01, and 0.001 were considered statistically significant. Hierarchical cluster analysis and Receiver operating characteristic analysis was performed using the same software.

2.9 Hierarchical cluster analysis

Hierarchical cluster analysis (HCA) was utilized to know the differences among the samples tested. HCA analysis was carried out using SPSS 16 software using Pearson's product-moment correlation coefficient with Euclidean separation ae utilized using Ward algorithm [14]. The clustering maximizes their similarity concerning measured characteristics to minimize errors in describing a large number of samples. Hierarchical groups are formed in the manner described for classification purposes of plants and animals in predicting the efficiency of the results [15].

2.10 Receiver operating characteristic analysis

Receiver operating characteristic (ROC) analysis allows the diagnostic performance of different tests by comparing the sensitivity and specificity of the samples tested. ROC curves were constructed by using SPSS 16 software. The ROC plot shows sensitivity against 1-specificity for each point with the threshold value between zero and one. The control was taken as reference point fixing the potential threshold limit of values as 95% of cut off points. The upper left-hand portion of the graph will have a region on the curve where potential threshold values occur that provides both high sensitivity and low specificity (1-specificity) of the curves [15]. Comparing the area under the ROC curves allows us to select the best test carried out in the experiment.

3 Results and discussion

Figures 1, 2 and 3 show the representative of the second derivative vector normalized spectra of control, Cu, Zn, and their metal mixtures. The peak assignment and the band area are

measured for various treatments are shown in Table 1. The response to metal toxicity showed changes in the spectra of –CH groups of lipids at 3100–2800 cm^{-1}. Binding of metals ions with amino acids/proteins showed changes occurring at 1500–1800 cm^{-1} regions. The phosphate groups of nucleic acids (DNA/RNA) structure occur in 600–1200 cm^{-1} regions [16]. The lipid membranes of *S. aureus* are characterized in the region 2900–2800 cm^{-1}. The band ~2957 cm^{-1} assigns to CH_3 asymmetric stretching of lipids. The band ~2930 cm^{-1} corresponds to CH_2 asymmetric stretching of lipids groups. The symmetric CH_3 & CH_2 stretching assigns to 2875 cm^{-1} and 2850 cm^{-1} mainly contributing to lipids. CO stretching of polysaccharides corresponds to 1745 cm^{-1}. The band ~1635 cm^{-1} was assigned to C=O stretching and N-H bending of amide I protein. Amide II rises due to N-H bending CN stretching of proteins at 1541 cm^{-1}. Amide III of proteins corresponds to 1316 cm^{-1}. The various bending vibration of lipids arises at 1462 cm^{-1}, 1458 cm^{-1}, and 1396 cm^{-1}. The phosphodiester groups (PO^{2-}) arise from phospholipids bands at 1339 cm^{-1}, 1233 cm^{-1},1174 cm^{-1}, and 1079 cm^{-1} which contributes to nucleic acids of *S. aureus*. Carbohydrates moieties of C-O stretching present at 1059 cm^{-1}. DNA/RNA of the nucleus corresponds to 994 cm^{-1} and 964 cm^{-1}. Also, the band area ratio of nucleic acid/protein, lipid/phosphorylated protein, and lipid/nucleic acid were calculated as suggested by Obinaju et al. [16]. It provides information on the compositional changes of lipids, proteins, nucleic acids, etc., in a bacterial population.

3.1 Toxicity impact of heavy metals Cu and Zn and their combinations in the lipid region

FTIR spectra in the 3100–2800 cm^{-1} region are generally dominated by the spectral characteristics of various membranes of phospholipids. We studied the effect of extracellular Zn and/or Cu metal ions that can exert significant and potentially deleterious effects on bacterial cell membranes composition and integrity. This happens through the variation of excess unsaturated fatty acids, which affects membranes fluidity [17]. Hence, we examine these metal ions stress on the fatty acid content of *S. aureus*. Our analyses show that *S. aureus* has a change in the band area of fatty acid compositions (CH_3/ CH_2 symmetric vibrations) as shown in Fig. 1a, b. The band area in the selected region 2900–2800 cm^{-1} shows changes in lipids due to toxicity compared with control. The reduction in CH_3 asymmetric band area of lipids arises for

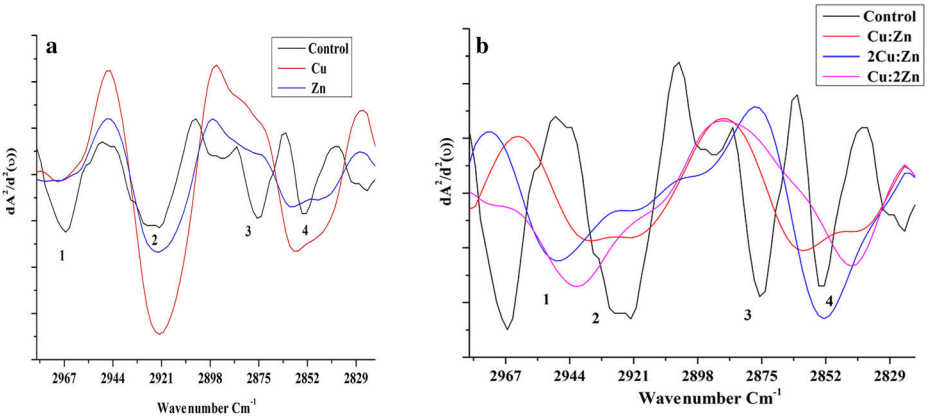

Fig. 1 Characteristic second derivative vector normalized FTIR spectra of *S. aureus* in the 2908–2820 Cm^{-1} region (A) Control, Cu and Zn toxicity (B) Metal mixtures at varying proportion

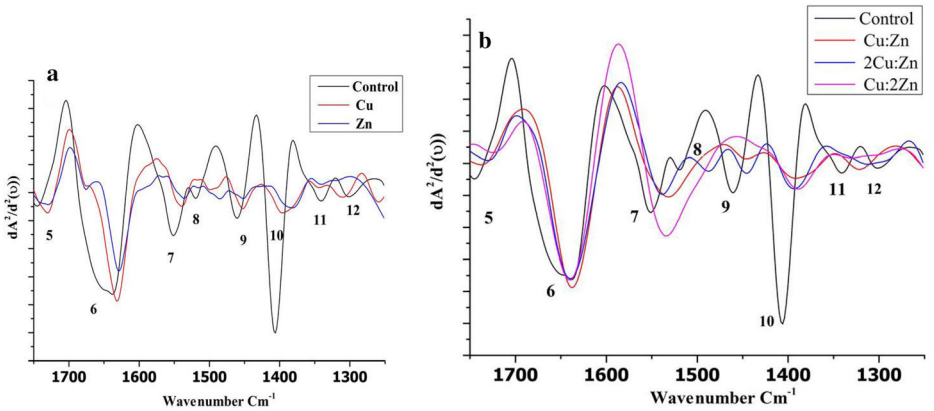

Fig. 2 Characteristic second derivative vector normalized FTIR spectra of *S. aureus* in the 1750–1250 Cm^{-1} region (A) Control, Cu and Zn toxicity (B) Metal mixtures at varying proportions

Cu and Zn metal treatment of *S. aureus* compared with control. For metal mixtures treatment (Cu: Zn) lipids bands decrease showing combined toxicity is greater than individual toxicity. The computed band area of Lipid/Phosphorylation (Fig. 4) shows a substantial reduction in lipid contents due to Zn treatment ($p < 0.001$). Goswami et al. [18] studied using FTIR and showed that Cu and Zn toxicity resulted in lipid contents reduction in bacterial strain *Rhodococcus opacus*. Rafig Gurbanov et al. [19] studied similar studies of Pb & Cd intoxication on *E.Coli* and *S. aureus* bacterial populations. Our reports (Fig.1a) in the band area of 2930 cm^{-1}, 2875 cm^{-1}, and 2850 cm^{-1} are well in good agreement with the literature discussed above. This shows a decrease in lipid content because of Cu and Zn intoxication. Our study shows that Zn toxicity has a higher effect on lipid contents compared to Cu. Further, the Cu and Zn interaction at various ratios 1:1, 1:2, 2:1 shows band area (Fig.1b) reduction resulting in, increase in toxicity.

Hassan et al. [17] studied Zn + Cu metal ion results in a change in the composition of fatty acid in *A.baumannii*. The results of our experiments show that Cu with the addition of Zn (Cu:2Zn) causes a decrease in lipid content. This shows Zn exhibits synergism effect with Cu. Further, the band area of lipid/phosphorylation ratio confirms the decreases in lipid significantly ($p < 0.001$) indicating that Zn exhibits greater toxicity than Cu. Thus, the toxicity

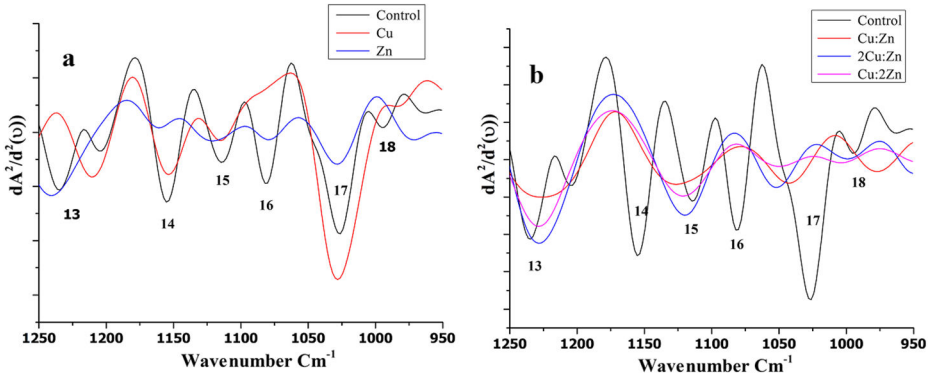

Fig. 3 Characteristic second derivative vector normalized FTIR spectra of *S. aureus* in the 1250–950 Cm^{-1} region (A) Control, Cu and Zn toxicity (B) Metal mixtures at varying proportions

Table 1 Frequency assignment and the band area of *S. aureus* treated with Cu, Zn and its mixtures

Peak Number	Wavenumber Cm^{-1}	Functional group	Control	Cu	Zn	Cu:Zn	2Cu:Zn	Cu:2Zn
1	2957	CH_3 antisymmetric stretching: lipids	5.26 ± 0.84	1.68 ± 0.07 [a]	1.80 ± 0.04 [a]	4.85 ± 0.96 [a]	3.82 ± 0.58 [a]	0.24 ± 0.03 [a]
2	2930	CH_2 antisymmetric stretching	7.92 ± 1.02	10.62 ± 1.13 [a]	10.77 ± 0.97 [b]	1.46 ± 0.09 [a]	0.38 ± 0.06 [a]	0.24 ± 0.02 [a]
3	2875	CH_3 symmetric stretching	2.99 ± 0.83	0.94 ± 0.08 [a]	0.56 ± 0.04 [a]	9.67 ± 0.86 [a]	5.47 ± 0.79 [c]	0.18 ± 0.04 [a]
4	2850	CH_2 symmetric stretching: mainly lipids	2.62 ± 0.63	1.28 ± 0.29 [a]	0.87 ± 0.07 [a]	0.14 ± 0.02 [c]	9.59 ± 1.03 [b]	0.15 ± 0.01 [a]
5	1745	CO stretch: polyester storage compounds, polysaccharides	66.78 ± 4.94	14.05 ± 1.58 [b]	5.98 ± 0.89 [b]	80.10 ± 7.04 [a]	9.46 ± 1.32 [a]	11.42 ± 1.75 [b]
6	1635	Amide I: protein C=O stretching, N—H bending	271.64 ± 18.9 4	171.21 ± 11.47 [a]	98.61 ± 6.84 [a]	322.68 ± 12.36 [a]	325.66 ± 13.06[b]	307.02 ± 9.69 [a]
7	1541	Amide II: protein, N-H bending, C—N stretching	61.71 ± 9.46	17.38 ± 1.37 [a]	1.42 ± 0.73 [b]	145.35 ± 10.65 [a]	79.72 ± 4.87 [b]	94.89 ± 16.37 [a]
8	1462	CH_2 scissoring: lipids	62.31 ± 4.82	23.56 ± 2.08 [a]	1.78 ± 0.77 [b]	34.92 ± 2.04 [a]	18.31 ± 1.26	14.32 ± 1.07 [a]
9	1458	CH_2 bending: lipids	79.82 ± 6.92	23.56 ± 3.05 [c]	1.78 ± 0.45 [b]	8.05 ± 0.79 [b]	21.87 ± 2.52[c]	11.77 ± 1.83 [b]
10	1396	COO^- symmetric stretching: fatty acids	156.38 ± 9.49	32.19 ± 2.04 [b]	4.65 ± 0.92 [a]	34.32 ± 1.57 [a]	43.74 ± 2.35 [b]	31.26 ± 2.02 [a]
11	1339	PO^{2-} antisymmetric stretching	29.89 ± 1.47	3.82 ± 0.68 [b]	1.94 ± 0.06 [a]	19.22 ± 1.62 [a]	3.61 ± 0.58 [b]	2.14 ± 0.08 [b]
12	1316	Amide III	14.98 ± 1.30	23.61 ± 3.31 [a]	9.96 ± 0.72 [a]	41.98 ± 3.72 [b]	5.23 ± 0.25 [a]	0.78 ± 0.06 [a]
13	1233	PO^{2-} antisymmetric stretching: mainly nucleic acids with minor contribution from phospholipids	21.17 ± 3.52	22.71 ± 2.79 [b]	35.08 ± 1.03 [a]	69.08 ± 5.07 [b]	92.79 ± 4.99 [a]	58.34 ± 2.04 [a]
14	1174	CO—O—C antisymmetric stretching: phospholipids	46.74 ± 2.47	48.62 ± 1.96 [c]	8.52 ± 0.75 [a]	54.02 ± 2.68 [a]	105.42 ± 8.42 [a]	63.85 ± 3.08 [a]
15	1112		34.72 ± 1.37	32.14 ± 1.57 [a]	0.63 ± .04 [a]	42.69 ± 1.73[a]	39.47 ± 1.38[a]	24.74 ± 1.02[a]
16	1079	PO^{2-} symmetric stretching: nucleic acids and phospholipids	27.45 ± 2.53	8.41 ± 0.69 [b]	1.40 ± 0.06 [a]	21.15 ± 3.71 [c]	32.29 ± 4.02 [a]	13.58 ± 1.38 [a]
17	1059	C–O stretching: polysaccharides	59.57 ± 2.41	91.94 ± 4.07 [a]	1.27 ± 0.04 [a]	18.96 ± 1.12 [b]	19.56 ± 1.40 [b]	5.43 ± 0.06 [a]
18	994	Ribose skeleton	4.85 ± 0.04	7.52 ± 0.85 [a]	5.25 ± 0.34 [a]	17.99 ± 0.04 [a]	5.63 ± 0.67 [a]	3.45 ± 0.64 [a]

[a] $p < 0.05$; [b] $p < 0.01$; [c] $p < 0.001$ with respect to control ($n = 3$)

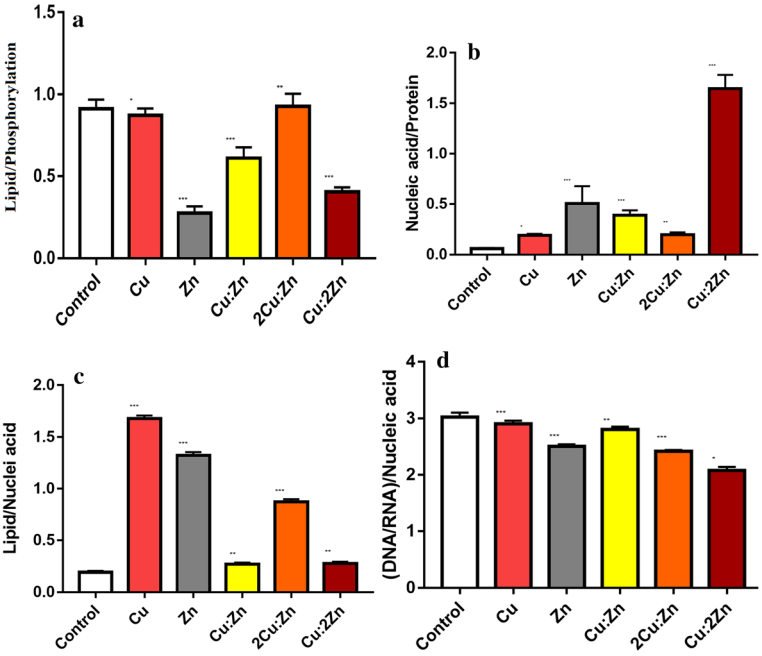

Fig. 4 Mean computed band area ratio of (a) Lipid/Phosphorylation (b) Nucleic acid/Protein (c). Lipid/Nucleic acid (d). DNA/RNA/ Nucleic acid (*$p < 0.05$, ** $p < 0.01$, ***$p < 0.001$) with respect to control

influence of Cu depletion in Zn stressed cells is because of failure to acquire enough amounts of Cu. This predicts cytoplasmic Cu accumulation of bacterial populations that also recognize other cations Zn^{2+} [17]. This further established changes in the phosphate band discussed in section 3.4. This complimentary information obtained in region 1470–1400 cm^{-1} shows the lipid bands at 1462 cm^{-1}, 1458 cm^{-1}, and 1396 cm^{-1} corresponds to CH_2 scissoring, CH_2 bending, and COO^- of fatty acids. The reduction in this band area is because of metal intoxication. This agrees well with other lipid regions (3100–2800 cm^{-1}) discussed in Section 3.2. Hassan et al. [17] obtained similar results due to Zn + Cu treatments showing a synergistic impact on *A. baumannii*. Similarly, the band emerging from the COO^- symmetric of fatty acids (~1396 cm^{-1}) decreases in Cu and Zn treatment of *S. aureus*. The Presence of Zn/ and Cu or in combination causes a fatty acid reduction. These changes in the fatty acid will influence membrane fluidity. It is proposed to be one of the mechanisms of bacterial adaption to extracellular stress [20].

3.2 Toxicity impact of heavy metals Cu and Zn and their combinations in the protein region

Amide bands dominating in the region 1600–1500 cm^{-1} are used for protein changes confirmation (Fig. 2a, b). Any decrease/increase in the band area is related to protein changes. The band area measured shows a high reduction in protein content due to Zn toxicity compared to Cu ($P < 0.01$). This may well support an increase in the binding of zinc with protein metallothionein. This regulates zinc level distribution in the microbes [21]. Further the combined toxicity effects resulted in the reduction of proteins when compared with individual

toxicants. In bacteria, Zn, or Cu binds with cysteine-rich polypeptides in bacterial resistance [22]. The Cu and Zn combinations (Cu:2ZN), surprisingly increases toxicity showing a band area of protein. Hassan et al. 2017 showed accumulation of Zn resulted in depletion of Cu in *A baumannii*. Bart A. Eijkelkamp et al. [23] studied that in *Streptococcus pneumonia* Zn (II) inhibits Mn (II) by binding with protein leading to increased susceptibility to oxidative stress. Our results show a change in Amide bands (I, II, III) of proteins playing an effective role in the defence mechanism. This decrease in the Amide band of proteins is due to inhibition of Cu (II) ions by the peptide. This forms a complex formation of Cu bonding to side peptide as described by Tsuneo Ishida [24]. The bioaccumulation study shows the accumulation of more Cu. The computed BCF values show a higher value as against Zn (Fig. 5). This shows the complex binding of the peptide chain by Cu in *S. aureus*. Besides, a copper transport mechanism (copA and copB) determines uptake of these metal ions which favours bioaccumulation [25]. The order of preference for cation binding to metallothionein is high for Zn^{2+} and low for Cu^{2+}. This probably explains a higher reduction in amide bands due to Zn toxicity. The presence of Zn abundance with Cu (Cu:2Zn) increases in the BCF value of Cu showing higher toxicity (Fig. 5). This high BCF probably explains the role of Cu in the periplasmic space that is considered as a covering membrane. In *S. pneumoniae* excess, Zn (II) antagonizes Mn (II) by protein binding mechanism reported by McDevitt et al. [26].

3.3 Toxicity impacts of heavy metals of Cu and Zn and their combinations in the carbohydrate region

The Fig. 3a, b shows the FTIR spectra of secondary derivative vector normalized in the regions 1200–950 cm^{-1}. The carbohydrate regions are dominating in 1200–950 cm^{-1} region. The measured band areas of the selected region are shown in Table 1. It is observed that the band area of *S. aureus* treated to metal toxicity increases for all treatment except for Cu:2Zn. The toxicity impact of Cu depletion in Zn stressed cells could be due to a failure of the cells to acquire enough amounts of Cu [17]. This may be because of cytoplasmic Cu accumulation of the bacterial systems that recognize other cations Zn. This confirms a decrease in phosphate

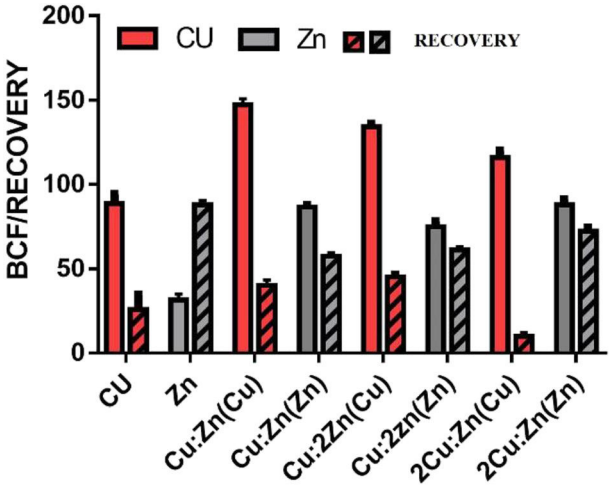

Fig. 5 Computed Bioconcentration factor (BCF) and Metal removal efficiency of *S. aureus* populations exposed to Cu, Zn and metal mixtures

band 1450 cm^{-1} observed at (2Zn: Cu). Further, the changes in the carbohydrate band area are influenced by Cu (II) ions on *S. aureus* owing to the damages of PGN as suggested by Tsuneo Ishida [22]. Our result confirms the changes in carbohydrates as studied from FTIR spectra. Similar results were reported by Joana Campos et al. [27] using FTIR in *Salmonella enterica* bacteria showing changes of phospholipids/DNA/ RNA with the sharp changes in the polysaccharide region. Similarly, Tom Grunert et al. [5] studied distinct spectral variation in 1200–800 cm^{-1} of *S. aureus*. Studies reported by Whelan et al. [28, 29] and Rafig Gurbanov et al. [30] shows how FTIR is used to monitor changes in nucleic acid bands by changes in DNA confirmation. The antisymmetric PO^{2-} gives information regarding nucleic acid which appears at 1233 cm^{-1}. This is also confirmed in our study with Cu-Zn metal interaction where the changes in band area is predominant when compared to control. This confirms interaction of Cu-Zn resulted in greater toxicity. Hence our results are in agreement with the other reports using FTIR to monitor DNA changes due to metal toxicity in *E. coli* and *S. aureus* bacterial populations [31, 32].

The complex formation of metal is important in the removal of toxic metals from the environment. It is well known that EPS are polysaccharides that are secreted by bacterial to overcome the metal toxicity. The measured band 1059 cm^{-1} corresponds to C-O stretching of polysaccharides. The decrease in band area resulted due to toxicity of these metals. This may be due to metal binding cation with sugar polymers resulting in changes in the band area [30–32]. Increase in band area due to Cu toxicity resulted in the production of extracellular polymers growth. Ferreira et al. [33] found similar results of extracellular polymers due to Cu, Zn, and Cd toxicity. The measured band area ~ 1059 cm^{-1} agrees with the results for Cu treatment against Zn treatment.

3.4 Toxicity impact of heavy metal and its mixture in the phosphate region

The band that arises in the 1250–950 cm^{-1} (Fig. 3a, b) region corresponds to the nucleic acid composition of *S. aureus* treated to various metals. Our FTIR study supports the changes in 994 cm^{-1} where the band area of Zn treatment has a significant reduction compared to Cu treatment. The band area measurement shows a 26% reduction in band area for DNA/RNA/ nucleic acid due to Cu:2Zn treatment. This shows Cu:2Zn treatment has greater toxicity affecting the DNA backbone of C-C stretching resulting in decreased band area (Fig. 3b). This result was supported by Guerra et al. [34] and Sanson et al. [35] in the case of *B. subtilis* where Zn (II) binds with high affinity to the DNA. Binding of zinc triggers an impairment of DNA but allows metallothionein production thereby resulting in cell survival at higher zinc levels. Similarly, Obinaju et al. [16] studied using FTIR and observed changes in DNA/RNA, carbohydrates bands due to toxicity bebzo[a]pyren on the bacterial cell population. The interaction of bacterium with metals is enveloped by S-layer of proteins in which phosphate groups on the cell wall bind closely. The main interaction mechanism of metals with a bacterial population is binding to organic phosphate and COO^- group. Merroun et al. [36] showed that carboxyl groups of S layer participate in binding of palladium which was shown by EXAFS and FTIR spectra.

3.5 Secondary structural study of protein in amide I band analysis

The Fourier self-deconvolution applied in the amide I regions reveals the existence of four bands as shown in Fig. 6a-f. Table 2 corresponds to the band area measurement of the secondary structure of proteins for control, Cu, Zn, and metal combination treatments. The band ~1677 cm^{-1} is assigned to ß turns of proteins. The α helix structure is assigned at

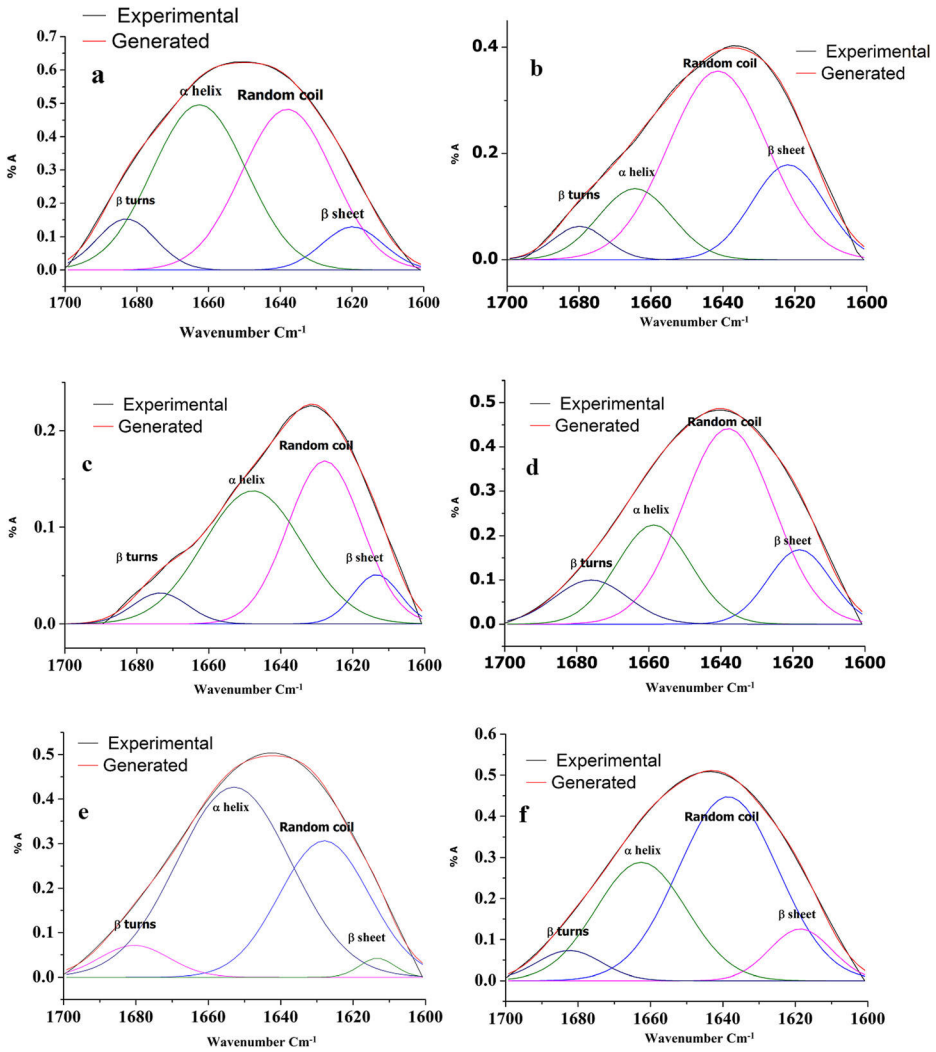

Fig. 6 Fourier self deconvolution deduced by curve fitting in Amide region (a). Control (b) Cu treatment (c) Zn treatment (d) Cu:Zn treatment (e) 2Cu:Zn treatment (f) Cu:2Zn treatment

1656 cm^{-1}. Random coil and ß sheet secondary structure of proteins corresponds to 1635 cm^{-1} and 1616 cm^{-1}. The Fig. 6a-f shows the secondary structure variation due to various treatments of metals. Among the various treatments examined studied Cu toxicity results in higher changes in ß sheet formation. She et al. [37] studied the secondary structural variation of protein due to the magnetic field on the bacterial population. The metal interaction Cu: Zn also shows significant changes in ß sheet formation. It is observed from our study that an increase in ß sheet and decrease in an α helix occurs for all treatment except for 2Cu:Zn treatments. Also, the random coil increases for this treatment. These results confirm the structural changes occurring in protein. This result confirms 2Cu:Zn treatment shows that Cu exhibits an antagonism effect.

Table 2 Secondary structural variation of protein in the Amide I regions of *S. aureus* population due to various metal treatments

Band Assignment	Spectral Range Cm^{-1}	% Band area					
		Control	Cu	Zn	Cu:Zn	2Cu:Zn	Cu:2Zn
1680–1690	β turns	8.36 ± 0.42	5.46 ± 0.36 [a]	5.93 ± 0.43[b]	9.84 ± 0.68 [a]	5.64 ± 0.45 [a]	5.94 ± 0.61 [a]
1660–1650	α helix	43.49 ± 1.05	15.18 ± 0.27 [b]	45.38 ± 1.12 [a]	22.46 ± 0.86 [a]	31.41 ± 0.94 [a]	59.22 ± 1.07 [a]
1645–1630	Random Coil	41.42 ± 0.78	57.43 ± 1.04 [a]	41.26 ± 0.86 [a]	53.95 ± 1.32 [a]	53.86 ± 1.04 [b]	33.25 ± 0.86 [a]
1610–1635	β sheet	7.32 ± 0.41	21.27 ± 1.08 [a]	7.72 ± 0.66 [a]	13.93 ± 0.79 [b]	9.28 ± 0.53 [a]	1.86 ± 0.06 [a]

[a] $p < 0.05$; [b] $p < 0.01$ with respect to control ($n = 3$)

3.6 Principal component analysis of the *S. aureus* sample subjected to heavy metal treatments

Figure 7 shows the PCA results obtained for various metals treatment of *S. aureus*. The plots indicate the control and treated samples are well separated according to eigenvalues. It shows that all the components are plotted in the positive region. The highest absolute eigenvalue relates to components 1 of 52% variation. Component 2 has 26% variation. The 3rd component is neglected because of the least variation and low eigenvalues. This PCA was obtained from absorption values in the entire region. The plot shows that control has the least value along PC1 whereas Cu and Zn treatment has high value along PC2. For metal interaction (Cu:Zn) of various ratios shows the highest positive value along PC1 and they are distinctly separated from control samples. FTIR spectra support this distinct variation due to various metal treatment studied in our case. The Cu:2Zn treated sample is predominant in influencing the changes studied followed by other combination ratios. This variation is because of changes in lipids, proteins, polysaccharides, and nucleic acid. Loading plots (Fig. 8) facilitate prominent frequency change that enables most of the variables studied. From the loading plot, it is seen that the amide region of proteins has a higher value (Fig. 8). The loading plots show a prominent peak responsible for discrimination of the samples treated to various Cu, Zn metal treatments. The loading plot shows PC1 has a higher value occurring in protein which accounts for maximum variation in the samples studied. Carbohydrates, fatty acids show the next important factors influencing the variation as observed from PC2 loading values. This account for the distinct grouping of S aureus treated due to metal treatments. This alteration and adaptation in the *S. aureus* are supported by bimolecular changes as revealed from the variation in the score plot. Similar studies were made by Kepenek et al. [38], Partouche et al. [39], Gupta et al. [9], and Kochan et al. [40] where PCA was employed on FTIR spectral data to determine the variability of a bacterial population.

3.7 Hierarchical cluster analysis (HCA)

An understanding of the *S. aureus* under different treatments are subjected to hierarchical clustering analysis using squared Euclidean distance method. They are displayed graphically

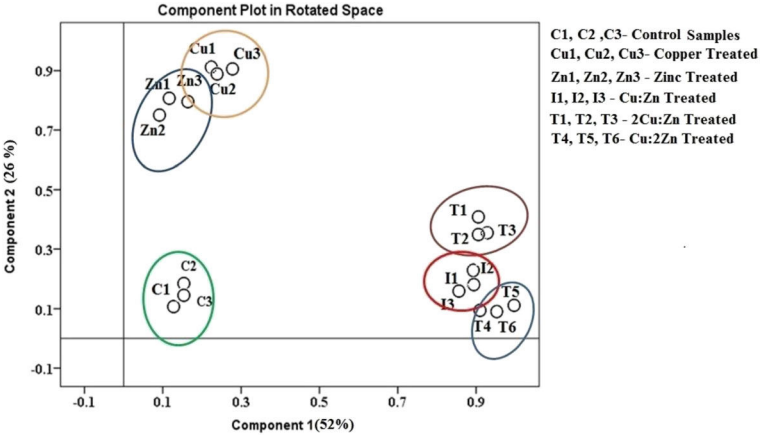

Fig. 7 PCA scatter plots of *S. aureus* populations of control, Cu, Zn, and metal mixture treated samples

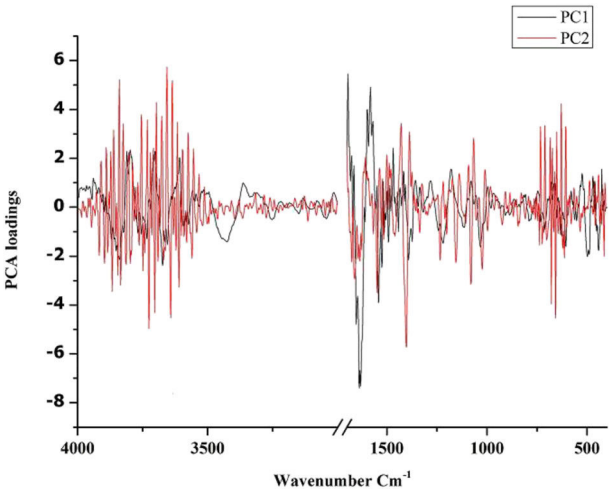

Fig. 8 Variation of the factor loading obtained from the PCA with the corresponding wavenumber of the *S. aureus* populations

(Fig. 9) as a dendrogram, by the Ward algorithm which relates to the dissimilarity scale. Similar cases are related by smaller distances which are visualized by closer separations. The distance present in the dendrogram shows how the composition of samples differs within an organism [14]. The first cluster corresponds to toxicity due to Cu-Zn metal interaction. The second cluster has two well-differentiated sub-clusters of Cu and Zn treatment. The third cluster results from control and Cu:2Zn treatment. This differentiation due to metal interaction results from the toxicity of Cu, playing a dominant role compared to Zn. The fourth cluster is well separated from individual metal treatments.

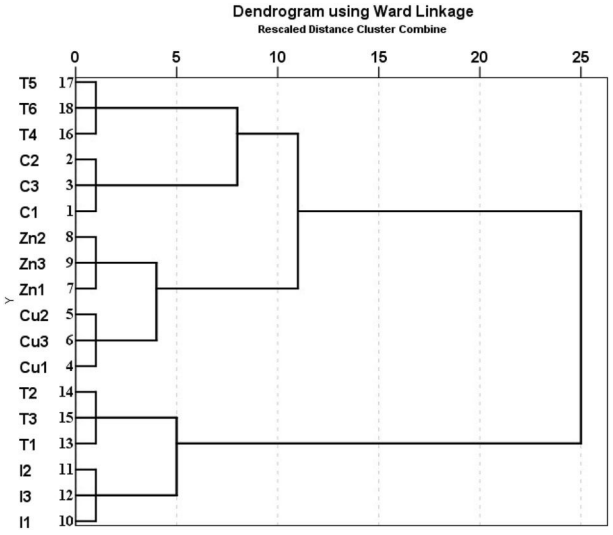

Fig. 9 Dendrogram of *S. aureus* bacterial populations treated with various Cu, Zn, and metal mixtures treatments showing group linkage obtained using the Ward algorithm

3.8 Analysis of reproducibility

The reproducibility of the sample replicates is measured by the parameter differentiation index D [13, 41]. Using correlation coefficients, the differentiation index (D value) of the identical spectra can be computed given by the relation [41]. The larger the deviation between the spectra, the greater the index values, thereby reaching the completely non-correlated spectra. The spectral region was separated as w_1 fatty acid, W_2, protein, and W_3 carbohydrates and nucleic acid groups. The window W_1 reflects changes in fatty acids. The window W_2 displays variation in the amide groups of proteins. The mixed regions W_3 detects the influence of polysaccharides and nucleic acid groups. These spectral windows are used to obtain the best identification of inter replicates variability as much as possible. Mean D values below 10 are considered good for strain reproducibility. The computed D value for the samples subjected to different metal treatments is represented in Table 3. The full spectra region is also considered to measure the reproducibility variations among the samples studied. In our study w_2 shows the highest D values. The windows W_1 and W_3 have a lower value (Table 3). The W_2 comprises of proteins region used for differentiation [4, 9, 41–43]. To check the reliability of our work the receiver operating characteristic curve was obtained to measure the diagnostic of our findings.

3.9 Receiver operating characteristic analysis

The ROC curve represents the sensitivity versus 1-specificity for all possible values of the experimental values. It gives information about the cut-off point of various samples studied. The diagnostic ability was measured by the area of the curve. The obtained ROC curve for various metal treatments lies in the higher range showing the reliability of our study (Fig.10). The highest ROC curve area was obtained for Cu:2Zn and 2Cu:Zn treatments. A similar conclusion was made by Sharaha et al. [44] using the ROC model from infrared spectroscopy to determine the accurate classification analysis of the *S. aureus* bacterial population. The measured Youden index ranges from 0.82 to 0.72 for all treatments. The highest Youden index is measured for Cu treatments. It gives the response and validation of the study.

Table 3 Differentiation index of *S. aureus* strain exposed to metal toxicity and its mixtures calculated for the 3 spectral windows and for the whole spectrum

Sample Treatment	Spectral window			Whole spectra
	W1	W2	W3	
Control	0.36	4.78	2.70	1.63
Cu	2.68	4.90	4.41	5.71
Zn	7.64	2.17	1.02	4.94
Cu:Zn	4.54	1.29	3.47	6.97
2Cu:Zn	8.67	2.68	7.42	4.70
Cu:2Zn	2.28	2.50	1.84	1.75

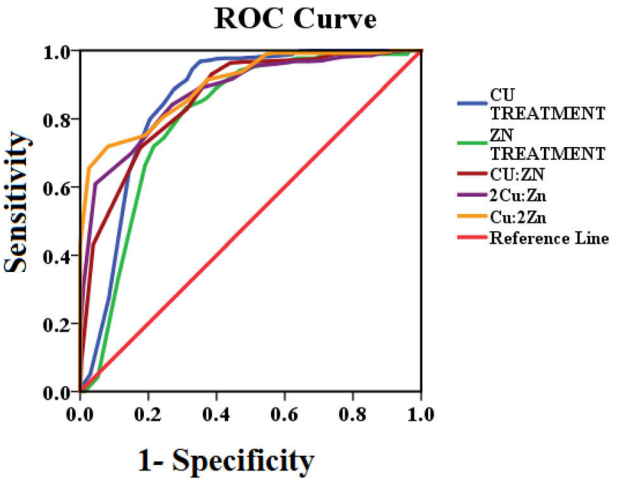

Fig. 10 Receiver operating characteristic curve for Cu, Zn and metal mixtures treated on the *S. aureus* populations

4 Conclusion

We examined the various molecular variations in the FTIR spectra due to Cu and Zn toxicity on *S. aureus*. Our study provides information that the toxicity mechanism of Cu is more pronounced than Zn. Further, the combined toxicity level Cu:2Zn shows increased toxicity resulting in changes at polysaccharides and protein levels. This shows the synergism exhibited among the metals studied. The spectral variation of *S. aureus*, resistant to metal treatment shows the changes occurring in the carbohydrates and protein regions. *S. aureus* bacteria produce cellulose-rich polysaccharide which was observed from FTIR spectra. This confirms binding occurs in this region. However, the secretion of EPS depends on the availability of nutrients and morphology of bacteria studied. This may be due to uptake or efflux of the metal ions from the cells. This results in the translocation of Zn and/or Cu from the cytoplasm in *S. aureus* and depends on the particular metal concentration present in the bacterial strain. Secondary structural changes of protein reveal an increase in ß sheet and a decrease in α helix due to metal treatments. PCA plots show the possible distinct variation of the *S. aureus* samples studied. The selected spectral range observed helps in evaluating the toxicity due to metal interaction on *S. aureus*. The ROC curve and the Youden index values validate our experimental study. This work shows how *S.aureus can* resist stress due to Cu-Zn metal mixtures in the environment. The study will help in understanding the capability of *S. aureus* in the defence mechanism due to Cu and/or Zn metals. The study gives an overview of the interaction mechanism of complex metal mixtures with regard to the molecular changes using FTIR coupled with chemometric techniques.

Acknowledgments The authors express thanks to the authorities, SAIF, IIT, Bombay, India for providing the necessary facilities in recording FTIR and ICP AES spectra.

Funding This research does receive any funding from government or private bodies.

Compliance with ethical standards

Conflict of interest There is no conflict of interest in this research work as declared by authors.

Ethical approval This study does not contain any animal model/experiment and hence does not require any ethical approval.

References

1. Silver, S.: Bacterial Heavy Metal Detoxification and Resistance Systems. In: Mongkolsuk, S., Lovett, P.S., Trempy, J.E. (eds.) Biotechnology and Environmental Science. Springer, Boston (1992). https://doi.org/10.1007/978-0-585-32386-2_14
2. Corbin, B.D., Seeley, E.H., Raab, A., Feldmann, J., Miller, M.R.: Metal chelation and inhibition of bacterial growth in tissue abscesses. Science **319**, 962–965 (2008). https://doi.org/10.1126/science.1152449
3. Ting-Ting, F., Xi, L., Qi-Sui, W., Zhi-Jun, Z., Peng, L., Zhang, C.-C.: Toxicity evaluation of CdTe quantum dots with different size on *Escherichia coli*. Toxicology in Vitro **26**(7), 1233–1239 (2012). https://doi.org/10.1016/j.tiv.2012.06.001
4. Lasch, P., Naumann, D.: Infrared Spectroscopy in Microbiology. In Encyclopedia of Analytical Chemistry, R.A. Meyers (Ed.). (2015). doi:https://doi.org/10.1002/9780470027318.a0117.pub2
5. Grunert, T., Jovanovic, D., Sirisarn, W., Johler, S., Weidenmaier, C., Schlz, M.E., Xia, G.: Analysis of *Staphylococcus aureus* wall teichoic acid glycoepitopes by Fourier transform infrared Spectroscopy provides novel insights into staphylococcal glycocode. Sci. Rep. **8**, 1889–1897 (2018). https://doi.org/10.1038/s41598-018-20222-6
6. Bae, W., Chen, X.: Proteomic study for the cellular responses to Cd^{2+} in *Schizosaccharomyces pombe* through amino acid coded mass tagging and liquid chromatography tandem mass spectrometry. Mol. Cell. Proteomics **3**, 596–607 (2004). https://doi.org/10.1074/mcp.M300122-MCP200
7. Al-Qadiri, H.M., Lin, M., Al-Holy, M.A., Cavinato, A.G., Rasco, B.A.: Detection of sublethal thermal injury in Salmonella enterica serotype typhimurium and listeria monocytogenes using Fourier transform infrared (FT-IR) spectroscopy (4000 to 600 cm(−1)). J. Food Sci. **73**(2), M54–M61 (2008). https://doi.org/10.1111/j.1750-3841.2007.00640.x
8. Gupta, A.D., Karthikeyan, S.: Individual and combined toxic effect of nickel and chromium on biochemical constituents in *E. coli* using FTIR spectroscopy and principal component analysis. Ecotoxicology and Environmental Safety **130**, 289–294 (2016). https://doi.org/10.1016/j.ecoenv.2016.04.025
9. Gupta, A.D., Karthikeyan, S., Chitra, A.: Resistance mechanism of Ni^{2+} ion individually and in combination with the Cr^{6+} ion in *Staphylococcus aureus* species to characterize the molecular changes studied using infrared spectroscopy coupled with chemometrics. Infrared Phys. & Technol. **94**, 126–133 (2018). https://doi.org/10.1016/j.infrared.2018.09.002
10. Kumar, M.M., Kumari, S.B., Kavitha, E., et al.: Spectral profile index changes as biomarker of toxicity in *Catla catla* (Hamilton, 1822) edible fish studied using FTIR and principal component analysis. SN Appl. Sci. **2**, 1233 (2020). https://doi.org/10.1007/s42452-020-3001-z
11. Phetsombat, S., Kruatrachue, M., Pokethitiyook, P., Upatham, S.: Toxicity and bioaccumulation of cadmium and lead in *Salvinia cucullata*. J. Environ. Biol. **27**, 645–652 (2006)
12. Zhou, M., Liu, Y., Zeng, G., et al.: Kinetic and equilibrium studies of Cr(VI) biosorption by dead *Bacillus licheniformis* biomass. World J. Microbiol. Biotechnol. **23**, 43–48 (2007). https://doi.org/10.1007/s11274-006-9191-8
13. Naumann, D.: FT-Infrared and FT-Raman spectroscopy in biomedical research. Appl. Spectros. Rev. **36**(2–3), 239–298 (2001). https://doi.org/10.1081/ASR-100106157
14. Ward, J.H.: Hierarchical grouping to optimize an objective function. J. Am. Stat. Assoc. **58**(301), 236–244 (1963). https://doi.org/10.1080/01621459.1963.10500845
15. Shine, J.P., Trapp, C.J., Coull, B.A.: Use of receiver operating characteristic curves to evaluate sediment quality guidelines for metals. Environ. Toxicol. Chem. **22**, 1642–1648 (2003). https://doi.org/10.1002/etc.5620220728
16. Obinaju, B.E., Fullwood, N.J., Martin, F.L.: Distinguishing nuclei-specific benzo[a]pyrene-induced effects from whole-cell alterations in MCF-7 cells using Fourier-transform infrared spectroscopy. Toxicol. **335**, 27–34 (2015). https://doi.org/10.1016/j.tox.2015.07.001
17. Hassan, K.A., Pederick, V.G., Elbourne, L.D.H., et al.: Zinc stress induces copper depletion in *Acinetobacter baumannii*. BMC Microbiol. **17**, 59–74 (2017). https://doi.org/10.1186/s12866-017-0965-y

18. Goswami, L., Arul Manikandan, N., Pakshirajan, K., et al.: Simultaneous heavy metal removal and anthracene biodegradation by the oleaginous bacteria *Rhodococcus opacus*. Biotech **7**, 37 (2017). https://doi.org/10.1007/s13205-016-0597-1
19. Gurbanov, R., Ozek, N.S., Gozen, Y.G., Severcan, F.: Quick discrimination of heavy metals resistan bacterial populations using infrared spectroscopy coupled with chemometrics. Anal. Chem. **87**, 9653–9661 (2015). https://doi.org/10.1021/acs.analchem.5b01659
20. Sakamoto, T., Murata, N.: Regulation of the desaturation of fatty acids and its role in tolerance to cold and salt stress. Cur Opin Microbiol. **5**(2), 208–210 (2002). https://doi.org/10.1016/s1369-5274(02)00306-5
21. Ruttkay-Nedecky, B., Nejdl, L., Gumulec, J., Zitka, O., Masarik, M., Eckschlager, T., Stiborova, M., Adam, V.: Rene Kizek.: the role of Metallothionein in oxidative stress. Int. J. Mol. Sci. **14**(6044–6066), (2013). https://doi.org/10.3390/ijms14036044
22. Blindauer, C.A., Harrison, M.D., Robinson, A.K., Parkinson, J.A., Bowness, P.W., Sadler, P.J., Robinson, N.J.: Multiple bacteria encode metallothioneins and SmtA-like zinc fingers. Mol. Microbiol. **45**, 1421–1432 (2002). https://doi.org/10.1046/j.1365-2958.2002.03109.x
23. Eijkelkamp, B.A., Morey, J.R., Ween, M.P.: Ong C-lY., McEwan AG., Paton JC., et al.: Extracellular zinc competitively inhibits manganese uptake and compromises oxidative stress management in *Streptococcus pneumoniae*. PLoS One **9**(2), e89427 (2014). https://doi.org/10.1371/journal.pone.0089427
24. Ishida, T.: Bacteriolyses of bacterial cell walls by Cu(II) and Zn(II) ions based on antibacterial results of dilution medium method and halo antibacterial test. J. Adv. Res. Biotech. **2**(2), 1–12 (2017). https://doi.org/10.15226/2475-4714/2/2/00120
25. Odermatt, A., Suter, H., Krapf, R.M.: Primary structure of two P-type ATPases involved in copper homeostasis in Enterococcus hirae. J. Biol. Chem. **268**(17), 12775–12779 (1993)
26. McDevitt, C.A., Ogunniyi, A.D., Valkov, E., Lawrence, M.C., Kobe, B.: A molecular mechanism for bacterial susceptibility to zinc. PLoS Pathog. **7**(11), e1002357 (2011). https://doi.org/10.1371/journal.ppat.1002357
27. Campos, J., Sousa, C., Mourão, J., Lopes, J., Antunes, P., Peixe, L.: Discrimination of non-typhoid Salmonella serogroups and serotypes by Fourier transform infrared spectroscopy: A comprehensive analysis. Int. J. Food Microbio. **285**, 34–41 (2018). https://doi.org/10.1016/j.ijfoodmicro.2018.07.005
28. Whelan, D.R., Bambery, K.R., Heraud, P., Tobin, M.J., Diem, M., McNaughton, D., Wood, B.R.: Monitoring the reversible B to A-like transition of DNA in eukaryotic cells using Fourier transform infrared spectroscopy. Nucleic Acids Res. **39**(13), 5439–5448 (2011). https://doi.org/10.1093/nar/gkr175
29. Whelan, D.R., Hiscox, T.J., Rood, J.I., Bambery, K.R., Don, M.N., Wood Bayden, R.: Detection of an *en masse* and reversible B- to A-DNA conformational transition in prokaryotes in response to desiccation. J. Roy. Soc. Interface 1120140454 (2014). https://doi.org/10.1098/rsif.2014.0454
30. Gurbanov, R., Tunçer, S., Mingu, S., Severcan, F., Gozen, A.G.: Methylation, sugar puckering and Z-form status of DNA from a heavy metal-acclimated freshwater *Gordonia* sp. J. Photochem. Photobiol. **198**, 111580 (2019). https://doi.org/10.1016/j.jphotobiol.2019.111580
31. Gurbanov, R.S., Ozek, N., Tunçer, S., Severcan, F., Gozen, A.G.: Aspects of silver tolerance in bacteria: infrared spectral changes and epigenetic clues. J. Biophotonics **11**(5), 11–e201700252 (2018). https://doi.org/10.1002/jbio.201700252
32. Gurbanov, R., Karadag, H., Karaçam, S., Samgane, G.: Tapioca starch modulates cellular events in oral probiotic *Streptococcus salivarius* strains. Probiotics Antimicrob. Proteins (2020). https://doi.org/10.1007/s12602-020-09678-z
33. Ferreira, M.L., Gerbino, E., Cavallero, G.J., Casabuono, A.C., Couto, A.S., Gomez-Zavaglia, A., Ramirez, S.A.M., Vullo, D.L.: Infrared spectroscopy with multivariate analysis to interrogate the interaction of whole cells and secreted soluble exopolimeric substances of *Pseudomonas veronii* 2E with Cd(II), Cu(II) and Zn(II). Spectrochim. Acta - Part A: Molec. Biomolec. Spectros. **228**(5), 117820–117828 (2020). https://doi.org/10.1016/j.saa.2019.117820
34. Guerra, A.J., Dann, C.E., Giedron, D.P.: Crystal structure of the zinc dependent MarR family transcriptional regulator AdcR in the Zn(II) bound state. J. Am. Chem. Soc. **133**, 19614–11617 (2011). https://doi.org/10.1021/ja2080532
35. Sanson, M., Makthal, N., Flores, A.R., Olsen, R.J., Musser, J.M., Kumaraswami, M.: Adhesin competence repressor(AdcR) from *Streptococcus pyogenes* controls adaptive responses to zinc limitation and contributes to virulence. Nucleic Acids Res. **43**, 418–432 (2015). https://doi.org/10.1093/nar/gku1304
36. Merroun, M.L.: Interactions between metals and bacteria: fundamental and applied research. In: Méndez-Vilas, A. (ed.) Communicating Current Research and Educational Topics and Trends in Applied Microbiology, pp. 108–119. Formatex, Mérida (2007)
37. She, Z., Hu, X., Zhao, X., Ren, Z., Ding, G.: FTIR investigation of the effects of ultra-strong static magnetic field on the secondary structures of protein in bacteria. Infrared Phys. and Technol. **52**(4), 138–142 (2009). https://doi.org/10.1016/j.infrared.2009.06.002

38. Kepenek, E.S., Severcan, M., Gozen, A.G., Severcan, F.: Discrimination of heavy metal acclimated environmental strains by chemometric analysis of FTIR spectra. Ecotoxicol. Environ. Safety **202**, 110953 (2020). https://doi.org/10.1016/j.ecoenv.2020.110953
39. Partouche, D., Militello, V., Gomez-Zavaglia, A., Wien, F., Sandt, C., Arluison, V.: *In situ* characterization of Hfq bacterial amyloid: a Fourier-transform infrared spectroscopy study. Pathogens **8**(1), 36 (2019). https://doi.org/10.3390/pathogens8010036
40. Kochan, K., Lai, E., Richardson, Z., Nethercott, C., Peleg, A.Y., Heraud, P., Wood, B.R.: Vibrational spectroscopy as a sensitive probe for the chemistry of intra-phase bacterial growth. Sensors **20**(12), 3452 (2020). https://doi.org/10.3390/s20123452
41. Naumann, D., Fijala, V., Labischinski, H., Giesbrecht, P.: The rapid differentiation and identification of pathogenic bacteria using Fourier transform infrared spectroscopic and multivariate statistical analysis. J. Molec. Struct. **174**, 165–170 (1988). https://doi.org/10.1016/0022-2860(88)80152-2
42. Choo-Smith, L.-P., Maquelin, K., van Vreeswijk, T., Bruining, H.A., Puppels, G.J., Ngo Thi, N.A., Kirschner, C., Naumann, D., Ami, D., Villa, A.M., Orsini, F., Doglia, S.M., Lamfarraj, H., Sockalingum, G.D., Manfait, M., Allouch, P., Endtz, H.P.: Investigating microbial (micro)colony heterogeneity by vibrational spectroscopy. Appl. Environ. Microbiol. **67**(4), 1461–1469 (2001). https://doi.org/10.1128/AEM.67.4.1461-1469.2001
43. Savic, D., Jokovic, N., Topisirovic, L.: Multivariate statistical methods for discrimination of lactobacilli based on their FTIR spectra. Dairy Sci. Technol. **88**, 273–290 (2008). https://doi.org/10.1051/dst:200800
44. Sharaha, U., Rodriguez-Diaz, E., Riesenberg, K., Bigio, I.J., Huleihel, M., Salman, A.: Using infrared spectroscopy and multivariate analysis to detect antibiotic resistant *Escherichia coli* bacteria. Analytical Chem. **89**(17), 8782–8790 (2017). https://doi.org/10.1021/acs.analchem.7b01025

Affiliations

Annika Durve Gupta[1] · **Esakimuthu Kavitha**[2] · **Shikha Singh**[1] · **Sivakumaran Karthikeyan**[3]

[1] Department of Biotechnology, B. K. Birla College, Kalyan, Maharashtra 421304, India

[2] Department of Physics, Dr. MGR Educational and Research Institute, Chennai, Tamil Nadu 600095, India

[3] Department of Physics, Dr. Ambedkar Government Arts College, Chennai, Tamil Nadu 600039, India

Food Chemistry 344 (2021) 128643

Contents lists available at ScienceDirect

Food Chemistry

journal homepage: www.elsevier.com/locate/foodchem

Structural and rheological changes of texturized mung bean protein induced by feed moisture during extrusion

Fatema Hossain Brishti [a], Shyan Yea Chay [a], Kharidah Muhammad [a], Mohammad Rashedi Ismail-Fitry [b], Mohammad Zarei [c], Sivakumaran Karthikeyan [d], F. Caballero-Briones [e], Nazamid Saari [a,*]

[a] Department of Food Science, Faculty of Food Science and Technology, Universiti Putra Malaysia, 43400 UPM, Serdang, Selangor, Malaysia
[b] Department of Food Technology, Faculty of Food Science and Technology, Universiti Putra Malaysia, 43400 UPM, Serdang, Selangor, Malaysia
[c] Department of Food Science and Technology, School of Industrial Technology, Faculty of Applied Sciences, Universiti Teknologi MARA, 40450 Shah Alam, Selangor, Malaysia
[d] Department of Physics, Dr. Ambedkar Government Arts College, Chennai, Tamil Nadu 600 039, India
[e] Instituto Politecnico Nacional, Materiales y Tecnologias para Energia, Salud y Medio Ambiente (GESMAT), CICATA Altamira, Km 14.5 Carretera Tampico-Puerto Industrial, 89600 Altamira, Mexico

ARTICLE INFO

Keywords:
Extrusion
Mung bean
Secondary structure
Structural properties
Sustainable food
Texturized vegetable protein

ABSTRACT

Mung bean protein isolate was texturized at different feed moisture contents (30.0, 49.3, and 60.0%) at a constant temperature (144.57 °C) to evaluate the changes in protein profile, solubility, thermal, structural (at secondary and tertiary levels) and rheological properties. SDS-PAGE, surface hydrophobicity, circular dichroism, FTIR spectroscopy, and fluorescence analyses revealed protein unfolding, aggregation, and structural rearrangement as a function of feed moisture content. Extrusion at 49.3% feed moisture produced texturized mung bean protein (TMBP) with favourable partial denaturation, the formation of small aggregates, improved solubility, and digestibility with strong gel forming behaviour, whereas 30.0 and 60.0% moisture content resulted in complete protein denaturation, the undesirable formation of large aggregates and weak gels. In conclusion, protein denaturation and formation of aggregates can be controlled by manipulating feed moisture content during extrusion, with 49.3% feed moisture prompting favourable partial denaturation to produce TMBP with desirable qualities for use as a vegetarian-based meat extender.

1. Introduction

Mung bean (*Vigna radiate* L.) is a leguminous crop predominantly grown in Asia and other parts of the world. In South Asia, the demand for mung bean reached 5.4 million tons between 2015 and 2016 (Schreinemachers et al., 2019), credited to high protein content (25–28%), low fat content (0.32–0.75 g/100 g) and easy digestibility (Hou et al., 2019; Khaket, Dhanda, Jodha, & Singh, 2015). As a protein-rich edible plant, mung bean demonstrates strong potential as a sustainable, economic, and environmentally-friendly source of "green protein" due to a lower carbon footprint compared to animal proteins like cattle and poultry.

To date, mung bean protein remains underutilized despite the potential of plant protein to be converted into other food products with extended shelf-life and versatility. For example, texturized vegetable protein (TVP), is a processed food fabricated from plants with the ability to mimic meat-like chewiness upon cooking. It is a healthy alternative to animal meat as it is cholesterol-free, low in fat, and high in protein. It is produced by extrusion, a multifunction operation where solid food material is forced through a die specifically designed for puffing food ingredients under different conditions of mixing, heating, and shear. During the process, a series of thermo-mechanical actions (protein denaturation, inactivation of enzymes, and anti-nutritional compounds) is applied to disrupt the native protein structure, forming a continuous viscoelastic mass (Riaz, 2011).

Despite the increased use of extrusion to produce TVP, little is known about the chemical reactions and structural changes of the protein molecules due to the diverse molecular composition of different proteins and intricate macromolecular interactions during extrusion (Verbeek & Van den Berg, 2010). Moreover, the characteristics of TVP relies heavily on the processing conditions including barrel temperature, feed

* Corresponding author.
E-mail address: nazamid@upm.edu.my (N. Saari).

https://doi.org/10.1016/j.foodchem.2020.128643
Received 29 March 2020; Received in revised form 10 November 2020; Accepted 11 November 2020
Available online 16 November 2020

moisture, feed composition (in terms of protein type, protein conformation, amino acid sequence), screw speed, extruder type, die geometry and screw configuration (Purwanti et al., 2010; Qi & Onwulata, 2011). This causes the final properties of the extruded product to differ from one sample to another, thus justifying the need to study the protein on a case-by-case basis.

Previous studies have reported the effect of extrusion on the structural properties and functionalities of whey protein isolate (Qi & Onwulata, 2011), wheat flour protein (Li & Lee, 1996), soybean protein isolate (Chen, Wei, & Zhang, 2011) and legume protein (Hood-Niefer and Tyler, 2010). Mung bean shows several favourable characteristics over soy protein isolate in terms of better functionality (gelling and foaming capacity), lower denaturation enthalpy (to promote texturization), and good amino acid profile (high lysine, isoleucine, and cystine) (Brishti et al., 2017). Additionally, mung bean protein is gluten-free, making it suitable for gluten intolerant individuals. Despite the numerous benefits of mung bean over other plant proteins, its potential as a food ingredient remains underexploited. The texturization of plant protein is not fully elucidated, particularly the molecular mechanism of protein interactions and structural alterations that occur during extrusion. Based on our previous work that optimized extrusion variables (feed moisture, barrel temperature, and screw speed) to produce texturized mung bean protein (TMBP) using response surface methodology, it was found that feed moisture solely affected the mung bean protein profile, irrespective of barrel temperature and screw speed (data not shown). Therefore, this current study aimed to investigate the sole effect of feed moisture on TMBP in terms of solubility, thermal, structural (including secondary and tertiary structure), and rheological properties, in comparison to the native mung bean protein, from an in-depth molecular aspect.

2. Materials and methods

2.1. Materials

Mung bean flour (product code: 9 556,066 312560) was purchased from Spicon products Sdn Bhd (Melaka, Malaysia). Sodium dodecyl sulfate, Coomassie Blue R250, ANS (8-anilinonaphthalene-1-sulfonic acid) fluorescent probe, β-mercaptoethanol, Ellman's reagent, and bovine serum albumin were purchased from Sigma-Aldrich Corporation (St Louis, MO, USA). All chemicals used were analytical grade.

2.2. Preparation of protein isolate

Mung bean protein isolate was prepared according to the method described by Thompson (1977) with slight modification. Briefly, 10 kg of mung bean flour was dispersed in 100 L of distilled water, with the pH adjusted to 9 using 3 mol L^{-1} NaOH, then stirred at 2000 rpm for 1 h at 30 °C in a stirred tank bioreactor equipped with six-bladed Rushton turbine (B. Braun Biotech International GmbH, Melsungen, Germany). The solution was centrifuged at 8586*g* using a continuous centrifugal machine (Model AS16VBNF, Alfa Laval Corporate AB, Lund, Sweden), and the pH of the supernatant adjusted to 4.5 using 3 mol L^{-1} HCl to precipitate the protein, which was then recovered by centrifugation at 8586*g*. The protein curd was freeze-dried for 48 h using a freeze dryer (VirTis Benchmark Freeze Dryer, SP Scientific, Stone Ridge, NY, USA). A total of 23 kg of mung bean protein was successfully prepared from 150 kg of mung bean flour. The proximate composition of the mung bean protein isolate was determined following AOAC (2005) standard method and recorded at 4.49% moisture (AOAC 934.01), 86.15% protein (AOAC 978.04), 1.11% fat (AOAC 954.01), 0.49% ash (AOAC 942.05), 0.55% fibre (AOAC 962.09), and 7.21% total carbohydrate (calculated by difference).

2.3. Preconditioning of protein isolate

Preconditioning was performed to incorporate the feed moisture into the mung bean protein powder before extrusion. Freeze-dried powder (86.15% protein and 1.11% fat) was ground and sieved by passing through a 150 μm screen. The moisture content was measured before preconditioning, with the appropriate amount of distilled water sprayed onto the powder to adjust the moisture content to the level required as per experimental design. The sample was mixed thoroughly using a hand blender until homogenous, gradually adding the water to avoid clumping. The moist samples were then sealed in polyethylene bags, equilibrated by storing at 4 °C for 24 h before extrusion. The moisture adjustment was performed according to the method of Serna-Saldivar (2012) using Eq. (1),

$$\text{Amount of water to add (mL)} = \left[\frac{100 - \%\ \textit{actual moisture content in protein isolate}}{(100 - \%\ \textit{desired moisture content in protein isolate})} - 1\right] \times \text{ amount of dry protein isolate powder} \quad (1)$$

2.4. Extrusion process

Extrusion was performed using a single screw stand-alone extruder (Model KE-19/25D, Brabender GmbH & Co. KG, Duisburg, Germany), with a spiral screw with the compression ratio of 3:1 and round die with a diameter of 10 mm. The extruder barrels were 19 mm in diameter and contained four heating zones. The screw speed and temperature of the extruder barrel were set at 80.66 rpm and 144.57 °C, respectively. The feed moisture content was fixed at three levels: low (30.0%), intermediate (49.3%), and high (60.0%). The extruder was fed manually through a conical hopper, keeping flights of the screw filled. After reaching a steady condition, the extruded product was collected and cooled at room temperature, then dried in a convection oven (Memmert GmbH + Co. KG, Schwabach, Germany) at 45 °C to a moisture content of 9–10% (wet basis) to produce TMBP. Dried TMBP was stored in a plastic container at −18 °C until further analysis. Prior to analysis, TMBP was ground into a fine powder using a grinder (IKA, MF 10 basic microfine grinder, Fullerton, CA, USA).

2.5. SDS-PAGE

SDS-PAGE was performed in a Mini-PROTEAN Tetra electrophoresis cell (Bio-Rad, Hercules, CA, USA), following the method of Laemmli (1970) using a 5% stacking gel and 12.5% separating gel. The mung bean protein isolate (MBPI, as control) was dissolved in phosphate buffer (10 mmol L^{-1}, pH 7.0, at 10 mg/mL), stirred for 12 h, homogenized, centrifuged at 7000*g* for 30 min and supernatant was collected. Then, 20 μL of the supernatant was mixed with 20 μL of sample buffer [0.125 mol L^{-1} Tris-HCl buffer, pH 8.0 containing 1% SDS (w/v), 0.05% bromophenol blue (w/v), 30% glycerol (v/v)]. The mixture was heated for 5 min at 90 °C and centrifuged at 8000*g* for 10 min. For TMBP, 5 mg of sample was dispersed in 1 mL of sample buffer, agitated at room temperature for 30 min, heated and shaken at 90 °C for 10 min, then centrifuged at 7000*g* at 20 °C for 5 min.

A 10 μL aliquot of the sample (MBPI/TMBP and protein marker) was

loaded into the gel well and electrophoresis was performed at 100 V for first 10 min, followed by 140 V for the next 30 min until the tracking dye ran toward the end of the gel. Finally, the gel was stained with Coomassie Blue R-250 solution (0.5% Coomassie Blue R-250 in 50% ethanol, 10% acetic acid, and 400% deionized water) and destained with a solution of 20% ethanol and 8% acetic acid.

2.6. Protein solubility

Protein solubility was determined according to the method of Morr et al. (1985) with minor modification. In brief, 0.5 g of MBPI or TMBP samples were dispersed into 50 mL of sodium phosphate buffer (10 mmol L^{-1}, pH 7.0), followed by continuous stirring for 2 h at room temperature. The solutions were then centrifuged at 7000 *g* for 15 min at 25 °C, filtered through Whatman No. 1 filter paper and analysed for soluble protein content via Lowry's method using bovine serum albumin (2 mg/mL) as standard. Percent protein solubility was expressed according to Eq. (2),

$$\text{Protein solubility } (\%) = \frac{\text{Protein content of the supernatant}}{\text{Total protein of the original sample}} \times 100\% \quad (2)$$

2.7. Thermal properties

Differential scanning calorimetry (Model DSC-823E, Mettler-Toledo International Inc., Columbus, OH, USA) was used to determine the thermal properties of the samples according to the method of Li, Wei, Fang, Zhang, & Zhang (2014) with slight modification. MBPI and TMBP samples (8–10 mg) were weighed in aluminium pans and sealed hermetically, then the pans were heated from 25 to 300 °C at a rate of 10 °C/min. The calibration was performed with indium. The peak temperature (T_d), onset temperature (T_o), endset temperature (T_e) and enthalpy (ΔH) were calculated using Mettler-Toledo STARe software system, version 9.x (Mettler-Toledo International Inc., Columbus, OH, USA).

2.8. Structural properties

2.8.1. Surface hydrophobicity (H_0)

H_0 was determined according to the method of Nakai (2003) using an ANS (8-anilino-1-naphthalenesulfonic acid) fluorescent probe. MBPI and TMBP samples were suspended in phosphate buffer (10 mmol L^{-1}, pH 7.0) to prepare protein solutions at 0.0035%, 0.0075%, 0.015%, 0.03% and 0.06% (w/v). Four millilitres of each solution was mixed with 20 mL of freshly prepared ANS solution (8 mmol L^{-1} ANS in 10 mmol L^{-1} phosphate buffer, pH 7.0), shaken vigorously, and kept in the dark for 10 min. The relative fluorescent intensity (RFI) was measured using a microplate spectrofluorophotometer (Model SpectraMax Gemini XPS, Molecular Devices LLC., San Jose, CA, USA) at $\lambda_{excitation} = 390$ nm and $\lambda_{emission} = 470$ nm. H_0 was calculated from the slope by plotting RFIs versus protein concentrations (%) as linear regression.

2.8.2. Sulfhydryl groups (SH) and disulfide bonds (S—S)

The sulfhydryl groups and disulfide bonds were estimated according to the method of Shimada and Cheftel (1988) with slight modification. In brief, 30 mg of MBPI and TMBP samples were dispersed in 10 mL of Tris-Glycine buffer (0.086 mol L^{-1} Tris, 0.09 mol L^{-1} Glycine and 0.04 mol L^{-1} EDTA, pH 8.0) containing 8 mol L^{-1} urea (total SH) or without 8 mol L^{-1} urea (free/exposed SH). An aliquot of 4 mL was mixed with 0.1 mL of Ellman's reagent [5,5′-dithiobis-(2-nitrobenzoic acid) in Tris-Glycine buffer, 4 mg/mL, pH 8.0]. The mixture was incubated in the dark at room temperature for 1 h, followed by centrifugation at 5000*g* for 10 min. The supernatant was collected, and the absorbance was measured at 412 nm against a reagent blank. The same procedure was followed to determine the free SH content. Total SH and free SH content were calculated according to Eq. (3),

$$\mu\text{mol SH/g} = \frac{73.53 \times A412 \times D}{C} \quad (3)$$

where A_{412} = absorbance at 412 nm; C = concentration of sample (mg/mL), D = dilution factor (1.01)

For the quantification of SS content, 1 mL of protein dispersion was added to 0.05 mL of β-mercaptoethanol and 4 mL of Tris-Glycine buffer, incubated for 1 h at room temperature before the addition of 10 mL of trichloroacetic acid (12%), mixed and centrifuged at 5000*g* for 10 min. The precipitate was resuspended in 10 mL of Tris-Glycine buffer, then 0.04 mL of Ellman's reagent was added. The mixture was incubated in the dark at room temperature for 30 min, followed by centrifugation at 5000 *g* for 10 min. The absorbance of the supernatant was measured at 412 nm against a reagent blank and the SS bond was calculated according to Eq. (4),

$$\mu\text{mol S} - \text{S/g} = \left(\frac{73.53 \times A412 \times D}{C} - \text{SHfree}\right) \Big/ 2 \quad (4)$$

where A_{412} = absorbance at 412 nm; C = concentration of sample (mg/mL), D = dilution factor (6.08).

2.9. Secondary structure

2.9.1. Circular dichroism (CD)

The CD spectra data were collected using a Circular Dichroism (JASCO J-815, Tokyo, Japan) following the method of Qi and Onwulata (2011). MBPI and TMBP samples (10 mg/mL) were dispersed in sodium phosphate buffer (33 mmol L^{-1}, pH 6.75) and centrifuged at 8000*g*. Afterward, the supernatant was collected and filtered through a cellulose filter (0.45 μm), and absorbance was measured in the far-UV region (190–250 nm) at 26 ± 2 °C. The CD spectra were obtained using cuvettes with 0.5 mm path length and a scan time of 4.0 S/Nm (under nitrogen environment), represented as the average of three consecutive scans and expressed as relative ellipticity (m degree) versus wavelength.

2.9.2. Fourier transform infrared spectroscopy (FTIR)

The secondary structures of MBPI and TMBP were characterized using an ATR-FTIR spectrometer (Model Spectrum-100, PerkinElmer, Inc., Waltham, MA, USA). The FTIR spectra were recorded in the region of 4000–500 cm^{-1} with a spectral resolution of 10 cm^{-1} and 32 scans, then analysed using OriginLab software (OriginLab Corporation, Northampton, MA, USA). Fourier self-deconvolution was conducted on the second derivative function of the amide I region (1700–1600 cm^{-1}) by the Gaussian curve fitting to get detailed information on the secondary structures (Long et al., 2015).

2.10. Tertiary structure (Intrinsic tryptophan fluorescence spectroscopy)

Intrinsic fluorescence spectroscopy was performed following the method of Qi and Onwulata (2011). Protein dispersions were prepared (10 mg/mL) in sodium phosphate buffer (33 mmol L^{-1}, pH 6.75) and centrifuged at 8000*g*. Then, the supernatant was collected and filtered through a cellulose filter (0.45 μm). Tryptophan fluorescence was measured using a quartz cell (1 cm path length) and Cary Eclipse Fluorescence Spectrometer (Agilent Technologies, Santa Clara, CA, USA). Protein solutions were excited at 295 nm and fluorescence was recorded from 300 to 450 nm.

2.11. Rheological properties

2.11.1. Time sweep

Rheological evaluation was performed using a controlled stress rheometer (Model Rheostress RS600, Thermo Fisher Scientific Inc., Waltham, MA, USA). Samples were dispersed in phosphate buffer (10 mM, pH 7.0) to form a protein dispersion of 25% (w/v). Then, 1 mL of

the dispersion was loaded onto the lower plate of the rheometer set at 25 °C, and the upper plate was lowered to contact the sample, with the gap between the two plates maintained at 1 mm. The storage (G′) and loss (G″) modulus of the samples were recorded as a function of time at a constant frequency (1 Hz) and constant shear stress (20 Pa) (Joshi, Adhikari, Aldred, Panozzo, & Kasapis, 2011).

2.11.2. Frequency sweep

The sample preparation was the same as the time sweep experiment. The storage and loss modulus of the samples were recorded as a function of dynamic frequency starting from 0.01 to 100 Hz at constant shear stress (20 Pa) (Joshi et al., 2011).

2.12. Statistical analysis

All results were analysed using one-way ANOVA followed by an independent *t*-test using SPSS software (version 17, SPSS Inc., Chicago, IL, USA). Data were expressed as means ± standard deviations from triplicate readings. All sample means were significantly different at $p \leq 0.05$.

3. Results and discussion

3.1. Protein profile of TMBP

The SDS-PAGE protein bands of MBPI, as control and TMBP extruded at different feed moisture contents are shown in Fig. 1. In MBPI, five major bands were observed at 15, 25, 26, 50 and 65 kDa, of which the 15 kDa band represented the 7S globulin subunit, 25 kDa represented the 11S globulin while 26, 50 and 65 kDa corresponded to the 8S globulin subunit (Fig. 1a). This finding was in line with Mendoza et al. (2001), whereby mung bean native protein 7S globulin comprised 16 kDa and 28 kDa, 11S comprised 24 kDa and 40 kDa and 8S comprised 26, 32, 48, and 60 kDa.

Upon texturization, different feed moisture contents (30.0, 49.3, and 60.0%) caused remarkable changes to the samples. Texturization at low (30.0%) and high (60.0%) feed moisture content displayed only a single, newly formed thin band on the gel (37 kDa, Fig. 1b), with the disappearance of 7S and 11S subunits. This implies denaturation of mung bean protein and formation of bulky protein aggregates with large molecular weight, which then separated out from the solvent environment and were thus unable to penetrate the pores in the SDS-PAGE separating gel to form protein band (Chen et al., 2011). In contrast, texturization at intermediate (49.3%) moisture content produced four bands (20, 22, 37 and 40 kDa, Fig. 1c) that were much thinner and narrower than the control MBPI, along with blurry band colours and decreased band intensity, indicative of partial protein depolymerization

Table 1
Protein solubility, thermal and structural properties of mung bean protein isolate (MBPI) and texturized mung bean protein (TMBP) samples extruded at 30.0, 49.3, and 60.0% feed moisture content.

Properties	MBPI	TMBP (30.0%)	TMBP (49.3%)	TMBP (60.0%)
Protein solubility (%)	71.06 ± 0.06^{b}	49.33 ± 0.48^{c}	75.32 ± 0.69^{a}	49.73 ± 0.76^{c}
Thermal properties				
T_d (°C)	158.00 ± 0.33^{a}	61.22 ± 0.48^{b}	60.54 ± 3.13^{b}	60.72 ± 3.98^{b}
ΔH (J g^{-1})	19.20 ± 2.11^{a}	0.45 ± 0.07^{b}	1.86 ± 1.51^{b}	0.41 ± 0.09^{b}
T_o (°C)	155.50 ± 0.29^{a}	47.20 ± 0.50^{b}	41.86 ± 1.35^{c}	49.33 ± 2.5^{b}
T_e (°C)	158.49 ± 0.31^{a}	73.55 ± 2.38^{b}	74.85 ± 4.94^{b}	78.37 ± 0.29^{b}
Structural properties				
Surface hydrophobicity	4691.65 ± 2.33^{a}	596.95 ± 0.02^{d}	747.76 ± 1.89^{c}	890.52 ± 9.57^{b}
Sulfhydryl group and disulfide bond				
Total SH group (μmol/g)	15.61 ± 0.71^{a}	16.43 ± 0.42^{a}	15.71 ± 0.23^{a}	15.79 ± 0.19^{a}
Exposed SH group (μmol/g)	9.59 ± 0.45^{b}	10.77 ± 0.15^{a}	7.72 ± 0.40^{c}	10.79 ± 0.18^{a}
S—S bond (μmol/g)	54.66 ± 0.59^{b}	41.30 ± 0.57^{d}	129.17 ± 3.02^{a}	49.29 ± 1.80^{c}

Mean ± s.d. in a row followed by different letters are significantly ($p \leq 0.05$) different.

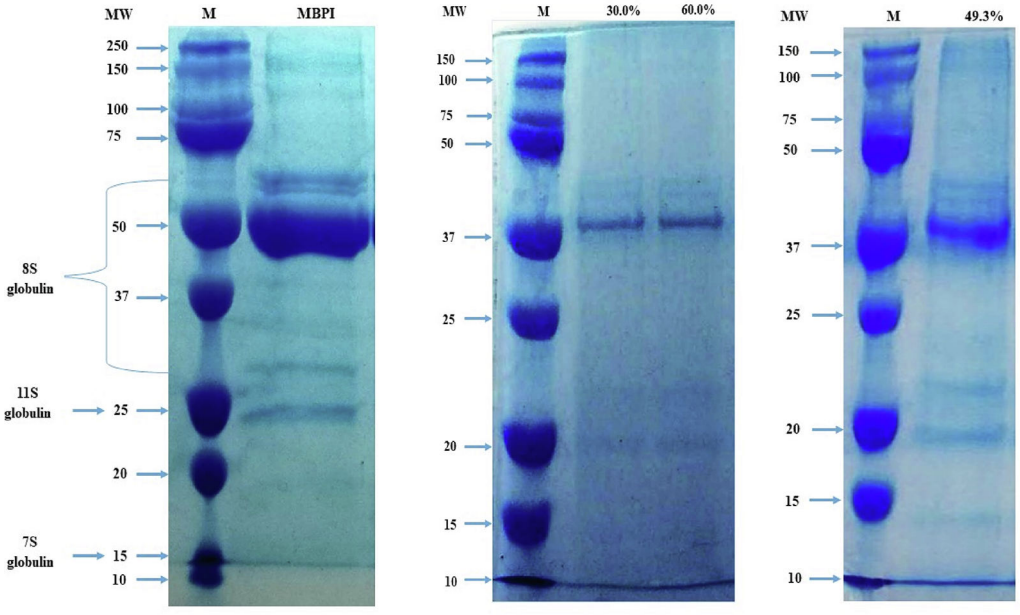

Fig. 1. SDS-PAGE protein bands of (a) mung bean protein isolate (MBPI, control), (b) texturized mung bean protein (TMBP, 30.0%, and 60.0%), and (c) texturized mung bean protein (TMBP, 49.3%). "M" represents the protein marker.

and denaturation that partially unfold the protein structure. This mechanism is desirable to facilitate texturization and produce a final product with good functional properties. The depolymerized proteins partially aggregate and form a network via inter or intramolecular disulfide bonds (S—S), as evidenced by the high disulfide bond content (129.17 μmol/g, Table 1) observed for TMBP texturized at 49.3% intermediate feed moisture content. Qi and Onwulata (2011) suggested that extrusion caused denaturation in texturized whey protein isolate, resulting in protein–protein aggregation through intermolecular S—S bond formation.

3.2. Protein solubility of TMBP

Protein solubility is an index of the functional property of a product and is estimated as the protein concentration in an aqueous solution that is not sedimented by centrifugal forces. It is mainly influenced by the polar and non-polar amino acid ratio, surface hydrophobicity, pH, temperature, processing condition (i.e. extrusion, drying, high-pressure treatment), degree of protein denaturation (partial or complete) and formation of protein aggregate (small or large) (Wagner et al., 2000). While protein solubility reduces when a protein molecule unfolds completely under prolonged heating, short-time heating could improve it. Similarly, partial denaturation (to some extent resembling native protein) and formation of small-sized protein aggregates (increased interactive surface region between protein and water molecules) facilitate the solubilization of protein molecules, thus improving the overall solubility.

Table 1 presents the protein solubility of MBPI (control) and TMBP samples, with TMBP produced at intermediate feed moisture recording the highest solubility of 75.32% compared to control (71.06%) and was significantly higher than TMBP produced at low and high feed moisture content. The improved solubility at intermediate feed moisture proves the occurrence of favourable partial protein denaturation which exposes all charged residues on the surface and refolds hydrophobic residues in the interior of protein structure (Damodaran, 2008). As evidenced by the SDS-PAGE gel pattern, texturization at 49.3% feed moisture partially depolymerized mung bean protein, forming smaller protein aggregates which improve its solubility (Damodaran, 2008). In contrast, the reduced protein solubility at the low feed moisture content (30.0%) could be attributed to the localized chemical modification which affected the solubility of texturized whey protein in a similar manner when it was extruded at 20–30% feed moisture level (Qi & Onwulata, 2011). It is also possible that the high shear rate (friction between sample and extruder screw) occurring at low feed moisture content, which gives rise to excessive denaturation and aggregation, forming large and hydrophobic protein clusters, lowered the solubility (Chen, Wei, Zhang, & Ojokoh, 2010; Damodaran, 2008). Texturization at 60.0% feed moisture content completely denatured mung bean protein, as depicted by SDS-PAGE gel bands. The large amount of water molecules present at this feed moisture content, along with applied heat inside the extruder, increases protein chain mobility and dynamic flexibility, thereby facilitating denaturation. When shear force is applied, denaturation is further intensified, causing extensive protein unfolding and formation of large insoluble aggregates, finally reducing the solubility (Damodaran, 2008).

3.3. Thermal properties of TMBP

Differential scanning calorimetry can be used to monitor structural and conformational changes of proteins due to processing treatments. It also serves as a base method to detect heat-induced protein denaturation or unfolding of protein structure. The denaturation temperature (T_d) indicates protein thermostability, while ΔH indicates the hydrophobic and hydrophilic interactions as well as the compactness of the proteins, whereby a larger ΔH depicts higher hydrophobicity and compactness. T_o and T_e indicate the onset and endset of denaturation temperatures.

Table 1 shows the thermal properties of MBPI (control) and TMBP samples extruded at 30.0, 49.3, and 60.0% feed moisture content. All parameters, including T_d, ΔH, T_o and T_e, reduced by more than two-folds when MBPI was texturized to produce TMBP. However, there was no significant difference between the texturized samples, indicating that thermal denaturation occurs because of extrusion rather than feed moisture levels. The decrease in T_d could be due to the action of feed moisture as plasticizer (Kitabatake & Doi, 1992), while lowered ΔH signifies reduced hydrophobicity and compactness of TMBP compared to MBPI, suggesting notable structural alteration during extrusion. The feed moisture content is concluded to play a critical role in denaturing the protein structure and facilitating protein melting inside the extruder barrel, making texturization possible.

3.4. Structural properties of TMBP

3.4.1. Surface hydrophobicity

The surface hydrophobicity of MBPI and TMBP were evaluated using ANS, a fluorescent probe that specifically binds to exposed hydrophobic clusters on protein molecules, eventually reflecting their surface hydrophobic properties. As shown in Table 1, the surface hydrophobicity of the control was significantly higher than all extruded samples, 4691.65 (unitless) compared to 596.95–890.52 for extruded samples. This significant reduction after extrusion could be attributed to the protein–protein crosslinking and formation of aggregates that cover most hydrophobic sites on the protein surface, thus inhibit the accessibility to ANS binding sites. This observation was in line with the SDS-PAGE results which showed the formation of protein aggregates that were too large to penetrate the gel, characterized by the absence of bands in Fig. 1b and band thinning in Fig. 1c.

Comparing the texturized samples, surface hydrophobicity increased significantly with increasing feed moisture content. A similar result was reported by Mozafarpour, Koocheki, Milani, and Varidi (2019) who observed an increment in surface hydrophobicity of soy protein concentrate when the feed moisture content increased from 18 to 25%. At low (30.0%) moisture content, surface hydrophobicity was less than the high (60.0%) moisture content, suggesting the formation of protein aggregates that behave differently when the feed moisture content changes. At 30.0% feed moisture, protein aggregates tend to bury hydrophobic groups within the core, resulting in decreased surface hydrophobicity, while at 60.0% moisture content, protein aggregates tend to expose hydrophobic groups to the surroundings, providing more binding sites for ANS (Celus, Brijs, & Delcour, 2007; Wang et al., 2019), resulting in increased surface hydrophobicity. Even though reduced surface hydrophobicity would improve the protein solubility, this occurs mainly in native, unmodified protein (i.e. MBPI before extrusion). Processed protein (i.e. TMBP after extrusion) behaves differently as a result of the complex chemical and structural alterations, leading to denaturation and aggregation during extrusion. As such, the intermediate moisture content of 49.3% produced TMBP with the highest solubility even though its surface hydrophobicity was not the lowest of the three texturized samples.

It can be concluded that the increase in feed moisture content during extrusion effectively increased surface hydrophobicity by denaturing mung bean proteins and exposing more hydrophobic domains, consequently making the protein structure more flexible. Surface hydrophobicity is a basic structural parameter strongly correlated to functional properties like emulsifying and foaming. Hence, regulating the feed moisture content during extrusion will produce desirable emulsion and foam properties required for different food product formulations.

3.4.2. Sulfhydryl groups (-SH) and disulfide bond content (S—S)

Intra- and intermolecular SH-SS interchange reactions are intricate in extrusion processing and play a significant role in the formation of relatively rigid proteins via crosslinking. Disulfide bonds, hydrophobic and electrostatic interactions are mainly responsible for the stabilization

of extruded protein structure (Akdogan, 1999). Table 1 shows the total -SH, exposed/free -SH and disulfide content of MBPI (control) and TMBP, with no significant difference in the total -SH content between control and texturized samples. Extrusion at 49.3% feed moisture content recorded the lowest exposed -SH content (7.72 μmol/g), possibly due to the oxidation of -SH groups to form sulfur oxidation products as well as involvement in protein–protein aggregation. Extrusion at 30.0% and 60.0% feed moisture content slightly increased the

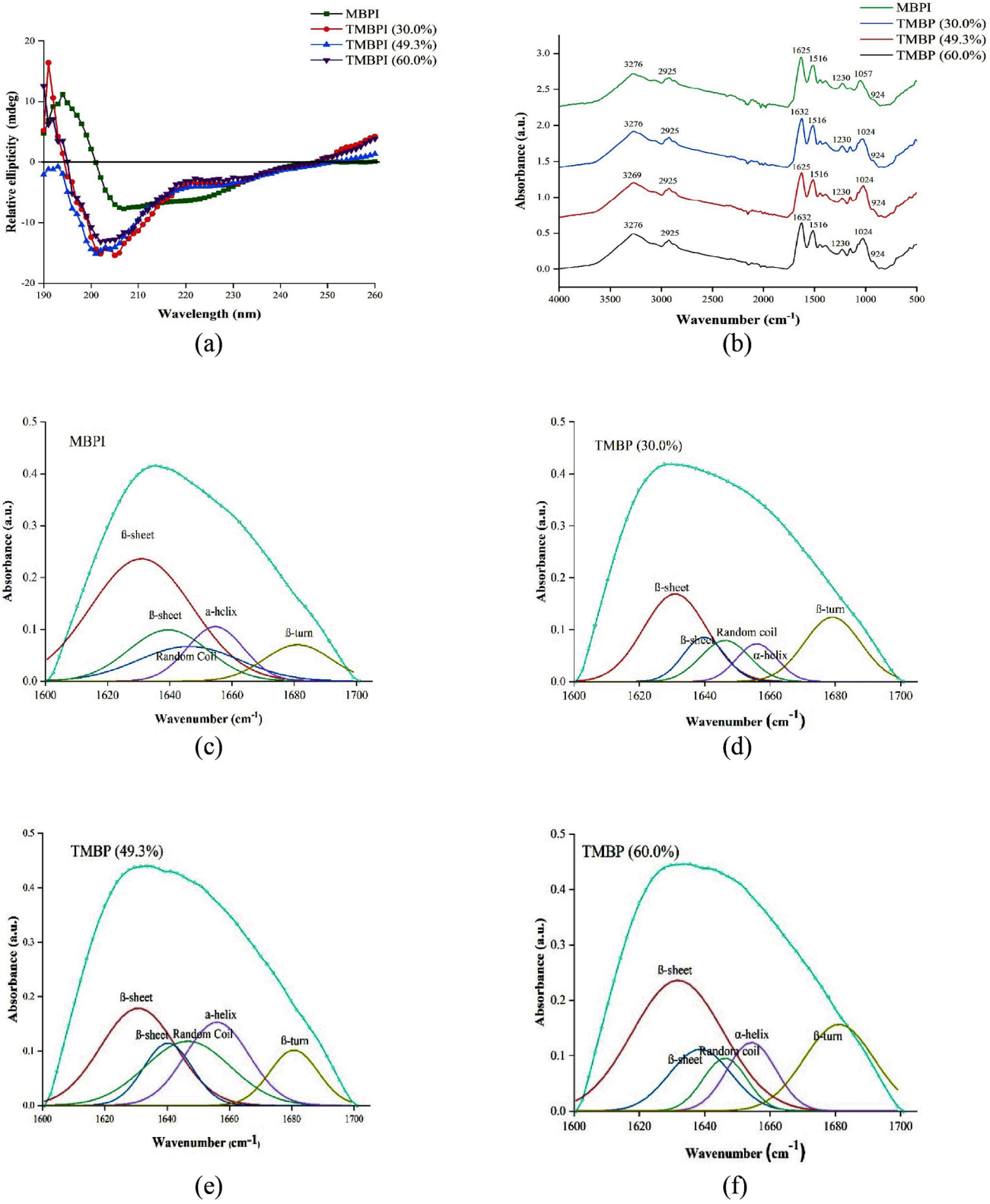

Fig. 2. Effects of extrusion feed moisture content on the secondary structure of texturized mung bean protein (TMBP) compared with mung bean protein isolate (MBPI, control). (a) Changes in the Far-UV CD spectra of MBPI and TMBP, (b) original FTIR spectra and Fourier self-deconvoluted curve-fitted spectra for (c) MBPI and TMBP extruded at (d) 30.0%, (e) 49.3% and (f) 60.0% feed moisture content.

exposed -SH content compared to control, suggesting spontaneous protein unfolding (Ma et al., 2018).

In terms of the disulfide bond, TMBP (49.3%) recorded the highest S—S content of 129.17 μmol/g, which was significantly higher than the control (54.66 μmol/g) as well as TMBP texturized at 30.0 and 60.0% feed moisture content, with values of 41.30 μmol/g and 49.29 μmol/g, respectively. It is interesting to note that S—S content increased with decreasing exposed -SH content for TMBP (49.3%). This increment in S—S content indicates the formation of new S—S bond through SH/SS interchange reactions. Similarly, increasing S—S bond with decreasing exposed -SH content was observed for heat-treated microfluidized soy protein isolate (Shen & Tang, 2012) and heat-treated soy protein isolate (Puppo et al., 2004). In contrast, the lowered S—S content for TMBP (30.0%) is suggestive of S—S bond disruption by severe mechanical shear stress inside the extruder barrel, as a result of severe friction under low moisture environment (Osen, Toelstede, Eisner, & Schweiggert-Weisz, 2015).

From these data, it can be concluded that texturization at different feed moisture contents results in the exposure of buried -SH groups to a different extent, leading to different degrees of protein aggregation via SH-SS interchange and sulfhydryl oxidation, consequently inducing protein structural rearrangement to different levels.

3.5. Secondary structural properties of TMBP

3.5.1. Circular dichroism (CD)

CD spectroscopy was performed to assess the unfolding properties of native mung bean proteins upon extrusion at different feed moisture contents. Fig. 2a depicts the CD spectra of MBPI (control) and TMBP samples detected in the far-UV region. The control MBPI spectrum illustrates a protein containing α-helical structure with a strong positive band (peak) at 194 nm and a β-sheet structure with a negative double band spanning from 207 to 224 nm. Extrusion at 30.0, 49.3, and 60.0% feed moisture contents induced changes in the secondary structure of TMBP compared to control. TMBP (49.3%) showed a reduction of ellipticity at 193 nm along with a blue shift of the negative double band at 201 and 205 nm, manifesting in significant secondary structural alteration. Also, the negative band at 220 nm indicated the presence of a random coil structure. In contrast, the CD spectrum of TMBP (30.0%) demonstrated a positive band at 191 nm, negative double band at 202 and 205 nm and a weak negative band at 221 nm, while for TMBP (60.0%), a positive band at 191 nm, a negative band at 202 nm and a weak negative band at 221 nm were observed.

Changes in the band magnitude and intensity are indicative of a drastic loss of native structures and interactions of aromatic amino acid residues during processing (Wang, Sun, Pu, & Wei, 2017). It is notable that due to the feed moisture content, texturization increases the structural flexibility of mung bean protein by increasing its ellipticity (positive or negative), depicted as different spectra patterns when MBPI was texturized into TMBP. Qi and Onwulata (2011) found that texturized whey protein isolate showed structural modification when extruded at the low moisture content (20%) rather than high moisture content (50%). Zhang et al. (2016) reported that moisture heat treatment of soy protein isolates during hydrothermal cooking resulted in a loss of native structure, confirmed by the decrease in ellipticity shown in their respective CD spectra.

3.5.2. Fourier transform infrared (FTIR) spectroscopy

FTIR spectroscopy is a powerful technique for structural and conformational characterization of proteins. The infrared spectrum in the range of 4000–400 cm^{-1} arises from the absorption of energy by stretching and bending motions of chemical bonds. In an IR spectrum, the amide I band (1700–1600 cm^{-1}) reveals secondary structural components of proteins, since this band is mainly attributed to C═O stretching vibrations (approximately 80%) with some C—H stretching and in-plane N—H bending. Specifically, the C═O stretching vibrations in proteins largely depend on their secondary structures, inter- or intramolecular effects, and hydrogen-bonding patterns. The amide I band consists of several overlapping protein structural components including α-helix, β-sheet, β-turn, and random coil (unordered structure). Fourier self-deconvolution (FSD) fitting was used to estimate the secondary structural components (Carbonaro & Nucara, 2010) of native MBPI, and TMBP extruded at 30.0, 49.3, and 60.0% feed moisture content.

Fig. 2b shows the FTIR spectra (4000–500 cm^{-1}) of MBPI and TMBP wherein small amount of trapped starch were observed at wavelength 924–1057 cm^{-1} for MBPI and 924–1024 cm^{-1} for TMBP extruded at 30.0, 49.3 and 60.0% feed moisture content. Likewise, Awais et al. (2020) detected starch in mung bean at wavelength 995–1022 cm^{-1} and 1022–1047 cm^{-1}. Fig. 2(c-f) shows the FSD curve fitting spectra of MBPI (control) and TMBP samples in 1700–1600 cm^{-1} region and Table 2 presents the peak area of each component. MBPI (control) exhibited typical plant protein structure, with low α-helix and high β-sheet content (Ma, Rout, & Mock, 2001). It is noteworthy that β-sheet content significantly reduced in all texturized samples compared with control, suggesting breakage of chemical bonds between protein molecules, and unfolding of original conformation, leading to denaturation and subsequent aggregation (Qi & Onwulata, 2011). The high content of β-sheets is responsible for the poor accessibility of proteolytic enzymes toward the protein substrate and may reduce protein digestibility (Long et al., 2015). With reduced β-sheet after texturization, the digestibility of TMBP is fostered. Interestingly, the random coil content of TMBP (49.3%) showed the highest peak area of 23.12% compared to control (14.64%), low (14.15%) and high feed moisture (7.96%), due to the partial denaturation at 49.3% feed moisture content, which alters protein conformation and exposes groups from the protein core (Afizah & Rizvi, 2014). In contrast, the significantly lower random coil content along with a high β-sheet content in TMBP (60.0%) could be attributed to the formation of dense, rigid protein aggregates. Zhou et al. (2016) reported the formation of rigid aggregates during extrusion, which caused a decrease in the random coil content. There was also a significant increment in β-turn content for all TMBP compared to control, indicating the occurrence of protein–protein aggregation during texturization (Wang et al., 2014), with TMBP (30.0 and 60.0% feed moisture) exhibiting more β-turn, thus more protein aggregates than TMBP (49.3%). The increment in α-helix content that occurs simultaneously with the decrement in β-sheets for TMBP (49.3%) compared to control and other texturized samples indicates that, despite melting of the monomer–monomer interface of legumin protein (hexameric species), the proteins survive the thermal treatment, forming new, desirable structure during texturization (Long et al., 2015).

From the above data, texturization at different feed moisture contents causes rearrangement of protein molecules into more suitable structures to adapt to the changes in the external environment. FTIR spectroscopy revealed the protein unfolding and structural rearrangement at a molecular level, providing insights for understanding mung bean protein bioavailability.

3.6. Tertiary structural properties of TMBP

Tryptophan fluorescence spectroscopy was applied to monitor the effect of feed moisture content on the tertiary structure of mung bean protein upon texturization. In plant proteins, tryptophan, tyrosine, and phenylalanine residues are natural chromophores responsible for fluorescence. As tryptophan residues are excited at 280 nm, any fluctuation in the fluorescence intensity could dictate possible alteration in the protein tertiary structure. Also, this intrinsic tryptophan fluorescence spectrum is useful in the study of protein unfolding (Albani, 2008; Wang et al., 2017).

Fig. 3 depicts the tryptophan fluorescence spectra of MBPI (control) and TMBP, with MBPI recording the highest fluorescence at $\lambda_{max} = 393$ nm, while TMBP produced at 30.0, 49.3 and 60.0% recorded maximum

Table 2
Secondary structure composition of mung bean protein isolate (MBPI) and texturized mung bean protein (TMBP) samples extruded at 30.0, 49.3, and 60.0% feed moisture content.

Properties	MBPI		TMBP (30.0%)		TMBP (49.3%)		TMBP (60.0%)	
Secondary structure composition	Area (%)	Peak (cm^{-1})	Area (%)	Peak (cm^{-1})	Area (%)	Peak (cm^{-1})	Area (%)	Peak (cm^{-1})
β-sheet	1631	46.82 ± 1.77^{a}	1632	38.92 ± 1.07^{c}	1631	30.11 ± 0.57^{d}	1631	42.72 ± 0.78^{b}
β-sheet	1639	16.83 ± 0.94^{a}	1638	12.40 ± 0.47^{bc}	1640	13.00 ± 0.33^{b}	1639	14.76 ± 0.96^{b}
Random coil	1646	14.64 ± 0.84^{b}	1647	14.15 ± 0.49^{b}	1647	23.12 ± 0.06^{a}	1646	7.96 ± 0.89^{c}
α-helix	1654	12.84 ± 0.76^{b}	1656	10.52 ± 0.01^{bc}	1656	22.21 ± 0.21^{a}	1654	13.74 ± 1.93^{b}
β-turn	1681	8.86 ± 0.77^{d}	1680	23.93 ± 1.19^{a}	1680	11.55 ± 0.39^{c}	1681	20.84 ± 1.15^{b}

Mean ± s.d. in a row followed by different letters are significantly ($p \leq 0.05$) different.

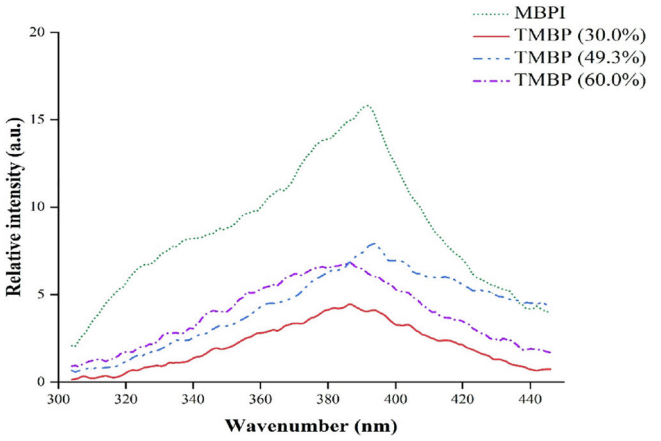

Fig. 3. Intrinsic tryptophan fluorescence spectra for mung bean protein isolate (control) and texturized mung bean protein samples extruded at different feed moisture content.

fluorescence at 389 nm, 396 nm, and 383 nm, respectively. When tryptophan residues are buried in the hydrophobic core of the protein structure, λ_{max} is typically < 330 nm, while in a polar environment λ_{max} shifts to a longer wavelength (bathochromic shifts), indicating a loss of protein tertiary or quaternary structure (Wang et al., 2017). In this study, the λ_{max} of MBPI and TMBP samples were all > 330 nm, indicating that tryptophan residues were in the polar environment both before and after extrusion. TMBP (49.3%) recorded similar λ_{max} to control (396 nm *vs.* 393 nm), indicative of partial protein unfolding and denaturation during extrusion, giving rise to a less compact protein structure in the final texturized product that partially resembles the tertiary structure of native mung bean protein, thus peaked at similar wavelengths. The decrease in λ_{max} of TMBP extruded at 30.0 and 60.0% feed moisture content could be related to protein–protein aggregation (Jiang et al., 2015).

Apart from λ_{max} shifting, changes in fluorescence intensity (FI) could also help to detect spatial changes in protein structure at the tertiary level. Texturization decreases the FI in all TMBP samples compared to control, as a result of fluorescence quenching through increased intermolecular hydrophobic interactions and protein–protein aggregation (Jiang et al., 2015). The highest protein–protein aggregation was observed for TMBP extruded at 30.0% feed moisture content, evidenced by its lowest FI.

3.7. Rheological properties of TMBP (Time and frequency sweep)

Time sweep elucidates the viscoelastic behaviour of samples as a function of time by keeping the strain, frequency, and temperature constant. During the test, the protein gel network continues to develop through progressive denaturation, as observed from the increasing storage modulus (G′) as a function of time. Fig. 4a shows the continuous increasing G′ values for all texturized samples as well as control, indicating that all protein samples demonstrate the ability to form a gel within the measured timeframe. As seen from Fig. 4a, G′ increases with increasing feed moisture content, possibly due to the rapid rearrangement of protein aggregates that promotes the formation of the gel network when the sample is treated under a high feed moisture environment.

Fig. 4(b–e) depicts the mechanical spectra of MBPI (control) and TMBP by plotting the storage modulus log (G′) and loss modulus log (G″) against frequency (ω). G′ and G″ are measures of elastic and viscous nature, respectively. The mechanical spectra for texturized samples reveal characteristic viscoelastic gel-forming behaviour with the elastic property dominating the viscous property within the entire angular frequency range except for TMBP (30.0%) (Fig. 4c–e). The stable, consistent G′ values for MBPI (control) and TMBP (49.3%) at all frequencies demonstrated the formation of a strong gel network. Additionally, the decreased complex viscosity (η*) with increasing frequency implied shear thinning behaviour in these samples, further confirming their gel-forming ability. In contrast, the G′ of TMBP extruded at 30.0 and 60.0% feed moisture content reduced with increasing frequency, indicating extensive protein denaturation which resulted in protein aggregation and weak gel formation. A similar result was reported by Tunick and Onwulata (2006) for extruded whey protein concentrate and isolate. Also, Osen (2017) reported viscoelastic gel formation by texturized pea protein isolate extruded at 55–65% feed moisture content.

Legume proteins are globular and tend to form a gel network when their structures are unfolded by heating. Hydrophobic interactions, hydrogen bonding, and disulfide bridges are the key contributors to gel network formation and stabilization (Gosal & Ross-Murphy, 2000; Damodaran, 2008). TMBP (49.3%) has significantly more disulfide bonds (Table 1) and shows consistent G′ values over the frequency range compared to TMBP (30.0 and 60.0%), indicative of a strong and stable gel network formation. Formation of such a gel is crucial during texturization, as it survives mechanical stress and heats better than weak gel. Gelling property is strongly relatable to meat-like juiciness, a feature deemed crucial for a meat extender product to mimic the mouthfeel of real meat. Juiciness is favourable as it improves the overall palatability and provides a pleasant eating experience. Heat-induced protein gelling is seen as a key functionality of muscle proteins and coherently, our results indicate a good heat-induced gelling of TMBP, leading to the formation of a strong network with good water-holding capacity, which is crucial to mimic typical meat texture and juiciness. Strong gels are less prone to syneresis, due to the formation of a well-defined three-dimensional structured matrix, thus can hold a large amount of water, retain water absorption and promote meat-like juiciness in the final food product. Thus, TMBP (49.3%) with retained juiciness is an excellent candidate for a plant protein-based meat extender that is available sustainably at an economic price.

4. Conclusion

This study evaluated the effect of manipulating feed moisture (30.0, 49.3, and 60.0%) on the characteristics of TMBP, showing that 49.3% is

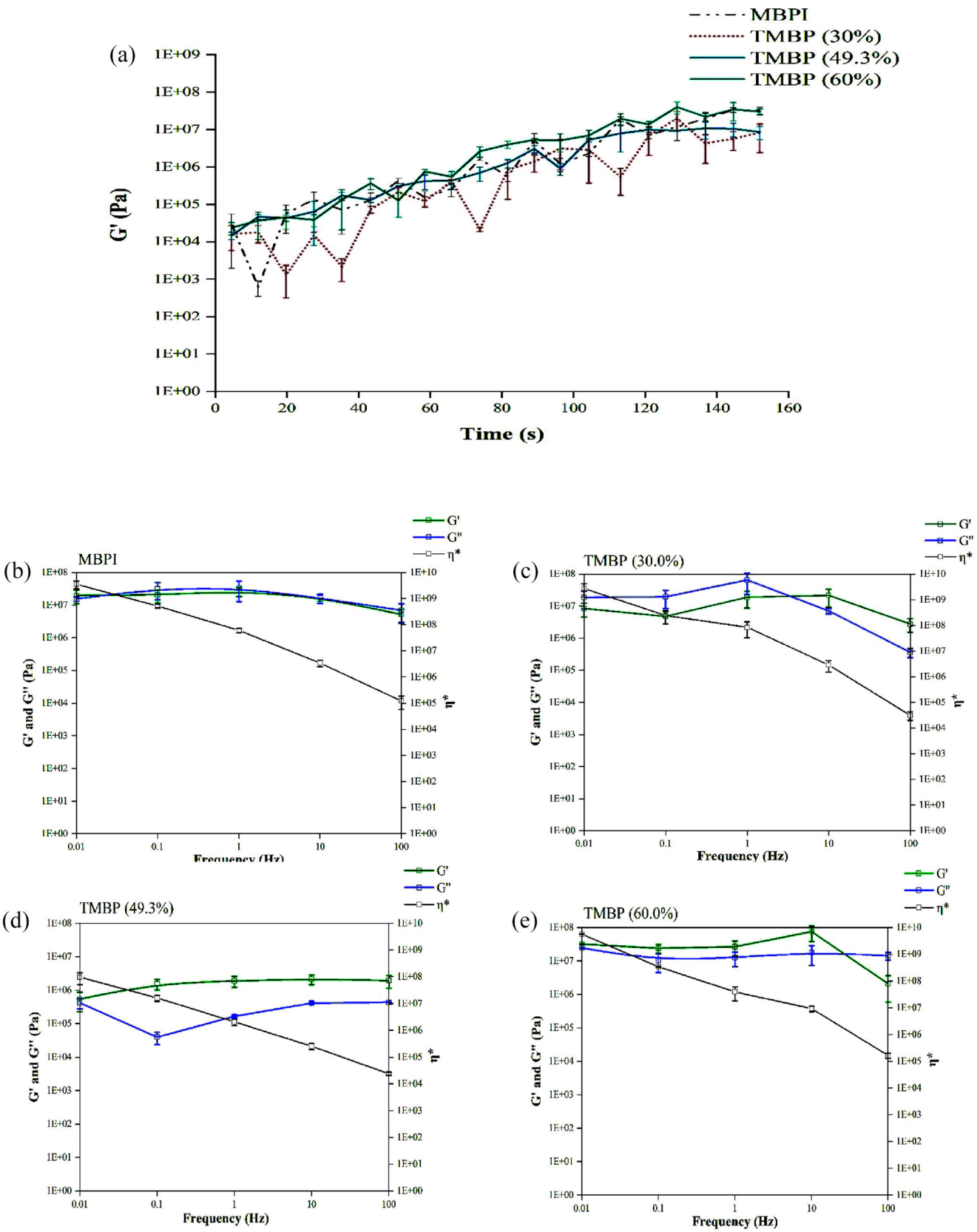

Fig. 4. Effects of extrusion feed moisture content on the rheological properties of texturized mung bean protein (TMBP) compared with mung bean protein isolate (MBPI, control). (a) Time sweep test for MBPI (control) and TMBP and frequency sweep test on the variation of the storage (G′) and loss modulus (G″) of (b) MBPI (control) and TMBP extruded at (c) 30.0%, (d) 49.3% and (e) 60.0% feed moisture content.

the optimum feed moisture content to produce TMBP with desirable qualities (partial denatured protein, improved protein solubility, improved digestibility, and stronger gel-forming behaviour). Partial denaturation was observed as protein band thinning in SDS-PAGE compared to native mung bean protein, improved digestibility is due to the increased α-helix along with reduced β-sheet content, while stronger gel-forming behaviour was due to the increased disulfide bond content, frequency-independent viscoelasticity and shear thinning. From a molecular point of view, surface hydrophobicity, secondary structural properties (circular dichroism, FTIR) and tertiary structural property (tryptophan fluorescence spectroscopy) revealed protein unfolding, aggregation, and structural rearrangement, substantiated by a significant reduction in thermal parameters (T_d, ΔH, T_o, T_e) after extrusion. Current work successfully elucidates the secondary and tertiary structural alteration in TMBP, at a molecular level, and demonstrates the occurrence of favourable partial protein denaturation at 49.3% feed moisture to improve the functional properties of the final product. Feed moisture content is an essential factor that should be carefully manipulated during the extrusion of plant proteins to achieve desirable quality and product performance as a vegetarian-based meat extender.

CRediT authorship contribution statement

Fatema Hossain Brishti: Conceptualization, Data curation, Formal analysis, Methodology, Investigation. **Shyan Yea Chay:** Validation, Writing - review & editing. **Kharidah Muhammad:** Resources, Supervision. **Mohammad Rashedi Ismail-Fitry:** Resources, Supervision. **Mohammad Zarei:** Validation, Writing - review & editing. **Sivakumaran Karthikeyan:** Software, Validation. **F. Caballero-Briones:** Software, Validation. **Nazamid Saari:** Conceptualization, Supervision, Funding acquisition, Resources.

Declaration of Competing Interest

The authors declare that they have no known competing financial interests or personal relationships that could have appeared to influence the work reported in this paper.

Acknowledgement

The financial support from Universiti Putra Malaysia, Malaysia, under Postgraduate Putra Initiative Grant Scheme GP-IPS/2018/9619900 (Vote no: 9619900) and scholarship from the Organization for Women in Science for the Developing World (OWSD) PhD fellowship as well as the Swedish International Development Cooperation Agency (SIDA) are gratefully acknowledged.

References

Afizah, M. N., & Rizvi, S. S. (2014). Functional properties of whey protein concentrate texturized at acidic pH: Effect of extrusion temperature. *LWT-Food Science and Technology, 57*(1), 290–298. https://doi.org/10.1016/j.lwt.2014.01.01.

Akdogan, H. (1999). High moisture food extrusion. *International Journal of Food Science & Technology, 34*(3), 195–207. https://doi.org/10.1046/j.1365-2621.1999.00256.x.

Albani, J. R. (2008). *Principles and applications of fluorescence spectroscopy*. John Wiley & Sons.

AOAC. (2005). *Official Methods of Analysis of AOAC International* (18 ed). Maryland, USA: Association of Official Analytical Chemists (AOAC) International.

Awais, M., Ashraf, J., Wang, L., Liu, L., Yang, X., Tong, L. T., … Zhou, S. (2020). Effect of controlled hydrothermal treatments on mung bean starch structure and its relationship with digestibility. *Foods, 9*(5), 664. https://doi.org/10.3390/foods9050664.

Brishti, F. H., Zarei, M., Muhammad, S. K. S., Ismail-Fitry, M. R., Shukri, R., & Saari, N. (2017). Evaluation of the functional properties of mung bean protein isolate for development of textured vegetable protein. *International Food Research Journal, 24*(4), 1595–1605.

Carbonaro, M., & Nucara, A. (2010). Secondary structure of food proteins by Fourier transform spectroscopy in the mid-infrared region. *Amino Acids, 38*(3), 679–690. https://doi.org/10.1007/s00726-009-0274-3.

Celus, I., Brijs, K., & Delcour, J. A. (2007). Enzymatic hydrolysis of brewers' spent grain proteins and technofunctional properties of the resulting hydrolysates. *Journal of Agricultural and Food Chemistry, 55*(21), 8703–8710. https://doi.org/10.1021/jf071793c.

Chen, F. L., Wei, Y. M., Zhang, B., & Ojokoh, A. O. (2010). System parameters and product properties response of soybean protein extruded at wide moisture range. *Journal of Food Engineering, 96*(2), 208–213. https://doi.org/10.1016/j.jfoodeng.2009.07.014.

Chen, F. L., Wei, Y. M., & Zhang, B. (2011). Chemical cross-linking and molecular aggregation of soybean protein during extrusion cooking at low and high moisture content. *LWT-Food Science & Technology, 44*(4), 957–962. https://doi.org/10.1016/j.lwt.2010.12.008.

Damodaran, S. (2008). Amino acids, peptides and proteins. *Fennema's Food Chemistry, 4*, 217–329.

Gosal, S. W., & Ross-Murphy, B. S. (2000). Globular protein gelation. *Current Opinion in Colloid & Interface Science, 5*, 188–194. https://doi.org/10.1016/S1359-0294(00)00057-1.

Hood-Niefer, S. D., & Tyler, R. T. (2010). Effect of protein, moisture content and barrel temperature on the physicochemical characteristics of pea flour extrudates. *Food Research International, 43*(2), 659–663. https://doi.org/10.1016/j.foodres.2009.09.033.

Hou, D., Yousaf, L., Xue, Y., Hu, J., Wu, J., Hu, X., … Shen, Q. (2019). Mung bean (*Vigna radiata* L.): Bioactive polyphenols, polysaccharides, peptides, and health benefits. *Nutrients, 11*(6), 1238. https://doi.org/10.3390/nu11061238.

Jiang, L., Wang, Z., Li, Y., Meng, X., Sui, X., Qi, B., & Zhou, L. (2015). Relationship between surface hydrophobicity and structure of soy protein isolate subjected to different ionic strength. *International Journal of Food Properties, 18*(5), 1059–1074. https://doi.org/10.1080/10942912.2013.865057.

Joshi, M., Adhikari, B., Aldred, P., Panozzo, J. F., & Kasapis, S. (2011). Physicochemical and functional properties of lentil protein isolates prepared by different drying methods. *Food Chemistry, 129*(4), 1513–1522. https://doi.org/10.1016/j.foodchem.2011.05.131.

Khaket, T. P., Dhanda, S., Jodha, D., & Singh, J. (2015). Purification and biochemical characterization of dipeptidyl peptidase-II (DPP7) homologue from germinated *Vigna radiata* seeds. *Bioorganic Chemistry, 63*, 132–141. https://doi.org/10.1016/j.bioorg.2015.10.004.

Kitabatake, N., & Doi, E. (1992). Denaturation and texturization of food protein by extrusion cooking. In J. L. Kokini (Ed.), *Food Extrusion Science and Technology* (pp. 361–371). M Karwe: CT Ho.

Laemmli, U. K. (1970). Cleavage of structural proteins during the assembly of the head of bacteriophage T4. *Nature, 227*(5259), 680. https://doi.org/10.1038/227680a0.

Li, M., & Lee, T. C. (1996). Effect of extrusion temperature on solubility and molecular weight distribution of wheat flour proteins. *Journal of Agricultural and Food Chemistry, 44*(3), 763–768. https://doi.org/10.1021/jf950582h.

Li, S., Wei, Y., Fang, Y., Zhang, W., & Zhang, B. (2014). DSC study on the thermal properties of soybean protein isolates/corn starch mixture. *Journal of Thermal Analysis and Calorimetry, 115*(2), 1633–1638. https://doi.org/10.1007/s10973-013-3433-4.

Long, G., Ji, Y., Pan, H., Sun, Z., Li, Y., & Qin, G. (2015). Characterization of thermal denaturation structure and morphology of soy glycinin by FTIR and SEM. *International Journal of Food Properties, 18*(4), 763–774. https://doi.org/10.1080/10942912.2014.908206.

Ma, C. Y., Rout, M. K., & Mock, W. Y. (2001). Study of oat globulin conformation by Fourier transform infrared spectroscopy. *Journal of Agricultural and Food Chemistry, 49*(7), 3328–3334. https://doi.org/10.1021/jf010053f.

Ma, W., Xie, F., Zhang, S., Wang, H., Hu, M., Sun, Y., … Li, Y. (2018). Characterizing the structural and functional properties of soybean protein extracted from full-fat soybean flakes after low-temperature dry extrusion. *Molecules, 23*(12), 3265. https://doi.org/10.3390/molecules23123265.

Mendoza, E. M. T., Adachi, M., Bernardo, A. E. N., & Utsumi, S. (2001). Mungbean [*Vigna radiata* (L.) Wilczek] globulins: Purification and characterization. *Journal of Agricultural and Food Chemistry, 49*(3), 1552–1558. https://doi.org/10.1021/jf001041h.

Morr, C. V., German, B., Kinsella, J. E., Regenstein, J. M., Van Buren, J. P., & Kilara, A. (1985). A collaborative study to develop a standardized food protein solubility procedure. *Journal of Food Science and Technology, 50*, 1715–1718. https://doi.org/10.1111/j.1365-2621.1985.tb10572.x.

Mozafarpour, R., Koocheki, A., Milani, E., & Varidi, M. (2019). Extruded soy protein as a novel emulsifier: Structure, interfacial activity and emulsifying property. *Food Hydrocolloids, 93*, 361–373. https://doi.org/10.1016/j.foodhyd.2019.02.036.

Nakai, S. (2003), Measurement of Protein Hydrophobicity. Current Protocols in Food Analytical Chemistry, 9: B5.2.1-B5.2.13.

Osen, R. (2017). Texturization of pea protein isolates using high moisture extrusion cooking (Doctoral dissertation, Technische Universität München).

Osen, R., Toelstede, S., Eisner, P., & Schweiggert-Weisz, U. (2015). Effect of high moisture extrusion cooking on protein–protein interactions of pea (*Pisum sativum* L.) protein isolates. *International Journal of Food Science & Technology, 50*(6), 1390–1396. https://doi.org/10.1111/ijfs.12783.

Puppo, C., Chapleau, N., Speroni, F., de Lamballerie-Anton, M., Michel, F., & Añón, C. (2004). Physicochemical modifications of high-pressure-treated soybean protein isolates. *Journal of Agricultural and Food Chemistry, 52*, 1564–1571. https://doi.org/10.1021/jf034813t.

Purwanti, N., van der Goot, A. J., Boom, R., & Vereijken, J. (2010). New directions towards structure formation and stability of protein-rich foods from globular proteins. *Trends in Food Science & Technology, 21*(2), 85–94. https://doi.org/10.1016/j.tifs.2009.10.009.

Qi, P. X., & Onwulata, C. I. (2011). Physical properties, molecular structures, and protein quality of texturized whey protein isolate: Effect of extrusion moisture content. *Journal of Dairy Science, 94*(5), 2231–2244. https://doi.org/10.3168/jds.2010-3942.

Riaz, M. N. (2011). Texturized vegetable proteins. *Handbook of Food Proteins, Woodhead Publishing, 395–418*. https://doi.org/10.1533/9780857093639.395.

Schreinemachers, P., Sequeros, T., Rani, S., Rashid, M. A., Gowdru, N. V., Rahman, M. S., … Nair, R. M. (2019). Counting the beans: Quantifying the adoption of improved mungbean varieties in South Asia and Myanmar. *Food Security, 11*(3), 623–634. https://doi.org/10.1007/s12571-019-00926-x.

Serna-Saldivar, S. O. (2012). *Production of breakfast cereals and snack foods*. In Cereal Grains: Laboratory Reference and Procedures Manual, CRC Press.

Shen, L., & Tang, C. H. (2012). Microfluidization as a potential technique to modify surface properties of soy protein isolate. *Food Research International, 48*(1), 108–118. https://doi.org/10.1016/j.foodres.2012.03.006.

Shimada, K., & Cheftel, J. C. (1988). Determination of sulfhydryl groups and disulfide bonds in heat-induced gels of soy protein isolate. *Journal of Agricultural and Food Chemistry, 36*(1), 147–153. https://doi.org/10.1021/jf00079a038.

Thompson, L. U. (1977). Preparation and Evaluation of Mung Bean Protein Isolates. *Journal of Food Science, 42*, 202–206. https://doi.org/10.1111/j.1365-2621.1977.tb01252.x.

Tunick, M. H., & Onwulata, C. I. (2006). Rheological properties of extruded milk powders. *International Journal of Food Properties, 9*(4), 835–844. https://doi.org/10.1080/10942910600669899.

Verbeek, C. J., & Van den Berg, L. E. (2010). Extrusion processing and properties of protein-based thermoplastics. *Macromolecular Materials and Engineering, 295*(1), 10–21. https://doi.org/10.1002/mame.200900167.

Wang, K., Sun, D. W., Pu, H., & Wei, Q. (2017). Principles and applications of spectroscopic techniques for evaluating food protein conformational changes: A review. *Trends in Food Science & Technology, 67*, 207–219. https://doi.org/10.1016/j.tifs.2017.06.015.

Wang, M.-P., Chen, X.-W., Guo, J., Yang, J., Wang, J.-M., & Yang, X.-Q. (2019). Stabilization of foam and emulsion by subcritical water-treated soy protein: Effect of aggregation state. *Food Hydrocolloids, 87*, 619–628. https://doi.org/10.1016/j.foodhyd.2018.08.047.

Wang, Z., Li, Y., Jiang, L., Qi, B., & Zhou, L. (2014). Relationship between secondary structure and surface hydrophobicity of soybean protein isolate subjected to heat treatment. *Journal of Chemistry, 2014*. https://doi.org/10.1155/2014/475389.

Wagner, J. R., Sorgentini, D. A., & Añón, M. C. (2000). Relation between solubility and surface hydrophobicity as an indicator of modifications during preparation processes of commercial and laboratory-prepared soy protein isolates. *Journal of Agricultural and Food Chemistry, 48*(8), 3159–3165. https://doi.org/10.1021/jf990823b.

Zhang, B., Yuan, D., He, X., Yang, X., Gao, Z., Wang, J., & Guo, Z. (2016). Physiochemical and conformational properties of soluble aggregates from soy protein isolates mediated by hydrothermal cooking: A comparative study with moisture heat treatment. *Journal of Food Technology, 1*, 1–9. https://doi.org/10.18689/mjft-1000101.

Zhou, L., Yang, Y., Ren, H., Zhao, Y., Wang, Z., Wu, F., & Xiao, Z. (2016). Structural changes in rice bran protein upon different extrusion temperatures: A Raman spectroscopy study. *Journal of Chemistry, 2016*. https://doi.org/10.1155/2016/6898715.

Journal of Molecular Structure 1244 (2021) 130964

Contents lists available at ScienceDirect

Journal of Molecular Structure

journal homepage: www.elsevier.com/locate/molstr

Two-trace two-dimensional (2T2D) correlation infrared spectral analysis of *Spirulina platensis* and its commercial food products coupled with chemometric analysis

E. Kavitha [a], L. Devaraj Stephen [b], Fatema Hossain Brishti [c], S. Karthikeyan [d,*]

[a] Department of Physics, Dr. MGR Educational, and Research Institute, Chennai, Tamil Nadu, 600095, India
[b] Department of Chemistry, SRM Valliammai Engineering College, Kattankulathur, Tamil Nadu, 603203, India
[c] Department of Food Science, Faculty of Food Science and Technology, Universiti Putra Malaysia, 43400 UPM, Serdang, Selangor Malaysia
[d] Department of Physics, Dr. Ambedkar Government Arts College, Chennai, Tamil Nadu, 600039, India

ARTICLE INFO

Article history:
Received 6 May 2021
Revised 20 June 2021
Accepted 21 June 2021
Available online 24 June 2021

Keywords:
2T2DCOS
Spirulina
Food products
Protein
Lipids
ROC

ABSTRACT

Spirulina plays an important role in the food industry due to its rich protein content and other nutritional values. 2D-COS spectral analysis is widely used nowadays in understanding the change in the molecular mechanism of biological samples. Two trace 2D-COS (2T2D-COS) is a technique that has gained much attention due to improved accuracy and higher spectral resolution. The selected band area measurement (Lipid/Amide I, Lipid/Carbohydrates, Amide I/ Amide II) shows that the samples S2 and S3 have higher quality among other samples. A positive correlation of increased lipid oxidation with lipid changes exists among all the samples studied. Synchronous spectra show auto peaks at 2870 cm^{-1}, 1624 cm^{-1}, 1034 cm^{-1} for samples S2 and S3 which helps in assessing food quality. Asynchronous negative cross-peaks (2870, 2815) indicate a higher presence of polysaccharides in the samples S1 and S4. The negative cross-peaks (1206, 1036) show deformation in the pyranose ring of polysaccharides in the S4 sample due to food processing. The negative PCA loading at 997 cm^{-1} shows the polymerization of carbohydrates mechanism occurring at glucan bands. Hierarchical cluster analysis shows clustering of dissimilar products occurring at a higher value. ROC curve depicts the higher reliability of our findings using 2T2D-COS.

1. Introduction

Food quality and protection have become an important issue due to the increase in adulteration of food products. The adulteration of various food items causes serious adverse health effects. Food fraud includes adulteration and substitution of low-value nutrients to increase food quality. [1]. Hence, it is necessary to develop a fast and price efficient method to control and detect fraud in food products. *Spirulina platensis* is a blue-green algae with a rich source of biologically active compounds. They are recognized as the most nourishing and complete of all food supplements. It is easily digested and its an effective anti-cancer protection. It has high protein (70%), fatty acids, polysaccharides, minerals [2]. The commercialization of *Spirulina* has attained more attention for use as food products and in pharmaceuticals.Researches are in progress for evaluating the potential of *Spirulina* as an ingredient in the manufacture of various food products [3]. The supplement of *Spirulina* is available as a tablet, capsule, or powdered form. This makes the algae species more popular and cultivated widely. A Spectroscopic method is a rapid, convenient, tool to control and detect adulterated food. FT-IR spectroscopy coupled with principal component analysis is highly informative in the analysis of metabolic changes and differentiation of the algal species in variable environmental conditions. It provides an accurate and effective method for quality detection and authentication.

Food processing is a critical step in improving bioaccessibility and produces beneficial nourishments [4]. The study reported that microalgae-containing food products have enhanced nutritional properties [5]. Bataller et al. [6]. indicated that the characteristic amide band of proteins, carbohydrates, and lipids are predominant in *Spirulina* which is studied using FTIR spectroscopy. This complex composition results in superpositions of IR bands which complicates their analysis. The development of multiple images at selected wavelengths reveals compositional changes on the quality of food products [7]. However, spectroscopy in association with chemometric methods is used to extract more interesting information. The chemometric tool such as Cluster Analysis (CA), Hierarchical Cluster Analysis (HCA) and Principal Component Analysis

* Corresponding author.
E-mail address: physicskarthik@gmail.com (S. Karthikeyan).

https://doi.org/10.1016/j.molstruc.2021.130964
0022-2860/

(PCA) are generally presented in a graphical pattern showing variation among the samples [8,9]. Among them, PCA is a common tool that reduces complex spectra to a small number of variables [10]. Lan et al. [11] successfully employed in the classification of food products using FTIR and PCA with respect to storage conditions. Yang et al. [12] successfully employed strategies to detect fraudulent adulteration of herbal medicines using IR and chemometric techniques.

The study suggested by various authors demonstrated the use of FTIR with chemometrics to detect adulteration of food products effectively [9,13,14]. Lafarga, et al. [3] suggested the importance of processing algae beneficial nutritional food products. The food adulteration of traditional herbal medicines *Radix Astragali* was studied by Yang et al. [12] and concluded that FTIR with PCA was feasible to detect the adulteration. Valand et al. [1] emphasized adulteration and authenticity of the food system have been practiced successfully using FTIR and chemometrics techniques. However, in the complex biological system, it is not possible to take out the characteristic information of adulterants using spectroscopic techniques due to the overlapping peaks. Hence the development of two-dimensional correlation infrared spectroscopy has a wide scope in the analysis and identification of natural products [15-16]. Thus two-dimensional correlation spectroscopy (2D-COS) plays a vital role in obtaining correlation information between different functional groups. It extracts the characteristic information of weak and overlapping peaks. It is a powerful analytical study, which provides new insights at the molecular level of understanding of biological samples [17,18]. It has the advantages of extracting abundant information from biological systems, which cannot be observed by conventional one-dimensional (1D) spectroscopy [19]. Hence it is widely used in food research [17,20]. 2D-COS studies in food and natural products effectively used identification, and real-time monitoring of vegetables, fruits and food products etc. [20,21,22].

Noda [22] (2018) introduced a new concept of Two-trace two-dimensional correlation spectra (2T2D-COS) which is generated only from a pair of spectra. It takes advantage of 2D-COS techniques in the sense it successfully distinguishes the weak signals of two spectra of different origins. Thus it provides abundant and useful characteristic information [23]. It has a good practical application in identifying unadulterated and adulterated food [12]. It is a powerful technique in finding the difference in overlapped peaks between the control and test sample. 2T2D correlation spectra help to correlate differences between two spectra. However, this method is not used much in food researches. Hence, we attempted to use this method to obtain useful information for food researchers. Moreover, limited or no studies are conducted using 2T2D-COS analysis of *Spirulina* and its food products and supplements. Hence our study focuses on the use of two-trace two-dimensional correlation along with chemometric tools in the analysis of *Spirulina*, and commercial products.

2. Material and methods

2.1. Sample culture and procurement

Spirulina platensis, the strain used in the present study was obtained from the Department of Botany, Dr Ambedkar government arts college, Chennai, Tamil Nadu, India. The strain was maintained in 500 mL sterilized Erlenmeyer flasks holding 100 mL Zarrouk's medium at 30±2 °C, pH 9 ± 0.1 with continuous lighting fluorescent tubes (2500 Lux) of 12:12 h light/dark. Zarrouk's medium served as the standard medium (SM) for *Spirulina* culture [24]. The culture was stirred twice daily shaking by hand for 30 days. The growth rate was measured by taking O.D(optical density) at 560 nm. The sample was harvested at the end of 30 days. It is taken as a control sample. The commercial sample of *Spirulina* food products and food supplements were purchased from a local market. The samples were labeled as papad- S1, tablet -S2, powder -S3 and semolina -S4

2.2. FTIR measurement

FTIR measurements, in the range of 4000–400 cm^{-1} were recorded using Perkin Elmer Spectrum FTIR spectrometer held at SAIF, IIT Chennai. Five replicates of control sample were freeze dried and mixed with KBr in the 1:20 ratio. The commercial samples were powedered directly mixed with KBr(1:20). They were pelletized using a hydraulic pellet press. Deuterated triglycine sulfate (DTGS) was used as a detector. The spectra were collected at 4 cm^{-1} resolution. A total of 20 scans were taken for each spectrum, for each sample. The collected spectra were further analyzed by origin 8.0 software.

2.3. Two- trace two-dimensional correlation spectra (2T2D-COS)

Two-trace two-dimensional correlation spectra(2T2D-COS) are constructed using 2Dshige v1.3 software [25-28]. It provides the correlation information between absorption peaks of different samples origin. Here control sample was taken as a standard reference in comparison with commercial products. It gives one to one correspondence between two different origin of samples. The synchronous and asynchronous spectra gives the characteristics information with good sensitivity.

2.4. Statistical analysis

Pearson correlation coefficient and one-way ANOVA were performed using SPSS 16.0. A probability level (p value) of less than 0.05, 0.01, and 0.001 were considered statistically significant. Principal Component Analysis (PCA), Hierarchical cluster analysis and Receiver operation characteristics analysis were also performed using the same software.

2.5. Hierarchical cluster analysis

Hierarchical cluster analysis was performed by Ward algorithm using SPSS 16.0 [29]. The results of the data are presented on a dendrogram scale. The clustering maximizes their similarity and minimizes the errors in distinguishing a large number of samples. The groups formed help in identifying the classification and prediction of the efficiency of the results [30,31]. The results look into the connectivity within and between samples presented in a tree form.

2.6. Principal component analysis (PCA)

The Principal Component Analysis (PCA) was done with SPSS 16.0. It is used in data reduction to a small number of factors from a large data. The PCA was applied to our mean-centered, second derivative, and vector normalized spectral data. It was done in the entire region of the spectrum. The factor reduction is obtained by transforming the variables into new variables called principal components. The results are obtained as scores and loadings [31]. It is utilized for quantitative methods in discriminating samples. The scores of the component were plotted to show sample variance from the FTIR information.

2.7. Receiver operating characteristic (ROC) analysis

Receiver operating characteristic (ROC) analysis allows for the diagnosis of the reliability of experiments carried out. ROC curve

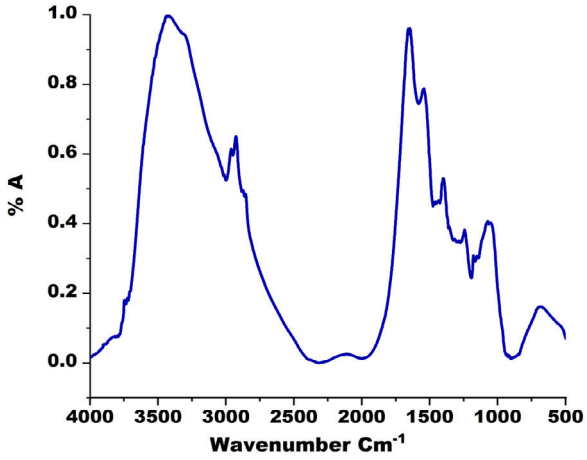

Fig. 1. Representive FTIR spectra of *Spirulina platensis* in the region 4000–500 cm^{-1}.

Table. 1
Tentative frequency assignment of the *Spirulina platensis* in the region 4000–400 cm^{-1}.

Wavenumber cm^{-1}	Frequency assignment
3416	OH stretching
3298	Amide A proteins
2960	CH_3 asymmetric stretching lipids
2930	CH_2 asymmetric stretching lipids
2852	CH_2 bending lipids and proteins
1645	Amide I of proteins
1539	Amide II of proteins
1456	CH_3 out of plane lipids proteins
1388	COO^- symmetric stretch of fatty and amino acids
1247	Amide III proteins
1147	C-O, C–C, C–O - C polysaccharides
1070	C–O stretching, Glycogen

was constructed by using SPSS 16 software. The ROC plot shows sensitivity against 1-specificity for each point with the threshold value between zero and one. It is widely used in biology nowadays in addition to other fields. The control was taken as a reference point with a threshold limit of 95%. It helps to validate the results of the experiment from the area under the curve (AUC). FTIR data of the samples was given as input and control taken as a reference

3. Results and discussion

Fig 1 shows representative FTIR spectra of *Spirulina* and its commercial samples recorded in the 4000–500cm^{-1} region. Table 1 shows the frequency assignment of the representative FTIR spectra of *Spirulina*. FTIR spectra of *Spirulina* have characteristic peaks corresponding to different biomolecules such as lipids(3050 - 2800 cm^{-1}) proteins(1600–1500 cm^{-1}) and polysaccharides (1300–1000 cm^{-1}) [9,32]. The OH vibrational stretching was observed around 3416cm^{-1}. The band at 3298 cm^{-1} corresponds to Amide A of proteins. The CH_3 and CH_2 asymmetric stretching of lipids corresponds to 2960 cm^{-1} and 2930 cm^{-1}. Lipids play an effective role with antioxidant property which is a unique characteristic of *Spirulina* [33]. The protein corresponds to three bands observed as Amide I (~1645 cm^{-1}) of $C = O$ stretching vibration, Amide II (1539 cm^{-1}) of N–H bending and C–N stretching vibrations and Amide III (1247 cm^{-1}) of proteins which provides significant growth for the algae. Carbohydrates reports to fungal metabolism observed at 1147 cm^{-1} and 1070cm^{-1} corresponding to C–O, C–C, C–O - C of polysaccharides and C–O stretching of glycogen [6]. The band at 1388 cm^{-1} corresponds to COO^- symmetric stretching of fatty acid and amino acids [34].

3.1. Band area measurement

The selected band area measurement of Amide I/Amide II, lipid/Amide I, lipid oxidation(1770-1729cm^{-1})/(2995-2816cm^{-1}) and lipid/carbohydrates, are shown in Fig 2a-2d. The selected band area such as Amide I (1705–1575 cm^{-1}), Amide II (1575–1480 cm^{-1}), Carbohydrates (1200–900 cm^{-1}), Lipid (3000–2800 cm^{-1}) was used to understand quantitative changes in biochemical compositions as reported by various authors [9,30-35]. Fig.(2a-2d) depicts a star delta graph showing selected band area measurement of *Spirulina* and its commercial samples. The ratio of band area of amide I/amide II shows changes in protein contents(Fig.2a). Results show the depletion of protein contents occurs in the samples which follow the order of S4>S1>S3>S2. Tao Wang et al. [36] studied IR spectra that fungal *Paxillus involutus* resulted in changes in the amide I/amide II bands with the changes in polysaccharides. From the band area of measurement of lipid/amide I a decrease in lipid contents was found in the commercial sample(Fig.2b) This result follows in the order of S4<S1<S3<S2. This shows the sample S4 has the least quality of protein and lipids and S2 has the highest value. The decrease in lipid oxidation resulted in lower values of lipids. It was measured from the band area of total oxidation of lipids (Fig. 2c). It follows in the order S2<S3<S1<S4. This shows S2 and S3 have lowest lipid oxidation. These results support us in finding the order of quality of *Spirulina* food supplements and products studied in comparison with control sample taken as standard. The change in carbohydrates contents is studied from the band area ratio of lipid/carbohydrates. The carbohydrates decrease in the order S1<S2<S4<S3 showing S1 has the lowest value and S3 has the highest value (Fig. 2d).

The results of the study reveal that S2 and S3 have a better quality of protein, lipid and carbohydrates compositions with the lowest lipid oxidations. Fig 3a-3d shows Pearson correlation heat map of various band area measurements for samples S1-S4. Sample S1 and S2 and S4 shows significant positive correlation (r = 0.960, P< 0.001) (r = 0.904, P<0.001) (r = 0.868, P< 0.001) with decrease in lipid and increased lipid oxidation (Fig. 3a-3d). Soto-Ramírez et al. [37] studied remarkable changes in carbohydrates in algae *C. vulgaris* due to biosorption metal using IR. Vojvodić [38] et al. studied cellular function mechanisms of microalgae *Chlorella sorokiniana* using FTIR and found alterations in the lipid due to environmental change in copper. Michalaka et al. [39] studied that prominent spectral changes in IR occur mainly due to carboxylate groups present on the *Arthrospira Spirulina*. The person correlation heat map show lipids changes negatively correlated with the increase in amide of protein S3 samples (r = 0.925, p<0.001)(Fig. 3c). Murdock etal [40] 2009 discussed an increase in lipid and carbohydrate relative to protein and phosphoryl groups in algae using IR employed with principal components analysis (PCA). He showed that FTIR is an efficient tool in monitoring structural changes of lipids, carbohydrates, proteins which are characteristic of functional groups of algae. Kosa Gergely et al. [41], studied changes in C–O and C–O-C absorption peaks of the cell wall polysaccharides (chitin, chitosan, α-glucan, mannan, etc.), in fungi and showed FTIR along with PCA is effective in understanding the biochemical changes. Bataller et al. [36] monitored biochemical changes in *Spirulina platensis* and found that FTIR with PLS-regression is a good analytical method of finding protein, carbohydrate and lipid content in *Spirulina* biomass during its growth. Dean et al. [42], determined lipid and carbohydrate changes in *Chlamydomonas reinhardtii* and *Scenedesmus subspicatus* microalgae using FTIR spectra. These results indicate the efficiency of FTIR to identify biochemical changes in algal cells in response quality of the product.

The region observed at 1200–900 cm^{-1} occurs due to C–O, C–C, C–O-C stretching vibration of polysaccharides [43]. These groups

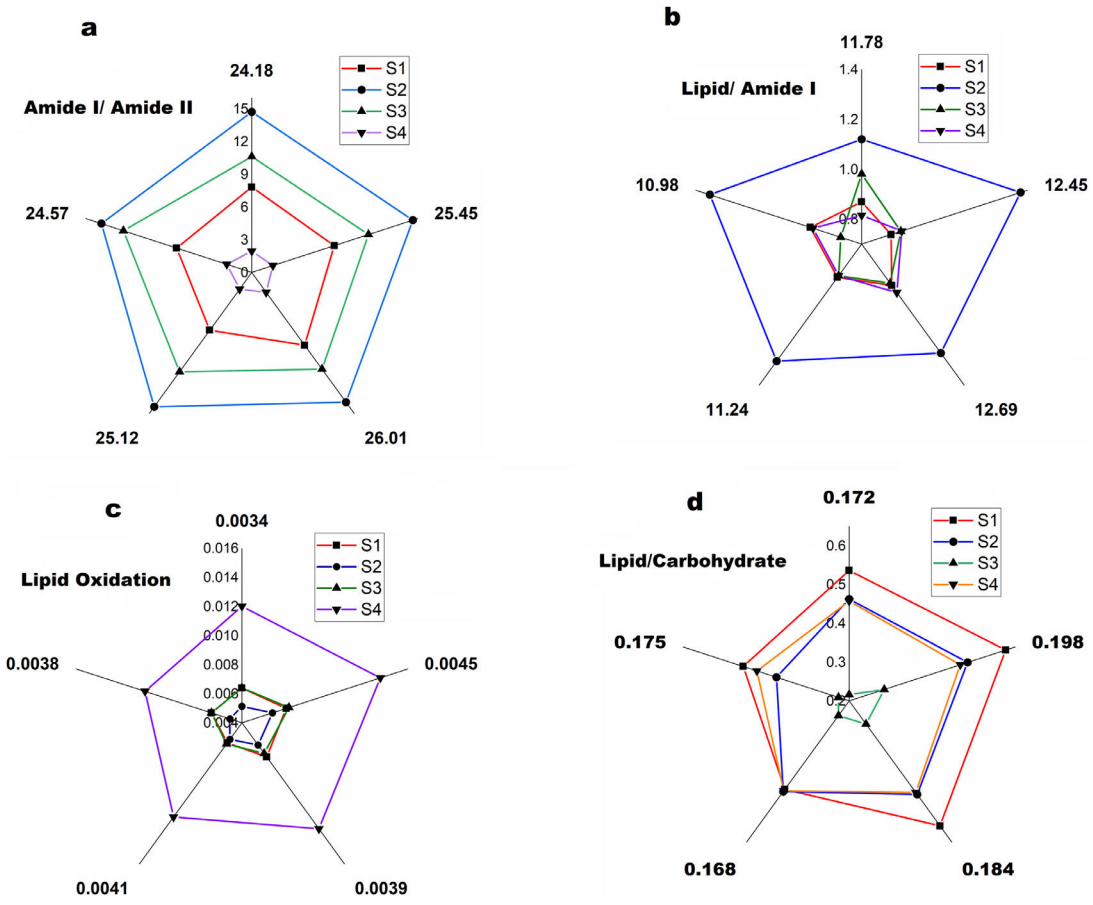

Fig. 2. Star delta graph showing band area measurement of *Spirulina platensis* control and its commercial products (a) Amide I/Amide II, (b) Lipid/Amide I (c) Total lipid oxidation and (d) Lipid/Carbohydrate.

Table 2
Synchronous 2T2D correlation cross peaks *Spirulina platensis* of different commercial products.

Sample	Auto Peaks	Assignment	Auto Peaks	Assignment
S1	2872	CH_3 symm stretch lipids	1034	C-C Stretch polyscharides
S2	2872	CH_3 symm stretch lipids	1624, 1034	Amide I (β sheet), C–C Stretch polyscharides
S3	2871	CH_3 symm stretch lipids	1627, 1034	Amide I (β sheet), C–C Stretch polyscharides
S3	2871	CH_3 symm stretch lipids	1031	C-C Stretch polyscharides

mainly occur in algae samples. Because of the complexity of the absorptions of various cellular polysaccharides specific assignments are rather difficult. In order to understand the quantitative and qualitative nature of the sample 2T2D correlation spectra were employed. We have employed 2T2D correlation spectroscopy which allows clarifying the different roles of carbohydrates and proteins with respect to lipids compounds which were discussed in the following section.

3.2. Synchronous 2T2D-COS spectral analysis

The 2T2D synchronous spectra in the range 3800–2800 cm^{-1} and 1800–900 $cm^{-1}$are shown for various commercial food products(Fig. 4a-4d). The Table. 2 shows auto peaks obsereved from 2T2D correlation spectra for samples. The synchronous map generated from the FTIR spectra has a predominant auto peak centered at 2871 cm^{-1}, 1624 $cm^{-1}$and 1034 cm^{-1} indicating lipids, protein and polysaccharides are mainly concentrated in the samples studied except S1 and S4. This shows the presence of abundant lipids, protein and carbohydrates. Mecozzi et al. [44] studied 2D-COS in characterizing lipid and protein changes in food samples.The carbohydrates and proteins show different characteristics because of significant components of subfractions present in the algae.

The more intense peaks at 2872 cm^{-1} were observed for S1 and S4 samples indicating high value lipids existing in the samples. The presence of these auto peaks shows samples have predominant lipids compositions which is the characteristics of the sample. The other samples S2 and S3 have less intense peaks. This signifies a decrease in the lipid's contents.

The two-auto peak observed at 1624 cm^{-1} and 1034 cm^{-1} signifies the presence of amide I of proteins and C–C stretching of polysaccharides for S2 and S3. The absence of auto peaks of 1624 cm^{-1}amide I and the presence of peak 1034 cm^{-1} show the presence of high value contents of polysaccharides in samples S1 and S4. Mecozzi et al. [45] studied biochemical changes in *Dunaliella tertiolecta*, algae sample using 2D-COS and PCA providing information on the mechanism of biochemical changes in algae samples

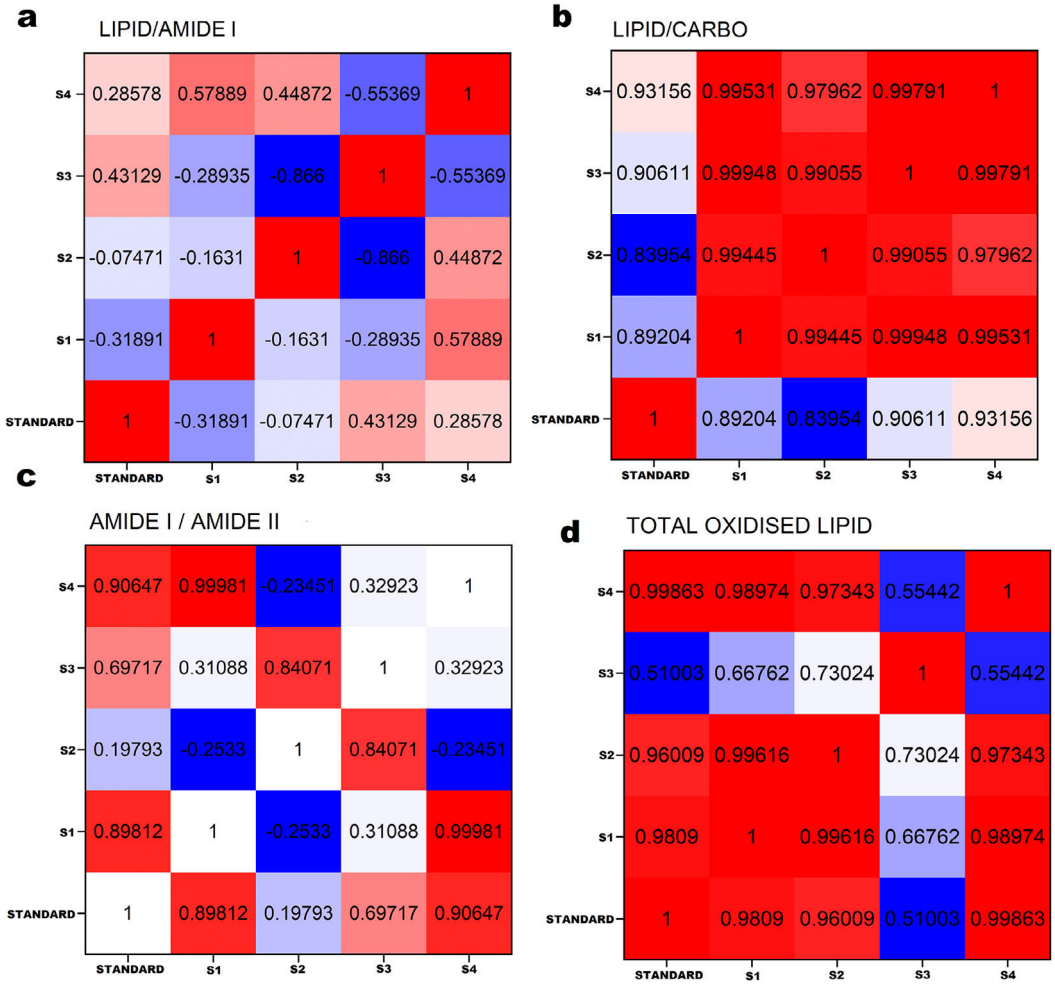

Fig. 3. Pearson correlation heat map showing different band area measurement among the *Spirulina platensis* samples (a) Lipid/Amide I (b) Lipid/Carbohydrate (c) Amide I/Amide II and (d) Total lipid oxidation.

3.3. Asynchronous 2T2D-COS spectral analysis

Fig 5a-5d shows asynchronous spectra obtained in the selected region 3000–2800 $cm^{-1}$and 1600–900 cm^{-1}. Table 3 shows the cross peaks obtained and their frequency assignment for the samples S1-S4. The asynchronous map which was asymmetric to the diagonal line displays cross peaks. This determines the sequence in spectral intensity changing with respect to control [22]. 2T2D analysis takes advantage that spectra measured in different conditions are directly compared independently [28]. The asynchronous negative cross peaks of S1 (Fig 4a) (2874, 2824) indicate that phospholipids are abundantly present in the control samples. In contrast, CH_2 stretching of pyranose rings are abundantly present in S1 sample. Such a differentiation of the specific origin of bands is clear in the advantage of 2T2D correlation which is not possible from the conventional spectra. The asynchronous spectra in the region 1800–900cm^{-1} show the presence of positive cross peaks (1126, 1036) indicating that C–O stretching of polysaccharides is abundantly present in the S1 sample than the control.

The asynchronous spectra of S2 show positive cross peaks at (2873, 2820) resulting in abundant presence of CH_2 stretching of pyranose ring than phospholipids in the S2 sample. This shows distinct variation of phospholipids and polysaccharides of pyranose ring between control and S2. Fig 5b shows asynchronous spectra obtained for the S2 sample in the region 1800–900cm^{-1}. The two positive cross peaks (1624, 1031) & (1624, 1125) indicate the presence of amide I of proteins in S2 indicating good quality. The asynchronous spectra of S3 (Fig 5c) show positive cross peaks (2879, 2819) which indicates a high amount of CH_2 stretching of pyranose ring of polysaccharides in S3 than phospholipids compared to control. The other positive cross peaks (1624, 1031) & (1624, 1125) show the presence of amide I of proteins (β sheet) dominated in the sample S3. The cross peaks observed for the sample S2 and S3 shows evidence of interaction mechanisms in lipids and carbohydrates between these molecules. Mecozzi et al. [46] reported different roles played by lipids, carbohydrates and proteins in algae using 2D-COS infrared spectra. Litwińczuk et al. [47] studied using 2D-IRCOS in bovine α-lactalbumin and observed changes in β-sheet/β-turn due to hydration effects. Ryu et al. [48] demonstrated pH-induced changes in α-lactalbumin/oleic acid (ALA/OA) by using 2D correlation spectroscopy and noticeable changes in auto peaks at 1659 cm^{-1} and 1636 cm^{-1} (shoulder) assigned to α-helix and β-sheet, respectively. Further analysis of 2D correlation spectra shows a change in intermolecular β-sheet to α-helices.

2T2D asynchronous spectra for S4 shows both positive and negative cross peaks (Fig 5d). The presence of positive cross peaks (2919, 2879) and (2971, 2879) shows higher amount of lipids and fatty acids in S4 than CH_2 stretching of the pyranose ring. The unique cross peaks confirm our finding that carbohydrates and lipids interaction play a different role due to external factors in food processing. This shows that conventional IR allows only changes in peak position and shift whereas two-

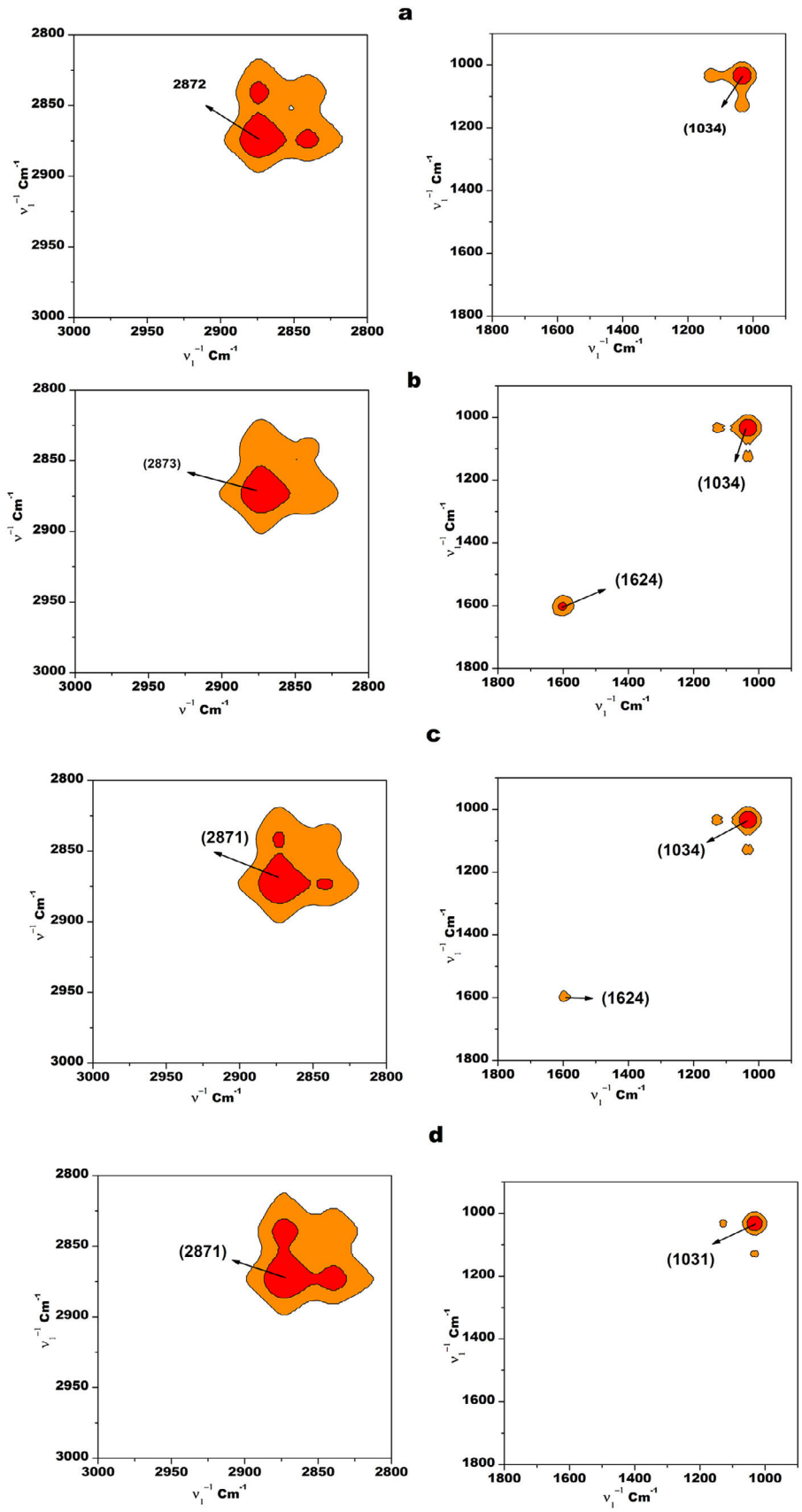

Fig. 4. Synchronous 2T2D correlation spectra obtained in the region 3000–2800 cm^{-1} and 1800–900 cm^{-1} of (a) Sample S1, (b) Sample S2 (c) Sample S3 (d) Sample S4.

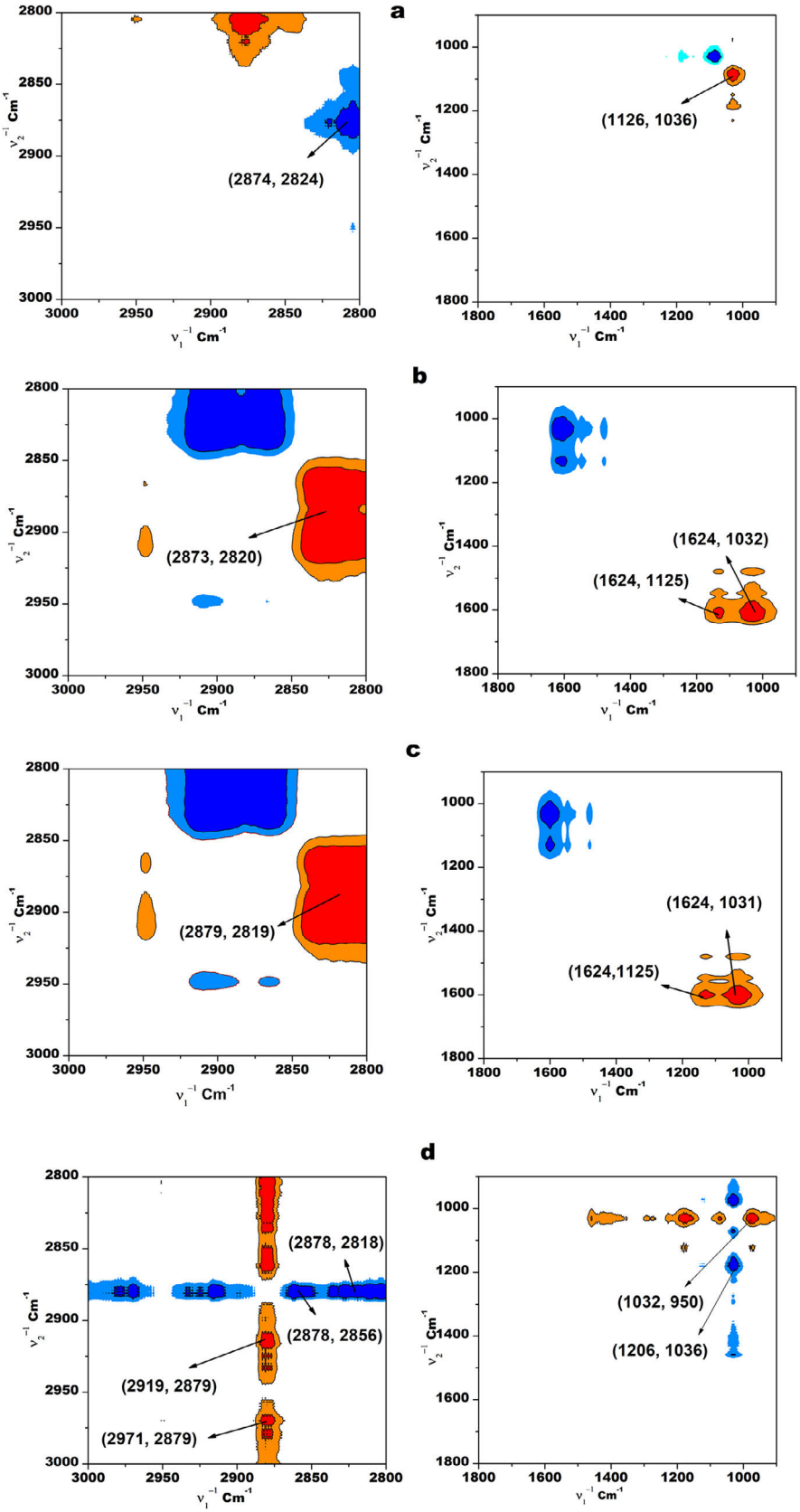

Fig. 5. Asynchronous 2T2D correlation spectra obtained in the region 3000–2800 cm^{-1} and 1800–900 cm^{-1} of (a) Sample S1, (b) Sample S2 (c) Sample S3 (d) Sample S4.

Table 3
Asynchronous 2T2D correlation cross peaks *Spirulina platensis* of different commercial products.

Sample	Asynchronous Assignment	Cross Peaks	Asynchronous Assignment	Asynchronous Assignment	Cross Peaks	Asynchronous Assignment
S1	CH_2 strech pyrnose ring	-(2874, 2824)	CH_2/CH_3 stretch phospholipids	C-O Stretch polyscharides	+(1126, 1036)	C-C Stretch polyscharides
S2	CH_2 strech pyrnose ring	+(2873,2820)	CH_2/CH_3 stretch phospholipids	Amide I (β sheet)	+(1624,1032) +(1624, 1125)	C-C Stretch polyscharides
				Amide I (β sheet)		
S3	CH_2 strech pyrnose ring	+(2879, 2819)	CH_2/CH_3 stretch phospholipids	Amide I (β sheet)	+(1624,1031) +(1624,1125)	C-C Stretch polysaccharides
				Amide I (β sheet)		C-O stretch polysaccharides
S4	CH_2asym lipids	+(2919, 2879)	CH_2 Strech pyranose ring	C-C Stretch polyscharides	+(1032, 950)	Glucan band (β anomer,
	CH_3 asymm lipids fatty acids	+(2971, 2879)	CH_2 Strech pyranose ring	C-C strech+ C-O strech + C-H	-(1206,1036)	C-H deformation)
	CH_2 strech pyrnose ring	-(2878, 2856)	C-H Strech pynose ring	deformation pyranose ring		C-C Stretch polyscharides
	CH_2strech pyrnose ring	(2878, 2818)	CH_2/CH_3 stretch phospholipids			

dimensional correlation allows significant correlation in changes in biomolecules present in our samples. The presence of negative cross peaks (2878, 2856) reveals a significant shift in frequency CH/CH_2 changes of pyranose ring of polysaccharides observed for the samples S4. It shows changes in polysaccharides compared to control [34]. This shift in frequency in polysaccharides arises due to interactions between hydrogen bonding related to the C–O-C fractions in the glucose unit. Carbohydrates cross linking results in polymerization due to specific interaction of external factors in food processing. The other negative cross peaks (2878,2818) show higher amount of phospholipids in control compared to S4. The study showed the role carbohydrates and lipids with significant changes observed in the S4 due to food processing such as mechanical pressing. The results of our study shows that CH_2/CH_3 of lipids and CH_2 stretch of pyranose ring are more abundantly present in S4 samples compared to control.

The week cross peaks +(1032, 950) show the presence of C–C stretching of polysaccharides than glucan band of C–H deformation in S4. Further negative cross peaks of (1206, 1036) confirms the higher amount of C–C/C–O stretching/C–H deformation of pyranose ring of polysaccharides in S4 sample [49]. Thus molecular degradation results in changes in polysaccharides released from the starch component during extrusion. Also, the hydrophilic groups of a starch bind with water molecules causing shear fragmentation during extrusion [50]. Further, the presence or absence of lipids bands in IR spectra of *Spirulina* food products is a measure of antioxidant property. This is due to various food treatments during production of commercial products. The heat map for the lipid/carbohydrates shows significant positive correlation exists among S4 sample with respect to control. These findings support our hypothesis of the cross-liking role played by lipid during food processing. It resulted in lipid oxidation changes. This was confirmed from the band area measurement shown in Fig. 3b. Thus 2T2D-COS allows us in discriminating samples based on the molecular changes which cannot be studied from 1D FTIR spectroscopy. Our study illustrates the use of 2T2D correlation to characteristics glycosidic linkages in the sample. For our case samples undergo various mechanical processing such as pressing, molding and heating to get final products. The absence of peaks at 1624 cm^{-1} shows evidence of changes in the biomolecules of S1 and S4. This peak is not linearly related to intensity changes compared to standard samples. The presence of evidence of out of phase components reflects the nonlinear relationship between biochemical changes and food processing techniques. Mecozzi et al. [46] studied similar results with 2DIR-COS for algae samples and observed interaction between fatty acids with respect to carbohydrates and proteins. Mecozzi et al. [44] studied that 2DIR-COS elucidate peculiar features of molecular modification occurring in algae samples. Qu Lei et al.[[51] utilized 2D-COS IR spectra effectively in discriminating Chinese herbal samples The synchronous spectra show a difference in auto-peaks observed in the range of 900–1100 cm^{-1}. Wang et al. [52] studied 2DIR-COS of rhizomes of Glycyrrhiza species with three auto-peaks at 908 cm^{-1}, 967 cm^{-1} and 1200 cm^{-1} corresponds to polysaccharides which are predominant in characterizing contents of the samples.

Adulteration of herbal medicine *Aquilariae Lignum Resinatum* was studied using two-dimensional (2D)correlation analysis showing simple and quick identification method of adulterated samples [52]. Yang et al. [53] investigated the 2T2D-IR correlation spectra with chemometrics in analyzing the adulterated milk. Vu et al. [54] employed 2T2D asynchronous correlation on dissimilar samples (gall bladder (GB) and bile juice) which helps in examining the metabolite compositions due to GB diseases. Thus the results obtained from 2T2D correlation analysis identify minute spectral features there by improving the accuracy and authentication of the samples studied.

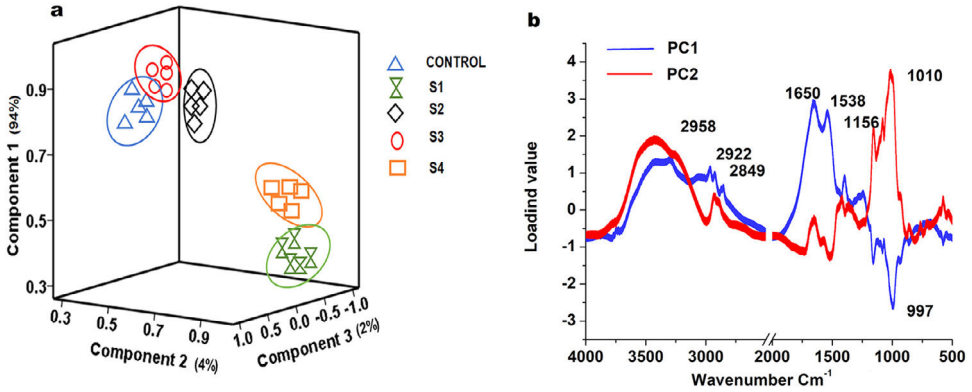

Fig. 6. (a). PCA scatter plots of *Spirulina platensis* of control and its commercial products (b)Variation of the factor loading obtained from the PCA with the corresponding wavenumber of the *Spirulina* platensis and its commercial products.

4. Principal component analysis

Fig.6a shows the PCA results obtained for various commercial *S platensis* and the control sample. The plots indicate the control and commercial food samples are well separated based on eigenvalues. The highest eigenvalue relates to components 1 with 94% variation. Component 2 has 4% variation. The 3rd component has the least value of 2% variation having low eigenvalues. This PCA was obtained from absorption values in the entire region. The plot shows that control has a high value along PC1 followed by the sample S3 and S4. The samples S1 and S4 have low values along PC2. The plots show a distinct variation of samples based on biochemical composition. The S3 and S4 sample is predominant in influencing the changes studied. This variation is due to the changes in lipids, proteins and polysaccharides. Loading plots show prominent frequency change that enables major biochemical changes of the variables (Fig. 6b). From the loading plot, the lipids and proteins have a higher value. This is responsible for the distinct separation of the samples studied. This supports bimolecular changes occurring in the sample as revealed from the scatter plot. Many studies reported the use of PCA on FTIR data to find the variability in biological samples [8,9,14,31]. Angelo Beratto-Ramos et al. [55] 2020 reported that FTIR along with PCA is used to identify carbohydrates 1–3-β-glucans and proteins in a seaweed *Macrocystis pyrifera*. Kokot et al. [56] demonstrated 2D correlation spectroscopy with PCA in analyzing changes in the hydrogen bonding network in cellulose. The loading plots(Fig. 6b) show positive loading values of lipids and carbohydrates along PC1. The negative loading value of PC1 occurs at 997cm^{-1} showing different mechanisms exhibited by polysaccharides of glucan bands. This occurs during the sample extrusion process. This supports the polymerization of carbohydrates moieties which occur during sample processing.

The high negative loadings values are strongly related to the changes in intra- and interchain H-bonds of cellulose structure during the sampling process. The differences that exist in a polysaccharide are shown by the negative loading(Fig. 6b). This helps in identifying the dissimilarity that exists among the samples studied. Similar reports of studies by Kokot et al. [56] using 2DIR with PCA showing positive/negative PC loading on cellulose structure on heating. This shows that the structural degradation and disruption of intrachain hydrogen bonding occurs in cellulose structure.

5. Hierarchical cluster analysis (HCA)

Spirulina platensis with different commercial food supplements is subjected to hierarchical clustering analysis using the Ward algorithm. They are displayed graphically (Fig.7) as a dendrogram.

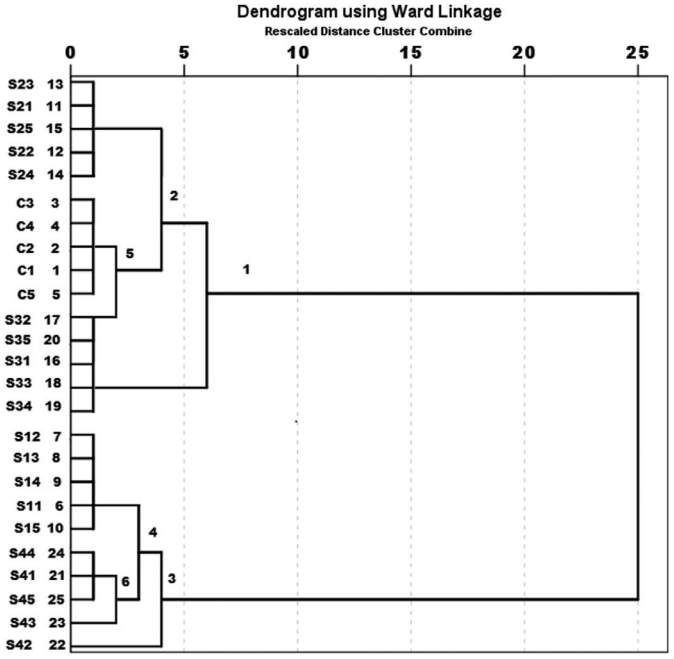

Fig. 7. Dendrogram of *Spirulina platensis* of control and its commercial products showing group linkage obtained using ward algorithm.

Similar cases are being visualized by closer separations. The larger distance in the dendrogram shows how the samples are separated [29]. The first cluster formed with two sub cluster (2 and 5) corresponds to the grouping of control samples with S2 and S3. The third cluster results from grouping of two well-differentiated subclusters (4 and 6) of commercial samples S1 and S4. The smaller distance in the range of 1–5 shows closer separation among the samples. The dissimilarity that exists among the various samples shows a higher scale in the range 8- 25. Thus dendrogram depicts clustering of samples, with the identical sample having closer separation. R. da Silva Leite et al. [9], Cao Z et al. [57] studied HCA in effective differentiation of biological samples.

6. Receiver operation characteristics analysis

The ROC curve represents the sensitivity versus 1-specificity of the experimental values. The information gives the effectiveness of the test carried. The obtained ROC curve for various commercial samples lies in the range of 0.84 to 0.87 showing the reliability of our study (Fig. 8). The highest ROC curve area was observed

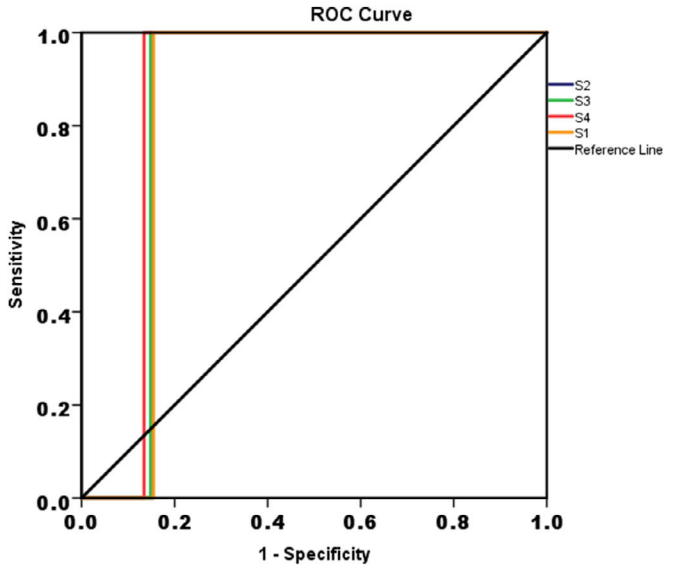

Fig. 8. Receiver operating characteristics curve for *Spirulina platensis* control and its commercial products .

for Sample S4 and S3. It gives the response and validation of the study. Güleken [58] et al. 2020 studied ROC analysis in quality performance of blood cancer of human samples. Many reports successfully employed FTIR data in utilizing the ROC curve for the effectiveness of the study in biological samples [30,59,59]. Our ROC results agree with the quality assessment of commercial *Spirulina* food products from the FTIR data.

7 Conclusion

We examined 2T2D-COS to assess specific aspects of molecular mechanisms observed for commercial products with respect to control. The information about changes in the biochemical compositions is used to assess the quality of commercial *Spirulina* products. The possibility of identification of functional group changes in food products reflects an important trend in the variations of chemical structure. The band area of Amide I/Amide II suggests studied samples have low protein contents for S1 and S4. This change in proteins, lipids and carbohydrates demonstrated rapid metabolic changes. The results show 2T2D-COS helps in understanding the changes in macromolecular compositions of *Spirulina* and its food products. We have examined the correlation between lipids and carbohydrates changes using 2T2D-COS techniques. The biggest difference between positive and negative loading from PCA results in discrimination among the samples. The dendrogram depicts dissimilarity that exists among the samples with high value. ROC analysis shows good reliability of the study for various commercial samples. Our results indicate 2T2D correlation infrared spectra helps in understanding the correlation in the functional groups mechanisms of *Spirulina* and its food products efficiently.

Declaration of Competing Interest

The authors have declared no conflict of interest.

CRediT authorship contribution statement

E. Kavitha: Formal analysis, Resources, Investigation, Methodology, Validation, Writing - review & editing. **L. Devaraj Stephen:** Formal analysis, Resources, Validation. **Fatema Hossain Brishti:** Software. **S. Karthikeyan:** Conceptualization, Data curation, Formal analysis, Resources, Investigation, Methodology, Supervision, Validation, Writing - original draft, Writing - review & editing.

Acknowledgement

The authors thank SAIF, IIT, Chennai,Tamil Nadu, India in helping with recording FTIR for the sample.

References

[1] Reema Valand, Sangeeta Tanna, Graham Lawson, Linda Bengtström, A review of Fourier Transform Infrared (FTIR) spectroscopy used in food adulteration and authenticity investigations, Food Addit. Contam.: part A 37 (1) (2020) 19–38, doi:10.1080/19440049.2019.1675909.
[2] Tomas Lafarga, José María Fernández-Sevilla, Cynthia González-López, Francisco Gabriel Acién-Fernández, Spirulina for the food and functional food industries, Food Res. Int. (2020) 109356, doi:10.1016/j.foodres.2020.109356.
[3] Tomás Lafarga, Erika Mayre, Gemma Echeverria, Inmaculada Viñas, Silvia Villaró, Francisco Gabriel Acién-Fernández, Massimo Castellari, Ingrid Aguiló-Aguayo, Potential of the microalgae nannochloropsis and tetraselmis for being used as innovative ingredients in baked goods, LWT 115 (2019) 108439, doi:10.1016/j.lwt.2019.108439.
[4] Ana Paula Batista, Alberto Niccolai, Patrícia Fradinho, Solange Fragoso, Ivana Bursic, Liliana Rodolfi, Natascia Biondi, Mario R. Tredici, Isabel Sousa, Anabela Raymundo, Microalgae biomass as an alternative ingredient in cookies: sensory, physical and chemical properties, antioxidant activity and in vitro digestibility, Algal. Res. 26 (2017) 161–171, doi:10.1016/j.algal.2017.07.017.
[5] Tomás. Lafarga, Effect of microalgal biomass incorporation into foods: nutritional and sensorial attributes of the end products, Algal Res. 41 (2019) 101566, doi:10.1016/j.algal.2019.101566.
[6] Butch G. Bataller, Sergio C. Capareda, A rapid and non-destructive method for quantifying biomolecules in Spirulina platensis via Fourier transform infrared–Attenuated total reflectance spectroscopy, Algal Res. 32 (2018) 341–352, doi:10.1016/j.algal.2018.04.023.
[7] Jessica Roberts, Aoife Power, James Chapman, Shaneel Chandra, Daniel Cozzolino, A short update on the advantages, applications and limitations of hyperspectral and chemical imaging in food authentication, Appl. Sci. 8 (4) (2018) 505, doi:10.3390/app8040505.
[8] Romdhane Karoui, Gerard Downey, Christophe Blecker, Mid-infrared spectroscopy coupled with chemometrics: a tool for the analysis of intact food systems and the exploration of their molecular structure– quality relationships–a review, Chem. Rev. 110 (10) (2010) 6144–6168, doi:10.1021/cr100090k.
[9] Da Silva Leite Romeu, Karthikeyan Sivakumaran, Salvador Hernandéz-Navarro, Marilza Neves do Nascimento, Norlan Miguel Ruiz Potosme, Paula Carrión-Prieto, Elma dos Santos Souza, Nitrogen influenced biomolecular changes on Physalis L. species studied using 2DCOS spectral analysis coupled with chemometric and Receiver operation characteristics analysis, Spectrochim. Acta Part A (2021) 249, doi:10.1016/j.saa.2020.119220.
[10] M.Pilar Callao, Itziar Ruisánchez, An overview of multivariate qualitative methods for food fraud detection, Food Control 86 (2018) 283–293, doi:10.1016/j.foodcont.2017.11.034.
[11] Weijie Lan, Catherine MGC Renard, Benoit Jaillais, Alexandre Leca, Sylvie Bureau, Fresh, freeze-dried or cell wall samples: which is the most appropriate to determine chemical, structural and rheological variations during apple processing using ATR-FTIR spectroscopy? Food Chem. 330 (2020) 127357, doi:10.1016/j.foodchem.2020.127357.
[12] Jun Yang, Chunling Yin, Xu Miao, Xiangru Meng, Zhimin Liu, Leqian Hu, Rapid discrimination of adulteration in Radix astragali combining diffuse reflectance mid-infrared Fourier transform spectroscopy with chemometrics, Spectrochim. Acta Part A 248 (2021) 119251, doi:10.1016/j.saa.2020.119251.
[13] Abdul Rohman, Sugeng Riyanto, Anggun Mart Sasi, Farahwahida Mohd Yusof, The use of FTIR spectroscopy in combination with chemometrics for the authentication of red fruit (Pandanus conoideus Lam) oil from sunflower and palm oils, Food Biosci. 7 (2014) 64–70 http://dx.doi.org/, doi:10.1016/j.fbio.2014.05.007.
[14] Lijuan Du, Weiying Lu, Boyan Gao, Jing Wang, Liangli Lucy Yu, Authenticating raw from reconstituted milk using fourier transform infrared spectroscopy and chemometrics, J. Food Qual. (2019) 2019, doi:10.1155/2019/5487890.
[15] Yew-Keong. Choong, Fourier Transform Infrared and Two-Dimensional Correlation Spectroscopy for Substance Analysis, Nicolic, G. Fourier Transf. (2017) 175–190 http://dx.doi.org/, doi:10.5772/66584.
[16] Zhaohong You, Liling Zhuo, Xiaoling Yang, Hanmei Hong, Zihao Liu, Zhaoyong Gong, Fang Cheng, Food research applications of two-dimensional correlation spectroscopy, Appl. Spectrosc. Rev. 50 (10) (2015) 840–858, doi:10.1080/05704928.2015.1087402.
[17] Isao. Noda, Modified two-dimensional correlation spectra for streamlined determination of sequential order of intensity variations, J. Mol. Struct. 1124 (2016) 197–206, doi:10.1016/j.molstruc.2016.01.092.
[18] Yukihiro Ozaki, Koichi Murayama, Yuqing Wu, Bogusława Czarnik-Matusewicz, Two-dimensional infrared correlation spectroscopy studies on secondary structures and hydrogen bondings of side chains of proteins, Spectroscopy 17 (2) (2003) 79–100 3.
[19] LI-Ying Liu, Ren-Jie Yang, Jing Zhang, Gui-Mei Gong, Yan-Rong Yang, Recent progress in two-dimensional correlation spectroscopy for the environmen-

tal detection and analysis, J. Mol. Struct. 1214 (2020) 128263, doi:10.1016/j.molstruc.2020.128263.
[20] Yeonju Park, Sila Jin, Isao Noda, Young Mee Jung, Emerging developments in two-dimensional correlation spectroscopy (2D-COS), J. Mol. Struct. (2020) 128405, doi:10.1016/j.molstruc.2020.128405.
[21] X.Z. Hu, S.Q. Liu, X.H. Li, et al., Geographical origin traceability of Cabernet Sauvignon wines based on Infrared fingerprint technology combined with chemometrics, Sci. Rep. 9 (2019) 8256, doi:10.1038/s41598-019-44521-8.
[22] Isao. Noda, Two-trace two-dimensional (2T2D) correlation spectroscopy–a method for extracting useful information from a pair of spectra, J. Mol. Struct. 1160 (2018) 471–478, doi:10.1016/j.molstruc.2018.01.091.
[23] Woosuk Sohng, Changhwan Eum, Hoeil Chung, Exploring two-trace two-dimensional (2T2D) correlation spectroscopy as an effective approach to improve accuracy of discriminant analysis by highlighting asynchronous features in two separate spectra of a sample, Anal. Chim. Acta 1152 (2021) 338255, doi:10.1016/j.aca.2021.338255.
[24] I. Noda, Generalized two-dimensional correlation method applicable to infrared, raman, and other types of spectroscopy, Appl. Spectrosc. 47 (1993) 1329–1336, doi:10.1366/0003702934067694.
[25] I. Noda, A.E. Dowrey, C. Marcoli, G.M. Story, Y. Ozaki, Generalized twod imensionalcorrelation spectroscopy, Appl. Spectrosc. 54 (2000) 236A, doi:10.1366/0003702001950454.
[26] Isao. Noda, Techniques useful in two-dimensional correlation and codistribution spectroscopy (2DCOS and 2DCDS) analyses, J. Mol. Struct. 1124 (2016) 29–41, doi:10.1016/j.molstruc.2016.01.089.
[27] Isao. Noda, Closer examination of two-trace two-dimensional (2T2D) correlation spectroscopy, J. Mol. Struct. 1213 (2020) 128194, doi:10.1016/j.molstruc.2020.128194.
[28] Ward Jr, H. Joe, Hierarchical grouping to optimize an objective function, J. Am. Stat. Assoc. 58 (301) (1963) 236–244, doi:10.1080/01621459.1963.10500845.
[29] Grzegorz Kalisz, Barbara Gieroba, Olga Chrobak, Magdalena Suchora, Agata L. Starosta, Anna Sroka-Bartnicka, Vibrational spectroscopic analyses and imaging of the early middle ages hemp bast fibres recovered from lake sediments, Molecules 26 (5) (2021) 1314, doi:10.3390/molecules26051314.
[30] Annika Durve Gupta, Esakimuthu Kavitha, Shikha Singh, Sivakumaran Karthikeyan, Toxicity mechanism of Cu 2+ ion individually and in combination with Zn 2+ ion in characterizing the molecular changes of Staphylococcus aureus studied using FTIR coupled with chemometric analysis, J. Biol. Phys. 46 (4) (2020) 395–414, doi:10.1007/s10867-020-09560-7.
[31] Claude. Zarrouk, Contribution a L'etude D'une cyanobacterie: Influence de Divers Facteurs Physiques et Chimiques sur la Croissance et la Photosynthese de Spirulina Maxima (Setchell Et Gardner) Geitler, University of Paris, Paris, 1966.
[32] Grace C. Esther Elizabeth, P. Kiruthika Lakshmi, S. Meenakshi, Seetharaman Vaidyanathan, S. Srisudha, M. Briget Mary, Biomolecular transitions and lipid accumulation in green microalgae monitored by FTIR and Raman analysis, Spectrochim. Acta Part A 224 (2020), doi:10.1016/j.saa.2019.117382.
[33] Zeynep Mine Şenol, Ülküye Dudu Gül, Rafig Gurbanov, Selçuk Şimşek, Optimization the removal of lead ions by fungi: explanation of the mycosorption mechanism, J. Environ. Chem. Eng. 9 (2) (2021), doi:10.1016/j.jece.2020.104760.
[34] Zanyar Movasaghi, Shazza Rehman, Dr Ihtesham ur Rehman, Fourier transform infrared (FTIR) spectroscopy of biological tissues, Appl. Spectrosc. Rev. 43 (2) (2008) 134–179, doi:10.1080/05704920701829043.
[35] Efstathia Skotti, Sophia Kountouri, Pavlos Bouchagier, Dimitrios I. Tsitsigiannis, Moschos Polissiou, Petros A. Tarantilis, FTIR spectroscopic evaluation of changes in the cellular biochemical composition of the phytopathogenic fungus Alternaria alternata induced by extracts of some Greek medicinal and aromatic plants, Spectrochim. Acta Part A 127 (2014) 463–472, doi:10.1016/j.saa.2014.02.113.
[36] Tao Wang, Zhaomo Tian, Anders Tunlid, Per Persson, Nitrogen acquisition from mineral-associated proteins by an ectomycorrhizal fungus, New Phytol. 228 (2) (2020) 697–711.
[37] Robinson Soto-Ramírez, Maria-Gabriela Lobos, Olivia Córdova, Paola Poirrier, Rolando Chamy, Effect of growth conditions on cell wall composition and cadmium adsorption in Chlorella vulgaris: a new approach to biosorption research, J. Hazard. Mater. (2021) 411, doi:10.1016/j.jhazmat.2021.125059.
[38] Snežana Vojvodić, Marina Stanić, Bernd Zechmann, Tanja Dučić, Milan Žižić, Milena Dimitrijević, Jelena Danilović Luković, Milica R. Milenković, Jon K. Pittman, Ivan Spasojević, Mechanisms of detoxification of high copper concentrations by the microalga Chlorella sorokiniana, Biochem. J. 477 (19) (2020) 3729–3741 PMID: 32936286, doi:10.1042/BCJ20200600.
[39] Izabela Michalak, Małgorzata Mironiuk, Katarzyna Godlewska, Justyna Trynda, Krzysztof Marycz, Arthrospira (Spirulina) platensis: an effective biosorbent for nutrients, Process Biochem. 88 (2020) 129–137, doi:10.1016/j.procbio.2019.10.004.
[40] Justin N. Murdock, David L. Wetzel, FT-IR microspectroscopy enhances biological and ecological analysis of algae, Appl. Spectrosc. Rev. 44 (4) (2009) 335–361, doi:10.1080/05704920902907440.
[41] Gergely Kosa, Achim Kohler, Valeria Tafintseva, Boris Zimmermann, Kristin Forfang, Nils Kristian Afseth, Dimitrios Tzimorotas, et al., Microtiter plate cultivation of oleaginous fungi and monitoring of lipogenesis by high-throughput FTIR spectroscopy, Microb. Cell Fact. 16 (1) (2017) 1–12.
[42] Andrew P. Dean, David C. Sigee, Beatriz Estrada, Jon K. Pittman, Using FTIR spectroscopy for rapid determination of lipid accumulation in response to nitrogen limitation in freshwater microalgae, Bioresour. Technol. 101 (12) (2010) 4499–4507.
[43] Halah Aalim, Zisheng Luo, Insight into rice (Oryza sativa L.) cooking: phenolic composition, inhibition of α-amylase and α-glucosidase, and starch physicochemical and functional properties, Food Biosci. 40 (2021) 100917, doi:10.1016/j.fbio.2021.100917.
[44] Mauro Mecozzi, Elena Sturchio, Effects of essential oil treatments on the secondary protein structure of Vicia faba: a mid-infrared spectroscopic study supported by two-dimensional correlation analysis, Spectrochim. Acta Part A 137 (2015) 90–98.
[45] M. Mecozzi, M. Pietroletti, R. Di Mento, Application of FTIR spectroscopy in ecotoxicological studies supported by multivariate analysis and 2D correlation spectroscopy, Vib. Spectrosc. 44 (2) (2007) 228–235.
[46] Mauro Mecozzi, Eva Pietrantonio, Marco Pietroletti, The roles of carbohydrates, proteins and lipids in the process of aggregation of natural marine organic matter investigated by means of 2D correlation spectroscopy applied to infrared spectra, Spectrochim. Acta Part A 71 (5) (2009) 1877–1884.
[47] Adriana Litwińczuk, Soo Ryeon Ryu, Laurence A. Nafie, Jong Wha Lee, Hugh I. Kim, Young Mee Jung, Bogusława Czarnik-Matusewicz, The transition from the native to the acid-state characterized by multi-spectroscopy approach: study for the holo-form of bovine α- actalbumin, Biochim. Biophys. Acta (BBA)-Proteins Proteom. 1844 (3) (2014) 593–606, doi:10.1016/j.bbapap.2013.12.018.
[48] Soo Ryeon Ryu, Bogusława Czarnik-Matusewicz, Rina K. Dukor, Laurence A. Nafie, Young Mee Jung, Analysis of the molten globule state of bovine α-lactalbumin by using vibrational circular dichroism, Vib. Spectrosc. 60 (2012) 68–72, doi:10.1016/j.vibspec.2012.02.006.
[49] Vlasta Mohaček-Grošev, Romano Božac, Gerwin J. Puppels, Vibrational spectroscopic characterization of wild growing mushrooms and toadstools, Spectrochim. Acta Part A 57 (14) (2001) 2815–2829, doi:10.1016/S1386-1425(01)00584-4.
[50] Qing-Bo Ding, Paul Ainsworth, Andrew Plunkett, Gregory Tucker, Hayley Marson, The effect of extrusion conditions on the functional and physical properties of wheat-based expanded snacks, J. Food Eng. 73 (2) (2006) 142–148.
[51] Lei Qu, Jian-bo Chen, Qun Zhou, Gui-jun Zhang, Su-qin Sun, Yi-zhen Guo, Identification of authentic and adulterated Aquilariae Lignum Resinatum by Fourier transform infrared (FT-IR) spectroscopy and two-dimensional correlation analysis, J. Mol. Struct. 1124 (2016) 216–220, doi:10.1016/j.molstruc.2016.01.056.
[52] Yang Wang, Ping Wang, Changhua Xu, Yan Yang, Jin Li, Tao Chen, Zheng Li, et al., Macro-fingerprint analysis-through-separation of licorice based on FT-IR and 2DCOS-IR, J. Mol. Struct. 1070 (2014) 1–9 http://dx.doi.org/, doi:10.1016/j.molstruc.2014.03.016.
[53] Renjie Yang, Rong Liu, Xu Kexin, Detection of adulterated milk using two-dimensional correlation spectroscopy combined with multi-way partial least squares, Food Biosci. 2 (2013) 61–67, doi:10.1016/j.fbio.2013.04.005.
[54] Tung Duy Vu, Woosuk Sohng, Eunjin Jang, Dongho Choi, Hoeil Chung, Feasibility of discrimination of gall bladder (GB) stone and GB polyp using voltage-applied SERS measurement of bile juice samples in conjunction with two-trace two-dimensional (2T2D) correlation analysis, Analyst 146 (3) (2021) 1091–1098, doi:10.1039/D0AN02115F.
[55] Angelo Beratto-Ramos, Cristian Agurto-Muñoz, Juan Pablo Vargas-Montalba, Rosario del, P. Castillo, Fourier-transform infrared imaging and multivariate analysis for direct identification of principal polysaccharides in brown seaweeds, Carbohydr. Polym. 230 (2020) 115561, doi:10.1016/j.carbpol.2019.115561.
[56] Serge Kokot, Boguslawa Czarnik-Matusewicz, Yukihiro Ozaki, Two-dimensional correlation spectroscopy and principal component analysis studies of temperature-dependent IR spectra of cotton–cellulose, Biopolym.: Orig. Res. Biomol. 67 (6) (2002) 456–469 10.1002/bip.10163.
[57] Zhen Cao, Zhenjie Wang, Zhonglin Shang, Jiancheng Zhao, Classification and identification of Rhodobryum roseum Limpr. and its adulterants based on fourier-transform infrared spectroscopy (FTIR) and chemometrics, PLoS ONE 12 (2) (2017) e0172359, doi:10.1371/journal.pone.0172359.
[58] Zozan Güleken, Başak Ünübol, Suat Toraman, Rabia Bilici, Oğuzhan Gündüz, Serap Erdem Kuruca, Diagnosis of opioid use disorder with high sensitivity and specificity by advanced computational analysis of Fourier transform infrared spectroscopy, Infrared Phys. Technol. 105 (2020) 103218, doi:10.1016/j.infrared.2020.103218.
[59] Maryam Ghassemi, Sahar Barzegari, Parastoo Hajian, Hanieh Zham, Hamid Reza Mirzaei, Farshad H. Shirazi, Diagnosis of normal and malignant human gastric tissue samples by FTIR spectra combined with mathematical models, J. Mol. Struct. 1229 (2021) 129493, doi:10.1016/j.molstruc.2020.129493.

UTTAR PRADESH JOURNAL OF ZOOLOGY

42(13): 74-83, 2021
ISSN: 0256-971X (P)

BIOCHEMICAL AND MOLECULAR ALTERATIONS IN THE GILLS OF FRESHWATER FISH *Oreochromis mossambicus* EXPOSED TO TANNERY EFFLUENT

M. SANKAR[1], T. KUMARAN[1] AND R. SARAVANAN[1*]

[1]Post Graduate and Research Department of Zoology, Dr. Ambedkar Government Arts College, Vyasarpadi, Chennai 600039, Tamil Nadu, India.

AUTHORS' CONTRIBUTIONS

This work was carried out in collaboration among all authors. All authors read and approved the final manuscript.

Article Information

Editor(s):
(1) Dr. Golam Mustafa, Center for Resource Development Studies Ltd., Bangladesh.
Reviewers:
(1) P. V. Krishna, Acharya Nagarjuna University, India.
(2) Shoaibe Hossain Talukder Shefat, Bangladesh.

Received: 10 April 2021
Accepted: 16 June 2021
Published: 19 June 2021

Original Research Article

ABSTRACT

The present study was to find out the effects of tannery effluent on the fingerlings of freshwater fish *Oreochromis mossambicus***.** The fishes were maintained at 10% concentration of tannery effluent in laboratory conditions for 30 days based on the lethal concentration studies. The gill tissue of the fishes was chosen for this study. Spectrophotometric analysis revealed a decline in total protein, DNA and RNA contents of the gills was statistically significant after exposure of the fishes to tannery effluent probable due to stress factors. Difference in intensity of genomic DNA between 750 and 1000bp was observed in the gill tissue in fishes exposed to tannery effluent, when DNA was subjected to agarose gel electrophoresis separation. Protein subunit separation by SDS-PAGE show high and low intensities in the protein bands obtained from the gills in the control and experimental fishes. DNA damage in the gills was confirmed by an increase in DNA damage by tail migration and by increase in percentage of mean DNA comet tail length formation.

Keywords: *Oreochromis mossambicus;* tannery effluent; gills; genomic DNA; protein subunits; comet assay.

1. INTRODUCTION

Aquatic ecosystem forms the final reservoir for a variety of chemicals used in industries and agriculture which in present days is becoming an alarming a global problem [1]. Tannery effluents are ranked as the highest pollutants among all industrial wastes. A number of tanning industries favour chrome tanning for processing leather. Only fraction of chromium (Cr) is utilized in tanning process and the rest is discharged as by-product of wastewater treatment [2]. Among the different forms of chromium hexavalent

**Corresponding author: Email: rsaravanan0268@gmail.com, rsaravanan51283@yahoo.com;*

chromium (Cr VI) is a potent carcinogen to humans and animals. It has the capacity to enters cells via surface transport systems and gets reduced to trivalent chromium (Cr III) inducing genotoxicity [3,4]. Chromium compounds exert genotoxic, mutagenic and carcinogenic effects on human life and animals. In ecotoxicological studies genotoxicity in aquatic animals can be assessed by alteration in DNA [5].

The gills participate in many important physiological functions in the fish, such as respiration, osmoregulation and excretion. These structures remains in close contact with the external environment and particularly sensitive to changes in the quality of the water are considered the primary target of the contaminants [6,7]. Gills are the primary route for the entry of pesticide [8]. The cellular damages observed in the gills in term of epithelium proliferation and necrosis can adversely affect the gaseous exchange and ionic regulation. The edematous changes in gill filaments are probably due to increased capillary permeability. Alterations like fusion of some secondary lamellae are a mechanism for defense. This result in the increase of distance between the external environment and the blood and thus serve as a barrier to the entry of contaminants [9].

Proteins play an important role in the maintenance of various physiological activities including growth, development, reproduction and sexual differentiation. Proteins are mainly involved in the architecture of the cell. It being the essential substance is needed for growth and development and also serves as energy source during the stress condition [10].

The nucleic acids play a major role in all biological activities and are regulators of all biological synthesis of proteins, which are structural and functional units of the biological systems. It is known that DNA functions as a primer in DNA and RNA polymerase reactions [11], and the inhibition in DNA content can result in the inhibition of both DNA and RNA synthesis. The synthesis of RNA plays an important role in protein synthesis. Apoptosis ultimately is cell death, which is caused due to chromatin condensation, internucleosomal DNA fragmentation, cellular shrinkage and membrane blebbing resulting in the formation of apoptotic bodies [12].

Comet assay is considered a suitable and rapid test for DNA-damaging potential in environmental and biomonitoring studies [13]. To quantify DNA lesions in individual cells for environmental monitoring was also reported [14]. Many researchers also conducted pilot study to assess the genotoxic effect under the laboratory scale [15].

In the present study, *Oreochromis mossambicus* was exposed to tannery effluent. Total protein, Nucleic acids DNA and RNA contents were determined in the gill tissue. This was followed by identification of base pairs and visualization of intensities of DNA bands / fragments by agarose gel electrophoresis, protein intensity changes were identified by polyacrylamide gel electrophoresis and single cell gel electrophoresis (comet assay) was performed to identify DNA damage.

2. MATERIALS AND METHODS

Collection of tannery effluent: Samples were collected from Common Effluent Treatment Plant (CETP) at Pallavaram in Chennai which treats around 3000 m^3/day of wastewater. The effluent was collected at a fixed point when the discharges from all the stages of processing are released together. The samples were collected during the month of November 2019. The raw effluent was collected in different polyethylene containers of 20 litres capacity and stored in dark at room temperature till further use.

2.1 Experimental Animals

Healthy juveniles fishes comprising fingerlings of *Oreochromis mossambicus* weighing about 4.0 to 4.5 gm approximately and 5.5 – 7.5 cm in length was procured from Bharat seed fish farm, Budur, Poondi, Tiruvallur District and were brought to the laboratory in polythene bags containing aerated water. This fish was selected for the study due hardy nature and was able to tolerate derelict water conditions. They are highly edible food fish with nutritive value.

2.2 Determination of Lethal Concentration (LC_{50})

The LC_{50} value of tannery wastewater was analyzed through a static renewal bioassay technique. Preliminary screening was carried out to determine the testing chemical as described by [16]. The effluent was mixed with tap water in appropriate dilution to get wide range of concentration. A range of 7 concentrations (50, 40, 30, 25, 20, 15, 10% / L of water) were selected for lethal dose studies. The mortality in each concentration were noted for 24, 48, 72 and 96 hour's exposure. The LC_{50} value (96 hour) was found to be at 20% concentration, for fingerlings of *Oreochromis mossambicus.* From this 50% of sub-lethal concentration was selected for the present study.

2.3 Analysis of Chromium in Raw Tannery Effluent Sample

The raw tannery effluent was estimated for total chromium, hexavalent chromium and trivalent chromium contents by following the standard methods of APHA [17].

2.4 Experimental Design

Acclimatized freshwater fish fingerlings of *Oreochromis mossambicus* were divided into two groups consisting of 10 fishes in each group.

Group I: Control group - Fishes maintained in dechlorinated toxicant free tap water

Group II: Experimental group - Fishes maintained in tannery effluent

All the groups of fishes were maintained in 30 L of water. Fishes of control group was maintained in 30 L tap water. Group-II fishes were exposed to sub-lethal concentration (10%) of the tannery waste water for a period of 30 days. No mortality was recorded during the period of study. The experimental set up was maintained promptly with the renewal of effluent water daily in group- II. The tubs were aerated with air stones attached to an air compressor to saturate oxygen. The fishes were fed with commercial fish feed twice a day regularly (2% of their body weight). Commercial food pellets with ingredients consisting of fish meal, wheat flour, soybean meal, yeast, vitamins and minerals were fed. Left over feed if any, was removed by siphoning, two hours post feeding to reduce contamination with food remains. Faecal residues were removed every 24 h through suction.

2.5 Collection of Tissue Samples

At the end of the experimental period, the control and the experimental fishes were randomly selected. The gill tissues were dissected out, carefully removed, washed in ice cold physiological saline (0.9 N) solution and weighed. Supernatants of gill tissue was processed as required for biochemical analysis and molecular studies.

2.6 Preparation of Tissue Supernatant and Estimation of Total Protein

About 1.0 g of the gill tissue was homogenized in ice cold Tris buffer (0.1 M, pH 7.4; 1:10, w/v) using a glass homogenizer and then centrifuged for 15 min at 10,000 g at 4°C in a refrigerated high speed centrifuge. The supernatant was used for estimation of total protein content which was performed by the method described earlier [18]. Bovine Serum Albumin (100-1000 µg) was used to prepare standard curve.

2.7 Extraction of Nucleic Acids

Nucleic acids was extracted by grinding the tissue with ice cold 10% TCA followed by centrifugation to separate them from the acid soluble compounds. The precipitated nucleic acids were then extracted with ethanol-ether to remove the interfering lipid material. It was then treated with 5% TCA for 15 minutes at 90^0C.Nucleic acids were extracted from the gill tissues following the method of [19].

2.8 Estimation of DNA and RNA

Portions of the TCA extract obtained were used for the DNA was determination by diphenylamine reaction method [20] and RNA was determination by orcinol reaction method [21].

2.9 Isolation of Genomic DNA by Agarose Gel Electrophoresis and Fragmentation Studies

Isolation of DNA from the gills of control and experimental fishes was performed by the method of [22].

2.10 Protein Profiling by Sodium Dodecyl Sulphate Polyacrylamide Gel Electrophoresis

SDS-PAGE was performed to determine tannery effluent induced protein profile changes in gill tissues of *Oreochromis mossambicus* at sub-lethal concentration according to protein subunit separation method [23].

2.11 Comet Assay to Assess DNA Damage

The control and experimental fishes were euthanized, the gills were excised immediately and washed with phosphate buffer solution (PBS), the gill tissues were transferred to microtubes for the cellular dissociation to be used in the comet assay. The method for cellular dissociation was based on [24]. The study of DNA damage by the alkaline Single cell gel electrophoresis (SCGE) / Comet assay was performed as a three layer procedure with slight modifications [25,26].

2.12 Statistical Analysis

Data was expressed as Mean ± SD. Software package SPSS 16.0 version was used to carry out the statistical analysis by Student "t" Test. The statistical significance was tested at 1% and 5% levels.

3. RESULTS AND DISCUSSION

The present study, evaluates the genotoxic effects of chromium present in tannery effluent in the gills of freshwater fish *Oreochromis mossambicus*. These freshwater fishes serve as indicators of heavy metal present in tannery effluent. The content of chromium in the raw tannery effluent collected from tanning industry was as 25.33 ppm, hexavalent chromium content was 19.45 ppm and trivalent chromium content was 5.56 ppm. The values reported are beyond the tolerance limit. The total protein content of the gill in experimental group was significantly declined ($P < 0.001$) after 30 days exposure of fishes to tannery effluent (Fig. 1) when compared to the fishes maintained in toxicant free water. Fishes maintained in tannery effluent showed a significant reduction in nucleic acid contents when compared to control after 30 days of exposure (Figs. 2 and 3).

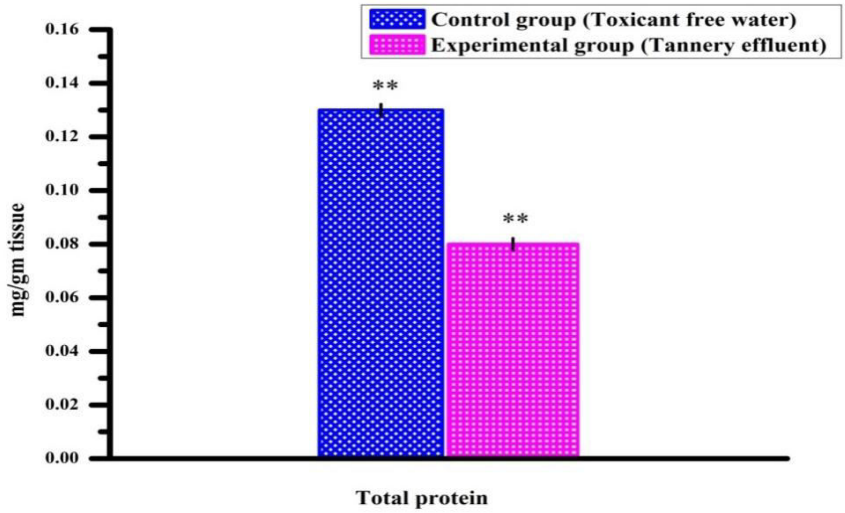

Fig. 1. Effect of tannery effluent on gill total protein content. Error bars show standard deviation and represents mean values of three experiments

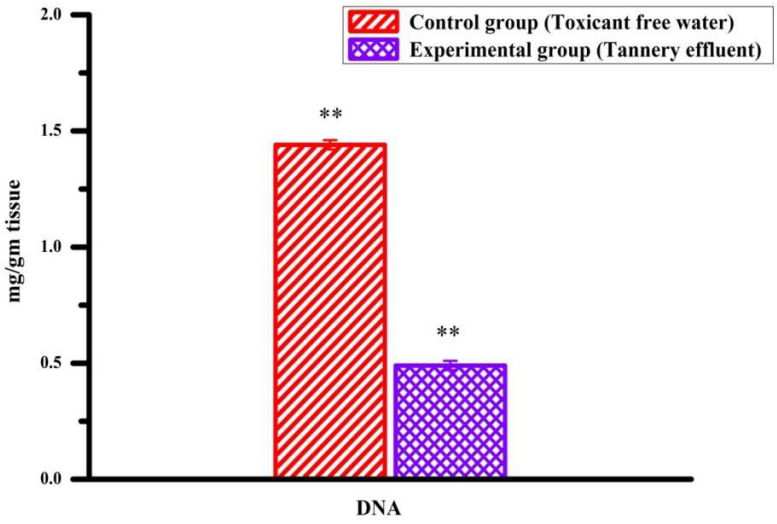

Fig. 2. Effect of tannery effluent on gill DNA content. Error bars show standard deviation and represents mean values of three experiments

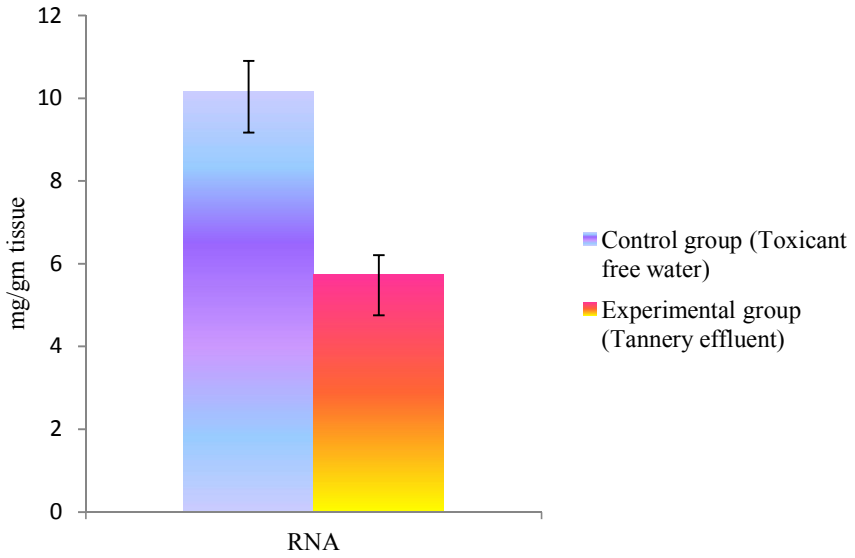

Fig. 3. Effect of tannery effluent on gill RNA content. Error bars show standard deviation and represents mean values of three experiments

When gill DNA of *Oreochromis mossambicus* from tannery exposed effluent and control was analysed on agarose gel, the presence of DNA fragments could be detected between 700bp and 1000bp when compared with molecular marker and difference in intensities of base pair subunits (Fig. 4).

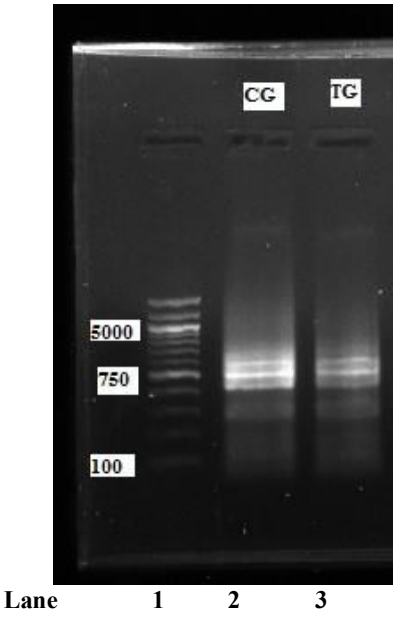

Fig. 4. Separation of genomic DNA in the gills of *Oreochromis mossambicus* exposed to tannery effluent. Lane-1 Molecular marker, Lane -2 Control gill (CG) and Lane-3 Test gill (TG)

Protein profiling by SDS-PAGE from gill of *Oreochromis mossambicus* was performed. (Fig. 5). Experimental gill tissue showed difference in protein intensities when compared to gill protein pattern of control fishes. The protein subunits of molecular weight 54 kDa, 124 kDa was observed with high intensity in tannery effluent treated fish. Low intensity protein subunits were appeared at 250 kDa.

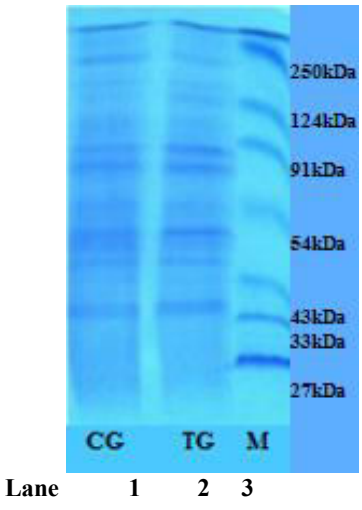

Fig. 5. SDS-PAGE analysis of tannery effluent induced protein profile changes in gills of *Oreochromis mossambicus*. Lane -1 Control gill (CG) , Lane -2 Test gill (TG) and Lane- 3: Molecular marker- (250, 124, 91, 54, 43, 33 and 27 kDa)

Fishes exposed to tannery effluent show variable score of DNA damage, the formation of comet tails in gill cells which was significantly higher ($p < 0.001$) in relation to control group (Figs. 6, 7).

The gills are the primary target of contaminants and for this reason, they are considered excellent indicators of environmental quality [27]. The depletion of total protein under the stress of tannery effluent toxicity observed in gill tissues of *Oreochromis mossambicus* in the present study indicates proteolysis, suggesting that the proteins were utilized to meet the excess energy demands imposed by exposure to effluent. Similar results were observed during methyl parathion toxicity in different tissues of *Channa punctatus* [28]. The alterations clearly indicate that stress brings about the metabolic reorientation in the tissues by raising energy resources.

a. Intact gill in control fish

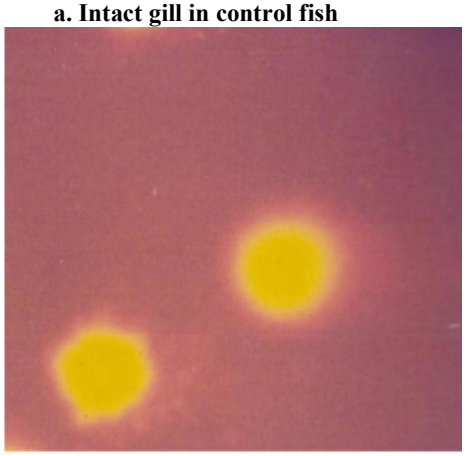

b. DNA damage showing tail formation

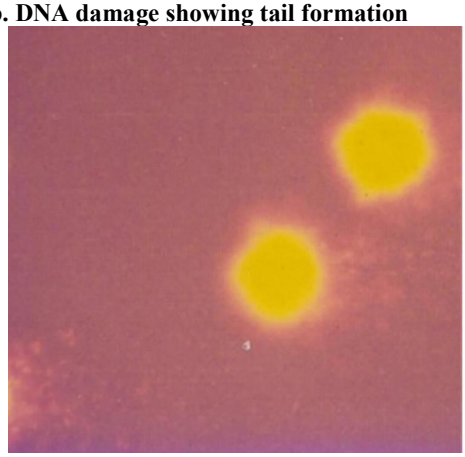

Fig. 6. Comet assay to assess the extent of gill damage in *Oreochromis mossambicus* exposed to tannery effluent

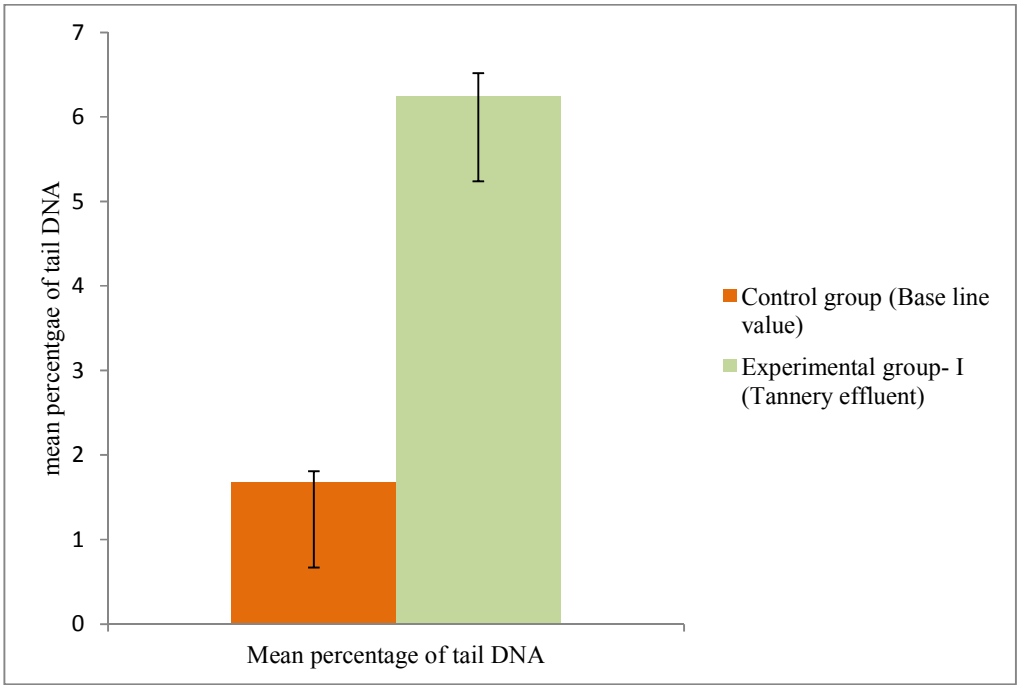

Fig. 7. Mean percentage of tail DNA formation in gills of fishes exposed to tannery effluent. Error bars show standard deviation and represents mean values of three experiments

Nucleic acid ratios provide significant information about the mechanism by which, they regulate the multifaceted activities of cells. The physico-chemical interaction of the pesticides with the cellular DNA produces primary lesions of the double stranded DNA such as breaks in single strand, double strand, cross-linking of DNA- protein and damage to nitrogenous bases purine and pyrimidine. The intactness of the DNA is the important part of the normal cellular process. DNA damage results from exposure to many contaminants, and is widely used as an indicator or biomarker of biological effects [29].

The decreased DNA content in the gill tissues of fishes exposed to tannery effluent present study might have been caused by the direct action of toxicant. Any alteration in nucleic acid content leads to variations in protein profile as evidenced from the present study [30,31]. The inhibition of RNA synthesis at transcription level may affect the protein content [32]. Significant decrease in RNA observed in the present study might have caused protein depletion in gills. The changes in DNA, RNA ratio results in eventual losses of cell structure, proliferation and formation of new tissue and tissue degradation with a total loss of cellular control mechanism [33].

The chromium compounds present in tannery effluent might have direct or indirect interaction with specific genes causing significant modulation of nucleic acids as reflected from the changes of electrophoretic analysis of the gill genomic DNA. Control gill tissue showed intense DNA sub-unit banding pattern. DNA banding with less intensity which is an indicator of necrosis was observed in experimental gill tissue. It could be suggested that long-term exposure upregulate both apoptotic and necrotic pathways in cells [34]. The changes observed in the gills of *Oreochromis mossambicus* in the present study, with less prominent appearance of base pairs in DNA subunits between 750 -1000 bp may be due to the effect of tannery effluent in experimental fishes. *Channa punctatus* exposed to methyl parathion show changes in DNA banding pattern of gills [35]. Protein electrophoretic banding pattern were also reported by various other investigators in *Cirrhinus mrigala* [36], *Danio rerio* [37] and *Oreochromis mossambicus* [38].

Difference in banding pattern was observed in control and tannery effluent treated fishes. When compared to control gill protein pattern, the experimental tissue showed difference in protein intensities. There is an increase in intensities of protein bands with molecular weights 124 KDa and 54 KDa, in control while a lesser intensity in protein subunits was noticed in the experimental gill tissue. This indicates that toxic nature of tannery effluent alters the protein expression. It may be due to the difference in chemical and structural properties of toxic compounds present in tannery effluent. The variations in protein subunit band patterns may be due to change in the turn over (synthesis /degradation) of various proteins. The electrophoretic bands represents the difference in the intensities of protein in gill tissue. Similar changes in protein banding patterns were noted in gills of *Clarias batrachus* exposed to rogorin [39]. Pesticides may significantly inhibit the expression of gene or multiple genes or may activate other set of genes to produce mRNAs which may subsequently be translated into stress induced proteins to survive in the pesticide stress environment [40,41,42].

DNA damage is an important mechanism of toxicity for a variety of pollutants, and therefore, is often used as an indicator of pollutant effects in eco-toxicological studies. Several studies on DNA damage employing the Comet assay performed on fish and molluscs revealed a direct effect of exposure to different contaminants [43,44].

The present study show enhanced DNA damage and formation of tail structures from region of the head DNA in gills of fishes exposed to tannery effluent. Fishes exposed to dichlorvos produced DNA strand breaks in the fishes exposed to sublethal concentrations indicating potential genotoxic properties to aquatic organisms [45]. Olive tail formation was reported in erythrocytes of *Catla catla* during *in-vivo* exposure of hexavalent chromium [46]. The DNA breaks with tail movement are possibly due to defective apoptosis or excessive production of reactive oxygen species. The comet assay results of the present study suggest that the mechanism of DNA damage can be through Cr (VI) which enters the system either by ingestion or absorption as an oxyanion. The absorbed chromium is metabolically reduced to Cr (V), Cr (IV) and finally to reduced trivalent (III) form. These reduced forms of chromium induce a wide range of genomic DNA damage, which makes chromium to inhibit the process of DNA replication within the cells [47].

To ensure the protection of water bodies, environmental monitoring report need to be done periodically in order to limit and prevent adverse environmental contaminations.

4. CONCLUSION

Protein and nucleic acid and contents are regarded as important biomarkers of the metabolic potential of cells, as these play a main role in regulating the different activities of cells. Gills, which are the vital structures in fishes, regulate the respiratory process.

Fishes exposed to tannery effluent in this study tend to lose the structural appearance of the gills and alter the functioning of biomolecules leading to adverse effects. Raw tannery wastewater without the required treatment protocols , when released from tanning industries directly into natural water bodies or when utilized for agriculture or aquaculture farming without sufficient and improper recycling may have adverse negative effects on development and growth of aquatic organisms.

COMPETING INTERESTS

Authors have declared that no competing interests exist.

REFERENCES

1. Adeogun AO, Chukwuka AV. Toxicity of industrial wastewater acting singly or in joint-ratios on *Clarias gariepinus*. American Journal of Environmental Science. 2012;8:366-375.
2. Majharul Islama SM, Md. Fazle Rohanib, Seyed Akib Zabeda, Md. Tarikul Islama, Rayeda Jannata, Yeasmin Akterc, Md. Shahjahana. Acute effects of chromium on hemato-biochemical parameters and morphology of erythrocytes in striped catfish *Pangasianodon hypophthalmus.* Toxicology Reports. 2020;7:664–670.
3. Matsumoto ST, Mantovani MS, Malagutti MJA, Dias AL, Fonseca IC, Marin-Morales MA. Genotoxicity mutagenicity of water contaminated with tannery effluent, as evaluated by the micronucleus test and comet assay using the fish (*Oreochromis niloticus)* and chromosome aberrations in onion root-tips. Genetics and Molecular Biology. 2006;29: 148-158.
4. Beyersmann D, Hartwig A. Carcinogenic metal compounds: Recent insight into molecular and cellular mechanisms. Archives of Toxicology. 2008;82:493–512.
5. Frenzilli G, Nigro M, Lyons BP. The comet assay for the evaluation of genotoxic impact in aquatic environments. Mutation Research. 2009;681:80-92**.**
6. Camargo MM, Martinez C. Histopathology of gills, kidney and liver of a Neotropical fish caged in an urban stream. Neotropical. Ichthyology. 2007;5:327-336.
7. Kakuta I. Murachi S. Physiological response of carp, *Cyprinus carpio*, exposed to raw sewage containing fish processing wastewater. Environmental Toxicology Water Quality. 1997;12:1-9.
8. Richmonds C, Dutta HM. Histopathological changes induced by malathion in the gills of bluegill, *Lepomis macrochirus*. Bulletin of Environmental Contamination and Toxicology. 1989;43:123-130.
9. Oliveira RCA, Pelletier E, Pfeiffer WC, Rouleau C. Comparative uptake, bioaccumulation and gill damages of inorganic mercury in tropical and nordic freshwater fish. Environmental Research. 2000;83:286-292.
10. Muthukumaravel K, Sivakumar B, Kumarasamy P, Govindarajan M. Studies on the toxicity of pesticide monocrotophos on the biochemical constituents of the freshwater fish, *Labeo rohita.* International Journal of Current research in Biochemistry and Biotechnology. 2013;2(10):20-26.
11. Haqqi TM, Adhami UM. Effect of apholate (ENT 26216, NSC 26812) on nucleic acids, total protein content and activity levels of aminotransferases (GOT, GPT), alkaline phosphatase and 5-nucleotidase in liver of male albino rats. Indian Journal of Experimental Biology. 1979;17:488- 492.
12. Monteiro SM, dos Santos NM, Calejo M, Fontainhas - Fernandes A, Sousa M. Copper toxicity in gills of the teleost fish, *Oreochromis niloticus,* Effects in apoptosis induction and cell proliferation. Aquatic Toxicology. 2009; 94(3): 219–228.
13. Muid KA, Shahjahan RM, Begum RRA. Zinc phosphide induced DNA damage in the blood cells of *Gallus* sp. using comet DNA assay. American Journal of Agricultural and Biological Sciences. 2012;**7**:82-87.
14. De Andrade VM, De Freitas TRO, De Silva J. Comet assay using mullet (*Mugil* sp.) and sea catfish (*Netuma* sp.) erythrocytes for the detection of genotoxic pollutants in aquatic environment. Mutation Research. 2004;560: 57-67.
15. Emmanouil C, Smart DJ, Hodges NJ, Chipman JK. Oxidative damage produced by Cr(VI) and repair in mussel (*Mytilus edulis* L.) gill. Marine Environmental Research. 2006;62:S292-S296.
16. Solbe JF. Freshwater. In: Handbook of Ecotoxicology. Peter Calins (ed) Blackwell Science Ltd. Osneymeed OX 20EL. 1975; 68(3).
17. APHA. American Public Health Association. Standard Methods for examination of water and wastewater. Washington DC, USA. 20th Edition; 1998
18. Lowry OH, Rosebrough NJ, Farr AL Randall RJ. Protein measurement with Folin-phenol reagent. Journal of Biological Chemistry. 1951; 193:265-275.

19. Schneider WC. Extraction and determination of total nucleic acids. Journal of Biological Chemistry. 1945;161:293-297.
20. Burton KC. A study of the condition and mechanism of the diphenylamine reaction for the colorimetric estimation of DNA. Biochemical Journal. 1956;62:315-323.
21. Cerioti G. Determination of nucleic acids in animal tissues. Journal of Biological Chemistry. 1955;214:59-70
22. Basnakian AG, James SJ. A rapid and sensitive assay for the detection of DNA fragmentation during early phases of apoptosis. Nucleic Acids Research. 1994;22(13):2714-2715.
23. Laemmli UK. Cleavage of structural proteins during the assembly of the head of bacteriophage T_4. Nature. 1970;22:680-685.
24. Monteiro VD, Cavalcante GSM, Vilela MBFA, Sofia SH, Martinez CBR. *In vivo* and *in vitro* exposures for the evaluation of the genotoxic effects of lead on the Neotropical freshwater fish *Prochilodus lineatus,* Aquatic Toxicology. 2011;7:291-298,
25. Singh NP, McCoy MT, Tice RR, Schneider EL. A simple technique for quantization of low levels of DNA damage in individual cells. Experimental and Cellular Research. 1988; 175:184–191.
26. Klaude Eriksson S, Nygren J, Ahnstrom G. The comet assay: Mechanisms and Technical considerations. Mutation. Research. 1996;363: 89-96.
27. Fatma AS, Mohammed. Histopathological Studies on *Tilapia zilli* and *Solea vulgaris* from lake Quran, Egypt. World Journal of Fisheries and Marine Sciences. 2009;1(1):29-39.
28. Padmavathy P, Veeriah K, Tata Rao S, Vivek CH. Methyl parathion 50% induced changes in enzymatic activities of the fish *Channa punctatus* (Bloch). Indian Journal of Applied Research. 2015;5(1):22-29.
29. Van der Oost R, Beyer J, Vermeulen NPE. Fish bioaccumulation and biomarkers in environmental risk assessment: A review. Environonmental Toxicology and Pharmacology. 2003; 13:57-149.
30. Raksheskar GA. Influence of cypermethrin on DNA, RNA and RNA/DNA ratio in gills of the freshwater fish *Channa striatus*. Bioscience Discussions. 2012;3:17-19.
31. Chandra Sekhara Rao J, Neelima P, Govinda Rao K, Gopala Rao N. Acute toxicity of cypermethrin (25% EC) on nucleic acids (DNA and RNA) in *Cyprinus carpio* (Linn.). International Journal of Recent Science. 2015; 6(7):5219-5224.
32. Singh KS, Singh SKS, Yadav RP. Toxicological and biochemical alterations of cypermethrin (synthetic pyrethroid) against freshwater teleost *Colisa fasciatus* at different seasons. World Journal of Zoology. 2010;5(7): 25-32.
33. Gowri B, Govindassamy P, Ramalingam V. Influence of cypermethrin on DNA and RNA content in different organs of freshwater fish *Cyprinus carpio*. Iranian Journal of Pharmaceutical Science. 2013;9(3):1-10
34. Datta S, Saha DR, Ghosh D, Majumdar T, Bhattacharya S, Mazumder S. Sub-lethal concentration of arsenic interferes with the proliferation of hepatocytes and induces *in vivo* apoptosis in *Clarias batrachus* L). Comp. Biochem. Physiol. Part C. 2007;145:339-349.
35. Veeraiah K, Padmavathi P,Tata Rao S, Vivek CH. Methyl parathion (50%EC) induced changes in protein and DNA banding pattern in the fish *Channa punctatus*. International Journal of Bioassays. 2015;4(1):3632-3637.
36. Veeraiah K, Jaya Raju K, Padmavathi P ,Samyuktha Rani A ,Vivek CH. Cadmium chloride induced changes in protein molecules of the freshwater fish *Cirrhinus mrigala* (Hamilton). Innovare Journal of Life Sciences. 2013;1(3):18-23.
37. Ahmed Hossam Mahmoud, Noura M. Darwish, Young Ock Kim, Ponnuswamy Viayaraghavan, Jun-Tack Kwon, Sae Won Na, Jae Chul Lee Hak-Jae Kim. Fenvalerate induced toxicity in Zebra fish, *Danio rerio* and analysis of biochemical changes and insights of digestive enzymes as important markers in risk assessment. Journal of King Saud University – Science. 2020;32:1569–1580.
38. Ganesan **N**, Samyappan K, Saravanan R. Assessment of DNA damage and apoptosis in the brain of freshwater fish *Oreochromis mossambicus* exposed to tannery effluent wastewater. Applied Ecology and Environmental Sciences. 2021;9(5):575-579. DOI: 10.12691/aees-9-5-8
39. Helen Chandra, Sajda, Sridhar S. Acute toxicity studies on the freshwater fish *Clarias batrachus* exposed to pesticide rogorin. Journal of Chemical and Pharmaceutical Sciences. 2015;8(1):34-39.
40. Ksenia, Cheshenko, Farzad, Pakdel, Helmut, Segner, Olivier, Kah, Rik, IL. Interference of endocrine disrupting chemicals with aromatase CYP 19 expression or activity and consequences for reproduction of teleost fish. General and Comparitive Endocrinology. 2008; 155: 31–62.

41. Palanisamy R, KumaresanV, Harikrishnan R, Arasu MV, Al-Dhabi NA, Arockiaraj J. Functional roles and gene regulation of tumor necrosis factor receptor 1 in freshwater striped murrel. Molecular Immunology. 2015;66:240–252.
42. Moon Young-Sun, Jeon, Hwang-Ju, Nam, Tae-Hoon, Choi, Sung-Deuk, Park, Byung-Jun, Ok, Yong Sik, Lee, Sung-Eun. Acute toxicity and gene responses induced by endosulfan in zebrafish (*Danio rerio*) embryos. Applied Biochem and Spectroscopic Bioavailability. 2016;28:14.
43. Carlos Eduardo Delfino Vieira, Maria Rita Perez, Raphael D'Anna Acayaba, Cassiana Carolina Montagner Raimundo, Claudia Bueno dos Reis Martinez. DNA damage and oxidative stress induced by imidacloprid exposure in different tissues of the Neotropical fish *Prochilodus lineatus* Chemosphere. 2018;195: 125- 134.
44. Lima PL, Benassi JC, Pedrosa RC, Wilhelm Filho D. Detection of DNA damage in haemocytes of *Mytella guaynensis* mussel from two mangroves on Santa Catarina Island, Brazil, using comet assay. Genetics and Molecular Biology. 2003;26(2):124.
45. Varo I, Navarro JC, Nunes B, Guilhermino L. Effects of dichlorvos aquaculture treatments on selected biomarkers of gilthead seabream (*Sparus aurata* L.) fingerlings. Aquaculture. 2007;266:87–96.
46. Kantha Deivi Arunachalam, Sathesh Kumar Annamalai, Jaya Krishna Kuruva. *In-vivo* evaluation of hexavalent chromium induced DNA damage by alkaline comet assay and oxidative stress in *Catla catla.* American Journal of Environmental Science. 2013;9(6): 470-482.
47. Nickens KP, Patierno R, Ceryak S. Chromium genotoxicity: A double-edged sword. Chemico-Biological Interaction. 2010;188:276-288.

Prediction, Cross Validation and Classification in the Presence COVID-19 of Indian States and Union Territories using Machine Learning Algorithms

P. Arumugam, V. Kadhirveni, R. Lakshmi Priya, Manimannan G

Abstract: ***The present study predicts, cross validate and classify the data of COVID-19 based on four machine learning algorithm with four major parameters namely confirmed cases, recoveries, deaths and active cases. The secondary sources of database were collected from Ministry of Health and Family Welfare Department (MHFWD), from Indian State and Union Territories up to March, 2021. Based on these background, the database classified and predicted various machine learning Algorithm, like SVM, kNN, Random Forest and Logistic Regression. Initially, the k-mean clustering analysis is used to perform and identified five meaningful clusters and is labeled as Very Low, Low, Moderate, High and Very High of four major parameters based on their average values. In addition the five clusters are cross validated using four machine learning algorithm and affected states were visualized with help of prediction and probabilities. The different machine learning models achieved cross validation accuracy of 88%, 97%, 91% and 91%. . Delhi, Uttar Pradesh and West Bengal were Moderately Affected States, Assam, Bihar, Chhattisgarh, Haryana, Gujarat, Madhya Pradesh, Odisha, Punjab, Rajasthan and Telangana are Low Affected States, wherein Tamil Nadu, Kerala, Andhra Pradesh and Karnataka are highly affected States. and Maharashtra the Very Highly Affected State. Rest of the States and Union Territories has Very Low affected Covid-19 Cases is clearly identified.***

Keywords: ***COVID-19, Machine Learning Algorithms, Prediction, Cross Validation and Classification.***

I. INTRODUCTION

The COVID-19 pandemic disease caused by SARS-CoV-2 virus and this virus was identified from Wuhan, China in the year 2019. World Health Organization declared world pandemic situation on 11th March, 2020, its spread over the world in a short period. Many people were affected by this virus and lost their lives, economy, jobs, Education, etc. In India, the first case is recorded from Kerala and it has spread over the Indian states and union territories. Recently, the second wave of COVID-19 spread is exponentially increasing in all states and union territories. The Indian government launched vaccine camps for the age group of above 45 to upper age people. The vaccine raises immunity in our human bodies and second dosage of vaccine is from 28 to 42 days.

Manuscript received on April 10, 2021.
Revised Manuscript received on April 17, 2021.
Manuscript published on May 30, 2021.
*Correspondence Author
P. Arumugam, Professor, Department of Statistics, Manonmaniam Sundaranar University, Tirunelveli (Tamil Nadu), India.
V. Kadhirveni, Research Scholar, Department of Statistics, Manonmaniam Sundaranar University, Tirunelveli (Tamil Nadu), India.
R. Lakshmi Priya, Assistant Professor, Department of Statistics, Dr. Ambedkar Government Arts College, Vyasarpadi, Chennai (Tamil Nadu), India.
Manimannan G*, Assistant Professor. Department of Statistics, TMG College of Arts and Science, Chennai (Tamil Nadu), India.

The main objective of this research paper is to identify the classification and visualization of affected persons using various machine learning and statistical algorithm.

II. BACKGROUND OF THE STUDY

In Data Mining the KDD (Knowledge Discovery in a Database) is the iterative process that uses to discover novel information and knowledge from large amounts of database. According to Han and Kamber, data mining software allows end-users to analyze data from different dimensions Also, categorize the details and summarize the relationships which are identified during the mining process [1]. Kamber and Han, classification falls into a supervised data mining technique. This process consists of two steps, the first step is learning setup, in which the model is constructed and trained with the help of a predetermined database with class labels. The second step is the place where the trained model is consumed to perform the predictions for given database and measure the accuracy level of the classifier algorithm model [1]. Most of the researches are focusing on behavior of predictive models in data mining (Padmavathi Janardhana). With the help of modern technologies, the researcher can collect a large number of various types of data with different types of parameters in relevant field. Then apply the data mining techniques very correctly and effectively to mine and absorb meaningful interpretations, predictions, etc. when comes to the medical science field, the above said process can be applied to many database like, predicting, classification and visualization of breast cancer, heart attack, oral diseases, diabetes, etc. [2] According to Manimannan G. *et. al.* classification is defined as a process that gives the model to describe and differentiate database classes or concepts to predict the class of objects whose class label is not known. Partitioning clustering algorithm, artificial neural networks, etc. are the major tools used for constructing these models in COVID-19 of Indian States [3]. In recent days, data mining has become an attractive discipline that is used in business, medical science, engineering, text mining and other professional field as well in information technology community. Data mining strategies can provide useful answers to a problem. The methods are Classification, Association, Clustering, Estimation, Novelty detection, sequencing deduction, etc [4] Rajkumar and G.S Reena carried out research using machine learning algorithms (such as K- nearest neighbor, Naive Bayes) for heart disease prediction.

Published By:
Blue Eyes Intelligence Engineering
and Sciences Publication

The data set consists of 3000 instances with 14 attributes. Dataset was divided as 70% for training and 30% for testing. According to the test results, Naïve bayes algorithm was selected as the algorithm with better performances when compared with KNN and Decision List [8].Halgurd S. Maghdid *et al*. have projected a new framework to detect corona virus disease using the inboard smartphone sensors. The designed AI (Artificial Intelligence) framework collects data from various sensors to predict the grade of pneumonia as well as predicting the infection of the disease [6]. The proposed framework takes uploaded CT Scan images as the key method to predict COVID-19 [5] Manimannan G. *et. al.* has used Silhouette distance measure for k- means clustering algorithm. It produced effective results and visualized their result in a simple manner. This technique achieved three meaningful groups and is labeled as C1, C2 and C3. C1 represents highly affected, C2 Moderate affected and C1 Low affected States and Union Territories [6].

III. DATABASE

The secondary source of database was collected from Ministry of Health and Family Welfare Department (MHFWD), from Indian State and Union Territories up to March, 2021 (Table 1). The database consists of four parameters namely confirmed cases, recoveries, deaths and active cases. Initially all parameters are classified using k-means algorithm and additionally tested and cross validated 10 folds stratified sampling methods with help of testing database 10 and training database 60 percent. Subsequently, the machine learning algorithm of kNN, SVM, Random Forest classification and Neural network cross validates the original database and gives better results.

Table 1. Sample Data and Parameters

	CL	: and Union Terrot	Cases	Deaths	Recoveries	Active
1	Very Low	Andaman and ...	5028	62	4960	6
2	High	Andhra Pradesh	891004	7177	882763	1064
3	Very Low	Arunachal Prad...	16840	56	16780	4
4	Low	Assam	217726	1096	214997	1633
5	Low	Bihar	262864	1548	261013	303
6	Very Low	Chandigarh	22589	357	21416	816
7	Low	Chhattisgarh	315486	3872	308269	3345
8	Very Low	Dadra and Nag...	3426	2	3404	20
9	Moderate	Delhi	642030	10931	629199	1900
10	Very Low	Goa	55607	802	54130	675
11	Low	Gujarat	275197	4418	267250	3529
12	Low	Haryana	273446	3064	267942	2440
13	Very Low	Himachal Prad...	59347	1003	57745	599
14	Very Low	Jammu and Kas...	127288	1968	124421	899
15	Very Low	Jharkhand	120436	1093	118823	520
16	High	Karnataka	956801	12379	936947	7475
17	High	Kerala	1083530	4342	1043473	35715
18	Very Low	Ladakh	9838	130	9669	39
19	Very Low	Lakshadweep	524	1	355	168
20	Low	Madhya Pradesh	266043	3877	258251	3915
21	Very High	Maharashtra	2252057	52610	2099207	100240
22	Very Low	Manipur	29305	373	28897	35
23	Very Low	Meghalaya	13983	148	13816	19
24	Very Low	Mizoram	4434	10	4415	9
25	Very Low	Nagaland	12217	91	12116	10
26	Low	Odisha	337929	1917	335322	690
27	Very Low	Puducherry	39932	670	39083	179
28	Low	Punjab	192040	5978	176660	9402
29	Low	Rajasthan	322078	2789	317257	2032
30	Very Low	Sikkim	6178	135	5994	49
31	High	Tamil Nadu	856917	12530	840180	4207
32	Low	Telangana	300536	1649	297032	1855

IV. METHODOLOGY

The following section describes various machine learning Data Mining Algorithms and Workflow (Figure 1):

4.1 k-mean Clustering Algorithm

MacQueen [7] suggests the term k-means for describing an algorithm of his that assigns each item to the cluster having the nearest centroids. The process composed of these three steps:

Step 1: Partition the items (input database) into k-initial clusters.

Step 2: Proceed through the list of items, assigning an item to the cluster whose centroid is nearest (using Euclidean distance measure). Recalculate the centroid for the cluster receiving the new item and for the cluster losing the item.

Step 3: Repeat Step 2 until no more reassignments take place.

4.2 Random Forest Classification Algorithm

Random Forest is a classification technique proposed by Breiman, 2001 [8]. When given a set of class-labeled database**,** Random Forest builds a set of classification trees. Each tree is developed from a bootstrap sample from the training data. Classification is based on majority vote from individually developed tree classifiers in the forest.

Step 1: Specify the name of the classifier. The default name is “Random Forest Classification”.

Step 2*:* State how many classification trees will be included in the forest, and how many attributes will be arbitrarily drawn for consideration at each node. If the latter is not specified, this number is equal to the square root of the number of attributes in the data.

Step 3: Brieman’s proposal is to grow the trees without any pre-pruning, but since pre-pruning often works quite well and is faster, the user can set the depth to which the trees will be grown.

Step 4: Produce a report.

Step 5: Tick Apply to communicate the changes to other widgets. Alternatively, click the box on the left side of the Apply button and changes will be communicated automatically.

4.3 Support Vector Machine (SVM)

Statistical learning aims at gaining knowledge, making predictions, making decisions or constructing model from a set of database, Statistical learning theory gained renewed momentum in data mining after the introduction of SVM developed by Vapnik. e*t. al* [9]. The Orange Data mining algorithm presents here:

Step 1: The learner can be given a name under which it will appear in other widgets.

Step 2: Classification type with test error settings. C-SVM and v-SVM are based on different minimization of the error function. On the right side, you can set test error bounds, Cost for C-SVM and Complexity bound for v-SVM.

Step 3: The next block of options deals with kernel, a function that

Published By:
Blue Eyes Intelligence Engineering
and Sciences Publication

transforms attribute space to a new feature space to fit the maximum-margin hyperplane, thus allowing the algorithm to create non-linear classifiers with Polynomial, RBF and Sigmoid kernels.

Step 4: Set permitted deviation from the expected value in Numerical Tolerance. Tick the box next to Iteration Limit to set the maximum number of iterations permitted.

Step 5: Produce a report and Click Apply to commit changes.

4.4 k-Nearest Neibours (k-NN))

This algorithm of k-Nearest Neibours (k-NN) in statistics is a non-parametric classification method first developed by Evelyn Fix et. al. 1951 [10] and later expanded by Thomas Cover [11]. It is used for classification and regression. In both the cases, input consists of the k closest training examples in data set. The output depends on whether k-NN is used for classification or regression: The Orange kNN algorithm is:

Step 1: A name under which it will appear in other widgets. The default name is “kNN”.

Step 2: Set the number of nearest neighbors, the distance parameter and weights as model criteria. In this paper, the researcher used Euclidean distance between two points.

Step 3: The Weights you can use are:Uniform: all points in each neighborhood are weighted equally.
Distance: closer neighbors of a query point have a greater influence than the neighbors further away.

Step 4: Produce a report in the Test and Score window.

4.5 Neural Network Algorithm

McCullough and Walter Pitts first proposed neural network algorithm in the year 1944 [12]. A Multil- Layer Perceptron (MLP) algorithm is used with back propagation in orange data mining:

Step 1: A name under which it will appear in other widgets. The default name is “Neural Network”.

Step 2: Set model parameters:

Step 3 Produce a report and the box is ticked (Apply Automatically), the widget will communicate changes automatically.

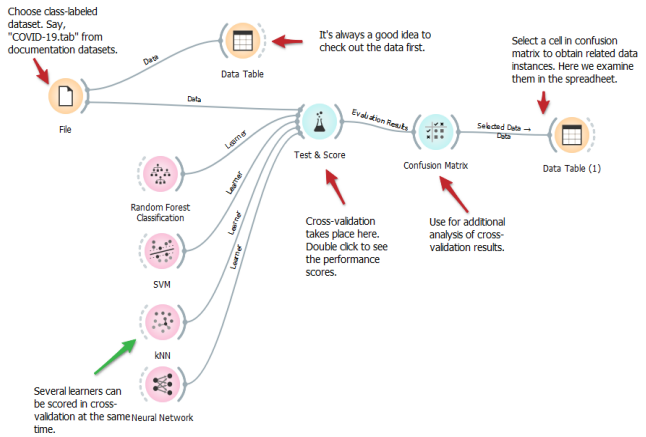

Figure 1. Workflow of various Machine Learning Algorithms

Reddy Prasad suggests a system at his paper to classify the patient with heart disease based on some features. Therefore, the proposed system can predict the presence of heart problems on a person based on the given data. He used logistic regression technology to perform classification and prediction. Further used sigmoid function for the representation processed [13].

V. RESULT AND DISCUSSION

The k-means algorithms achieved five meaningful clusters and are labeled as five categories of States and Union Territories of India affected by COVID-19 (Table 2). And also the same result produced the cross validation machine learning algorithm in Table 4 to 7.

Table 2: Final Cluster of k-means Algoritm

Final Cluster Centers					
	Cluster				
	1 (Low)	2 (High)	3 (Very Low)	4 (Very High)	5 Moderate)
Conformed Cases	36553.44	947063.00	276334.50	2252057.00	607981.67
Deaths	499.39	9107.00	3020.80	52610.00	9984.67
Recoveries	35794.89	925840.75	270399.30	2099207.00	595758.33
Active Cases	259.17	12115.25	2914.40	100240.00	2238.67
Number of Case in each Cluster	10	4	18	1	3

Table 3 shows the various model accuracy of training data. This is a very high value of accuracy and it is reasonable to expect that the model would be useful to predict new, previously unknown, instance of COVID-19 problem. Rest of the data may be outlier due to data variation in the study period.

The confusion matrix can be used to define a number of performance criteria commonly used in model evaluation suggested by Ali, 2005 [14]. The following section describes various measures of the test score:

5.1 AUC (Area under Curve)

AUC stands for "Area under the ROC Curve." That is, AUC measures the entire two-dimensional area underneath the entire ROC curve from (0,0) to (1,1).

An **ROC** curve (Receiver Operating characteristic Curve) is a graph showing the performance of a classification model at all classification thresholds. This curve plots two parameter, they are True Positive Rate and False Positive Rate.

True Positive Rate (**TPR**) is a synonym for recall and is therefore defined as follows:

$$TPR = \frac{TP}{TP + FN}$$

False Positive Rate (**FPR**) is defined as follows:

$$FPR = \frac{FP}{FP + TN}$$

5.2 Classification Accuracy (CA)

Accuracy is one metric for evaluating classification models. Informally, accuracy is the fraction of predictions and formally has the following definition:

$$Accuracy = \frac{Number\ of\ Correct\ Predictions}{Total\ Number\ of\ Predictions}$$

Published By:
Blue Eyes Intelligence Engineering
and Sciences Publication

Accuracy=Number of correct predictions shared by the Total number of predictions. For binary classification, accuracy can also be calculated in terms of positives and negatives as follows:

$$Accuracy = \frac{TP + TN}{TP + TN + FP + FN}$$

Where TP = True Positives, TN = True Negatives, FP = False Positives, and FN = False Negatives.

5.3 F1 Score

The F1 score is calculated by using the following formula:

$$F_1 = 2 * \frac{Precision * Recall}{Precision + Recall} = \frac{TP}{TP + \frac{1}{2}(FP + FN)}$$

5.4 Precision

Precision is given by:

$$\frac{True\ Positive}{True\ Positive\ + False\ Positive}$$

5.5 Recall

Recall Measure is computed by using the formula:

$$\frac{True\ Positive}{True\ Positive\ + False\ Negative}$$

The Models of AUC, CA, F1, Precision and Recall measure accuracy value closer to 1 is the best fitted model and closer to 0 is not a good fitted model . In this study all the measures are closter to 1 and these models are best fitted models using machine learning algorithms.

Table 3: Test Score of Various Algorim

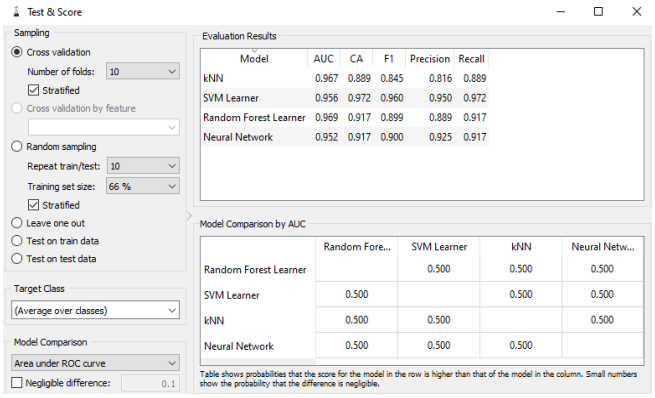

Table 4: Confusion Matrix of Random Forest Learner

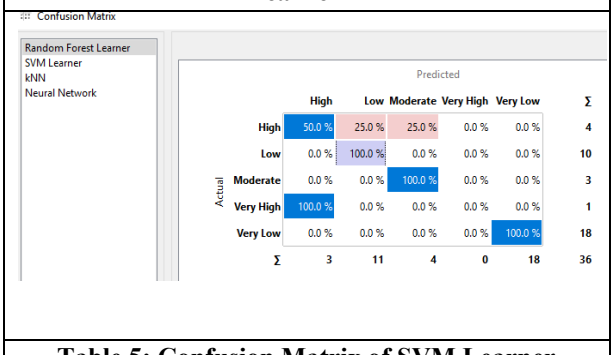

Table 5: Confusion Matrix of SVM Learner

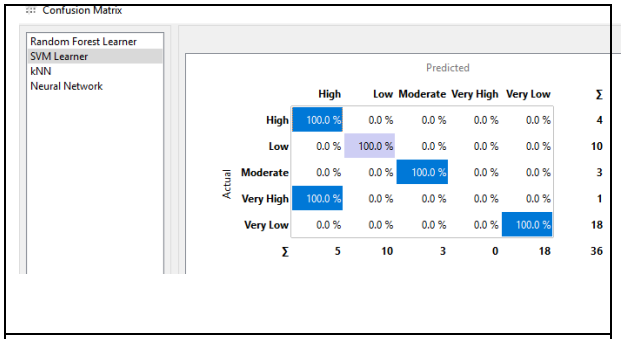

Table 6. Confusion Matrix of kNN

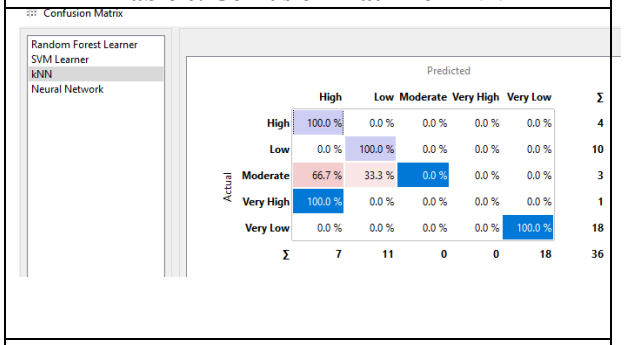

Table 7. Confussion Matrix of Neural Network

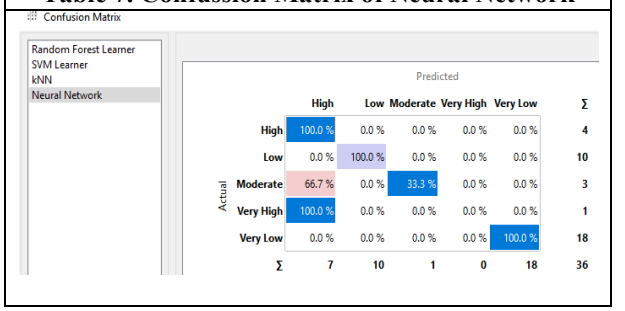

Table 8. Prediction and Probilities of States and Union Teritories

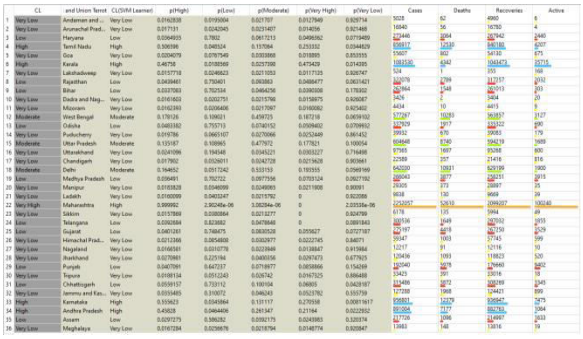

Based on the above models, Machine Learning algorithm achieved better prediction and proximities in all the methods. On the whole ten percentages of prediction and proximities are misclassified due to different models and noisy data. The different machine learning models cross validation and classification accuracy are 88%, 97%, 91% and 91%. The Classification of States and Union Territories were named as Very Low Affected (VLA), Low Affected (LA), Moderately Affected (MA), Highly Affected (HA) and Very Highly Affected (VHA) States and Union Territories of India by COVID-19 cases.

Published By:
Blue Eyes Intelligence Engineering and Sciences Publication

Maharashtra is correctly classified as Very High Affected States, Delhi, Uttar Pradesh and West Bengal falls in Moderately Affected States, Assam, Bihar, Chattisgarh, Haryana, Gujarat, Madhya Pradesh, Odisha, Punjab, Rajasthan and Telangana falls in Low Affected States, and Tamilnadu, Kerala Andhra Pradesh and Karnataka forms a group of highly affected States. Remaining States and Union Territories falls in Very Low affected by Covid-19 Cases (Table 8). The second wave of COVID-19 also started from March 2021. The government is taking necessary action to prevent and control the spread of COVID. Also our government advices our people to take vaccination over and above 45 years of age.

VI. CONCLUSION

In this section the researcher predicts and classifies the data of COVID-19 based on four machine learning algorithm with four major parameters namely confirmed cases, recoveries, deaths and active cases. The secondary sources of database were collected from Ministry of Health and Family Welfare Department (MHFWD), from Indian State and Union Territories up to March, 2021. Based on these background, the database classified and predicted various machine learning Algorithm, like SVM, kNN, Random Forest and Logistic Regression. Initially, k-means clustering analysis is used to perform and identified five meaningful clusters and is labeled as Very Low, Low, Moderate, High and Very High of four major parameters based on their average values. In addition the five clusters are cross validated using four machine algorithm and affected states are visualized in the table with help of prediction and probabilities. The different machine learning models cross validation and classification accuracy are 88%, 97%, 91% and 91%. The Classification of States and Union Territories were named as Very Low Affected (VLA), Low Affected (LA), Moderately Affected (MA), Highly Affected (HA) and Very Highly Affected (VHA) States and Union Territories of India by COVID-19 cases. Maharashtra is correctly classified as Very High Affected States, Delhi, Uttar Pradesh and West Bengal falls in Moderately Affected States, Assam, Bihar, Chattisgarh, Haryana, Gujarat, Madhya Pradesh, Odisha, Punjab, Rajasthan and Telangana falls in Low Affected States and Tamilnadu, Kerala Andhra Pradesh and Karnataka forms a group of highly affected States. Remaining States and Union Territories falls in Very Low affected by Covid-19 Cases (Table 8).

REFERENCES

1. Han J. Pei and M. Kamber (2011), Data Mining: Concepts and Techniques. Elsevier, 2011.
2. Padmavathi Janardhana et.al, (2015), Effectiveness of Support Vector Machines in Medical Data mining Journal Of Communications Software And Systems, Vol. 11, No. 1, Pp. 25-30.
3. Prediction of Affected and Deceased Population Trend of COVID-19 in India using Statistical Analysis, International Journal of Scientific and Innovative Mathematical Research(IJSIMR) Volume 8, Issue 2, 2020, PP 37-43.
4. A.B. M. Shawkat Ali and Saleh A. Wasimi (2016). Data Mining: Methods and Techniques, Cengage Learning India private Imitated, New Delhi.
5. Halgurd S. Maghdid, Kayhan Zrar Ghafoor, Ali Safaa Sadiq, Kevin Curran, and Khaled Rabie (2020). A novel AI-enabled framework to diagnose coronavirus covid 19 using smartphone embedded sensors: Design study. Computer Science, Cornel University. pp.1-7.
6. Manimannan G. et. al (2020), Clustering Study of Indian States and Union Territories by coronavirus (COVID-19) using k-mean algorithm, International Journal of Data Mining and Emerging Technologies, Vol.9 Issue-2, pp.43-51.
7. MacQueen (2015), Applied Multivariate Statistical Analysis, Prentice Hall, New Delhi
8. Breiman, L (2001), Random Forests. Machine Learning **45,** 5–32.
9. H. Drucker, Donghui Wu and V. N. Vapnik (1999), "Support vector machines for spam categorization," in *IEEE Transactions on Neural Networks*, vol. 10, no. 5, pp. 1048-1054
10. Evelyn Fix and Joseph L Hodges Jr (1951). Discriminatory analysis-nonparametric discrimination: consistency properties. Technical report, DTIC Document.
11. Thomas M Cover and Peter E Hart (1967). Nearest neighbor pattern classification. IEEE Transactions on Information Theory, 13(1):21-27.
12. McCulloch, W. S. & Pitts, W. (1943) BulL Math Biophys. 5, 115-133.
13. R. Prasad, P. Anjali, S. Adil, and N. Deepa, “Heart Disease Prediction using Logistic Regression Algorithm using Machine Learning,” Mach. Learn., vol. 8, no. 3, p. 4.
14. S. Ali. And S. Wasimi (2005). Data Mining: Methods and Techniques, Cengage Learning India.

AUTHORS PROFILE

P. Arumugam., Department of Statistics, Monomaniam Sundaranar University, Tirunelveli.

V. Kadhirveni, Department of Statistics, Manonmaniam Sundaranar University, Tirunelveli

R. Lakshmi Priya, Department of Statistics, Dr. Ambedkar Govt. Arts College, Vyasarpadi, Chennai

Manimannan G., Department of Statistics, TMG College of Arts and Science, Chennai

Published By:
Blue Eyes Intelligence Engineering and Sciences Publication

Data mining Application of Data Reduction and Clustering Domain of Textile Database

M. Salomi, R. Lakshmi Priya, Manimannan G, N. Manjula Devi

Abstract: ***This research paper attempts to identify the textile data structure and hidden pattern of original database with certain important parameters. The main objectives of this study are to identify the first n number of factors that explained over the study period. Initially factor analysis is performed to extract factor scores. Principal extraction is performed through Data mining package with sixteen textile fabrics parameters. Factor extraction is aimed to uncover the intrinsic pattern among the textile parameters considered and an important point of factor analysis is to extract factor scores for further investigation. Thus, factor analysis consistently resulted in three factors for the whole datasets. The amount of total variation explained is over 75 percent in factor analysis with varimax rotation. The factor loadings or factor structure matrix with unassociated rotation methods are not always easy to interpret. The nonhierarchical k-mean clustering is also used to identify meaningful cluster based on their parameter means of original database.***

Keywords: Data Mining, Principal Component Analysis, k-mean Clustering, Sillohoutte plot and Scatter plot,

I. INTRODUCTION

Normally a textile industry uses fibres, yarn and fabrics for testing their properties based on the quality. In general, for every end-use, the mechanical properties of fabrics are of special interest, this study how these properties are related to fabric. Yarn properties could help in make a decision how to produce a suitable fabric at a minimum cost when its likely range of use is known. The textile industry depends on raw materials such as cotton, jute and silkfibres. The fibres were acquired from natural resources. After mining, materials are then sent to spinning mills for processing and yarns are produced. Yarn structure and properties are primarily influenced by fibre properties based on their length, fineness and cross-sectional shape.The spinning method consists of ring, rotor and airjet and process variables based on their twist insertion rate, rotor speed, nozzle pressure, etc. Classifying of yarns is another important need in assessing textile quality control for business purposes, since it provides a useful means of expressing yarn standards in the market.

II. REVIEW OF LITERATURE

Many scholars quoted their research, the traditional methods; it is done by a similarity of measurements of various quality related variables with their values as suggested in a standard, which is diverse for different countries. Yarns are used for producing fabrics.

Revised Manuscript Received on October 20, 2020.

M. Salomi, Assistant Professor, Department of Statistics, Madras Christian College, Chennai (Tamil Nadu), India.

R. Lakshmi Priya, Assistant Professor, Department of Statistics, Dr. Ambedkar Govt. Arts College, Chennai (Tamil Nadu), India.

Manimannan G, Assistant Professor, Department of Mathematics, TMG College of Arts and Science, Chennai (Tamil Nadu), India.

N. Manjula Devi, Bio Statistician, Department of Community Medicine, Karpaka Vinayakar Institute of Medical Sciences, Chengalpet, (Tamil Nadu), India.

These fabrics can be classified according to weave structure, knitting method, base material used such as cotton, jute and silk. Syntheticmaterial is based on polyester, softness or roughness of the material. The classification is very essential for textile industry. Textile technologists have introduced various methods for solving the above mentioned problems. Most of the measurement properties are obtained using Kawabata instrument. Kawabata (1980) and his associates established the *Kawabata Evaluation System for Fabrics (KES-F),* which is used to measure mechanical properties of fabrics. It's shown to offer benefit over other instruments in the routine dimensions of the properties. Fabric is tested for their tensile, bending, shearing, compression, surface properties and also for thickness and weight. To categorize a fabric based on measurements, some scientific methodology is to be implemented. The relationship between yarn structure and tensile properties has been studied extensively. A number of statistical models have been developed for textile parameters. More number of publications of research papers shows that fabric handle received wide attention from scientist and technologists from very early days. Fabric database handle has become one of the most likely areas of textile research during the past twenty years. Fabric 'hand' or 'handle' is defined as the quality of a fabric or yarn assessed by the reaction obtained from the sense of touch. KES-F system of assessment of hand value has been used by fibre, yarn and fabric producers all over the world. Many researchers have used multivariate statistical methods of Cluster Analysis, Principal Component Analysis in the study of fabric hand. Recently, Rong, Slater and Fei (1994) have used cluster analysis method for grading of yarns in textile industry. Pan, Zeronian and Ryu(1993) suggest statistical methods such as PCA, Variable Cluster Analysis, D-optimal method and multi collinearity tests for identifying the most important mechanical properties. Pan, Yen, Zhao and Yang (1988) have conversed classification of fabrics by hierarchical clustering methods. Recently Artificial Neural Network technique (ANN) has been applied for textile database for the classification purpose by Ramesh, Rajamanickam and Jayaraman (1995)

III. DATABASE

The database consists of three data sets, combined together which has 105 fabric samples with 16 KES-F parameters. In the present study, the combined data sets as well as individual data sets are analyzed. All data setwas subjected to normality test and equality of variance test and the same established. The three data sets are, Data Set 1 comprises different types of Polyester Fabrics (Regular/Micro fibres). It includes 27 fabric samples with 16 parameters (Table 1).

Data Set 2 consists of 40 Lyocell/Viscose fabric samples with 16 KES-F parameters and Chemically Treated Polyester fabric samples constitute Data set 3.

Table 1. Sixteen Textile Parameters and their abbreviation

Parameters and their Abbreviation
1. Linearity of the Stress Strain Curve (LSSC)
2. Tensile Energy (TE):
3. Tensile Resilience (TR)
4. Bending Rigidity (BR):
5. Hysteresis of Bending (HB):
6. Shear Rigidity (SR):
7. Hysteresis of Shear Force (HSF):
8. Hysteresis of Shear Force 2 (2HSF) :
9. Linearity of the Compression Curve (LCC):
10. Work of Compression Curve (WCC):
11. Compressional Resilience (CR):
12. Coefficient of Surface Friction (CSF):
13. Mean Deviation of Coefficient of Friction (MDCF):
14. Surface Roughness (SR):
15. Fabric Thickness (FT):
16. Fabric Weight (FW):

IV. METHODOLOGY

4.1 MacQueen k-means Clustering Algorithm

In general context, one of the most popular clustering algorithms suggested by MacQueen (1967) known as ***k-means*** is used to identify q classes in the data set. This technique uses Euclidean distance measure computed on textile paparameters to partition or group the data set into mutually exclusive groups such that the members of each group are as close as possible to one another and different groups are as far as possible. Thus, ***k***-means clustering assigns group labels to data sets which are unknown initially based on the nuclei of clusters or groups as seed points exhibited in factor analysis. The number of cluster is determined as a part of clustering procedure. In its simplest report, the process is composed of three steps.

Step 1:: Partition the data sets in to ***k*** initial clusters.

Step 2:The initial cluster starts from *k=2…n* based cluster centroid. The distance is computed using Euclidean distance with standardized or unstandardized observations. Recalculate the centroids for the cluster receiving the new item and the cluster losing the item.

Step 3: Repeat Step 2 until no more reassignment takes place.

Rather than starting with partition of all items in to *k* preliminary groups in Step 1, Specify ***k*** initial centroids and proceed Step 2.The final assignment of items to clusters will be, to some extent depends upon initial partition or initial selection of seed points. The present study deals with textile database with sixteen parameters as input data matrix. Centroids are calculated and assigned the samples based on Euclidean distance measure. The cemtroids are calculated by using following equations.

$$d(x,y)=\sum_{i=1}^{n}|y_i - x_i|$$

4,2 Data Mining k- Mean Clustering Methods

The data mining widget applies the k-Means clustering algorithm to data and outputs of textile dataset in which cluster index is used as a class attribute. The original class attribute, if it exists, is moved to Meta attributes. The scores of clustering results for various k are also shown in the widget. The following algorithm execute the widget

Step 1: Initially, select the number of clusters.

Fixed: *The* algorithm clusters data in a specified number of clusters.

Optimized: widget shows clustering scores for the selected cluster range:

Silhouette: This method contrasts average distance to elements in the same cluster with the average distance to elements in other clusters

Inter-cluster distance: This measures distances between clusters, normally between centroids values

Distance to centroidsmeasures distances to the arithmetic means of clusters.

Step 2: Select the initialization method:

k-Means++ to evaluate first centre is selected randomly and subsequent are chosen from the remaining points with probability proportioned to squared distance from the closest center values

Random initialization clusters are assigned randomly at first and then updated with further iterations. *Re-runs* to evaluate how many times the algorithm is run from random initial positions; the result with the lowest within-cluster sum of squares will be used and **maximal** *iteration***s** is the maximum number of iterations within each algorithm run can be set manually.

Step 3: The output widget create a new dataset with appended cluster information. Select how to append cluster information based on class, feature or Meta attribute and name the column.

Step 4: If Apply automatically is ticked, the widget will assign changes automatically. Alternatively, click *Apply* button.

Step 5: Produce a report for a given database.

Step 6:Scores of clustering results for various k in Table 2

4.3 Principal Component Analysis

Principal Component Analysis (PCA) is generally preferred for purposes of data reduction and variable reduction but not when the goal is to detect the latent construct or factors. Factor analysis is similar to principal component analysis, in that factor analysis also involves linear combinations of variables withPCA linear transformation of input data.

4.3.1 Inputs of Data:

Textile database as a input dataset with sixteen parameters

4.3.2 Outputs

The outputs based on PCA transformed data Eigen Values Components.

Principal Component Analysis (PCA) computes the PCA linear transformation of the input data. It outputs either a transformed dataset with weights of individual instances or weights of Principal Components Analysis.

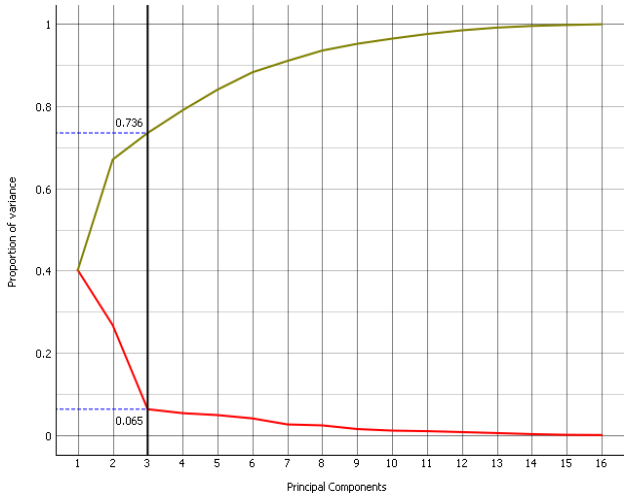

Figure 1. PCA Screw Plot for Extracted Components

4.3.3 Data mining Algorithm for Principal Component Analysis

Step 1: The file Widget to import the database from various formats of data file like, .dat. txt. CSV, .tab, etc. (Three sets of database with sixteen parameters)

Step 2: Select the number of principal components to be included in output. It is the best to choose as few as possible with variance covered as high as possible.

Step 3: Set how much variance to be covered with principal components.

Step 4: Normalize data to adjust the values to common scale.

Step 5: When Apply Automatically is ticked, the widget will automatically communicate all changes. Alternatively, click *Apply*.

Step 6: Press *Save Image* to save the created image to your computer. Produce a report.

Step 7: Principal components graph, where the red (lower) line is the variance covered per component and the green (upper) line is cumulative variance covered by components. The number of components of transformation can be selected either in Components Selection input box or by dragging the vertical cutoff line in the graph(Figure 1).

4.3.4 Proposed Algorithm for k++ (k-means)

In this section, the researcher explains the widget with the following schema.

Step 1: The file Widget to import the database from various formats of data file like, .dat. txt. CSV, .tab, etc. (Three sets of database with sixteen parameters)

Step 2: The k- mean widget analyze for any given data and group them for requirements. The k-mean widget by default i=2 clusters, then increase up to i=n meaningful clusters, then stop the iteration process.

Step 3: Data widget shows that grouped data of k- mean clustering.

Step 4: Select Row Widget to highlight the grouped data.

Step 5: Finally, the scatter plot widget, to visualize the grouped data using k-means clustering method (Figure 2)

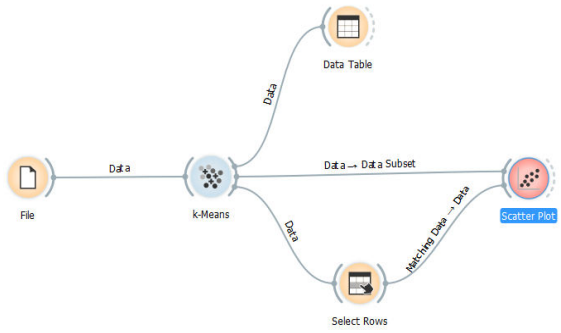

Figure 2. k- Means Work Flow

V. RESULT AND DISCUSSION

The input textile database load the file widget, the k-mean widget divides it into three clusters and presentedin Data Table. The interesting parts are the Scatter Plotachieved from Select Rows widget (Figure 3). Since k-means added the cluster index as a class attribute, the scatter plot will color the points according to the clusters they are shown inFigure 3.

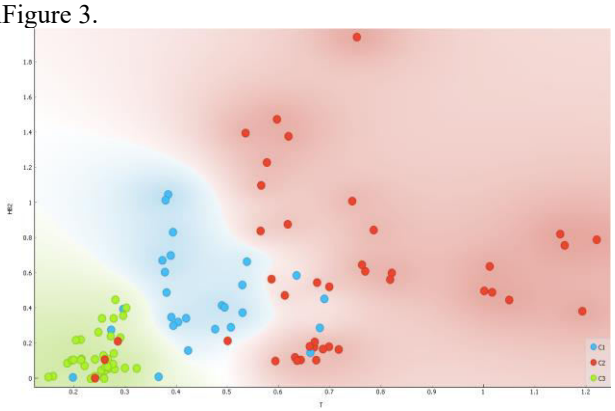

Figure 3. Scatter Plot for k- Means

It may be noticed that removal of noisy data or attributes to be unusedclasses in Select Rows widget is unchecked. This is important: if the widget modifies the attributes, it outputs a list of modified instances and the scatter plot cannot compare them with original data.Conceivably a simpler way to test the match between clusters and the original classes is to use Distributions widget (Figure 4).

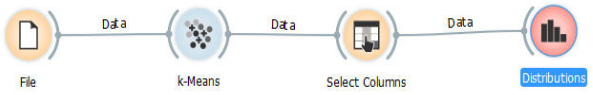

Figure 4. k- Means Distribution Work Flow

The widget visualizes normal attributes bar chart for three datasetonly. This is achieved by Select Columns widget: Reinstate the original class *textile* Data set as the class and put the cluster index among the attributes. The match is perfect for 27 Polyester Fabrics: all parameters of Polyester Fabrics are in first cluster (blue). 40 Lyocell/Viscose fabrics are in second cluster (red), while two ended up in first. Chemically Treated Polyester fabric samples are in third cluster and 38 in the second.

The following figure represents the cluster information of three data sets (Figure 5).

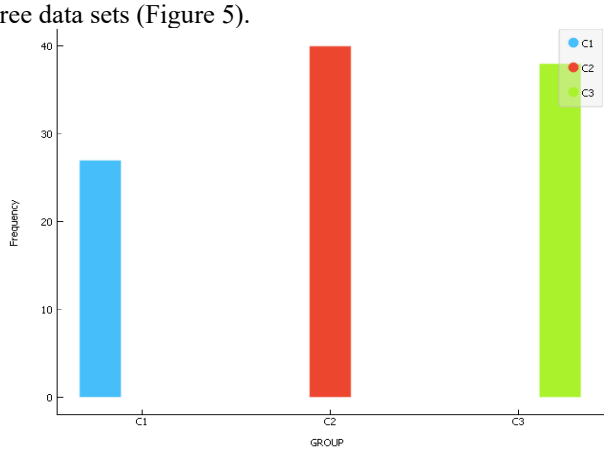

Figure 5. k- Means Classification Work Flow

Principal Component Analysis can be used to simplify visualizations of large datasets. The researcher used the Textile Fabricsdataset to show how visualization of dataset with PCA can be improved. The transformed data in Scatter Plot and Silhouette plot shows a cleardistinction between classes than the default locations (Figure 6-8)

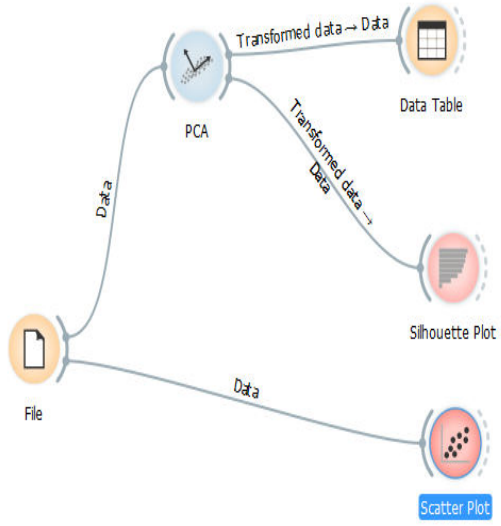

Figure 6. Principal Component Analysis Work Flow

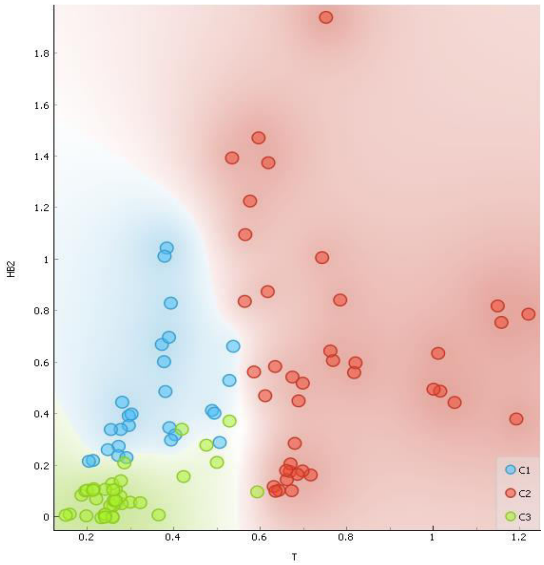

Figure 7. Scatter Plot for Principal Component Analysis

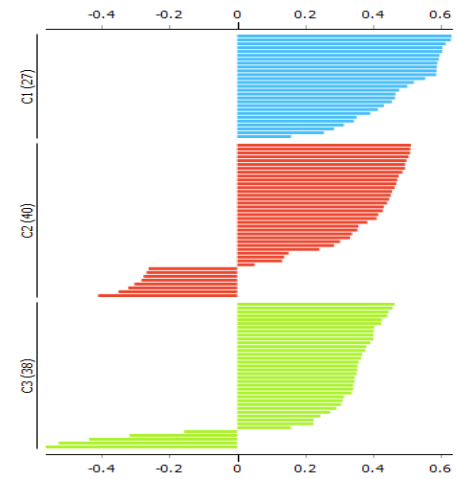

Figure 8. Silhouette for Principal Component Analysis

The below flow diagram widget provides two outputs: transformed data and principal components. Transformed data are weights for individual instances in new coordinate system, while components are system descriptors based on their weights for principal components. When fed into the Data Table widget, both outputs in numerical form can be achieved. In order to provide a more clean visualization of workflow, two data tables were used, but one can also choose to edit the links in such a way that it displays data in just one data table widget. It is necessary to create two links and connect the *Transformed data* and *Components* inputs to *Data* to extract PCA output. The following workflow shows the performance of PCA (Figure 9).

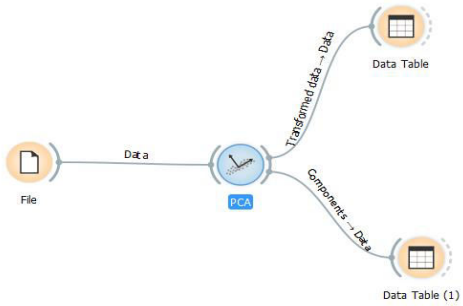

Figure 9. Principal Component Analysis Workflow for Components and Transformed Data

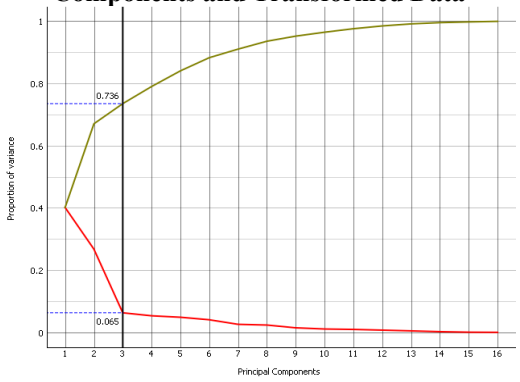

Figure 10. Screw Plot for Components and Transformed Data

The Screw plot shows that variance and number factor in textile database (Figure 10). The total variance explained 75 percent with three factors and they are labeled as, Polyester Fabrics, Lyocell/Viscose fabrics and Chemically Treated Polyester fabrics. The three extracted factor scores are shown in the following table. Finally, the removed three factor component score are listed in next table of factor scores (Table 1 to 2).

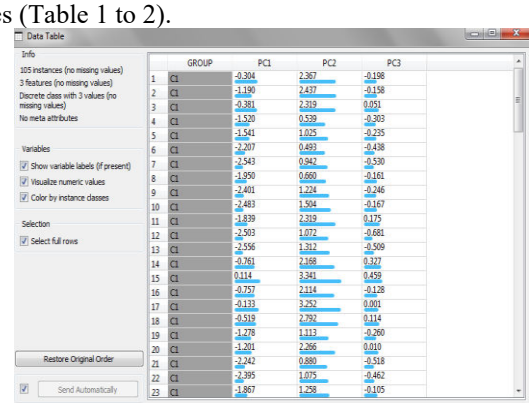

Table 1. PCA Extracted Factor Score

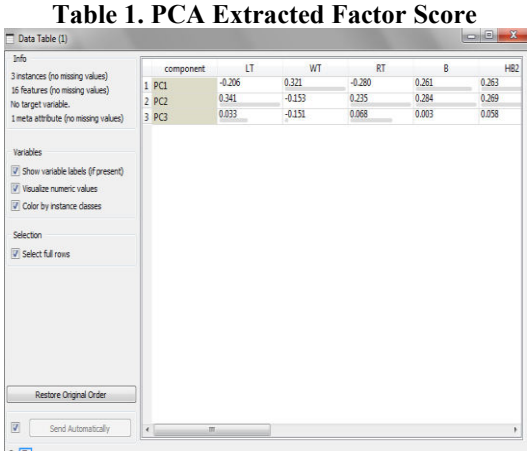

Table 2. PCA Extracted Factor Component Score

VI. CONCLUSION

The main objective of this study is to identify the first **n** number of factors that explained over 75 percent of variation in the data set. Initially factor analysis is performed to extract factor scores. Principal extraction is performed through data mining package on sixteen textile fabrics database. Factor extraction is aimed to uncover the intrinsic pattern among the ratios considered and an important point of factor analysis is to extract factor scores for further investigation. Thus, factor analysis consistently resulted in three factors for the three datasets. The amount of total variation explained is over 75 percent in factor analysis. The factor loadings or factor structure matrix with unassociated rotation methods are not always easy to interpret. Both Varimax and Quatrimax orthogonal criterion are employed to improve the interpretability of the set of variables on factors. Though both rotations are almost similar in structure, the grouping of variables is more meaningful under Varimax rotation. Variables have been ordered and grouped by sizes of loadings to facilitate interpretation. Factor analysis results show that the set of variables are highly correlated with their respective factors. After identifying all significant loadings, an attempt is made to assign meaning to the factors and hence factors are labeled as ***Polyester Fabrics, Lyocell/Viscose fabrics and Chemically Treated Polyester fabrics*** respectively. The naming of factors is based on previous study and also with clustered variables on factors. In addition, the mechanical properties stability of all the samples was measured to certain extent without any uncertainty though the number of samples kept varying during the study period.

REFERENCES

1. Chen Y and Collier B J(1997), Characterizing Fabric End-Use by Fabric Physical Properties, Textile Research Journal, Vol. 67, No. 4, pp.247-252.
2. G.K. Gupta (2012), Introduction to Data Mining with Case Studies, PHI Learning Private Limited, New Delhi, India.
3. Kawabata S. (1980), The Standardisation and Analysis of Hand Evaluation, 2nd Edition, The Textile Machinery Society of Japan, Osaka, Japan.
4. MacQueen, J. Some methods for classification and analysis of multivariate observations. Proceedings of the Fifth Berkeley Symposium on Mathematical Statistics and Probability, Volume 1: Statistics, 281--297, University of California Press, Berkeley, Calif., 1967
5. Pan N, Zeroniam S H and Ryu H S(1993), An Alternative Approach to the Objective Measurements of Fabrics, Textile Research Journal, Vol.63, pp.33-43.
6. Pan N, Yen K C, Zhao S J and Yang S R(1988), A New Approach to the Objective Evaluation of Fabric Handle from Mechanical Properties(Fuzzy Cluster Analysis for Fabric Handle Sorting), Textile Research Institute, pp.565-571.
7. Ramesh M.C., Rajamanickam R. & Jayaraman S. (1995). The Prediction of Yarn Tensile Properties by Using Artificial Neural Networks, J. Text. Inst., 86: 3, pp. 459 – 469.
8. Rong G H, Slater K and Fei R C(1994), The Use of Cluster Analysis for Grading Textile Yarns, Journal Textile Institute, Vol. 85, No.3, pp.389-396.
9. R. Ruhin Kouser and R. Gunasundri (2015), Data Warehousing and Data Mining, Lakshmi Publications, Chennai, India

AUTHORS PROFILE

Dr. Manimannan G. M. Sc. M. Phil. Ph. D, PGDCA,, MCA. He has good research experience by working for many Project Guidance and consultation work in application of Statistics, Neural Networks and Data Mining. He has published more than seventy research papers in various National and International journals.

Dr. Salomi M. M. Sc. M. Phil. Ph. D, She has good research experience by working for many project guidance and consultation work in application of Statistics and Bio – Statistics. She has published more than twenty research papers in various national and International journals.

Dr. R. Lakshmi Priya M. Sc. M. Phil. Ph. D, She has good research experience by working for many project Guidance and consultation work in application of Statistics and Data Mining. She has published more than forty five research papers in various National and International journals.

Ms. N. Manjula Devi M. Sc (Bio Statistics), She has good research experience by working for few project Guidance and consultation work in application of Bio Statistics and Data Mining. She has published more than Ten research papers in various National and International journals.

.

Applied Ecology and Environmental Sciences, 2021, Vol. 9, No. 5, 575-579
Available online at http://pubs.sciepub.com/aees/9/5/8
Published by Science and Education Publishing
DOI:10.12691/aees-9-5-8

Assessment of DNA Damage and Apoptosis in the Brain of Freshwater Fish *Oreochromis mossambicus* Exposed to Tannery Effluent Wastewater

N. Ganesan, K. Samyappan, R. Saravanan*

Department of Zoology, Dr Ambedkar Government Arts College, Vyasarpadi, Chennai 600039, Tamil Nadu, India
*Corresponding author: rsaravanan51283@yahoo.com

Received April 17, 2021; Revised May 22, 2021; Accepted May 30, 2021

Abstract The present study was designed to evaluate the effect of tannery effluent on the fingerlings of freshwater fish *Oreochromis mossambicus.* The fishes were maintained at 10% concentration of tannery effluent for a period of 30 days. Apoptosis was studied by activity of caspases. Caspase 3 and 9 activity showed significant alteration. DNA seperation by agarose gel electrophoresis shows difference in intensity of genomic DNA between 750-1000 bp in fishes exposed to tannery effluent. DNA damage was also confirmed by Comet assay which showed an increase in DNA damage and tail migration was indicated by increase in percentage of mean DNA comet tail length formation.

Keywords: *Oreochromis mossambicus, Tannery effluent, Brain, Caspases 3 and 9, Genomic DNA, Comet assay*

Cite This Article: N. Ganesan, K. Samyappan, and R. Saravanan, "Assessment of DNA Damage and Apoptosis in the Brain of Freshwater Fish *Oreochromis mossambicus* Exposed to Tannery Effluent Wastewater." *Applied Ecology and Environmental Sciences*, vol. 9, no. 5 (2021): 575-579. doi: 10.12691/aees-9-5-8.

1. Introduction

Tannery effluents are ranked as the highest pollutants among all industrial wastes. Recently, majority of tanning industries favour chrome tanning for processing leather. Unfortunately only fraction of chromium (Cr) is utilized in tanning process and the rest is discharged as by-product of wastewater treatment [1]. Aquatic ecosystem is the final sink for many chemicals used in industry and agriculture and has become a global problem [2]. It is well known that Cr (VI) is a potent carcinogen to humans and animals as it enters cells via surface transport systems and gets reduced to Cr (III) inducing genotoxicity [3,4]. Chromium compounds are known to have toxic, genotoxic, mutagenic and carcinogenic effects on man and animals. Genotoxicity in aquatic animals can be assessed by DNA alteration which is an important mechanism of toxicity for a variety of pollutants and therefore is often used as an indicator of pollutant effect in ecotoxicological studies [5].

Brain is the master of all living organism as it is the controlling centre for all the receptors and effector organs. Because of its structural complexity and functional diversity brain performs a number of complex biological functions that are essential for survival. The blood brain barrier (BBB) is a physical and metabolic barrier between the brain and systemic circulation which functions to protect the brain and systemic circulation from circulating drugs, toxins and xenobiotics [6].

Apoptosis is a physiological cell death, defined by internucleosomal DNA fragmentation, chromatin condensation, cellular shrinkage and membrane blebbing resulting in the formation of apoptotic bodies. Apoptotic cell death occurs in two different pathways; extrinsic or the receptor apoptotic pathway and intrinsic or the mitochondrial apoptotic pathway, both working with caspase-3 activation [7]. There are two modes of cell death, necrosis and apoptosis. Apoptosis may occur with many different pollutants such as heavy metals and insecticides.

It has been proposed in the present study, to examine the genotoxic evaluation of chromium present in tannery effluent and its effects on the brain tissue of freshwater cultivable fish *Oreochromis mossambicus.* This would provide data supporting the usefulness of freshwater fish as indicators of heavy metals. The brain tissue is analysed for caspases activity, brain genomic DNA was separated to identify the base pairs and differences in their intensities, visualization of DNA fragments by gel documentation and single cell gel electrophoresis (comet assay) was performed to identify the extent DNA damage.

2. Materials and Methods

Collection of tannery effluent: Samples were collected from Common Effluent Treatment Plant (CETP) at Pallavaram in Chennai which treats around 3000 m^3/day of wastewater. The effluent was collected at a fixed point when the discharges from all the stages of processing are released together. The samples were collected during the month of November 2019. The raw effluent was collected in different polyethylene containers of 20 litres capacity and stored in dark at room temperature till further use.

Experimental animals: Active and healthy juveniles fishes comprising fingerlings of both sexes of *Oreochromis mossambicus* weighing about 4.0 to 4.5 gms approximately and 5.5 – 7.5 cms in length was procured from Bharat seed fish farm, Budur, Poondi, Tiruvallur District and were brought to the laboratory in polythene bags containing aerated water.

Determination of lethal concentration (LC_{50}): The LC_{50} value of tannery waste water was analyzed through a static renewal bioassay technique. Preliminary screening was carried out to determine the testing chemical as described by Solbe [8]. The effluent was mixed with tap water in appropriate dilution to get wide range of concentration. A range of 7 concentrations (50, 40, 30, 25, 20, 15, 10 % / L of water) were selected for lethal dose studies. The mortality in each concentration were noted for 24, 48, 72 and 96 hours exposure. The LC_{50} value (96 hour) was found to be at 20% concentration, for fingerlings of *Oreochromis mossambicus.* From this 50% of sublethal concentration was selected for the study.

Experimental Design: Acclimated freshwater fish fingerlings of *Oreochromis mossambicus* were divided into two groups consisting of 5 fishes in each group.

Group I: Control group - Fishes maintained in dechlorinated toxicant free tap water

Group II: Experimental group - Fishes maintained in tannery effluent

All the groups of fishes were maintained in 30 L of water. Fishes of control group was maintained in 30 L tap water. Group-II fishes were exposed to sublethal concentration (10%) of the tannery waste water for a period of 30 days. No mortality was recorded during the period of study. The experimental set up was maintained promptly with the renewal of effluent water daily in group- II. The tubs were aerated with air stones attached to an air compressor to saturate oxygen. The fishes were fed with commercial fish feed twice a day daily (2% of their body weight). Commercial food pellets with ingredients consisting of fish meal, wheat flour, soybean meal, yeast, vitamins and minerals were fed. Left over feed if any was removed by siphoning, two hours post feeding to reduce contamination with food remains. Faecal residues were removed daily through suction.

At the end of the experiment, fishes were euthanized by decapitation of cervical region and brain tissues were carefully removed, washed twice in ice cold physiological saline (0.9 N) solution and weighed. Tissue samples were homogenized and processed as required for different molecular analysis.

Analysis of chromium in raw tannery effluent : The raw tannery effluent total chromium content , hexavalent and chromium content was analysed by following the standard methods as given by APHA [9].

Activity of Caspases and Apoptosis: The commercially available lysis buffer for tissues were used. The cells were resuspended in 50 µL of chilled cell lysis buffer and homogenated. The cells are incubated on ice for 10 minutes and then centrifuged at 10,000 x g for 1 minute. The supernatant (cytosolic extract) are transferred to a fresh tube and put on ice for immediate assay. Caspases activity was determined by the method of Baharara Javad *et al.,* [10] by using Caspase-3 assay kit (colorimetric) (ab39401) and Caspase- 9 assay kit (colorimetric) (ab65608).

Isolation of genomic DNA by Agarose Gel Electrophoresis and fragmentation studies: Isolation of DNA was performed by the method of Basnakian and Jill James [11].

Collection and Cellular dissociation of brain tissue for comet assay: The control and experimental fishes were euthanized, the brain were excised immediately and washed with phosphate buffer solution (PBS), the brain tissues were transferred to microtubes for the cellular dissociation to be used in the comet assay. The method for cellular dissociation was based on Monteiro *et al*., [12].

3. Results and Discussion

Content of Chromium in raw tannery effluent: The content of chromium in the raw tannery effluent was 25.33 ppm and hexavalent chromium was 19.45 ppm. The values obtained were beyond the tolerance limit.

Caspases activity: The percentage activity of caspase 3 and caspase 9 was increased in brain of the fishes exposed to tannery effluent by 7.23 % and 6.70 % respectively, when compared with the control percentage activity baseline value (Figure 1a & Figure 1b).

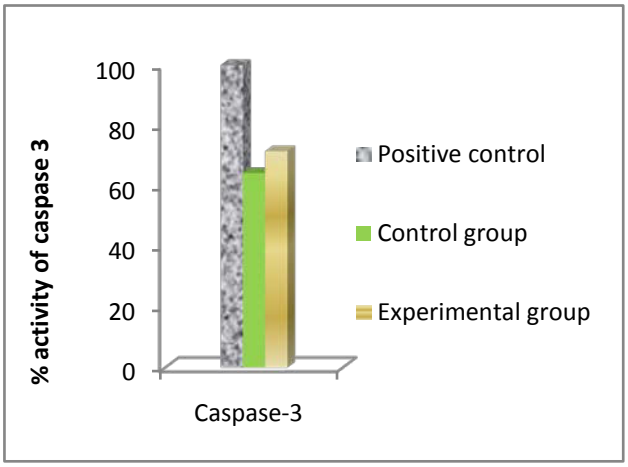

Figure 1a. Effect of tannery effluent on the caspase-3 activity in brain of freshwater fish *Oreochromis mossambicus* (Values are (n=2) and expressed as % activity of caspase-3)

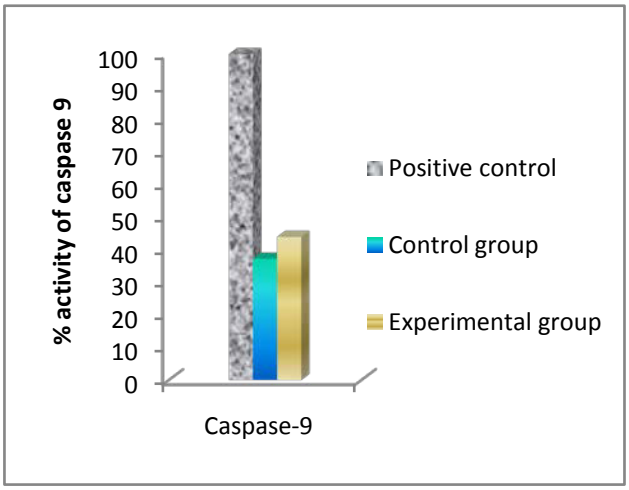

Figure 1b. Effect of tannery effluent on the caspase-9 activity in brain of freshwater fish *Oreochromis mossambicus* (Values are (n=2) and expressed as % activity of caspase -9)

Isolation of genomic DNA and its separation: Brain DNA of *Oreochromis mossambicus* from tannery exposed effluent and control was analysed on agarose gel, the presence of DNA fragments could be detected between 750 bp and 1000bp when compared with molecular marker and difference in intensities of base pair subunits were noticed (Figure 2).

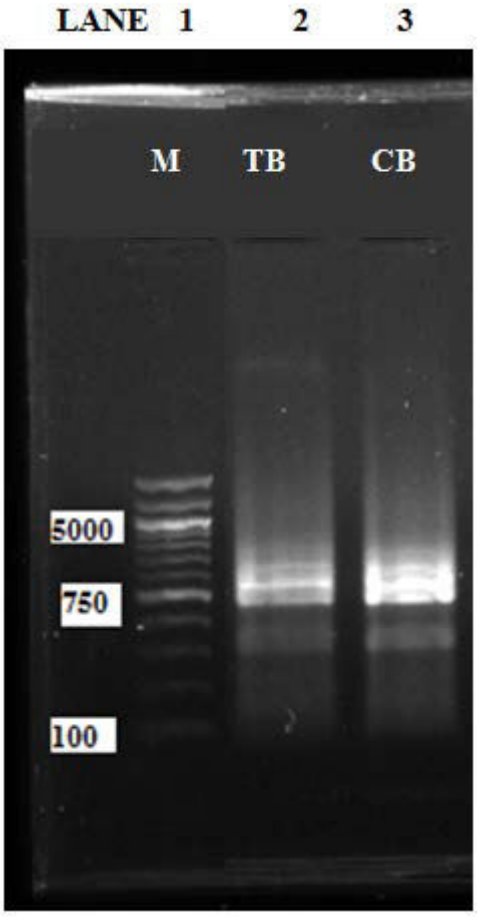

Figure 2. Separation of DNA by agarose gel electrophoresis and identification of genomic DNA in brain of freshwater fish *Oreochromis mossambicus* fingerlings exposed to tannery effluent (Lane -1: Molecular marker, Lane -2 Test brain (TB) and Lane- 3 Control brain (CB))

Comet studies: Fishes exposed to tannery effluent show variable score of DNA damage, the formation of comet tails in brain cells was significantly higher by 3.28% ($p < 0.001$) in fishes exposed to tannery effluent when compared to the control group of fishes (Figure 3 & Figure 4).

The brain has a large membrane surface due to axon extensions and neuronal dendrites that are rich in polyunsaturated fatty acids and high intake of oxygen, making them particularly vulnerable to reactive oxygen species (ROS) attack [13]. The generation of ROS triggered by oxidative stress is related to apoptotic cell death via the mitochondrial apoptosis pathway. Bcl-2, which plays an important role in promoting cell survival, pro-apoptotic protein actions, regulates the antioxidant pathway and ROS generation sites to prevent apoptosis and cellular damage [14].

Caspase-3 activation is important for the execution phase of apoptosis involving pesticide exposure [15,16]. In our study, caspase-3 activity was increased in the brain tissue of the fishes exposed to tannery effluent. This reveals that toxic compounds present in tannery effluent may activate caspase-3 and may induce brain cell apoptosis in freshwater fish *Oreochromis mossambicus.* Two possible mechanisms may be mentioned in this event are ROS generation may cause caspase 3 activation and increased Ca may induce apoptotic cell death [17]. The observed DNA damage is possibly due to direct interactions of toxic compounds present in tannery effluent with cellular DNA due to ROS generation causing strand breaks in DNA [18].

Cytochrome-C promotes activation of caspase-9 followed by downstream events leading to apoptosis as evident from increase in the activity of casapse-9 in the brain tissue of fishes exposed to tannery effluent. Caspase-9 triggers mitochondrial morphological changes and ROS production [19]. It is clear from the present study that tannery effluent like other environmental toxicants activates the expression of apoptotic genes and down regulates the expression of anti-apoptotic genes after activation of caspase-9 and caspase-3 which is required for efficient execution of apoptosis [20]. Expression of apoptotic genes was identified by upregulation of caspase 3 and caspase 9 after the exposure of zebrafish to monocrotophos [21]. Oxidative stress has been reported to inhibit expression of Bcl-2 mRNA in zebrafish. Similar mechanisms could be suggested in the present study for the increase in caspase activity.

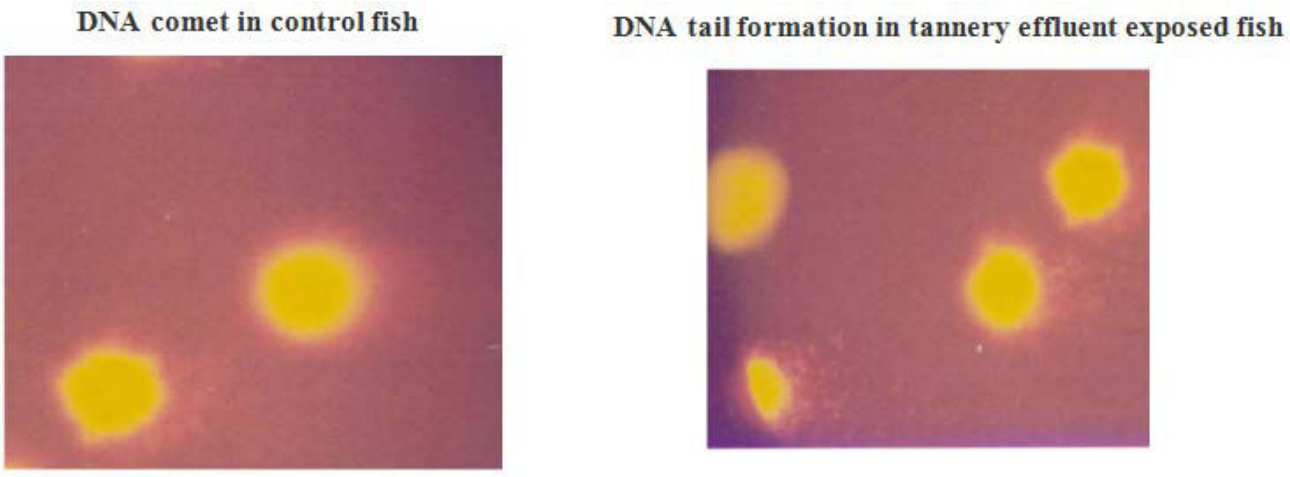

Figure 3. Comet Assay and identification of DNA damage in brain of freshwater fish *Oreochromis mossambicus* fingerlings exposed to tannery effluent

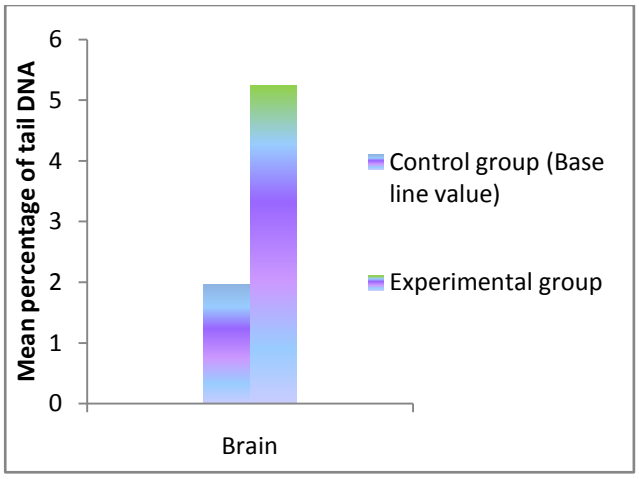

Figure 4. Effect of tannery effluent on the mean percentage of tail DNA by Comet assay in brain of freshwater fish *Oreochromis mossambicus* (Values are (n=2) and expressed as Mean percentage of tail DNA formed)

In this study DNA banding patterns were analysed by the isolation of genomic DNA from brain tissue and its separation on an agarose gel. Distinct bands were observed between 750-1000bp in the control brain tissue of *Oreochromis mossambicus*, while disappearance or less prominent appearance of base pairs in DNA subunits between 750-1000bp were observed in experimental fishes. Such changes may be attributed to the effect of tannery effluent. Similar changes in DNA banding pattern were observed in brain of *Channa punctatus* exposed to methyl parathion [22]. DNA smearing with less intensity which could be an indicator of necrosis was observed in experimental brain tissue, between 750bp-1000bp suggesting that long-term exposure may upregulate both apoptotic and necrotic pathways in cells [23].

The comet assay studies revealed have that tail length/ movement was maximum. The present study showed a consistently enhanced DNA fragmentation and formation of distinct tail from the region of the head. DNA in brain of fishes exposed to tannery effluent for 30 days. The DNA breaks as evidenced by tail movement are possibly due to defective apoptosis, or excessive production of reactive oxygen species. From the comet assay results we can also conclude that the mechanism of DNA damage can be described as follows: The Cr (VI) enters the system either by ingestion or by absorption as an oxyanion. The absorbed chromium is metabolically reduced to Cr (V), Cr (IV) and finally to reduced trivalent (III) form. These reduced forms have been shown to induce a wide range of genomic DNA damage, which make chromium to inhibit DNA replication [24].

4. Conclusion

Raw tannery wastewater without the required primary, secondary or tertiary treatment, when released from tanning industries directly into natural water bodies or when used for agriculture or aquaculture practices without proper recycling may have adverse negative effects on life aquatic organisms. To ensure the protection of water bodies, environmental monitoring report need to be done periodically in order to limit and prevent adverse environmental contaminations.

References

[1] Noorjahan, C.M., Physicochemical Characteristics, Identification of bacteria and biodegradation of industrial effluent, *Journal of Bioremediation and Biodegradation,* 5, 219-223, 2014.

[2] Adeogun, A.O. and A.V. Chukwuka. Toxicity of industrial wastewater acting singly or in joint-ratios on *Clarias gariepinus*, *American. Journal of Environmental. Sciences,* 8, 366-375, 2012.

[3] Matsumoto. S.T., Mantovani, M.S., Malagutti, M.J.A., Dias, A.L., Fonseca, I.C.and Marin-Morales, M.A., Genotoxicity mutagenicity of water contaminated with tannery effluent, as evaluated by the micronucleus test and comet assay using the fish (*Oreochromis niloticus)* and chromosome aberrations in onion root-tips, *Genetics and Molecular Biology,* 29, 148-158, 2006.

[4] Beyersmann, D. and Hartwig, A, Carcinogenic metal compounds: recent insight into molecular and cellular mechanisms, *Archives of Toxicology*, 82, 493-512, 2008.

[5] Frenzilli G., Nigro, M.and Lyons, B.P.,. The comet assay for the evaluation of genotoxic impact in aquatic environments, *Mutation Research.* 681.80-92, 2009.

[6] Eliceiri, B.P., Gonzalez, A.M. and Baird, A., Zebrafish model of the blood brain barrier. Morphological and permeability studies. *Methods in Molecular Biology,* 686, 371-378, 2011.

[7] Monteiro, S.M., dos Santos, N.M., Calejo, M., Fontainhas - Fernandes, A and Sousa, M., Copper toxicity in gills of the teleost fish, *Oreochromis niloticus,* Effects in apoptosis induction and cell proliferation, *Aquatic Toxicology*, 94 (3), 219-228, 2009.

[8] Solbe JF. Freshwater. In: Handbook of Ecotoxicology. Peter Calins (ed) Blackwell Science Ltd. Osney meed OX 20EL 68, 3, 1975.

[9] APHA - American Public Health Association. Standard Methods for examination of water and wastewater. Washington DC, USA. 20th Edition, 1998.

[10] Baharara Javad, Ramezani, Divsalar, Mousavi and Seyedarabhi, Induction of apoptosis by green synthesized gold nanoparticles through activation of caspase-3 and 9 in human cervical cancer cells, *Avicenna Journal of Medical Biotechnology,* 8(2), 75-83. 2016.

[11] Basnakian, A.G. and James, S.J, A rapid and sensitive assay for the detection of DNA fragmentation during early phases of apoptosis. *Nucleic Acids Research*, 22 (13), 2714-2715, 1994.

[12] Monteiro V, D. Cavalcante, G.S.M.,. Vilela, M.B.F.A., Sofia, S.H. and Martinez, C.B.R. *In vivo* and *in vitro* exposures for the evaluation of the genotoxic effects of lead on the Neotropical freshwater fish *Prochilodus lineatus, Aquatic Toxicology,* 291-298, 7, 2011.

[13] Wang, X. and Michaelis, E.K., Selective neuronal vulnerability to oxidative stress in the brain. *Frontiers of Aging and Neuroscience,* 2, 12-20, 2010.

[14] Deng, J., Yu, L. and Liu, C., Hexabromocyclododecane - induced developmental toxicity and apoptosis in zebrafish embryos, *Aquatic Toxicology*, 93(1), 29-36, 2009.

[15] Piner. P. and Uner N., Oxidative and apoptotic effects of lambda-cyhalothrin modulated by piperonyl butoxide in the liver of *Oreochromis niloticus, Environmental Toxicology and Pharmacol*ogy, 33 (3), 414-420, 2012.

[16] Topal A, Atamanalp M, Oruc E, Kirici M and Kocaman EM, Apoptotic effects and glucose-6-phosphate dehydrogenase response in liver and gill tissues of rainbow trout treated with chlorpyrifos,. *Tissue and Cell Research*, 4 , 490-496 , 2014.

[17] Misra, S., Hamilton, C and Niyogi, S., Induction of oxidative stress by selenomethionine in isolated hepatocytes of rainbow trout (*Oncorhynchus mykiss*), *Toxicology invitro.,* 26; 621-629, 2012.

[18] Cao, J., Chen, J., Wang, J., Klerks, P.and Xie, L.,. Effects of sodium fluoride on MAPK's signaling pathway in the gills of a freshwater teleost, *Cyprinus carpio. Aquatic. Toxicology*. 16(152C), 164-172, 2014.

[19] Matthew Brentnall, Luis Rodriguez-Menocal, Rebeka Ladron De Guevara, Enrique Cepero and Lawrence H Boise Caspase-9, caspase-3 and caspase-7 have distinct roles during intrinsic apoptosis. *BMC Cell Biology*, 1471 (21), 14-32, 2013.

[20] Gao, D., Xu, Z., Qiao, P., Liu, S., Zhang, L., He, P., Zhang, X., Wang, Y. and Min, W., Cadmium induces liver cell apoptosis through caspase-3A activation in purse red common carp (*Cyprinus carpio*), *PLOSONE,* 8 (12), 2013.

[21] Kuppuswamy, J.M. and Seetharaman, B. Monocrotophos based pesticide alters the behavior response associated with oxidative indices and transcription of genes related to apoptosis in adult Zebrafish (*Danio rerio*) brain. *Biomedical and Pharmacology Journal*, 13 (3), 1291-1304, 2020.

[22] Veeraiah, K. , Padmavathi ,P., Tata Rao, S. and Vivek, C.H., Methyl parathion (50%EC) induced changes in protein and DNA banding pattern in the fish *Channa punctatus, International Journal of Bioassays,* 4(1), 3632-3637, 2015.

[23] Datta, S., Saha, D.R., Ghosh D, Majumdar T, Bhattacharya, S and Mazumder, S. Sub-lethal concentration of arsenic interferes with the proliferation of hepatocytes and induces *in vivo* apoptosis in *Clarias batrachus* (L), *Comparative Biochemistry and Physiology*, Part C, 145, 339-349, 2007.

[24] Nickens, K.P., Patierno, R. and Ceryak, S., Chromium genotoxicity: A double-edged sword, *Chemical Biological Interaction*, 188, 276-288, 2010.

UTTAR PRADESH JOURNAL OF ZOOLOGY

42(9): 50-59, 2021
ISSN: 0256-971X (P)

EVALUATION OF CYTOTOXICITY AND ANTI-CANCER ACTIVITY OF *Solanum torvum* STEM EXTRACT ON NORMAL VERO AND HUMAN BREAST CANCER MCF - 7 CELL LINE

D. SHANTHI[1], K. RAJA[1] AND R. SARAVANAN[1*]

[1]Department of Zoology, Dr Ambedkar Government Arts College, Vyasarpadi, Chennai 600039, Tamil Nadu, India.

AUTHORS' CONTRIBUTIONS

This work was carried out in collaboration among all authors. Author RS designed the study, performed the statistical analysis, wrote the protocol and wrote the first draft of the manuscript. Authors DS and KR managed the analyses of the study. Author DS managed the literature searches. All authors read and approved the final manuscript.

Article Information

Editor(s):
(1) Dr. Ana Cláudia Correia Coelho, University of Trás-os-Montes and Alto Douro, Portugal.
Reviewers:
(1) Md Sadique Hussain, Lovely Professional University, India.
(2) S. Mabel Parimala, St. Xavier's College, India.

Received: 20 February 2021
Accepted: 27 April 2021
Published: 01 May 2021

Original Research Article

ABSTRACT

Limited plants have been screened for their complete biological and pharmacological nature. In the present research investigation an attempt was made to decipher the medicinal value of aqueous extract of *Solanum torvum* (*S.torvum*) stem. Phytochemical screening of the aqueous extract of *S.torvum* stem in the present study ascertain the presence of flavonoids, phenols, saponins, alkaloids, coumarins, sterols, proteins and reducing sugars. Further, the potentiality of aqueous extract of *S.torvum* stem was assessed for its cytotoxic effect on Normal Vero cell line and anticancer activity on Human breast adenocarcinoma cell line by 3-(4,5dimethylthiazole-2-yl)-2,5-diphenyl tetrazolium bromide assay and compared with normal drug target doxorubicin. A 24-hour incubation cell proliferation study reduced the cell viability of MCF-7 breast cancer cell lines. *In vitro* studies on cytotoxicity analysis on Vero cell line revealed that the aqueous stem extract of *S.torvum* show mild toxicity and further it was found to be effective in the prevention of cell proliferation by MCF-7 cell lines.

Keywords: Phytochemical analysis; doxorubicin; cell viability; tryphan blue; selectivity index.

**Corresponding author: Email: rsaravanan51283@yahoo.com;*

1. INTRODUCTION

Cancer is still a growing health problem world-wide characterized by their regular proliferation of the cells, as a cell progresses from normal to cancerous tissue, the biological imperative to survive and perpetuate drives fundamental changes in cells behavior [1]. In 2012, it was estimated that there were 14 million new cases and 8.2 million cancer related deaths and by the year 2050, this could increase to 27 million cases, 17 million deaths and 75 million persons living with cancer [2]. Breast cancer is the second leading cause of mortality among women. Breast cancer is generally treated in recent days by radiotherapy, hormonal or chemotherapy. Intensive therapy with chemotherapeutical agents usually results in adverse effects [3].

Doxorubicin (Dox) is one of the most effective agents in the treatment of breast cancer patients, even if it shows severe side effects in the form of typhlitis, cardiotoxicity, nephrotoxicity, hepatotoxicity and other toxicities. Dox is an anthracyclin antibiotic, which remains an important agent in many chemotherapy regimens [4]. Although Dox is currently considered to be one of the most effective agents in the treatment of human breast cancer, its chemotherapeutic use is associated with severe side effects to non tumor tissues, such as the heart, liver, and kidney, thus greatly limiting its clinical application [5].

Nature becomes a great source of medicinal treatment for millions of years. Much of the world's biological diversity remains unexplored as a source of novel biological compounds and the search for new bioactive agents from natural sources, including extreme environmental niches is expanding. Unique bioactive compounds have many pharmacological activities. Medicinal plants occupy an important position for being the paramount sources of drug discovery in the modern era. The medicinal value of herbal plants lies in bioactive substances called phytochemicals that produced infinite physiological action of human body immense therapeutic quality. Experimental animal studies indicate that many phytochemicals in plants are potential antioxidants and possess anticancer properties [6].

Solanum is the largest genus in the family Solanaceae, comprising of about 2000 species distributed in the subtropical and tropical regions of the world. *S. torvum* belongs to the family Solanaceae and is distributed throughout the Southern parts of India. It is common name is Turkey berry and known as Sundaikkai in Tamil and Bhankatiya in Hindi. This is a shrub which grows upto 5 mt tall and cultivated in the tropics for its tasty immature fruits [7]. Many plants of this family are economically significant species and have received considerable attention in chemical and biological studies.

Several pharmacologically active potential chemical compounds which include flavonoids, steroidal saponins, steroidal alkaloids, sterols, lignans, phenolic compounds, coumarins terpenes, and glycosides have been identified from this genus which present wide range of pharmacological activities to different tumors such as breast cancer, colorectal cancer and prostate cancer cell lines [8]. Secondary metabolite compounds like alkaloids, sapogenin, chlorogenin, solasodine, solamargine, solanine and tomatidine were isolated from leaf and stem of *Solanum* species [9,10].

Clinical research revealed that nutraceutical factors can defend cancers. The antioxidant power of herbal resources and their bioactive compounds, have been linked to their potentialities to inhibit multiplication of oncogenic cells by minimizing oxidative stress, which may play key role in the progression of cellular disintegration underlying tumor growth. Research reports have identified that antioxidant supplementation may inhibit breast cancer recurrence and mortalities [11]. Pharmacological studies reveal that the stem, roots and fruits of *S. torvum* have cytotoxic, anti-tumor, anti-bacterial, anti-viral and anti-inflammatory properties [12].

Studies reported earlier on *S. torvum* highlights extensively on the pharmacological properties of its fruits using various solvent systems on cancer cell lines and was found to be extremely effective in the prevention of cell proliferation of the mammary gland breast adenocarcinoma cell lines [13]. Studies pertaining to the pharmacologic action of aqueous extract of stem of *S. torvum* on Vero and MCF-7 cell lines are scanty. In this study an attempt was made to find the effect of aqueous extract of *S. torvum* stem on normal Vero and MCF-7 cell lines to unravel the cytotoxic effect and the anticancer activity respectively.

2. MATERIALS AND METHODS

2.1 Collection and Identification of Plant Material

Stems of *S. torvum* used for the study were collected from in and around Kanchipuram District, Tamil Nadu during the months of February and March, 2018. Fresh plant specimen collected was authenticated by Dr.P.Jayaraman, Director, Plant Anatomy Research Center, Tambaram, Chennai (Registration No.PARC/2018/3855).

2.2 Extraction of Plant Material

The plants were freshly collected, the stem portions were separated from the shoots. The stems were washed with running tap water and rinsed in distilled water. The stems were shade dried for two week complete dryness. The dried stems were powdered, using mechanical grinder. They were ground well to fine powder and then transferred into air-tight containers until further use.

2.3 Cold Extraction

5 g of *S. torvum* dried stem powder was soaked in 50ml of distilled water in a 250ml conical flask. The flask was plugged with cotton wool and aluminium foil. The conical flask was placed in a shaker for 24 h. The extract was filtered using Whatman filter paper to get the crude plant extract of the stem. The filtered extract in the form of concentrated paste were used for the study. The aqueous extract was evaluated for preliminary phytochemical screening [14].

2.4 Procurement and Maintenance of Cell Lines

Normal Vero (African green monkey kidney) and MCF-7 cell lines were procured from National Centre for Cell Sciences (NCCS), Pune, India. The cell lines procured were maintained at Life Teck Research Centre, Arumbakkam, Chennai, Tamilnadu, India. The cells were maintained in Minimal Essential Media (MEM) and were supplemented with 10% Fetal Bovine Serum (FBS), Penicillin (100 IU / ml) and Streptomycin (100 µg/ml) in a humidified atmosphere of 5% CO_2 at 37°C.

2.5 Cell Viability Assay: *In vitro* Studies

Aqueous extract of *S. torvum* stem was analyzed for its cytotoxicity in Normal Vero cell line and for Anticancer activity in MCF-7 cell line based on the principle of (MTT) assay [15].

2.6 Maintenance of Vero and MCF-7 Cell Lines

Cells (1×10^5/well) were plated in 24-well plates and incubated in 37°C with 5% CO_2 condition. After the cell reaches the confluence, the prepared sample plant extract was added and incubated for 24 h. After incubation, the sample was removed from the well and washed with phosphate-buffered saline (pH 7.4) 100 µl/well without serum. 5mg/ml of 0.5% (MTT) was added and incubated for 4 h. After incubation, 1.0 ml of 0.1% DMSO was added to all the wells. The absorbance at 570 nm was measured with UV-spectrophotometer using DMSO as the blank in triplicates. Measurements were performed and the concentration required for a 50% inhibition (IC_{50}) was determined. Standard drug Doxorubicin was used to compare the cell viability of the stem extracts. Cell control and sample control is included in each assay to compare the complete the cell viability assessments.

The % cell viability was calculated using the following formula:

% Cell Viability =
Absorbance of sample / Absorbance of control cells × 100

2.7 Morphological Studies of Vero and MCF-7 Cells after 24 h Incubation

The aqueous stem extract-treated cell lines (Normal Vero and MCF-7) were observed and photographed under inverted animal cell culture microscope (LABOVERT-FS) under 40 x objective.

2.8 Cell Viability Analysis - Trypan Blue Dye Exclusion Method

A simple cell count method was performed to assess live and dead cells using hemocytometer and Trypan blue, a vital dye. This assay was based on the assumption that the dead cells will take up the dye and viable cells will not take up dye [16]. Cell count was performed for MCF-7 cell lines treated with aqueous stem extract by staining with trypan blue dye. The dead and live cells counted were obtained from the IC_{50} concentration at the end of 24 h incubation. The percentage of viable cells (live cells) and non-viable cells (dead cells) from the aqueous extract treated cell line were calculated. The percentage growth inhibition was calculated as using the following formula

% Growth Inhibition (Dead cells) =
Total Cells - Dead Cells / Total Cells × 100

2.9 Determination of Selectivity index (SI):

The degree of selectivity of the aqueous extract of *S. torvum* stem is expressed by its SI value. The SI value was calculated based on the effect of the extraction Normal Vero cell line and MCF- 7 cell line [17]. The SI value of the extract was calculated using the formula:

SI = CC_{50} normal vero cell line / IC_{50} cancer cell line

Cytotoxic concentration of (CC_{50}) of normal Vero cell line and inhibitory concentration (IC_{50}) of MCF-7 cell line.

3. RESULTS

Phytochemical analysis of the aqueous extract of *S. torvum* stem showed the presence of various specific phytoconstituents such as flavonoids, alkaloids, phenols, saponins, coumarins, sterols, proteins and reducing sugars (Table 1).

3.1 Cytotoxicity and Anti-Cancer Activity of Aqueous Stem Extract of *S. torvum* on Normal Vero

3.1.1 Cell line and MCF -7 cell line

The percentage cell viability shown by Vero cell line treated with aqueous stem extract was 97.96% at 7.8 µg/ml and 52.03% at1000 µg/ml. The IC_{50} was also recorded at 1000 µg/ml during 24 h of incubation (Fig. 1). Normal Vero cells treated with doxorubicin showed maximum cell viability at 1000 µg/ml with a minimal cell death. The results of Vero cell lines were statistically significant ($p< 0.05$) when compared among the various concentrations treated with stem extracts.

The MCF-7 cells treated with the stem extract showed percentage cell viability of79.78 % at 7.8 µg/ml and 29.25 % at 1000 µg/ml. The IC_{50} is value of 50.17 % reported at 125 µg/ml concentration at 24 h of incubation (Fig. 2). The reference standard drug doxorubicin treated with the stem extracts showed percentage cell viability of 55.89 % at 7.8 µg/ml and 12.29 % at 1000 µg/ml. The IC_{50} value of 49.17 % was reported at 125 µg/ml.

The statistical significance was calculated among the various concentrations of Doxorubicin ($p< 0.05$) treated with stem extracts , MCF-7 treated with stem extracts ($p< 0.05$) and between the various concentrations of doxorubicin and MCF-7 treated with stem extracts ($p< 0.05$).

Table 1. Phytochemical screening of aqueous extract of S. *torvum* stem

S.No	Phytochemical compounds	*S.torvum* stem extract
1	Flavanoids	+
2	Alkaloids	+
3	Phenols	+
4	Coumarin	+
5	Triterpenes	-
6	Saponins	+
7	Steroids	+
8	Proteins	+
9	Reducing Sugars	+
10	Anthraquinones	-
11	Anthocyanins	-
12	Tannins	-

Presence of the compound (+) and absence of the compound (-)

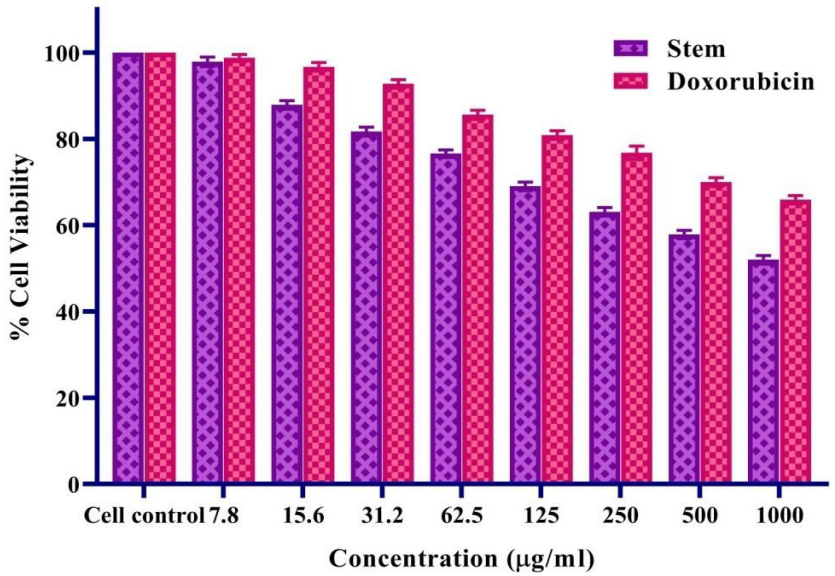

Fig. 1. Graph representing the cytotoxicity of *S. torvum* aqueous stem extract on normal Vero cell line at 24 h incubation compared with Doxorubicin. Values expressed as Mean ± SD (n = 3)

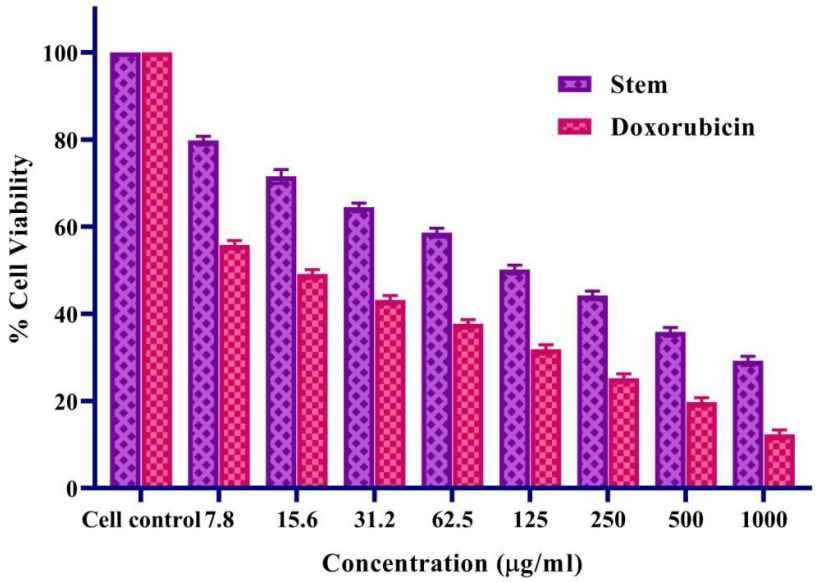

Fig. 2. Graph representing the anticancer activity of *S. torvum* aqueous stem extract on MCF-7 cell line at 24 h incubation compared with Doxorubicin. Values expressed as Mean ± SD (n = 3)

3.2 Morphological Studies of Vero Cells Treated with Aqueous Extract of *S. torvum* stem

Vero cells are uniformly spread in confluent layer with long and elongated shape in appearance. At highest concentration of 1000 µg /ml of stem extract the treated cells lose their normal cytostructure and show polygonal shape with shrunken cells at the end of 24 h incubation (Fig. 3).

3.3 Morphological Studies of MCF-7 Cells Treated with Doxorubicin

MCF-7 cells treated with DOX show changes in cell cytostructure and loss of cells as the concentration increases which substantiates a dose-dependent effect (Fig. 4).

3.4 Morphological Studies of MCF-7 Cells Treated with Aqueous Extract of Stem

MCF-7 cells treated with different concentrations of the extract show reduction in number of cells as the concentration increases. Cells show loss of regular shape and size. Majority of cells are with flattened structures with cell to cell contact disappearing (Fig. 5).

3.5 Cell Count of Live and Dead Cells by using Trypan Blue Dye Exclusion Method

MCF-7 breast cancer cell line treated with aqueous extract of stem show variation in the number of live and dead cells. The cell viability was 53.84% and cell death was 46.16% at IC_{50} concentration of 125µg /ml (Table 2).

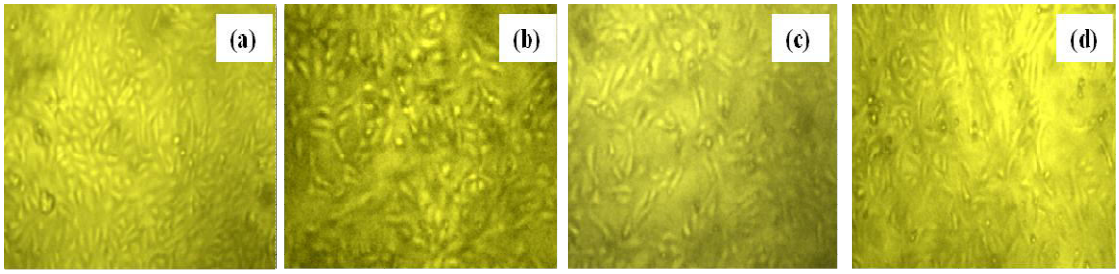

Fig. 3. Photomicrograph of *S. torvum* aqueous extract of stem on the morphology of normal Vero cell line at different concentrations (a) Control (b) 7.8 µg/ml (c) 125 µg/ml (d) 1000µg/ml

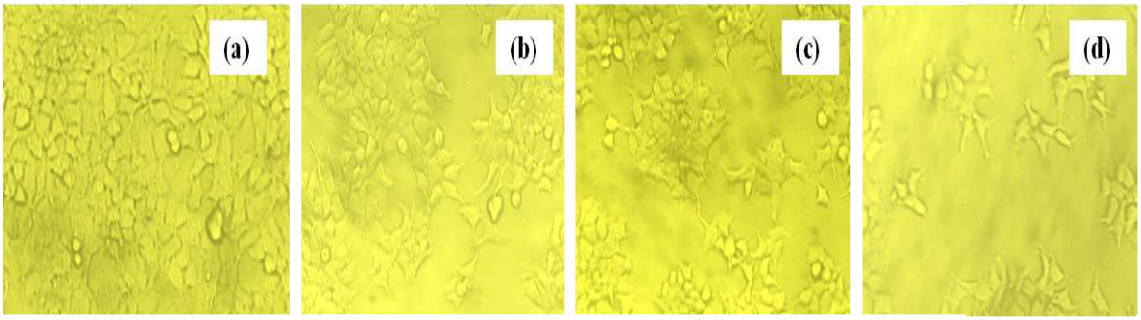

Fig. 4. Photomicrograph representing anticancer effect of Doxorubicin on MCF-7 cell line at different concentrations (a) Control (b) 7.8 µg/ml (c) 125 µg/ml (d) 1000µg/ml

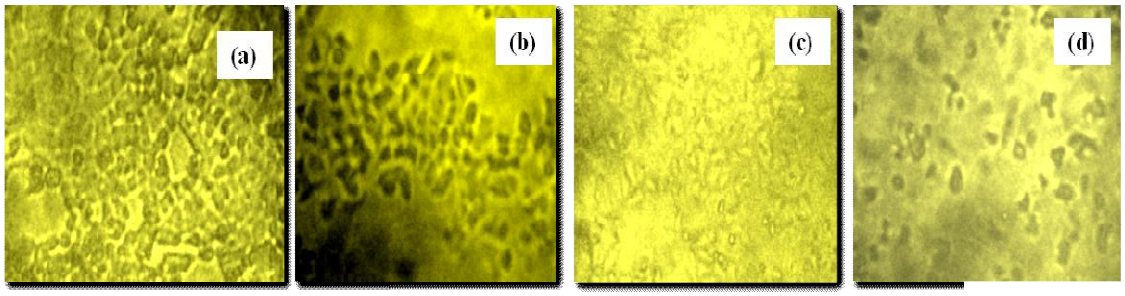

Fig. 5. Photomicrograph of *S. torvum* aqueous extract of stem on the morphology of MCF-7 cell line at various concentrations (a) Normal MCF-7 Cell line (b) 1000µg/ml (c)125 µg/ml (d) 7.8 µg/ml

Table 2. Cell count to observe live and dead cells of MCF-7 cell line treated with aqueous extract of *S. torvum* stem by Trypan blue dye at IC_{50} concentration

No of live cells	142
No of dead cells	123
% Cell viability	53.84
% Cell death	46.16

3.6 Selectivity Index (SI)

The SI for (CC_{50}) of Vero cell line and (IC_{50}) of MCF-7 cell line for cells treated with aqueous extract of stem was 8 after 24 h of incubation (Table 3).

Table 3. SI of (CC_{50}) of normal Vero cell line and (IC_{50}) of MCF-7 cell line treated with aqueous extract of stem of *S. torvum* at 24 h of incubation

CC_{50} of Vero (µg/ml)	1000
IC_{50} of MCF-7(µg/ml)	125
SI	8

4. DISCUSSION

The major health concern of the 21st century is cancer, which has no boundaries and can affect any human organ. It is a very complex disease to understand because it has many cellular physiological systems such as cell signaling and apoptosis. The most common cancer treatments are chemotherapy, hormone therapy, radiation and surgery. Chemotherapy, the most popular treatment provides patients with systemic anti-cancer drugs to manage uncontrolled cancer cell proliferation [18].

The raw materials from the herbals form the base for drug production in pharmaceuticals. Understanding of the interaction of various constituents of medicinal herbs, would help in formulating and designing drug to act on the cancerous cells without harming the normal cells of the body [19,20].

In the present study cytotoxicity analysis on Vero cell line revealed that the aqueous stem extract of *S. torvum* exhibited 50% toxicity at the maximum concentration. The CC_{50} was found at 1000 µg/ml for Normal Vero cell line when treated with the aqueous extract of *S. torvum* stem at 24 h of incubation showed 50.32 % of cell viability and 49.68% cell death respectively.

The IC_{50} was found at 125 µg/ml for human breast cancer MCF-7 cell line when treated with the aqueous extract of *S. torvum* stem after 24 h of incubation. The MCF-7 cell line treated with aqueous extract of stem

show 51.70 % of cell viability and 48.30% cell death respectively. The extract was effective in reducing the cell viability of MCF-7 breast cancer cell lines. The IC_{50} was determined based on inhibitory concentration that induced 50% inhibition on the growth of the treated cells as compared to the untreated cells.

The phytochemical analysis in the present study shows presence of phytoconstituents such as flavonoids, alkaloids, phenols and saponins in the aqueous extract of stem which may have contributed to the anti-proliferative effect. The observed cytotoxic and anticancer action of the aqueous extract of *S. torvum* stem are in accordance with earlier studies carried out on the properties of *Solanum* phytoconstituents [21]. The phytocompounds isolated from Solanaceae family have been reported to possess several medicinal values, antioxidant and anticancer properties [22,23]. Flavonoids which prevent oxidative cell damage have shown to possess anti-proliferative role in cancer cells. This compound has profound effects on signal transduction mechanisms in cell proliferation and angiogenesis [24].

Solanum genus have also been shown to contain steroidal glycoalkaloids and steroidal saponins with significant cytotoxic and anti-tumor activities that have a close structural relationships [25]. Saponins react with cholesterol rich plasma membrane of cancer cells and inhibit their proliferation. Studies have demonstrated that several classes of compound including phenolic compounds, terpenes and coumaric acid may possibly act synergistically to inhibit cell proliferation and induce apoptosis in cancer cells [26]. The anti-proliferative effect observed in MCF-7 cell line in the present study can be attributed to the combined integrated mechanism of action of the phytochemicals present in *S. torvum* stem aqueous extracts. The qualitative analysis of these phytochemicals from the extract also substantiates this role.

Considerable amount of sterol content in aqueous extract of *S. torvum* stem have been reported. The anticancer activity of *S. torvum may* be attributed partially to steroidal alkaloid and steroidal saponins substances present in the stem [27].

The cytotoxic action indicates that the aqueous stem extract probably contain secondary metabolites or novel compounds which may inhibit cellular division in cancer cells [28]. Studies on *S. erianthum* revealed high cytotoxic and anticancer activity which is attributed to presence of compounds like flavonoids and phenols [29].

Aqueous extract of *S. torvum* stem was found to be extremely effective in the prevention of cell proliferation of breast adenocarcinoma cell lines. The extract if tested in animal models or administered in human may prevent cell proliferation by possible mechanism which could directly combine with cell receptor and elicit cellular apoptosis. Plant derived phytochemicals coupled with chemotherapy has gained much importance now-a-days in alleviating the proliferation of various carcinomas with minimal side effects [30].

Cell viability was also performed by staining the cells treated with trypan blue. The dead and live cells were counted from IC_{50} concentrations of 24 h incubation. About 53.84% live cells and 46.16% dead cells were identified. Trypan blue is water soluble dye and it is insoluble in membrane lipids. Chromophore is negatively charged and does not interact with cells unless the membrane is damaged. This could have been the possible mechanism in the present study when dead or non-viable cells show membrane damage and take up the dye whereas the viable cells do not take up the dye and are transparent as revealed from the cell count of the study [31].

Morphological alterations in Vero and MCF-7 cell lines clearly validated that extract of *S. torvum* induced drug dosage response in the present study. Microscopic observations clearly revealed Vero cells with regular shape and size at lower concentrations of the extract and with loss of their normal cytostructure at higher concentration. MCF-7 cells are seen in clusters, spindle shaped at lower concentrations. Cells with flattened structures are seen with increase in concentration of the extract at 24 h of incubation. The progressive changes seen are in a dose-dependent manner.

Cell morphological analysis indicated a significant loss of cell structure and disruption of cellular organelle integrity following treatment of the MCF-7 cell lines with aqueous extract of stem which can be correlated to non-viable cells exposed to trypan blue. Similar morphological changes were observed in MCF-7 cells treated with *Pongamia glabra* seed oil extract [32] and alkaloid extract of leaf from *Excoecaria agallocha* [33].

The degree of selectivity of the compounds is expressed by its SI value. The greater SI value (above 2) of a compound suggests selective toxicity and differential action against the target cells, while a compound with SI value (less than 2) indicates general toxicity of the pure compound which can also cause cytotoxicity in normal cells [34]. The IC_{50} values are used to determine the SI of each extract

which represents the overall activity between normal cell line and cancer cell line. The SI value for the present study on Normal Vero cell lines and MCF-7 breast cancer cell lines is calculated as 8 for cells treated with aqueous extract *S. torvum* of stem. 'Therapeutic index' is an important parameter to select samples for developing drugs [35,36].

Chemotherapy is routinely used for cancer treatment although its success is quite limited, due to severe side effects caused by drug resistance, targeting of healthy cells and metabolic stress. Dox increases the oxidative stress, which kills cancer cells and induces an inflammatory microenvironment, with cellular toxicity. Dox alone is not a preferable drug. A myriad of plant products have shown very promising anticancer properties *in vitro*, but they have yet to be evaluated in humans. However, some phytochemicals have shown a chemopreventive effect and the ability to sensitize cancer cells [37].

The results of the present study suggest that the uptake of the bioactive compounds from aqueous extract of *S. torvum* stem may suppress growth of cancer cells *in vitro* in breast cancer cell line MCF-7 and may prevent breast cancer development and proliferation induced by carcinogens. Isolation and characterization of specific bioactive compounds from the stem of this plant will be promising for its further development as an anticancer drug through molecular docking studies and in-silico predictions.

5. CONCLUSION

Information on ethnopharmacognosy is to gain knowledge for an effective method in the discovery of new anti-infective molecules from medicinal herbal plants.MCF-7 breast cancer cells serves as an excellent source of *in vitro* model for studying the mechanism of tumor response as well as complex relationships between binding and biological systems. This medicinal plant *Solanum torvum* can be considered for drug development and synthesis. The present information related with these secondary biomolecules will lead to new sources in search of lead molecules for curing cancer related ailments.

ACKNOWLEDGEMENT

The authors thank Dr. (Mrs). I. Seethalakshmi, Director, Life Teck Research Centre, Arumbakkam, Chennai, Tamilnadu for the laboratory assistance rendered in procurement and maintenance of cell lines used in the study. The authors are grateful to Tamil Nadu State Council For Higher Education (TANSCHE),Government of Tamilnadu, for the grant of financial assistance provided under the Teacher's Minor Research Project Scheme, 2017- 2018 for the conduct of this research work.

COMPETING INTERESTS

Authors have declared that no competing interests exist.

REFERENCES

1. Ashworth A, Christopher LJ, Reis-Filho S. Genetic interactions in cancer progressions and treatment. Cell. 2011;145(1):30-38.
2. Cancer Statistics. Available:http://www.cancer.gov/about-cancer/what-is-cancer/statistics Accessed on 21/04/2020.
3. Neves MP, Cravo S, Lima RT, Vasconcelos MH, Nascimento MS, Silva AM. Solid-phase synthesis of 21-hydroxychalcones. Effects on cell growth inhibition, cell cycle and apoptosis of human tumor cell lines. Bioorganic Medicinal Chemistry. 2012;20:25-33.
4. Iwamoto T. Clinical application of drug delivery systems in cancer chemotherapy: Review of the efficacy and side effects of approved drugs. Biological Pharmacology Bulletein. 2013;36:715 718.
5. Rashid S, Ali N, Nafees S, Ahmad ST, Arjumand W, Hasan SK, Sultana S. Alleviation of doxorubicin induced nephrotoxicity and hepatotoxicity by chrysin in Wistar rats. Toxicology Mechanics Methods. 2013;23:337 345.
6. Mahassni SH, Al-Reemi RM. Apoptosis and necrosis of human breast cancer cells by an aqueous extract of garden cress (*Lepidium sativum*) seeds. Saudi Journal of Biological Science. 2013;20(2):131-139.
7. Solowey E, Lichtenstein M, Sallon S, Paavilainen H, Solowey E, Lorberboum-Galski H. Evaluating medicinal plants for anticancer activity. Science World Journal. 2014;1-12.
8. Kaunda JS, Zhang YJ. The Genus *Solanum*: An ethnopharmacological, phytochemical and biological properties review. Natural Products Bioprospecting. 2019;9(2):77-137.
9. Chopra RN, Nayar SL, Chopra IC. Glossary of Indian medicinal plants, National Institute of Science Communication. New Delhi.1996;20-50.
10. Jaiswal BS. *Solanum torvum*: A review of its traditional uses, phytochemistry and pharmacology. International Journal of Pharmacy and Biological Sciences. 2012;3(4):104 -111.

11. Lee AV, Oesterreich S, Davidson NE. MCF-7 cells-changing the course of breast cancer research and care for 45 years. Journal of National Cancer Institute. 2015;107(7):1-8.
12. Khatoon N, Jain P, Choudhary AK. Phytochemical studies on seed and leaf extract of *Solanum torvum* (Sw). Indo American Journal of Pharmaceutical Research. 2015;5:1649-1653.
13. Jaikumar B, Jasmine R. A review on a few medicinal plants possessing anticancer activity against human breast cancer. International Journal of Pharmaceutical Technology and Research. 2016;9(3): 333-365.
14. Harborne JB. Phytochemical methods. In: Chapman &, Hall. New York. 1984;4-5.
15. Mosmann T. Rapid colorimetric assay for cellular growth and survival: Application to proliferation and cytotoxicity assays. Journal of Immunological Methods. 1983;65:55-63.
16. Jauregui HO, Hayner NT, Driscoll JL, Williams- Holland R, Lipsky MH, Gallen PM. Trypan blue dye uptake and lactate dehydrogenase in adult rat hepatocytes freshly isolated cells, Cell Suspensions and Primary Monolayer Cultures. *In-vitro*. 1981;17:1100-1110.
17. Badisa RB, Darling-Reed SF, Joseph P, Cooperwood JS, Latinwo LM. Selective cytotoxic activities of two novel synthetic drugs on human breast carcinoma MCF-7 cells. Anticancer Research. 2009;29:2993-2996.
18. Kalaiyarasi D, Manobharathi V, Mirunalini S. Development of nano drugs: A promising avenue for cancer treatment. Research Journal of Biotechnology. 2021;16(4):234-244.
19. Isha S, Monika T, Avinash R, Astha T. Antimicrobial, Antioxidant and bioactive compounds from four Folk medicinal plants of Solan, Himachal Pradesh, India. Research Journal of Biotechnology. 2021;16(4):44-51
20. Biswas J, Roy M, Mukherjee A. Anticancer drug development based on phytochemicals. Journal of Drug Discovery, Development and Delivery. 2015;2(1) :1-6.
21. Badmus JA, Ekpo OE, Hussein AA, Meyer M, Hiss DC. Cytotoxic and cell cycle arrest properties of two steroidal alkaloids isolated from *Holarrhena floribunda* (G. Don) leaves. BMC Complementary and Alternative Medicine. 2019;19:112-120
22. Kalebar VU, Hoskeri JH, Hiremath SV, AB Kalebar RV, Sonappanavar KL, Agadi BS. Pharmacognostical and phytochemical analysis of *Solanum macranthum* (Dunal) Fruits. J Pharmacognsy and Phytochemistry. 2019;8:284–290.
23. Kalebar VU, Joy H. Hoskeri, Shivaprakash V. Hiremath, Murigendra B. HiremathMB. *In-vitro* cytotoxic effects of *Solanum macranthum* fruit. Dunal Extract with Antioxidant Potential. Clinical Phytoscience. 2020;6:24- 29
24. Pandey S. *In vivo* antitumor potential of extract from different parts of *Bauhinia variegate* Linn. against b16f10 melanoma tumor model in c57bl/6 mice. Applied Cancer Research. 2017;37:33-39
25. Omran R, Al-Taee ZM, Hayder O Hashim, Al-Jassani MJ. Extraction of phenolic compounds as antioxidants from some plants and their cytotoxic activity against breast cancer cell line. Asian Journal of Pharmaceutical and Clinical Research. 2017;10(7):349-355.
26. Jayakumar K, Murugan.K. Evaluation of major phytochemicals in the leaves and fruits of *Solanum mauritianum* Scop.: A potential herbal drug. International Journal of Research in Ayurveda and Pharmacy. 2016; 7(2):58-60.
27. Kalebar VU, Hoskeri JH, Hiremath SV, Hiremath MB. *In vitro* antiproliferative effect of aqueous extract of *Solanum macranthum* fruits on MDA-MB-231 triple negative breast cancer cell line. Journal of Applied Biology and Biotechnology. 2020;8(1):28–32.
28. Panigrahi, Muthuraman MS , Natesan R, Pemiah B. Anticancer activity of ethanolic extract of *Solanum torvum* (Sw). International Journal of Pharmacy and Pharmaceutical Sciences. 2014;6 (1):93-98 .
29. Radhika M, Ramakrishnaiah H, Krishna V, Deepalakshmi AP, Naveen Kumar S. Cytotoxic activity of methanolic extract of *Solanum erianthum*. International Journal of Pharmacy and Pharmaceutical Science. 2015;7(2):106-108
30. Fekry MI, Ezzat SM, Salama MM, Alshehri OY, Al-Abd AM. Bioactive glycol alkaloides isolated from *Solanum melongena* fruit peels with potential anticancer properties against hepatocellular carcinoma cells. Science Reports. 2019;9:1-11.
31. Chung DM, Kim JH, Kim JK. Evaluation of MTT and Trypan blue assays for radiation induced cell viability test in HepG 2 cells, International Journal of Radiation Research. 2015;13(4):331-335.
32. Arulvasu C, Vasantha Suppriya S, Babu G. Anticancer activity of *Pongamia glabra* seed oil extract against selected human cancer cell lines. International Research Journal of Pharmacy. 2012;3(8):131-134
33. Deepa M, Darsan MB, Ramalingam C. *In vitro* evaluation of the antioxidant, anti-

inflammatory and antiproliferative activities of the leaf extract of *Excoecaria agallocha* L. International Journal of Pharmacy and Pharmaceutical Sciences. 2016; 7(11):346-352.

34. Wardihan, Rusdi M, Alam G, Lukmanand A, Manggau M. Selective cytotoxicity evaluation in anticancer drug screening of *Boehmeria virgata* (Forst) guill leaves to several human cell lines: HeLa, WiDr, T47D and Vero. Dhaka University Journal of Pharmaceutical Science. 2013;12(2):87-90.
35. Artun FT, Karagoz A , Ozcan G, Melikoglu G, Anil S, Kultur S, Sutlupinar N. *In vitro* anticancer and cytotoxic activities of some plant extract on HeLa and Vero cell lines. Journal of Balkan Union of Oncology. 2016;21(3):720-725
36. Senthilraja P, Kathiresan K. *In vitro* cytotoxicity MTT assay in Vero, HepG2 and MCF -7 cell lines study of marine yeast. Journal of Applied Pharmaceutical Science. 2015;5(3):80-84.
37. Zeinoddini S, Nabiuni M, Jalali H. The synergistic cytotoxic effects of doxorubicin and *Viola odorata* extract on human breast cancer cell line T47-D. Journal of Cancer Research and Therapeutics. 2019;15: 1073-1079.

Antioxidant potential of aqueous extract of immature fruit and developing shoot of *Solanum torvum* (*Swartz*)

D. Shanthi, K. Raja and R. Saravanan
Post Graduate and Research Department of Zoology,
Dr Ambedkar Government Arts College, Vyasarpadi, Chennai 600039,Tamil Nadu
email: rsaravanan0268@gmail.com
Corresponding author: Dr R. Saravanan

ABSTRACT

The role played by free radicals which are highly reactive oxygen species has become increasingly relevant in various of degenerative diseases. Focus on natural antioxidants in medicinal plants are gaining momentum in present days reflecting the immense valuability of Ayurveda, Naturopathy and Siddha medicine in treatment of ailments. The present study will focus on the antioxidant potential of aqueous extract of *Solanum torvum* immature fruits and developing shoot which contribute to the scavenging of free radicals. *In vitro* antioxidant potential of aqueous extracts of *Solanum torvum* immature fruits and developing shoot was assessed by 1,1-Diphenyl-2-Picryl hydrazyl (DPPH), Superoxide anion and Nitric oxide (NO_2) at various concentrations (200 µg, 400 µg, 600 µg, 800 µg and 1000 µg). In the present study a significant antioxidant potential was found in the aqueous extracts of immature fruits.

Keywords: *Solanum torvum*, immature fruits, developing shoots, *in vitro* antioxidant activity, DPPH, Superoxide anion and nitric oxide.

Introduction

Herbals are considered to be promising source of medicine in the traditional healthcare system. The efficacy and safety of herbal medicine have turned the major pharmaceutical population towards medicinal plant research. There is a need for more effective, less toxic and cost effective antioxidants and antimicrobials from natural sources to treat various non- communicable and communicable diseases (Singh et al., 2002).

. The role played by free radicals which are highly reactive oxygen species has become increasingly relevant. They initiate or propagate development of diseases such as cancer, liver and cardiovascular disorders. The oxidation induced by reactive oxygen species can result in cell membrane disintegration, membrane protein damage and DNA mutation (Jayakumar et al ., 2016a). Antioxidants with free radical scavenging activity play an important role in protecting damage by reactive oxygen species (Darkwah et al., 2018).

Solanum torvum (*S.torvum*) have revealed cytotoxic activities, antimicrobial, anti-viral activity, anti- inflammatory and anti-tumour (anticancer) activity (Joseph Sakah Kaunda and Ying-Jun Zhang,2019) . The present study will focus

on the free radical scavenging activity of aqueous extract of *S.torvum* immature fruits and developing shoots which contribute to the quenching of free radicals.

Materials and Methods

Collection and Identification of Plant Material

Immature fruits and developing shoots of *S.torvum* (Plate-1) used for the study were collected from in and around Kancheepuram District, Tamil Nadu during May 2018. Fresh plant specimens collected were authenticated by Dr. P. Jayaraman, Director, Plant Anatomy Research Center, Tambaram, Chennai. Registration No. (PARC/2018/3855).

Plate 1: ***Solanum torvum*** **plant**

Processing and Preservation of Plant Materials

Immature fruits and developing shoots of *S.torvum* (Plate- 2) were separated from freshly collected plants, washed in running tap water and rinsed in distilled water. The plant materials were chopped into small pieces and were shade dried for two weeks for complete dryness. The dried plant materials were powdered, using mechanical grinder. They were ground well to fine powder and then transferred into airtight containers until further use.

Plate 2 : Dried immature fruit and developing shoot of ***Solanum torvum***

Preparation of Aqueous Extract: Cold Water Extraction

5 gm powdered samples of *S.torvum* dried immature fruits and developing shoots were soaked and dissolved in 50 ml of distilled water in a 250 ml conical flask. The flask was plugged with cotton wool and aluminium foil and was placed in a shaker for 24 hrs. The filtrate was concentrated in a Soxhlet apparatus to get the crude plant extracts. The extract was filtered using Whatman filter paper No1. The filtered extracts in the form of a concentrated paste was used for the study.

Determination of *in vitro* Antioxidant Activity of *Solanum torvum*

The aqueous extracts of dried immature fruits and developing shoots of *S.torvum* was assayed for antioxidant activity by the following methods. DPPH radical scavenging activity (Clarke et al., 2013), Superoxide anion radical scavenging assay (Nishimiki et al., 2002) and NO_2 radical scavenging assay (Garret,1974)

Results

The antioxidant potential of the aqueous extracts of immature fruits and developing shoots of *S.torvum* was assessed at various concentrations of 200 µg ,400 µg ,600 µg, 800 µg and 1000 µg by *in vitro* studies.

DPPH radical scavenging activity

The reaction capability of DPPH radical scavenging activity was determined by the decrease in its absorbance induced by antioxidants. At 200–1000 µg, the antioxidant activities of the aqueous extract of *S.torvum* immature fruits ranged from 25.85% to 49.43%. and for developing shoots from 20.84% to 39.83% and the standard BHT were 61.53% and 27.03 - 89.04%, respectively (Table -1, Figure- 1). Aqueous extract of *S.torvum* immature fruits show higher antioxidant activity when compared to the developing shoot extracts.

Table 1: DPPH radical scavenging activity of aqueous extract of immature fruit and developing shoot of *Solanum torvum*

Concentration (µg/ml)	BHT	Immature Fruit	Developing Shoot
200	61.53 ± 0.01	25.85 ± 0.01	20.84 ± 0.02
400	67.62 ± 0.01	31.73 ± 0.02	22.72 ± 0.01
600	74.87 ± 0.02	39.82 ± 0.02	29.17 ± 0.01
800	82.57 ± 0.01	42.51 ± 0.01	35.71 ± 0.01
1000	89.04 ± 0.02	49.43 ± 0.01	39.83 ± 0.01

Values are Mean ± SD of three (n = 3) independent analysis of the extract
Values expressed as % radical scavenging activity

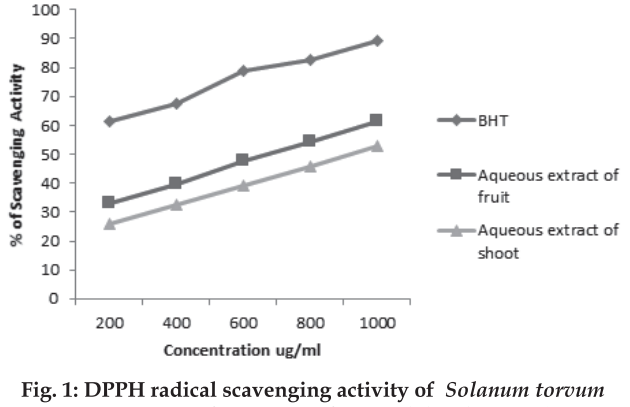

Fig. 1: DPPH radical scavenging activity of *Solanum torvum* aqueous extract of immature fruit and developing shoot

Superoxide anion radical scavenging activity

At 200–1000 µg, the superoxide radical scavenging activity of aqueous extracts of *S.torvum* immature fruits was varied from 31.41 % – 52.27% and that of the standard ascorbic acid was 57.29 % – 95.70 %. Radical scavenging activity of aqueous extracts of *S.torvum* developing shoots was 25.15 % at 200 µg concentration of the extract and at 1000 µg concentration of the extract it was found to be 41.73% (Table -2; Figure- 2). From 400 µg to 1000 µg superoxide anion radical scavenging activity was higher in the aqueous extracts of fruits.

Table 2: Superoxide anion radical scavenging activity of aqueous extract of immature fruit and developing shoot of *Solanum torvum*

Concentration (µg/ml)	Ascorbic acid	Immature Fruit	Developing Shoot
200	57.29 ± 0.12	31.41 ± 0.01	25.15 ± 0.01
400	67.83 ± 0.05	36.35 ± 0.01	32.61 ± 0.01
600	78.32 ± 0.01	44.73 ± 0.02	39.45 ± 0.03
800	85.92 ± 0.02	47.57 ± 0.06	40.45 ± 0.02
1000	95.76 ± 0.02	52.27 ± 0.01	41.73 ± 0.02

Values are Mean ± SD of three (n = 3) independent analysis of the extract
Values expressed as % radical scavenging activity

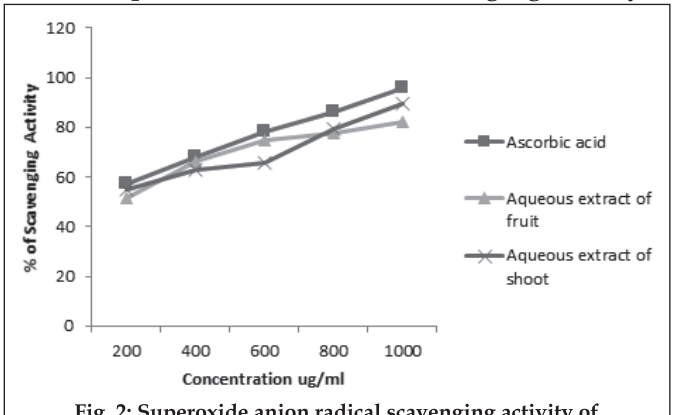

Fig. 2: Superoxide anion radical scavenging activity of *Solanum torvum* aqueous extract of immature fruit and developing shoot

NO_2 radical scavenging activity

The nitric oxide scavenging activity of aqueous extracts of *S.torvum* immature fruits was minimal at

29.57% at 200 µg concentration of the extract, whereas the maximum activity was 55.12% at 1000 µg concentration of the extract. *In vitro* nitric oxide scavenging activity of aqueous extracts of *S.torvum* developing shoots was 19.38% at 200 µg concentration of the extract and 41.21 % at 1000 µg concentration of the extract (Table -3; Figure- 3). The percentage antioxidant potential was higher in the aqueous extracts of *S.torvum* immature fruits when it was compared with the developing shoots.

Table 3: NO_2 radical scavenging activity of aqueous extract of immature fruit and developing shoot of *Solanum torvum*

Concentration (µg/ml)	Ascorbic acid	Immature Fruit	Developing Shoot
200	22.56 ± 0.02	29.57 ± 0.01	19.38 ± 0.01
400	34.41 ± 0.01	39.51 ± 0.05	25.19 ± 0.01
600	43.02 ± 0.01	44.41 ± 0.01	29.81 ± 0.01
800	54.84 ± 0.01	47.02 ± 0.05	35.51 ± 0.01
1000	66.56 ± 0.13	55.12 ± 0.01	41.21 ± 0.01

Values are Mean ± SD of three (n = 3) independent analysis of the extract; Values expressed as % radical scavenging activity

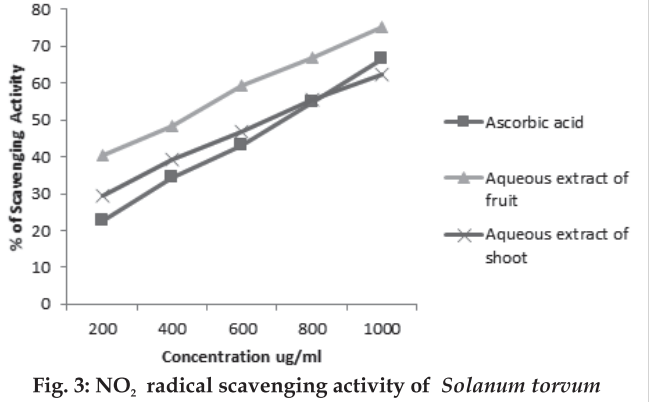

Fig. 3: NO_2 radical scavenging activity of *Solanum torvum* aqueous extract of immature fruit and developing shoot

Discussion

The results obtained from the present study indicates that the aqueous extracts of immature fruit and developing shoot of *S.torvum* possess antioxidant properties and could serve as free radical inhibitors or scavengers, or act as primary antioxidants (Kannan. et al ., 2012; Abdul Aziz et al .,2016) DPPH is widely used to evaluate the free radical scavenging capacity (Abdul kadir et al ., 2015). The aqueous extracts of *S.torvum* immature fruit and developing shoot exhibited concentration-dependent radical scavenging activity. The antioxidant potential of aqueous extract and BHT as reference solution was evaluated for its ability to quench the synthetic DPPH radical in the present study.

The antioxidant potential increases with an increase in the concentration of the extracts. Dose-dependent DPPH scavenging activity of was reported. The proton radical scavenging action is known to be one of the various mechanisms for measuring antioxidant activity (Fitriansyah et al., 2018). Earlier studies show hydro-alcoholic extract of Desmodium gangeticum have the proton-donating ability and can serve as free radical inhibitors or scavenger, acting possibly as primary antioxidant (Usha and Suriyavathana, 2012). The reaction of DPPH with aqueous extracts of S.torvum immature fruit and developing shoot was slower when compared to BHT.

The antioxidant potential of aqueous extract of *S.torvum* immature fruit and developing shoot was analysed for the extracts potential to scavenge superoxide anions. The aqueous extract of *Solanum torvum* immature fruit and developing shoot exhibited concentration-dependent radical scavenging activity, which show an increase in percentage inhibition with an increase in concentration, being compared with the standard ascorbic acid.

Superoxide anions is one of the potent reactive oxygen species which are produced from molecular oxygen. They are involved in the formation of hydrogen peroxide, hydroxyl radical and singlet oxygen (Hemmani and Parihar ,1998). These compounds induce oxidative damage to biomolecules such as lipids, protein and nucleic acids associated with cellular structures of the living organisms (Nishimiki et al., 2002). Results of this study clearly indicates that aqueous extract of *S.torvum* immature fruit and developing shoot is a potent scavenger of superoxide radicals.

The present study show an increase in percentage inhibition of free radical scavenging activity of NO_2 with increasing concentration of the aqueous extract of *S.torvum* immature fruit and developing shoot. The activity of synthetic antioxidant ascorbic acid was more pronounced than that of the extract which indicates the dose-dependent antioxidant potential of nitric oxide.

Nitric oxide is another free radical produced in mammalian cellular system involved in regulation of various physiological processes. Several degenerative diseases are associated with its increased production (Nathan,1992). The development of drugs to target and prevent its overproduction is gaining importance for treating various chronic inflammatory diseases (Shen et al., 2002). In the present study, the aqueous extract of *S.torvum* was assessed for its inhibitory effect on nitric oxide production. Nitric oxide radical generation was inhibited by immature fruit and developing shoot aqueous extract of *S.torvum*. The percentage inhibition of nitric oxide by the immature fruit extracts of *S.torvum* seems to be more predominant in the study.

Antioxidant activity of the alkaloids in plant S mauritianum has been reported against hydrogen peroxide induced oxidative damage in human erythrocytes (Jayakumar. et al ., 2016b). Flavonoid compounds which contain hydroxyl functional groups, are responsible for the antioxidant effect in plants (Kalita et al.,2012) Phytochemical compounds present in the aqueous extract of *S.torvum* immature fruit and developing shoot are likely to contribute to the antioxidant potential of aqueous extract (Gandhiappan and Rengasamy 2012; Thenmozhi, and Mahadeva Rao, 2012).

Conclusion

Plants are considered to be promising source of medicine in the traditional healthcare system. The present study indicates the antioxidant potential of aqueous extracts of unripe immature fruit and developing shoots of *S.torvum* which paves way to test whether it serves as inhibitors, scavengers or act as primary antioxidants in prevention of free radical formation.

Acknowledgement

The authors are grateful to **Tamilnadu State Council For Higher Education (TANSCHE)**, Department of Higher Education, Government of Tamilnadu, for the grant of financial assistance under the Teacher's Minor Research Project Scheme during the year 2017- 2018.

References

1. Abdul Aziz R. Abdul Kadir , Nashriyah Mat, Md M. Hasan and Md S. Jahan, 2016 *In vitro* antioxidant activity of the ethanolic extract from fruit, stem and leaf of *Solanum torvum*. Sci Asia; 42: 184-189
2. Abdul kadir A R, D D Zawawi, A K Yunusa and M S Jahan 2015 *In vitro* anti-oxidant potential, total phenolic content and total flavonoid content of methanolic flower and seed extract of miracle tree (*Moringa Oleifera* Lam.). *Aust J Basic Appl Sci*, 9: 27–31
3. Clarke G, K N, Ting, C Wiart and J Fry 2013. High correlation of 2,2-diphenyl-1-picrylhydrazyl (DPPH) radical scavenging, ferric reducing activity potential and total phenolics content indicates redundancy in use of all three assays to screen for antioxidant activity of extracts of plants from the Malaysian rainforest. *Antioxidants*; 2: 1–10.
4. Darkwah W K, M B Adinortey, A Weremfo, F K Abrokwah and E Afriyie, 2018 Total phenolic, flavonoid and alkaloid contents, oxidative DNA damage protective and antioxidant properties of methanol and aqueous extracts of *Dissotis rotundifolia* whole plant. *Free Radicals Antioxidants*; 8(2): 55-59
5. Fitriansyah SN, D L Aulifa, Y Febriani and E Sapitri. 2018 Correlation of total phenolic, flavonoid and carotenoid content of *Phyllanthus emblica* extract from bandung with DPPH scavenging activties. *Pharmacog J*, 10(3): 447-452

6. Gandhiappan J and R Rengasamy 2012 Comparative study on antioxidant activity of different species of Solanaceae family. Adv *Appl Sci Res*; 3:1538–1544.
7. Garret DC.1964 The quantitative analysis of drugs, In: Champman and Hall, Japan.1; 3: 456 – 458
8. Hemmani T and Parihar MS 1998 Reactive oxygen species and oxidative DNA damage. *Ind. J. Physiol. Pharmacol*; 42: 440–444.
9. Jayakumar K, VGM Krishnan and K Murugan, 2016a Evaluation of antioxidant and antihemolytic activities of purified caulophyllumine-A from *Solanum mauritianum. J Pharmacogn. Phytochem* ; 5(2) :195-199.
10. Jayakumar K, S S Sumayya and K Murugan. 2016b Evaluation of mitigating effect of purified solasodine from *Solanum mauritianum* against hydrogen peroxide induced oxidative damage in human erythrocytes. *Inter J Appl Biol Pharma Tech*; 2: 1-9
11. Joseph Sakah Kaunda and Ying-Jun Zhang, 2019 The Genus *Solanum*: An Ethnopharmacological, Phytochemical and Biological Properties Review. *Nat Prod Bioprospect*., 9(2): 77–137.
12. Kalita S, G Kumar, L Karthik and K V Rao. 2012 *In vitro* antioxidant and DNA damage inhibition activity of aqueous extract of *Lantana camara* (Verbenaceae) leaves. *Asian Pac J Trop Biomed*; 2(3): 1675-1679
13. Kannan M, B. Dheeba S. Gurudevi and A.J A Ranjit Singh 2012 Phytochemical, antibacterial and antioxidant studies on medicinal plant *Solanum torvum J Pharma Res* ; 5(5): 2418-2421
14. Nathan C.1992 Nitric oxide as a secretory product of mammalian cells. *FASEB J*, 6:305 - 3064.
15. Nishimiki M, N A Rao and K Yagi, 2002 The antioxidant activity, reducing power, superoxide anion radical scavenging. *J Ethnopharm*; 79: 325–332.
16. Shen SC, W R Lee, H Y Lin, H C Huang, Ch Ko and L L Yang 2002 *In vitro* and *in vivo* inhibitory activities of rutin, wogonin, and quercetin on lipopolysaccharide - induced nitric oxide and prostaglandin E(2) production. *Eur J Pharmacol*,; 446 :187-194.
17. Singh R P, K N Chidambara Murthy and G K Jayaprakash, 2002 Studies on antioxidant activity of pomegranate peel and seed extracts using in vitro models. *J Agric Food Chem*; 50: 86-89
18. Thenmozhi, A. and U S Mahadeva Rao 2012 Comparative free radical scavenging potentials of different parts of *Solanum torvum. Free Rad. Antioxid*; 2: 24–29.
19. Usha V and M Suriyavathana 2012 Free radical scavenging activity of ethanolic extracts of *Desmodium gangeticum J Acute Med* ; 2 : 36-42

■

.

Government of Maharashtra **Ismail Yusuf College**
of Arts, Science and Commerce Jogeshwari (East), Mumbai -60.

(35)

Journal of Molecular Structure 1240 (2021) 130593

Contents lists available at ScienceDirect

Journal of Molecular Structure

journal homepage: www.elsevier.com/locate/molstr

Contemporary studies on growth and characterization of Magnesium doped γ-glycine – A potential optoelectronic NLO material

K. Premlatha[a], N.R. Rajagopalan[b], P. Krishnamoorthy[a,*]

[a] Department of Chemistry, Dr.Ambedkar Government Arts College,Chennai600039, Tamil Nadu, India
[b] Department of Chemistry, St.Joseph's College of Engineering, Chennai600 119, Tamil Nadu, India

ARTICLE INFO

Article history:
Received 22 February 2021
Revised 12 April 2021
Accepted 27 April 2021
Available online 6 May 2021

Keywords:
SHG efficiency
UV studies
LDT
NLO
Etching
Vicker's test

ABSTRACT

The optical quality magnesium doped γ-glycine single crystal has been grown by slow evaporation method. The grown crystal was identified as $P3_1$ space group based on single crystal X-ray diffraction analysis. The obtained unit cell dimensions a = 7.05 Å, b =7.05 Å, c =5.51Å and $\alpha = \beta = 90^{o}$ and $\gamma = 120^{o}$ showed that the crystal is hexagonal. The transmittance of the crystal is measured and the UV cut off wavelength was found to be 340 nm and band gap of the crystal is found to be 3.5hν. The various functional groups associated with the grown single crystal have been characterized by FT-IR studies, measured in the range from 450–4000 cm^{-1}. The hardness number and Mayer index value calculated using Microhardness studies established the good mechanical strength of the grown crystal. Simple harmonic generation studies showed that the crystal is having NLO nature. To get the knowledge of crystal surface morphology, SEM studies were carried out. The decomposition temperature of the crystal was identified using TG-DSC studies which indicated that the crystal is thermally stable up to 492.5°C. The laser damage threshold (LDT) studies also supported the suitability of the crystal towards non linear optical applications. Etching studies indicated the minimal dislocations in the crystal growth mechanism. The present study clearly shows that the grown crystal is having potential applications in NLO-optoelectronic devices.

1. Introduction

In the ever expanding frontier area of non linear optics, the various non linear optical (NLO) materials of organic, inorganic, semi-organic single crystal with their unique properties, such as giant intrinsic charge carrier mobility, record thermal conductivity, super stiffness and excellent light transmission have been the point of attraction and interest of researchers [1-3]. A variety of crystals with suitable size and perfection were required for integrated circuits materials and have been synthesized and reported in literature [4,5].

In recent years, there is a tremendous growth of amino acid based semi-organic single crystal owing to their potential applications in optoelectronic devices through their wide transparency windows, desirable thermal stability, high laser damage threshold, simplified procedures of fabrication process and device integration easy fabrications and integrating into devices [6-9]. Glycine is the best amino acid which exhibit the promising physical and chemical properties related to ideal applications [10]. γ-glycine is the best alternative for KDP crystal which shows typical and significant NLO and intrinsic property [11-13].

Recent researches coordinate with the semi - organic non linear optical materials which are used to develop the low power laser driven non linear optical system [14-15]. The amino acid γ-glycine is the best raw material to grow the semi-organic crystal [16]. Glycine based various semi-organic crystals such as glycine doped potassium thiourea chloride [17], L-tartaric acid crystals doped with glycine [18], glycine zinc chloride [19], Ni^{2+} doped glycine sodium sulphate [20], glycine doped ammonium dihydrogen phosphate [21] have been reported in the literature. In this context, the current work mainly focuses on the growth and characterisation of Magnesium doped glycine (MGG) towards its NLO applications, by means of X-ray diffraction analysis, Vicker's micro hardness studies, optical properties, Infra red spectral analysis, SEM –EDAX, Second harmonic generation investigation, NMR, and TG-DSC analysis.

2. Materials and methods

Pure chemicals with analytical grade have been chosen and all studies were carried out at room temperature. MGG single crystal is synthesized by slow evaporation technique. The glycine and

* Corresponding author.
E-mail address: krishthiresearch1@gmail.com (P. Krishnamoorthy).

https://doi.org/10.1016/j.molstruc.2021.130593
0022-2860/

ISSN 0974-3618 (Print)
0974-360X (Online)
www.rjptonline.org

RESEARCH ARTICLE

Evaluation of Cytotoxicity of normal Vero and Anticancer Activity of Human Breast Cancer Cell Lines by Aqueous Unripe Fruit Extract of *Solanum torvum*

D. Shanthi, R. Saravanan
Post Graduate and Research Department of Zoology, Dr Ambedkar Government Arts College, Vyasarpadi, Chennai 600039, Tamil Nadu.
*Corresponding Author E-mail: **rsaravanan51283@yahoo.com**

ABSTRACT:
In the present study aqueous extract of *Solanum torvum* unripe fruits was used to evaluate its cytotoxic effect and anticancer activity through *in vitro* studies by 3-(4, 5 dimethyl thiazole-2-yl)-2, 5-diphenyl tetrazolium bromide-MTT assay) on Normal VERO cell line and MCF-7 (Human breast adenocarcinoma cell line). Aqueous extracts of *Solanum torvum* unripe fruits was found to be effective in the prevention of cell proliferation by breast adenocarcinoma cell lines at 1000 µg/ml from the results obtained during 24 hours of incubation.

KEYWORDS: Unripe fruits of *Solanum torvum,* Normal VERO cell line, MCF-7 (Human breast adenocarcinoma cell line), MTT assay.

INTRODUCTION:

Medicinal plants occupy an important position for being the paramount sources of drug discovery in the modern era. The medicinal value of these plants lies in bioactive substances called phytochemicals that produce a definite physiological action of human body. According to World Health Organization (WHO) medicinal plants would be the best source to obtain a variety of drugs. The use of plant extracts and phytochemicals with known antimicrobial properties can be of great significances in therapeutic treatment[1].

Cancer is still a growing health problem world-wide characterized by the irregular proliferation of the cells, as a cell progresses from normal to cancerous tissue, the biological imperative to survive and perpetuate drives fundamental changes in cells behaviour[2]. Cancer risk can be reduced by avoidance of exposure to harmful biological, chemical and physical agents, in addition to the habitual consumption of cancer protective foods.

Breast cancer is generally treated in recent days by radiotherapy, hormonal or chemotherapy. In most of the case, the patients experience adverse side effects from the therapy. Intensive radio or chemotherapeutical agents usually results in nausea and failure of bone marrow function[3]. Cancer cells are resistant to action of chemical drugs[4].

Bioassay and animal studies indicates that many phytochemicals in the plants are potential antioxidants and possess anticancer properties[5]. In this scenario, secondary metabolites from herbals may be the best remedy and alternative for curing cancer[6]

Solanum torvum (*S.torvum)* have revealed cytotoxic activities, antimicrobial, anti-viral activity, anti-inflammatory, anti-tumour (anticancer) activity[7,8]. Anticancer phenolic compounds have also been isolated from leaves and seeds of this plant[9]. Extracts of the aerial parts of *S.torvum* was found to be extremely effective in the prevention of cell proliferation of the mammary gland breast adenocarcinoma cell lines[10].

The fruit of *S.torvum* is edible and nutritive, It is commonly known as Sundaikai in Tamil. We have chosen to study the cytotoxic and anticancer properties of the unripe fruit in the present study. Normal VERO cell line was used to evaluate its cytotoxic effect. Breast

Received on 10.04.2020 Modified on 13.07.2020
Accepted on 28.09.2020
Research J. Pharm. and Tech. 2021; 14(7):3504-3508.
DOI: 10.52711/0974-360X.2021.00607

cancer line (MCF7- Human breast adenocarcinoma cells) was used in the study to find out the anticancer activity.

MATERIALS AND METHODS:

Collection and Identification of Plant Material:

Unripe fruits of *Solanum torvum* used for the study were collected from in and around Kancheepuram District, Tamil Nadu. Fresh plant specimen collected was authenticated by Dr. P. Jayaraman, Director, Plant Anatomy Research Center, Tambaram, Chennai. Registration No. (PARC/2018/3855).

Processing and Preservation of Plant Materials:

The plants were freshly collected, the leaves and fruits were separated from the stem. Fruits were washed with running tap water and rinsed in distilled water. The fruits were chopped into small pieces and were shade dried for two weeks for complete dryness. The dried fruits were powdered, using mechanical grinder. They were ground well to fine powder and then transferred into airtight containers until further use.

Preparation of Aqueous Extract: Cold Water Extraction:

5gm of the dried unripe fruit powder samples was soaked and dissolved in 50ml of distilled water in a 250 ml conical flask. The flask was plugged with cotton wool and aluminium foil and was placed in a shaker for 24 hrs. The filtrate was concentrated in a Soxhlet apparatus to get the crude extract. The extract was filtered using Whatman filter paper No 1. The filtered extracts in the form of concentrated paste were used for the study.

Obtaining Cell lines, its sub culture and maintenance:

Normal VERO cell line and Cancer cell line type MCF-7 (Human breast adenocarcinoma cells) were obtained from National Centre for Cell Sciences (NCCS), Pune. The cell lines procured were maintained at Life Teck Research Centre, Arumbakkam, Chennai, Tamil Nadu

The cells were maintained in Minimal Essential Media (MEM) and was supplemented with 10 % Foetal Bovine Serum (FBS), Penicillin (100U/ml) and Streptomycin (100µg/ml) in a humidified atmosphere of 5% CO_2 at 37^0C.

Cell viability and Antiproliferative studies:

***In vitro* studies:** Cytotoxicity analysis of Normal Vero cell line and Anticancer activity of the aqueous unripe fruit extracts of *Solanum torvum* on MCF-7 (Breast cancer cell line) was performed based on the principle of MTT assay.[11]

Preparation of two-fold serial dilutions of the leaf extracts for cytotoxicity and anticancer analysis:

Weighed extracts of *Solanum torvum* unripe fruits were separately dissolved in distilled dimethyl sulfoxide (DMSO) and the volume was made up with Dulbecco's modified eagle medium (DMEM) supplemented with 2% inactivated FBS to obtain a stock solution of 1 mg/ml^{-1} concentration and sterilized by filtration.

Incubation of Vero and MCF7 cell lines:

Cells (1×10^5/well) were plated in 24-well plates and incubated in 37^0C with 5% CO_2 condition. After the cell reaches the confluence, the prepared extract was added and incubated for 24 hrs. After incubation, the sample was removed from the well and washed with phosphate-buffered saline (pH 7.4) 100µl/well without serum. 5 mg/ml of 0.5% MTT was added and incubated for 4 hours. After incubation, 1ml of DMSO was added in all the wells. The absorbance at 570nm was measured with UV- spectrophotometer using DMSO as blank in triplicates. The average absorbance of the triplicates are represented in the table. Measurements were performed and the concentration required for a 50% inhibition (IC_{50}) was determined.

The % cell viability was calculated using the following formula:

% Cell viability = A570 of treated cells/A570 of control cells × 100

Morphological studies of the cells:

The unripe fruit aqueous extract treated cell lines (Normal Vero and MCF7) were observed and photographed under inverted animal cell culture microscope (Labovert-FS) under 10 x objective.

RESULTS:

Cytotoxicity of aqueous unripe fruit extract of *Solanum torvum* on normal Vero cell line:

The maximum cell viability of 86.75% was observed in 7.8µg/ml of plant extract at 24 hrs. The minimum cell viability of 51.42% was observed in 1000 µg/ml concentration of plant extract at 24 hrs. The IC_{50} was recorded at 1000µg/ml at 24hrs (Table 1; Fig 1).

Table 1: Cytotoxicity of aqueous unripe fruit extract of *Solanum torvum* on normal Vero cell line

Concentration (µg/ml)	Absorbance (Average O.D of three replicates)	Cell viability (%)
1000	0.559	**51.42**
500	0.600	55.19
250	0.664	61.08
125	0.719	66.14
62.5	0.787	72.40
31.2	0.843	77.55
15.6	0.891	81.96
7.8	0.943	86.75
Cell control	1.087	100

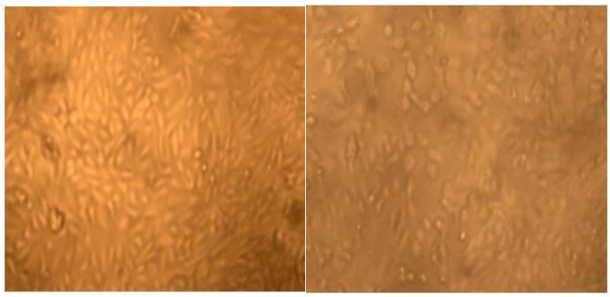

a. Control cells **b. 1000 µg/ml**

a. Control cells (Vero cell line) without extract treated
b. Vero cell line treated with extract and appearance of cells at 1000 µg/ml (IC_{50})

Fig 1: Morphology of Normal Vero cell line treated with aqueous unripe fruit extract of *Solanum torvum* at 24 hours of incubation

Anticancer activity of aqueous unripe fruit extract of *Solanum torvum* on MCF7 human breast cancer cell line:

The maximum cell viability of 74.26% was observed in 7.8µg/ml of fruit extract at 24 hrs. The minimum cell viability of 25.38% was observed in 1000µg/ml concentration of fruit extract at 24 hrs. The IC_{50} was reported in 62.5µg/ml at 24 hrs. (Table 2; Fig 2).

Table 2: Anticancer activity of aqueous unripe fruit extract of *Solanum torvum* on MCF7 human breast cancer cell line

Concentration (µg/ml)	Absorbance (Average O.D of three replicates)	Cell viability (%)
1000	0.216	25.38
500	0.269	31.60
250	0.335	39.36
125	0.399	46.88
62.5	0.458	**53.81**
31.2	0.521	61.22
15.6	0.585	68.74
7.8	0.632	74.26
Cell control	0.851	100

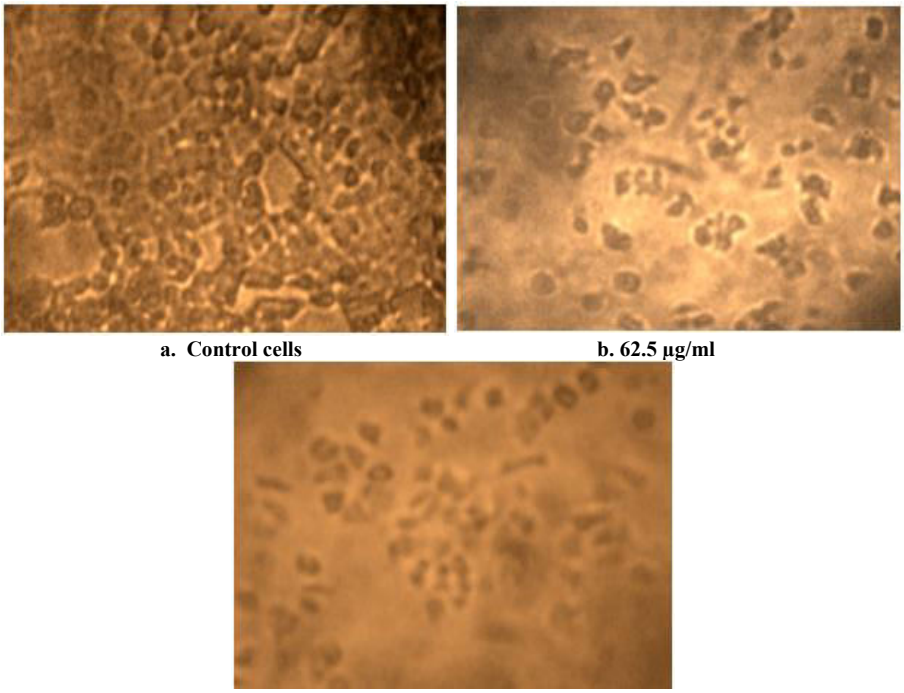

a. Control cells **b. 62.5 µg/ml**

c. 1000 µg/ml

Fig 2 : Morphology of MCF 7 cancer cell line treated with aqueous unripe fruit extract of *Solanum torvum* at 24 hours of incubation

a. Control cells (MCF7cell line) without extract treatment
b. MCF7 cell line treatment with extract and appearance of cells at 62.5 µg/ml (IC_{50})
c. MCF7 cell line treatment with extract and appearance of cells at 1000 µg/ml with minimal cell viability

DISCUSSION:

Phytochemicals are increasingly used in treatment of cancer because of their availability and potential anti-cancer activity when compared with chemotherapy[12,13,14].

The cytotoxicity analysis of aqueous extract of *S. torvum* unripe fruit on Vero cell line revealed that the extract is devoid of toxic effect, while the extracts were effective in reducing the cell viability of MCF-7 cell line in the present study at 1000µg/ml. The cytotoxic action indicates that they probably contain secondary metabolites or novel compounds that may inhibit cellular division[15,16]. A number of species of the genus *Solanum* have been shown to contain steroidal glycoalkaloids and steroidal saponins with significant cytotoxic and antitumour activities[17].

Thus the cytotoxic and anticancer activity of *S. torvum* can be attributed to steroidal alkaloids and steroidal saponins substances present in unripe fruit extracts in the present study. Similar results were observed in cancer cells treated with ethanolic leaf extract and ethanolic fruit extract of *Solanum paniculatum*[18].

Morphological changes are a consequence of characteristic, molecular and biochemical change occurring in cancer cells[19]. The control Vero cells and MCF7 cells without extract treatment did not show any morphological changes, whereas a monolayer cell destruction was observed in both cell lines treated with the extracts. The polygonal cells shows shrinkage. The increase in cell shrinkage is in a dose-dependent manner which can be attributed to the growth inhibitory effect of the aqueous extract of *Solanum. torvum* unripe fruit[20].

The extract if tested or administered in human may prevent cell proliferation by directly combining with cell receptors or enzymes and by initiating cell arrest or cell apoptosis. Plant derived chemicals coupled with chemotherapy has gained much importance now-a-days in alleviating the proliferation of various carcinomas with less side effects[21]

Earlier reports on various cell lines are in support with the present study. The apoptotic activity of *Kydia calycina* methanolic leaf extract was evaluated for ROS generation and caspase-3 activity on different cell lines. The results showed that the extract has significantly increased the ROS production and caspase-3 levels in the cell cultures in a dose dependent manner[22]. Methanolic extract of *Ficus racemosa* show cytotoxic activity against HL-60 and HepG2 cell line with profound IC50 values and shown negligible toxicity against normal cell line HEK-293T[23.] Anticancer activity of *Maytenus emarginata* leaves and stems: were assessed by using antimitotic activity by *Allium cepa* method, seed germination assay by green gram seeds and brine shrimp lethality test using Artemia salina eggs showed cytotoxic effects of the extracts studied[24]. *In vitro* anticancer activity of ethanolic and ethyl acetoacetate extracts of sweet cherry, *Prunus avium* was evaluated. against human breast cancer cell line MCF-7 by MTT assay. The bioactive molecules exhibited potential capability to inhibit the cancer cell when compared with standard drug doxorubicin and expression of cell growth inhibition[25].

Many natural products from marine sources are also endowed with promising anti-cancer activity, thus representing invaluable leads in the plans for drug discovery[26]. It also reported that bioactive compounds have been isolated from *Moringa oleifera* and used extensively for treatment of cancer[27]. Ethyl acetate leaf extract of *Azima tetracantha* has been shown to have pronounced anticancer potential against MCF-7 cell lines while compared to that of the stem extract[28]. Petroleum ether and chloroform extracts of *Barleria gibsoni* leaves showed significant ant proliferative effects against MDA MB 4355 (Human breast cancer) by SRB assay method due to presence of phytoconstituents present in the plant[29]. Anticancer activity of *Maytenus emarginata* on Ehrlich's Ascites Carcinoma treated mice proved to have an effect in cancer cells[30].

The treatment or chemotherapy given for cancer patient is costly so the treatment should be non-toxic and economic. India is having an unexplored data of hidden treasure of medicinal plants. There are anticancer medicinal plants abundantly present in India. Bioactive constituents can be isolated and patented[31]. The potential uses of large number of herbal drugs are limited due to their poor absorption and poor bioavailability after oral administration. Phytosome technology has been effectively used to enhance the bioavailability of many popular herbal extracts including milk thistle, ginkgo biloba, grape seed, green tea, hawthorn and ginseng can be developed for various therapeutic uses or dietary suppliments[32,33]. Similar method of phytosome technology can be adopted to deliver the bioactive constituents present in the unripe fruit of *Solanum torvum* used in the present study since this fruit is nutritive and edible in nature.

CONCLUSION:

Herbals are natural store house of phytochemicals with immense therapeutic quality. Proper understanding of synergistic interactions of various constituents of anticancer herbs, would help in formulating and designing drug to attack the cancerous cells without harming the normal cells of the body.

ACKNOWLEDGEMENT:

The authors are grateful to Tamil Nadu State Council for Higher Education, Chennai for the grant of financial assistance under Minor Research Project Scheme. We thank Dr. (Mrs). I. Seethalakshmi, Director, Life Teck Research Centre, Arumbakkam**,** Chennai for the laboratory assistance rendered in procurement and maintenance of cell lines.

CONFLICT OF INTEREST:

None declared.

REFERENCES:

1. Yomgam Yumge, Rohita Sharma, Om Prakash Arya, Yumbi Yomgam Phytochemical screening and antifungal activities of three medicinal plants from Arunachal Pradesh, Indian Journal of Medicinal Plants Studies. 2017; 5(3): 278-283
2. Dai X, Cheng H, Bai Z, Li J. Breast cancer cell line classification and its relevance with breast tumor subtyping. Journal of Cancer.

2017; 8(16): 3131-3141
3. Neves MP, Cravo S, Lima RT, Vasconcelos MH, Nascimento MS, Silva AM. Solid-phase synthesis of 21-hydroxychalcones. Effects on cell growth inhibition, cell cycle and apoptosis of human tumor cell lines. Bioorganic Medicinal Chemistry; 2012; 20: 25-33.
4. Mahassni SH, Al-Reemi RM. Apoptosis and necrosis of human breast cancer cells by an aqueous extract of garden cress (*Lepidium sativum*) seeds. Saudi Journal of Biological Science. 2013; 20(2)**:** 131-139.
5. Jayakumar K, Murugan K Purified solasodine and caulophyllumine: A from *Solanum mauritianum.* against MCF-7 breast cancer cell lines in terms of cell growth, cell cycle and apoptosis. Research Journal of Pharmacognosy and Phytochemistry. 2017a; 6(1)**:** 472-478
6. Solowey E, Lichtenstein M, Sallon S, Paavilainen H, Solowey E, Lorberboum-Galski H. Evaluating medicinal plants for anticancer activity. Science World Journal. 2014; 1-12.
7. Arthan D, Svasti J, Kittakoop P, Pittayakhachonwut D, Tanticharoen M, Thebtaranonth Y Antiviral isoflavonoid sulfate and steroidal glycosides from the fruits of *Solanum torvum.* Phytochemistry. 2002; 59: 459–463
8. Wiart C, Mogana S, Khalifah S, Mahan M, Ismail S. Buckle M. Antimicrobial screening of plants used for traditional medicine in the state of Perak, Peninsular Malaysia. Fitoterapia. 2004 ;**75**: 68–73
9. Amarnath Kanchana, Monvalli Balakrishnan. Anti-cancer effect of saponins isolated from *Solanum trilobatum* leaf extract and induction of apoptosis in human larynx cancer cell lines. International Journal of Pharmacy and Pharmaceutical Sciences. 2011; l3 (4): 65-71
10. Jaikumar B, Jasmine R. A review on a few medicinal plants possessing anticancer activity against human breast cancer. International Journal of Pharmacy and Technology Research. 2016; 9(3): 333-365.
11. Mosmann T. Rapid colorimetric assay for cellular growth and survival: Application to proliferation and cytotoxicity assays. Journal of Immunology and Metabolism. 1983; 65: 55-63.
12. Mohammad Mijanur Rahman, Md. Asaduzzamam Khan. Anticancer potential of South Asian plants. Natural Products and Bioprospecting. 2013; 3: 74-88
13. Biswas J, Roy M, Mukherjee a Anticancer drug development based on phytochemicals. Journal of Drug Discovery. Development and Delivery. 2015; 2(1) :1-6.
14. Amutha. R, Ramesh. K, Sudha. A, Rathika. S, Pandiselvi. P. Preclinical assessment of *Solanum trilobatum* leaf extracts as DNA damaging anticancer agent in the management of breast cancer. International Journal of Latest Engineering, Management and Research. 2017; 2 (9): 23-27
15. Panigrahi, Meenakshi Sundaram Muthuraman, Ravichandran Natesan, Brindha Pemiah 2014 Anticancer activity of ethanolic extract of *Solanum torvum* (SW). International Journal of Pharmacy and Pharmaceutical Sciences. 2014; 6(1): 93-98
16. Maya Nair, S Kamala Soren, Virendra Singh, Bibari Boro Anticancer activity of fruit and leaf extracts of *Averrhoa bilimbi* on MCF-7 human breast cancer cell lines: A Preliminary Study. Australian Journal of Pharmacotheraphy. 2016; 4(2): 76-84
17. Joseph Sakah Kaunda**,** Ying-Jun Zhang, The genus *Solanum*: An Ethnopharmacological, Phytochemical and Biological Properties Review. Natural Products and Bioprospecting**.** 2019; 9(2): 77–137.
18. Vieira PM, Santos SC, Chen Chen L. Assessment of mutagenicity and cytotoxicity of *Solanum paniculatum* L extracts using *in vivo* micronucleus test in mice. Brazilian Journal of Biology.2010; 70(3): 601-606
19. Arulvasu C, Vasanth Supriya S, Gajendra Babu. Anticancer activity of *Pongamia glabra* V seed extract against selected human cancer cell lines. International Research Journal of Pharmacy. 2012; 3(8): 131-134
20. Dehghan-Nayeri N, Darvishi M, Mashati P, Younesian O. Comparison of cytotoxic activity of herbal extracts on the most commonly used breast cancer cell lines (MCF7 and SKBR3): A systematic review. Journal of Research in Pharmacy.2020; 24(1): 1-22.
21. Jumpa-Ngern P, Kietinun S, Sakpakdeejaroen I, Cheomung A and Na-Bangchang K. Pharmacokinetics of piperine following single dose administration of benjakul formulation in healthy Thai subjects. African Journal of Pharmacy and Pharmacognosy.2013; 7(10): 560-566
22. Baburao Bhukya, Harikiran Lingabathula, Narsimhareddy Yellu. Evaluation of Anti Cancer Activity of *Kydia calycina* Roxb. Leaf Extract on Different Cancer Cell Lines. Research. Journal of. Pharmacognosy and Phytochemistry. 2017; 9(4): 197-202.
23. Prakash S. Sukhramani, G. Vidyasagar, Piyush M. Patel. In-vitro screening of *Ficus racemosa* for Anticancer activity. Research Journal Pharmacognosy and Phytochemistry. 2013; 5(3): 119-122.
24. 24.P Nagaveni, G Krishna Mohan, Switi B Gaikwad. Anticancer Activity of *Maytenus emarginata* Leaves and Stems: A Comparative Study. Research Journal. Pharmacognosy and Phytochemistry. 2015; 7(2): 101-106.
25. 25.M Lavanya, Asish Bhaumik, A Gopi Reddy, Ch Manasa, B Kalyani, S Sushmitha. Evaluation of Anticancer Activity of Ethanolic and Ethylacetoacetate Extracts of Sweet Cherry Against Human Breast Cancer Cell Line MCF-7. Research Journal Pharmacology and Pharmacodynamics.2016; 8(2): 65-70
26. 26.Nachiket S Dighe, Shashikant R Pattan, Deepak S Musmade, Abhijeet N Merekar, Manisha S Kedar, Deepak K Thakur, Pratik V Patel. Recent Synthesis of Marine Natural Products with Anticancer Activity: An Overview. Research Journal Science and Technology. 2009; 1(2): 63-70.
27. Qureshi Md. Shamim, Patel Jitendra, Venkateshwar Reddy A, Syed Safiullah, P Mohapatra. Phytochemicals and Pharmacological Activities of *Moringa oleifera* Lam. Research J. Pharmacology and Pharmacodynamics. 2010; 2(2): 183-186.
28. B. Edwin Jose, P. Muralidharan. Effect of *Azima tetracantha* Lam on Human Breast Cancer Cells MCF-7. Research Journal Science and Technology. 2019; 11(2): 109-112.
29. Firoj A. Tambolia, Harinath N. Inhibitory Effects of Successive Solvant Extracts of *Barleria gibsoni* Dalz. on the Proliferation of MDA MB 4355 (Human Breast Cancer) and Hep G2 (Liver Cancer Cell line). Asian Journal of Pharmaceutical Research. 5(4): 2015; 183-185.
30. 30.Salla Pujitha, A. Jaswanth, A. Ganesh, Irfana Begum, Noor Jahan. Evaluation of Anticancer activity of *Maytenus emarginata* on Ehrlich's Ascites Carcinoma treated mice. Asian Journal of Research in Pharmaceutical Sciences. 2018; 8(3): 133-136.
31. 31.Chandrasekar. R, Sivagami. B, M. Niranjan Babu. A Pharmacoeconomic Focus on Medicinal Plants with Anticancer Activity. Research. Journal of. Pharmacognosy and Phytochemistry. 2018; 10(1): 91-100.
32. Patel Chirag J., Satyanand Tyagi, Patel Pinkesh, Alpesh Yadav. Phytosomes: A Current Trend for Enhancement of Bioavailability of Polar Phytoconstituents Research. Journal of. Pharmaceutical. Dosage Forms. and Technology. 6(1): Jan.-Mar. 2014; Page 44-49.
33. K. Selvaraju, K.S.G. Arulkumaran, K. Karthick, K. Vengadesh Prabhu, J. Padma Preetha, R. Arrivukkarasu. Phytosomes – An Advanced Herbal Technology. Research Journal of. Pharmacognosy and Phytochemistry 2011; 3(5): 191-194

UTTAR PRADESH JOURNAL OF ZOOLOGY

42(1): 6-11, 2021
ISSN: 0256-971X (P)

CRUSTACEAN TAXONOMY- A SOLUTION FOR CONSERVING ITS BIODIVERSITY IN INDIA

H. SRUTHI[1*] AND N. THIRUNAVUKKARASU[1]

[1]Department of Zoology, Dr. Ambedkar Government Arts College (Autonomous), Chennai-39, India.

AUTHORS' CONTRIBUTIONS

This work was carried out in collaboration between both authors. Author HS designed and searched literature for completing this article and author NT helped in correction of this article.

Article Information

Editor(s):
(1) Dr. Villagomez Cortes Jose Alfredo Santiago, Professor, University of Veracruz, Mexico.
Reviewers:
(1) Ivan Pandourski, Institute of Biodiversity and Ecosystem Research, Bulgaria.
(2) Artur Chahud, University of São Paulo, Brazil.
(3) Farhana Shafiq Ghory, University of Karachi, Pakistan.

Received: 02 November 2020
Accepted: 07 January 2021
Published: 04 February 2021

Review Article

ABSTRACT

Crustaceans play major role in ecological enhancement and improvement in economic value of Indian fisheries. Due to over exploitation and constant demand, various species of crustaceans in wild had gradually decreased from 1996 to 2016 all around India which lead to great ecological imbalance. According to IUCN Red Data List 2019 about 27% of selected crustaceans are in threatened category globally whereas in India about 1.54% of crustaceans are in threatened category and about 37.5% of crustacean data are deficient. Out of 17.5% of global endemic crustacean species about 5.9% of endemic crustaceans are found in India but the worst scenario is the population of these species too has deteriorated due to over exploitation. This will lead to enormous loss to biodiversity by not finding any clue about unexplored extinct species. At this juncture, taxonomy plays key role in assessment of species in the wild and employs in assisting conservative programs for documenting biodiversity. It also provides checklist for in-situ conservation of those species which in turn help in elevating the economic development of crustacean fisheries. It will also help in creating awareness on the alarming condition of biodiversity loss. This article explains the exact scenario of crustacean population in India and highlights the role of taxonomy in its conservation.

Keywords: Biodiversity; crustaceans; taxonomy; in-situ conservation.

1. INTRODUCTION

India is one of the 17 world's biodiversity rich countries harboring variety of flora and fauna. India's unique geography makes it a potential biodiversity hotspot in the world. Aquatic biodiversity of India is again one of the most peculiar and dynamic biome making it a suitable habitat for variety of organisms. Still, about 91% of species in the ocean are awaited for description [1]. Globally, India

**Corresponding author: Email: shruthisai.shruthi@gmail.com;*

International Journal of Ecology and Environmental Sciences
www.ecologyjournal.in
Online ISSN: 2664-7133, Print ISSN: 2664-7125
Received: 02-06-2021, Accepted: 17-06-2021, Published: 02-07-2021
Volume 3, Issue 3, 2021, Page No. 01-04

An investigation on microbial quality of salted and Sun dried fishes from Pulicat lake fishermen villages

Vijayananth S[1], B Venkatarathanam[1], C Sheeba Anitha Nesakumari[2], R Muthezhilan[3], Thirunavukkarasu N[4*]
[1] Department of Advanced Zoology and Biotechnology Dr. Ambedkar Government Arts College (Autonomous), Vyasarpadi, Chennai, Tamil Nadu, India
[2] Department of Zoology, Madras Christian College Autonomous, Tambaram, Chennai, Tamil Nadu, India
[3] Department of Marine Biotechnology, AMET University, Chennai, Tamil Nadu, India
[4] Associate NCC Officer, Faculty of Zoology, Dr Ambedkar Government Arts College (Autonomous), Vyasarpadi, Chennai, Tamil Nadu, India

Abstract
The present study has executed to investigate the microbial quality of the salted and sundried fishes around the Pulicat dry fish market. There were four varieties chosen for this study. The varieties of dry fishes were anchovy (*Stolephorous commersonni*), sardine (*Sardinella longiceps*), mackerel (*Rostrelliger kanagurta*) and silver bellies (*Leiognathus* sp.). The bacterial and fungal infestation was found in the dried fishes. The bacterial strains were total heterotrophic bacteria, *Escherichia coli, Vibrio cholera, V. parahaemolyticus, Salmonella* sp., and *Shigella sp.* The maximum total heterotrophic bacterial count was observed in fish silver bellies (5.2×10^4) followed by anchovy (4.8×10^4), mackeral (4.1×10^4) and sardine (3.9×10^4) respectively. Whereas checking the *Escherichia coli* load on the maximum was observed in mackeral (33) followed by anchovy (27), silver bellies (26) and sardine (21) respectively. The fungal infestations were *Aspergillus* sp., *Mucor* sp., *Fusarium* sp., *Penicillium* sp. and *Verticilium* sp. This study revealed that, the quality of processed dried fishes were found with microbiological infestation of different contaminants. Such products should be properly cooked before consumption. Consumers should be continuously sensitized to raise awareness of the existence of such microbes in order to encourage adequate cooking of fish prior to consumption.

Keywords: microbial contamination, sundried fishes, salted fishes, Pulicat Lake

Introduction

Human have been eating sea food since the beginning of recorded history. Fish was the most reliable protein food. Dried fish have relatively low contribution both in terms and quality and value in price. Most of the fishes among by catch are dried in the sun after salting. Although it is a common practice to salt the fish before drying certain varieties of *Anchoviella* are dried without salting. Highly salted fish retards microbial growth. For low salt product halophilic or holotolorent populations consisting of gram negative organism will prevail. Pathogen growth in the finished product as a result of inadequate drying of fishery products can cause consumer illness. Dried products are usually considered shelf stable and are, therefore, often stored and distributed unrefrigerated (Nair, 2003) [4]. Water is the measure of the amount of water in a food that is available for the growth of microorganisms, including pathogens. A water activity of 0.85 or below will prevent the growth and toxin production of pathogens, including *Staphylococcus aureus* and *Clostridium botulinum*.
Poor hygiene condition is because they dry fish are placed on mat, sandy substratum or hung in raised rack/ pole. During handling fish gets contaminated with various types of bacteria if the time temperature condition favours organism grows and multiply and lead to spoilage. Human health on consumption of such fish is dangerous and it can lead to food poisoning and problem to public health. Hygiene and sanitation, therefore plays a vital role in fish handling. In this perspectives the study has planned to isolate and enumerate the bacteria and fungi from four commercially important fishes *viz*, anchovy (*Stolephorous commersonni*), sardine (*Sardinella longiceps*), mackerel (*Rostrelliger kanagurta*) and silver bellies (*Leiognathus* sp.).

Materials and methods

Four dry fish samples were taken for this present study. The dry fishes were sardine (*Sardinella longiceps*) (Fig.1), mackerel (*Rostrelliger kanagurta*) (Fig.2), anchovy (*Stolephorous commersonni*) (Fig.3) and silver bellies (*Leiognathus* sp) (Fig.4).

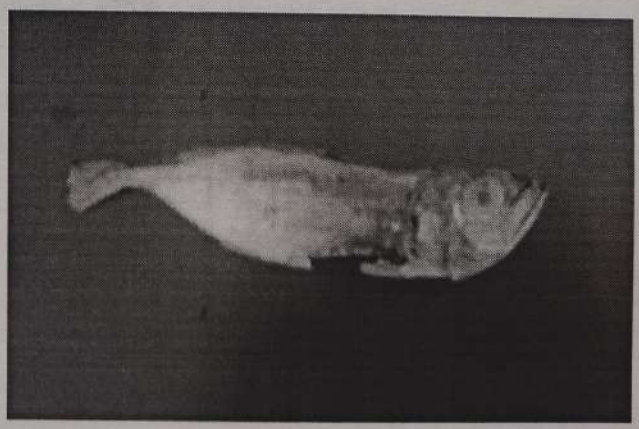

Fig 1: Sample A (*Sardinella longiceps*)

International Journal of Ecology and Environmental Sciences
www.ecologyjournal.in
Online ISSN: 2664-7133, Print ISSN: 2664-7125
Received: 29-05-2021, Accepted: 11-06-2021, Published: 29-06-2021
Volume 3, Issue 2, 2021, Page No. 266-270

Production and characterization of glucosamine hydrochloride from crustacean shell wastes

R Sumithraa[1], T Vijaykumar[1], C Sheeba Anitha Nesakumari[2], R Muthezhilan[3], Thirunavukkarasu N[4*]
[1] Department of Advanced Zoology and Biotechnology, Dr. Ambedkar Government Arts College (Autonomous), Vyasarpadi, Chennai, Tamil Nadu, India
[2] Department of Zoology, Madras Christian College (Autonomous), Tambaram, Chennai, Tamil Nadu, India
[3] Department of Marine Biotechnology, AMET University, Chennai, Tamil Nadu, India
[4] Department of Advanced Zoology and Biotechnology, Dr. Ambedkar Government Arts College (Autonomous), Vyasarpadi, Chennai, Tamil Nadu, India

Abstract
The bycatch resources of crustaceans were taken from Royapuram Fish Landing Centre, Kasimedu, Chennai. The stomatopod - *Harpiosquilla gonyptes* and shrimps - *Panapenaeopsis maxillipedo* and *Penaeus indicus* were collected and chitin was extracted from the shells of the crustacean samples. The chitin further used for the production of glucasomaine hydrochloride. The glucasoamine hydrochloride was derived from the chitin by acid hydrolysis. The samples were confirmed through FT-IR spectrum against standard glucosamine hydrochloride. The stomatopod *H. gonyptes* shows the peaks at 3676 cm^{-1}, 3404cm^{-1}, 2848 cm^{-1}, 1629 cm^{-1} and 1012 cm^{-1}. The *P. maxillipedo* shows the peaks at 3712 cm^{-1}, 3408 cm^{-1}, 2370 cm^{-1}, 1629 cm^{-1}, 1095 cm^{-1} and 1033 cm^{-1}. Whereas the peaks through FT-IR of the shrimp *P. indicus* shows 3676 cm^{-1}, 3404 cm^{-1}, 2372 cm^{-1}, 1641 cm^{-1} and 1186 cm^{-1}. In the present study the intense bands were observed 3400 cm^{-1} (*H. gonyptes*), 3408 cm^{-1} (*P. maxillipedo*) and 3404 cm^{-1} (*P. indicus*) which reveals that association of O-H and N-H stretching. The peaks at 1629 cm^{-1} (*H. gonyptes*), 1629 cm^{-1} (*P. maxillipedo*) and 1641 cm^{-1} (*P indicus*) which reveals that association of NH_2. Whereas the peaks at 1012 cm^{-1} (*H. gonyptes*), 1095 cm^{-1} & 1033 cm^{-1} (*P. maxillipedo*) and 1186 cm^{-1} (*P. indicus*) which reveals that association of secondary alcohol -OH. All the above peaks levels were confirm that samples were glucosamine hydrochloride. The present study was found as simple, efficient and suitable for the preparation of glucasoamine from crustacean shells thereby recycling crustacean wastes.

Keywords: crustacean shell waste, chitin, glucosamine hydrochloride

Introduction

The major economically important group of crustaceans include lobster, shrimps, and crabs about 40-50 % of total weight of crustaceans goes as waste while processing for human food and the slower degradation of crustacean shell waste has become the major concern in sea food processing industries. Proper use of crustacean wastes allows recovery of value added by products which are having potential applications in the field of food and medicine (Santos *et al.*, 2012; Khor and Lim, 2003; Cira *et al.*, 2002; Healy *et al.*, 1994; Acosta *et al.*, 1993) [9, 4, 2, 3, 1]. Glucosamine has been prepared from various crustaceans. Glucosamine is an amino monosaccharide acting as a preferred substrate for the constitution of glycosaminoglycan chains. Glucosamine has anti-Cancer (Jung *et al.*, 2012; Oh *et al.*, 2007) [5, 8]. Anti-inflammatory (Nagaoka *et al.*, 2011) [7] and antibacterial (Kim, 2011) [6] effects. Glucosamine and its derivative like N-acetylglucosamine (GlcNAc) and D-glucosamine hydrochloride (GlcNHCl) have attracted much attention owing to their therapeutic activity in arthritis and been approved as a food supplement by FDA. Glucosamine is a poly-hydroxylatedprimary amine, used in the body as a molecular element for special macromolecules, the proteoglycans, and important constituents of the articular cartilage. Glucosamine hydrochloride, Glucosamine sulphate and N-acetylglucosamine are the commonly used glucosamine derivatives.

System line, which contains glucosamine, is promoted for use among young athletes. Elation, another fruit-flavoured beverage containing glucosamine, is produced by Coca-Cola and Procter & Gamble. Glucosamine hydrochloride can be considered as a nutraceutical by virtue of its properties. As a pharmaceutical product its preparation has only begun now in India. A number of products have been launched in the Indian market with glucosamine hydrochloride and glucosamine sulphate as the major ingredient. Glucosamine is a highly valued commercial product and hence the details of its production technology and its chemical properties are not widely available in literature. In this context it is felt that the technologies for the production of glucosamine hydrochloride in the purest form with maximum yield and least investment will help the industry significantly.
Adverse effects of glucosamine by any route are minimal with gastrointestinal symptoms, drowsiness, headache, and skin rash being reported. Although no known interactions exist between glucosamine and foods or other herbal supplements, there are two well-documented interactions between glucosamine and antidiabetic and cancer chemotherapy drugs. Glucosamine might increase insulin resistance or decrease insulin production resulting in elevated blood glucose levels. This increase in blood glucose may require increases in administered insulin and/or hypoglycemic agents such as sulfonylureas and metformin.

Nutritional Quality Evaluation of Mud Crab *Scylla tranquebarica* (Fabricius, 1798)

N. Thirunavukkarasu[1*], K. Maheshkumar[2] and A. Shanmugam[3]

[1]Department of Advanced Zoology and Biotechnology, Dr. Ambedkar Government Arts College (Autonomous), Vyasarpadi, Chennai-600 039, Tamilnadu, India

[2]Department of Advanced Zoology and Biotechnology, Government Arts College for Men (Autonomous), Nandanam, Chennai – 600 025, Tamilnadu, India

[3]Centre of Advanced Study in Marine Biology, Faculty in Marine Sciences, Annamalai University, Parangipettai-608 502, Tamilnadu, India

ABSTRACT : Fish demand in recent years has been growing not only because of the increasing needs of the growing population especially from developing countries, as a nutritious and functional food. In this present study focused on investigate the meat content variation, proximate analysis of mud crab *Scylla tranquebarica* along with aminoacids, fattyacids, vitamins and minerals. In the nutritional evaluation the meat content yield in male (18.21 – 28.65%) and female (18.45 – 25.92%). The carbohydrate content in the body ranged from 0.59 to 2.23%, claw (0.68-2.87%), legs (0.76-2.76%), hepatopancreas (1.40-1.71%) and ovary (2.27- 3.47%). The protein content in the body (65.48-72.24%), claw (69.5-80.29%), legs (69.47-74.7%), hepatopancreas (71.06-75.92%) and ovary (73.21-82.11%). Total aminoacid content in the meat of *S. tranquebarica* was 46.352AA%. The Arginine (7.925AA%) and Leucine (3.356AA%) were in higher values and Methionine (1.738%) was lower among the essential aminoacids. Whereas in the nonessential aminoacids the percentage contribution was 21.68%. The glutamic acid (8.098AA%) and Aspartic acid (4.243AA%) were in higher values and serine (1.879AA%) was lower in the nonessential aminoacids. The proline, cystine, asparagine, glutamine and tryptophan were not detected. The lipid content in the body (1.6-2.09%), claw (1.83-2.06%), legs (1.58-2.08%), hepatopancreas (1.58-2.09%) and ovary (1.98-2.43%). The fatty acids composition showed quantitative differences in the individual acids. Total fatty acids accounted to 49.84% total saturated fatty acids (SFA), followed by Mono unsaturated fatty acids (MUFA) and polyunsaturated fattyacid (PUFA) by 40.34% and 9.81% respectively. The moisture content in the body (73.5-81.8%), claw (73.5-80.16%), legs (73.23-79.6%), hepatopancreas (57.33-67.5%) and ovary (58.6-62.3%). The ash content in the body (2.46-3.53%), claw (2.53-3.91%), legs (2.98-4.33%), hepatopancreas (2.67-4.82%) and ovary (3.8-4.15%). The result shows the vitamin C in higher values of 425.05MG followed by vitamin B_1 (21.285MG) and vitamin B_6 (18.03MG). The niacinamide (0.6213MG) and vitamin B_{12} (0.085MG) were trace in level. The vitamin A and vitamin E detected 1450IU and 10.51IU. respectively. The minerals of iron present in the higher values (154.2mg) among the other minerals followed by phosphorus (15.80mg) and calcium (1.367mg). The remainings are presented a little amount. The calorific values in the body (1.310-1.447 kcal/g), claw (1.396-1.584kcal/g)), legs (1.401-1.480kcal/g)), hepatopancreas (1.422-1.525kcal/g) and ovary (1.472-1.670kcal/g).

Keywords: *Mud crab, Scylla, Nutrition, Proximate composition, Vitamins, Minerals*

*Corrosponding author E-mail: marinethiru@gmail.com

Development of Mud Crab Culture Technology and its Economics Profile

N. Thirunavukkarasu[1*], S. Vijayananth[2] and P. Desingu[3]

[1]Department of Advanced Zoology and Biotechnology, Dr.Ambedkar Government Arts College (Autonomous), Vyasarpadi, Chennai-600 039.

[2]Department of Biochemistry, Chennai National Arts and Science College, Avadi, Chennai – 600 054.

[3]The Marine Products Export Development Authority (MPEDA), Thanjavur.

ABSTRACT : Mud Crab, *Scylla spp* occur throughout tropical zones where they form the basis of small but important inshore fisheries. Their size, high meat yield, delicacy and flavor, mud crabs are sought after as a quality food item. As they are easily caught using very simple traps or nets, remain alive for considerable periods after capture. Ponds selected in Madalapattu of Cuddalore District at Uppanar creeks for crab culture. Earthen ponds of 0.5ha with sandy clay bottom were used. The ponds were provided with net fencing along the inner side of the bunds to prevent theescape of crabs. Salinity (6-35 ppt), temperature (22-27°C), pH (8.1-9.6) and dissolved oxygen (5.5-8.9mg/l) were noted in the culture pond and the required water exchange and liming were given. BOD between 4.3 to 8.9 mg/l and the COD between 10.1 to 36.4 mg/l were noted. Phosphorus value varied during study of period was 0.29 to 2.80 mg and the nitrogen value was 1.58 to 5.80 mg. Water depth of 0.5 to 1.0m was maintained in the pond. The stocking density is about 1 no. / sq.m. Stocking has to be done by proper acclimatization procedures. Hide outs were provided in the pond bottom for reducing cannibalism and improving survival. Trash fish chopped into small pieces were provided as feed daily in two rations of 40% (morning) and 60% (evening). The daily ration is adjusted according to the biomass in the pond from an initial level of 8% during the first month to about 4% during the fifth month. Selective harvesting required to remove the harvestable size in several times during the culture period. This also allow smaller crab to grow faster thus helping to shorten the culture duration. This type of harvest was done with lift net or scoop net. Complete harvest can be done by the end of 120 – 150 days by lift net/scoop net and hand picking after draining the pond. The details of economic and cost estimates for crab grow-out culture was carried out in 0.5 ha pond. The capital expenses including bund maintenance, net fencing, cost of check trays, hideouts etc. was estimated at Rs.32,450/-. While the operational expenses were estimated Rs.3,16,430/- the stocking density of 1no./sq.m and a survival of 60% a production of about 1,800 kg estimated, yielding an estimated sale value realization of Rs.4,36,500/-.

Keywords: *Mud crab, Scylla, Culture, Economics*

*Corresponding author: E-mail: marinethiru@gmail.com